Ultrafast Electron Diffraction

Volume One

Thesis By

Hyotcherl Ihee

In Partial Fulfillment of the Requirements for the Degree of
Doctor of Philosophy

California Institute of Technology
Pasadena, California
2001

(Submitted April 30, 2001)

ACKNOWLEDGMENT

This thesis represents the combined efforts of many people. First and foremost is Prof. Ahmed Zewail, my advisor, whose scientific insight, encouragement, enthusiasm, support, guidance, and energy have carried me through my graduate career here at Caltech. I vividly remember the first day I met him. Although my English was so poor at that time, which later led him to confess that he could not understand much of what I was saying, he saw through me without any prejudice and gave me the golden opportunity to work on my PhD project in ultrafast electron diffraction (UED) lab. Especially I greatly appreciate his patience and trust in my ability to do good science. Without him, the completion of my PhD would not have been possible.

I have been very fortunate to work with many talented postdoctoral fellows and students. I have learned from interactions with my colleagues not only scientifically but also personally and culturally. I thank the first and second generation UED people; Chuck Williamson, Hans Frey, Stefen Preuss, and Jianming Cao. Chuck taught me the basics of electron diffraction and Hans and Chuck helped me to build an interest in machining. I really enjoyed working with Jianming Cao days and nights. I also thank the third generation UED people; Vladimir Lobastov, Udo Gomez, Ramesh Srinivasan, Boyd Goodson, Chong-Yu Ruan, and Jon Feenstra. Vladimir and Gomez always encouraged me to look at scientific problems in different perspectives. Ramesh and Boyd always tried to help me in many ways. I feel that my English has improved greatly since I met Boyd. He helped me correct my many kinds of manuscripts. I

always enjoyed having discussions with Ruan. Special thanks to Jon for proofreading my thesis. All UED people have been good friends at all times.

I am also grateful to my other former and present colleagues. Although they were not directly involved in my project, interactions with them always gave me motivation and encouragement. These include Spencer Baskin, Chaozhi Wan, Dongping Zhong, Sang Kyu Kim, Carsten Kötting, Eric Diau, Hern Paik, Theis Solling, Joseph Casanova, Shouzhong Zou, Hans-Christian Becker, Samir Pal, Xiaogang Qu, Nam Joon Kim, Hotae Kim, Robert Clegg, Zee Kim, Marianas Chachisvillis, Torsten Fiebig, Klaus Møller, Marcos Motzkus, Sing Chong, Søren Pedersen, Jennifer Herek, Qianli Liu, Ahmed Heikel, Osama Abou-Zied, Thorsten Bernhardt, Steven De Feyter, and Brent Horn.

I would like to thank the committee members; Professors Ahmed Zewail, Mitchio Okumura, Brian Stoltz, Doug Rees, Vincent Mckoy, and John Richards for their encouragement and friendship. I also thank Prof. Bill Goddard and Jeremy Kua for having invited me into the world of quantum calculations.

Words would be never enough to thank my family for their unconditional love, support, and encouragement. I would like to thank also all my friends for their friendship and support. Finally all thanks to Him who created me and loves me forever.

Financial support for this research was made through the National Science Foundation, the Air Force Office of Scientific Research, and the Office of Naval Research.

ABSTRACT

Molecular dynamics is now routinely studied on femtosecond time scales using various spectroscopies. However, direct structural information of all nuclear coordinates involved in such dynamical processes requires resolution in time by x-ray or electron diffraction. The focus of this laboratory has been the development of ultrafast electron diffraction (UED) for recording structures in motion, which exploits the six-orders-of-magnitude higher scattering cross section of electrons compared with x-rays. Conventional electron diffraction has been developed over the last several decades to become an enormously powerful technique for determining the static structures of molecules in the gas phase; the subsequent implementation of pulsed electron sources has added a temporal dimension to such studies. In UED, a femtosecond (fs) laser pulse is used to initiate a reaction, but unlike other ultrafast spectroscopies, the subsequent laser pulses normally used to probe the progress of the reaction are replaced with ultrashort pulses of electrons. Time-resolved diffraction patterns are then recorded at fixed time delays relative to the zero-of-time. This directly reflects the changing internuclear distances in the species under study.

For these UED studies, there exist a number of significant experimental challenges, including: (i) the problem of independently determining the temporal overlap (zero-of-time) of the pump and probe pulses *in situ* for clocking the change; (ii) the problem of low electron flux required to minimize space-charge induced temporal broadening of electron pulses; and (iii) the problem of low scattering and sensitivity caused by the absence of long-range order present in solids, and the low

density of molecules in gases. These challenges to the realization of UED have been surmounted over the last decade, and UED now approaches the combined spatial and temporal resolution necessary for tracking all nuclear coordinates during the making and breaking of chemical bonds, thereby permitting the direct observation of molecular structural dynamics in real time. In addition, the diffraction-difference method—which employs the subtraction of a reference diffraction signal from the signals recorded over the course of the reaction—can be used to select the contributions resulting only from changes in structure in the species under study, thereby enhancing the sensitivity of UED to chemical change. Contributions only from the products can be also isolated by adding the appropriately scaled parent diffraction signal at negative time to the difference curves, thus canceling out the parent contribution in each curve.

The first reaction studied by UED was the dissociation of CH_2I_2 into CH_2I and I with fs laser pulses. The second-generation apparatus allowed us to see the amplitude change in the scattering intensity on the picosecond time scale resulting from dissociation. Since this work, UED experiments have successfully investigated the course of several prototypical chemical reactions. For example, the molecular structures and branching ratios of the final products were determined in the dissociation of $Fe(CO)_5$ upon two-photon excitation at 310 nm. A simple intermediate, CF_2, was generated by fragmentation of CF_2I_2 and its molecular structure was precisely determined and compared with other experiments and theoretical calculations. Furthermore, the molecular structure of the transient $Fe(CO)_4$ species

was elucidated and compared with available theoretical predictions, permitting identification of the specific electronic energy state of the intermediate and the primary reaction pathway. UED was applied to another organometallic compound, namely $(C_5H_5)Co(CO)_2$ and the molecular structures of the intermediate and final products were observed. A preliminary analysis showed that either C_5H_5 and other species can be selectively generated depending on the excitation wavelength. Further analysis will elucidate their molecular structures. The elimination of iodine from 1,2-diiodotetrafluoroethane ($C_2F_4I_2$) was also studied with the second-generation apparatus, providing early results which suggested that the molecular structure of the C_2F_4I radical intermediate is not bridged in nature, but instead is "classical," resembling the structure of the parent species.

The need for greater sensitivity and resolution, as well as the desire to study more complex reactions, led to the development of our third-generation UED apparatus. This new machine, with vast improvements in pulsed electron flux, repetition rate, detection sensitivity, and experimental stability, permits the direct imaging of complex chemical reactions with unprecedented spatial and temporal resolution. The spatial and temporal resolution of UED approached ~0.01 Å and ~1 ps, respectively, and we were sensitive to ~1% changes in the mole fractions of the various chemical species over the course of the reaction. In its first application, the non-concerted elimination of iodine from a haloethane ($C_2F_4I_2$) was re-visited and the molecular structure of the transient C_2F_4I radical was determined for the first time. Two prototypical cyclic hydrocarbons, 1,3,5-cycloheptatriene (CHT) and 1,3-

cyclohexadiene (CHD), were also studied with temporal and spatial resolution of ~5 ps and ~0.04 Å respectively. At high internal energies of ~4 eV, these molecules displayed markedly different behavior. For CHT, wherein excitation resulted in the reformation of the parent, the observed diffraction change was explained with an equipartitioned model of hot structures—indicating rapid energy redistribution (within a few picoseconds). For CHD, photo-induced ring opening was shown to result in hot but highly non-equilibrium structures even up to 400 ps, with energy trapped in large-amplitude motions comprised of torsion and asymmetric stretching. These studies promise a new direction of research for studying transient structural changes both in equilibrium and non-equilibrium complex systems. The results presented here provide the new limit of improved detection sensitivity, versatility, and resolution of UED, as well as the potential for its diverse applications. The extension to even more complex systems, a process that has already begun in our laboratory, represents our next challenge in UED.

COLLABORATIONS AND REFERENCES

Williamson, J. C.; Cao, J.; Ihee, H.; Frey, H.; Zewail, A. H.
"Clocking transient chemical changes by ultrafast electron diffraction"
Nature **1997**, *386*, 159-162.

Ihee, H.; Cao, J.; Zewail, A. H.
"Ultrafast electron diffraction: structures in dissociation dynamics of $Fe(CO)_5$"
Chem. Phys. Lett. **1997**, *281*, 10-19.

Cao, J.; Ihee, H.; Zewail, A. H.
"Ultrafast electron diffraction: determination of radical structure with picosecond time resolution"
Chem. Phys. Lett. **1998**, *290*, 1-8.

Cao, J.; Ihee, H.; Zewail, A. H.
"Ultrafast electron diffraction and direct observation of transient structures in a chemical reaction"
Proc. Natl. Acad. Sci. **1999**, *96*, 338-342

Ihee, H.; Zewail, A. H.; Goddard, W. A., III.
"Conformations and Barriers of Haloethyl Radicals (CH_2XCH_2, X = F, Cl, Br, I): Ab Initio Studies"
J. Phys. Chem. A **1999**, *103*, 6638-6649.

Ihee, H.; Lobastov, V. A.; Gomez, U. M.; Goodson, B. M.; Srinivasan, R.; Ruan, C.-Y.; Zewail, A. H.
"Direct Imaging of Transient Molecular Structures with Ultrafast Diffraction"
Science **2001**, *291*, 458-462.

Ihee, H.; Kua, J.; Goddard, W. A., III.; Zewail, A. H.
"CF_2XCF_2X and CF_2XCF_2 radicals (X = Cl, Br, I): Ab Initio Studies and Comparison with Experiments"
J. Phys. Chem. A, 2001, *105*, 3623-3632.

Ihee, H.; Cao, J.; Zewail, A. H.
"Ultrafast electron diffraction of transient $Fe(CO)_4$: Determination of molecular structure and reaction pathway"
Angew. Chem., Int. Ed. Engl. **2001**, 40, 1532-1536.

Ruan, C.-Y.; Lobastov, V. A.; Srinivasan, R.; Goodson, B. M.; Ihee, H.; Zewail, A. H.
"Ultrafast diffraction and structural dynamics – The nature of complex molecules far from equilibrium"
Proc. Natl. Acad. Sci. **2001**, in press.

TABLE OF CONTENTS

Volume One

Volume Two

CHAPTER ONE

ULTRAFAST ELECTRON DIFFRACTION

1.1 Studying Chemical Reactions In Real Time

Molecules respond to photons in various ways, such as scattering and absorption. If the energy of the photon matches the difference in the energy between two states of a molecule, the molecule can absorb the photon and undergoes a transition from the initial state to the final state. The excited molecule may have many different fates; it can remain in the excited state for some time, it can dissociate into various fragments, it can isomerize into other conformers, it can convert into other spin state through intersystem crossing, or it can fall back into the original ground state with or without accompanying radiation. The goal of many physical chemists is to discern the fate and follow the dynamics of the photo-excited molecule, which necessarily involves the identification of reaction channels and the measurement of the reaction rate. The time scales of the reaction rate depend on the nature of the reaction and spans several orders of magnitude from femtoseconds to days. For example, most fundamental processes such as bond-breaking and bond-making takes usually sub-picosecond while the whole process of protein-folding may take days.

1.1.1 Pump-Probe Experiments

One of the most natural ways to monitor time-dependent processes is to pump the molecule with a photon (which defines the reaction time zero) and to probe the behavior of the excited molecule in time-resolved manner. This basic scheme, so called pump-probe has been very powerful over the last decades. Following ultrafast processes such as bond-breaking and bond-making and catching short-lived

intermediate species necessitate probing tools with time scales comparable to those such ultrafast events. Progress has been made in obtaining such ultrashort optical pulses reaching the atomic-scale time resolution of picoseconds (ps) and femtoseconds (fs).[1-6] In the typical experimental scheme of femtosecond spectroscopy, a femtosecond laser pulse elevates the molecules to an excited state in a coherent manner, creating a wave packet. The transient behavior of the wave packet is subsequently probed by additional sequentially delayed fs laser pulses, thereby providing insight into the dynamics of the reaction by sampling its progress in real time.

1.1.2 Problems With Optical Probes

In traditional pump-probe experiments, the probing methodology encompasses a variety of techniques, including laser-induced fluorescence, transient absorption, and multiphoton ionization. The excited molecules or fragments in a certain energy state can be excited with the probe pulse into upper states. If the upper states fluoresce, then the magnitude of this laser-induced fluorescence can be monitored with time. If the energy state does not fluoresce or the fluorescence yield is too small to detect, this method cannot be used. The magnitude of the absorption transition also can be monitored. However, it is not unusual that many different species simultaneously have absorption at the same wavelength and the transient signal often is mixture of multiple species. Multiphoton ionization has the advantage over other techniques in that any species can in principle be ionized and monitored with time. However, the common

problem with detecting ion signals is multiple sources for the particular ions.

Although these optical probing methods have been extremely powerful in elucidating the ultrafast dynamics of various reactions, they have two intrinsic problems; they are unable to give molecular structural information and they provide information relevant to only a few selected trajectories or reaction channels.

Inability to provide structural information With femtosecond temporal resolution, it is possible to observe the coherent motion of a vibrational wave packet on the excited potential energy surface. Since the molecular structure is closely related with the energy structure of the molecule, in principle, this observed motion can be transformed to give the trajectories of all nuclei involved in the reaction—if the potential energy surface is known. However, detailed potential energy surfaces are often difficult to obtain, and conventional femtosecond spectroscopies do not, in general, supply a complete picture of the molecular structures involved in a given reaction. For example, the relationship between the energy structure and the molecular structure is so direct in diatomic molecules that a traditional femtosecond spectroscopy can reveal the molecular structure of such simple diatomics. The relationship gets more obscure for bigger molecules and the detailed structural information such as bond lengths and angles are impossible to directly measure with conventional optical tools.

Bright only to a subspace The traditional probing methodologies such as laser-induced fluorescence, multiphoton ionization, and transient absorption necessarily involve the interaction of the optical probing pulses and the species of interest. The most common interaction is the optical transition, which can be bright only to selected subspaces rather than the whole phase space. Therefore, the signal may not provide the whole picture but only a subset of all the reaction trajectories and channels. There exist other optical probing methods such as intense-field dissociative ionization and coulomb explosion which are in principle not supposed to depend on particular optical resonances. However, these techniques have a potential risk of perturbing the reaction too much and the interpretation of the transient signal is not straightforward. In addition these methods depend on the ionization cross section and are influenced by the ion fragmentation.

1.1.3 Solution: Diffraction As The Probe

Direct information regarding static molecular structures can be routinely obtained by diffraction methods. The elastic scattering of x-rays or electrons or neutrons from molecules (or crystals) produces interference patterns that depend on relevant structural parameters, such as internuclear separations and mean amplitudes of vibration. It should be also noted that the scattering process is in general bright to the whole phase space, thereby ensuring that the complete picture can be obtained rather than a few selected pathways. In summary, the diffraction methods can provide solutions to the problems associated with using the optical pulses as probing tools.

Thus, the combination of diffraction techniques with femtosecond pump-probe spectroscopy can provide the spatiotemporal resolution necessary for tracking all nuclear coordinates over the course of chemical reactions, thereby permitting the direct observation of the structural dynamics of molecules.[7]

1.2 Comparisons Of Diffraction And Spectroscopies As Probes

Diffraction methods and spectroscopic tools as probes can be compared in the following areas: information content, cross section, and selectivity.

1.2.1 Information Content

The transient signals obtained by monitoring the magnitude of the laser-induced fluorescence, absorption at particular wavelength, and photo-generated ions typically give the information about the population change of particular species associated with the transient signals. As described in **1.1.2**, molecular structural informations generally cannot be extracted from these transient signals. In contrast, the diffraction pattern contains not only the populations of the species but also detailed structural informations such as bond-lengths and angles. Also diffraction signals provide informations about all the species in the interaction region while the optical signal usually conveys informations about only one or a few species. In other words, a diffraction signal is composed of the contributions from the complete trajectories of all present species (whole phase space) whereas the optical signal is contributed only from a subset of the whole phase space.

1.2.2 Cross Section

The elastic scattering cross sections of electrons, x-rays, and neutrons depend on the atomic number. The scattering cross section of neutrons is most sensitive to the change of the atomic number. The scattering cross sections of electrons and x-rays

depend also on the wavelength of the scattering particles whereas that of neutrons does not. The magnitudes of the scattering cross sections increase in the order of neutrons (~10^{-24} cm^2), x-rays (~10^{-23} cm^2), and electrons (~10^{-17} cm^2). The absorption cross sections (~10^{-18} cm^2) and ionization cross sections depend on the molecule and the optical wavelength. A simple comparison of the cross section may give the impression that the scattering particles should have better sensitivities than the optical tools. However, the ionization or absorption methods generally have better signal-to-noise ratio than the scattering methods due to the following reasons. First, optically generated signals such as an absorption signal and photo-induced ions can convey complete information (*e.g.*, population of the species) with only one event, while multiple events are necessary to convey complete information (molecular structures and populations) in diffraction signal. Second, unlike most optical transition signals, a diffraction signal contains significant background mostly coming from atomic scattering. Third, as explained in greater detail in **1.2.3**, the scattering particles cannot discriminate between different species in the molecular beam, resulting in the signal being overwhelmed by a majority of unreacted parent molecules whereas optical signals can be tuned to yield results originating only from reactants.

1.2.3 Selectivity and sensitivity

Optical transitions by nature are more selective than the scattering process. Generally, it is possible to tune the wavelength of the laser light so that a particular species of interest can be probed. In contrast, the scattering particles diffract every

species present in the interaction region. As explained in **1.2.2**, the high selectivity of the optical methods plays an important role in improving the signal-to-noise ratio and sensitivity to certain species compared to the diffraction method. However, in the case that many reaction pathways co-exist, the absolute branching-ratio is hard to obtain unless the probing cross section is known. On the other hand, since the diffraction signal contains contributions from every species, the absolute branching ratio can be easily obtained. Although the errors get bigger for minor channels and it might be impossible to pick up extremely minor channels, the diffraction signal guarantees that the major channels are observed.

1.3 Time-Resolved Electron Diffraction

1.3.1 Ultrafast Electron Diffraction

The focus of this laboratory has been the development of ultrafast electron diffraction (UED)[8-15] for recording structures in motion, which exploits the six-orders-of-magnitude higher scattering cross section of electrons compared with x-rays. Conventional electron diffraction has been developed over the last several decades to become an enormously powerful technique for determining the static structures of molecules in the gas phase[16,17]; the subsequent implementation of pulsed electron sources has added a temporal dimension to such studies.[18-20] As with ultrafast spectroscopic methods,[3-5] UED utilizes a femtosecond (fs) laser pulse to initiate a chemical reaction; however, instead of using additional laser pulses to probe the reaction's progress, UED employs ultrashort pulses of electrons. Time-resolved diffraction patterns are then recorded at fixed time delays which directly reflect the changing internuclear distances in the species under study.

The advantages of UED are two-fold. First of all, it can yield the molecular structures of short-lived intermediates or unusual species such as radicals.[11,12,15] Second, temporal behavior of these transient structures can be followed.[11-13,15]

1.3.2 Electron Diffraction On Unstable Species

Actually, conventional electron diffraction was sometimes utilized for the study of unstable species like radicals, but just for a few special cases. Ultrafast electron diffraction is an ideal tool for generating unstable species and studying their

molecular structures.[11-13,15] In the past, there were some efforts to study structures of unstable molecules such as free radicals by electron diffraction.[21-31] Some special organic free radicals such as Di-t-butyl-nitroxide[32] and 2,2,6,6-tetramethyl-4-piperidone-1-oxyl[29] are stabilized by steric interactions or electron delocalization and can be synthesized and stored for a long time. Therefore, the study of these special radicals can be done following the usual procedure of gas electron diffraction. For the usual radicals which can not be stored and synthesized, thermal decomposition was the approach utilized by other researchers. The specific radical of interest was obtained by heating the appropriate parent molecules. For example, triphenylmethyl radical was generated from hexaphenylethane, difluoroamino radical (NF_2) from tetrafluorohydrazine (N_2F_4),[23] Indenyl radical (C_9H_7) from diindenylcobalt ($Co(C_9H_7)_2$),[25] Allyl radical from 1,5-hexadiene.[30] Although this method was quite effective for a few specific cases, in general mixtures involving numerous species of unknown composition are generated.[26-28] For example, Kohl and coworkers used the thermal decomposition of $BrCCl_3$ and CBr_4 in attempts to study the structures of CCl_3 and CBr_2 radicals, respectively, by using a sophisticated oven for thermal decomposition.[26,28] However, the specific radical of interest is contaminated by too many other species produced by the thermal decomposition. For the case of the thermal decomposition of CBr_4, a mixture containing singlet CBr_2, triplet CBr_2, CBr_3, CBr_4, C_2Br_6, Br_2 can be produced,[28] and for $BrCCl_3$, the thermal decomposition generated mixtures of not only CCl_3 radical but also other potential species such as $BrCCl_2$, C_2Cl_6, BrCl and Br_2.[26] This is why there exist only several unstable species

that have been studied by thermolosys. The major problem with thermolysis is its lack of control over the possible product. In this respect, laser photolysis can be an optimal means for generating desired species. While the thermal decomposition suffers the possibility of various thermal reactions in the sample reservoir, laser pulse is a clean tool that can be used for the collision-free molecular beam. In addition, its wavelength, phase, and intensity can be tuned to generate only desired species.

1.3.3 Time-Resolved Electron Diffraction

Several groups have employed time-resolved electron diffraction to investigate the structural aspects of short-lived chemical systems. In the early experiments as an attempt to test the possibility of such technique, Ischenko *et al.* studied the structure of photofragmented species using 1 μs electron pulses made with an electromagnetic chopper.[33] They used infrared multiphoton dissociation of CF_3I molecules to obtain CF_3 radicals and showed qualitative evidence of molecular scattering intensity changes due to photofragmentation. Rood and Milledge combined electron diffraction with flash photolysis to reveal the geometries of excited molecules and radicals in the photodecomposition of ClO_2 and photolysis of biacetyl.[34] Diffraction patterns were recorded with a 0.5 ms electron pulse created from an electromagnetic chopper. They claimed that the theoretical curve from a mixture of candidate photo-products approached the experimental curve, but existence of a ClO radical could not be unambiguously determined. Bartell and coworkers have shown that the phase transition in molecular clusters can be studied with electron diffraction.[20] For

example, 10 nm clusters of CCl_4 were generated from a pulsed nozzle source with neon carrier gas, and a set of diffraction patterns, over a range of flight times of clusters after their formation, was obtained. With this experimental scheme, they showed the structural change of the clusters on the microsecond time scale. Ewbank *et al.* improved the temporal resolution of electron diffraction to the nanosecond regime by utilizing a laser-initiated electron pulse and a linear diode array detector.[35,36] In their experimental setup, two synchronized excimer lasers generated optical and electron beams. Their studies on the laser-decomposition of CS_2 and photoisomerization of 1,2-dichloroethenes are supported by theoretical calculations concerning the composition and energetics of photoproducts.

1.3.4 Recent Advancements: UED

While the above studies hinted at the possibility of using diffraction to study chemical dynamics, it was still not possible to directly investigate fundamental events such as bond breakage, bond formation, and intramolecular vibrational energy redistribution, which normally take place on the ps to fs time scales. In order to dramatically improve the temporal resolution of pulsed electron diffraction, in 1991 Zewail and coworkers proposed that a femtosecond laser system could be incorporated with electron diffraction to obtain, in a general way, the precise evolution of atomic coordinates on the fs time scale in a manner analogous to the pump-probe techniques commonly practiced in femtosecond spectroscopy.[8] However, realizing this concept is non-trivial; in order for time-resolved, pulsed electron diffraction to be feasible for

studying the ultrafast structural dynamics in gas-phase chemical reactions, a number of significant experimental challenges must first be addressed. These include: 1) the low electron flux required to minimize space-charge induced temporal broadening of electron pulses resulting from Coulombic repulsion of negatively-charged electrons; 2) the need for independently determining the temporal overlap of the pump (light) and probe (electron) pulses within the sample in order to clock the initiation of the chemical reaction; 3) the low scattering and sensitivity due to the absence of long-range order present in solids; 4) the low density of molecules in gases; and 5) the rapid rise in complexity of theoretical models used to interpret the scattering data as the number of atoms involved in the reaction increases.

In addition to these difficulties, the mismatch in velocities between the pump laser (traveling at the speed of light) and the probe electrons (traveling at ~1/3 the speed of light at 30 keV) broadens the overall time resolution of diffraction experiments.[37] Since the speeds of the pump laser pulse and the probe electron pulse are very different, molecules in different regions of the interaction volume experience different time delays. Due to this velocity mismatch, a smaller interaction volume of laser, electron, and molecular beams is preferred. This effect has already been considered in our experimental setup.[35,36] Thus, the space-charge effect and velocity mismatch together conspire to constrain the practical temporal resolution of our UED experiment to the picosecond rather than the femtosecond regime.

Our efforts to address these difficulties began with the first-generation UED apparatus, with which it was demonstrated that electron diffraction patterns could be

recorded with picosecond temporal resolution. The lessons learned from the first-generation machine guided the design of our second-generation apparatus, which allowed us to see the amplitude change in the scattering intensity on the picosecond time scale resulting from dissociation of CH_2I_2 with fs laser pulses.[10] Since this work, UED experiments have successfully investigated the course of several prototypical chemical reactions. For example, the molecular structures and branching ratios of the final products were determined in the dissociation of $Fe(CO)_5$ upon two-photon excitation at 310 nm.[11] A simple intermediate, CF_2, was generated by fragmentation of CF_2I_2 and its molecular structure was precisely determined and compared with other experiments and theoretical calculations.[12] Furthermore, the molecular structure of the transient $Fe(CO)_4$ species was elucidated by UED and compared with available theoretical predictions, permitting identification of the specific electronic energy state of the intermediate and the primary reaction pathway.[14] The elimination of iodine from 1,2-diiodotetrafluoroethane ($C_2F_4I_2$) was also studied with the second-generation apparatus, providing early results which suggested that the molecular structure of the C_2F_4I radical intermediate is not bridged in nature, but instead is "classical," resembling the structure of the parent species.[13] Although the data permitted the course of the reaction to be followed, and suggested the nature of the intermediate structure given two possible models, the signal–to–noise ratio and resolution was not yet sufficient to elucidate the molecular structures involved.

The need for greater sensitivity and resolution, as well as the desire to study more complex reactions, led to the development of our third-generation UED

apparatus.[15] This new machine, with vast improvements in pulsed electron flux, repetition rate, detection sensitivity, and experimental stability, permits the direct imaging of complex chemical reactions with unprecedented spatial and temporal resolution. In its first application,[15] the capabilities of the new apparatus were demonstrated in the study of two prototypical reactions: the non-concerted elimination of iodine from a haloethane ($C_2F_4I_2$), and the electrocyclic ring opening of 1,3-cyclohexadiene, a hydrocarbon with no heavy atoms. In the $C_2F_4I_2$ experiments, the spatial and temporal resolution of UED approached ~0.01 Å and ~1 ps, respectively, and we were sensitive to ~1% changes in the mole fractions of the various chemical species over the course of the reaction. Moreover, the molecular structure of the transient C_2F_4I radical was determined for the first time.

UED also provides a novel method for studying structural phenomena in molecules at high internal energy. Studies of molecular structures at or near their equilibrium configurations have long provided information on their geometry in terms of bond distances and angles. However, far-from-equilibrium structures are relatively unknown—especially for complex systems—and generally, neither their dynamics nor their average geometries can be extrapolated from equilibrium values. Two prototypical cyclic hydrocarbons, 1,3,5-cycloheptatriene (CHT) and 1,3-cyclohexadiene (CHD), were studied with temporal and spatial resolution of ~5 ps and ~0.04 Å respectively. At high internal energies of ~4 eV, these molecules displayed markedly different behavior. For CHT, wherein excitation resulted in the reformation of the parent, the observed diffraction change was explained with an equipartitioned

model of hot structures—indicating rapid energy redistribution (within a few picoseconds). For CHD, photo-induced ring opening was shown to result in hot but highly non-equilibrium structures even up to 400 ps, with energy trapped in large-amplitude motions comprised of torsion and asymmetric stretching. These studies promise a new direction of research for studying transient structural changes in non-equilibrium complex systems.

References

1. Chergui, M. *Ultrafast Chemical and Physical Processes in Molecular Systems* (World Scientific, Singapore, 1996).
2. Manz, J. & Wöste, L. *Femtosecond Chemistry* (VCH, New York, 1995).
3. Castleman, A. W., Jr. 10 years of femtochemistry - A historical perspective. *J. Phys. Chem. A. - Ten Years Of Femtochemistry* **102**, June 4 issue (1998).
4. Sundström, V. *Femtochemistry and Femtobiology: Ultrafast Reaction Dynamics at Atomic-Scale Resolution* (World Scientific, Singapore, 1997).
5. Zewail, A. H. Femtochemistry: Atomic-Scale Dynamics of the Chemical Bond. *J. Phys. Chem. A* **104**, 5660-5694 (2000).
6. Zewail, A. H. *Femtochemistry: Ultrafast Dynamics of the Chemical Bond* (World Scientific, Singapore, 1994).
7. Tanimura, Y., Yamashita, K. & Anfinrud, P. A. Femtochemistry. *Proc. Natl. Acad. Sci. USA* **96**, 8823-8824 (1999).
8. Williamson, J. C. & Zewail, A. H. Structural femtochemistry: Experimental methodology. *Proc. Natl. Acad. Sci.* **88**, 5021-5025 (1991).
9. Dantus, M., Kim, S. B., Williamson, J. C. & Zewail, A. H. Ultrafast Electron Diffraction. 5. Experimental Time Resolution and Applications. *J. Phys. Chem.* **98**, 2782-2796 (1994).
10. Williamson, J. C., Cao, J., Ihee, H., Frey, H. & Zewail, A. H. Clocking transient chemical changes by ultrafast electron diffraction. *Nature* **386**, 159-

162 (1997).

11. Ihee, H., Cao, J. & Zewail, A. H. Ultrafast electron diffraction: structures in dissociation dynamics of $Fe(CO)_5$. *Chem. Phys. Lett.* **281**, 10-19 (1997).

12. Cao, J., Ihee, H. & Zewail, A. H. Ultrafast electron diffraction: determination of radical structure with picosecond time resolution. *Chem. Phys. Lett.* **290**, 1-8 (1998).

13. Cao, J., Ihee, H. & Zewail, A. H. Ultrafast electron diffraction and direct observation of transient structures in a chemical reaction. *Proc. Natl. Acad. Sci. USA* **96**, 338-342 (1999).

14. Ihee, H., Cao, J. & Zewail, A. H. Ultrafast electron diffraction of transient $[Fe(CO)_4]$: Determination of molecular structure and reaction pathway. *Angew. Chem. Int. Ed.*, in press (2001).

15. Ihee, H. *et al.* Direct Imaging of Transient Molecular Structures with Ultrafast Diffraction. *Science* **291**, 458-462 (2001).

16. Hargittai, I. & Hargittai, M. *Stereochemical Applications Of Gas-Phase Electron Diffraction* (VCH, New York, 1988).

17. Karle, J. *Structural Chem.* **2**, 91 (2000).

18. Williamson, S., Mourou, G. & Li, J. C. M. Time-resolved Laser-Induced Phase Transformation in Aluminum. *Phys. Rev. Lett.* **52**, 2364-2367 (1984).

19. Ischenko, A. A., Spiridonov, V. P., Schäfer, L. & Ewbank, J. D. The stroboscopic gas electron diffraction method for investigation of time-resolved structural kinetics in photoexcitation processes. *J. Mol. Struct.* **300**, 115-140

(1993).

20. Bartell, L. S. & Dibble, T. S. Observation of the Time Evolution of Phase Changes in Clusters. *J. Am. Chem. Soc.* **112**, 890-891 (1990).

21. Andersen, P. An Electron Diffraction Investigation of Triphenylmethane in the Gas Phase. *Acta Chem. Scand.* **19**, 622-628 (1965).

22. Andersen, B. & Andersen, P. An Electron Diffraction Investigation of the Di-t-butylnitroxide Free Radical. *Trans. Amer. Cryst. Assoc.* **2**, 193-196 (1966).

23. Bohn, R. K. & Bauer, S. H. An Electron Diffraction Study of the Structures of NF2 and N2F4. *Inorg. Chem.* **6**, 304-309 (1967).

24. Schäfer, L. Electron Diffraction as a Tool of Structural Chemistry. *Appl. Spectrosc.* **30**, 123-149 (1976).

25. Schäfer, L. Electron Diffraction Studies of Free Radicals. I. Indenyl. *J. Am. Chem. Soc.* **90**, 3919-3925 (1968).

26. Leggett, T. L. & Kohl, D. A. Electron diffraction study of the thermal decomposition of BrCCl3. *J. Chem. Phys.* **59**, 611-616 (1973).

27. Leggett, T. L., Kennerly, R. E. & Kohl, D. A. An electron diffraction investigation of the reaction intermediate in the gas-phase bromination of ethylene. *J. Chem. Phys.* **60**, 3264-3267 (1974).

28. Ivey, R. C., Schulze, P. D., Leggett, T. L. & Kohl, D. A. On an electron diffraction study of the structure of the dibromomethylene radical. *J. Chem. Phys.* **60**, 3174-3177 (1974).

29. Andersen, P., Astrup, E. E., Frederichsen, P. S. & Nakken, K. F. An Electron

Diffraction Investigation of 2,2,6,6-Tetranethyl-4-piperidone-1-hydroxyl. *Acta Chem. Scand. A* **28**, 671-674 (1974).

30. Vajda, E. *et al.* Molecular Structure of Allyl Radical from Electron Diffraction. *J. Am. Chem. Soc.* **108**, 4352-4353 (1986).

31. Belova, N. V. *et al.* Structure And Energy Studies Of β-Diketonates. 5. Structure Of The Y(DPM)2 Radical From Gas-Phase Electron Diffraction Data. *J. Struct. Chem.* **38**, 395-402 (1997).

32. Andersen, B. & Andersen, P. An Electron Diffraction Investigation of the Molecular Structure of Di-t-butylnitroxide Free Radical in the Vapor Phase. *Acta Chem. Scand.* **20**, 2728-2736 (1966).

33. Ischenko, A. A. *et al.* A Stroboscopic Gas-Electron Diffraction Method for the Investigation of Short-Lived Molecular Species. *Appl. Phys. B* **32**, 161-163 (1983).

34. Rood, A. P. & Milledge, J. Combined Flash-photolysis and Gas-phase Electron Diffraction Studies of Small Molecules. *J. Chem. Soc. Far. Trans. 2* **80**, 1145-1153 (1984).

35. Ewbank, J. D. *et al.* Time-Resolved Gas Electron Diffraction Study of the 193-nm Photolysis of 1,2-Dichloroethenes. *J. Phys. Chem.* **97**, 8745-8751 (1993).

36. Ischenko, A. A., Schäfer, L., Luo, J. Y. & Ewbank, J. D. Structural and Vibrational Kinetics by Stroboscopic Gas Electron Diffraction: The 193 nm Photodissociation of CS2. *J. Phys. Chem.* **98**, 8673-8678 (1994).

37. Williamson, J. C. & Zewail, A. H. Ultrafast electron diffraction. Velocity

mismatch and temporal resolution in crossed-beam experiments. *Chem. Phys. Lett.* **209**, 10-16 (1993).

CHAPTER TWO

UED EXPERIMENT

2.1 Experimental Scheme

A schematic of our experimental setup is shown in Figure 2.1.1. It consists of a femtosecond laser system, an ultrafast electron gun, a free-jet molecular beam, and a single-electron detection system. The electron pulse, the laser pulse, and the molecular beam are arranged in a crossed-beam geometry, and the overlap of the three beams is controlled within 10 μm. The chemical reaction is initiated with the fs laser pulse and probed with the ps electron pulses. The two-dimensional diffraction images at each delay time were recorded in the charge-coupled device camera. The time delays between the fs laser and the ps electron pulses were precisely controlled by a computer-driven translational stage. The proper overlap of electron beam, pump laser beam, and molecular beam was critical to catch the structural change.

Femtosecond laser pulses were generated from the CPM laser and further amplified through the PDA. A beam splitter separated the output beam into a pump beam and an electron generation beam so that the majority of the PDA output went into the pump arm. The pump arm contained the computer-driven translation stage and the second harmonic generation crystal (KD*P), where the pump laser beam was frequency-doubled from 620 nm to 310 nm. The output power after the second harmonic generation was about 70 to 350 μJ.

For electron beam generation, the remaining light entered a Michelson interferometer. Just one arm of the interferometer was used for the usual diffraction experiment; the streaking experiment required two electron pulses. The laser beam from the Michelson interferometer was frequency-doubled through the KD*P crystal.

The output beam (310 nm, 1 μJ) illuminated the photocathode for photoelectron generation. The ultrashort electron pulse was generated when the femtosecond laser pulse struck the silver photocathode in back illumination mode. These electrons were accelerated to the extraction pinhole, and focused and shaped by electrostatic lenses and the final pinhole. The direction of the output electron beam was controlled by the deflection plates so that the electron beam intersects the molecular beam.

The molecular sample entered the diffraction chamber in a free-jet expansion through a needle. The needle, inlet tube, and sample holder were heated with wrapped heating tapes in the case that the sample had insufficient vapor pressure at room temperature.

A pump and probe diffraction experiment was conducted typically using a 310 nm pump laser. After finding time zero from the lensing experiment, several time delays between the excitation laser pulse and the probing electron pulse were chosen for a time resolved UED experiment. In some cases, two points before time zero were chosen to confirm that there was no change before time zero as compared to after time zero. The alignment procedure of electron and molecular beams was the same as for the ground state diffraction data. The laser beam was brought to the interaction volume by watching the needle shadow as in the lensing experiment. The laser beam size at the interaction volume was enlarged to 350 mm from its tightly focused size during the lensing experiment. An NG-12 filter (95% transmittance), located in the laser path for the electron beam generation, was used to limit the number of electrons in the electron beam. An automated macro program managed the diffraction procedure

and diffraction images were recorded at each time step during each scan. The translation stage was repeatedly scanned over the chosen time steps to average slow fluctuations in laser and electron intensity over the course of the experiment. After each scan, the position of the electron beam was checked with a short time exposure.

The following section provides a more detailed information about each component.

2.2 The 2nd Generation UED Apparatus

2.2.1 Femtosecond Laser System

The laser system (Fig. 2.2.1) consisted of a colliding-pulse mode-locked ring dye laser (CPM) and a four-stage pumped dye amplifier (PDA). Femtosecond laser pulses (100 MHz, 200 pJ) are generated from the CPM laser and further amplified through the PDA. The main components of the CPM laser system are ring cavity mirrors, four prisms, a gain jet (Rhodamine 6G/ethylene glycol), and an absorber jet (3,3'-diethyloxadicarbocyanine (DODCI) / ethylene glycol). A CW argon ion laser (Coherent, Innova 310) pumps the gain jet at a power of about 4~7 W, and the saturable absorber induces mode-locking of the CW beam into a femtosecond laser beam. Four Brewster-angle prisms are inserted into the ring cavity to reduce the pulse duration by compensating for group velocity dispersion.

The PDA consists of an Nd:YAG laser (30 Hz, Spectra Physics GCR-4), four amplifying dye cells, and an absorber dye jet. The second harmonic (532 nm) of the Nd:YAG is divided into four beams, and each beam pumps the dye cells. The femtosecond laser is amplified by several orders of magnitude while passing through the four dye cells. The saturable absorber jet, which is placed after the second stage, blocks amplified spontaneous emission (ASE) and transmits the femtosecond laser, and two pinholes, located after the first and third stages, filters ASE spatially. The output power after the PDA is about 1-4 mJ and an autocorrelation experiment yielded a pulse duration full-width at half maximum of about 150 to 300 fs.

Figure 2.2.2 represents a schematic laser setup. A beam splitter of 95% / 5% separates the output beam into a pump beam and an electron generation beam so that 95% of the PDA output goes into the pump arm. The pump arm contains the computer-driven translation stage and the second harmonic generation crystal (KD*P), where the pump laser beam is frequency-doubled from 620 nm to 310 nm. The output power after the second harmonic generation is about 70 to 350 μJ. For electron beam generation, the remaining 5% enters a Michelson interferometer. Just one arm of the interferometer is used for the usual diffraction experiment; the streaking experiment requires two electron pulses. The laser beam from the Michelson interferometer is frequency-doubled through the KD*P crystal. The output beam (310 nm, 1 μJ) illuminates the photocathode for photoelectron generation.

2.2.2 Vacuum Chambers

The vacuum chamber is divided into three sections: electron gun chamber, diffraction chamber, and detection chamber (see Figure 2.2.3). The electron gun chamber and the diffraction chamber are separated by a butterfly valve and a vertical slit (2 mm × 8 mm). The fiber optic window, which has a scintillator on it, separates the diffraction chamber and the detection chamber by an o-ring seal, and the phosphor scintillator is protected with a sliding cover. Differential pumping is achieved by introducing a small diffusion pump (Varian HS2, 285 l/s) system beneath the electron gun and a larger (700 l/s) oil diffusion pump (Edwards, Diffstak MK2 160) for the diffraction chamber. The system pressures are monitored by ionization gauges. By

separating the electron gun chamber from the diffraction chamber and pumping the two chambers differentially, the electron gun maintains a pressure of 5×10^{-7} Torr or less, which is low enough to prevent arcing and to increase the longevity of the silver photocathode. A pressure below 10^{-6} Torr is attained for the diffraction chamber in the absence of the molecular beam. When the molecular beam is operating, the pressure is as high as 10^{-4} Torr, and a trap between the gate valve and the diffusion pump for the diffraction chamber is filled with liquid nitrogen to condense the chemicals. To prevent water condensation on the cooling unit of the detection chamber, the same mechanical pump (Alcatel 2010, 6.8 cfm) for the electron gun chamber is used to pump out the detection chamber. The diffraction chamber has its own mechanical pump (Alcatel 2012A, 11 cfm) independent of the electron gun chamber. The electron gun chamber and the diffraction chamber are shielded with a μ-metal sheet to prevent the earth's magnetic field from affecting the electron beam pathway.

2.2.3 Detection System

Figure 2.2.4 shows a schematic of the detection system. The photoionization-induced lensing experiment, required to find time zero, uses small distortions of the electron beam profile and requires very high resolution (< 15 μm). This high resolution is also necessary to line up the needle for the diffraction experiments since proper alignment of the electron beam relative to the needle is important. For these purposes, a small CCD chip (Texas Instruments, TC211), with good resolution (~14

μm), operated in the direct electron bombardment mode is installed inside the diffraction chamber. This chip has 192 by 165 active pixels and each pixel has a dimension of 13.7 μm by 16 μm. A pixel (picture element) is the smallest unit collecting charge in the CCD chip. The pre-amplifier circuit, including this chip, is mounted on the phosphor screen protection cover and a thermoelectric cooling chip (Melcor, FC series frigichip, FC 0.45-66-05-2L) is introduced to dissipate the heat generated from the CCD. The back side of the CCD chip is adhered to the cold side of the frigichip using a heat sink compound. The hot side is thermally coupled to the wall of the diffraction chamber through the screen cover with a heat sink compound. The equilibrium temperature of the cold side is -20 °C without any other cooling system. This temperature is low enough to reduce the thermal noise generated in the CCD chip during lensing experiments, since short exposure time (1-2 seconds) is usually sufficient for this. To block any scattered light hitting the CCD, the surface of the CCD chip is coated with a 2000 Å aluminum film using a home-built evaporation chamber.

For the diffraction data, the detection system inside the detection chamber is used. The detection system consisted of a phosphor screen, a fiber optic window, a fiber optic taper, an image intensifier, another fiber optic taper, a CCD chip, and a cooling system. The components are coupled with an optical coupling compound. The fiber optic window (2 inch diameter, 1/4 inch thick) was coated with phosphor (P-20, 4 mg/cm^2, CRT Scientific), and on top of the phosphor a thick 3000 Å aluminum film (CRT Scientific) is applied to cut down the scattered laser light and any other

light. This thick aluminum film effectively blocks the light and transmits the electrons. The scattered electrons from the interaction volume hit the phosphor screen and their kinetic energy is transformed into photons (~545 nm), which are transported to the image intensifier through the fiber optic window and taper (40 mm to 18 mm). In this step, most of the photons from the undiffracted electrons, which contains over 88% of the electron intensity in a small area, are blocked by a beamstop. The beamstop is a 700 Å-aluminum film coated on the center of the wider side of the big fiber optic taper. The transported photons are further amplified through the image intensifier (Hamamatsu, V3063U-04).

The gated image intensifier is controlled by a home-built power electronic controller, which is triggered after the Nd:YAG laser fired during the exposure. The function of intensification is regulated by the gate voltage of the photocathode following the triggered signal, and the gain is adjusted by varying the screen voltage. The delay of the gate is optimized so that the image intensifier amplifies the diffraction signal effectively without introducing any unwanted signal from scattered light. The optimum width of the gate is determined by increasing the width until the spontaneous emission of the image intensifier reached the maximum value.

The intensified photons illuminate the CCD chip (SITe, SI502A) through a smaller fiber optic taper (18 mm to 12.5 mm) and develop electron-hole pairs on the pixels of the CCD chip. The SITe CCD chip, which is operated in front-illumination mode, consisted of 512 by 512 pixels (each pixel, 24 μm by 24 μm). The cooling system is very similar to that of a small TI CCD inside the diffraction chamber except

that the thermoelectric cooling chip had larger capacity (Melcor, 2 stage cascade frigichip, 2CP 085-065-71-31L), and the cold side is cooled by circulating water. The equilibrium temperature of the SITe CCD chip is maintained at -40 °C, which is enough to reduce most of the dark noise.

Software (HPC-1) and electronics from SpectraSource Instruments are used to control the SITe CCD; many modifications were made on the electronics for better performance. The TI CCD can be controlled using basically the same electronics with further modification on the camera head circuit in order to deal with the different clocking signals and pin connections. The camera head, power supply, and computer are all connected with each other to transfer voltages, signals, data, *etc.* The software interface controls the exposure feature and data collection. A remote shutter, which is controlled by the camerahead power supply, is placed in the path of the femtosecond laser before the 95% / 5% beam splitter. The charge collected during the exposure at each pixel of the CCD chip is converted into a corresponding voltage through the pre-amplification stage in the CCD chip. The voltage is further amplified by the home-made pre-amplification circuit, and is transported into the camera head circuit. In the camera head, the 16-bit analog to digital converter transforms the voltage into a two byte integer (analog to digital converted unit, ADU). An optocoupler circuit electrically separates the computer and the camera head, and the data transfer rate from camera to computer is kept rather low (50 kHz) following the processing frequency of the analog to digital converter chip. A single electron, detected by the SITe CCD, creates 1600 ADU counts and is spread over 4 pixels at an image

intensifier gain of 10^4. The readout noise of the SITe CCD chip is about 6 or 7 counts per pixel. The computer (486/33 MHz IBM compatible) is equipped with 16 Mbyte of RAM, a 300-Mbyte SCSI hard, and a 150-Mbyte tape drive to deal with a large amount of data because each image of 512 by 512 needs 0.5 Mbyte.

2.2.4 Ultrashort Electron Pulse Generation

The construction of our electron gun (Fig. 2.2.5) is based on the design of the Elsayed-Ali group.[1] The cylindrically symmetric gun consisted of a photocathode, an extraction pinhole, and four focusing electrodes. The body was made of ceramic, and stainless steel was used for the remaining parts. The photocathode was made by coating a quartz window with a 450 Å silver film in a home-built evaporation chamber. Silver was chosen for the photocathode following Tsang's research.[2] Tsang found that a 310 nm laser could generate photoelectrons from a thin silver film in a one-photon process although the work-function of bulk silver (~4.3 eV) is much higher than 310 nm (~4.0 eV). The aluminum final pinhole (2 mm diameter) is installed to clean the tail. The distance between the photocathode and the extraction pinhole aperture (200 μm diameter) is 2.6 mm. The electron gun is powered by a variable high-voltage power supply (Glassman, EH40) and four home-built voltage dividers. The optimized voltages applied for the photocathode, extraction pinhole, first electrode, second electrode, and third electrode are typically -18.00 , -10.92, -2.01, -2.00, and -10.20 kV respectively. The final pinhole is grounded. The extraction field was 2.72 kV/mm.

Three pairs of aluminum deflection plates are mounted at the end of the electron gun. The first pair, consisting of 1 inch long plates 4 mm apart, are the streaking electrodes. The remaining two pairs are deflection electrodes, which control the horizontal (3.0 pixels / 10 V on the SITe CCD) and vertical position (3.5 pixels / 10 V on the SITe CCD) of the electron beam. The deflection plates are 0.5 inches long and 6 mm apart. During collection of the diffraction data, the streaking electrodes are grounded, and one of each pair of deflection plate is also grounded. The deflection voltages used to bring the electron beam to the center spot in the detector are usually less than 50 V.

The ultrafast electron pulse was generated when the femtosecond laser pulse (310 nm, 1 μJ) strikes the silver photocathode in back illumination mode. The electrons are accelerated to the extraction pinhole and focused and shaped by electrostatic lenses and the final pinhole (Fig. 2.2.6). The direction of the output electron beam is controlled by the deflection plates. As mentioned before, a smaller interaction volume is preferable because of velocity mismatch. To reduce the interaction volume, the electron beam size in the interaction volume should be small. The electrode voltages are adjusted so that the electron beam focal point is near the interaction volume beneath the molecular beam needle. The electron beam diameter at the interaction volume is about 300 μm, which is close to the optimum value for our system. In addition to the small electron beam size in the interaction volume, the electron beam should have a well-collimated profile since the small spot size on the detector is necessary for a high spatial resolution of the diffraction pattern. The

obtained electron beam size on the phosphor screen detector is about 380 μm resulting in the overall spatial resolution of diffraction images of ~0.1 $Å^{-1}$. The divergence of the electron beam is ~1.8 mrad.

2.2.5 Sample Inlet System And Beam Alignment

The molecular sample enters the diffraction chamber in a free-jet expansion through a needle (150 μm, inner diameter). A schematic is shown in Figure 2.2.7. When the sample has insufficient vapor pressure at room temperature, the needle, inlet tube, and sample holder are heated with wrapped heating tapes. The position of the needle is controlled by an XYZ position translator (±5 μm on all axes, Thermionics, EC-1275-1-1-2). The shadow from the needle tip is used to adjust the positions of the electron and laser beams and to determine the beam sizes. Proper overlap of the laser, electron, and molecular beams within several microns is critical for a successful experiment. The usual procedure is the following: first, the electron beam position is deflected to hit the beam stop on the detector and then the needle is moved so that the electron beam is just below (within 50 microns) the needle tip using the needle shadow of electron beam. Finally, the pump laser beam is fine-tuned watching the needle shadow of the laser beam.

2.3 Pre-Requisite Experiments

2.3.1 Measuring e-Pulse Width With Streak Experiment

Figure 2.3.1 shows a schematic of the experimental setup for the streak experiment, which is used to determine the temporal duration of the electron pulse. High voltages of opposite polarities are applied to the two streaking plates connected to photoconductive switches (iron-doped indium phosphide substrate); the photoconductive switches were biased with reversed voltages from a fast RC circuit. For example, the upper plate has an initial voltage of 1 kV, and the photoconductive switch for the upper plate has -1 kV in the opposite arm, while the lower plate is initially applied with -1 kV, and its photoconductive switch is biased with 1 kV in the opposite arm. When the femtosecond laser pulse strikes and activates the photoconductive switches simultaneously, the switches become conductive, so that a time dependent electric field is ramped across the streaking plates. A very fast rate of voltage change is required to disperse single picosecond pulses (an order of 1 kV / ns). If the electron pulse happens to travel the gap between the plates at the time the electric field changes very quickly, the field gradient between the two plates converts the temporal profile of the electron pluse into a spatial profile: the head of the electron beam would experience larger upward voltage than the tail part resulting in the spread of the temporal width of electron pulse across the detector. To convert the measured spatial width to a corresponding temporal width, a well-established temporal reference is required. This temporal reference is achieved by using a pair of electron pulses rather than one electron pulse. A pair of laser pulses with well-defined pulse

separation Δt_{ps} are created through the use of a Michelson interferometer, which is incorporated into the pump laser arm. This pair of laser pulses generates a pair of electron pulses with the same temporal separation Δt_{ps} at the photocathode. The arrival of the electron pulse between the streaking plates is synchronized with the voltage crossing at the plates by adjusting an optical delay line in the pathway of the laser beam for activating the photoconductive switches. In the case of two electron pulses, the first electron pulse would experience an upward potential and the second pulse would receive a downward potential; the head of the first pulse would feel a larger upward potential than the tail part of the first pulse while the tail of the second pulse would experience a larger downward potential than the head part of the second pulse. After streaking, the two streaked electron pulses are separated by a distance D_{pix} (in pixels) on the CCD detector. The streak velocity, in pixels per picosecond, is calculated from Δt_{ps} and D_{pix} (streak velocity = $D_{pix}/\Delta t_{ps}$). A sufficient number of single shot streak image pairs are recorded for a wide range of laser intensities, which is achieved by varying neutral density filters in the laser beam path. The separation Δt_{ps} is fixed to 66.7 ps, which is obtained by separating the two laser pulses by 20 mm. The spatial separation D_{pix} caused by the streaking voltage is 134 pixels on average. Therefore the average streak velocity is 2 pixels/ps, which corresponds to 1.6×10^8 m/s. To determine the number of electrons and the width of the electron pulse in the streaking direction (L_m), the background corrected intensity and the full-width at half-maximum are measured for each streaked electron pulse detected on the CCD detector. The ADU counts are converted to the number of electrons by one electron =

1600 ADU at the gain 10^4 of the image intensifier. The length L_m is a function of the finite size of the unstreaked electron beam (L_u) and the streak-transformed temporal length of the pulse (L_s). The pulse profile is assumed to be a Lorentzian shape so that the total length is expressed as $L_m = L_u + L_s$. A series of unstreaked single shot images are also taken for a wide range of laser intensities, and each of the measured L_u is used to calculate L_s, which is converted into units of time using the streak velocity.

Figure 2.3.2 shows examples of streaked images with low and high intensities, and Figure 2.3.3 shows the plot of temporal width of the electron beam with the number of electrons per pulse. The results show that an order of magnitude variation in the number of electrons can be obtained with one kind of filter. This fact reflects the fluctuation in laser intensity. Using various filters (transmittance of 21% to 100%), a range of the number of electrons per pulse is obtained (an order of 10^1 to 10^4). We observe that the photoelectrons are generated in a one-photon process although a two-photon effect takes over for higher laser intensity. The temporal duration of the electron beam (subpicosecond to >15 ps) increases with the number of electrons per pulse, and can be controlled by changing filters. There is a linear relationship between the number of electrons per pulse and the electron pulse width; 1000 electrons per 1 ps.

2.3.2 Finding Time-Zero With Lensing Experiment

A time coordinate for an ultrafast reaction can be obtained by establishing the zero of time, which is defined as the time when both pulses intersect in the molecular

beam simultaneously. Careful measurement of the laser and electron beam paths can narrow the time zero window to within a hundred picoseconds, but recording diffraction patterns, analyzing them, and finding the changes in diffraction patterns is not an efficient way to find time zero because each set of diffraction data, which actually corresponds to one data point, needs at least several hours of exposure time to show the amplitude change in the scattering intensity function. This fact imposes the necessity of another way of finding time zero.

The photoionization-induced lensing effect is utilized to establish the time zero. The basic principle is schematically represented in Fig. 2.3.4. The pump laser pulse passing through the molecular beam photoionizes a fraction of the sample via a multiphoton effect, and produces a mixture of positive ions and negative electrons. Electrons, with their excess kinetic energy acquired from the laser pulse, diffuse very quickly compared to the relatively heavy positive ions remaining stationary on the picosecond time scale. The femtosecond laser pulse forms a cylinder of positive ions, which acts like a lens for the incident electron pulse. When the electron pulse from the electron gun travels through this region of high population of positive ions, a Coulombic field between electrons and positive ions distorts the electron pulse. The change of the unscattered electron beam profile can be used to search for time zero.

For the photoionization-induced lensing, the pump laser beam was focused very tight (50-100 μm diameter) onto the molecular beam to increase the ion population and to reduce the velocity mismatch effects to ~1 ps. The number of electrons per pulse was constrained so that the electron beam had a temporal duration

of ~5 ps. The electron beam images with and without the pump laser are recorded on the TI CCD operated in direct bombardment mode. The vertical profiles are averaged and the square of the difference from the background profile without the pump laser is calculated and plotted against the time delay. Figure 2.3.5 (top) shows an example of the electron beam image with and without the laser beam and vertical profiles. Figure 2.3.5 (bottom) shows the experimental photoionization-induced lensing transient for a molecular beam of CH_2I_2. This chemical was chosen for this experiment because of its relatively high extinction coefficient (850 $l$cm^{-1}mol^{-1}) at 310 nm.[3-6] The transient profile consists of two components: a very sharp spike with full-width at half maximum of 4 ps and a smooth rise with rise time of ~30 ps. The slow rise can be explained by the aforementioned theory. Since the ionization energy of CH_2I_2 is ~9.46 eV[7] and the photon energy of the excitation laser pulse (310 nm) is ~4 eV, three photons are needed to ionize the CH_2I_2, resulting in an excess energy of 2.54 eV (3×4 - 9.46). After ionization, the electron carries the remaining energy (2.54 eV) as its kinetic energy, and escapes the plasma cylinder with the velocity of ~0.9 μm / ps. Since the spatial dimension of the positive cylinder would presumably follow the size of excitation laser beam (50 μm diameter), an electron in the cylinder center would escape within about 30 ps, which corresponds to the observed slow rise time. In some lensing experiments, a sharp spike is observed reproducibly as shown in Figure 2.3.6. The nature of the sharp spike is temporarily assigned to the effect of the field formed by ionized species in the needle tip. Further systematic study will be needed to define

the origin of this phenomenon. Nevertheless, the spike helps to define the time zero within a few picoseconds.

2.4 Requirements For Samples

UED has the potential to be applied to study the reaction dynamics of a wide range of chemicals. However, in practice, the applicability is limited to the chemicals satisfying the following characteristics because of the available laser power and wavelength, and the simplicity of the sample inlet system: 1) high absorption cross section at the available wavelengths, 2) high vapor pressure (1~10 torr at the needle tip) in available conditions, 3) pronounced structural changes upon photo-induced reaction, 4) easy to deal with—stable, non-flammable, non-toxic, 5) relatively high symmetry—not too complex, 6) high degree of scattering, 7) commercially available. Although the applicability of UED will expand as the technology advances, it is worth considering the points 1) to 3) in greater details (the following sections). Above all these requirements, of course, the chemistry displayed by the chemicals upon light irradiation should be interesting and the following reactions may be of particular interest for UED: 1) intermediate structure with a lifetime longer than the total experimental temporal resolution, 2) reactions that are hard to study with the conventional femtosecond spectroscopic tools, 3) systems with time scales faster than the resolution of nanosecond time-resolved electron diffraction.

2.4.1 Vapor Pressure

Gas phase electron diffraction requires that the vapor pressure in the interaction volume should be high with typical pressure ranging 1~10 torr at the

needle tip. For this reason, most chemicals studied in this laboratory are in gas-phase (Ar, Xe, N_2, CO_2, CF_3I, SF_6) or liquid-phase (CCl_4, CH_2I_2, CF_2I_2, $C_2F_4I_2$, CH_2=CH-CH_2I, CHD, CHT, Pyridine, $Fe(CO)_5$, $Co(C_5H_5)(CO)_2$) at room temperature. In the case that the vapor pressure of 1 to 10 torr cannot be reached, the exposure time and electron flux should be increased to compensate for the decrease of the scattering intensity. On the other hand, if the pressure is higher than this range, the diffraction pattern may suffer from the multiple scattering. A few solid samples such as CHI_3 and CH_2ICH_2I have been tried. The biggest problem was thermal reactions that occurred during the heating of the sample to attain a reasonable vapor pressure. In the case of CHI_3, a considerable fraction of it decomposed into Iodine-containing species prior to reaching the scattering chamber. In the case of CH_2ICH_2I, most of it decomposed into CH_2CH_2 and I_2.

Since the pressure at the needle tip (i.e., in the interaction volume) is not directly measured, it is still questionable until proven whether the pressure is indeed in the range of 1 to 10 torr. In the 2nd generation UED, we used 8 g of CH_2I_2 (MW = 267.8 g/mol) over 5.5 hours, which corresponds to Q = (n / t) = 0.0055 mol/h. The pressure can be estimated by using the relationship of

$$p = n \cdot R \cdot T / V = n \cdot R \cdot T / (v \cdot t \cdot A) \qquad (2.4.1.1)$$

where v is molecular velocity, V the total volume of the gas sample, n the number of molecules in mol, A the cross section of the needle, and t the total time to flow. T_{needle} = 160 °C = 433 K. The velocity of the molecule can be estimated using

$$v = (3 \cdot R \cdot T/(MW))^{1/2}. \qquad (2.4.1.2)$$

Combining these two equations, (2.4.1.1) and (2.4.1.2), gives us the final equation,

$$p = (n / t)\cdot(R\cdot T\cdot(MW))^{1/2} / (3^{1/2}\cdot A). \qquad (2.4.1.3)$$

With 300 μm as the diameter of the average molecular beam, the pressure p is estimated to be ~3 torr, which falls within the range. Since the conditions for other chemicals are similar to that of CH_2I_2, it is reasonable to conclude that the gas pressures used in the 2nd generation UED experiments are very similar to the conventional value of 1 – 10 torr.

In the 3rd generation UED experiments, ~35 ml of sample is usually consumed for 30 to 36 hours. The typical molecules studied have molecular weights of ~80 g/mol (79.10 for Pyridine, 80.13 for CHD, and 92.14 for CHT) and molecular densities of ~0.9 (0.978 for Pyridine, 0.841 for CHD, and 0.888 for CHT). These values come up with (n / t) = ~0.015 mol/h, which is almost three times higher than that of CH_2I_2 in the UED2. On the other hand, the MW is three times less than that of CH_2I_2. Plugging all these numbers into the above master equation for the pressure shows that the gas pressure in UED3 is about twice as much as that in UED2. Therefore, the gas pressure in UED3 is still in the conventional range of 1-10 torr and the multiple scattering should not be a concern.

Except for the gas sample, the temperatures of the sample reservoir, the manifold, and the needle are usually kept higher than room temperature. To prevent any clogging of the chemical in the needle tip, the general wisdom is to maintain the needle temperature higher than the manifold temperature, which is kept higher than the sample temperature. To estimate the right temperature to get the right pressure is

not trivial. If the whole sample inlet system is in equilibrium, the Clausius-Clapeyron equation

$$dp/dT = \Delta H_{vap}/(T \cdot \Delta V_{vap}) \quad (2.4.1.4)$$

can be applied to estimate the temperature and to obtain a certain equilibrium pressure. The change in volume (ΔV_{vap}) can be approximated as

$$\Delta V_{vap} = V_m(\text{gas}) - V_m(\text{liquid}) \approx V_m(\text{gas}) \approx R \cdot T/p. \quad (2.4.1.5)$$

A wide range of liquids give ~85 $JK^{-1}mol^{-1}$ as their molar entropy of vaporization. This simple law (Trouton's rule) is approximate, but provides a useful way to estimate ΔH_{vap};

$$\Delta H_{vap} = T_b \cdot 85\ JK^{-1}mol^{-1} \quad (2.4.1.6)$$

where T_b is the boiling point. For example, Trouton's rule (combined with the Clausius-Clapeyron equation) gives vapor pressure of 97 torr at 40 °C for $Fe(CO)_5$ while a much accurate empirical pressure-temperature relationship for $Fe(CO)_5$ gives ~70 torr. As shown in Table 2.4.1, room temperature should be more than enough to get 10 torr. However, the actual temperatures of the sample and the needle had to be raised much higher than room temperature because the needle has a limited throughput. To get 10 torr at the needle tip, the backing pressure should be much higher than this. As seen in Table 2.4.1, the estimated pressure in the sample container is about 100 torr.

Table 2.4.2 lists the temperature setting used for the samples studied in the 2nd generation UED. The needle temperature is slightly lower than the boiling temperature except for the case of $CpCo(CO)_2$. Generally, the lower temperature is preferred lest

the sample should thermally decompose. For the 3rd generation UED setup, the needle temperature is generally higher than the boiling temperature and the sample is kept near the boiling temperature. It turned out that these samples did not suffer much from thermal decomposition.

2.4.2 Absorption Cross Section

The "actual" signal of interest in UED is the change of diffraction patterns upon light illumination. The change of diffraction patterns is proportional to several factors: the number of molecules in the interaction volume, the number of photons to excite the molecules, the number of electrons to scatter and give a diffraction signal, the degree of structural changes induced by photo-excitation, and the fraction of excited molecules and products. All these issues are discussed in section (**2.5**) for consideration of the signal-to-noise ratio. With all other conditions identical, the fraction of excited molecules and products is directly proportional to the absorption cross section, and this section gives a few considerations regarding the absorption cross section and the fraction of excited and/or product molecules.

Estimation of the fraction of the excited molecules can be obtained by using the Beer-Lambert law, which can be expressed in several forms

$$I = I_0 \cdot e^{-\kappa \cdot p \cdot l} \qquad (2.4.2.1a)$$

$$I = I_0 \cdot e^{-\sigma \cdot N \cdot l} \qquad (2.4.2.1b)$$

$$I = I_0 \cdot 10^{-\varepsilon \cdot c \cdot l} \qquad (2.4.2.1c)$$

Where I_0 is the incident photon intensity, I is the photon intensity after the sample, p is the pressure in atm at the reference temperature T, l is the cell length in cm, N is the number of molecules per cm^3, c is the concentration in $mol \cdot liter^{-1}$, κ is the absorption cross section in $atm^{-1} \cdot cm^{-1}$, σ is the absorption cross section in $cm^2 \cdot molecule^{-1}$, and ε is the extinction coefficient in $liter \cdot mol^{-1} \cdot cm^{-1}$. The interconversion among κ, σ, and ε can be obtained using the following relationships:

$$\sigma = 3.72 \times 10^{-20} \cdot \kappa \qquad (2.4.2.2a)$$

$$\varepsilon = 9.73 \cdot \kappa \qquad (2.4.2.2b)$$

$$\sigma = 3.8 \times 10^{-21} \cdot \varepsilon \qquad (2.4.2.2c)$$

Let Φ_0 the number of photons before absorption, Φ the number of photons after absorption, and $\Delta\Phi$ the number of photons absorbed by the sample. The Beer-Lambert law (2.4.2.1b) tells us

$$\begin{aligned} \mathrm{Log_e}(I_0 / I) &= \mathrm{Log_e}(\Phi_0 / \Phi) = \mathrm{Log_e}((\Phi + \Delta\Phi) / \Phi) \\ &= \mathrm{Log_e}(1 + \Delta\Phi / \Phi) = \sigma \cdot N \cdot l \end{aligned} \qquad (2.4.2.3)$$

Now we need to consider the magnitude of $\Delta\Phi$ compared with Φ. The upper limit for $\Delta\Phi$ is the total number of molecules (n) in the interaction volume V ($= A \cdot l$), where A is the area covered by the laser light. With $p = 1 \sim 10$ torr and $T = 300$ K, the gas law $PV = nRT$ gives us $n = 10^{12} - 10^{13}$ molecules. The number of photons before absorption Φ_0 can be calculated by

$$\Phi_0 = E / (h \cdot \nu) \qquad (2.4.2.4)$$

where E is the energy of the incident light, h is Planck's constant, and v is the frequency. A laser pulse with 100 μJ at 266 nm has $\Phi_0 = \sim 10^{16}$ photons. Therefore $\Phi = \Phi_0 - \Delta\Phi \approx 10^{16}$ photons. Since $\Delta\Phi / \Phi \approx 10^{-3} \sim 10^{-4}$, eq. (2.4.2.3) can be approximated as

$$\Delta\Phi / \Phi \approx \sigma \cdot N \cdot l \qquad (2.4.2.5)$$

The number of absorbed photons per the total number of molecules can be expressed as

$$\Delta\Phi / (A \cdot N \cdot l) = \sigma \cdot \Phi / A = \sigma \cdot E / (A \cdot h \cdot \nu) \qquad (2.4.2.5)$$

In the limit of a one-photon absorption process, the maximum value of $\Delta\Phi / (A \cdot N \cdot l)$ is 1, which means that every molecule in the interaction volume absorbs one photon. The energy (E_{Max}) necessary to reach this limit, then, can be expressed as

$$E_{Max} = A \cdot h \cdot \nu / \sigma \qquad (2.4.2.6)$$

For example, $C_2F_4I_2$ has $\sigma_{266nm} = 2 \times 10^{-18}$ cm^2 at 266 nm. With the radius of the interaction volume 200 μm, eq. (2.4.2.6) yields ~470 μJ. The actual energy used for the UED experiment on the $C_2F_4I_2$ reaction was ~100 μJ.

Even if E_{Max} is applied, the actual fraction of excited molecules cannot reach 1 when a linearly polarized laser pulse is used. This is because eq. (2.4.2.6) neglects the transition dipole moment of the molecule and only 1/3 of the molecules are properly aligned to match the transition dipole and the polarization of the laser. This is assuming that the pulsewidth is longer than the dissociation time and shorter than the rotational time. In principle, if we have enough power, it will be possible to create two beams with perpendicularly polarized directions, and excites 2/3 of the population.

Table 2.4.4 lists the absorption cross section of the molecules studied in this laboratory and also some other molecules which may be investigated in the future. Due to consideration of the signal-to-noise ratio, molecules with relatively high absorption cross sections have been chosen for our UED experiments. Successful chemicals have absorption cross section of at least 0.8×10^{-18} cm^2 and as high as 6.8×10^{-18} cm^2. Molecules with low absorption cross sections can be, in principle, studied as long as compensation is made for the signal-to-noise ratio.

2.4.3 Structural Changes

Another important factor affecting the change of diffraction patterns is the degree of structural change and its actual impact on the diffraction pattern. Some reaction may induce a big change in the diffraction pattern whereas another reaction only produces little or no change. To quantify this factor, a useful coefficient can be defined as

$$i = |\text{Change in the diffraction pattern}| \,/\, |\text{Diffraction pattern of the reactant}| \qquad (2.4.3.1)$$

The value of this coefficient i depends on the choice of the diffraction curves (sM(s) or $f(r)$ or $I_M(s)$). Most quantitative and meaningful definition can be obtained by using $I_M(s)$.

$$i = \Sigma |I_M^{Product} - I_M^{Reactant}| \,/\, \Sigma |I_M^{Reactant}| \qquad (2.4.3.2)$$

where $I_M^{Reactant}$ is the molecular scattering intensity of the reactant and $I_M^{Product}$ is that of the product. For example, the H-shift reaction of CHT produces the same species,

CHT, thereby giving us $i \approx 0$. In contrast, the dissociation of I_2 into two Iodine atoms will yield $i \approx 1$. In other words, if the same number of molecules are excited and turned into the final products, the change in the diffraction patterns will be much more pronounced in the I_2 dissociation than in the H-shift of CHT. This coefficient i plays an important role in consideration of the signal-to-noise ratio.

2.5 Practical Considerations

Two critical factors characterizing UED are considered here; temporal resolution and signal-to-noise ratio. These two parameters are closely related and usually one must be compromised to increase the other. Suggestions for improvement are also included.

2.5.1 Temporal Resolution

The temporal resolution of time-resolved electron diffraction experiments has been improved by several orders of magnitude over the last decade, and has now reached a few picoseconds (ps) with the advance of ultrafast electron diffraction. Although this ps time resolution is short enough to study the molecular structure of short-lived and long-lived intermediate species with a life time longer than several picoseconds[8], the vibrational motions, direct bond-breaking and bond-making processes[9] cannot be captured. Therefore, the ultimate goal would be the femtosecond regime, in which the fundamental bond-making and bond-breaking processes occur. The plausibility of femtosecond time resolution is investigated and several important factors relevant to accomplishing this time scale are considered in this section.

Total temporal resolution The total temporal resolution (Δt) of ultrafast electron diffraction depends on the pulsewidth of laser beam (Δt_{laser}), the electron beam (Δt_e), and the velocity-mismatch (Δt_{VM}) according to[10]:

$$(\Delta t)^2 = (\Delta t_{laser})^2 + (\Delta t_e)^2 + (\Delta t_{VM})^2. \qquad (2.5.1.1)$$

In the present UED system, Δt_{laser} = 0.1 ps, Δt_e = 0.5 ~ 10 ps, and $\Delta t_{VM} \approx$ 1.5 ps, resulting in the total temporal resolution of a few picoseconds. So, to achieve the femtosecond time resolution, Δt_e and Δt_{VM} should be reduced significantly.

The temporal width of electron pulses Even the present electron gun can generate subpicosecond electron pulses, but a reasonable electron flux can be obtained only when $\Delta t_e >$ 2 ps. The Δt_e can be reduced further by better designs of electron guns while not losing the necessary flux. For example, Δt_e has been improved by an order of magnitude for the last five years. Reducing Δt_e with the present electron gun system requires that the signal-to-noise ratio should be sacrificed or the exposure time should be greatly increased to maintain the signal-to-noise ratio of the diffraction change. In summary, there is still room for the improvement on Δt_e.

The velocity mismatch Sample molecules within the interaction volume of UED experiments experience a distribution of time delays between the pump laser pulse and the probing electron pulse. This velocity mismatch[11] depends on many parameters such as the widths of the laser beam, the electron beam, and the molecular beam, and the velocity vectors of the laser and electron beams. The sensitivity of Δt_{VM} to these parameters also varies. The most critical factors are the angle between the laser beam and electron beam, the speed of electrons, the width of the laser beam, and the width of the molecular beam. The width of the molecular beam gets important only when it is smaller than the width of the laser and electron beams. The width of electron beam is not so important, which is actually good news when the signal-to-noise ratio is considered. So, as far as the velocity mismatch is concerned, increasing

the speed of electrons and reducing the width of the laser beam can be quite effective in improving Δt_{VM}. Even with the present experimental setup, a sub-picosecond Δt_{VM} can be achieved by making the width of the laser beam extremely small. However, one needs to consider not only the velocity mismatch but also the effect of reducing the laser beam width on the signal-to-noise ratio.

2.5.2 Signal-To-Noise Ratio

To consider the signal-to-noise ratio, several parameters need to be defined.

The number of molecules covered by beams $N_{m\text{-}e}$ is the number of molecules covered by the electron beam pathway. w_m, w_e, and w_l are the widths of the molecular beam, the electron beam, and the laser beam, respectively. The volume ($V_{m\text{-}e}$) of the molecular beam covered by the electron beam can be as

$$V_{m\text{-}e} = \pi \cdot (w_e/2)^2 \cdot w_m \qquad (2.5.2.1)$$

The gas law gives us $N_{m\text{-}e}$ as

$$N_{m\text{-}e} = N_A \cdot p \cdot V_{m\text{-}e}/(R \cdot T) = N_A \cdot p \cdot \pi \cdot (w_e/2)^2 \cdot w_m/(R \cdot T) \qquad (2.5.2.2)$$

In the same way, the number ($N_{m\text{-}l}$) of molecules covered by the laser beam can be expressed as

$$N_{m\text{-}l} = N_A \cdot p \cdot V_{m\text{-}l}/(R \cdot T) = N_A \cdot p \cdot \pi \cdot (w_l/2)^2 \cdot w_m/(R \cdot T) \qquad (2.5.2.3)$$

Among the molecules covered by the electron beam, the number ($N_{m\text{-}e\text{-}l}$) of molecules excited by the laser beam is roughly

$$N_{m\text{-}e\text{-}l} = N_A \cdot p \cdot V_{m\text{-}e\text{-}l}/(R \cdot T) = N_A \cdot p \cdot \pi \cdot (w_l/2)^2 \cdot w_e/(R \cdot T) \qquad (2.5.2.4)$$

In the point of diffraction, the molecules that are exposed to electrons but do not see the laser light is waste. Therefore the ratio (overlap parameter) of $N_{m\text{-}e\text{-}l}$ and $N_{m\text{-}e}$ is an important parameter to consider.

$$N_{m\text{-}e\text{-}l}/N_{m\text{-}e} = w_l^2/(w_m \cdot w_e) \qquad (2.5.2.5)$$

The number of excited molecules From eq. (2.4.2.5), the fraction (f_{ex}) of molecules that absorb one photon can be expressed as

$$f_{ex} = \sigma \cdot E_{pulse}/(\pi \cdot (w_l/2)^2 \cdot h \cdot \nu) \qquad (2.5.2.6)$$

where E_{pulse} is the energy per pulse. The total number of molecules absorbing one photon is

$$f_{ex} \cdot N_{m\text{-}l} = \sigma \cdot E_{pulse} \cdot N_A \cdot p \cdot w_m/(h \cdot \nu \cdot R \cdot T) \qquad (2.5.2.7)$$

However, in most cases, the number of molecules experiencing both the laser beam and electron beam is smaller than the above value.

$$f_{ex} \cdot N_{m\text{-}e\text{-}l} = \sigma \cdot E_{pulse} \cdot N_A \cdot p \cdot w_e/(h \cdot \nu \cdot R \cdot T) \qquad (2.5.2.8)$$

The actual observed fraction of change comes as

$$f_{ex}\,(N_{m\text{-}e\text{-}l}/N_{m\text{-}e}) = \sigma \cdot E_{pulse}/(\pi \cdot (w_l/2)^2 \cdot h \cdot \nu)\,(N_{m\text{-}e\text{-}l}/N_{m\text{-}e}) \qquad (2.5.2.9)$$

As shown in **2.4.2**, in most cases, only one third can be excited. So eq. (2.5.2.9) can be modified to take this factor into account.

$$(1/3)\,f_{ex}\,(N_{m\text{-}e\text{-}l}/N_{m\text{-}e}) = (1/3)\,\sigma \cdot E_{pulse}/(\pi \cdot (w_l/2)^2 \cdot h \cdot \nu)\,(N_{m\text{-}e\text{-}l}/N_{m\text{-}e}) \qquad (2.5.2.10)$$

$$(1/3)\,f_{ex} = (1/3)\,\sigma \cdot E_{pulse}/(\pi \cdot (w_l/2)^2 \cdot h \cdot \nu) \qquad (2.5.2.11)$$

In Table 2.5.1, the expected fraction change ($(1/3) \cdot f_{ex}$) and the actual change experienced by electrons ($(1/3) \cdot f_{ex} \cdot (N_{m\text{-}e\text{-}l}/N_{m\text{-}e})$) are tabulated on the basis of actual

experimental parameters in the 2nd generation UED. The ($N_{m\text{-}e\text{-}l}/N_{m\text{-}e}$) values are consistent, ranging 40 to 50%. This means that only half of the molecules in the electron beam path are actually illuminated by the laser beam. Table 2.5.2 shows the values for the 3rd generation UED. The values are similar to those of the 2nd generation, but generally better.

The number of electrons Let the number of electrons per pulse $N_{e\text{-}pulse}$. Generally the $N_{e\text{-}pulse}$ is proportional to Δt_e, and the relationship between N_e and Δt_e depends on the electron gun design ($c_{e\text{-}gun}$ is a constant to characterize the electron gun).

$$N_{e\text{-}pulse} = c_{e\text{-}gun} \cdot \Delta t_e \tag{2.5.2.12}$$

If the scattering cross section ($\sigma_e(s)$) is known, the total number of scattered electrons can be expressed as

$$N_e \cdot \sigma_e(s) \cdot N_{m\text{-}e} = N_e \cdot \sigma_e(s) \cdot N_A \cdot p \cdot \pi \cdot (w_e/2)^2 \cdot w_m/(R \cdot T) \tag{2.5.2.13}$$

where N_e is the total number of electrons. If the fraction of $I_M(s)$ over $I(s)$ is known, the total number of electrons contributing to $I_M(s)$ is

$$\begin{aligned} & N_e \cdot \sigma_e(s) \cdot N_{m\text{-}e} \cdot I_M(s)/I(s) \\ & = (I_M(s)/I(s)) \cdot N_e \cdot \sigma_e(s) \cdot N_A \cdot p \cdot \pi \cdot (w_e/2)^2 \cdot w_m/(R \cdot T) \end{aligned} \tag{2.5.2.14}$$

The repetition rate and exposure time Now let us introduce a parameter for the total experimental exposure time (t_{exp}). Let the laser repetition rate r_{rep} and the number of electrons per pulse $N_{e\text{-}pulse}$. Then,

$$N_e = r_{rep} \cdot N_{e\text{-}pulse} \cdot t_{exp} \qquad (2.5.2.15)$$

The signal-to-noise ratio of ground state data Since the scattering process follows Poisson statistics, the signal-to-noise ratio (SNR_{ground}) of a ground state is

$$SNR_{ground} = c_{ground} \cdot (N_e \cdot \sigma_e(s) \cdot N_{m\text{-}e} \cdot I_M(s)/I(s))^{1/2}$$

$$= c_{ground} \cdot ((I_M(s)/I(s)) \cdot N_e \cdot \sigma_e(s) \cdot N_A \cdot p \cdot \pi \cdot (w_e/2)^2 \cdot w_m/(R \cdot T))^{1/2} \qquad (2.5.2.16)$$

where c_{ground} is a constant. Plugging in the repetition rate and the exposure time gives

$$SNR_{ground} = (N_e \cdot \sigma_e(s) \cdot N_{m\text{-}e} \cdot I_M(s)/I(s))^{1/2}$$

$$= ((I_M(s)/I(s)) \cdot r_{rep} \cdot N_{e\text{-}pulse} \cdot t_{exp} \cdot \sigma_e(s) \cdot N_A \cdot p \cdot \pi \cdot (w_e/2)^2 \cdot w_m/(R \cdot T))^{1/2} \qquad (2.5.2.17)$$

We can see that the signal-to-noise ratio for the ground state data can be boosted up by simply increasing the number of electrons per pulse, the pressure of the molecular beam, the widths of the electron beam and the molecular beam, the repetition rate, and the exposure time. Note that SNR_{ground} is proportional to $r_{rep}^{1/2}$ and $t_{exp}^{1/2}$.

The signal-to-noise ratio of the time-resolved data In the time-resolved diffraction experiments, the actual signal of interest is the change of the diffraction pattern. Therefore, the number of scattered electrons due to the chemical change should be considered. The number of scattered electrons contributing to $\Delta I_M(s)$ after excitation is

$$N_e \cdot \sigma_e(s) \cdot f_{ex} \cdot N_{m\text{-}e\text{-}l} \cdot I_M^{Product}(s)/I^{Product}(s) \qquad (2.5.2.18)$$

It should be noted that these electrons do not necessarily show changes in actual diffraction pattern. To account this, the coefficient i introduced in **2.4.3** should be included.

$$i \cdot N_e \cdot \sigma_e(s) \cdot f_{ex} \cdot N_{m\text{-}e\text{-}l} \cdot I_M^{Product}(s)/I^{Product}(s) \qquad (2.5.2.19)$$

Since the difference signal comes as eq. (2.5.2.17) and the noise still remains as the square root of eq. (2.5.2.14), the final signal-to-noise ratio (SNR_{diff}) for a time-resolved diffraction experiment is

$$SNR_{diff} = c_{diff}\cdot(i\cdot N_e\cdot\sigma_e(s)\cdot f_{ex}\cdot N_{m\text{-}e\text{-}l}\cdot I_M(s)/I(s))/(N_e\cdot\sigma_e(s)\cdot N_{m\text{-}e}\cdot I_M(s)/I(s))^{1/2}$$

$$= c_{diff}\cdot i\cdot f_{ex}\cdot(N_{m\text{-}e\text{-}l}/N_{m\text{-}e}^{1/2})\cdot(N_e\cdot\sigma_e(s)\cdot I_M(s)/I(s))^{1/2} \qquad (2.5.2.20)$$

where c_{diff} is a constant. Plugging in eq. (2.5.2.6) for f_{ex}, eq. (2.5.2.4) for $N_{m\text{-}e\text{-}l}$, (2.5.2.2) for $N_{m\text{-}e}$, eq. (2.5.2.12) for $N_{e\text{-}pulse}$ gives

$$SNR_{diff} = 1/2\cdot(c_{diff}\cdot N_A/\pi/R)^{1/2}\cdot(i\cdot\sigma)\cdot(p/w_m)^{1/2}\cdot(\sigma_e(s)\cdot I_M(s)/I(s))^{1/2}$$

$$\cdot(E_{pulse}/(h\cdot\nu))\cdot r_{rep}^{1/2}\cdot t_{exp}^{1/2}\cdot(c_{e\text{-}gun}\cdot\Delta t_e)^{1/2}\cdot \qquad (2.5.2.21)$$

The term $1/2\cdot(N_A/\pi/R)^{1/2}$ is simply a constant. The term $i\cdot\sigma$ is characteristic of the chemical reaction under investigation. As shown in **2.4**, the absorption cross section and the actual impact of the chemical change on the diffraction change are critical. The term $(p/w_m)^{1/2}\cdot$ characterizes the molecular beam. The $(1/w_m)^{1/2}$ factor comes in because a decreasing w_m decreases the dead volume (the region that sees the electrons but do not see the laser light). The term $(\sigma_e(s)\cdot I_M(s)/I(s))^{1/2}$ is characteristic of the scattering and diffraction process. The term $E_{pulse}/(h\cdot\nu)$ is characteristic of the excitation laser pulse. The term $(c_{e\text{-}gun}\cdot\Delta t_e)^{1/2}$ is characteristic of the electron gun and the chosen temporal pulse width of the electron pulse. SNR_{diff} is proportional to $r_{rep}^{1/2}$ and $t_{exp}^{1/2}$ as SNR_{ground}.

So far the effect of the photon noise (Noi_{light}) caused by the scattered laser light coming into the detection system has been neglected. How the photon noise scales

with the photon energy is not clear at this point. Including the photon noise in eq. (2.5.2.20) gives

$$SNR_{diff} = c_{diff}(i \cdot N_e \cdot \sigma_e(s) \cdot f_{ex} \cdot N_{m\text{-}e\text{-}l} \cdot I_M(s)/I(s)) \\ /[(N_e \cdot \sigma_e(s) \cdot N_{m\text{-}e} \cdot I_M(s)/I(s))^{1/2} + Noi_{light}] \quad (2.5.2.22)$$

If Noi_{light} dominates ($Noi_{light} \gg (N_e \cdot \sigma_e(s) \cdot N_{m\text{-}e} \cdot I_M(s)/I(s))^{1/2}$),

$$SNR_{diff} = c_{diff}(i \cdot N_e \cdot \sigma_e(s) \cdot f_{ex} \cdot N_{m\text{-}e\text{-}l} \cdot I_M(s)/I(s))/(Noi_{light}) \quad (2.5.2.23)$$

If the photon noise follows Poisson statistics, it is proportional to the square root of the total photon energy

$$Noi_{light} = c_{light} \cdot E^{1/2} \quad (2.5.2.24)$$

where c_{light} is a constant. Then SNR_{diff} is independent of r_{rep} and t_{exp}. This has never been observed. Therefore, we can see that Noi_{light} cannot be the dominant over other noises. In general, this can be expressed as

$$Noi_{light} = c_{light} \cdot E^{z} \quad (2.5.2.25)$$

c_{light} and z can be experimentally obtained using eq. (2.5.2.22).

References

1. Aeschlimann, M. *et al.* A picosecond electron gun for surface analysis. *Rev. Sci. Instrum.* **66**, 1000-1009 (1995).
2. Tsang, T. Measurement of femtosecond electron bunches from metal photocathodes. *Appl. Phys. Lett.* **63**, 871-873 (1993).
3. Kawasaki, M., Lee, S. J. & Bersohn, R. Photodissociation of molecular beams of methylene iodide and iodoform. *J. Chem. Phys.* **63**, 809-814 (1975).
4. Koffend, J. B. & Leone, S. R. Tunable Laser Photodissociation: Quantum Yield Of I*(2P1/2) From CH_2I_2. *Chem. Phys. Lett.* **81**, 136-141 (1981).
5. Pence, W. H., Baughcum, S. L. & Leone, S. R. Laser UV Photofragmentation of Halogenated Molecules. Selective Bond Dissociation and Wavelength-Specific Quantum Yields for Excited I($^2P_{1/2}$) and Br($^2P_{1/2}$) Atoms. *J. Phys. Chem.* **85**, 3844-3851 (1981).
6. Hunter, T. F. & Kristjansson, K. S. Yield Of I($^2P_{1/2}$) In The Photodissociation Of CH_2I_2. *Chem. Phys. Lett.* **90**, 35-40 (1982).
7. Baughcum, S. L. & Leone, S. R. Photofragmentation infrared emission studies of vibrationally excited free radicals CH_3 and CH_2I. *J. Chem. Phys.* **72**, 6531-6545 (1980).
8. Cao, J., Ihee, H. & Zewail, A. H. Ultrafast electron diffraction and direct observation of transient structures in a chemical reaction. *Proc. Natl. Acad. Sci. USA* **96**, 338-342 (1999).

9. Zewail, A. H. *Femtochemistry: Ultrafast Dynamics of the Chemical Bond* (World Scientific, Singapore, 1994).

10. Dantus, M., Kim, S. B., Williamson, J. C. & Zewail, A. H. Ultrafast Electron Diffraction. 5. Experimental Time Resolution and Applications. *J. Phys. Chem.* **98**, 2782-2796 (1994).

11. Williamson, J. C. & Zewail, A. H. Ultrafast electron diffraction. Velocity mismatch and temporal resolution in crossed-beam experiments. *Chem. Phys. Lett.* **209**, 10-16 (1993).

12. Kimura, K. & Nagakura, S. n -> σ* Absorption spectra of saturated organic compounds containing bromine and iodine. *Spectrochim. Acta* **17**, 166-183 (1961).

13. Wannenmacher, E. A. J., Felder, P. & Huber, J. R. The simultaneous three-body dissociation of CF_2I_2. *J. Chem. Phys.* **95**, 986-997 (1991).

14. Kotzian, M., Rosch, N., Schroder, H. & Zerner, M. C. Optical Spectra of Transition-Metal Carbonyls: $Cr(CO)_6$, $Fe(CO)_5$ and $Ni(CO)_4$. *J. Am. Chem. Soc.* **111**, 7687-7696 (1989).

15. Gerck, E. Quantum yields of $I(^2P_{1/2})$ for CF_3I, C2F5I, i-C_3F_7I, n-C3F7I, n-$C_6F_{13}I$, and 1,2-$C_2F_4I_2$ at 308 and 248 nm. *J. Chem. Phys.* **79**, 311-315 (1983).

16. Wasserman, E. P., Bergan, R. G. & Moore, C. B. IR Flash Kinetic Spectroscopy of Transients Generated by Irradiation of (h_5-C_5H_5)$Co(CO)_2$ in the Gas Phase and in Solution. *J. Am. Chem. Soc.* **110**, 6076-6084 (1988).

17. McDiarmid, R. & Sabljic, A. Valence transitions in 1,3-cyclopentadiene, 1,3-

cyclohexadiene, and 1,3-cycloheptadiene. *J. Chem. Phys.* **83**, 2147-2152 (1985).

18. Benzler, J., Linkersdorfer, S. & Luther, K. Density dependence of the collisional deactivation of highly vibrationally excited cycloheptatriene in compressed gases, supercritical fluids, and liquids. *J. Chem. Phys.* **106**, 4992-5005 (1997).

19. Perkampus, H.-H., Sandeman, I. & Timmons, C. J. (eds.) *UV ATLAS of Organic Compounds* (Verlag Chemie, London, 1966).

20. Phillips, J. P., Lyle, R. E. & Jones, P. R. (eds.) *Organic Electronic Spectral Data* (Interscience Publishers, New York, 1960).

21. Haszeldine, R. N. Studies in Spectroscopy. Part III. The Ultra-violet Absorption Spectra of Halogen-containing Aliphatic Iodo-compounds, and the Relative Stability of Free Halogen-containing Alkyl Radicals. *J. Chem. Soc. (London)* **Part 2**, 1764-1771 (1953).

Table 2.4.1 The temperatures and pressures for the samples studied in the second generation UED

	$Fe(CO)_5$	CH_2I_2	CF_2I_2	$C_2F_4I_2$	$CpCo(CO)_2$
Boing point (T_b)	103 °C	181 °C	80 °C	113 °C	140 °C/710 mm
Calculated T to get 10 torr	−8 °C	46 °C	−25 °C	−2 °C	19 °C
Actual T used for sample	40 °C	110 °C	21 °C	41 °C	95 °C
Estimated p for sample	97 torr	114 torr	100 torr	73 torr	203 torr
Actual T used for needle	70 °C	163 °C	44 °C	63 °C	151 °C

Table 2.4.2 The temperatures of the needle, manifold, and sample container for the chemicals studied in the 2nd generation UED. In the case that muptiple experiments were performed for the sample, only one experiment is arbitrarily chosen and their temperatures are reported here.

	T_b	T_{needle}	$T_{manifold}$	T_{sample}
CH_2I_2	181 °C	163 °C	155 °C	108 °C
CF_2I_2	80 °C	44 °C	39 °C	33 °C
$Fe(CO)_5$	103 °C	68 °C	65 °C	38 °C
$C_2F_4I_2$	113 °C	63 °C	55 °C	41 °C
$CpCo(CO)_2$	140 °C	151 °C	144 °C	95 °C

Table 2.4.3 The temperatures of the needle, manifold, and sample container for the chemicals studied in the 3rd generation UED. In the case that muptiple experiments were performed for the sample, only one experiment is arbitrarily chosen and their temperatures are reported here.

	T_b	T_{needle}	$T_{manifold}$	T_{sample}
$C_2F_4I_2$	113 °C	120 °C	100 °C	60 °C
CHD	80 °C	120 °C	100 °C	80 °C
CHT	116 °C	130 °C	120 °C	110 °C
Pyridine	115 °C	130 °C	120 °C	100 °C

Table 2.4.4 The absorption cross sections of the molecules studies in UED and other molecules that have been considered and have potential to be investigated in the future are presented for the typical wavelengths available for CPM laser and Ti:Sapphire laser. The molecules already studied in UED are indicated in bold style.

Chemical	Absorption cross section	Ref.
CH_2I_2	**$\sigma_{310\ nm} = 3.2 \times 10^{-18}\ cm^2$**	12
	$\sigma_{266\ nm} = 1.3 \times 10^{-18}\ cm^2$	
	$\sigma_{200\ nm} = 6.8 \times 10^{-18}\ cm^2$	
CF_2I_2	**$\sigma_{307\ nm} = 2.3 \times 10^{-18}\ cm^2$**	13
	$\sigma_{266\ nm} = 1.9 \times 10^{-18}\ cm^2$	
	$\sigma_{200\ nm} = 38 \times 10^{-18}\ cm^2$	
$Fe(CO)_5$	**$\sigma_{310\ nm} = 3 \times 10^{-18}\ cm^2$**	14
	$\sigma_{266\ nm} = 18 \times 10^{-18}\ cm^2$	
	$\sigma_{200\ nm} = 114 \times 10^{-18}\ cm^2$	
$C_2F_4I_2$	**$\sigma_{310\ nm} = 0.8 \times 10^{-18}\ cm^2$**	15
	$\sigma_{266\ nm} = 2 \times 10^{-18}\ cm^2$	
	$\sigma_{200\ nm} > 3.5 \times 10^{-18}\ cm^2$	
$CpCo(CO)_2$	**$\sigma_{310\ nm} = 5.3 \times 10^{-18}\ cm^2$**	16

CHD (1,3-cyclohexadiene) 	$\sigma_{310\ nm} < 0.001 \times 10^{-18} cm^2$ **$\sigma_{266\ nm} = 6.9 \times 10^{-18}\ cm^2$** $\sigma_{200\ nm} = 18 \times 10^{-18}\ cm^2$	17
CHT (cycloheptatriene) 	$\sigma_{310\ nm} = 0.038 \times 10^{-18} cm^2$ **$\sigma_{266\ nm} = 4.2 \times 10^{-18}\ cm^2$** $\sigma_{200\ nm} = 38 \times 10^{-18}\ cm^2$	18
Pyridine 	$\sigma_{310\ nm} < 0.01 \times 10^{-18}\ cm^2$ **$\sigma_{266\ nm} = 2.7 \times 10^{-18}\ cm^2$** $\sigma_{200\ nm} = 19 \times 10^{-18}\ cm^2$	19
$Cr(CO)_6$	$\sigma_{310\ nm} = 6.5 \times 10^{-18}\ cm^2$ $\sigma_{266\ nm} = 30 \times 10^{-18}\ cm^2$ $\sigma_{200\ nm} = 31 \times 10^{-18}\ cm^2$	14
$Ni(CO)_4$	$\sigma_{310\ nm} = 1.9 \times 10^{-18}\ cm^2$ $\sigma_{266\ nm} = 17 \times 10^{-18}\ cm^2$ $\sigma_{200\ nm} = 69 \times 10^{-18}\ cm^2$	14
	$\sigma_{310\ nm} < 0.001 \times 10^{-18} cm^2$ $\sigma_{266\ nm} < 0.1 \times 10^{-18}\ cm^2$ $\sigma_{200\ nm} = 4.7 \times 10^{-18}\ cm^2$	17
	$\sigma_{310\ nm} < 0.001 \times 10^{-18} cm^2$	17

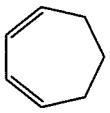	$\sigma_{266\ nm} = 0.9 \times 10^{-18}\ cm^2$ $\sigma_{200\ nm} = 10 \times 10^{-18}\ cm^2$	
CHI_3	**$\sigma_{310\ nm} = 5.7 \times 10^{-18}\ cm^2$** $\sigma_{266\ nm} = 4.8 \times 10^{-18}\ cm^2$ $\sigma_{200\ nm} > 6.8 \times 10^{-18}\ cm^2$	12
Acetone	$\sigma_{266\ nm} = 68 \times 10^{-18}\ cm^2$	NIST
Acetone	$\sigma_{266\ nm} = 0.1 \times 10^{-18}\ cm^2$ $\sigma_{195\ nm} = 35 \times 10^{-18}\ cm^2$	20
Allyl alcohol	$\sigma_{273\ nm} = 39 \times 10^{-18}\ cm^2$	20
Epoxypropane	$\sigma_{272\ nm} = 31 \times 10^{-18}\ cm^2$	20
Allyl Iodide	**$\sigma_{266\ nm} = 2.3 \times 10^{-18}\ cm^2$**	21
ICH_2CH_2I	**$\sigma_{266\ nm} = 5.2 \times 10^{-18}\ cm^2$**	21
Cyclooctatetraene 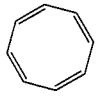	$\sigma_{310\ nm} = 0.8 \times 10^{-18}\ cm^2$ $\sigma_{266\ nm} = 1.0 \times 10^{-18}\ cm^2$ $\sigma_{200\ nm} = 96 \times 10^{-18}\ cm^2$	19
1,3,5-cyclooctatriene 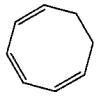	$\sigma_{267\ nm} = 15 \times 10^{-18}\ cm^2$	20

Table 2.5.1 Estimated overlap parameters for the 2nd generation UED

	$Fe(CO)_5$	CH_2I_2	$C_2F_4I_2$
E_{pulse}	250 μJ	250 μJ	450 μJ
σ	3×10^{-18} cm^2	3.2×10^{-18} cm^2	0.8×10^{-18} cm^2
λ	310 nm	310 nm	310 nm
w_l	~400 μm	~400 μm	~400 μm
$(1/3)\cdot f_{ex}$	0.31	0.33	0.15
$(1/3)\cdot f_{ex}$ $(N_{m\text{-}e\text{-}l}/N_{m\text{-}l})$	0.12	0.15	0.08
$(N_{m\text{-}e\text{-}l}/N_{m\text{-}l})$	0.39	0.45	0.53

Table 2.5.2 Estimated overlap parameters for the 3rd generation UED

	$C_2F_4I_2$	CHD	CHT	Pyridine
E_{pulse}	~100 μJ	~100 μJ	~100 μJ	~150 μJ
σ	2×10^{-18} cm^2	6.9×10^{-18} cm^2	4.2×10^{-18} cm^2	2.7×10^{-18} cm^2
λ	267 nm	267 nm	267 nm	267 nm
w_l	~350 μm	~400 μm	~400 μm	~400 μm
$(1/3)\cdot f_{ex}$	0.09	0.25	0.15	0.14
$(1/3)\cdot f_{ex}$ $(N_{m\text{-}e\text{-}l}/N_{m\text{-}l})$	0.08	0.12	0.06	0.07
$(N_{m\text{-}e\text{-}l}/N_{m\text{-}l})$	0.88	0.48	0.40	0.50

Figure Captions

Figure 2.1.1: A schematic of the experimental setup used here for ultrafast electron diffraction (2^{nd} generation). It is composed of a fs excitation laser, a ps pulsed-electron source, a free-expansion molecular beam, and a two-dimensional single-electron detection system. The electron pulse, the laser pulse, and the molecular beam are arranged in a crossed-beam geometry. The fs laser pulse is directed to the molecules in the interaction volume in the molecular beam and initiates a chemical reaction. After a certain time delay, the ps electron pulse arrives at the interaction volume and scatters off the molecules composed of the parent molecule and other photo-induced species. The interference pattern (diffraction) of the scattering electron wave at each time delay is recorded in the two-dimensional single-electron detection system. The time delays are controlled by a computer-driven translational stage.

Figure 2.2.1: (Top) The colliding-pulse, mode-locked ring dye laser (CPM) which generates femtosecond laser pulses for the UGED laboratory. SA: saturable absorber; OC: output coupler (2%); G: refraction grating for observing laser pulse spectrum. (Bottom) The pulsed dye amplifier (PDA) for amplifying the output of the CPM. SA: saturable absorber; BS: beam splitter; C#: dye cell; PH: pinhole spatial filter; CL: cylindrical lens; F: filter; CM: dichroic mirror; S: beam stop.

Figure 2.2.2: A schematic of laser setup: M, mirror; L, lens; BS, beam splitter; SHG, second harmonic generation crystal (KD*P).

Figure 2.2.3: A schematic of UED apparatus consisting of an electron gun chamber, a diffraction chamber and a detector chamber. Two fs laser pulses are used; the first initiates the chemical change and the second generates the electron pulse.

Figure 2.2.4: Detection scheme. Incident electrons either directly bombard a small CCD or strike a phosphor-coated fused fibber-optic window. Light emitted from the phosphor is amplified by an image intensifier and brought to a scientific-grade CCD. Both CCDs are thermoelectrically cooled.

Figure 2.2.5: UED electron apparatus. Photoelectrons were extracted from the photocathode through a pinhole, and collimated and focused with electrostatic optics in the electron gun. The electron beam traveled through a final pinhole, deflection plates, and exited the electron gun chamber via a butterfly valve and differential-pumping aperture. In the scattering chamber, electrons passed under the molecular beam nozzle tip and were detected either by direct bombardment on a CCD, or by emission from a phosphor scintillator.

Figure 2.2.6: Dimensions of the ultrashort electron gun.

Figure 2.2.7: A schematic of the sample inlet system. The molecular sample enters the diffraction chamber in a free-jet expansion through a needle. When the sample has insufficient vapor pressure at room temperature, the needle, inlet tube, and sample holder are heated with wrapped heating tapes. The position of the needle is controlled by an XYZ position translator.

Figure 2.3.1: A schematic of the experimental setup for the streak experiment; M, mirror; L, lens; BS, beamsplitter; SHG, KD*P crystal; VD, variable delay; R, 5 MΩ resister; C, 500 pF capacitor.

Figure 2.3.2: Surface contour plots of low and high-intensity streaked electron pulse pairs. Each pair comes from two incident light pulses, one of which is delayed by 66.7 ps. The horizontal coordinate is the streaking axis. The temporal durations of pulses with high electron numbers (top trace -- 7400 e^-, 6.6 ps; 3790 e^-, 4.3 ps) are broadened by space-charge effects. For low electron numbers (bottom trace -- 295 e^-, 0.5 ps; 150 e^-, 0.5 ps), measurement of the pulse width is limited by the resolution of the streak experiment. The electron pulse width was obtained by subtracting the width of the unstreaked electron beam (4 pix) from the width of the streaked pulses (Lorentzian profiles).

Figure 2.3.3: Measured electron pulse widths as a function of the number of electrons. The streak velocity was 2.1 pix/ps, or 1.6×10^8 m/s. The sweep voltage is ~1 kV/ns. Uncertainty in the pulse width measurements was on the order of 1 ps. The bottom curve is replotted from the top curve with a logarithmic temporal axis. There is a linear relationship between the number of electrons per pulse and the electron pulse width; 1000 electrons per 1 ps.

Figure 2.3.4: Sequence of photoionization-induced lensing. (Top Left) Excitation laser is incident on the molecular beam. (Top Right) Excitation laser ionizes molecules within the sample through multiphoton absorption. The nascent electrons exit the interaction region within picoseconds, while the positive ions remain behind.

(Bottom) The incident electron beam is deflected by the horizontal column of positive charge, and the altered beam shape is detected on the direct bombardment CCD.

Figure 2.3.5: (Top) Change in the electron beam vertical profile with time. The nozzle tip is located on the left side of each profile. (Bottom) Typical Photoionization-induced lensing (PIL) transient. No lensing occurs in the absence of the molecular beam.

Figure 2.3.6: Examples of PIL transients, recorded on different days, which exhibit very fast initial rises. The left-hand figure shows that the horizontal electron beam profile is unaffected by lensing.

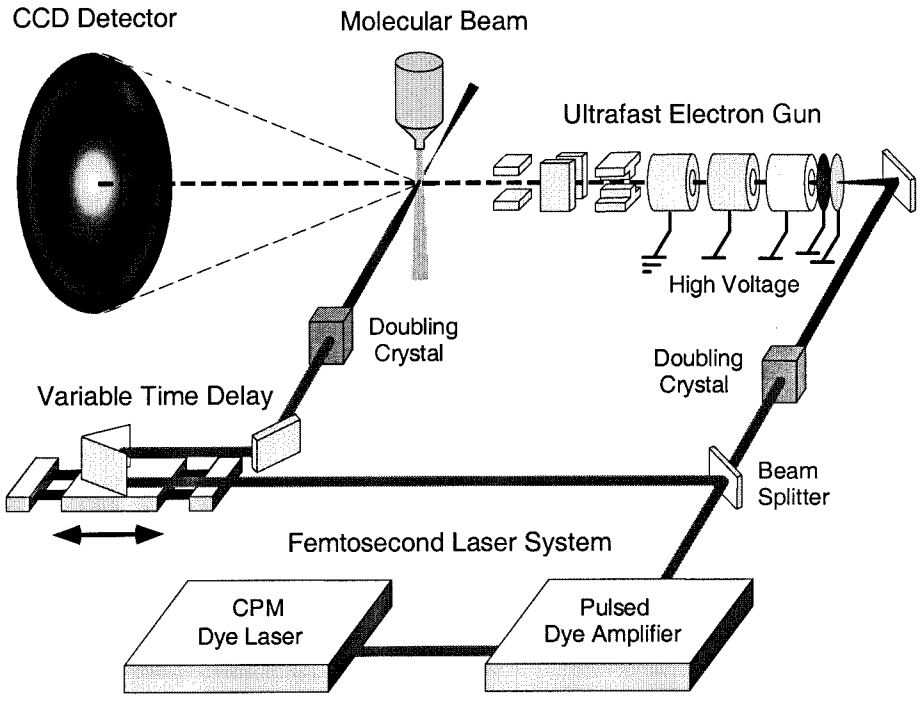
CCD Detector
Molecular Beam
Ultrafast Electron Gun
High Voltage
Doubling Crystal
Doubling Crystal
Variable Time Delay
Beam Splitter
Femtosecond Laser System
CPM Dye Laser
Pulsed Dye Amplifier

Figure 2.1.1

Colliding Pulse, Mod-Locked Ring Dye Laser

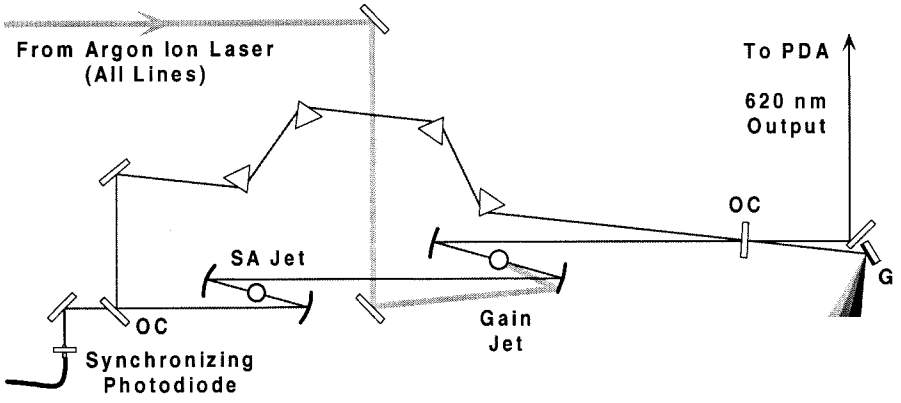

Pulsed Dye Amplifier

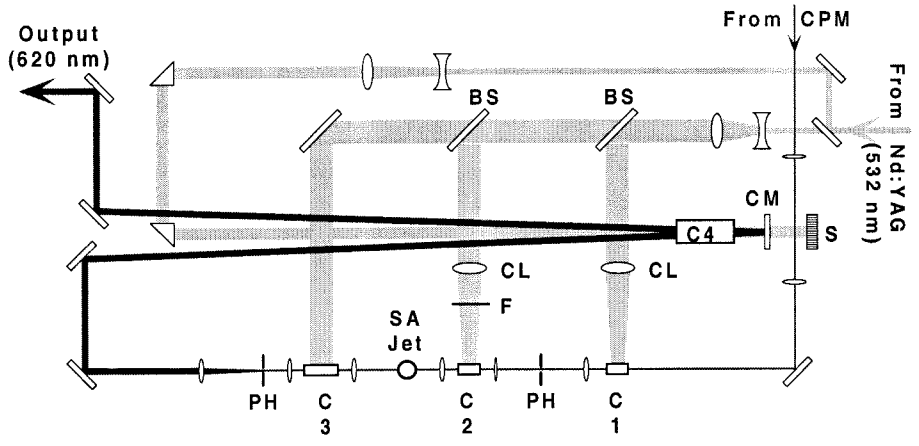

Figure 2.2.1

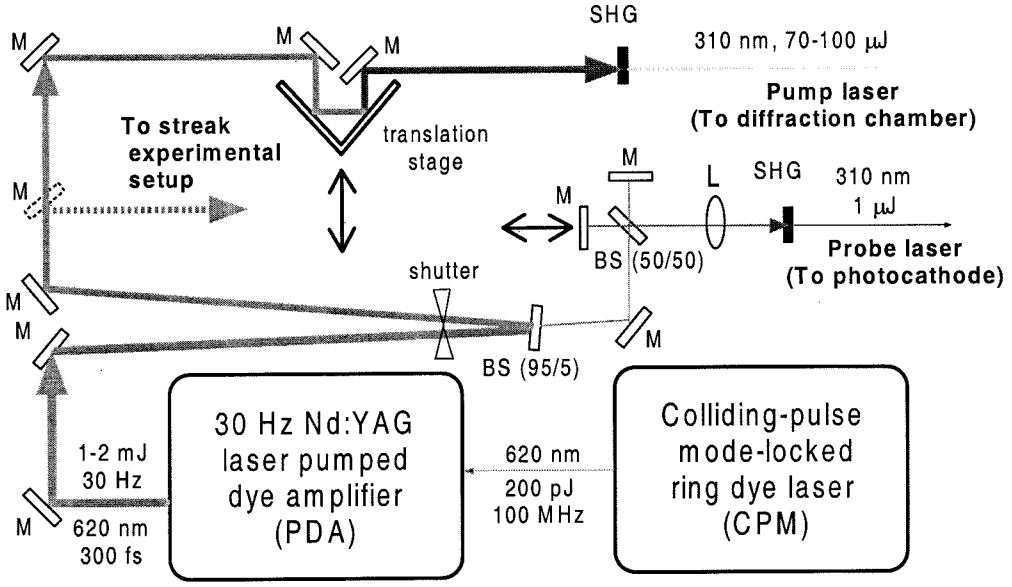
SHG
310 nm, 70-100 μJ
Pump laser
(To diffraction chamber)
M
M
M
To streak
experimental
setup
translation
stage
M
M
L
SHG
310 nm
1 μJ
Probe laser
(To photocathode)
BS (50/50)
shutter
M
M
BS (95/5)
M
30 Hz Nd:YAG
laser pumped
dye amplifier
(PDA)
1-2 mJ
30 Hz
M
620 nm
300 fs
620 nm
200 pJ
100 MHz
Colliding-pulse
mode-locked
ring dye laser
(CPM)

Figure 2.2.2

Chamber system

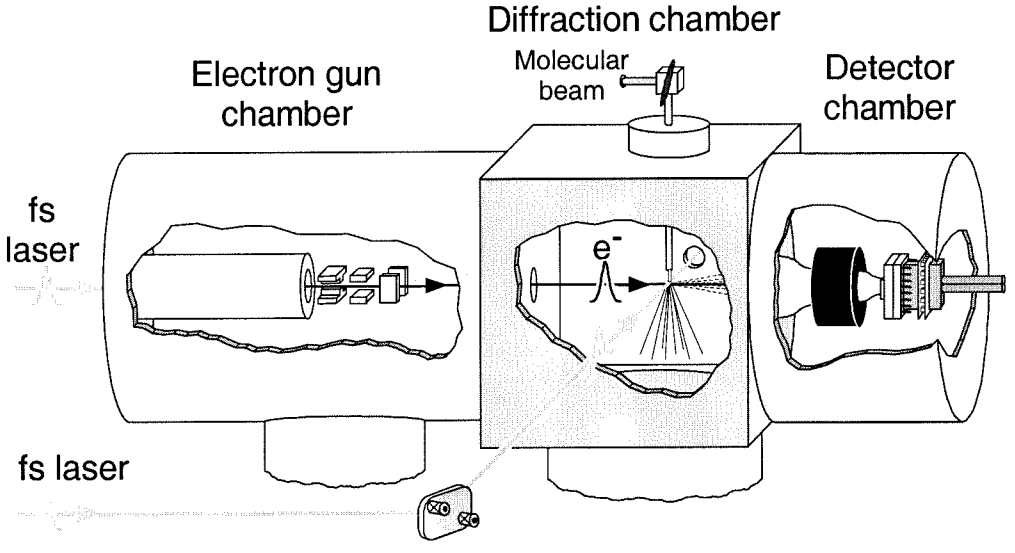

Figure 2.2.3

Detection system

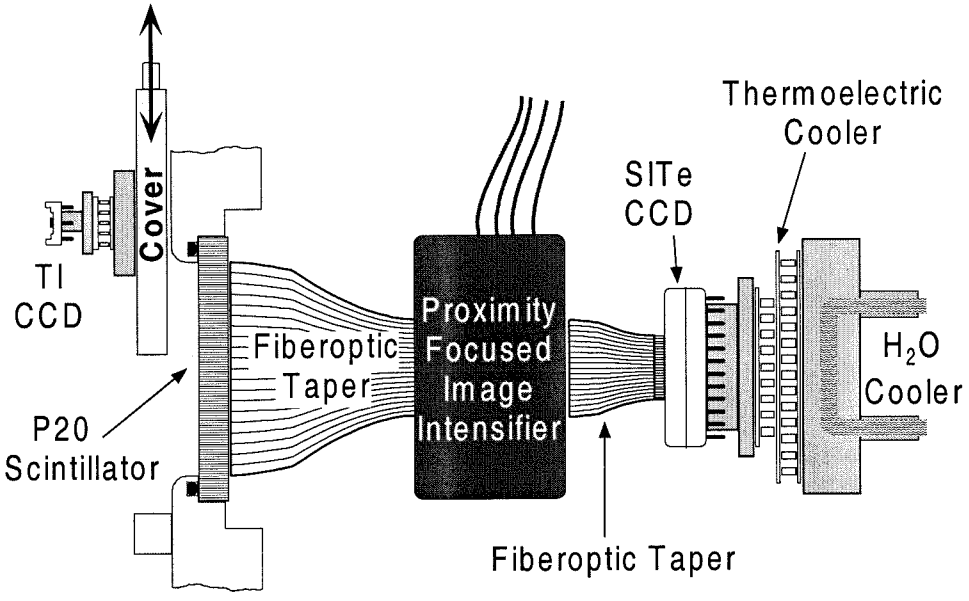

Figure 2.2.4

UED electron apparatus

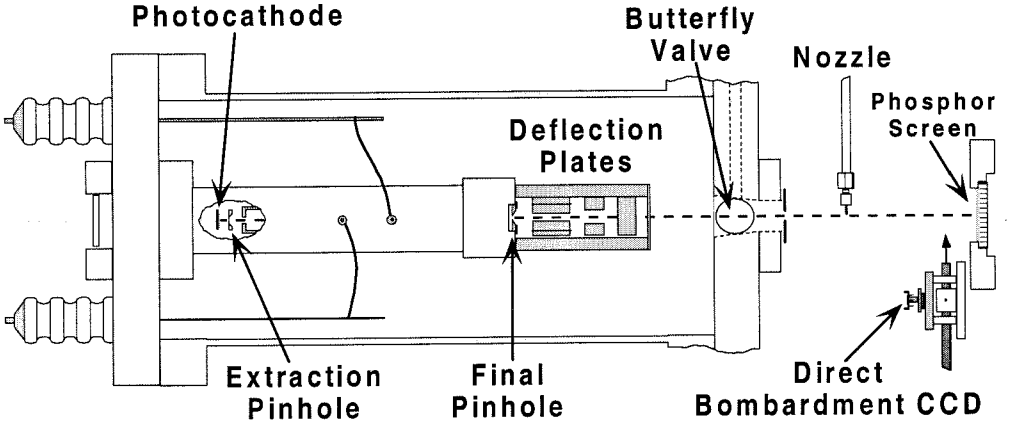

Figure 2.2.5

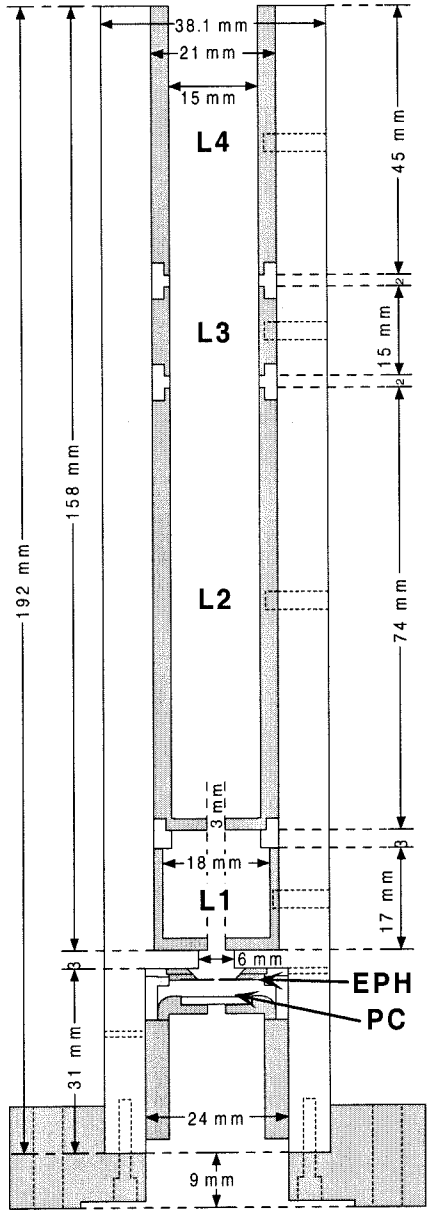
38.1 mm
21 mm
15 mm
L4
L3
L2
L1
45 mm
15 mm
74 mm
17 mm
3 mm
18 mm
6 mm
EPH
PC
192 mm
158 mm
31 mm
24 mm
9 mm

Figure 2.2.6

Sample inlet system

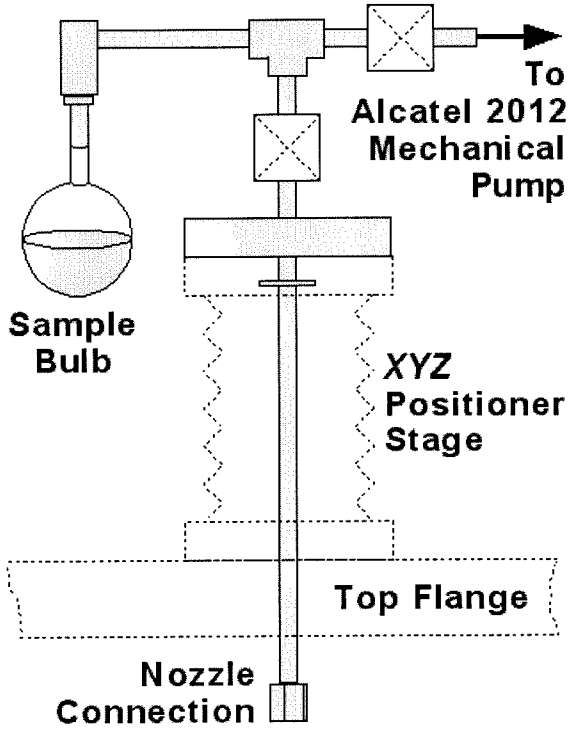

Figure 2.2.7

Streak experiment to measure e-beam width

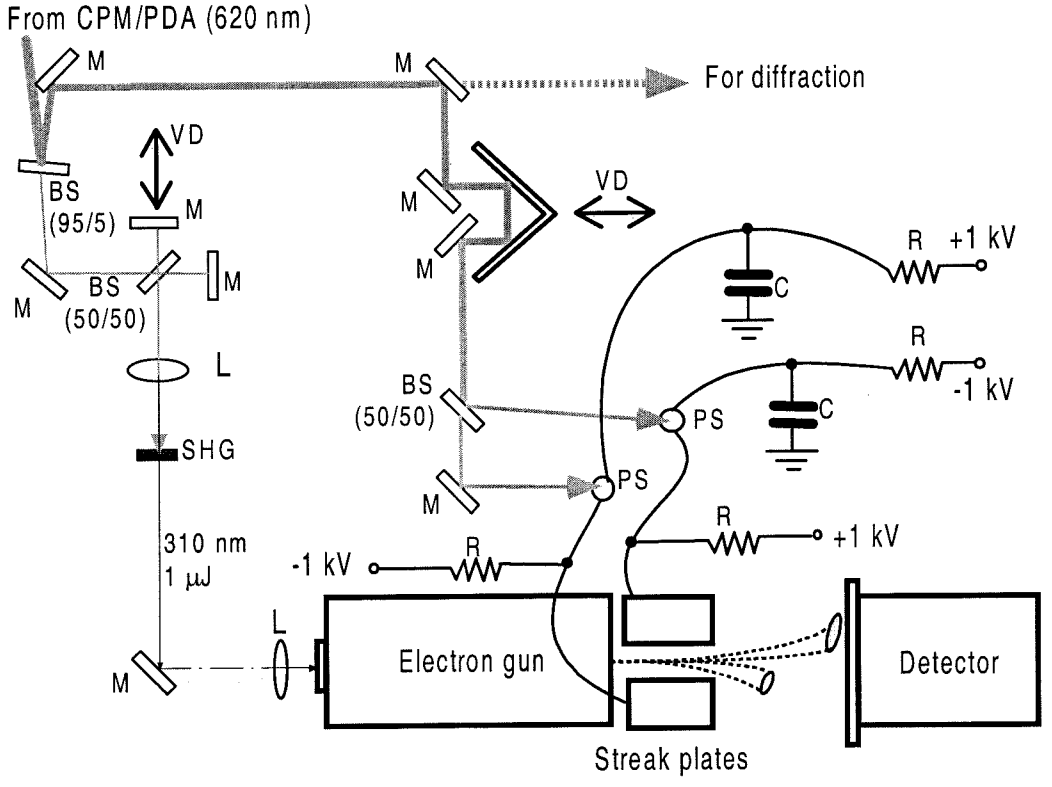

Figure 2.3.1

Streak image pairs

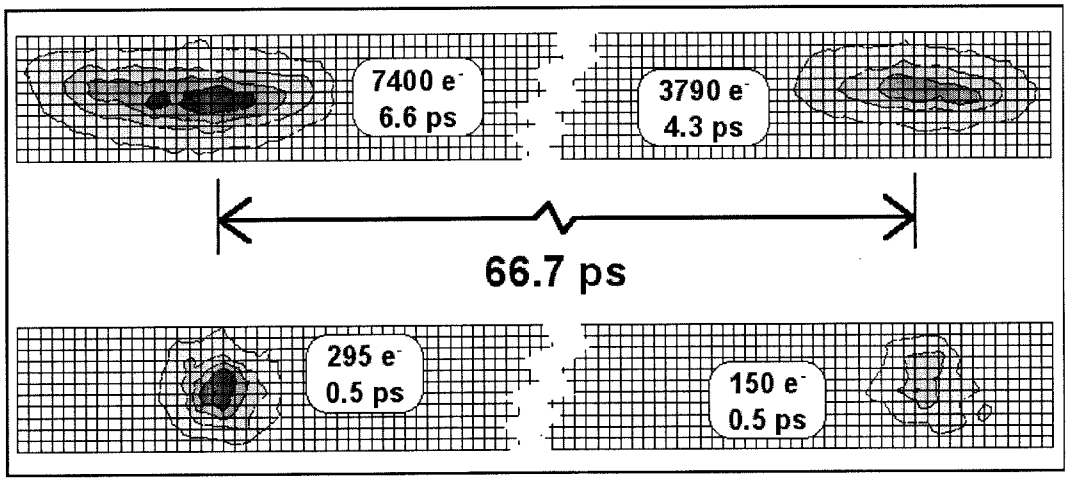

Figure 2.3.2

Pulse width vs. number of electrons

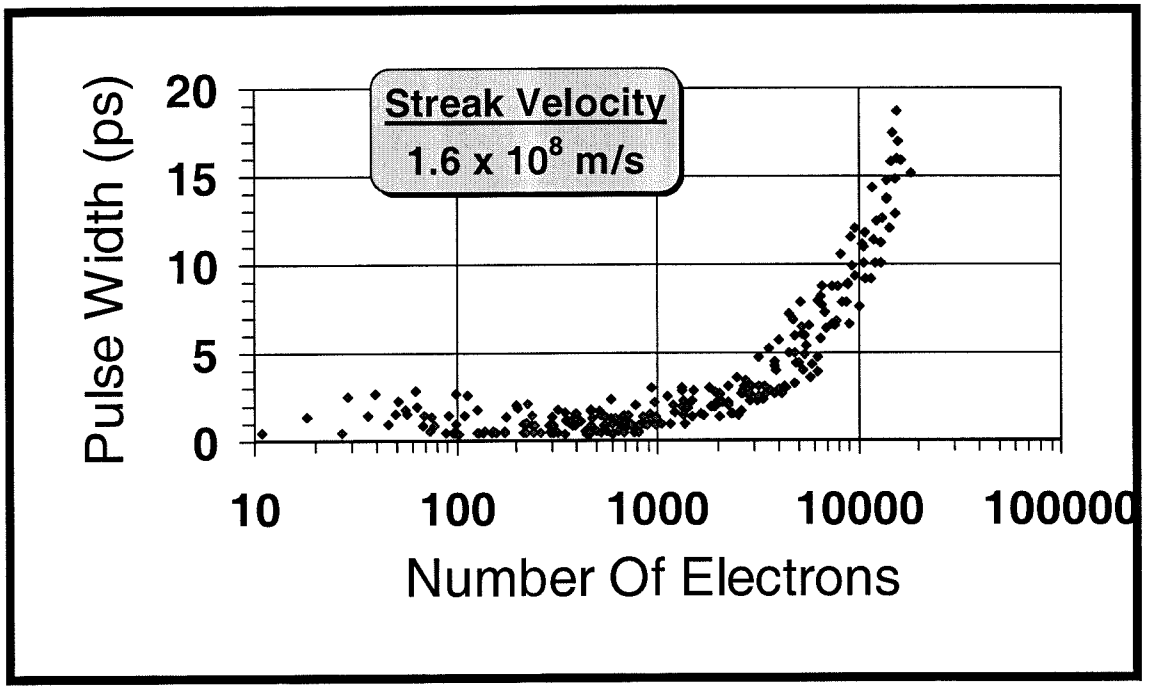

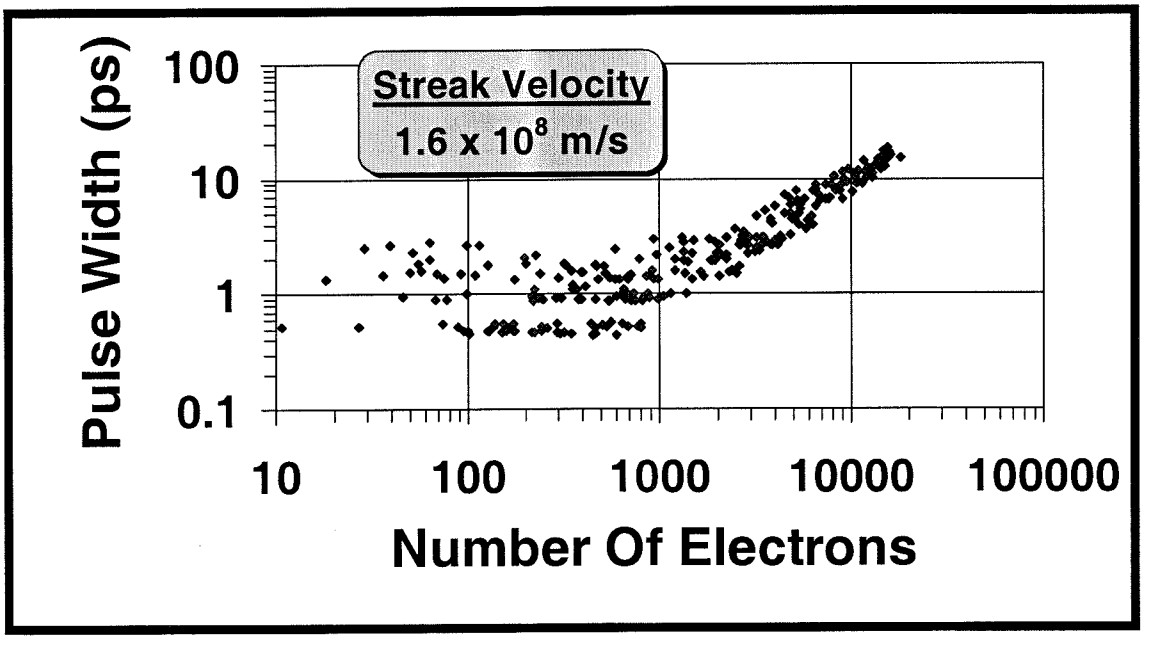

Figure 2.3.3

Photoionization-induced lensing

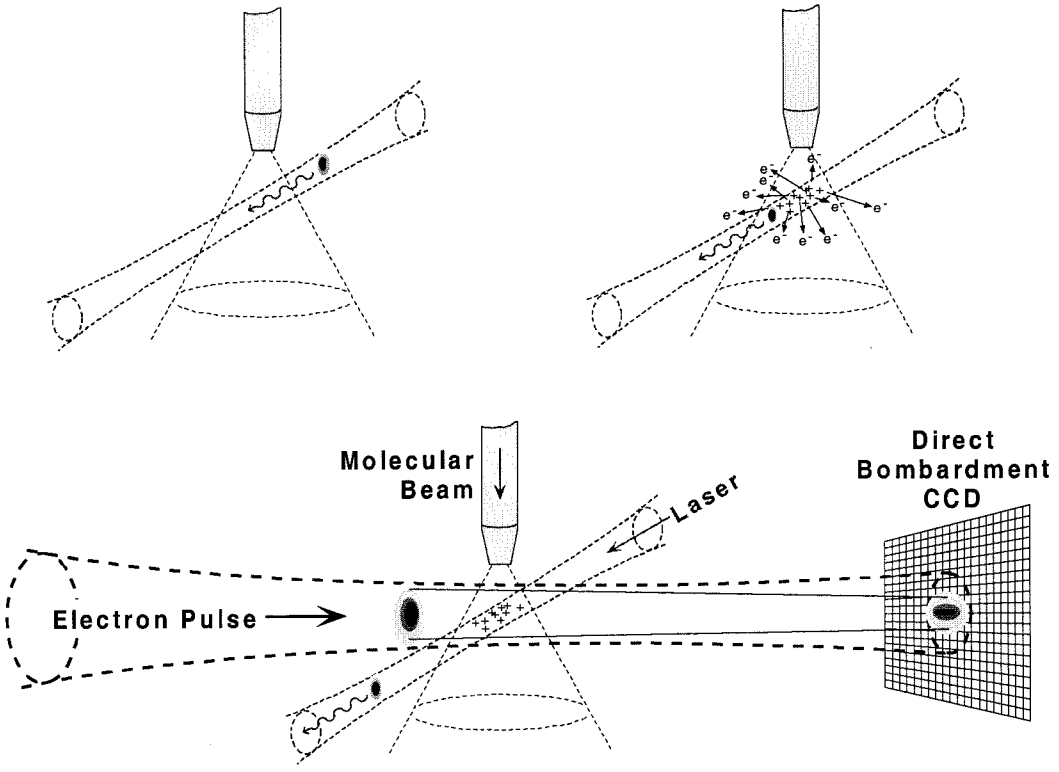

Figure 2.3.4

Change in the electron beam vertical profile with time

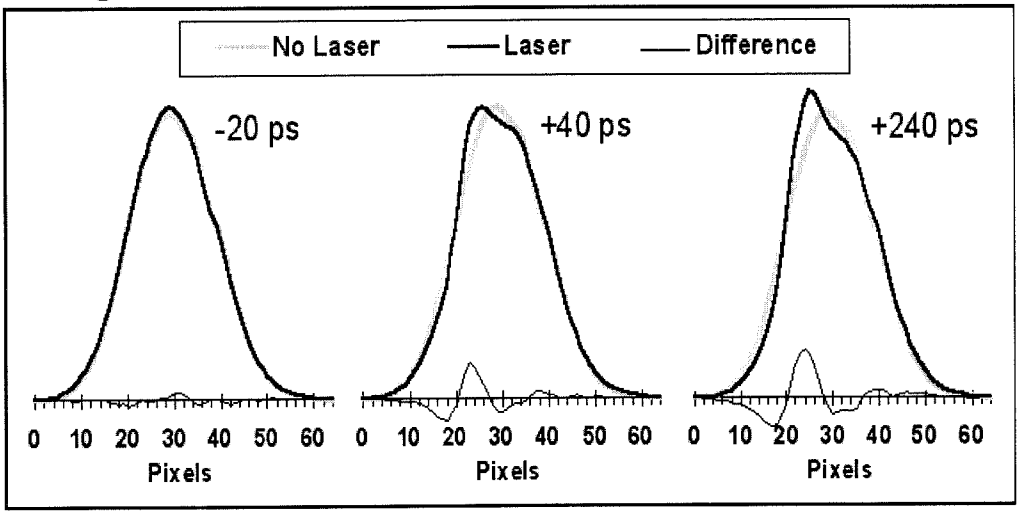

Typical PIL transient

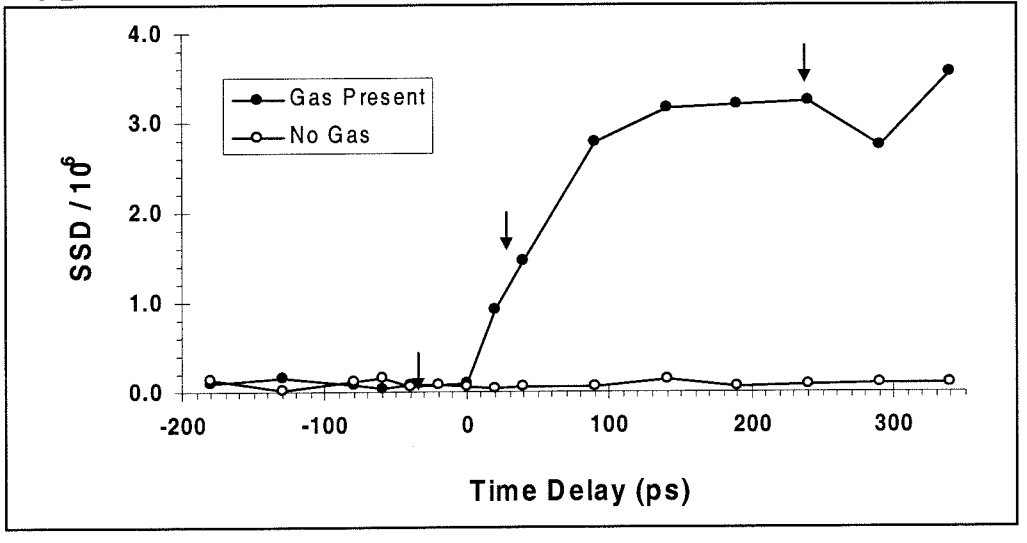

Figure 2.3.5

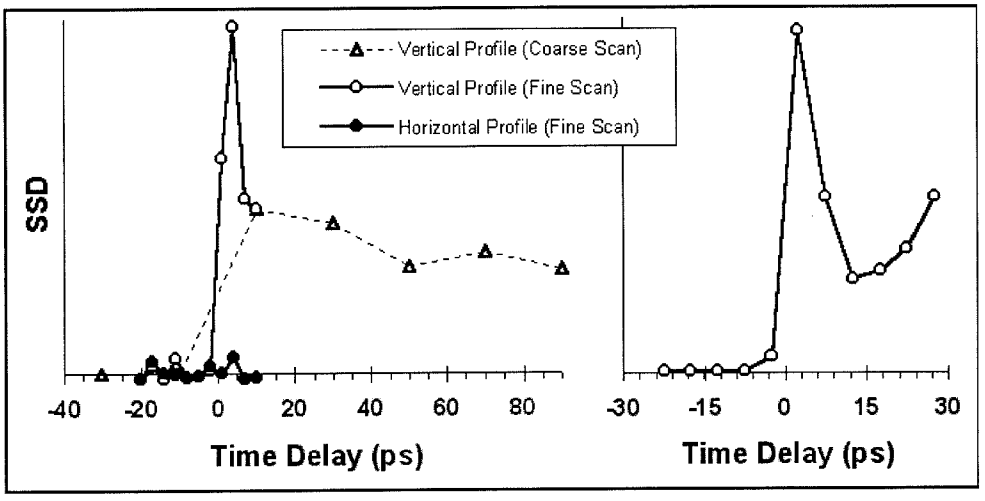
Vertical Profile (Coarse Scan)
Vertical Profile (Fine Scan)
Horizontal Profile (Fine Scan)
SSD
-40
-20
0
20
40
60
80
Time Delay (ps)
-30
-15
0
15
30
Time Delay (ps)

Figure 2.3.6

CHAPTER THREE

ADVANCEMENT OF UED APPARATUS

3.1 The 3rd Generation UED Apparatus

The need for greater sensitivity and resolution, as well as the desire to study more complex reactions, led to the development of our third-generation UED apparatus (Fig. 3.1.1). This new machine, with vast improvements in pulsed electron flux, repetition rate, detection sensitivity, and experimental stability, permits the direct imaging of complex chemical reactions with unprecedented spatial and temporal resolution. The spatial and temporal resolution of UED approached ~0.01 Å and ~1 ps, respectively, and we were sensitive to ~1% changes in the mole fractions of the various chemical species over the course of the reaction. A brief description of the 3rd generation machine with the comparisons to the 2nd generation apparatus is given.

3.1.1 Laser System

The laser system consisted of a mode-locked Ti:Sapphire oscillator and a Ti:Sapphire regenerative amplifier system. Femtosecond laser pulses (82 MHz, ~120 fs @ 11 nm bandwidth, ~8.5 nJ) are generated from the Tsunami (Spectra Physics, fs standard configuration Model 3960) system. The average output power is ~700 mW with a pump energy of 4.5 W. The tuning range is 735 – 840 nm. An all solid-state, diode pumped CW Visible laser (Spectra Physics, MilleniaV) equipped with two fiber-coupled 20 W diode laser bars pumps the Ti:Sapphire oscillator. The gain medium inside the solid-state laser is Neodymium yttrium vanadate (Nd:YVO_4) and its maximum output is 5 W at 532 nm.

The femtosecond amplification system consists of two Nd:YLF lasers (Spectra

Physics, Merlin, ~250 ns pulses @ 1 kHz, 10 mJ) and a Ti:Sapphire regenerative amplifier system (Spectra Physics, "Super" Spitfire). The second harmonics (527 nm) of the Nd:YLF are used to pump the Ti:Sapphire regenerative amplifier, which creates ~120 fs pulses with 3 mJ per pulse. A tripler (Uniwave fs TP-1A system) is used to triple the fs pulses from 800 nm to 266 nm. The typical output energy is ~400 μJ.

A beam splitter separates the output beam into a pump beam and an electron generation beam so that the majority of the tripler output goes into the pump arm. For electron beam generation, the remainder enters a Michelson interferometer. Just one arm of the interferometer is used for the usual diffraction experiment; streaking experiments require two electron pulses. One of the laser beams in the Michelson interferometer goes through computer-driven translation stage and is directed onto the photocathode for photoelectron generation.

3.1.2 Electron gun

The construction of our electron gun is based on the design provided by the Elsayed-Ali group. The cylindrically symmetric gun consisted of a photocathode, an extraction mesh, and a magnetic lensing system. The photocathode was made by coating a sapphire window with a 450 Å silver film using a home-built evaporation chamber. Usually about −30 kV is applied to the photocathode and the extraction mesh is grounded. The extraction field is 6 kV/mm, which is more than two times better than that of the 2nd generation electron gun (2.72 kV/mm). The focusing of the electron pulse is achieved by a magnetic lens. Three pairs of aluminum

deflection plates are mounted at the end of the electron gun. The last pair is the streaking electrodes. The remaining two pairs are deflection electrodes, which control the horizontal and vertical position of the electron beam.

The ultrafast electron pulse was generated when the femtosecond laser pulse (266 nm) strikes the silver photocathode in back illumination mode. This electrons are accelerated to the extraction mesh, and focused and shaped by magnetic lens. The direction of the output electron beam is controlled by the deflection plates. As mentioned before, a smaller interaction volume is preferable because of velocity mismatch. To reduce the interaction volume, the electron beam size in the interaction volume should be small. The electrode voltages are adjusted so that the electron beam focal point is near the interaction volume beneath the molecular beam needle. The electron beam diameter at the interaction volume is about 350 μm. In addition to the small electron beam size in the interaction volume, the electron beam should have a well-collimated profile since the small spot size on the detector is necessary for a high spatial resolution of the diffraction pattern. The divergence of the electron beam is almost an order of magnitude better than that of the 2nd generation.

3.1.3 Vacuum Chambers

The vacuum chamber is divided into four sections: the electron gun chamber, the diffraction chamber, and the time-of-flight chamber for mass spectrometry (see Figure 3.1.1). The electron gun chamber and the diffraction chamber are separated by a small hole. Differential pumping is achieved by introducing a turbo pump system

beneath the electron gun and a large oil diffusion pump for the diffraction chamber. The detection chamber is separated from the diffraction chamber by an o-ring seal and from the time-of-flight chamber by a gate valve. The system pressures are monitored by ionization gauges. By separating the electron gun chamber from the diffraction chamber and pumping the two chambers differentially, the electron gun maintains a pressure of 5×10^{-8} Torr or less, which is low enough to prevent arcing and to increase the longevity of the silver photocathode. A pressure below 10^{-7} Torr is attained for the diffraction chamber in the absence of the molecular beam. When the molecular beam is operating, the pressure is as high as 10^{-4} Torr, and a trap just above the diffusion pump for the diffraction chamber is filled with liquid nitrogen to condense the chemicals. To prevent water condensation on the cooling unit of the detection chamber, the same mechanical pump for the diffraction chamber is used to pump out the detection chamber. The electron gun chamber has its own mechanical pump independent of the diffraction chamber.

3.1.4 Detection System

The basic design of the detection system in the 3rd generation machine is very similar to that of the 2nd generation. The detection system consists of a phosphor screen, a fiber optic window, a fiber optic taper, an image intensifier, a CCD chip, and a cooling system. The components are coupled with an optical coupling compound. The fiber optic window was coated with phosphor and on top of the phosphor a thick aluminum film (CRT Scientific) is applied to cut down the scattered laser light and

any other light. This thick aluminum film effectively blocks the light and transmits the electrons. The scattered electrons from the interaction volume hit the phosphor screen and their kinetic energy is transformed into photons, which are transported to the image intensifier through the fiber optic window and taper. The transported photons are further amplified through the image intensifier (Photometrics).

The intensified photons illuminates the CCD chip (Kodak) and develops electron-hole pairs on the pixels of the CCD chip. The Kodak CCD chip consisted of 1024 by 1024 pixels. The cooling system is very similar to that of the 2nd generation.

3.1.5 Experimental Scheme

Figure 3.1.2 shows a schematic of the 3rd generation UED. The basic pump-probe scheme is actually the same as in the 2nd generation. The main differences are as follows: 1) The translational stage is in the pathway of the laser beam for electron beam generation instead of the pump beam, 2) A common frequency conversion step (tripler) is used to obtain the correct wavelength for both the pump and probe beams and the output beam from the tripler is split later.

3.2 Improvements Over The 2nd Generation

The third-generation UED apparatus has been greatly advanced over the 2nd generation machine with vast improvements in pulsed electron flux, repetition rate, detection sensitivity, and experimental stability. These improvements all together resulted in the better temporal resolution and signal-to-noise ratio, details of which are considered in the following chapters. Other improvements are also discussed in the last section.

3.2.1 Temporal Resolution

A typical electron pulse width in the 3rd generation is ~4 ps and the overall total temporal resolution including the velocity mismatch (~1.5 ps) is less than 5 ps. Compared with the 2nd generation, where 7 – 10 ps is the usual temporal resolution, the temporal resolution has improved nearly by a factor of two. However, the number of electrons per pulse has been improved by a factor of six. For example, the 3rd generation electron pulse with a pulse width of 4 ps contains ~25,000 electrons whereas the 2nd generation pulse contains ~4,000 electrons at the same pulse width of 4 ps. Therefore, if we use the same number of electrons, the 3rd generation can offer a sub-ps electron pulse and the only limiting factor in the temporal resolution is the velocity mismatch. By reducing the beam waist of the electron beam further and focusing the laser beam more tightly, a sub-ps temporal resolution can now be obtained.

3.2.2 Signal-To-Noise Ratio

The signal-to-noise ratio for the diffraction-difference derived in **2.5** is recalled here:

$$SNR_{diff} = \tfrac{1}{2}\cdot(c_{diff}\cdot N_A/\pi/R)^{1/2}\cdot(i\cdot\sigma)\cdot(p/w_m)^{1/2}\cdot(\sigma_e(s)\cdot I_M(s)/I(s))^{1/2}$$

$$\cdot(E_{pulse}/(h\cdot\nu))\cdot r_{rep}^{1/2}\cdot t_{exp}^{1/2}\cdot N_{e\text{-}pulse}^{1/2}. \qquad (3.2.2.1)$$

The term $\tfrac{1}{2}\cdot(N_A/\pi/R)^{1/2}$ is simply a constant. The term $i\cdot\sigma$ is characteristic of the chemical reaction under investigation. The term $(p/w_m)^{1/2}$ characterizes the molecular beam. The term $(\sigma_e(s)\cdot I_M(s)/I(s))^{1/2}$ is characteristic of the scattering and diffraction process. The term $E_{pulse}/(h\cdot\nu)$ is characteristic of the excitation laser pulse. The term $N_{e\text{-}pulse}^{1/2}$ is characteristic of the electron gun and the chosen temporal pulse width of the electron pulse.

The change in the wavelength of the excitation laser from 310 nm in the 2nd generation to 266 nm in the 3rd generation actually decreases SNR_{diff} by ~12% due to the term $1/(h\cdot\nu)$. E_{pulse} has been reduced from ~250 μJ in the 2nd generation to ~150 μJ in the 3rd generation, which decreases SNR_{diff} by additional ~50% since SNR_{diff} is linearly proportional to E_{pulse}. The great improvement in the repetition rate from 30 Hz to 1 kHz increases SNR_{diff} by ~577% due to the term $r_{rep}^{1/2}$. The larger number of electrons (~25,000 electrons per pulse) compared to that of the 2nd generation (~6000 electrons per pulse) kHz increases SNR_{diff} by additional ~200% due to the term $N_{e\text{-}pulse}^{1/2}$. If other conditions such as the molecular beam profile, absorption cross section, the identity of the molecule, and total experimental time are kept the same, the overall

improvement in the signal-to-noise ratio for the diffraction-difference is ~500% compared with the 2nd generation machine.

The signal-to-noise ratio for the ground-state data derived in **2.5** gives

$$SNR_{ground} = ((I_M(s)/I(s))\cdot r_{rep}\cdot N_{e\text{-}pulse}\cdot t_{exp}\cdot \sigma_e(s)\cdot N_A\cdot p\cdot \pi\cdot (w_e/2)^2\cdot w_m/(R\cdot T))^{1/2} \quad (3.2.2.2)$$

Since SNR_{ground} does not depend on the characteristics of the laser pulse, the improvement in SNR_{ground} is even larger than in SNR_{diff}, reaching 1150%.

In summary, the 3rd generation apparatus has achieved improvements in the signal-to-noise ratio by a factor of five for the ground-state data and a factor of ten for the time-resolved data.

3.2.3 Other improvements

The most striking improvement is the reliability and stability of the whole system. We used to suffer a rather frequent arcing of the electron gun in the 2nd generation and had to constantly watch the behavior of the electron beam and move the electron beam into the right position whenever it shifts. This kind of problem has been extremely rare in the 3rd generation. The 3rd generation detection system has also never failed whereas the almost home-made 2nd generation detection system often gave many troubles and slowed down progress. In addition, the 3rd generation machine is equipped with the capability of time-of-flight mass spectrometry. This provides a complementary means to monitor the identity of the reactant and product molecules.

After a few adjustments, a traditional pump-probe femtosecond spectroscopy can also be performed in the 3rd generation machine.

The shift of the excitation wavelength from 310 nm to 267 nm has greatly increased the number of molecules whose absorption cross sections are high enough to give a decent signal-to-noise ratio in reasonable experimental time. Since many molecules have vast absorption cross section at 200 nm, two-photon absorption using 400 nm may open a new way of inducing many interesting reactions in the future.

Figure Captions

Figure 3.1.1: The UED apparatus is principally comprised of a commercial femtosecond laser system (Spectra Physics), an electron gun, a high-vacuum scattering chamber, a molecular beam, a 2-D detection system, and a time-of-flight mass spectrometer (*MS-TOF*) with retractable accelerating grids. The laser produces ultra-violet 120 fs pulses (1 kHz repetition rate) which are directed into a beam splitter (*BS*). Approximately 90% of the laser power is then guided into the scattering chamber to initiate reactions, while the remainder is directed into a delay line and then focused onto a photocathode within the electron gun to generate electron pulses (30 keV, λ: 0.067 Å). Diffracted electrons are detected with a 2-D imager constructed around a Photometrics CCD camera. The inset shows the results of an *in situ* streaking experiment, demonstrating the sub-picosecond precision with which the electron pulses are generated.

Figure 3.1.2: A schematic of the 3rd UED apparatus consisting of an electron gun chamber, a diffraction chamber and a detector chamber. Two fs laser pulses are used; the first initiates the chemical change and the second generates the electron pulse.

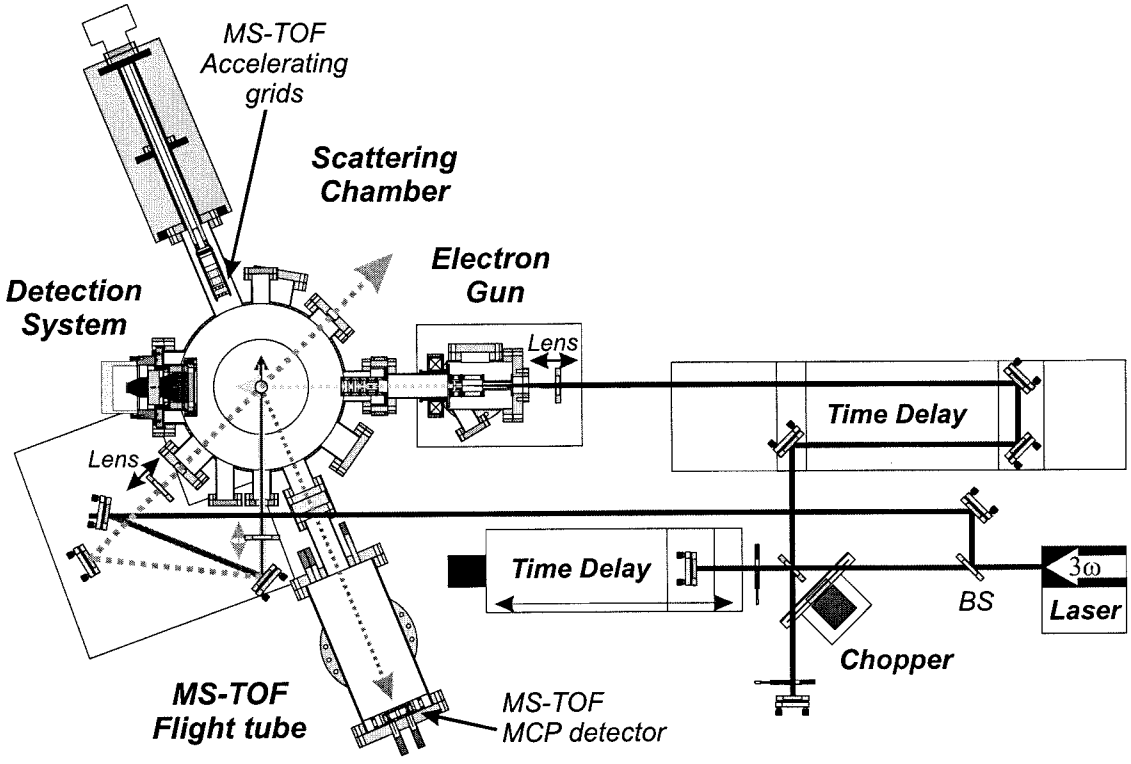
MS-TOF
Accelerating
grids
Scattering
Chamber
Electron
Gun
Detection
System
Lens
Time Delay
Lens
Time Delay
3ω
BS
Laser
Chopper
MS-TOF
Flight tube
MS-TOF
MCP detector

Figure 3.1.1

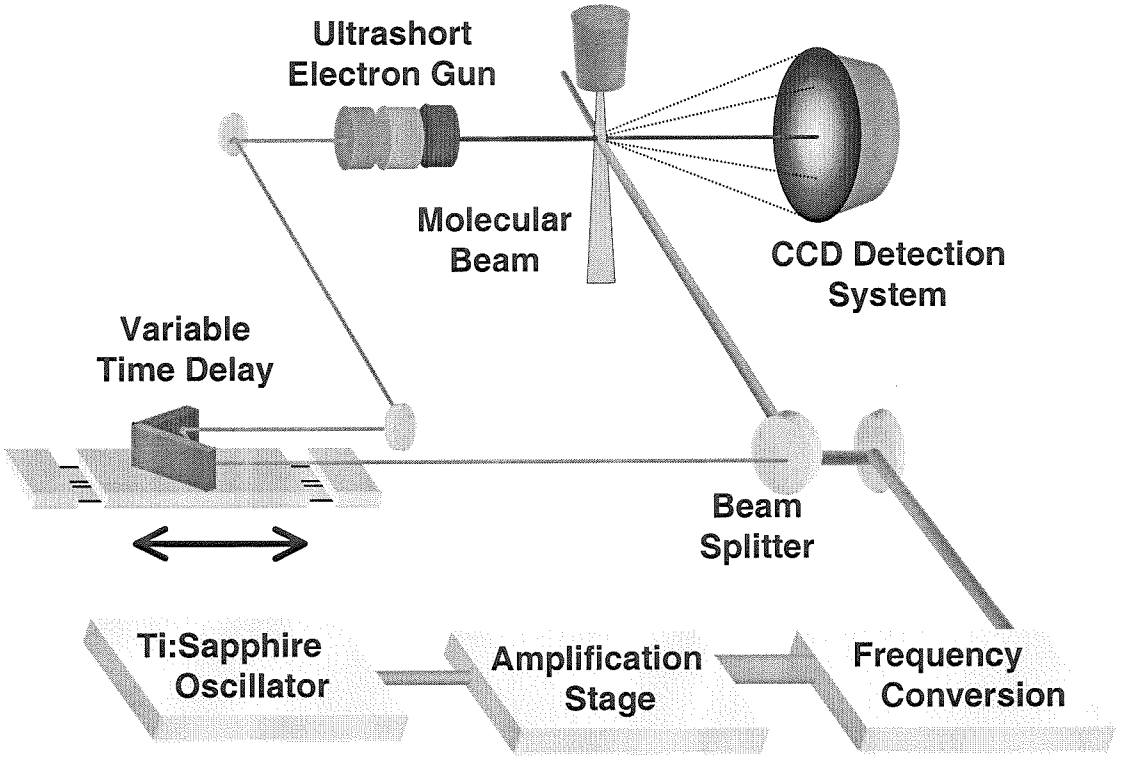
Ultrashort
Electron Gun
Molecular
Beam
CCD Detection
System
Variable
Time Delay
Beam
Splitter
Ti:Sapphire
Oscillator
Amplification
Stage
Frequency
Conversion

Figure 3.1.2

CHAPTER FOUR

UED DATA ANALYSIS

4.1 Electron Diffraction From Ground-State Molecules

4.1.1 Overview Of Basic Formalism

The general theory of gas-phase electron diffraction is well established (see for example, Ref. [1,2]); this section summarizes the basic formulas used in the analysis of conventional scattering patterns and the subsequent extraction of internuclear separations. The electron scattering intensity is typically expressed as a function of s, the magnitude of the momentum transfer between an incident electron and an elastically scattered electron:

$$s = \frac{4\pi}{\lambda}\sin\left(\frac{\theta}{2}\right) \qquad (4.1.1.1)$$

where λ is the de Broglie wavelength of the electrons (0.067 Å at 30 keV) and θ is the scattering angle.

The total scattering intensity, I, is a sum of scattering contributions from individual atoms (atomic scattering, I_A) superimposed with interference terms from all atom-atom pairs (molecular scattering, I_M):

$$I(s) = I_A(s) + I_M(s). \qquad (4.1.1.2)$$

If it is assumed that the electronic potentials of each atom in the molecule are independent (the independent atom model), the atomic scattering intensity may be written as a sum of elastic and inelastic scattering contributions

$$I_A(s) = C\sum_{i=1}^{N}\left(|f_i(s)|^2 + 4\frac{S_i(s)}{a_0{}^2 s^4}\right) \qquad (4.1.1.3)$$

where N is the number of atoms in the molecule, f_i and S_i are the elastic and inelastic

scattering amplitudes for atom i, a_0 is the Bohr radius, and C is a proportionality constant. The contributions from spin-flip scattering amplitudes (g_i) have not been included as they are generally neglected for high-energy electron diffraction experiments.[3]

For the purpose of structural determination, only I_M is of interest because it contains the information regarding internuclear separations. The molecular scattering intensity of an isotropic sample can be written as a double sum over all N atoms in the molecule:

$$I_M(s) = \sum_{i=1}^{N}\sum_{\substack{j=1 \\ i\neq j}}^{N} |f_i||f_j|\cos(\eta_i - \eta_j)\exp\left(-\tfrac{1}{2}s^2 l_{ij}^2\right)\frac{\sin(sr_{ij})}{sr_{ij}}, \qquad (4.1.1.4)$$

where f_i is the elastic scattering amplitude for the ith atom, η_i is the corresponding phase term, r_{ij} is the internuclear separation between atoms i and j, l_{ij} is the corresponding mean amplitude of vibration, and C is a proportionality constant. The scattering factors f and η depend on λ, s, and atomic number Z; tables of f and η are available in the literature.[2,4] The relative contribution of each atomic pair to the total molecular scattering intensity is roughly proportional to Z_iZ_j / r_{ij}. $I_M(s)$ can also be written as a single sum over the number of unique internuclear separations N_{IS} in the molecule:

$$I_M(s) = 2\sum_{k=1}^{N_{IS}} n_k |f_{i(k)}||f_{j(k)}|\cos(\eta_{i(k)} - \eta_{j(k)})\exp\left(-\tfrac{1}{2}s^2 l_k^2\right)\frac{\sin(sr_k)}{sr_k} \qquad (4.1.1.5)$$

The number of times a specific atom pair occurs in the molecule (containing the same

elements i and j, the same r, and the same l) is given by n_k. The oscillations in $I_M(s)$ are rapidly damped, however, because the scattering factors $f_i(s)$ decrease like s^2. This means that $I_M(s)$ decays approximately with s^5, and the modified molecular scattering intensity, $sM(s)$, is often used instead of $I_M(s)$ in order to highlight the oscillatory behavior of the diffraction signal at higher values of s.[1] The modified molecular scattering intensity can be defined either as:

$$sM(s) = s\frac{I_M(s)}{I_A(s)} \qquad (4.1.1.6a)$$

or

$$sM(s) = s\frac{I_M(s)}{|f_a||f_b|}, \qquad (4.1.1.6b)$$

where a and b correspond to two chosen atoms in the molecule (usually atoms with relatively high Z). In our current analysis, eq. (4.1.1.6a) was used (unless indicated otherwise). The corresponding radial distribution curve, $f(r)$, may be derived from $sM(s)$ via a Fourier (sine) transform:

$$f(r) = \int_0^{s_{max}} sM(s)\sin(sr)\exp\left(-k_d s^2\right)ds\,, \qquad (4.1.1.7)$$

where the damping constant k accounts for the finite s range of the detector. Ideally the upper limit on the integral should be ∞, which is experimentally impossible. In our experiments, the available experimental scattering intensity, $sM^E(s)$, typically ranged from s_{min} = 1.5 Å^{-1} to s_{max} = 18.5 Å^{-1} while the conventional diffraction data are typically recorded out to an s_{max} on the order of 40 Å^{-1}. The exponential term with coefficient k_d is included to damp spurious oscillations in $f(r)$ caused by cutting off the

integration at s_{max}. For the range from 0 to s_{min}, the theoretical scattering intensity, $sM^T(s)$, is appended to avoid distortions of the radial distribution baseline. Correction for non-nuclear scattering can be included so as to express the radial distribution curve as a sum of Gaussian functions, with each peak representing a given internuclear separation in the molecule.[5] Although all structural information is contained in the molecular scattering function, the radial distribution curve is more intuitive for qualitative interpretation because it directly reflects the relative density of internuclear distances in the molecule. Each unique internuclear separation yields one peak in the $f(r)$ curve, and the area under each peak is approximately proportional to:

$$\text{Peak Area} \propto n Z_i Z_j / r_{ij}\,, \qquad (4.1.1.8)$$

when k_d is equal to zero. The FWHM of each peak is related to the mean amplitude of vibration l_{ij}, and also s_{max}. Since $f(r)$ is related to internuclear probability distributions, the measurement of molecular scattering intensities offers a direct method of observing the evolution of a wave packet.

4.1.2 Scattering From An Atom

The theoretical derivation results in two key equations. The first equation is for the molecular scattering electron intensity, I_M, which contains intramolecular interference terms and hence structural parameters. Other intensity contributions, such as atomic scattering and inelastic scattering, contain no interference terms and are removed from the experimental data during data analysis.

The derivation of the molecular scattering and radial distribution functions is

developed in the following way. First, the atomic scattering is formulated and its solution is applied to the scattering from only one molecule. Then, an ensemble of molecules in thermal equilibrium is introduced. The relationship between $I_M(s)$ and internuclear probability amplitudes is reconsidered, leading to a definition of the radial distribution function. Finally, the effect of the non-equilibrium state is considered.

A simple picture of atomic scattering is shown in Figure 4.1.1. An electron beam travels along the z-axis, encounters the electric field of an atom centered at the origin, and scatters in all directions. Three initial assumptions are made about this interaction: 1) The electrons scatter elastically, without exchanging energy with the atom. 2) The atomic potential does not change with time. 3)The atomic potential has spherical symmetry. One consequence of the third assumption is that the scattered electron intensity must have cylindrical symmetry about the z-axis and depend only on the angle θ.

Schrödinger's wave equation must be solved to find the probability amplitude of the scattered electrons. As a result of the second assumption, the time-independent equation can be used:

$$\hat{H}\psi = E\psi, \qquad (4.1.2.1)$$

where ψ is the wave function and E is the sum of the kinetic and potential energies of an electron. The Hamiltonian operator can be expressed as follows if V describes the atomic potential energy:

$$\hat{H} = \frac{\hat{p}^2}{2m_e} + V = -\frac{\hbar^2}{2m_e}\nabla^2 + V, \qquad (4.1.2.2)$$

Before scattering occurs, the incident electron beam can be described as a plane wave:

$$\psi_I = A\exp(i\,\mathbf{k}_0\cdot\mathbf{z}) = A\exp(i\,k_0 z), \tag{4.1.2.3}$$

The magnitude of $\mathbf{k}_0$ is given by:

$$|\mathbf{k}_0| = k_0 = \frac{2\pi}{\lambda_e} = \frac{\sqrt{2m_e c^2 KE + KE^2}}{\hbar c}, \tag{4.1.2.4}$$

where λ_e is the relativistic de Broglie wavelength and KE is the kinetic energy. The electron beam's current density is calculated from:

$$I = \frac{\hbar}{2im_R}\left(\psi^*\nabla\psi - \psi\nabla\psi^*\right), \tag{4.1.2.5}$$

In the asymptotic limit of large R, the atom will appear as a point source of spherical waves with some functional dependence on θ. The wave amplitude of the scattered electrons must also have a $1/R$ dependence in order to conserve electron density, so the functional form of the scattered wave amplitude is chosen to be:

$$\psi_S(\mathbf{R}) \xrightarrow{R\to\infty} \frac{A}{R} f(\theta) e^{ikR}, \tag{4.1.2.6}$$

In this equation, $f(\theta)$ is the scattering amplitude and $|\mathbf{k}| = |\mathbf{k}_0|$ because the scattering process is elastic. $|f(\theta)|^2$ is the differential scattering cross section $d\sigma$ for unit solid angle $d\Omega$. According to eqs. (4.1.2.5), the intensity of the scattered wave is equal to:

$$I = \frac{\hbar k_0}{mR^2} f^2(\theta)|A|^2 = \frac{I_0}{R^2} f^2(\theta), \tag{4.1.2.7}$$

so an equation for $f(\theta)$ must be derived in order to predict the scattered intensity.

The total wave function is a sum of the incident and scattered waves:

$$\psi(\mathbf{R}) \xrightarrow{R\to\infty} \psi_I(\mathbf{R}) + \psi_S(\mathbf{R}), \tag{4.1.2.8}$$

and $\psi(\mathbf{R})$ must satisfy Schrödinger's equation. Inserting Eq. (4.1.2.2) into Eq. (4.1.2.1) yields:

$$-\frac{\hbar^2}{2m_e}\nabla^2\psi(\mathbf{R}) + V(\mathbf{R})\psi(\mathbf{R}) = E\psi(\mathbf{R}), \tag{4.1.2.9}$$

This equation can be greatly simplified by defining $U(\mathbf{R})$ as:

$$U(\mathbf{R}) = \frac{2m_R}{\hbar^2}V(\mathbf{R}), \tag{4.1.2.10}$$

With Eqs. (4.1.2.4) and (4.1.2.10), Eq. (4.1.2.9) becomes:

$$\left(\nabla^2 + k_0^2\right)\psi(\mathbf{R}) = U(\mathbf{R})\psi(\mathbf{R}), \tag{4.1.2.11}$$

This equation should be solved under the boundary condition in Eq. (4.1.2.8). As a first step, a more detailed illustration of the scattering center is introduced in Figure 4.1.2, where the atomic potential with volume Γ is displaced from the origin by $\mathbf{r}_0$. This modifies Eq. (4.1.2.11) to:

$$\left(\nabla^2 + k_0^2\right)\psi(\mathbf{R}) = U(\mathbf{R}-\mathbf{r}_0)\psi(\mathbf{R}), \tag{4.1.2.12}$$

The scattered intensity is detected at point P at the end of $\mathbf{R}$, and $\mathbf{r}$ points to an infinitesimal volume element $d\mathbf{r}$ of the potential. By the aid of the Green's function[2] the final $\psi(\mathbf{R})$ yields as:

$$\psi(\mathbf{R}) = Ae^{ik_0z} - \frac{e^{ikR}}{4\pi R}\left[\int_{V_0}\exp(-i\mathbf{k}\cdot\mathbf{r} - i\mathbf{k}\cdot\mathbf{r}_0)U(\mathbf{r})\psi(\mathbf{r}+\mathbf{r}_0)d\mathbf{r}\right], \tag{4.1.2.13}$$

Comparing this equation with Eq. (4.1.2.8) shows that the scattered wave ψ_S is equal to the second term of Eq. (4.1.2.8). In order to evaluate the integral, it is assumed that the scattered wave amplitude is negligible compared with the incident wave: $\psi_S << \psi_I$, which means that single-scattering events occur. After applying this approximation called the first Born approximation,. the scattered wave is given by:

$$\psi_S(\mathbf{R}) = \frac{Ae^{ikR}}{R}\exp\left(i(\mathbf{k}_0 - \mathbf{k})\cdot\mathbf{r}_0\right)\left[-\frac{1}{4\pi}\int_{V_0} U(\mathbf{r})\exp\left(i(\mathbf{k}_0 - \mathbf{k})\cdot\mathbf{r}\right)d\mathbf{r}\right], \tag{4.1.2.14}$$

The momentum transfer vector **s** for the scattered electron is defined as:

$$\mathbf{s} = \mathbf{k}_0 - \mathbf{k}, \tag{4.1.2.15}$$

Since $\mathbf{k_0}$ and **k** have the same magnitude, **s** has a magnitude given by:

$$|\mathbf{s}| = s = 2k_0\sin(\theta/2) = \frac{4\pi}{\lambda_e}\sin\left(\frac{\theta}{2}\right), \tag{4.1.2.16}$$

In old days, some diffractionists described the magnitude of the momentum transfer with the variable q instead of s:[5]

$$q = \frac{40}{\lambda_e}\sin\left(\frac{\theta}{2}\right) = \frac{10}{\pi}s, \tag{4.1.2.17}$$

Substitution of **s** into Eq. (4.1.2.14) gives:

$$\psi_S(\mathbf{R}) = \frac{Ae^{ikR}}{R}\exp\left(i\mathbf{s}\cdot\mathbf{r}_0\right)\left[-\frac{1}{4\pi}\int_{V_0} U(\mathbf{r})\exp\left(i\mathbf{s}\cdot\mathbf{r}\right)d\mathbf{r}\right], \tag{4.1.2.18}$$

Comparing this equation with Eq. (4.1.2.6) shows that the portion of $\psi_S(\mathbf{R})$ in square brackets is equal to $f(\theta)$ in Eq. (4.1.2.6):

$$f(s) = -\frac{1}{4\pi}\int_{V_0} U(\mathbf{r})e^{i\mathbf{s}\cdot\mathbf{r}}d\mathbf{r}, \qquad (4.1.2.19)$$

A potential function $U(\mathbf{r})$ is required in order to evaluate $f(s)$. The Coulombic potential for an atom can be written as a sum of the attractive point-charge-like potential of the nucleus and the repulsive diffuse potential of the electron cloud distribution $\rho(\mathbf{r}')$:

$$V(\mathbf{r}) = -\frac{Ze^2}{r} + e^2\int_{V_0}\frac{\rho(\mathbf{r}')}{|\mathbf{r}-\mathbf{r}'|}d\mathbf{r}', \qquad (4.1.2.20)$$

Using this potential, one can show that:[2]

$$f(s) = \frac{2m_e e^2}{\hbar^2}\left(\frac{Z - F_X(s)}{s^2}\right), \qquad (4.1.2.21)$$

where $F_X(s)$ is the x-ray scattering function:

$$F_X(s) = 4\pi\int_0^\infty r\rho(r)\frac{\sin(sr)}{s}dr, \qquad (4.1.2.22)$$

The elastic electron scattering amplitude depends on Z and decreases with scattering angle like s^2. To summarize, under the first Born approximation the elastic electron scattering amplitude from a spherically-symmetric atom at position $\mathbf{r}_0$ is found to be:

$$\psi_s(\mathbf{R}) = \frac{Ae^{ikR}}{R}f(s)\exp(i\mathbf{s}\cdot\mathbf{r}_0), \qquad (4.1.2.23)$$

So far only an atom has been considered. The next section advances into the case of molecule.

4.1.3 Scattering From One Molecule

A molecule can be described as a collection of atoms whose positions are defined by the vector set $\{\mathbf{r}_1, \mathbf{r}_2, \ldots, \mathbf{r}_N\}$. The chemical binding between atoms in a molecule removes spherical symmetry from the potential functions of individual atoms. Nevertheless, as a zeroth-order approximation, a molecule can be pictured as a collection of non-interacting atoms; the Independent Atom Model (IAM). Since the electric field from core electrons and nuclear charge is still spherically symmetric, an electron passing close to an atomic nucleus is less affected by the chemical bonding. For this reason, IAM has been proved to be robust enough for practical purpose in larger scattering angles above 5 Å^{-1} The weaker asymmetric field due to molecular orbital electrons is significant only when the impact parameter is large, and the momentum transfer is small.

Using IAM, the scattered electron wave amplitude from a molecule is written as a sum of Eq. (4.1.2.23) over each atom:

$$\psi_s(\mathbf{R}) = \frac{A}{R} e^{ikR} \sum_{i=1}^{N} f_i(s) \exp(i\mathbf{s}\cdot\mathbf{r}_i), \tag{4.1.3.1}$$

The intensity of scattered electrons is again calculated using the equation for the Schrödinger current Eq. (4.1.2.5):

$$I(s) = \frac{I_0}{R^2} \left(\sum_{i=1}^{N} f_i(s) \exp(i\mathbf{s}\cdot\mathbf{r}_i) \right) \left(\sum_{i=1}^{N} f_i(s) \exp(-i\mathbf{s}\cdot\mathbf{r}_i) \right), \tag{4.1.3.2}$$

This multiplication of two series can be reindexed as a double summation of a product:

$$I(s) = \frac{I_0}{R^2} \sum_{i=1}^{N} \sum_{j=1}^{N} f_i(s) f_j(s) \exp\left[i\mathbf{s}\cdot(\mathbf{r}_i - \mathbf{r}_j) \right], \tag{4.1.3.3}$$

This equation shows that the scattered intensity depends on the internuclear separation vector $\mathbf{r}_{ij} = \mathbf{r}_i - \mathbf{r}_j$ for all atom pairs in the molecule, bonded and non-bonded. This double sum can be broken apart into an atomic contribution containing no structural information, and a molecular contribution containing the interference terms:

$$I(s) = I_A(s) + I_M(s) = \frac{I_0}{R^2}\left(\sum_{i=1}^{N} f_i^2(s) + \sum_{i=1}^{N}\sum_{\substack{j=1 \\ i\neq j}}^{N} f_i(s) f_j(s) \exp\left(i\mathbf{s}\cdot\mathbf{r}_{ij}\right)\right)$$

, (4.1.3.4)

Usually the incoherent inelastic scattering terms are included in $I_A(s)$:

$$I_A(s) = \frac{I_0}{R^2}\sum_{i=1}^{N}\left(f_i^2(s) + \frac{4S_i(s)}{a_0^2 s^4}\right), \quad (4.1.3.5)$$

where $S_i(s)$ are the inelastic scattering factors and a_0 is the Bohr radius.

4.1.4 Scattering From An Ensemble of Molecules

The molecular scattering intensity $I_M(s)$ of Eq. (4.1.3.4) results from just one rigid molecule with a specific orientation defined by $\{\mathbf{r}_1, \mathbf{r}_2, \ldots, \mathbf{r}_N\}$. To model experimental data, $I_M(s)$ must be averaged over all the distributions of whatever physical parameters describe the sample molecules (e.g., orientation, electronic state, vibrations):

$$I_M(s) = C\sum_{i=1}^{N}\sum_{\substack{j=1 \\ i\neq j}}^{N} f_i(s) f_j(s) \left\langle \exp\left(i\mathbf{s}\cdot\mathbf{r}_{ij}\right)\right\rangle_{\substack{\text{Molecular} \\ \text{Distribution}}}, \quad (4.1.4.1)$$

An incident electron accelerates as it approaches an atomic nucleus and the de Broglie wavelength contracts. After the electron leaves the influence of the atomic

potential, λ_e returns to its original value, but the phase of the scattered wave differs from that of a wave traveling the same path with constant λ_e. While the first Born approximation gives only real scattering amplitudes, the second Born approximation yields complex amplitudes containing a phase shift, and Schomaker and Glauber defined the complex $f(s)$ to be:

$$f(s) = |f(s)|e^{i\eta(s)}, \qquad (4.1.4.2)$$

where $\eta(s)$ is the argument of $f(s)$. η is positive for an attractive potential and negative for a repulsive potential. The correction to the magnitude is small enough that the first Born approximation can still be used for $|f(s)|$. The phase shift is more pronounced at larger scattering angles and depends on Z. A new formula for the molecular scattering intensity is now:

$$I_M(s) = C\sum_{i=1}^{N}\sum_{\substack{j=1 \\ i\neq j}}^{N} \mathrm{Re}\left[f_i(s) f_j^*(s) \left\langle \exp\left(i\,\mathbf{s}\cdot\mathbf{r}_{ij}\right)\right\rangle_{\substack{\text{Molecular} \\ \text{Distribution}}} \right], \qquad (4.1.4.3)$$

Averaging over an isotropic sample gives:

$$I_M(s) = C\sum_{i=1}^{N}\sum_{\substack{j=1 \\ i\neq j}}^{N} \mathrm{Re}\left[|f_i(s)||f_j(s)| \exp\left(i\left[\eta_i(s) - \eta_j(s)\right]\right)\right] \frac{\sin(sr_{ij})}{sr_{ij}}, \qquad (4.1.4.4)$$

which simplifies to:

$$I_M(s) = C\sum_{i=1}^{N}\sum_{\substack{j=1 \\ i\neq j}}^{N} |f_i(s)||f_j(s)| \cos\left(\eta_i(s) - \eta_j(s)\right) \frac{\sin(sr_{ij})}{sr_{ij}}, \qquad (4.1.4.5)$$

Thus, the scattering intensity from two atoms of very different Z contains an additional interference term which causes splitting in the radial distribution curve peak.

More accurate values of $f(s)$ are obtained by solving the Schrödinger equation using the method of partial waves, where it is rewritten in terms of spherical coordinates. Tabulated values of $|f(s)|$, $\eta(s)$, and the inelastic scattering factor $S(s)$ are available in the literature as functions of s, Z, and electron kinetic energy.

4.1.5 Effect Of Molecular Vibration

High-energy electron scattering is in the attosecond time scale, the nuclear motions are essentially frozen on this time scale. Therefore, an incident electron scatters from a target molecule as if the molecule was in fact rigid. Because of random vibrational motion, however, molecules are frozen in different internuclear configurations throughout the sample, and the ensemble is represented by an average structure, not an absolute structure. To account for vibrational motion in the diffraction pattern, the "Molecular Distribution" average occurring in Eq. (4.1.4.1) must include a vibrational average in addition to the spatial-orientation average:

$$I_M(s) = C\sum_{i=1}^{N}\sum_{\substack{j=1\\ i\neq j}}^{N}|f_i||f_j|\cos(\eta_i-\eta_j)\left\langle\left\langle\exp(i\mathbf{s}\cdot\mathbf{r}_{ij})\right\rangle_{Sptl}\right\rangle_{Vib}, \qquad (4.1.5.1)$$

If a molecule's spatial orientation can be considered independent of its vibrational motion, it can be de-coupled and the spatial-orientation average can be carried out first as in **4.1.4**:

$$I_M(s) = C\sum_{i=1}^{N}\sum_{\substack{j=1\\ i\neq j}}^{N}|f_i||f_j|\cos(\eta_i-\eta_j)\left\langle\frac{\sin(sr_{ij})}{sr_{ij}}\right\rangle_{Vib}, \qquad (4.1.5.2)$$

To average over vibrational motion, each internuclear separation r_{ij} is assigned a

probability $P_{ij}(r)dr$ of having r_{ij} between r and $r + dr$. This leads to:

$$I_M(s) = C\sum_{i=1}^{N}\sum_{\substack{j=1 \\ i\neq j}}^{N}|f_i||f_j|\cos(\eta_i - \eta_j)\int_0^{\infty}\frac{\sin(sr)}{sr}P_{ij}(r)dr, \qquad (4.1.5.3)$$

4.1.6 Harmonic Approximation And Thermal Equilibrium

An analytical description of $P_{ij}(r)$ is necessary for the integration in Eq. (4.1.5.3). In harmonic approximation, each atom-atom pair (even the non-bonded pairs) can be simplified as a perfect harmonic oscillator. For an ensemble of harmonic oscillators in equilibrium at temperature T, the average over all vibrational states ψ_v gives a Gaussian probability distribution as a function of the variable x:

$$P_{ij}^{T}(x) = \frac{\sum_{v=0}^{\infty}|\psi_v(x)|^2\exp(-E_v/kT)}{\sum_{v=0}^{\infty}\exp(-E_v/kT)} = \frac{1}{l_h\sqrt{2\pi}}\exp\left(-\frac{x^2}{2l_h^2}\right), \qquad (4.1.6.1)$$

where x is the displacement from the equilibrium distance, $x = r - r_e$. The variable l_h is the mean amplitude of vibration of a harmonic oscillator at T. In general,

$$l^2 = \langle x^2\rangle - \langle x\rangle^2, \qquad (4.1.6.2)$$

and

$$l_\alpha = \hbar/\sqrt{2\mu\omega_e}, \qquad (4.1.6.3)$$

for the ground vibrational state of a harmonic oscillator. Using the gaussian probability distribution from Eq. (4.1.6.1), the integral in Eq. (4.1.5.3) becomes:

$$\frac{1}{l_h\sqrt{2\pi}}\int_{-\infty}^{\infty}\exp\left(-\frac{x^2}{2l_h^2}\right)\frac{\sin\left[s(r_e+x)\right]}{s(r_e+x)}dx, \qquad (4.1.6.4)$$

This integral does not have an analytical solution and further approximations are made; the denominator can be written as a binomial expansion:

$$\frac{1}{r_e+x} = \frac{1}{r_e}\left(1-\frac{x}{r_e}+\frac{x^2}{r_e^2}-\ldots\right), \qquad (4.1.6.5)$$

If x is small compared to r_e, the first two terms of the expansion are the most significant. This and further expanding the sine functions using angle-sum relations give:

$$\frac{\exp\left(-\frac{1}{2}s^2l_h^2\right)}{sr_e}\left[\sin(sr_e)-\frac{sl_h^2}{r_e}\cos(sr_e)\right], \qquad (4.1.6.6)$$

This equation can be further simplified by noting that $sl_h^2/r_e << 1$. For small y it is true that $\sin y \approx y$ and $\cos y \approx 1$, so the portion in square brackets can be simplified using an angle-difference relation:

$$\sin(sr_e)\cos\left(sl_h^2/r_e\right)-\cos(sr_e)\sin\left(sl_h^2/r_e\right) = \sin\left[s\left(r_e-l_h^2/r_e\right)\right], \qquad (4.1.6.7)$$

In summary, if all atom-atom pairs are modeled as harmonic oscillators and thermal equilibrium (Boltzman distribution) is established, the elastic electron scattering intensity from an unordered gaseous sample of vibrating molecules can be expressed as:

$$I_M(s) = C\sum_{i=1}^{N}\sum_{\substack{j=1\\ i\neq j}}^{N}|f_i||f_j|\cos(\eta_i-\eta_j)\exp\left(-\tfrac{1}{2}s^2l_h^2\right)\frac{\sin(sr_a)}{sr_e}, \qquad (4.1.6.8)$$

where the effective internuclear separation r_a is related to the equilibrium internuclear

separation r_e by:

$$r_a = r_g(1) = r_e - l_h^2 / r_e \,, \tag{4.1.6.9}$$

$r_g(1)$ is the center of gravity of $P(r)/r$. The l_h can be expressed as:

$$l_h = \frac{h}{8\pi^2 \mu \nu} \coth\left(\frac{h\nu}{2kT}\right) \tag{4.1.6.10}$$

4.1.7 Influence Of Anharmonicity

The description of the vibration can be made more accurate by considering a more realistic potential than the harmonic oscillator. This can be done by expanding about the harmonic oscillator gaussian distribution:[6,7]

$$P_{ij}^T(x) = \frac{A_P}{l_h\sqrt{2\pi}} \exp\left(-\frac{x^2}{2l_h^2}\right)\left[1 + \sum_{n=1}^{\infty} c_n x^n\right], \tag{4.1.7.1}$$

where the c_n are expansion coefficients and the normalization constant A_P is close to unity:

$$A_P = \left(1 + \sum_{m=1}^{\infty} \frac{(2m)!}{2^m m!} c_{2m} l_h^{2m}\right)^{-1}, \tag{4.1.7.2}$$

After incorporating corrections for centrifugal distortion, δr, the vibrational displacement x is:

$$x = r - r_e - \delta r \,, \tag{4.1.7.3}$$

One can show that:[7]

$$I_M(s) = C\sum_{i=1}^{N}\sum_{\substack{j=1 \\ i\neq j}}^{N} |f_i||f_j| \cos(\eta_i - \eta_j) \exp\left(-\tfrac{1}{2}s^2 l_m^2\right) \frac{\sin\left[s\left(r_a - \kappa s^2\right)\right]}{s r_e}, \tag{4.1.7.4}$$

where l_m is an effective mean amplitude of vibration close in value to l_h, and r_a and κ are series expansions including weighted terms of l_h^2.

Often the ground-state of the Morse anharmonic oscillator provides sufficient precision. The Morse oscillator expansion coefficients for Eq. (4.1.7.1) are:

$$c_1 = a; \qquad c_2 = 0; \qquad c_3 = a/6l_h^2, \tag{4.1.7.5}$$

where a is the anharmonicity constant and all other c_n are equal to zero. With these parameters, r_a and κ are approximated by:

$$r_a = r_g - l_h^2/r_e, \tag{4.1.7.6}$$

$$r_g = r_e + \tfrac{3}{2}al_h^2 + \delta r, \tag{4.1.7.7}$$

$$\kappa = al_h^4/6, \tag{4.1.7.8}$$

$$l_m = l_h^2 + (3/2)a^2l_h^4 \tag{4.1.7.9}$$

Values of a for different atom-atom pairs are tabulated in the literature.[8] Diffractionists often set a equal to 2 Å^{-1} for all bonded atom pairs and a equal to 0 Å^{-1} for all non-bonded atom pairs. Combining Eqs. (4.1.7.6) and (4.1.7.7) gives:

$$r_a \approx r_e + (3/2)\cdot a\cdot l_h^2 + dr - l_h^2/r, \tag{4.1.7.10}$$

It should be noted that this equation is strictly valid only for a diatomic when the potential can be approximated as a Morse oscillator and its vibrational levels have a Boltzman distribution. In general, the moment method gives the following expressions for polyatomic molecules in thermal equilibrium.

$$r_a \cong r_e + <\Delta r> - \frac{<(\Delta r)^2>}{r_e} + \delta r \tag{4.1.7.11}$$

$$l_m \cong < (\Delta r)^2 >^{1/2}$$

(4.1.7.12)

$$\kappa \cong \frac{< \Delta r^3 > -3 < \Delta r >< \Delta r^2 >}{6} \qquad (4.1.7.13)$$

An equation similar to eq. (4.1.7.10) can be used:

$$r_a \approx r_e + (3/2) \cdot a \cdot l_m^2 + dr - l_m^2 / r, \qquad (4.1.7.14)$$

if the following relationship can be established.

$$< \Delta r >= \frac{3}{2} a < (\Delta r)^2 >= \frac{3}{2} a l_m^2 \qquad (4.1.7.15)$$

It should be noted that this relationship is not really valid except for a Morse oscillator. It is always questionable whether internuclear distances in a polyatomic molecule can be approximated as Morse oscillators.

Three different kinds of internuclear separation (r_e, r_a, r_g) have been introduced so far, but many others are also found in the literature. These distances (summarized in Table 4.1.1) can be classified into two different types; operational parameters and parameters with well-defined physical meaning. Among these, r_e is the distance between nuclear equilibrium positions, i.e., the location of the potential well minimum. The distances reported for theoretical structure calculations are usually r_e distances. The complications arise because the apparent distance measured in electron diffraction and other spectroscopies is generally not r_e. Therefore, the relationships between these distances are necessary for meaningful interpretations of the experimentally observed distances.

For a polyatomic molecule, the displacements perpendicular to the direction of the connection between two atoms also must be taken into account. Consider two nuclei, i and j, separated by r_e. The instantaneous separation, r_{ij}, can be expressed as:

$$(r_{ij})^2 = (\Delta x_{ij})^2 + (\Delta y_{ij})^2 + (r_e + \Delta z_{ij})^2 \qquad (4.1.7.16)$$

where Δx_{ij} is the instantaneous displacement along x axis. Then, after dropping the subscript for simplicity, eq. (4.1.7.16) becomes

$$r_{ij} = (r_e + \Delta z)\sqrt{1 + \frac{(\Delta x)^2 + (\Delta y)^2}{(r_e + \Delta z)^2}} \qquad (4.1.7.17)$$

If $(\Delta x_{ij})^2 + (\Delta y_{ij})^2 << (r_e + \Delta z_{ij})^2$,(which is true in general), this equation can be approximated as:

$$r_{ij} \approx (r_e + \Delta z)\left[1 + \frac{(\Delta x)^2 + (\Delta y)^2}{2(r_e + \Delta z)^2}\right] = r_e + \Delta z + \frac{(\Delta x)^2 + (\Delta y)^2}{2(r_e + \Delta z)} \qquad (4.1.7.18)$$

r_g is the average value of r_{ij} and with the approximation of dropping Δz in the denominator and adding the centrifugal stretching δr for completeness,

$$r_g = \langle r_{ij} \rangle \approx r_e + < \Delta z > + \frac{< (\Delta x)^2 + (\Delta y)^2 >}{2 r_e} + \delta r \qquad (4.1.7.19)$$

In the classical description, δr can be expressed as,

$$\delta r = \frac{2kT}{r_e K} \qquad (4.1.7.20)$$

where K is the force constant of the bond. For a diatomic where Δx and Δy are absent, this equation becomes identical to eq. (4.1.7.7) with

$$< \Delta z > = \frac{3}{2} a l^2 \qquad (4.1.7.21)$$

It should be emphasized again that this is true only for a Morse oscillator. Above, the following relationship (eq. (4.1.7.6)) was derived,

$$r_a = r_g - l_h^2 / r_e = r_g - <(\Delta z)^2> / r_e \qquad (4.1.7.22)$$

Combining eqs. (4.1.7.13) and (4.1.7.16) gives

$$r_a = r_e + <\Delta z> + \frac{<(\Delta x)^2 + (\Delta y)^2>}{2r_e} - \frac{<(\Delta z)^2>}{r_e} + \delta r \qquad (4.1.7.23)$$

At present, UED typically provides a precision on the order of 0.01 Å^{-1} because diffraction data is recorded out to an s_{max} of only 20 Å^{-1} at best. Even with extremely large vibrational motion ($l_h \approx 0.3$ Å), the anharmonicity term κs^2 in Eq. (4.1.7.8) is much smaller than 0.01 Å^{-1} and can be neglected in most cases. The centrifugal correction term dr is also very small (much less than 0.01 Å^{-1}) and is usually neglected. The difference between r_a and r_e is usually less than 0.01 Å. The exponential damping term $\exp\left(-\frac{1}{2}s^2 l_h^2\right)$ alters the molecular intensity by 10% or more at a scattering position of s = 10 Å^{-1}.

4.1.8 The Radial Distribution Curve

As derived in the previous section, the molecular scattering intensity from vibrating molecules with isotropic spatial orientation is:

$$I_M(s) = C\sum_{i=1}^{N}\sum_{\substack{j=1 \\ i\neq j}}^{N} |f_i||f_j| \cos(\eta_i - \eta_j) \int_0^\infty \frac{\sin(sr)}{sr} P_{ij}(r) dr, \qquad (4.1.8.1)$$

$P_{ij}(r)$ is a radial distribution function: the normalized probability density that atoms i and j are separated by a distance r. Qualitative interpretation of diffraction data is

simplified by transforming the reciprocal-space data to yield a distribution function $D(r)$ related to $P_{ij}(r)$. Instead of comparing experimental $I_M(s)$ curves with theoretical calculations for different structural models, internuclear separations can be read directly from the maxima in $D(r)$. To obtain $D(r)$, a modified scattering intensity $M(s)$ is derived from Eq. (4.1.8.1):

$$M(s)=C\sum_{i=1}^{N}\sum_{\substack{j=1\\ i\neq j}}^{N} g_{ij}(s)\int_0^{\infty}\frac{\sin(sr)}{sr}P_{ij}(r)dr, \qquad (4.1.8.2)$$

where $g(s)$ is a leveling function and $D(r)$ is defined as the sum:

$$D(r) = \sum_{i=1}^{N}\sum_{\substack{j=1\\ i\neq j}}^{N} g_{ij}(s)\frac{P_{ij}(r)}{r} = 2\sum_{k=1}^{N_{IS}} n_k g_k(s)\frac{P_k(r)}{r}, \qquad (4.1.8.3)$$

If g_k is independent of s, then $D(r)$ is a true sum of all radial distribution functions $P_k(r)$ weighted by $1/r$ and the constant terms g_k. After substituting in $D(r)$ and multiplying by s, Eq. (4.1.8.2) becomes:

$$sM(s) = C\int_0^{\infty} D(r)\sin(sr)dr, \qquad (4.1.8.4)$$

and thus $D(r)$ and $sM(s)$ are related by a sine-transform:

$$D(r) = C'\int_0^{\infty} sM(s)\sin(sr)ds, \qquad (4.1.8.5)$$

Formerly, g_k was approximated

$$g_k(s)=s^4 f_{i(k)}f_{j(k)}, \qquad (4.1.8.6)$$

to compensate for the s^2 fall off in the scattering factors. If the scattering effects from planetary electrons are ignored (F_X = 0 in Eq. (4.1.2.21)), then their g_k is a constant

equivalent to:[9]

$$g_k = cZ_{i(k)}Z_{j(k)}, \tag{4.1.8.7}$$

This aids in the interpretation of $D(r)$ because the area under the curve:

$$\int_0^\infty D(r)dr = 2\sum_{k=1}^{N_{IS}} n_k g_k \int_0^\infty \frac{P_k(r)}{r}dr = 2\sum_{k=1}^{N_{IS}} n_k g_k \int_{-r_{e,k}}^\infty \frac{P_k\left(r_{e,k}+x\right)}{r_{e,k}+x}dx, \tag{4.1.8.8}$$

can be simplified by recalling that the $P_k(r)$ are highly localized about $r_{e,k}$ and are normalized to have unit area:

$$\int_0^\infty D(r)dr \approx 2\sum_{k=1}^{N_{IS}} \frac{n_k g_k}{r_{e,k}} \int_{-\infty}^\infty P_k\left(r_{e,k}+x\right)dx = 2c\sum_{k=1}^{N_{IS}} n_k \frac{Z_{i(k)}Z_{j(k)}}{r_{e,k}}, \tag{4.1.8.9}$$

So by assuming that the $g_k(s)$ are constant and that nuclear scattering dominates GED, the area under a peak in the distribution curve is proportional to the atomic numbers of the atoms involved, and inversely proportional to their internuclear separation (Eq. (4.1.1.8)).

Two formulations of $g_{ij}(s)$ are commonly used in modern GED analysis[1,10-12]. The Western U.S.-Western European school (Norwegian school) writes $g_{ij}(s)$ as:[1,13-32]

$$g_{ij}(s) = \frac{|f_i||f_j|}{|f_a||f_b|}\cos\left(\eta_i - \eta_j\right), \tag{4.1.8.10}$$

where a and b are two atoms in the molecule. In this version, $D(r)$ is truly proportional to $P(r)/r$ for homonuclear diatomic molecules because $g_{ij}(s)$ becomes 1. The Eastern U.S.-Eastern European-Japanese school (American school) writes $g_{ij}(s)$ as:[5,11,12,33-50]

$$g_{ij}(s) = \frac{|f_i||f_j|}{I_A(s)}\cos(\eta_i - \eta_j), \qquad (4.1.8.11)$$

on the grounds that the resulting distribution curve has a flatter baseline.

The $D(r)$ distribution curve defined in Eq. (4.1.8.5) cannot be calculated from experimental scattering intensities because the data is recorded over a finite range of s. A modified radial distribution curve $f(r)$ (also called $\sigma(r)/r$) is calculated instead:

$$f(r) = C' \int_0^{s_{max}} sM(s)\sin(sr)\exp(-k_d s^2)ds, \qquad (4.1.8.12)$$

The exponential damping function reduces the ringing in $f(r)$ caused by the cut off at s_{max}. If k_d is sufficiently large, $f(r)$ and $D(r)$ are related by:

$$f(r) = \frac{1}{2\sqrt{\pi k_d}} \int_{-\infty}^{\infty} D(\rho)\exp\left[-(r-\rho)^2/4k_d\right]d\rho, \qquad (4.1.8.13)$$

which shows that $f(r)$ is the convolution of $D(r)$ with a gaussian, smoothing $D(r)$ and broadening the peaks. In practice, k_d is chosen such that $\exp(-k_d s_{max}^2) \approx 0.1$.

4.2 Electron Diffraction During Chemical Reaction

4.2.1 Time-Dependent Scattering

In UED, the photons in the excitation laser pulse are absorbed by the molecules in the interacting volume, and the excited molecules may undergo many kinds of reaction pathways. They may stay in the excited state, or dissociate into fragments, or isomerize into other conformers, or fall into the ground state again through internal conversion (avoided crossing or conical intersection), or convert into other spin states via intersystem conversion. As a result, the scattering intensity in UED varies with time t, depending on the chemical reaction. Therefore, the time-dependent scattering intensity[51-58] needs to be defined. Two kinds of notation have been used in the literature.[54,55]

$$I(t; s) = I(s, t) \tag{4.2.1.1}$$

This time-dependent scattering intensity, $I(s, t)$, is composed of the time-dependent atomic contribution

$$I_A(t; s) = I_A(s, t) \tag{4.2.1.2}$$

and the time-dependent molecular intensity.

$$I_M(t; s) = I_M(s, t) \tag{4.2.1.3}$$

In other words, according to Eq. (4.1.3.4),

$$I(s, t) = I_A(s, t) + I_M(s, t) \tag{4.2.1.4}$$

Unlike the ground-state data, the scattering intensity at time $t > 0$, $I(t > 0; s)$, contains contributions from more than one molecular species—not just the parent molecule, but also intermediates and products of the reaction. Therefore, the time-

resolved $I(t; s)$ can be written as a sum of the individual scattering intensities from each species at time t, $I_\alpha(t; s)$:

$$I(t;s) = \sum_\alpha I_\alpha(t;s) = \sum_\alpha (I_M(t;s)_\alpha + I_A(t;s)_\alpha) = \sum_\alpha I_M(t;s)_\alpha + \sum_\alpha I_A(t;s)_\alpha \quad (4.2.1.5)$$

where α indexes all possible structures occurring over the course of the reaction. If the elastic ($f(s)$) and inelastic ($S(s)$) scattering factors are time-independent, I_A should be time-invariant. (Eq. (4.1.3.5)). Although, in general, the possibility cannot be ruled out that photons perturb the electrons in the parent molecules and other photo-induced species and alter these scattering factors, the primary part is $I_M(s, t)_\alpha$ (or $I_M(s, t)_\alpha$). The next section gives more details regarding this.

4.2.2 Time-Dependent Molecular Intensity

Eq. (4.1.7.4) derived in **4.1** is for standard gas phase electron diffraction experimental conditions: an isotropic gaseous sample in thermal equilibrium, with vibrational population concentrated in the low-lying states. Therefore, Eq. (4.1.7.4) cannot be used in UED, and all perturbations of the sample must be accounted for in the theoretical model by averaging over a description of the molecular distribution:

$$I_M(s) = C\sum_{i=1}^{N}\sum_{\substack{j=1 \\ i\neq j}}^{N} |f_i||f_j| \mathrm{Re}\left[\exp\left(i\left(\eta_i - \eta_j\right)\right)\left\langle \exp\left(i\,\mathbf{s}\cdot\mathbf{r}_{ij}\right)\right\rangle_{\substack{\text{Molecular} \\ \text{Distribution}}}\right] \quad (4.2.2.1)$$

Since $\mathbf{r}_{ij}$ is now dependent on time t, $I_M(s, t)$ should be re-written as:

$$I_M(s,t)=C\sum_{i=1}^{N}\sum_{\substack{j=1\\ i\neq j}}^{N}|f_i||f_j|\mathrm{Re}\left[\exp\left(i\left(\eta_i-\eta_j\right)\right)\left\langle\exp\left(i\mathbf{s}\cdot\mathbf{r}_{ij}(t)\right)\right\rangle_{\substack{\text{Molecular}\\ \text{Distribution}}}\right] \quad (4.2.2.2)$$

It should be noted that this equation is valid only under the independent atom approximation. The molecular scattering intensity for a particular species can be expressed as in Eq. (4.2.2.2):

$$I_M(s,t)_\alpha=C\sum_{i=1}^{N}\sum_{\substack{j=1\\ i\neq j}}^{N}|f_i||f_j|\mathrm{Re}\left[\exp\left(i\left(\eta_i-\eta_j\right)\right)\left\langle\exp\left(i\mathbf{s}\cdot\mathbf{r}_{ij}(t)\right)\right\rangle_{\substack{\text{Molecular}\\ \text{Distribution}}}\right] \quad (4.2.2.3)$$

as far as it is understood that the sums go over only that particular species. Various parameters relevant to electron diffraction include the vibrational population, the rotational population, spatial orientation, and composition. Although the effect of the rotational excitation has not been captured yet in UED, the effect of the vibrational excitation (**6.1**) and the effect of a high temperature (**6.2**) have been observed in the products of the various reactions using UED.

4.2.3 Vibrational Excitation

Since the excitation by laser light often induces vibrational excitations, the vibrational levels should be incorporated. Eq. (4.2.2.2) can be expressed as

$$I_M(s,t)=C\sum_{i=1}^{N}\sum_{\substack{j=1\\ i\neq j}}^{N}|f_i||f_j|\mathrm{Re}\left[\exp\left(i\left(\eta_i-\eta_j\right)\right)\sum_{v}p_v(t)\left\langle v\left|\exp\left(i\mathbf{s}\cdot\mathbf{r}_{ij}\right)\right|v\right\rangle_{\text{rot}}\right] \quad (4.2.3.1)$$

where $p_v(t)$ is the population of the vth vibrational state and $\langle\ldots\rangle_{rot}$ means the rotational averaging. Note that the time dependence of $\mathbf{r}_{ij}(t)$ in Eq. (4.2.2.3) is adsorbed to $p_v(t)$ in Eq. (4.2.3.1). In most time, the molecules and photo-generated

species in UED can be approximated as randomly oriented. Therefore, spatial averaging can be done first: [55,59,60]

$$I_M(s,t)=C\sum_{i=1}^{N}\sum_{\substack{j=1\\ i\neq j}}^{N}|f_i(s)||f_j(s)|\cos(\eta_i(s)-\eta_j(s))\int P(r_{ij},t)\frac{\sin(sr_{ij})}{sr_{ij}}dr_{ij}, \quad (4.2.3.2)$$

where $P(r_{ij}, t)$ is the time-dependent probability density function. In the case that the distribution (weighting coefficient, $w_v(t)$) of the vibrational energy states is known, $P(r_{ij}, t)$ can be expressed as the sum of the probability distribution ($P_{ij,v}(r)$) of vibrational state v for atom pair i, j.

$$P(r_{ij},t)=\sum_{v}w_v(t)P_{ij,v}(r), \quad (4.2.3.3)$$

Then, Eq. (4.2.3.2) becomes

$$I_M(s,t)=C\sum_{i=1}^{N}\sum_{\substack{j=1\\ i\neq j}}^{N}|f_i||f_j|\cos(\eta_i-\eta_j)\sum_{v}w_v(t)\int_0^{\infty}\frac{\sin(sr)}{sr}P_{ij,v}(r)dr \quad (4.2.3.4)$$

This equation can be freely applicable to general cases as far as the molecules or the photo-generated species can be considered as a randomly oriented ensemble. Therefore, experimental electron diffraction data for a variety of problems both in equilibrium and in non-equilibrium can be interpreted using this equation. The next section concerns the effect of the high internal energy of the photo-products and the concept of equilibrium and non-equilibrium conditions are introduced.

4.2.4 Equilibrium And Non-Equilibrium Conditions

Once a molecule absorbs a photon or photons, the energy (hv) of photons is used to bring the molecule into different states or species. If the energy difference of the final state and the initial state is denoted as $E_{i\text{-}f}$, the rest of the photon energy ($hv - E_{i\text{-}f}$) is the available energy (E_{avail}) for the final state; E_{avail} is partitioned into the translational, vibrational, and rotational energies.

$$E_{avail} = hv - E_{i-f}\,, \tag{4.2.4.1}$$

In the case that the initial state already has some internal energy (vibrational and rotational energies), this also should be added into the total available energy.

$$E_{avail} = E_{trans} + E_{rot} + E_{vib}\,, \tag{4.2.4.2}$$

where E_{trans}, E_{rot}, and E_{vib} stand for translational, rotational, and vibrational energy, respectively.

If the available energy is completely thermalized among modes, and a Boltzman distribution is established within each mode, the temperature of the system can be estimated using the thermodynamic functions[61]. For linear polyatomic molecules,

$$E_{avail} = \frac{3}{2}NkT + \frac{2}{2}NkT + NkT\sum_{j=1}^{3N-5}\left[\frac{\Theta_{vj}}{2T} + \frac{\Theta_{vj}/T}{\exp(\Theta_{vj}/T)-1}\right], \tag{4.2.4.3}$$

and for nonlinear polyatomic molecules,

$$E_{avail} = \frac{3}{2}NkT + \frac{3}{2}NkT + NkT\sum_{j=1}^{3N-6}\left[\frac{\Theta_{vj}}{2T} + \frac{\Theta_{vj}/T}{\exp(\Theta_{vj}/T)-1}\right], \tag{4.2.4.4}$$

where Θ_{vj} is the vibrational temperature of the jth vibrational mode. Note that only one temperature T is common to all the translational, rotational, and vibrational modes and describes the temperatures of these modes. In general, there is no guarantee that this

type of complete thermal distribution can be established. Therefore, more general cases should be considered. If dissociation processes are involved, the temperature for the translational mode can be decoupled from the other modes. In this case, the available energy should be recalculated by subtracting the translational energy and the new temperature can be estimated by dropping the first terms in Eqs. (4.2.4.3) and (4.2.4.4) as far as a complete thermal equilibrium can be established among the rotational and vibrational modes. For linear polyatomic molecules,

$$E_{avail} - E_{trans} = \frac{2}{2}NkT + NkT\sum_{j=1}^{3N-5}\left[\frac{\Theta_{vj}}{2T} + \frac{\Theta_{vj}/T}{\exp(\Theta_{vj}/T)-1}\right], \qquad (4.2.4.5)$$

and for nonlinear polyatomic molecules,

$$E_{avail} - E_{trans} = \frac{3}{2}NkT + NkT\sum_{j=1}^{3N-6}\left[\frac{\Theta_{vj}}{2T} + \frac{\Theta_{vj}/T}{\exp(\Theta_{vj}/T)-1}\right], \qquad (4.2.4.6)$$

Special orientation in the chemical dynamics of the reaction process may result in that the temperature for the rotational modes differs from those of other modes. In this case, the rotational energy should be subtracted from the available energy in a separate step and the terms for the rotational modes (the second terms in Eqs. (4.2.4.3) and (4.2.4.4)) should be dropped. For linear polyatomic molecules

$$E_{avail} - E_{rot} = \frac{3}{2}NkT + NkT\sum_{j=1}^{3N-5}\left[\frac{\Theta_{vj}}{2T} + \frac{\Theta_{vj}/T}{\exp(\Theta_{vj}/T)-1}\right], \qquad (4.2.4.7)$$

and for nonlinear polyatomic molecules,

$$E_{avail} - E_{rot} = \frac{3}{2}NkT + NkT\sum_{j=1}^{3N-6}\left[\frac{\Theta_{vj}}{2T} + \frac{\Theta_{vj}/T}{\exp(\Theta_{vj}/T)-1}\right], \qquad (4.2.4.8)$$

In the case that both the translational and rotational modes should be decoupled from the vibrational modes, for linear polyatomic molecules,

$$E_{avail} - E_{trans} - E_{rot} = NkT \sum_{j=1}^{3N-5} \left[\frac{\Theta_{vj}}{2T} + \frac{\Theta_{vj}/T}{\exp(\Theta_{vj}/T) - 1} \right], \qquad (4.2.4.9)$$

and for nonlinear polyatomic molecules,

$$E_{avail} - E_{trans} - E_{rot} = NkT \sum_{j=1}^{3N-6} \left[\frac{\Theta_{vj}}{2T} + \frac{\Theta_{vj}/T}{\exp(\Theta_{vj}/T) - 1} \right], \qquad (4.2.4.10)$$

So far a complete thermal equilibrium in the vibrational modes has been assumed. This assumption means that the available energy for the vibrational modes is partitioned with a complete equilibrium between modes (intermode) and a complete Boltzman distribution within modes (intramode). Now, these concepts can be generalized by considering incomplete intermode and intramode equilibrium conditions. In general, four possibilities arise. 1) Complete intermode equilibrium and complete intramode thermalization, 2) Complete intermode equilibrium and incomplete intramode thermalization, 3) Incomplete intermode equilibrium and complete intramode thermalization, 4) Incomplete intermode equilibrium and incomplete intramode thermalization.

Incomplete intermode equilibrium means, at least as a first-order approximation, that the available energy for the whole vibrational modes is not partitioned into each vibrational mode according to Eqs. (4.2.4.3) – (4.2.4.10). This general case can be expressed as

$$E_{vib} = \sum_{j=1}^{3N-6} E_{vj} \,, \tag{4.2.4.11}$$

Even in this case, the temperature (T_{vj}) for each vibrational mode can be defined if the intramode thermalization occurs

$$E_{vj} = Nk\left(\frac{\Theta_{vj}}{2} + \frac{\Theta_{vj}}{\exp(\Theta_{vj}/T_{vj})-1}\right), \tag{4.2.4.12}$$

In contrast, incomplete intramode thermalization makes the definition of temperature meaningless. In this case, eq. (4.2.3.2) should be used directly.

Since a diatomic has only one vibrational mode, there is no complication from the intermode energy partitioning. Therefore, effects of the intramode energy distribution on the electron diffraction signal can be effectively visualized for a model diatomic molecule. In Figure 4.2.1, the upper panel (a) represents the complete intramode thermalization. An increased l value (red) from a thermal (Boltzmann) vibrational population (left) results in broadening of the $f(r)$ curve (middle) and damping of the $sM(s)$ curve (right). The bottom panel represents two hypothetical cases of incomplete intramode thermalization; low-lying and higher-lying inverted (non-Boltzmann) vibrational populations modeled with Gaussian distributions. The low-lying inverted populations will cause broadening of the $f(r)$ curve and damping of the $sM(s)$ curve similar to the Boltzman case above. Higher-lying populations (green) can lead to outright bifurcation of the internuclear density and significant changes in the frequency components of the $sM(s)$ scattering signal.

4.2.5 Convolution With Probe Electron Pulse

In the actual UED experiment, the probe electron beam has a finite pulse width. The intensities in 4.2.3 are derived without including this effect. If the electron pulse profile ($I_e(t', t)$) is known, the intensity observed by this electron pulse can be expressed as

$$I(s,t) = \int_{t',t'+\tau} I_e(t',t) I(s,t') dt', \qquad (4.2.5.1)$$

where t is the delay time and τ is the electron pulse width.

4.2.6 Scattering Equations Used In UED

In **4.1**, the standard equation for the molecular scattering has been derived.

$$I_M(s) = C\sum_{i=1}^{N}\sum_{\substack{j=1 \\ i\neq j}}^{N} |f_i||f_j| \cos(\eta_i - \eta_j) \exp\left(-\tfrac{1}{2}s^2 l_m^2\right) \frac{\sin\left[s\left(r_a - \kappa s^2\right)\right]}{s r_e}, \qquad (4.2.6.1)$$

In the actual analysis, this equation is re-indexed according to atomic pairs:

$$I_M(s) = C\sum_{i=1}^{K} n_i g_i(s) \exp\left(-\tfrac{1}{2}s^2 l_i^2\right) \frac{\sin\left[s\left(r_i - \kappa_i s^2\right)\right]}{s r_i}, \qquad (4.2.6.2)$$

where K is the number of nonequivalent internuclear distances, n_i is the multiplicity, g_i is the scattering function, r_i is the internuclear distance, l_i is the mean amplitude of vibration, and κ_i is the asymmetry constant. Here, r_i is the r_a value and eq. (4.1.7.14) is used to relate r_a and r_e.

$$r_a \approx r_e + (3/2)\cdot a \cdot l^2 + dr - l^2/r, \qquad (4.2.6.3)$$

It should be noted that eqs. (4.2.6.2) and (4.2.6.3) are strictly valid only when the following conditions are fully met.

1) The molecules have random orientations.
2) The molecules are in thermal equilibrium following Boltzman distribution.
3) The potential energy of the internuclear distances (both direct and in-direct bonds) can be approximated as Morse oscillators.
4) The vibrations have small amplitudes.

Bond Length The r_e values are obtained from three sources. 1) Other previously published data from electron diffraction, 2) Ab initio calculation. 3) Empirical relationships. The static structure of most molecules studied by UED have already been studied by conventional electron diffraction or spectroscopic tools. Usually, r_g distances are reported. These values are converted into r_e values using eq. (4.1.7.7). Ab initio calculations provide r_e values directly and in some cases these ab initio values are used. Especially, the products and intermediate structures in UED are unstable species hard to study with the conventional electron diffraction method and therefore the experimental structure parameters are generally not available. In this case, the ab initio calculation is the major source. The structural parameters of similar species may be used as a starting point, but should be refined later.

Mean Amplitude Of Vibration The l values are obtained from three sources. 1) From literature, 2) Normal mode analysis using an approximate quadratic force field.

3) Empirical relationships to r values. The values reported in the literature are usually for room temperature. In the case where l values for elevated temperatures are needed, eq. (4.1.6.10) can be used to estimate approximate values by treating each internuclear pair as a harmonic oscillator. In some cases, ASYM40 program[62] is used to calculate the l values from an approximate quadratic force field. A detailed description of the theory behind this can be found in the book by Cyvin[63] and Califano[64]. In the harmonic approximation, the mean-square amplitude of a normal coordinate Q_i is given by

$$\delta_i = \langle Q_i^2 \rangle \frac{h}{8\pi^2 c\omega_i} \coth\left(\frac{hc\omega_i}{2kT}\right) \qquad (4.2.6.4)$$

where ω_i is the (harmonic) vibrational frequency in cm^{-1}. The mean-square amplitudes of the normal coordinates can be arranged in the form of a diagonal matrix

$$\boldsymbol{\delta} = \langle \mathbf{QQ'} \rangle \qquad (4.2.6.5)$$

whose non-zero elements are given by eq. (4.2.6.4). The mean-square amplitude matrices for other coordinates are simply obtained from eq. (4.2.6.4) by using the linear transformations between the normal and the other coordinates. For example, a symmetry coordinate **S** can be given as

$$\mathbf{S} = \mathbf{LQ} \qquad (4.2.6.6)$$

And we obtain

$$\boldsymbol{\Sigma}^S = \langle \mathbf{SS'} \rangle = \mathbf{L} \langle \mathbf{QQ'} \rangle \mathbf{L'} \qquad (4.2.6.7)$$

The mean amplitude of vibration in electron diffraction is usually defined in terms of the change ($\mathbf{R} = \Delta\mathbf{r}$) in the internal coordinate **r**. We need a conversion between **S** and **R**.

$$\mathbf{R} = \mathbf{VS}, \text{ and } \mathbf{S} = \mathbf{UR}, \text{ and } \mathbf{V} = \mathbf{U}' \qquad (4.2.6.8)$$

Then we have

$$\mathbf{\Sigma}^{\mathbf{R}} = \langle \mathbf{RR}' \rangle = \mathbf{V\Sigma}^{\mathbf{S}}\mathbf{V}' = \mathbf{VL}\delta\mathbf{L}'\mathbf{V}' = \mathbf{U}'\mathbf{L}\delta\mathbf{L}'\mathbf{U} \qquad (4.2.6.9)$$

Now the famous Wilson's **GF** matrix comes and **L** can be obtained using the following well-known equations.

$$|\mathbf{GF} - \lambda\mathbf{E}| = 0, \quad \mathbf{GFL} = \mathbf{L}\Lambda, \quad \mathbf{F}^{-1} = \mathbf{L}\Lambda^{-1}\mathbf{L}', \mathbf{G} = \mathbf{LL}' \qquad (4.2.6.10)$$

where the element of Λ is given by

$$\lambda_i = 4\pi^2\nu_i^2 \qquad (4.2.6.11)$$

The relationships between the **GF** matrices in the symmetry coordinate and **gf** matrices in the internal coordinate is straightforward.

$$\mathbf{G} = \mathbf{UgU}', \quad \mathbf{F} = \mathbf{UfU}' \qquad (4.2.6.12)$$

Experimental vibrational frequencies or ab initio calculations after appropriate scaling can be used to optimize the quadratic force field. It should be noted that the calculated *l* values from ASYM40 are strictly valid only in the harmonic limit.

For CC and CH pairs, which are most common in hydrocarbons and vast amount of experimental data have been accumulated, there exist empirical relationships[65-68] between *l* and *r* such as

$$l(\mathrm{CC}) = -0.071856 + 0.124162\, r - 0.028974\, r^2$$

$$\text{for } 1.2086 \le r \le 1.549 \qquad (4.2.6.13)$$

$$l(\mathrm{CC}) = 0.013837 + 0.023398\, r - 0.000147\, r^2$$

$$\text{for } 1.217 \le r \le 5.618 \qquad (4.2.6.14)$$

$$l(\mathrm{CH}) = 0.050134 + 0.027368\, r - 0.001805\, r^2$$

$$\text{for } 1.080 \le r \le 4.677 \qquad (4.2.6.15)$$

General Cases As discussed in **4.2.1**, **4.2.2**, and **4.2.3**, in UED, there is no guarantee that the intermediate and product species establish equilibrium states and the assumptions made above may not be hold any more. If the standard eq. (4.2.6.2) is still used to fit the experimental data from non-standard situations, the finally obtained structural parameters can lose their original meanings, but still can reflect some valuable information as long as proper interpretations are incorporated.

As far as the sample can be still considered to be randomly oriented, eq. (4.2.3.2) can be used.

$$I_M(s) = C\sum_{i=1}^{N}\sum_{\substack{j=1 \\ i\neq j}}^{N} |f_i(s)||f_j(s)|\cos(\eta_i(s)-\eta_j(s))\int P(r_{ij})\frac{\sin(sr_{ij})}{sr_{ij}}dr_{ij}\,, \qquad (4.2.6.16)$$

In some cases, this equation can be re-indexed according to atomic pairs:

$$I_M(s) = C\sum_{i=1}^{K} n_i g_i(s)\int P(r_i)\frac{\sin(sr_i)}{sr_i}dr\,, \qquad (4.2.6.17)$$

Now the problem boils down to how to model $P(r)$ to fit the experimental data. Ab initio calculations, in principle, can provide the vibrational wave functions for each internuclear pairs and $P_v(r)$ corresponding to each vibrational wave function can be calculated since

$$P_v = |\psi_v|^2 \tag{4.2.6.18}$$

. However, as shown in eq. (4.2.3.3), the overall $P(r)$ is the sum of $P_v(r)$,

$$P(r)=\sum_v w_v P_v(r), \tag{4.2.6.19}$$

and all w_v's should be fit, which is not realistic at least for the moment. To reduce the number of variables, the distribution (w_v's) can be approximated as some form of function with a few parameters. A more realistic approach would be to approximate $P(r)$ as a sum of a few Gaussian functions with each gaussian having three variables; width, position, and height.

$$P(r)=\sum_m^M \frac{h_m}{\sqrt{\pi} l_m} \exp\left(-\frac{(r-(r_e+\Delta_m)^2)}{2{l_m}^2} \right), \tag{4.2.6.20}$$

where m is the index for Gaussian functions, M is the number of Gaussian functions, h_m is the coefficient satisfying the normalization condition, Δ_m is the shift of the center of the Gaussian function from r_e, and l_m is the width of the Gaussain function. Plugging eq. (4.2.6.20) into eq. (4.2.6.17) gives

$$I_M(s)=C\sum_{i=1}^K n_i g_i(s) \int \sum_m^M \frac{h_m}{\sqrt{\pi} l_m} \exp\left(-\frac{(r_i-(r_{e,i}+\Delta_{m,i})^2)}{2{l_{m,i}}^2} \right) \cdot \frac{\sin(sr_i)}{sr_i} dr, \tag{4.2.6.21}$$

This can be re-written as:

$$I_M(s)=C'\sum_{i=1}^K n_i g_i(s) \sum_m^{M_i} h_{m,i} \exp\left(-\frac{{l_{m,i}}^2 s^2}{2} \right) \frac{\sin\left(s((r_{e,i}+\Delta_{m,i})-{l_{m,i}}^2/(r_{e,i}+\Delta_{m,i}))\right)}{sr_{e,i}} \tag{4.2.6.22}$$

4.3 Overview Of Diffraction Data Analysis

The rest of this chapter discusses the most essential part of UED: a method of analyzing the diffraction images downloaded from the charge-coupled device and stored on the computer hard drive and obtaining time-resolved structural parameters of gas-phase molecules. The software required to complete these tasks is part of an in-house, custom program written for the UED laboratory.

4.3.1 Two Major Parts: Data Processing And Data Analysis

Data analysis can be broken down into two major steps. First, a one-dimensional data file of raw scattering intensity had to be extracted from two-dimensional CCD images taken during a single experiment. Second, the raw scattering intensity is analyzed, yielding the structural parameters. This process involves corrections for the background intensity in order to generate the modified molecular scattering function $sM^E(s)$ and the radial distribution function $f^E(r)$, and least-squares refinements to minimize the difference between the theoretical model and the experimental intensity.

4.3.2 Conversion From CCD Pixel To Momentum Transfer *s*

The numerical values of 1-D raw intensity obtained after converting the 2-D images into a 1-D intensity is usually given in CCD pixel distance. Since the theoretical scattering intensity is calculated in terms of the momentum transfer s, the CCD pixel distance should be converted to s prior to actual data analysis of the

diffraction intensity. This conversion is straightforward.

$$s = \frac{4\pi}{\lambda_e}\sin\left[\frac{1}{2}\arctan\left(\frac{w_{pix}r}{L}\right)\right] \approx 2\pi\frac{w_{pix}r}{L\lambda_e} \qquad (4.3.2.1)$$

where λ_e is the de Broglie electron wavelength, L is the camera length, w_{pix} is the effective CCD pixel width at the scintillator, r is in pixels, and $L\lambda_e$ is known as the camera constant. For a precise determination of structural parameters, the approximation in Eq. (4.3.2.1) is usually not recommended, and L and λ_e need to be determined individually.

4.3.3 Determination of L and λ_e

In principle, both L and λ_e can be determined by recording diffraction patterns from highly symmetric gas molecules such as CO_2, CCl_4, SF_6, or benzene or with thin, polycrystalline films[69] whose structural parameters are precisely known, at many acceleration voltages (λ_e depends on the acceleration voltage) and many different camera lengths. The two variables can be fit using more than two sets of data in combinations of many λ_e and L. A set of diffraction patterns from a thin film of aluminum was recorded for this purpose, but the uncertainty in the values of L and λ_e obtained by fitting two variables simultaneously were in reality too big to be useful.

In the 2nd generation UED, the camera length was measured by a ruler. A typical measurement gave the camera length of ~100 mm with an error of ~0.5 mm. This 0.5% uncertainty was an order of magnitude larger than in standard GED values for L. The measured L value was incorporated into the fit of the diffraction patterns

from an aluminum film to obtain λ_e.

In the 3rd generation UED, a set of diffraction patterns from a thin film of aluminum was also recorded, but was not used in the actual determination of L and λ_e. Instead, λ_e was calculated using the nominal value of the acceleration voltage (30 kV) and L was fit using diffraction patterns of either N_2 or CO_2.

4.4 Conversion Of 2-D Image Into 1-D Curve

The conversion of the 2-D diffraction image to a 1-D intensity distribution, $I(r_{pixel})$, as a function of pixel radius r_{pixel}, is completed by calculating the average intensity as a function of pixel radius from the center for each diffraction image. In UED, not one but many 2-D diffraction images (N_{frame} is the total number of images) are recorded at each delay time so that averaging the intensities from many images increases the total signal-to-noise ratio of the final 1-D intensity. The detailed procedures are different in the 2nd and 3rd generation, depending on the order of averaging and converting.

4.4.1 The 2nd Generation

Figure 4.3.1 gives a schematic of the data processing procedure used in the 2nd generation. The 2-D diffraction images from the CCD are first converted to one-dimensional intensity curves ($I(r_{pixel}, t)_i$, i = 1 to N_{frame}) by calculating the average intensity as a function of pixel radius from the primary beam center for each diffraction image. The experimental total scattering intensity curve $I(r_{pixel}, t)$ at different delay times (t) is obtained by further averaging all the $I(r_{pixel}, t)_i$ at each delay time.

$$I(r_{pixel}, t) = \Sigma_i (I(r_{pixel}, t)_i / N_{frame}) \qquad (4.4.1.1)$$

In most cases, a set of images with the electron beam blocked is also obtained. These images do not contain any contributions from electron scattering but the contributions

mainly from the scattered laser light. These images are processed in the same and the final 1-D intensity curve, $I_{Laser}(r_{pixel}, t)$, is obtained. Finally, the scattered-laser-light-free total intensity curve, $I_{final}(r_{pixel}, t)$ at each delay time was obtained by subtracting $I_{Laser}(r_{pixel}, t)$ from $I(r_{pixel}, t)$.

$$I_{final}(r_{pixel}, t) = I(r_{pixel}, t) - I_{Laser}(r_{pixel}, t) \quad (4.4.1.2)$$

Then, the total raw scattering intensity in s, $I(s, t)$, is obtained by converting the pixel radius to the momentum transfer parameter (s) according to Eq. (4.3.2.1). An experimental data file containing the one standard deviation ($\sigma_{Tot}(r_{pixel})$) as a function of pixel radius for each data set at different delay times was also generated for the molecular structural fitting.

4.4.2 The 3rd Generation 2-D Image Processing

The digital nature of our data acquisition permits the use of a variety of powerful image processing techniques that aid in the isolation of molecular diffraction signals; a schematic that summarizes our image processing methods is given in Fig. 3. The accessibility of the individual pixels in the digitized images allows us to treat each pixel as an independent detector statisically characterized by its own mean intensity and standard deviation. Following the acquisition of a series of n raw 2-D diffraction images (A_i, $i = 1, 2, ..., n$) with the CCD camera (at a given time point), unwanted random events (caused, for example, by spontaneous emission and cosmic rays) are removed from each raw image, and a processed, averaged 2-D image, $\overline{A}_0$, is generated according to the following iterative procedure.

For each A_i, a corresponding binary "mask" image, M_i, is created, for which a given pixel, $M_i(x,y)$, has a value of 1 if the corresponding pixel in A_i is valid (the conditions for validity are outlined below), or has a value of 0 otherwise. Initially, $M_i(x,y) = 1$ for all coordinates for all n images. In the first step of each processing loop, an average value, $\overline{A}(x, y)$, is obtained for the signal intensity at each pixel:

$$\overline{A}(x, y) = \frac{\sum_{i}^{n} M_i(x, y) \cdot A_i(x, y)}{\sum_{i}^{n} M_i(x, y)}, \qquad (4.4.2.1)$$

where $A_i(x,y)$ is the signal intensity for the pixel with coordinates (x,y) in the ith image, and $\sum_{i}^{n} M_i(x, y)$ is the number of pixels contributing acceptable values of $A_i(x,y)$, and is $\leq n$. During this step $\overline{A}(x, y)$ and $\sigma(x, y)$ (the standard deviation of the averaged scattering intensity) are calculated for each pixel in $\overline{A}$. In order to remove the signal spikes from random events, each A_i is then submitted to a pixel-by-pixel rejection criterion requiring that $\overline{A}(x, y) - 4\sigma(x, y) \leq A_i(x, y) \leq \overline{A}(x, y) + 4\sigma(x, y)$ for all pixels: if a given value for $A_i(x,y)$ does not meet this criterion then the corresponding value of $M_i(x,y)$ in the mask image is set to zero. This processing cycle is typically repeated three times, with the $\overline{A}(x, y)$ values, $\sigma(x, y)$ values, and the M_i mask images updated after each cycle. At the conclusion of the last cycle, the final 2-D binary mask (M') is generated, which now ensures that inactive pixels (and pixels manually removed due to systematic problems) do not contribute to the scattering

intensity used for analyzing diffraction data. This final mask is multiplied by the final averaged $\overline{A}$ image to yield $\overline{A}_0$, which is now used for all further analysis. All averaged images, including background images and the reference gas images, were generated by this procedure.

A processed, averaged background image ($\overline{B}_0$), obtained under identical conditions as the molecular diffraction image (e.g., exposure time, laser light scattering, etc.)—except *without* the presence of the gas sample under study—is then subtracted from each $\overline{A}_0$. After this background subtraction, each 2-D molecular diffraction image is then divided by a corresponding 2-D image, $\overline{X}_0$, obtained from a monatomic reference gas (xenon):

$$R^{2D} = \frac{\overline{A}_0 - \overline{B}_0}{\overline{X}_0 - \overline{B'}_0}, \qquad (4.4.2.2)$$

where $\overline{B'}_0$ is the corresponding background image for $\overline{X}_0$. This division by the smoothly decaying diffraction intensity[56] of the reference gas not only permits the direct visualization of molecular interferences in the 2-D ratio image, but also removes most of the systematic errors associated with the apparatus function of the detector. Each R^{2D} is then converted to an experimental 1-D total intensity curve, $R^E(pix)$, by calculating the average intensity as a function of pixel radius, $\rho(pix)$, from the electron beam center, according to the relation:

$$\sqrt{x^2 + y^2} < \rho < \sqrt{(x+1)^2 + (y+1)^2} \quad . \qquad (4.4.2.3)$$

Corresponding values for the standard deviation of the scattering intensity at each

pixel radius, $\sigma(pix)$, are also calculated, permitting a second round of spike rejection in the final calculation of $R^E(pix)$. The $\sigma(pix)$ values are then used later as the weighting function in least squares refinements. Finally, $R^E(pix)$ is converted to $R^E(s)$ by calculating the scattering angle θ from the pixel dimensions and the camera length L (which is defined as the distance between the scattering volume beneath the sample nozzle and the detection screen). The camera length for these experiments was 13.39 cm, and was calibrated by comparing experimentally derived diffraction data obtained from high-purity nitrogen gas with literature values.[1] The division by the reference gas scattering intensity is accounted for by multiplying $R^E(s)$ by the theoretical scattering intensity of the reference gas, $I^T_{ref}(s)$:

$$I^E(s) = R^E(s) \times I^T_{ref}(s). \qquad (4.4.2.4)$$

approximation in Eq. (4.3.2.1) is usually not recommended, and L and λ_e are needed to be determined individually.

4.4.3 Time-Resolved Experiments: Normalization

In order to follow the structural changes that occur over the course of a given chemical reaction, we record a series of averaged 2-D diffraction images with varying time delay, t, between the pump (laser) and probe (electron) pulses. Each of these images thus reflects the transient behavior of the molecular structures at the corresponding temporal delay following laser excitation. However, before considering any time-dependent behavior of the diffraction signals, we normalize the total intensity of each $\overline{A}_0(t)$ 2-D image; this is done by first calculating the mean image

intensity of each image, $\langle \overline{A}_0(t) \rangle$, according to the relation:

$$\langle \overline{A}_0(t) \rangle = \frac{\sum_{x,y}^{512} M'(x,y;t) \cdot \overline{A}_0(x,y;t)}{\sum_{x,y}^{512} M'(x,y;t)}, \qquad (4.4.3.1)$$

where $\overline{A}_0(x,y;t)$ is the signal intensity at the pixel with coordinates (x,y) in the averaged 2-D image acquired at time delay t, $M'(t)$ is the binary mask image corresponding to $\overline{A}_0(t)$, and 512 is the effective number of pixels along both x and y. The quantity $\langle \overline{A}_0(t) \rangle^{-1}$ obtained at each time delay is then used as the normalization constant for the corresponding averaged 2-D image.

4.5 Methods Of Data Analysis In UED

4.5.1 A Brief Review Of Conventional Methods

This section attempts to present a neat summary of the main ideas relevant to the data analysis of the ground state data. The total experimental scattering intensity is commonly described as a sum of three components:

$$I^E(s) = I_M(s) + I_A(s) + I_{Det}(s) \qquad (4.5.1.1)$$

where $I_M(s)$ is the molecular scattering intensity, $I_A(s)$ is the atomic scattering intensity, including inelastic terms, and $I_{Det}(s)$ represents contributions from the detector and experimental artifacts. Since $I_M(s)$ is the only term containing structural information, $I_A(s)$ and $I_{Det}(s)$ are sometimes lumped together as a single, generic background term, $I_B^E(s)$:

$$I^E(s) = I_B^E(s) + I_M^E(s), \qquad (4.5.1.2)$$

where $I_B^E(s)$ contains contributions from atomic scattering, $I_A(s)$, and the experimental background response. Most analytic treatments make the reasonable assumption that $I_B(s)$ is a smooth function compared to $I_M(s)$, and all higher frequency oscillations in the scattering intensity are due solely to molecular interference terms. Different approaches diffractionists have used to remove $I_B(s)$ from Eq. (4.5.1.2) are reviewed in **A.3**.

The general approaches may be divided into two major schools; the Eastern U.S.-Eastern European-Japanese school and the Western U.S.-Western European school. The former works with the ratio I_M/I_A, reasoning that certain theoretical errors will cancel, and compensates radial distribution analyses for effects of planetary

electrons by additive corrections. The latter[13-22] works with I_M itself, reasoning that extraneous scattering errors will drop out, and compensates for planetary electrons in radial distribution analyses by multiplicative corrections.

In the Eastern U.S.-Eastern European-Japanese school, they deal with $M(s)$.

$$M(s) = I/I_A - 1 = I_M/I_A. \qquad (4.5.1.3)$$

The advantages are (a) the s-dependence is almost removed in $M(s)$ compared to I_M. (b) any theoretical imperfections are presumably canceled out. (c) more sensitive $I_B(s)$ can be obtained with $M(s)$ rather than $I(s)$. First, I_0, "the leveled intensity", is obtained by dividing the experimental total intensity by the theoretical atomic scattering intensity.

$$I_0 = I^E/I_A{}^T \qquad (4.5.1.4)$$

The initial trial background function may be drawn by a visual estimate to cleave the molecular oscillations more or less evenly, or it may be derived by a polynomial fit with a computer as discussed elsewhere.[33] It is desirable to refine the initial trial background function as the analysis progresses, according to the criteria proposed by Karles[27-29], namely, the background must be kept smooth and the derived $f_c(r)$ radial distribution function be everywhere nonnegative. Once a trial background function has been selected, it is possible to compute a trial reduced intensity function

$$M^E(s) = ([I^E(s)/I_B(s)] - 1). \qquad (4.5.1.5)$$

The index of resolution R is then introduced for a better fit;

$$M^E(s) = R \cdot M^T(s). \qquad (4.5.1.6)$$

Usually, R is first kept as unity for every s, and then after obtaining the I_m's, $R(s)$ is

allowed to vary. In an ideal fit, R approached unity.

The principal difficulty in obtaining $M(s)$ is that I_A is itself not directly observable. Nevertheless, $M(s)$ may be established within limits by applying a certain criteria[29]. Heretofore, one of the less desirable features of automatic analyses of reduced intensity functions has been that background functions, obtained subjectively, have been frozen until $f(r)$ is analyzed. A least squares fit on the total experimental scattering intensity $I^E(s)$ can be done by minimizing the function[33]:

$$\chi^2 = \Sigma_i w_i [I_0^T(s) - I_0^E(s)]^2 \qquad (4.5.1.7)$$

where w_i were weighting factors over different regions of the pattern, $I^T(s)$ was given by:

$$I_0^T(s) = I_B(s)[1 + R \cdot M^T(s)] \qquad (4.5.1.8)$$

and the parameterized background curve was:

$$I_B(s) = A\exp(-\alpha s) + \sum_n a_n s^n \qquad (4.5.1.9)$$

The order of the polynomial in the background curve was limited to prevent the introduction of spurious oscillations. For experimental data which do not include the region below s $\approx$ 7 Å^{-1}, it is sufficient to neglect the exponential term. Background smoothness is guaranteed by limiting the degree of the polynomial. At scattering angles corresponding s smaller than 6 or 7 Å^{-1}, the division of experimental by calculated atomic intensities does not level the data as satisfactorily as it does at larger angles. Inside this limit, the derived background functions usually fall off rapidly as the scattering angle decreases. The imperfect leveling might be from a deficiency in

the theory. The coefficient A is allowed to vary freely and α is kept constant at a value in the range of 0.5 to 2. The atomic background intensity function, I_A, itself, has gentle bumps in it arising from the shell-like structure of atoms. Unless the total intensity function is leveled by a suitably bumpy calculated I_A^T as described above, the smoothness criterion breaks down and the accuracy of the analysis is diminished. An initial trial background need not involve the manual plotting and visual selection typical of the previous scheme. The simplest procedure is to feed the initial background in as a constant representing the approximate mean leveled intensity. A procedure which may be somewhat more accurate is to obtain, by least squares, the parameters of a low-order polynomial which best follows the trends of $I_0(s)$. Another procedure is to calculate I_B^T from $I_0^T(s) = I_B^T(s)[1 + R \cdot M^T(s)]$ assuming trial values for the molecular parameters and using the experimental $I_0(s)$. The calculated I_B^T can then be fitted using $I_B^T(s) = A \cdot \exp(-\alpha s) + \sum_n a_n s^n$ with a least-squares method. All of these procedures have been used successfully. The last alternative is the most accurate, of course, if good guesses are available for bond lengths and amplitudes. It is obviously the procedure most likely to introduce an operator bias into the analysis, however.

Other variants on background-correction techniques included refinement of the radial distribution curve[5], least squares fitting of the background curve (rather than $I(s)$)[50], and optimization of the smoothness of the background curve[48]. More recently, various fitting mechanisms have replaced the single background function like Eq. (4.5.1.8) with a series of splines, third- or fifth-order polynomials applied piecewise across the scattering intensity curve[70-72]. The splines have been optimized for

smoothness and continuity of the first and second differentials at the joints. More detailed descriptions are presented in **A.3**.

In the Western U.S.-Western European school, $I^E(s)$ is not divided by $I_A{}^T$. Instead, $I^E(s)$ is multiplied by s^4 or $1/|f_a||f_b|$ to bring out the molecular interference terms.

$$I^{\cancel{E}}(s) = I^E(s) \times L(s) \tag{4.5.1.10}$$

where $L(s)$ is a leveling function, which can take many forms.

$$L(s) = s^n \ (n = 3 \text{ or } 4) \tag{4.5.1.11a}$$

$$L(s) = 1/|f_a||f_b| \tag{4.5.1.11b}$$

$$L(s) = s/|f_a||f_b| \tag{4.5.1.11c}$$

$$L(s) = 1/I_A(s) \tag{4.5.1.11d}$$

$$L(s) = s/I_A(s) \tag{4.5.1.11d}$$

$$L(s) = 1/I_{Ref}(s) \tag{4.5.1.11e}$$

$$L(s) = s/I_{Ref}(s) \tag{4.5.1.11f}$$

In the case of Eq. (4.5.1.11d), $I^{\cancel{E}}(s)$ actually becomes identical to I_0 in Eq. (4.5.1.4), and $I^{\cancel{E}}(s)$ becomes the ratio curve $R^E(s)$ if Eq. (4.5.1.11f) is used. $I^{\cancel{E}}(s)$, then, is used for further analysis. Usually, the first step is the removal of background ($I'_B{}^E(s)$).

$$I'_M{}^E(s) = I^{\cancel{E}}(s) - I'_B{}^E(s) \tag{4.5.1.12}$$

Then, $sM^E(s)$ can be obtained by

$$sM^E(s) = [s/L(s)]\cdot[I^{\cancel{E}}(s) - I'_B{}^E(s)] \tag{4.5.1.13}$$

The modified experimental molecular scattering intensity can be defined as

$$sM^{E}(s) = s\frac{I^{E}(s) - I_{B}{}^{E}(s)}{I_{A}(s)} \qquad (4.5.1.14a)$$

in the case of Eq. (4.5.1.11d), or

$$sM^{E}(s) = s\frac{I^{E}(s) - I_{B}{}^{E}(s)}{|f_{a}\|f_{b}|}. \qquad (4.5.1.14b)$$

in the case of Eq. (4.5.1.11b).The least squares can be done by minimizing the function

$$\chi^2 = \Sigma_i w_i [sM^{T}(s) - sM^{E}(s)]^2 \qquad (4.5.1.15)$$

In general, the fit of the background function and the fit of the structural parameters are performed iteratively until a self-consistent fit is obtained.

4.5.2 Data Analysis Of Ground-State Data

Figure 4.5.1 shows a schematic of our approach in analyzing the ground state data. It was not possible to obtain a universal curve for $I'_{B}{}^{E}(s)$ with merely a calibration of the detector because the amount of scattered laser light (absent in the conventional experiments but present in UED) and other factors varied from experiment to experiment and with each molecular system. Instead, background curves were independently estimated for each experiment. Such background curves may be estimated using a variety of methods, three of which are described below:

(1) A crude yet often effective approximation is a low-order polynomial curve fit through all the data points of $I^{E}(s)$.

A more rigorous way of obtaining $I'_{B}{}^{E}(s)$ utilizes the fact that $I'_{M}(s)$ is a

sinusoidal function, cycling above and below zero several times over the experimental detection range. At each of these crossings or zero points, Eq. (4.5.1.2) shows that the raw experimental scattering intensity must be equal to $I'_B(s)$. The theoretical zero points can be identified with an adequate model of the molecular structure, and a smooth curve can be fit through $I^E(s)$ at those zero points. This fitted curve is the experimental background curve. This approach introduces a set of zero-positions, s_n, of s where the theoretical molecular intensity curve, $I'_M{}^T(s)$, crosses zero: i.e., $I'_M{}^T(s_n) = 0$. If $I'_M{}^T(s)$ approaches $I'_M{}^E(s)$, it should then hold from Eq. (4.5.1.2) that $I^E(s_n) = I'_B{}^E(s_n) + I'_M{}^E(s_n) = I'_B{}^E(s_n) + 0 = I'_B{}^E(s_n)$ at the zero-positions, s_n. Therefore, $I'_B{}^E(s)$ can be approximated by fitting a polynomial curve through $[s_n, I^E(s_n)]$.

(2) A third way to estimate $I'_B{}^E(s)$ is to express it independently as a polynomial curve defined by the variable coefficients of each order,

$$I'_B{}^E(s) = A\cdot\exp(-\alpha\cdot s) + \Sigma a^n\cdot s^n \qquad (4.5.2.1)$$

and to find these variables by minimizing χ^2 in Eq. (4.5.1.15). This method should produce the exact same background as the second method if there is no systematic error. In the case that this third method is applied, the theoretical atomic scattering intensity ($R_A{}^T(s)$) can be incorporated into $I'_B{}^E(s)$.

$$I'_B{}^E(s) = A\cdot\exp(-\alpha\cdot s) + \Sigma a^n\cdot s^n + k\, I'_A{}^T(s) \qquad (4.5.2.2)$$

where k is a scaling factor between the theory and experiment. An example is shown in Figure 4.5.2.

4.5.3 Diffraction Difference Approach

Unlike the ground-state data, the scattering intensity at time $t > 0$, $I(t > 0; s)$, contains contributions from more than one molecular species—not just the parent molecule, but also intermediates and products of the reaction. Therefore, the time-resolved $I(t; s)$ can be written as a sum of the individual scattering intensities from each species at time t, $I_\alpha(t; s)$:

$$I(t;s) = \sum_\alpha I_\alpha(t;s), \tag{4.5.3.1}$$

where α indexes all possible structures occurring over the course of the reaction. If the molecular structures of the species formed (transient or otherwise) do not change significantly over the course of the reaction within our time resolution (a satisfactory approximation for the decomposition of $C_2F_4I_2$ studied in this work), we may partition the time dependence of $I_\alpha(t; s)$ into the relative concentration of species α by writing

$$I(t;s) = \sum_\alpha I_\alpha(t;s) \approx \sum_\alpha p_\alpha(t) \cdot I_\alpha(s), \tag{4.5.3.2}$$

where $p_\alpha(t)$ is the population (or mole fraction) of a given species α and $I_\alpha(s)$ is the time *independent* scattering intensity from that species. In the present case, we will consider α to refer to parent, intermediate, and product structures.

Because there is no selectivity in the detection of excited species (all species present will scatter the incident electrons regardless of their participation in the chemical reaction), in most cases the vast majority (>85-90%) of the diffracting media is comprised of non-reacting parent molecules; $p_{parent} >> p_{intermediate}$ or $p_{product}$. Furthermore, the molecular scattering intensity from a reaction fragment is usually

weaker than that from a parent molecule because it has fewer internuclear pairs. Therefore, in order to accentuate the diffraction signal arising from structural changes occurring over the course of the reaction, we employed the so-called diffraction-difference method (Fig. 4.5.3), whereby we obtain the diffraction-difference signal, $\Delta I(t; t_{ref}; s)$, from the relation

$$\Delta I(t; t_{ref}; s) = I(t; s) - I(t_{ref}; s) \ , \qquad (4.5.3.3)$$

where t_{ref} refers to the reference time (e.g., prior to the arrival of the reaction-initiating laser pulse). Combining Eqs. (4.5.3.2) and (4.5.3.3) gives

$$\Delta I(t; t_{ref}; s) \approx \sum_{\alpha} p_{\alpha}(t) \cdot I_{\alpha}(s) - \sum_{\alpha} p_{\alpha}(t_{ref}) \cdot I_{\alpha}(s) = \sum_{\alpha} \Delta p_{\alpha}(t; t_{ref}) \cdot I_{\alpha}(s). \qquad (4.5.3.4)$$

Eq. (4.5.3.4) thus presents $\Delta I(t; t_{ref}; s)$ in terms of the *changing populations* of the molecular structures involved—a particularly useful approximation when the structures of individual species do not change considerably over the course of the reaction. If the molecular structure of a given species does undergo significant structural change over the course of the experiment, it will be necessary to refine its structural parameters at each point in time.

The diffraction-difference method has several general advantages. First, the large (unwanted) background signal from atomic scattering is a common contribution to all images—regardless of time and fragmentation—and can, therefore, be essentially removed by subtraction. It follows from the definition of the total scattering intensity, I^E (= $I_M{}^E + I_B{}^E$), that the experimental difference curve is given by

$$\Delta I^E(t; t_{ref}; s) = \Delta I_M{}^E(t; t_{ref}; s) + \Delta I_B{}^E(t; t_{ref}; s). \quad (4.5.3.5)$$

Because $I_B{}^E$ is comprised mostly of atomic scattering, I_A, which is unchanged over the course of a chemical reaction, $\Delta I_B{}^E(t; t_{ref}; s)$ should be nearly zero. Thus, the total diffraction signal, $I(t; s)$, is dominated by the background intensity, $I_B{}^E(t; s)$, but the diffraction-difference curve is dominated by the molecular scattering intensity, $I_M{}^E(t; s)$:

$$\Delta I^E(t; t_{ref}; s) \approx \Delta I_M{}^E(t; t_{ref}; s). \quad (4.5.3.6)$$

Second, any intrinsic systematic error of the detection system will be greatly reduced (or effectively eliminated) by the subtraction. Third, each diffraction-difference curve reflects comparable contributions from the parent and products, in contrast to the original raw data, which contains only a relatively small fraction of products (and/or intermediates) with the vast majority of the signal originating from the parent. Therefore, the significance of the product contribution is dramatically enhanced in $\Delta I(t; t_{ref}; s)$: $|\Delta p_{parent}| \approx |\Delta p_{intermediate}| \approx |\Delta p_{product}|$. Note that the diffraction-difference method does not depend on the specific formulae used to express I_M.

Prior to analyzing the diffraction-difference signals, high-frequency noise was reduced with low-pass Fourier filtering (performed via convolution with a parabolic cut-off function valued 1.0 at 0.0 Å and 0.0 at ≈8.7 Å). This filter, which was carefully chosen to prevent any significant damping of higher-frequency components of the diffraction signal, reduced the standard deviation values resulting from least-squares fitting by about half compared to similar analyses of unfiltered data but did not significantly alter the results of the fit.

As mentioned earlier, because I_B^E is comprised mostly of atomic scattering, I_A, which is unchanged over the course of a chemical reaction, $\Delta I_B^E(t; t_{ref}; s)$ should be nearly zero. In UED experiments, however, a residual background of a small intensity have been observed. The origin of this small baseline is not completely known, but has been attributed to the effect of the photo-generated ions formed in the molecular beam. This residual baseline can be estimated using the same approaches used for the ground state data (**4.5.2**):

A crude yet often effective approximation is a low-order polynomial curve fit through all the data points of $I^E(s)$. An example of the baseline removal with this method is given in Figures 4.5.4 and 4.5.5. Figure 4.5.4 shows the time-resolved raw diffraction-difference curves (divided by reference gas) for a CHD ring-opening reaction (**6.1**). After the baseline removal, a new set of data is obtained in Figure 4.5.5. One can see that the baseline is removed quite effectively. A more rigorous way of obtaining $\Delta I_B^E(t; t_{ref}; s)$ utilizes the fact that $\Delta I_M^E(t; t_{ref}; s)$ is a sinusoidal function, cycling above and below zero several times over the experimental detection range. In other words, the zero-positions (s_n) of $\Delta I_M^T(t; t_{ref}; s)$ are used, and, $\Delta I_B^E(t; t_{ref}; s)$ is approximated by fitting a polynomial curve through $[s_n, \Delta I_M^E(t; t_{ref}; s)]$. A third way is to express $\Delta I_B^E(t; t_{ref}; s)$ independently as a polynomial curve defined by the variable coefficients of each order,

$$\Delta I_B^E(t; t_{ref}; s) = \Sigma a^n \cdot s^n \qquad (4.5.3.7)$$

and to find these variables by minimizing χ^2 (for example Eq. (4.5.5.1)). This method should produce the exact same background as the second method if there is no

systematic error.

4.5.4 Modified diffraction-difference approach: Product-Isolated method

The diffraction-difference method, which is described in the previous section, proved to be quite useful and successful in analyzing UED data.[54,73-76] However, the diffraction-difference method has its own drawback; since the diffraction-difference signal is composed of the newly formed products and the reacting parents, sometimes it is not so convenient to examine the detailed structural features only from the products. To remedy this problem, the original version of diffraction-difference approach can be modified as follows. First, using the diffraction-difference method, the experimental difference curve $\Delta I^E(t; t_{ref}; s)$ is fitted with a theoretical difference curve $\Delta I^T(t; t_{ref}; s)$ to yield $\Delta p_\alpha(t; t_{ref})$. By scaling the parent diffraction signal obtained at a negative time by the fraction of parent molecules depleted at each time point ($\Delta p_{parent}(t; t_{ref})$) and adding the scaled parent diffraction signal ($\Delta p_{parent}(t; t_{ref}) \cdot I_{parent}(s)$) to the diffraction difference curve, the parent contribution is canceled out. The product-isolated signal ($piI(t; s)$) can be expressed as

$$piI(t; s) = I(t;t_{ref};s) - \Delta p_{parent}(t;t_{ref}) \cdot I_{parent}(s) = \sum_{\alpha \neq parent} \Delta p_\alpha(t;t_{ref}) \cdot I_\alpha(s). \quad (4.5.4.1)$$

In practice, this product-isolated method has two major advantages over the original diffraction-difference method. First, the absence of the parent signal amplifies the sensitivity of the product signal. Second, by adding the experimental intensity at the reference time, any systematic errors relevant to the parent structure should be

eliminated. The modified analysis scheme is shown in Figure 4.5.6.

4.5.6 Least-Squares Refinement

The basic principle of the least-squares refinement can be summarized as follows. We have a model function (f) as a function of parameters $x_1, x_2, \ldots, x_n$ to use to fit experimental observations.

$$f = f(x_1, x_2, \ldots, x_m) \tag{4.5.5.1}$$

where m is the number of fitting parameters. f can be, for example, $I_M{}^T(s)$, $sM^T(s)$, $I^T(s)$, $R^T(s)$, $\Delta I_M{}^T(s)$, $\Delta sM^T(s)$, $\Delta I^T(s)$, or $\Delta R^T(s)$, to just name a few, and x_m's can be r's, l's, h's, Δ's, scaling factors or fractions. Neglecting higher order terms in eq. (4.5.5.1),

$$f = f(x_1{}^0, x_2{}^0, \ldots, x_m{}^0) + \left(\frac{\partial f}{\partial x_1}\right)_0 \Delta x_1 + \left(\frac{\partial f}{\partial x_2}\right)_0 \Delta x_2 + \ldots \left(\frac{\partial f}{\partial x_m}\right)_0 \Delta x_m \tag{4.5.5.2}$$

In a matrix notation,

$$\mathbf{F}_N = \mathbf{F}_N{}^0 + \mathbf{A}_{Nm}\mathbf{X}_m \tag{4.5.5.3}$$

where N is the number of the data points. The difference between the theory ($\mathbf{F}_N$) and the observed value ($\mathbf{F}^E$) can be defined as V.

$$\mathbf{V} = \mathbf{F}_N - \mathbf{F}^E \tag{4.5.5.4}$$

Combining eqs. (4.5.5.3) and (4.5.5.4) gives

$$\mathbf{V} = \mathbf{F}_N{}^0 - \mathbf{F}^E + \mathbf{A}_{Nm}\mathbf{X}_m = -\mathbf{N} + \mathbf{AX} \tag{4.5.5.5}$$

Introducing the weight matrix $\mathbf{W}_{NN} = \mathbf{W}$, the least-squares criterion is to minimize the following function:

$$\chi^2 = \mathbf{V'WV} \tag{4.5.5.6}$$

where **V′** means the transpose of **V**. If the weight matrix can be approximated as a diagonal matrix with w_k as the kth diagonal element, eq. (4.5.5.6) can be expressed as:

$$\chi^2 = \sum_k^N \left[w_k \left(f_k{}^E - f_k \right)^2 \right] \tag{4.5.5.7}$$

The minimum of eq. (4.5.5.6) can be obtained by finding the solution of the following equation.

$$(\partial/\partial \mathbf{X})(\mathbf{V'WV}) = \mathbf{A'WV} = \mathbf{0} \tag{4.5.5.8}$$

Combining eqs. (4.5.5.5) and (4.5.5.8) gives,

$$\mathbf{BX} = \mathbf{Y} \text{ where } \mathbf{B} = \mathbf{A'WA} \text{ , } \mathbf{Y} = \mathbf{A'WN} \tag{4.5.5.9}$$

And the solutions are

$$\mathbf{X} = \mathbf{B}^{-1}\mathbf{Y} \tag{4.5.5.10}$$

Here the elements of **X**, **B**, ad **Y** are

$$\mathbf{X};\ \delta x_i \tag{4.5.5.11}$$

$$\mathbf{B};\ B_{ij} = \sum_k^N \left[w_k \left(\frac{\partial f_k}{\partial x_k} \right)^0 \left(\frac{\partial f_k{}^E}{\partial x_k} \right)^0 \right] \tag{4.5.5.12}$$

$$\mathbf{Y};\ Y_i = \sum_k^N \left[w_k N_k \left(\frac{\partial f_k}{\partial x_k} \right)^0 \right] \tag{4.5.5.13}$$

The standard deviations of the parameters determined, $\sigma(x_i)$, and the correlation coefficients between the parameters, $\rho(x_i x_j)$, may be expressed as follows:

$$\sigma(x_i) = \left(\frac{\sum_k^N \left[w_k \left(f_k{}^E - f_k \right)^2 \right]}{N - m} \right)^{1/2} \left(B_{ii}{}^{-1} \right)^{1/2} \tag{4.5.5.14}$$

$$\rho(x_i x_j) = \frac{\sum_k^N \left[w_k \left({f_k}^E - f_k \right)^2 \right]}{N - m} \left[\sigma(x_i)\sigma(x_j) \right]^{-1} \left({B_{ij}}^{-1} \right) \qquad (4.5.5.15)$$

There is a strong correlation between the parameters x_i and x_j if $|\rho(x_i x_j)|$ is close to 1, and are uncorrelated when x_i and x_j = 0. Traditionally, a so-called R factor has been used in the electron diffraction community.

$$R = \left(\frac{\sum_k^N \left[w_k \left({f_k}^E - f_k \right)^2 \right]}{\sum_k^N \left[w_k \left({f_k}^E \right)^2 \right]} \right)^{1/2} \qquad (4.5.5.16)$$

Formerly, the weighting function cannot be determined experimentally and different form of empirical formulae have been introduced depending on the researcher. In UED, however, since the individual pixels in the digitized images are easily accessible, the weighting function can be more rigorously estimated. For example, the standard deviation ($\sigma(r_{pixel})$) for each r_{pixel} can be calculated using

$$\sigma(r_{pixel}) = \left(\frac{\sum_i^{N_{pixel}} (I - I_i)^2}{N_{pixel} \cdot (N_{pixel} - 1)} \right)^{1/2} \qquad (4.5.5.17)$$

where N_{pixel} is the number of pixels satistfying eq. (4.4.2.3) in **4.4**, I is the average intensity, and I_i is the intensity of each individual pixel. Also, the scattering process follows Poisson statistics, the standard deviation can be estimated as

$$\sigma = (\text{signal})^{1/2} \qquad (4.5.5.18)$$

Once σ's are known, w's can be approximated as

$$w_k = 1 / \sigma_k^2 \qquad (4.5.5.19)$$

If f is different from I in eq. (4.5.5.17), w_k should be accordingly adjusted with appropriate error propagation.[77]

Refinements of the diffraction data were performed with software developed in-house using a procedure (similar to that used in conventional GED[1]) that iteratively minimizes the statistical χ^2. For example, for a given difference curve, $\Delta R^E(t; t_{ref}; s)$, the determination of the relative fractions or structural parameters of each molecular species was made by minimizing

$$\chi^2 = \sum_{s_{\min}}^{s_{\max}} \frac{[\Delta sM^T(t;t_{ref};s) - \frac{1}{S_c}\Delta sM^E(t;t_{ref};s)]^2}{[\sigma(s)]^2}, \qquad (4.5.5.20)$$

where the $\Delta sM(s)$ is the difference modified molecular scattering intensity, $\sigma(s)$ is the standard deviation of $\Delta sM^E(t; t_{ref}; s)$ at each s position (over the available range), and S_c is a scaling factor (whose magnitude is determined by the amplitude of the ground-state signal). The $\sigma(s)$ values are calculated from the corresponding values of $\sigma(pix)$[74] with appropriate error propagation.[77] Actually the optimal scaling factor can be analytically obtained by finding the S_c value satisfying the following equation.

$$\frac{\partial \chi^2}{\partial S_c} = 0, \qquad (4.5.5.21)$$

In UED, the scaling factor is obtained by fitting the data taken at a negative time delay (the ground state data) and this value is kept fixed for fitting the diffraction-difference curves.

Starting from an assumed initial product distribution and the structural

parameters for each species, the software first fits the residual background, $\Delta I_B^E(t; t_{ref}; s)$, with the experimental $\Delta I^E(t; t_{ref}; s)$ values at the zero-positions (s_n) of the theoretical $\Delta I_M^T(t; t_{ref}; s)$ curve. Then the experimental $\Delta sM^E(t; t_{ref}; s)$ curve is obtained with the background-free ΔI through Eq. (4.5.1.14), and χ^2 is calculated to evaluate the quality of the fit. This procedure is repeated until the best least-squares fit between theoretical and experimental $\Delta sM(s)$ curves is reached (i.e., until χ^2 is minimized). In the fitting algorithm, the absolute amplitude of the diffraction-difference signal may then be scaled to that of the ground-state signal to give the relative number densities of every species at each time delay over the course of the experiment.

References

1. Hargittai, I. & Hargittai, M. *Stereochemical Applications Of Gas-Phase Electron Diffraction* (VCH, New York, 1988).
2. Bonham, R. A. & Schäfer, L. in *International Tables For X-Ray Crystallography* (eds. Ibers, J. A. & Hamilton, W. C.) 176 (Kynoch Press, Birmingham, 1974).
3. Yates, A. C. *Phys. Rev.* **176**, 173 (1968).
4. Sellers, H. L., Schäfer, L. & Bonham, R. A. *J. Mol. Struct.* **49**, 125 (1978).
5. Bonham, R. A. & Bartell, L. S. Rapid Procedure for Rigorous Analysis of Electron Diffraction Data. *J. Chem. Phys.* **31**, 702-708 (1959).
6. Kuchitsu, K. & Bartell, L. S. Effects of Anharmonicity of Molecular Vibrations on the Diffraction of Electrons. II. Interpretation of Experimental Structural Parameters. *J. Chem. Phys.* **35**, 1945-1949 (1961).
7. Kuchitsu, K., Fukuyama, T. & Morino, Y. Average Structures of Butadiene, Acrolein, and Glyoxal Determined by Gas Electron Diffraction and Spectroscopy. *J. Mol. Struct.* **1**, 463-479 (1967-68).
8. Hargittai, I. in *Stereochemical Applications of Gas-Phase Electron Diffraction* (eds. Hargittai, I. & Hargittai, M.) 1-54 (VCH, New York, 1988).
9. Debye, P. The Influence of Intramolecular Atomic Motion on Electron Diffraction Diagrams. *J. Chem. Phys.* **9**, 55-60 (1941).
10. Schäfer, L. Electron Diffraction as a Tool of Structural Chemistry. *Appl.*

Spectrosc. **30**, 123-149 (1976).

11. Viervoll, H. Electron Diffraction Investigation of Molecular Structures. I. Application of Fourier Analysis to the Rotating Sector Method. *Acta Chem. Scand.* **1**, 120-132 (1947).

12. Bartell, L. S. in *Physical Methods of Chemistry* (eds. Weissberger, A. & Rossiter, B. W.) (Wiley, New York, 1972).

13. Hedberg, K. & Iwasaki, M. Least-Squares Refinement of Molecular Structures from Gaseous Electron Diffraction Sector-Microphotometer Intensity Data. I. Method. *Acta Cryst.* **17**, 529-533 (1964).

14. Iwasaki, M., Fritsch, F. N. & Hedberg, K. Least-Squares Refinement of Molecular Structures from Gaseous Electron Diffraction Sector-Microphotometer Intensity Data. II. Adaptation to Automatic Computation. *Acta Cryst.* **17**, 533-537 (1964).

15. Bastiansen, O., Fritsch, F. N. & Hedberg, K. Least-Squares Refinement of Molecular Structures from Gaseous Electron Diffraction Sector-Microphotometer Intensity Data. I. Refinements of Cyclopropane. *Acta Cryst.* **17**, 538-543 (1964).

16. Seip, H. M. Studies on the Failure of the First Born Approximation in Electron Diffraction I. Uranium Hexafluoride. *Acta Chem. Scand.* **19**, 1955-1968 (1965).

17. Seip, H. M. & Stølevik, R. Studies on the Failure of the First Born Approximation In Electron Diffraction II. Osmium Tetraoxide. *Acta Chem.*

Scand. **20**, 385-394 (1966).

18. Seip, H. M. & Seip, R. Studies on the Failure of the First Born Approximation in Electron Diffraction IV. Molybdenum- and Tungsten Hexafluoride. *Acta Chem. Scand.* **20**, 2698-2710 (1966).

19. Seip, H. M. & Stølevik, R. Studies on the Failure of the First Born Approximation in Electron Diffraction III. Tellurium Hexafluoride. *Acta Chem. Scand.* **20**, 1535-1545 (1966).

20. Arnesen, S. & Seip, H. M. Studies on the Failure of the First Born Approximation in Electron Diffraction V. Molybdenum- and Tungsten Hexacarbonyl. *Acta Chem. Scand.* **20**, 2711-2727 (1966).

21. Andersen, B. & Andersen, P. An Electron Diffraction Investigation of the Molecular Structure of Di-t-butylnitroxide Free Radical in the Vapor Phase. *Acta Chem. Scand.* **20**, 2728-2736 (1966).

22. Andersen, B., Seip, H. M., Strand, T. G. & Stølevik, R. Procedure and Computer Programs for the Structure Determination of Gaseous Molecules from Electron Diffraction Data. *Acta Chem. Scand.* **23**, 3224-3234 (1969).

23. Gundersen, G. & Hedberg, K. Molecular Structure of Thionyltetrafluoride, SOF_4. *J. Chem. Phys.* **51**, 2500-2507 (1969).

24. Hagen, K. & Hedberg, K. Conformational Analysis. I. Molecular Structure, Composition, Trans-Gauche Energy and Entropy Differences, and Potential Hindering Internal Rotation of Gaseous Oxalyl Choride as Determined by Electron Diffraction. *J. Am. Chem. Soc.* **95**, 1003-1009 (1973).

25. Hedberg, L. in *Abstracts Fifth Austin Symposium on Gas Phase Molecular Structure* 37-43 (Austin, TX, 1974).

26. Bastiansen, O., Hedberg, L. & Hedberg, K. Reinvestigation of the Molecular Structure of 1,3,5,7-Cylcooctatetraene by Electron Diffraction. *J. Chem. Phys.* **27**, 1311-1317 (1957).

27. Karle, I. L. & Karle, J. Internal Motion and Molecular Structure Studied by Electron Diffraction. *J. Chem. Phys.* **17**, 1052-1058 (1949).

28. Karle, I. L. & Karle, J. Internal Motion and Molecular Structure Studied by Electron Diffraction. II. Interpretation and Method. *J. Chem. Phys.* **18**, 957-962 (1950).

29. Karle, I. L. & Karle, J. The Background Scattering of CO_2 and CCl_4, Correction. *J. Chem. Phys.* **18**, 565 (1950).

30. Almeningen, A., Bastiansen, O., Seip, R. & Seip, H. M. The Molecular Structure of Hexafluorobenzene. The Application of Least-Squares Calculation on the Electron Diffraction Intensity Data. *Acta Chem. Scand.* **18**, 2115-2124 (1964).

31. Beagley, B., cruickshank, W. J. & Hewitt, T. G. Molecular Strucures of P_4O_{10} and P_4O_9. *Trans. Frad. Soc.* **63**, 836-845 (1967).

32. Seip, H. M., Strand, T. G. & Stolevik, R. Least-Squares Refinements and Error Analysis Based on Correlated Electron diffraction Intensities of Gaseous Molecules. *Chem. Phys. Lett.* **3**, 617-623 (1969).

33. Bartell, L. S., Kohl, d. A., Carroll, B. L. & Gavin, J. R. M. Least-Squares

Determination of Structures of Gas Molecules Directly from Electron-Diffraction Intensities. *J. Chem. Phys.* **42**, 3079-3084 (1965).

34. Hastings, J. M. & Bauer, S. H. An Electron Diffraction Investigation of the Structures of Neopentyl Chloride and Silico-Neopentyl Chloride. The Determination of Intensities through the Use of a Ratating Sector. *J. Chem. Phys.* **18**, 13-26 (1950).

35. Bregman, J. & Bauer, S. H. An Electron Diffraction Study of Ketene Dimer, Methylketene Dimer and b-Propiolactone. *J. Am. Chem. Soc.* **77**, 1955-1965 (1955).

36. Keidel, F. A. & Bauer, S. H. Structure of Toluene, Phenylsilane, and Diphenyldichlorosilane. *J. Chem. Phys.* **25**, 1218-1227 (1956).

37. Kuchitsu, K. An Electron Diffraction Investigation of the Molecular Structure of 1,4-Dichlorobutyne. I. Determination of Bond Distances and Angles. *Bul. Chem. Soc. Japan.* **30**, 391-399 (1957).

38. Kuchitsu, K. An Electron Diffraction Investigation of the Molecular Structure of 1,4-Dichlorobutyne. II. A Study of Internal Rotation by Use of Halos in Small Angle Region. *Bul. Jap. Chem. Soc.* **30**, 399-402 (1957).

39. Morino, Y. & Kuchitsu, K. Electron Diffraction Study on the Rotational Isomerism in n-Propyl Chloride. *J. Chem. Phys.* **28**, 175-184 (1958).

40. Morino, Y. & Kuchitsu, K. Molecular Structure and Internal Rotation of Hexachloroethane, Hexachlorodisilane, and Trichloromethyl-trichlorosilane. *J. Chem. Phys.* **28**, 185-197 (1958).

41. Bonham, R. A. & Bartell, L. S. The Molecular Structure and Rotational Isomerization of n-Butane. *J. Am. Chem. Soc.* **81**, 3491-3498 (1959).

42. Bartell, L. S., Kuchitsu, K. & DeNeui, R. J. Mean and Equilibrium Molecular Structures of Methane and Dueteromethane as Determined by Electron Diffraction. *J. Chem. Phys.* **35**, 1211-1218 (1961).

43. Shibata, S., Bartell, L. S. & Gavin, J. R. M. Molecular structure and Bonding of InC_5H_5. *J. Chem. Phys.* **41**, 717-722 (1964).

44. Morino, Y., Kuchitsu, K. & Murata, Y. A Critical Examination of the Statistical Method for the Analysis of Gas Electron Diffraction Data. *Acta Cryst.* **18**, 549-557 (1965).

45. Shibata, S. & Bartell, L. S. Electron-Diffraction Study of Water and Heavy Water. *J. Chem. Phys.* **42**, 1147-1151 (1965).

46. Murata, Y. & Morino, Y. Correlation of Observation in the Least-Squares Calculation for the Analysis of Gas Electron Diffraction Data. *Acta Cryst.* **20**, 605-609 (1966).

47. Bartell, L. S. A New Approach to Error Analyses in Electron Diffraction. *Acta Cryst.* **A25**, S76 (1969).

48. Shibata, S. & Bartell, L. S. Least-Squares Determination of Molecular Structures from Gaseous Electron Diffraction Data. I. Slope and Curvature Criteria for Background. *J. Mol. Struct.* **9**, 1-9 (1971).

49. D'Antonio, P., George, C., Lowrey, A. H. & Karle, J. Electron Diffraction Investigation of Dimetyl Diselenide. *J. Chem. Phys.* **55**, 1071-1075 (1971).

50. Shibata, S. Least-Squares Determination of Molecular Structures from Gaseous Electron-Diffraction Data. II. Polynomial Expression of Background. *Bul. Chem. Soc. Jap.* **45**, 1631-1634 (1972).

51. Geiser, J. D. & Weber, P. M. Pump-probe diffraction imaging of vibrational wave functions. *J. Chem. Phys.* **108**, 8004-8011 (1998).

52. Liu, W.-K. & Lin, S. H. Theory of gas-phase time-resolved ultrafast electron diffraction. *Phys. Rev. A* **55**, 641-647 (1997).

53. Ben-Nun, M., Martínez, T. J., Weber, P. M. & Wilson, K. R. Direct imaging of excited electronic states using diffraction techniques: theoretical considerations. *Chem. Phys. Lett.* **262**, 405-414 (1996).

54. Cao, J., Ihee, H. & Zewail, A. H. Ultrafast electron diffraction and direct observation of transient structures in a chemical reaction. *Proc. Natl. Acad. Sci. USA* **96**, 338-342 (1999).

55. Ischenko, A. A., Ewbank, J. D. & Schäfer, L. Structural and Vibrational Kinetics by Time-Resolved Gas Electron Diffraction: Stochastic Approach to Data Analysis. *J. Phys. Chem.* **99**, 15790-15797 (1995).

56. Lobastov, V. A., Ewbank, J. D., Schäfer, L. & Ischenko, A. A. Instrumentation for time-resolved electron diffraction spanning the time domain from microseconds to picoseconds. *Rev. Sci. Instrum.* **69**, 2633-2643 (1998).

57. Ischenko, A. A., Schäfer, L., Luo, J. Y. & Ewbank, J. D. Structural and Vibrational Kinetics by Stroboscopic Gas Electron Diffraction: The 193 nm Photodissociation of CS_2. *J. Phys. Chem.* **98**, 8673-8678 (1994).

58. Ischenko, A. A., Ewbank, J. D. & Schäfer, L. Structural kinetics by stroboscopic gas electron diffraction. Part 1. Time-dependent molecular intensities of dissociative states. *J. Mol. Struct.* **320**, 147-158 (1994).

59. Bonham, R. A. & Fink, M. *High Energy Electron Scattering* (Van Nostrand Reinhold, New York, 1974).

60. Kohl, D. A. & Shipsey, E. J. Elastic electron scattering from state-selected molecules. *Z. Phys. D* **24**, 33-38 (1992).

61. McQuarrie, D. A. *Statistical Mechanics* (Harper & Row, New York, 1973).

62. Hedberg, L. & Mills, I. M. ASYM20: A Program for Force Constant and Normal Coordinate Calculations, with a Critical Review of the Theory Involved. *J. Mol. Spectrosc.* **160**, 117-142 (1993).

63. Cyvin, S. J. *Molecular Vibrations and Mean Square Amplitudes* (Elsevier Publishing Company, Amsterdam, 1968).

64. Califano, S. *Vibrational States* (John Wiley & Sons, London, 1976).

65. Cyvin, S. J. & Mastryukov, V. S. Relations between mean amplitudes of vibration and corresponding internuclear distances II. Bonded carbon-carbon distances. *J. Mol. Struct.* **30**, 333-337 (1976).

66. Mastryukov, V. S. & Cyvin, S. J. Relations between mean amplitudes of vibration and corresponding internuclear distances I. Bonded and nonbonded carbon-carbon distances. *J. Mol. Struct.* **29**, 15-25 (1975).

67. Mastryukov, V. S. & Osina, E. L. The relationship between vibrational amplitudes and internuclear distances IV. Amplitudes for element-hydrogen

distances. *Zhu. Struk. Khim.* **17**, 172-174 (1976).

68. Mastryukov, V. S., Osina, E. L., Vilkov, L. V. & Cyvin, S. The relationship between vibrational amplitudes and internuclear distances V. Bonded and nonbonded CH distances. *Zhu. Struk. Khim.* **17**, 80-85 (1976).

69. Taguchi, M. & Iijima, T. Construction of an Electron Diffraction Unit for Gases as Fitted for the Use of Photographic Sheet Films. *Jpn. J. Appl. Phys.* **23**, 1509-1517 (1984).

70. Spiridonov, V. P., Prikhod'ko, A. Y. & Butayev, B. S. Computer-Generated Backgrounds for Gas-Phase Electron Diffraction Analysis. *Chem. Phys. Lett.* **65**, 605-609 (1979).

71. Novikov, V. P. Application of Spline Functions in Programs for Gas Phase Electron Diffraction Analysis. *J. Mol. Struct.* **55**, 215-221 (1979).

72. Mijlhoff, F. C. Computer-Drawn Backgrounds For Gas Phase Electron Diffraction Analysis Using Spline Functions. *J. Mol. Struct.* **27**, 447 (1975).

73. Ihee, H., Cao, J. & Zewail, A. H. Ultrafast electron diffraction: structures in dissociation dynamics of $Fe(CO)_5$. *Chem. Phys. Lett.* **281**, 10-19 (1997).

74. Cao, J., Ihee, H. & Zewail, A. H. Ultrafast electron diffraction: determination of radical structure with picosecond time resolution. *Chem. Phys. Lett.* **290**, 1-8 (1998).

75. Ihee, H. *et al.* Direct Imaging of Transient Molecular Structures with Ultrafast Diffraction. *Science* **291**, 458-462 (2001).

76. Ihee, H., Cao, J. & Zewail, A. H. Ultrafast electron diffraction of transient

[$Fe(CO)_4$]: Determination of molecular structure and reaction pathway. *Angew. Chem. Int. Ed.*, in press (2001).

77. Taylor, J. R. *An Introduction to Error Analysis: the Study of Uncertainties in Physical Measurements* (The University Science Book, Mill Valley, CA, 1982).

Table 4.1.1. The most important internuclear distance parameters[1,2]

Operational parameters

r_a: effective internuclear distance in the expression of the molecular contribution to electron scattering intensities

r_0: effective internuclear distance obtained from the rotational constants (usually, though not always, refers to the ground vibrational state)

r_s: effective internuclear distance determined from the isotropic substitution coordinates of the respective atoms

Parameters with well-defined physical meaning

r_e: equilibrium distance between the positions of atomic nuclei corresponding to the minimum of the potential energy

r_v: distance between average nuclear positions in the vth vibrational state

r_α^0 / r_z: distance between average nuclear positions in the ground vibrational state

r_α: distance between average nuclear positions in thermal equilibrium at temperature T

r_g: average bond length (or generally, average internuclear distance) at temperature T

Figure Captions

Figure 4.1.1: Atomic scattering geometry. An incident electron beam propagates along the z-axis and scatters off an atom at the origin. Scattered intensity, detected in the far field at R, is a function of the angle θ.

Figure 4.1.2: Atomic scattering geometry. The incident electron beam propagates along the z-axis and scatters from an atom displaced from the origin by r_0. Scattered intensity is measured in the far field at point P. The scattered intensity is integrated over all infinitesimal volume elements dr.

Figure 4.2.1: Effects of high vibrational energy on the electron diffraction signal for a model diatomic molecule. **a**, An increased l value (red) from a thermal (Boltzmann) vibrational population (left) results in broadening of the $f(r)$ curve (middle) and damping of the $sM(s)$ curve (right). **b**, Inverted (non-Boltzmann) vibrational populations modeled with Gaussian distributions (left). Low-lying inverted populations (red) will cause broadening of the $f(r)$ curve and damping of the $sM(s)$ curve similar to the Boltzmann case above. Higher-lying populations (green) can lead to bifurcation of the internuclear density and significant changes in the frequency components of the $sM(s)$ scattering signal.

Figure 4.5.1: Schematic of the processing procedure for 2-D diffraction images and ground-state data analysis.

Figure 4.5.2: An example of the application of the third method of the background removal described in **4.5.2**. The upper panel shows the original raw data (ratio curve) along with the scaled theoretical atomic scattering intensity and the residual polynomial background. The middle panel shows the raw ratio curve after the subtraction of the scaled atomic scattering intensity and the lower panel shows the final ratio curve after further subtraction of the residual background obtained from the least-squares minimization of χ^2.

Figure 4.5.3: Schematic of the diffraction-difference analysis procedure for time-resolved experiments.

Figure 4.5.4: Time-resolved raw diffraction-difference curves (divided by reference gas) for a CHD ring-opening reaction (**6.1**).

Figure 4.5.5: Residual background (baseline) is removed from the raw diffraction-difference curves shown in Figure 4.5.4. One can see that the baseline is removed quite effectively.

Figure 4.5.6: Schematic of the modified diffraction-difference analysis procedure including the product-isolated method.

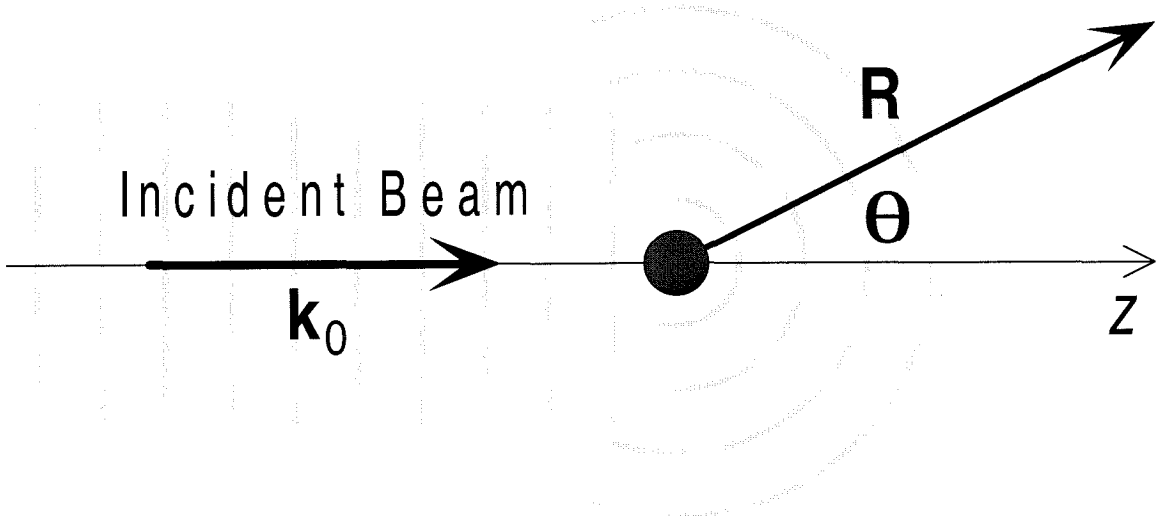

Figure 4.1.1

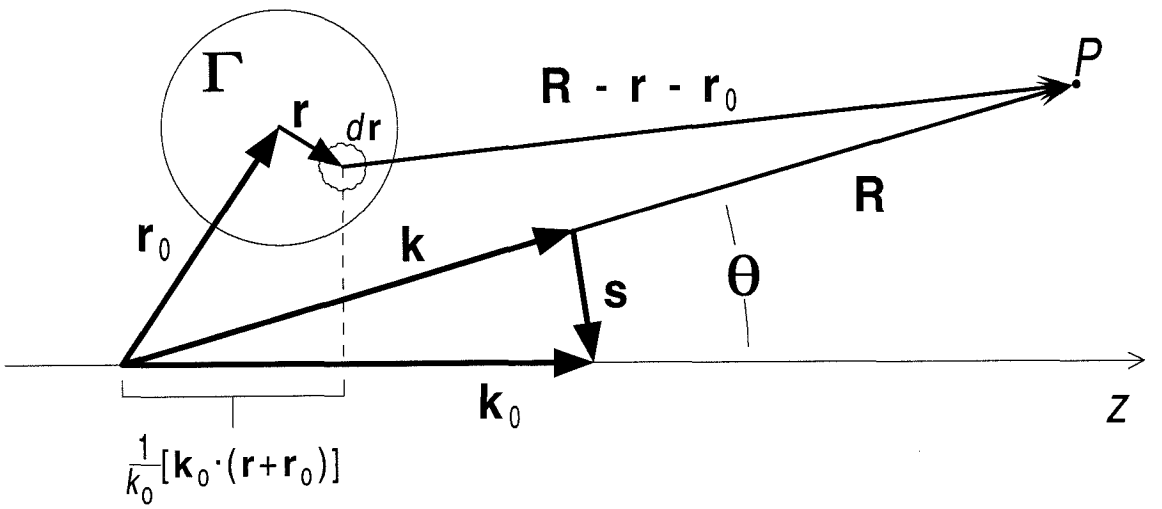

Figure 4.1.2

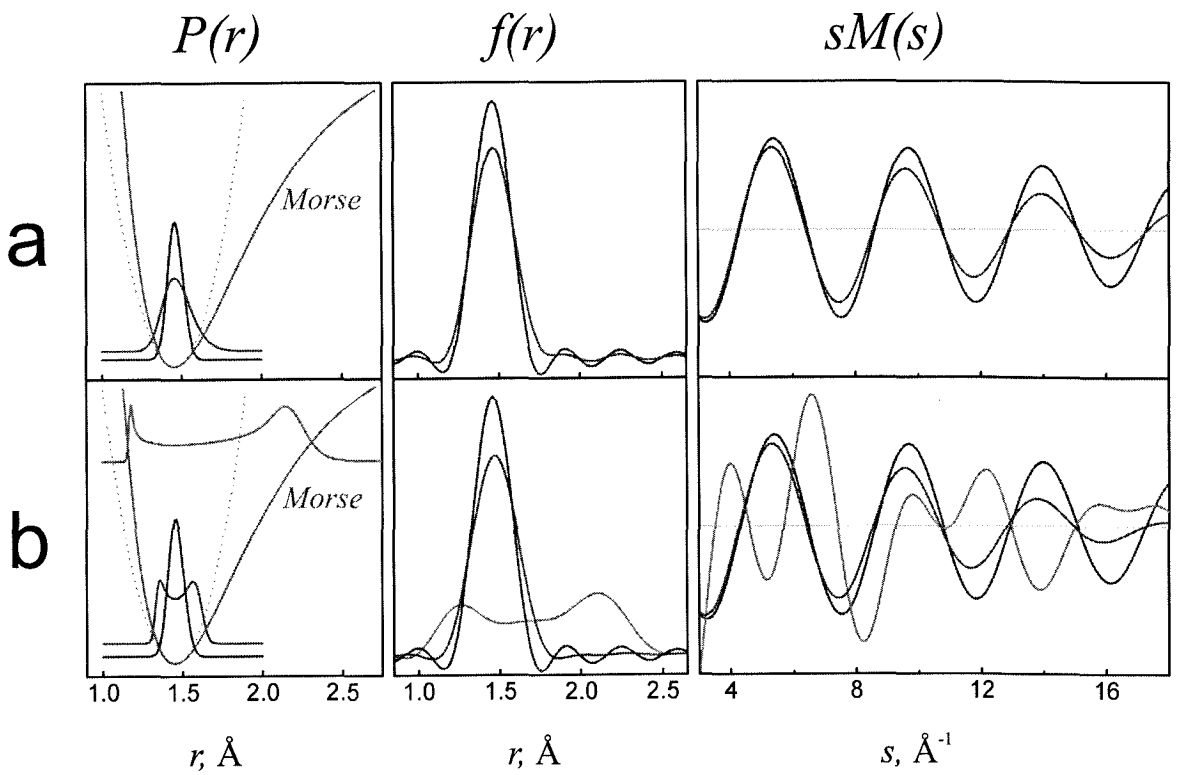

Figure 4.2.1

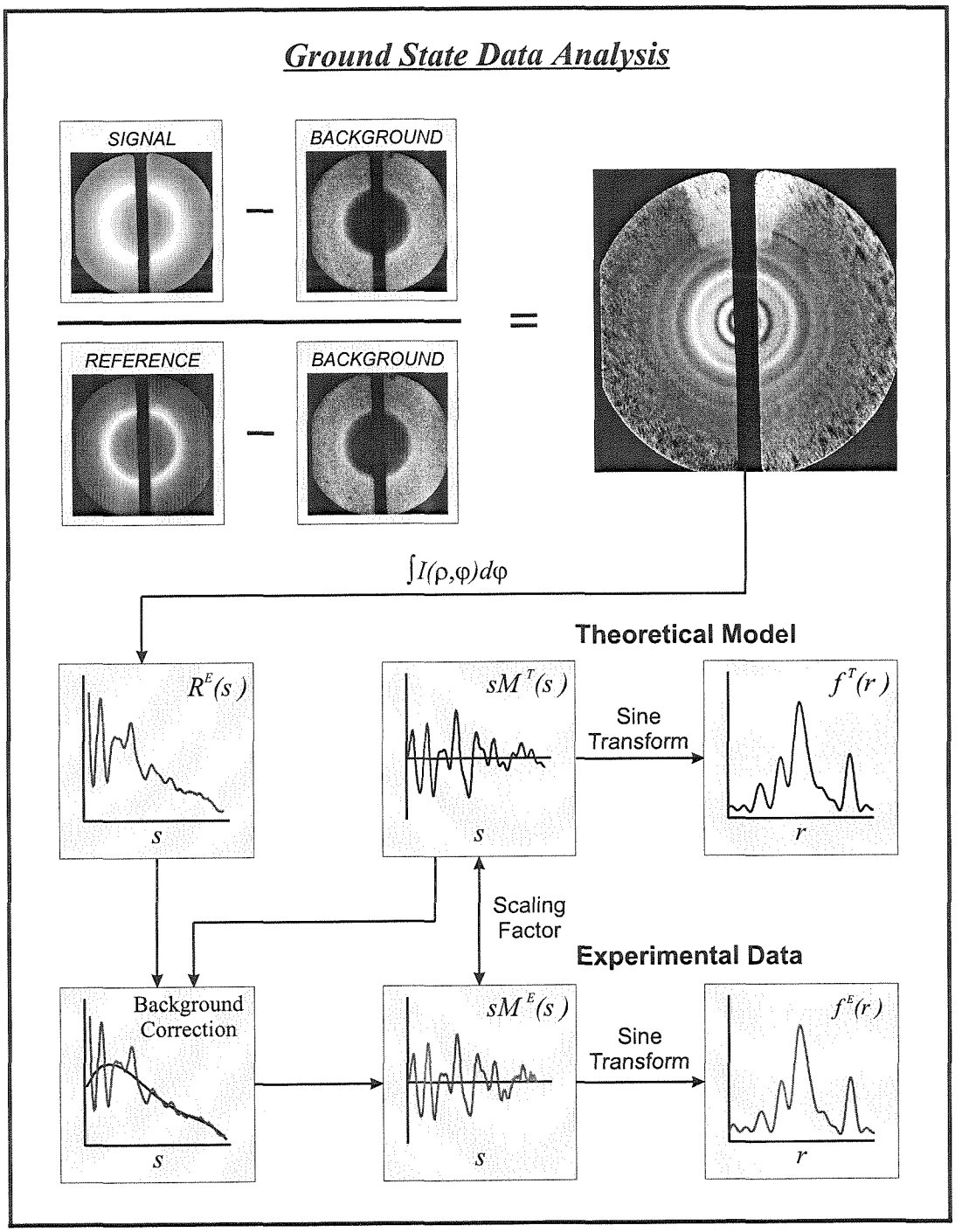
Ground State Data Analysis
SIGNAL
BACKGROUND
REFERENCE
BACKGROUND
$\int I(\rho,\varphi)d\varphi$
Theoretical Model
$R^E(s)$
$sM^T(s)$
Sine Transform
$f^T(r)$
Scaling Factor
Experimental Data
Background Correction
$sM^E(s)$
Sine Transform
$f^E(r)$
s
r

Figure 4.5.1

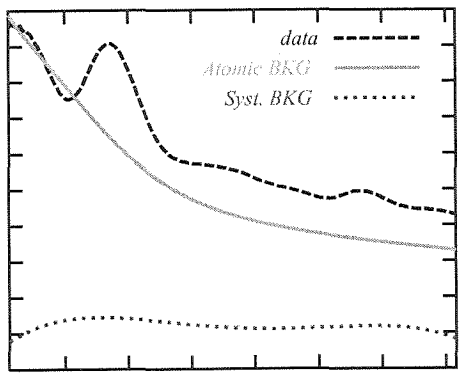

s (Å^{-1})

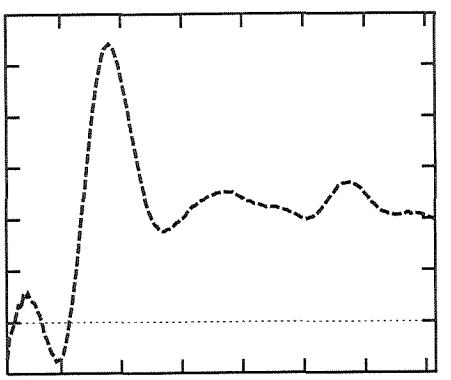

s (Å^{-1})

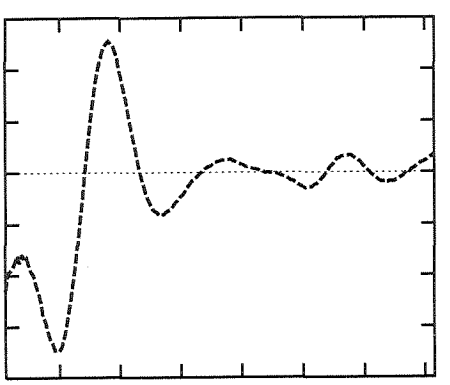

s (Å^{-1})

Figure 4.5.2

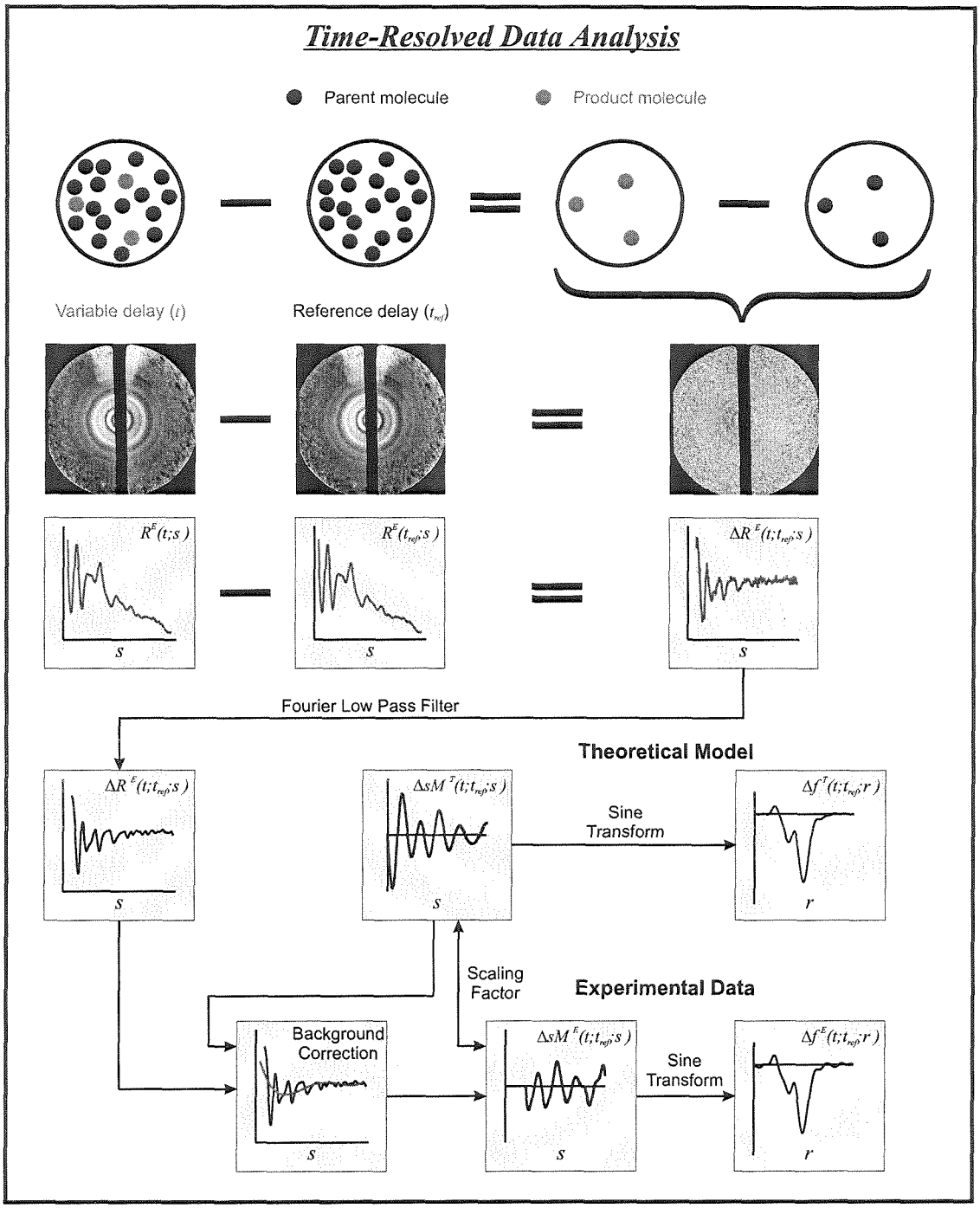
Time-Resolved Data Analysis
Parent molecule
Product molecule
Variable delay (t)
Reference delay (t_ref)
R^E(t;s)
R^E(t_ref;s)
ΔR^E(t;t_ref;s)
s
Fourier Low Pass Filter
Theoretical Model
ΔsM^T(t;t_ref;s)
Sine Transform
Δf^T(t;t_ref;r)
r
Scaling Factor
Experimental Data
Background Correction
ΔsM^E(t;t_ref;s)
Δf^E(t;t_ref;r)

Figure 4.5.3

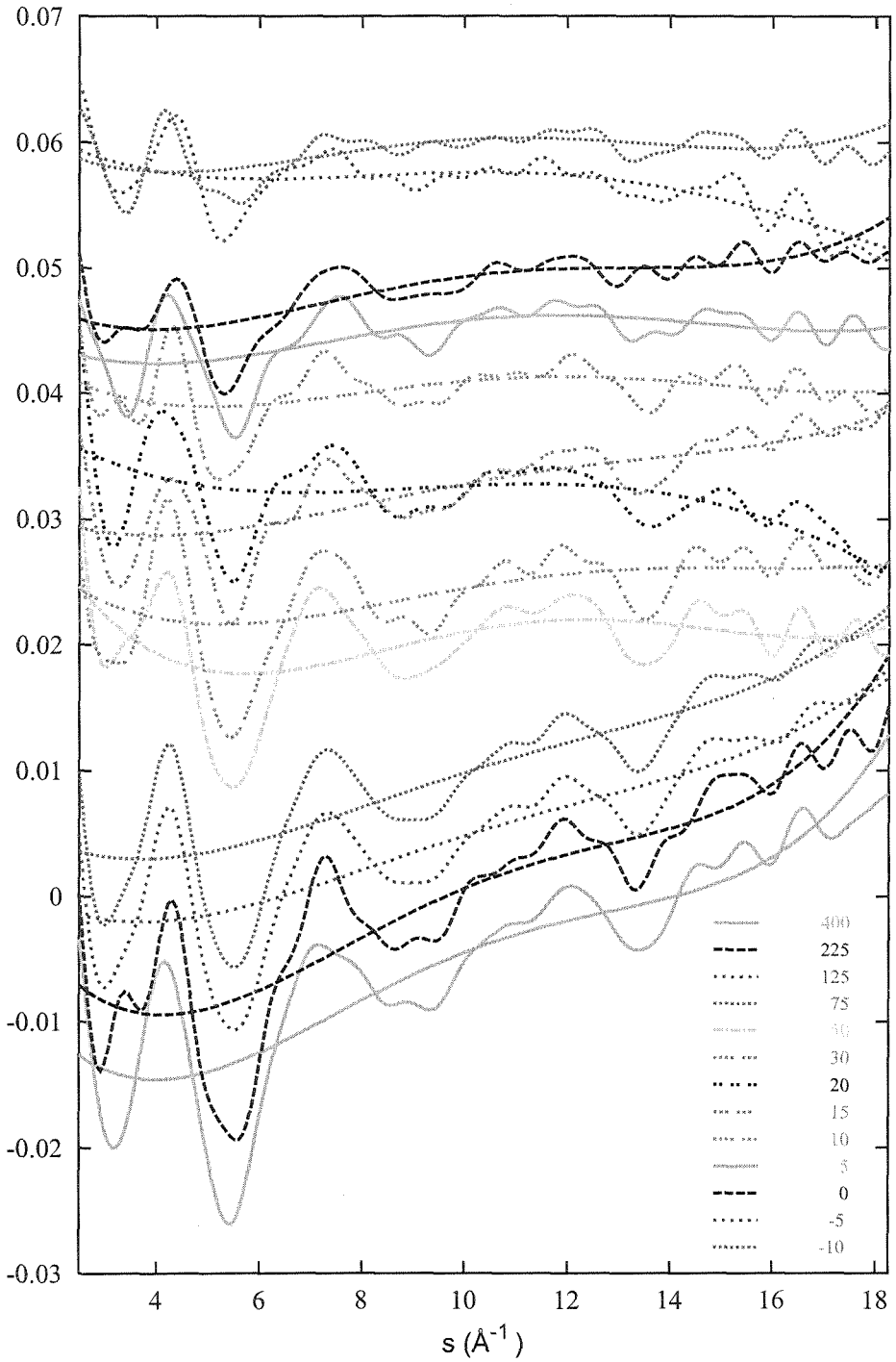
0.07
0.06
0.05
0.04
0.03
0.02
0.01
0
-0.01
-0.02
-0.03
4
6
8
10
12
14
16
18
s (Å-1)
400
225
125
75
50
30
20
15
10
5
0
-5
-10

Figure 4.5.4

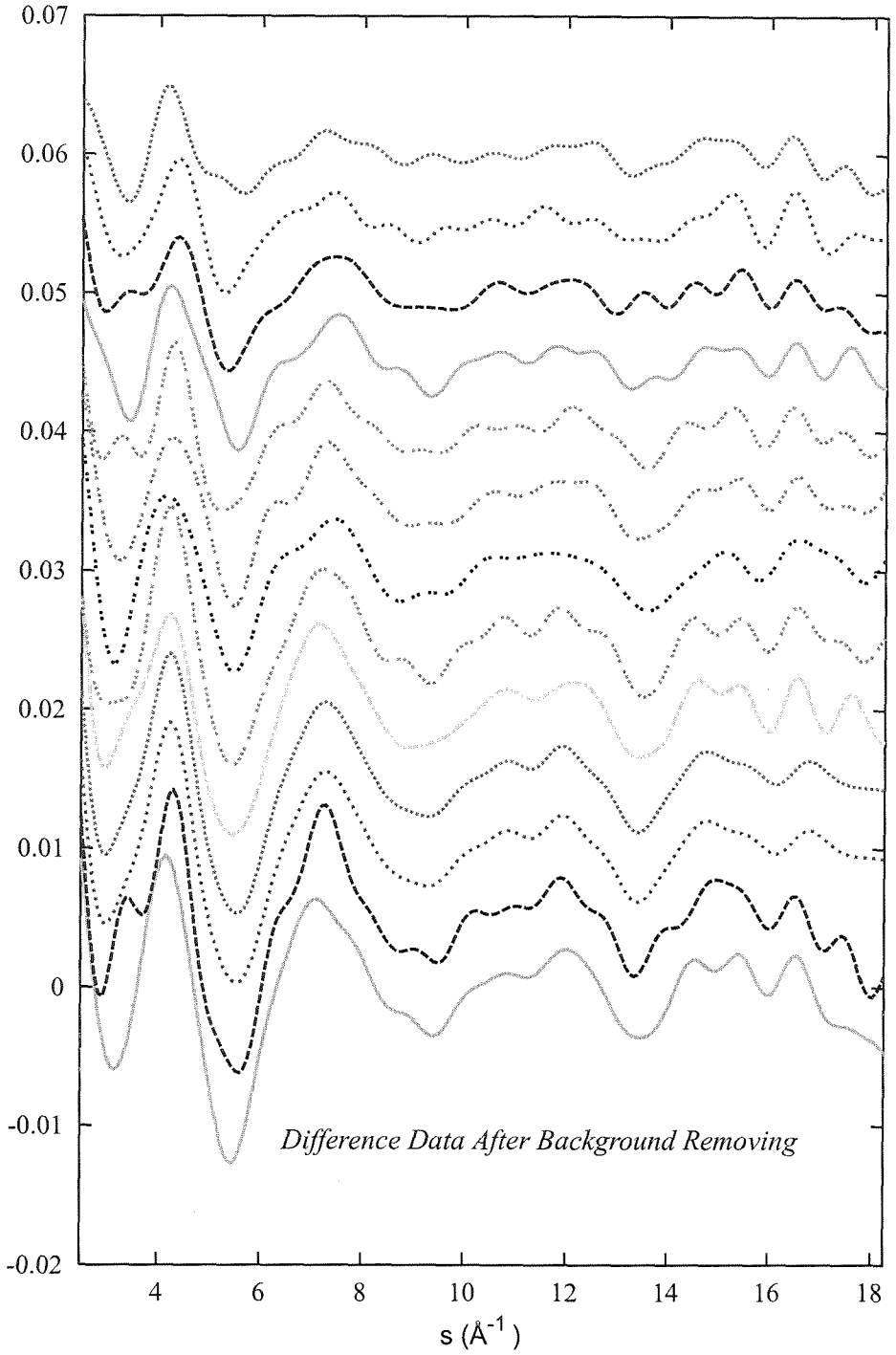
0.07
0.06
0.05
0.04
0.03
0.02
0.01
0
-0.01
-0.02
4
6
8
10
12
14
16
18
s (Å-1)
Difference Data After Background Removing

Figure 4.5.5

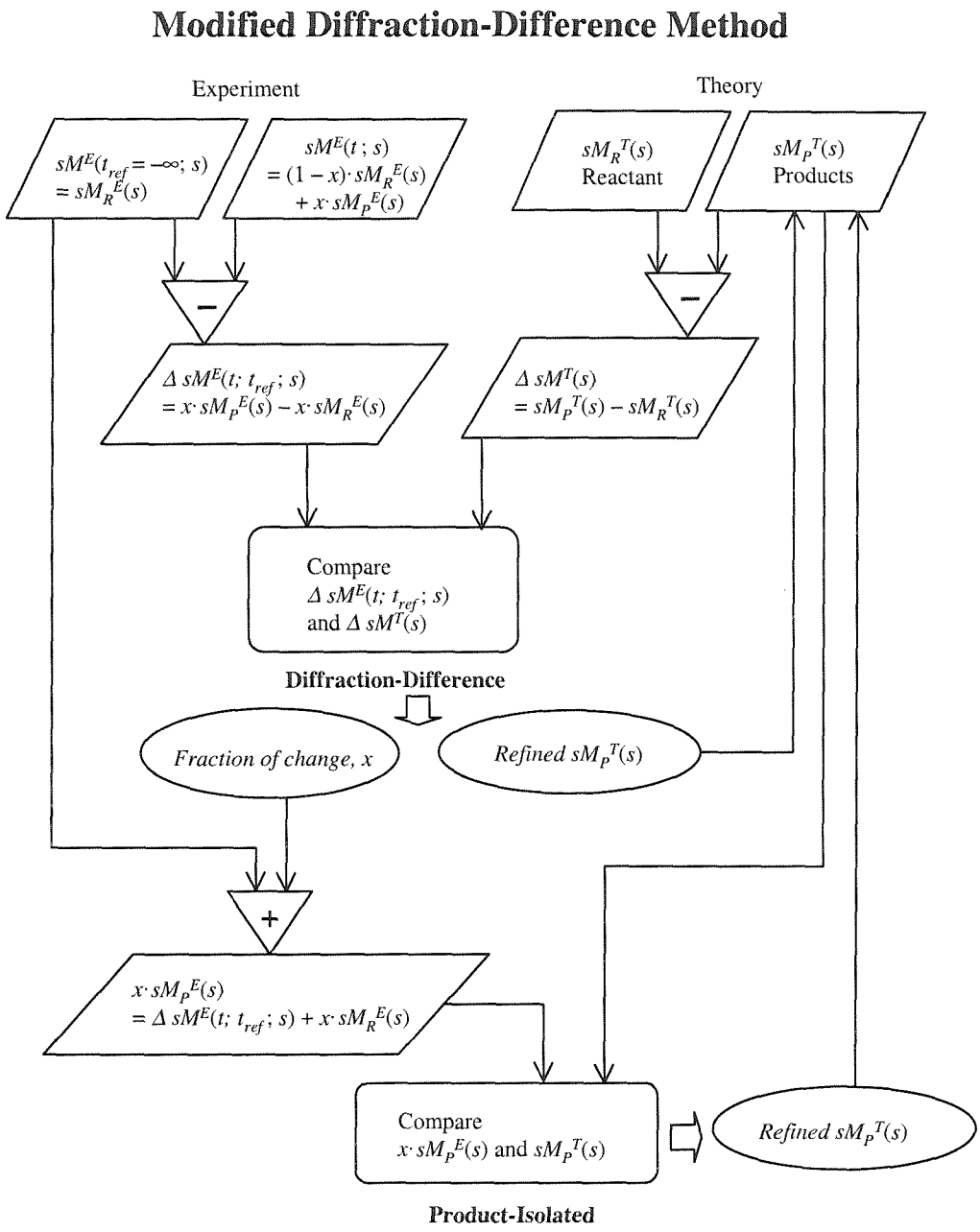
Modified Diffraction-Difference Method
Experiment
Theory
$sM^E(t_{ref} = -\infty; s) = sM_R{}^E(s)$
$sM^E(t; s) = (1-x)\cdot sM_R{}^E(s) + x\cdot sM_P{}^E(s)$
$sM_R{}^T(s)$ Reactant
$sM_P{}^T(s)$ Products
−
−
$\Delta\, sM^E(t; t_{ref}; s) = x\cdot sM_P{}^E(s) - x\cdot sM_R{}^E(s)$
$\Delta\, sM^T(s) = sM_P{}^T(s) - sM_R{}^T(s)$
Compare $\Delta\, sM^E(t; t_{ref}; s)$ and $\Delta\, sM^T(s)$
Diffraction-Difference
Fraction of change, x
Refined $sM_P{}^T(s)$
+
$x\cdot sM_P{}^E(s) = \Delta\, sM^E(t; t_{ref}; s) + x\cdot sM_R{}^E(s)$
Compare $x\cdot sM_P{}^E(s)$ and $sM_P{}^T(s)$
Refined $sM_P{}^T(s)$
Product-Isolated

Figure 4.5.6

Ultrafast Electron Diffraction

Volume Two

Thesis By

Hyotcherl Ihee

In Partial Fulfillment of the Requirements for the Degree of
Doctor of Philosophy

California Institute of Technology
Pasadena, California
2001

(Submitted April 30, 2001)

TABLE OF CONTENTS

Volume One

Volume Two

CHAPTER FIVE

APPLICATIONS TO HALOALKANES

5.1 $CH_2I_2 \rightarrow CH_2I + I$ @ 310 nm

5.1.1 Introduction

CH_2I_2 was chosen as the first molecule to apply the 2nd generation UED apparatus since it satisfied the following good UED sample criteria. 1) It is volatile enough under moderate heating to provide a few torr of pressure at the molecular beam nozzle orifice. 2) It has a relatively high absorption cross-section at 310 nm, which is the second harmonic of the fundamental wavelength of 620 nm from CPM/PDA laser system. 3) After absorbing one photon of 310 nm, CH_2I_2 loses one Iodine atom. This dissociation involves the depopulation of the I..I internuclear distance, which is the biggest contributor in the molecular scattering of electrons. Therefore, considerable change is expected after the loss of the Iodine atom. In addition, the dynamics of CH_2I_2 has been well studied by other techniques, thereby providing a good ground for comparison of the new technique of UED with other well-established techniques.

Diiodomethane is a yellowish transparent liquid at room temperature (mp: 6 °C) and its boiling point is 182 °C. The absorption cross-section at 310 nm is 3.25×10^{-18} cm^2. (see **2.4.2**) The absorption begins in the near UV and three photochemical reactions are energetically possible at 310 nm:

$$CH_2I_2 \rightarrow CH_2I + I\ (^2P_{3/2}) \qquad (5.1.1.1)$$

$$CH_2I_2 \rightarrow CH_2I + I^*\ (^2P_{1/2}) \qquad (5.1.1.2)$$

$$CH_2I_2 \rightarrow CH_2 + I_2 \qquad (5.1.1.3)$$

Among these reactions, the third channel where the molecular iodine is generated is symmetry-forbidden in the wavelength we used, so only the first two channels are available. Even if the third channel is actually active as shown by other femtosecond experiments, the actual branching ratio is extremely small compared to the other two channels and it is doubtful that UED would even pick it up. I and I* are formed on the lowest electronic states with B_1 symmetry, and the transition moment lies along the I...I internuclear separation. At 310 nm, 20-25% of the reaction proceeds along the I* channel.

5.1.2 Experimental Setup And Method

In order to probe ps and sub-ps changes and the associated orientational anisotropy with UED, three basic experiments must be incorporated into our apparatus: measurement of the electron pulsewidth, accurate clocking of the reaction, and detection of single electrons (necessary to reduce the electron flux and minimize space-charge broadening). To this end the second-generation UED apparatus (Fig. 5.1.1) was developed. The apparatus is composed of a fs laser, an ultrafast electron gun, a free-jet expansion source, and a newly designed two-dimensional single-electron detection system. Femtosecond laser pulses were created using a colliding-pulse mode-locked ring dye laser. The output was directed through a four-stage pulsed dye amplifier with no pulse compression (620 nm, 2-3 mJ, 30 Hz, 300 fs). For initiation of the reaction, 95% of this beam was doubled (310 nm, ~250 μJ). The remainder (also doubled) was focused onto a back-illuminated, negatively-biased

photocathode to generate the electron pulse via the photoelectric effect.

The ejected photoelectrons were accelerated through a series of electrostatic lenses that collimate and focus the electron beam; for 19 keV, λ is 0.088 Å. The position of the electron beam was controlled with horizontal and vertical deflectors. Two closely spaced metal plates were used for streaking experiments. The vacuum system was divided into two chambers and differentially pumped. The sample molecules entered the vacuum chamber in a free-jet expansion mounted on an *xyz* positioning stage. The scattering chamber background pressure with gas flow was $\sim 2\times10^{-4}$ torr. To provide a sufficient gas pressure beneath the needle tip, the temperatures of the sample, the manifold, and the needle were maintained at 108, 153, and 163 °C, respectively. Both chambers were shielded with μ-metal to reduce the effects of earth's magnetic field.

The component most critical to the success of UED is the detection system. The electron flux must be very low in order to keep the temporal resolution ultrafast. Early on we recognized that all of the scattered electrons must be detected for the experiment to succeed, and we introduced the two-dimensional charge-coupled device (CCD) as a detector in a direct electron bombardment mode. In order to increase the longevity and flexibility of the single-electron detection system, our second-generation apparatus now employs two CCDs: one is a small, direct-bombardment device installed in the scattering chamber, and the other is a large, scientific-grade device mounted in a separate chamber at the end of a phosphor scintillator / fiber optic / image intensifier chain.

To confirm the time resolution of the apparatus, we have measured the electron pulse duration *in situ* as a function of the number of electrons per pulse using the high-speed deflection technique in a streak camera arrangement. Streak velocities (which measure the conversion from temporal to spatial resolution, as shown in Fig. 5.1.2) attained with this setup are on the order of 1.6×10^8 m/s, or ~2 pixels/ps on the detector. The resolution of the streak experiment is therefore ±0.5 ps. Streak images spanning three orders of magnitude of electron number are shown in Fig 5.1.2. For electron intensities on the order of 10^4 electrons per pulse, the width is typically ~10 ps. The laser and electron beam waists at overlap was measured to be 450 ± 50 μm, so the velocity mismatch contribution[7] to the total experimental temporal resolution is ~4 ps.

To clock chemical changes, we must establish the zero of time (t_0). A streak camera or photo-triggered deflection plates can give t_0 to within 10-20 ps, but these methods require some extrapolation and do not duplicate the design of crossed-beam experiments. Another approach is to rely on changes in the diffraction pattern of the system under investigation, but this is not an independent means of finding t_0. More importantly, this method is simply not practical for gas-phase work because of the long integration times required to obtain a single data point.

In the clocking technique developed here for UED, we use the crossed-beam geometry of the actual diffraction experiment rather than relying on scattered electrons. The idea is to let the initiation laser pulse create a Coulombic field (by ionization), which deflects the unscattered electron beam only during and after the

laser pulse passes through. The phenomenon, termed lensing, occurs because the field focuses the charged electron beam. Fig. 5.1.2 shows the degree of lensing versus time; the lensing is a maximum when the laser and electron pulses are temporally overlapped. The results accurately show the precise $t = 0$ (to ~2 ps) and hence allow a direct clocking of changes in the diffraction experiment with ps resolution. We recorded lensing transients as a function of the position, polarization, and diameter of the pump laser, and conducted control experiments where no gas was flowing and where the sample source tip was far or near to the interaction region.

After successfully establishing t_0, we conducted the first time-resolved gas-phase electron diffraction experiment with picosecond resolution. Diiodomethane (CH_2I_2) was selected as our prototype system since the loss of an iodine atom after dissociation at 310 nm is a major structural change and it occurs in less time than the rotational period (~10 ps)[1,2]. To clock the change, diffraction images were recorded on the CCD at delays of -20 ps, 0 ps, and up to +70 ps.

5.1.3 Results And Discussion

The experimental modified molecular scattering intensity, $sM(s)$, was obtained at each time point

$$sM(s) = s\frac{I_{Tot}(s) - I_{Back}(s)}{|f_a||f_b|}, \qquad (5.1.3.1)$$

where I_{Tot} is the total scattering intensity, I_{Back} is the background (including atomic) scattering intensity, and f_a and f_b are atomic scattering amplitudes. Typical $sM(s)$ raw

data taken at -20 ps are shown in Fig. 5.1.3. The theoretical fits, calculated from structural parameters (see also Fig. 5.1.4 caption) of CH_2I_2, are superimposed on the experimental data. To unambiguously establish the magnitude of the change with time, we also recorded a $sM(s)$ in the absence of the fs initiation laser and obtained the residual by subtracting the $sM(s)$ at -20 ps from the $sM(s)$. The residual is essentially flat (Fig. 5.1.3), indicating that the two are identical. Thus, the $sM(s)$ at -20 ps is a calibration point in time, independent of any theoretical fit. The change in the diffraction pattern as a function of time is shown in two sets of data having differing temporal resolutions (15 ps and 30 ps); the $\Delta sM(s)$ curves are relative to the -20 ps data.

Radial distribution curves were obtained from the $sM(s)$ curves according to the standard GED equation:

$$f(r) = \int_0^{s_{max}} sM(s)\sin(sr)\exp(-ks^2)ds \qquad (5.1.3.2)$$

where the constant k is a damping coefficient included for the limited s range. Fig. 5.1.4 shows the experimental and theoretical $f(r)$ obtained from the -20 ps $sM(s)$ curves of Fig. 5.1.3. The time-evolution of $\Delta f(r)$ is also presented for the two sets of data. At positive time the amplitudes of the dominating C-I and I···I peaks decrease, corresponding to the loss of an iodine atom. Both the $sM(s)$ and $f(r)$ representations of our diffraction data clearly show a chemical change occurring as the delay between the fs laser pulse and the ps electron pulse sweeps from negative, to zero, and to positive times. From the $f(r)$ data, we obtained the standard deviation for more than 100

diffraction images for each data set, and established that the signal-to-noise ratio is better than 60. Thus, we could detect a change as small as 3%, which is five times less than the changes reported here.

Breakage of one C-I bond reduces the I···I peak twice as quickly as the C-I peak since CH_2I_2 has two C-I bonds and one I···I internuclear separation. This is observed in our data, corroborated with theoretical simulations of $f(r)$ (not shown) which account for the percentage change of CH_2I_2 to CH_2I and I. Similar time-resolved studies were made for $C_2F_4I_2$ and CHI_3. Quantitative analysis in the future should yield the changes due to the second C-I bond breakage, and elucidate the structure of the intermediate. Last, ground-state diffraction patterns of three other molecules (CF_3I, CCl_4, and SF_6) were recorded with our new UED apparatus. As mentioned earlier, the diffraction patterns were converted to experimental $sM(s)$ curves and radial distribution functions. The experimental and theoretical agreement is very good.

The photon energy, hν, at the wavelength of 310 nm was 93 kcal/mol. This photon energy is partitioned into dissociation energy for the first C-I bond breakage (D_0^I), electronic energy (E_{el}; 0 kcal/mol for I and 22 kcal/mol for I*), and remaining available energy (E_{avail}). The latter can be divided further into the internal energy of the photofragment (E_{int}) and the translational energy (E_{trans}).

$$h\nu = D_0^I + E_{el} + E_{avail} = D_0^I + E_{el} + E_{int} + E_{trans}. \qquad (5.1.3.3)$$

The second C-I bond breaks only when the internal energy is larger than the dissociation energy for the second Iodine (D_0^{II}). Considering the energetics of the first

and second C-I bond breakage reactions,

$$CH_2I_2 \rightarrow CH_2I + I\ (2P3/2) \qquad \Delta E = D_0^{I} = 51\ \text{kcal/mol}$$

$$E_{avail} = h\nu - \Delta E = 93 - 51 = 42\ \text{kcal/mol} \qquad (5.1.3.4)$$

$$CH_2I_2 \rightarrow CH_2I + I^*\ (2P1/2) \qquad \Delta E = D_0^{I} + E_{el} = 51 + 22 = 73\ \text{kcal/mol}$$

$$E_{avail} = h\nu - \Delta E = 93 - 73 = 20\ \text{kA/mol} \qquad (5.1.3.5)$$

$$CH_2I \rightarrow CH_2 + I \qquad \Delta E = D_0^{II} = 63\ \text{kcal/mol} >> E_{avail} \qquad (5.1.3.6)$$

One can see that the second bond breakage with the one-photon process is energetically impossible.

5.2 $CF_2I_2 \rightarrow CF_2 + 2I$ @ 310 nm

5.2.1 Introduction

CH_2I_2 was nearly an ideal molecule for demonstrating our ability to detect a chemical change with UED. Its dynamics at 310 nm consisted of a simple step-function reaction and no further changes sensitive to electron diffraction occurred after a few ps. Diffraction changes due to C-I bond breakage in CH_2I_2 molecules upon irradiation at 307 nm were successfully detected on the picosecond time scale. After observing this and demonstrating how reactions are clocked (**5.1**), our effort was directed to resolving a temporal evolution of new structures in the chemical reactions. The reaction of CF_2I_2 was chosen for this project because energetics at 310 nm allow both Iodine atoms to dissociate. In the hope that intermediate structures could be obtained in this two-step reaction, UED was applied to this system.

Fragmentation of CF_2I_2 following UV excitation has been studied by photofragment translational spectroscopy. After absorbing one UV photon, several dissociation channels are energetically possible, which include radical channels and a three-body dissociation channel:

$$CF_2I_2 \rightarrow CF_2I + I \qquad \text{(channel 1)}$$

$$\rightarrow CF_2I + I^* \qquad \text{(channel 2)}$$

$$\rightarrow CF_2 + I + I \qquad \text{(channel 3),}$$

depending upon the photon energy. As mentioned, a photon at 308 nm wavelength provides enough energy for both I atoms to come off. The photon energy, hν, in the experiment was 93 kcal/mol with a wavelength of 310 nm. This photon energy is

partitioned into dissociation energy for the first C-I bond breakage (D_0^I), electronic energy (E_{el}; 0 kcal/mol for I and 22 kcal/mol for I*), and remaining available energy (E_{avail}). The latter can be divided further into the internal energy of the photofragment (E_{int}) and the translational energy (E_{trans}).

$$h\nu = D_0^I + E_{el} + E_{avail} = D_0^I + E_{el} + E_{int} + E_{trans}. \qquad (5.2.1.1)$$

The second C-I bond breaks only when the internal energy is larger than the dissociation energy of the second C-I bond (D_0^{II}). Considering the energetics of the first and second C-I bond breakage reactions,

$$CF_2I_2 \rightarrow CF_2I + I\ (^2P_{3/2}) \qquad \Delta E = D_0^I = 51 \text{ kcal/mol}$$

$$E_{avail} = h\nu - \Delta E = 93 - 51 = 42 \text{ kcal/mol} \qquad (5.2.1.1)$$

$$CF_2I_2 \rightarrow CF_2I + I^*\ (^2P_{1/2}) \qquad \Delta E = D_0^I + E_{el} = 51 + 22 = 73 \text{ kcal/mol}$$

$$E_{avail} = h\nu - \Delta E = 93 - 73 = 20 \text{ kcal/mol} \qquad (5.2.1.2)$$

$$CF_2I \rightarrow CF_2 + I \qquad \Delta E = D_0^{II} \approx 12 \text{ kcal/mol} < E_{avail} \qquad (5.2.1.3)$$

One can see that both channels have higher available energy than the second dissociation energy. According to the results of photofragment translational spectroscopy, E_{trans} for the first channel and the second channel is centered at 15 kcal/mol and 10 kcal/mol respectively. Therefore, the internal energy E_{int} is 27 kcal/mol for the first channel and 10 kcal/mol for the second channel, which means that most of the second C-I bonds break via the first channel and few break via the second C-I bond. The results also showed that the branching ratio of the first channel to the second channel is 1:2. It is not unreasonable to expect that about 30% of CF_2I generated from CF_2I_2 will be fragmented further by consuming the available internal

energy. For example, if we generate 15% CF_2I out of CF_2I_2, we might to be able to see at least 4% CF_2 generation.

In addition, the molecule CF_2I_2 has a high absorption coefficient (see **2.4.2**) at 307 nm wavelength and its possible product radicals have higher scattering intensities than those of CH_2I_2.[3] The reaction was activated with 307 nm excitation laser pulses and snapshots of diffraction images were recorded at different delay times. Actually the dissociation of CF_2I_2 was found to be completed within 4 ps. On this ps time scale, the major product detected was CF_2 radical and its structure was determined with an improved accuracy of one order of magnitude higher than in the study of $Fe(CO)_5$,[4] by analyzing the diffraction-difference curves at each delay time.

5.2.2 Experimental Setup And Method

The ps time-resolved electron diffraction was performed in the second-generation UED apparatus developed in this laboratory. It is composed of a femtosecond laser, a picosecond electron gun, a free-jet expansion sample source, and a two-dimensional single-electron detection system. Femtosecond laser pulses from a colliding-pulse mode-locked ring dye laser were amplified in a four-stage pulsed dye amplifier pumped by a Nd:YAG laser at 30 Hz. The amplified pulses (614 nm, 3-4 mJ/pulse, 30 Hz, ~400 fs pulse width) were then split (with a beam splitter) into two beams. The clocking laser pulse (95%) was first frequency-doubled with a KDP crystal (>500 μJ at 307 nm), then directed and focused on the scattering gas sample beneath the needle of the free-jet expansion source.

To generate the electron pulse, part of the remaining 5% was doubled and focused onto a back-illuminated photocathode in the electron gun compartment. The ultrashort photoelectron pulse was then accelerated to 18.8 keV (de Broglie wavelength is 0.088 Å), collimated and focused onto the scattering volume. The two-dimensional diffraction images at a given delay time were recorded in a charge-coupled device (CCD) at the end of a phosphor scintillator/fiber optic/image intensifier chain in the detection chamber. Time delays between the fs laser pulse and the ps electron pulse were controlled by a computer-driven translational stage.

The electron pulse, the laser pulse and the molecular beam were arranged in a cross-beam geometry, and the overlap of the three beams was controlled within 10 μm accuracy. The camera length was measured to be 102.4 mm. For our current setup, the time resolution was determined by the electron pulse width. With a flux of ~6000 electrons per pulse in our experiment, the corresponding temporal width is ~7 ps. The total temporal resolution, including the contributions from the pump laser pulse width (~1.5 ps) and group velocity mismatch effect (~3 ps), is less than 8 ps. After establishing the time zero by the lensing approach within ± 2 ps accuracy *in situ*, the diffraction images at -150, 0, +12 and +162 ps delay times were recorded.

The sample was purchased from the Shanghai Institute of Organic Chemistry. Our F^{19} NMR measurements showed that the sample purity was better than 99%. UV and infrared absorption spectra were obtained and were consistent with published results[5]. After connection to the diffraction chamber, the sample was further purified by four cycles of freeze-and-thaw to remove air and the residual impurities. To

increase the gas density in the scattering volume, the sample cell, the gas line and the nozzle were heated to 33, 39 and 44 °C, respectively. The gas pressure in the scattering chamber during the experiment was ~3×10^{-4} torr.

5.2.3 Data Analysis

At each delay time, a series of over 200 two-dimensional diffraction images (85 second average exposure time for each image), including the images of scattered laser light without the electron beam, were recorded with the CCD detector. The conversion of the two-dimensional diffraction image to a one-dimensional intensity distribution, $I(r_{pixel})$, as a function of pixel radius r_{pixel}, was completed with home-built software by providing the center pixel coordinates (undiffracted electron beam spot) and the background offsets (CCD dark noise) of each image, and calculating the average intensity as a function of pixel radius from the center for each diffraction image. Then, the experimental total scattering intensity curve $I_{Tot}(r_{pixel})$ at different delay times, including that of scattered laser light $I_{Laser}(r_{pixel})$, was obtained by further averaging all the $I(r_{pixel})$ at each delay time. Finally, the scattered-laser-light-free total intensity curve $I_{Tot}(s)$ at each delay time was obtained by subtracting $I_{Laser}(r_{pixel})$ from $I_{Tot}(r_{pixel})$ and through the conversion of pixel number to momentum transfer s. An experimental data file containing the one standard deviation ($\sigma_{Tot}(r_{pixel})$) as a function of pixel radius for each data set at different delay times was also generated for the molecular structural fitting.

To monitor the structural changes due to dissociation, we followed the

diffraction-difference approach developed in our laboratory. First, the modified molecular scattering intensity for the parent molecule (-150 ps data) was calculated with CF_2I_2 structural parameters obtained in the conventional gas phase electron diffraction (GED) according to:

$$sM^{Exp}(s) = s\frac{I_M(s)}{|f_a||f_b|}, \qquad (5.2.3.1)$$

where f_a and f_b are atomic scattering amplitudes (both are iodine atoms in our case), and I_M is the molecular scattering intensity. I_M, is composed of interference terms from all atom-atom pairs and contains molecular structural information and, is given by:

$$I_M = I_{Tot}(s) - I_{Back}(s) \quad , \qquad (5.2.3.2)$$

where $I_{Back}(s)$ is the background intensity profile. Then, the theoretical $sM^{Theo}(s)$ was normalized to the $sM^{Exp}(s)$ with a scaling factor S_C for comparison. The corresponding radial distribution curve, which provides the relative density of internuclear distances in a molecule, was also generated by Fourier transforming $sM(s)$ curves using the standard equation in GED:

$$f(r) = \int_0^{s_{max}} sM(s)\sin(sr)\exp(-ks^2)ds, \qquad (5.2.3.3)$$

where the constant k (k = 0.02 Å^2) is a damping coefficient included for the limited s range.

To extract the transient radical structures, the difference total intensity data, ΔI_{Tot}, was obtained by subtracting I_{Tot} at -150 ps from I_{Tot} at each positive delay time. ΔI_{Tot} was used instead of I_{Tot} for the analysis of transient structural changes, because of

the enhanced product contribution to diffraction intensity, reduced background scattering intensity and cancellation of systematic error in the diffraction-difference curve. The determination of the fractions and structural parameters of each fragment, for a given difference total intensity curve, ΔI_{Tot}, was made using home-developed software in an iterative manner, similar to that used in conventional GED, by minimizing the Chi-square:

$$\chi^2 = \sum_{pixel} \frac{(S_c \cdot \Delta sM^{Theo}(s) - \Delta sM^{Exp}(s))^2}{\sigma_i^2} \quad , \qquad (5.2.3.4)$$

where the $\Delta sM(s)$ is the difference modified molecular scattering intensity, σ_i is the one standard deviation of $\Delta sM^{Exp}(s)$ at each pixel position (or s position), and the summation is over all pixels (17 to 225). $\Delta s^{Exp}M(s)$ is obtained from ΔI_{Tot} through Eq. (1). σ_i was calculated with experimental $\sigma_{Tot}(r_{pixel})$ for each data set obtained in the radial sum and the error propagation rules. First, the $\sigma_{sM(s)}$ for the experimental $sM(s)$ curve was generated by:

$$\sigma_{sM(s)} = \sqrt{2} \cdot \sigma_{Tot}(r_{pixel}) \cdot \frac{s}{|f_a||f_b|}, \qquad (5.2.3.5)$$

where the factor $\sqrt{2}$ accounts for the subtraction of I_{Back} (Eq.(5.2.3.2)). Then, the standard deviation for the difference curve ($\Delta sM^{Exp}(s) = sM^{Exp}(s) - sM^{Exp}_{-150\,ps}(s)$) was finally calculated as:

$$\sigma_i = \sqrt{\sigma^2 + \sigma^2_{-150\,ps}} \quad . \qquad (5.2.3.6)$$

By starting from an assumed product distribution and the structural parameters for each species, the software first fits the residual background with the experimental ΔI_{Tot} values at the zero points of the theoretical $\Delta I_M(s)$. Then the experimental $\Delta sM(s)$ is obtained with the background-free ΔI_{Tot} through Eq. (5.2.3.1), and χ^2 was calculated to evaluate the goodness of the fit. This whole procedure is repeated until the best least-square fit between theoretical and experimental $\Delta sM(s)$ curves is reached (minimum of χ^2). During fitting, the scaling factor was fixed at the value of the data set for the parent molecules (data at -150 ps).

With one-photon absorption at 307 nm, a CF_2I_2 molecule can dissociate in two different pathways: CF_2I + I and CF_2 + 2I. In the fitting, we first floated the structural parameters and the population for both radicals. The contribution of CF_2I radical to the diffraction intensity was found negligibly small, less than 1%. For the further refinement, only CF_2I_2 molecule and CF_2 radical were included. The CF_2I_2 structural parameters were kept fixed at the value obtained in conventional GED. The fraction of CF_2, the internuclear distances r(C-F) and r(F···F), and the mean amplitudes of vibration l(C-F) and l(F···F) were fitted. The fitting results for structural parameters and populations are summarized in the Table 5.2.1. The errors are three standard deviations of the fitting. The χ^2 and R value, which is frequently used as a measure of goodness of fit in electron diffraction, are also listed in the Table 5.2.1. The R was is calculated as:

$$R^2 = \frac{\sum \frac{1}{\sigma_i^2} \cdot (S_c \cdot \Delta sM^{Theo}(s) - \Delta sM^{Exp}(s))^2}{\sum \frac{1}{\sigma_i^2} \cdot \left(\Delta sM^{Exp}(s)\right)^2} \quad . \qquad (5.2.3.7)$$

5.2.4 Ground State Data

The structure of the parent molecule was also fitted with the non-linear least-square method, and results are summarized in Table 5.2.1. Other error sources, such as the uncertainties of camera length and electron wavelength, were estimated and included in the final error analysis. Agreement between UED results and those of conventional GED is very good considering the extremely low flux of our ps electron pulse. Note that our k value is 0.02 $Å^2$ and the peaks in *f(r)*, which reflect relative density of internuclear distances, is less resolved than those reported in the literature with smaller values of k ranging from 0.01 to 0.0025 $Å^2$. The fitting for the parent molecule is not as good as those of difference curves because of the much larger background scattering intensity and the presence of the systematic error in the detector.

5.2.5 Time-resolved data

The experimental *sM(s)* and *f(r)* curves at -150 ps and the difference *ΔsM(s)* and *Δf(r)* curves at different delay times, relative to the data of CF_2I_2 at -150 ps, are shown in Fig. 5.2.1. The theoretical *sM(s)* and *f(r)*, calculated with the structural parameters from conventional GED studies, and the fitting results for *ΔsM(s)* and *Δf(r)*

are also imposed on each data set for comparison. The absence of temporal evolution after +12 ps indicates that the whole fragmentation process takes place on the ultrafast time scale. Since no CF_2I radical was detected even at the time zero, as shown in Table 5.2.2, the estimated bond breakage time for both iodine atoms of a CF_2I_2 molecule is less than 4 ps at 307 nm. Note that the fraction of CF_2 product detected at 0 ps is 18%, higher than half of the total final fraction (~26%). This indicates that the actual time zero determined in this experiment is at about + 1.4 ps.

A theoretical simulation was also carried out to further test the robustness of this method. A theoretical diffraction-difference curve, $\Delta I^{Sim}(r_{pixel})$ was generated by summing $\Delta I_{Back}(r_{pixel})$, $\Delta I_M(r_{pixel})$ and $\Delta I_{Noise}(r_{pixel})$. $\Delta I_{Back}(r_{pixel})$ was the experimental background determined in the diffraction-difference analysis and $\Delta I_M(r_{pixel})$ is the theoretical difference curve calculated with fitting results for the difference curve at given delay time. $\Delta I_{Noise}(r_{pixel})$ was generated with a Gaussian random number generator by feeding in the σ_i obtained from Eq. (5.2.3.6) with experimental $\sigma_{Tot}(r_{pixel})$. Then, the $\Delta sM^{Sim}(s)$ and $\Delta f^{Sim}(r)$ were generated from $\Delta I^{Sim}(r_{pixel})$ with the same procedure as in the above data analysis. The agreement between the theoretical simulation and the experimental data was found to be very good. As shown in Table 5.2.2, the χ^2 of the fitting for each diffraction-difference curve is comparable to the number of data points, 208. Both χ^2 values and simulation results indicate that the diffraction-difference curves contain mostly random noise, and the contribution of systematic errors is negligibly small. This confirms the advantages of the diffraction-

difference method in extracting transient structures with UED compared to fitting the I_{Tot} directly.

To visualize the contribution of product CF_2 to the scattering intensity, $\Delta sM^{CF_2}(s)$ and $\Delta f^{CF_2}(r)$ curves containing only the CF_2 signal were also generated at each delay time, as shown in Fig. 5.2.2. The curves were obtained through the diffraction-difference curves by adding a fraction of scattering intensity from parent molecules, e.g. $\Delta sM^{CF_2}(s)$ at 162 ps was obtained by adding 26.6% of the experimental $sM(s)$ at -150 ps to $\Delta sM(s)$ at 162 ps delay time, to compensate its negative contribution to the difference curves. Even though the parent CF_2I_2 scatters electrons much stronger than the CF_2 radical, the CF_2 signal is clearly seen at each delay time, as shown in Fig. 5.2.2. The errors in the $\Delta sM^{CF_2}(s)$ and $\Delta f^{CF_2}(r)$ are larger than those in diffraction-difference curves $\Delta sM(s)$ and $\Delta f(r)$, because the error in $sM(s)$ at -150 ps has been propagated through the addition.

Fragmentation of CF_2I_2 following UV excitation has been studied by photofragment translational spectroscopy. After absorbing one UV photon, several dissociation channels are energetically possible, which include radical channels and a three-body dissociation channel:

$$CF_2I_2 \rightarrow CF_2I + I \quad \text{(channel 1)}$$

$$\rightarrow CF_2I + I^* \quad \text{(channel 2)}$$

$$\rightarrow CF_2 + I + I \quad \text{(channel 3)},$$

depending upon the photon energy. For 308 nm wavelength, the reported branching ratio was 5:10:2 (39%:59%:12%). The available energy for the CF_2I radical in channel

2 was measured to be 8.6 kcal/mol, less than D_{02} ,the dissociation energy of second iodine atom, which is 12.0 kcal/mol.[5,6] Therefore, having 26% dissociation of parent molecules, about 16% final products should be CF_2I radicals, if only one photon absorption takes place. However, for comparison with our experimental results, we must consider the different fluence of the laser pulses used. For translational spectroscopy experiments, the fluence was ~0.01 J/cm^2 (~10^7 W/cm^2) from a ns laser, but in our experiments, a much higher laser power ~5×10^{11} W/cm^2 was used. It is highly probable that the product CF_2I radical subsequently absorbs another photon (ladder switching)[7,8] and further dissociates rapidly into CF_2 + I. If enough energy is partitioned into the translational energies of the photofragments, the final CF_2 radical will be in the ground electronic state. A femtosecond transition-state spectroscopy experiment will establish the nature of these channels, as was done in the case of the reaction of $C_2F_4I_2$.[9,10]

5.2.6 Molecular structure of CF_2

The structure of CF_2 radical has been studied both theoretically and experimentally. [11] [12] [13-17] The equilibrium geometry of both ground state (X^1A_1) and the first excited state ($^3B_1$) of CF_2, which lies about 2.42 eV above the ground state, were measured with microwave spectrum[12], UV absorption spectroscopy[11] and laser-induced fluorescence spectroscopy[13]. The internuclear distances r(C-F) and r(F···F) for these two states were determined to be 1.30 Å and 2.06 Å (∠FCF = 104.9°) for ground state[11], and 1.325 Å and 2.29 Å (∠FCF = 119.4°) for the first excited state[13],

respectively. These values are also supported by *ab initio* calculations[13-17]. The internuclear distances of the CF_2 radical (1.30 Å and 2.06 Å) determined here by UED in the reaction suggest that the radicals formed after dissociation at 307 nm are in the ground state. The mean amplitudes of vibration determined by UED (0.04 Å and 0.06 Å) are also consistent with the values (0.045 Å and 0.053 Å) we calculated using the force field[13] for CF_2 in the ground state.

In conclusion, with the achievement of direct monitoring of the transient radical structure with high accuracy on the picosecond time scale by using the temporal diffraction-difference method, UED now has the potential for wider applications.

5.3 $C_2F_4I_2 \rightarrow C_2F_4I + I \rightarrow C_2F_4 + 2I$ @ 310 nm

5.3.1 Introduction

Ultrafast electron diffraction (UED) is a unique method for studying the structural changes of complex molecular systems. Here, we report the first UED study of the evolution of short-lived intermediates in the course of a chemical change. Specifically, we observe the transient intermediate in the elimination reaction of 1,2-diiodotetrafluoroethane ($C_2F_4I_2$) by which produces the corresponding ethylene derivative is reproduced by the breakage of two carbon-iodine, C-I, bonds. The evolution of the ground-state intermediate (C_2F_4I radical) is directly revealed in the population change of a single chemical bond, namely the second C-I bond. The elimination of two iodine atoms was shown to be non-concerted, with reaction time of the second C-I bond breakage being 17 ± 2 ps. The structure of the short-lived C_2F_4I radical is closer to the classical radical structure than to the bridged radical structure. This leap in our ability to record structural changes on the ps and shorter time scales bodes well for many future applications in complex molecular systems.

Significant progress has already been made in the probing of chemical reactions on the femtosecond (fs) time scale. In these femtochemistry[18-21] experiments, the nuclear motions on the time scale of bond breaking and bond making are monitored by an initial pulse to establish the zero-of-time (clocking) and probing pulses to view the motion; typical probes are optical and IR spectroscopy, photoelectron spectroscopy, mass spectrometry, and non-linear optical techniques[22]. In this laboratory, efforts have been made to include diffraction techniques in order to

map out ultrafast structural changes, especially in complex molecular systems[3,23]. Electron diffraction of molecules in their ground state has been a powerful tool over the past fifty years[24], and both electron and x-ray methods are now being advanced in several laboratories[3,23,25-32] for the studies of structural changes. Our focus here and before has so far been on gas-phase ultrafast electron diffraction (UED) of isolated chemical reactions.

Elsewhere, we have reported the latest advance in UED[3], by which major challenges were surmounted: the very low number densities of gas samples, the absence of the long-range order that is present in crystals, which enhances coherent interference, and the challenging task of determining *in situ* the zero-of-time when diffraction changes are on the picosecond (ps) and sub-ps time scale. With UED, molecular structures[33] and branching ratios[4] of final products have been determined on the ps time scale. The diffraction change before and after the chemical reaction was observed[3]. However, no direct observation of transient structural changes in the course of the reaction has so far been reported. In this article, we report the first such observation of the temporal evolution of short-lived intermediates probed with ultrafast electron diffraction.

5.3.2 Experimental

The UED experiments were performed using the second-generation apparatus developed in this laboratory[3]. It is composed of a fs excitation laser, a ps pulsed-electron source, a free-expansion molecular beam, and a two-dimensional single-

electron detection (camera) system. All of these are part of a complex apparatus which has been described in more detail elsewhere[3]. The electron pulse, the laser pulse and the molecular beam are arranged in a crossed-beam geometry, and the overlap of the three beams is controlled within 10 μm accuracy. With a flux of ~7000 electrons per pulse in our experiment, the corresponding pulse width is ~8 ps[3]. The total temporal resolution, including the contributions from the pump laser pulse width (~0.7 ps) and the ~3 ps group-velocity mismatch effect[34], is less than 10 ps[4,33].

The chemical reaction was initiated with the fs laser pulse (450 μJ at 307 nm), and probed with the ps electron pulses at 18.8 keV (de Broglie wavelength 0.088 Å). The two-dimensional diffraction images at each delay time were recorded with the charge-coupled device (CCD) camera. Time delays between the fs laser and the ps electron pulses were precisely controlled by a computer-driven translational stage. After the establishment of the time zero by the lensing approach[3], the time-resolved diffraction images at -150, 0, +10, +20, +30 and +330 ps delay times were recorded with ± 2 ps accuracy (see below); at each delay time, a series of over 360 diffraction images was collected. For the experiments reported here, the $C_2F_4I_2$ sample (Lancaster, 98%) was further purified by several cycles of freeze-and-thaw. The gas nozzle temperature was 72°C, and the estimated gas density in the scattering volume was ~10 torr.

5.3.3 The Approach: UED

In time-resolved experiments with UED, the *actual* signal being monitored is the net *change* of a diffraction pattern resulting from a chemical reaction. In order to

follow the course of the fs-initiated structural change in the presence of ground-state species (typically 90%), we followed the *diffraction-difference approach* developed in our laboratory[4,33]. This approach, compared with simply analyzing the I_{Tot} (see below), has critical advantages: elimination of background scattering intensity, enhancement of product contribution to diffraction intensity, and cancellation of systematic errors in the diffraction-difference curve.

The diffraction data was analyzed following our previous procedure[4,33,35]. The two-dimensional diffraction images from the CCD were first converted to one-dimensional intensity curves by calculating the average intensity as a function of pixel radius from the primary beam center for each diffraction image. Then, the total raw scattering intensity, $I_{Tot}(s)$, was obtained by further averaging of all images at each time delay and converting the pixel radius to the momentum transfer parameter (s); $s = (4\pi/\lambda)\sin(\theta/2)$, where λ is the de Broglie wavelength of the electrons and θ is the scattering angle.

The $sM(s)$ curve was calculated with the structural parameters[36] obtained by conventional gas-phase electron diffraction. The $sM(s)$ is given by:

$$sM(s) = s\frac{I_M(s)}{|f_a||f_b|}, \qquad (5.3.3.1)$$

where f_a and f_b are the atomic scattering amplitudes (I and F atoms in our case), and I_M is the molecular scattering intensity. I_M is composed of interference terms from all atom-atom pairs and contains the molecular structural information: $I_M = I_{Tot}(s) - I_B(s)$, where $I_B(s)$ is the background intensity profile. In the calculation, the theoretical $sM(s)$

was normalized to the experimental $sM(s)$ with a scaling factor.

The corresponding radial distribution curve, which provides the relative density of internuclear distances in a molecule, was generated by Fourier transforming $sM(s)$ using the standard equation[37,38]:

$$f(r) = \int_0^{s_{max}} sM(s)\sin(sr)\exp(-ks^2)ds, \qquad (5.3.3.2)$$

where the constant k (k = 0.02 Å^2) is the known damping coefficient included for a limited s range.

In order to monitor the transient structural change, we introduced the temporally-resolved diffraction difference as $\Delta I(t;\ t_{ref};\ s)$, where t_{ref} refers to the reference time: $\Delta I(t;\ t_{ref};\ s)$ is simply $I_{Tot}(t;\ s)$ minus $I_{Tot}(t_{ref};\ s)$. Typically, we scan diffraction from, say –150 ps to +330 ps, with an accuracy of 2 ps. Thus we can easily obtain $\Delta I(t;\ -150\ ps;\ s)$ which displays the evolution as a function of time and in reference to the –150 ps diffraction data (the ground state structure). It follows from the definition of I_{Tot} (= I_M + I_B) that ΔI will give $I_M(t) - I_M(t_{ref})$. In so doing, the background signal is eliminated, thus leaving the molecular structure (I_M) signal. Furthermore, because I_M for a chemical reaction has contributions from both reactant and product structures, ΔI gives, as demonstrated below, the product(s) contribution as it evolves with time; even if the fraction of product(s) is small, this approach avoids the dominance of the reactant diffraction in the signal.

For the sake of comparison with theory, molecular structural calculations were performed using the Jaguar 3.0 program[39]. The LAV3P basis set[40] was employed for

the I atom and 6-31G* for the C and F atoms. For the parent molecule, both restricted Hartree-Fock (RHF) and density functional theory (DFT; B3PW91) were used to obtain the optimized structures. With RHF, the optimized structures of $C_2F_4I_2$ reproduce the experimental structures (21) very well (the deviation was at most 0.01 Å for bond length and 1° for angle), while using DFT, the deviation was somewhat larger. For the anti and gauche radicals, the structures optimized at the RHF level of theory were used for diffraction data analysis. Compared with the parent molecule, the radicals have a longer C-I bond, but a shorter C-C bond. Single point calculations with the localized second order Møller-Plesset (MP2) method at the RHF optimized structures showed that the anti structure is ~2 kcal/mol more stable than the gauche structure of the radical. The symmetrically bridged radical was found to be a transition state with ~62 kcal/mol higher energy than the anti species.

5.3.4 Ground State Data

In Fig. 5.3.1, we present a modified molecular scattering intensity, *sM(s)*, and the corresponding radial distribution function, *f(r)*, for the parent molecule $C_2F_4I_2$ (data at –150 ps). For consistency, we compared our results at –150 ps for the ground-state structure of the two isomers (anti and gauche) of $C_2F_4I_2$ with that of static diffraction experiments[36]. The fraction of anti and gauche isomers was obtained by a least-square fitting and found to be 75% and 25%, respectively. This result is in excellent agreement with the value of 76% and 24% obtained (at our gas temperature of 72°C) from the temperature dependence curve of Hedberg and coworkers[36].

5.3.5 Time-Resolved Data

For the chemical reaction investigated here, we consider its two elementary steps with the different structures involved:

$$\mathbf{RS} \xrightarrow{\tau_1} \mathbf{IS} \xrightarrow{\tau_2} \mathbf{PS}, \qquad (5.3.5.1),$$

where the reactant structure (RS), in this case $C_2F_4I_2$, forms the intermediate in τ_1, while the intermediate structure (IS), C_2F_4I, transforms in time τ_2 to the final product structure (PS), C_2F_4. Following the approach outlined above, we can now obtain *ΔI(t; -150 ps; s)*. In Fig. 5.3.2, we show the experimental results for the corresponding *ΔsM(s)* and *Δf(r)* as a function of time; all data was referenced to t_{ref} = -150 ps. For each *ΔI*, the corresponding *ΔsM(s)* and *Δf(r)* curves were obtained through equations (5.3.3.1) and (5.3.3.2), respectively. The ground-state structure, which is the data for –150 ps, is shown in Fig. 5.3.1. Note that the contribution in the radial distribution function from the F··I and C··I internuclear separations is evident near ~3 Å. The I··I internuclear separation is at ~5 Å (anti), and that of C-F is at ~1.3 Å. In Fig. 5.3.2, the increase of the peak intensity at ~3 Å with time is clear, while the peak intensity at ~5 Å remains constant after 10 ps.

To follow the time evolution of individual structures, we obtained *ΔI(t; +10 ps; s)*. As before, $\Delta I(t; +10\,ps; s) = I_M(t) - I_M(+10\,ps)$, and, therefore,

$$\Delta I(t;+10\,ps;s) = \sum_i [I_i(t) - I_i(+10\,ps)] \qquad i = \text{RS, IS, PS} \qquad (5.2.5.2).$$

It is evident that the evolution of the structures in the reaction can be observed as these three terms for *reactant*, *intermediate* and *product* structure are distinct in some of their internuclear separations, and their contribution to the diffraction difference is therefore unique. For example, the change in I_{RS} will be most pronounced at the I··I internuclear separation, while changes in I_{IS} and I_{PS} will be observed at the C-I, C··I and F··I distances. The dynamic time scale of the process is also evident. If, for example, the reaction proceeds with $\tau_1 << \tau_2$ ($\tau_1 < t_{ref}$ = 10 ps) in a non-concerted pathway, then $\Delta I(t;\ +10\ ps;\ s)$ will arise only from I_{IS} and I_{PS} via equation (5.2.5.2), with the depletion of I_{IS} shown by population changes of the C-I, C··I, and F··I separations. Because the population of other internuclear separations, C-F, C-C, and F··F, is essentially unchanged, their contribution to the evolution in time of $\Delta I(t;\ +10\ ps;\ s)$ will be zero. In Fig. 5.3.3, we display the theoretical simulations for the reaction studied, but for different dynamical time scales, τ_1 = 200 fs and τ_2 = 17 ps.

Fig. 5.3.4 displays the $\Delta f(t;\ +10\ ps;\ r)$ diffraction data for the investigated reaction. The temporal evolution of the C-I, C··I, and F··I internuclear separations is clearly observed. In Fig. 5.3.5, the change of the population of the ground-state C_2F_4I intermediate and C_2F_4 product with time shows that the second bond breakage occurs in 17 ± 2 ps. The measurements were made both for the build up of C_2F_4 structure and the decay of C_2F_4I structure (Fig. 5; bottom and top). The first bond breakage must occur on a time scale shorter than 10 ps, and this is consistent with the spectroscopic detection of I atoms on the fs time scale[9,10]; it occurs in ~ 200 fs. In Fig. 5.3.4, it is seen that the intensity of peaks corresponding to depletion of C-I (~2.2 Å), C··I (~3.1

Å) and F··I (~2.9 and ~3.1 Å) nuclear separations is gradually increasing with time due to the secondary C-I bond breakage. The absence of an I··I component (~5 Å) in $\Delta f(r)$ confirms that the population of unreacted parent molecules remains constant after 10 ps (see Fig. 5.3.5) and is, therefore, absent in the difference curves. Hence, the decomposition of $C_2F_4I_2$ is a two-step non-concerted process involving the intermediate C_2F_4I radical ground-state structure.

The maximum internal energy for the radical is ~42 kcal/mol;[10] the barrier for the second bond breakage is ~15 kcal/mol. Using state detection on the fs time scale, a typical reaction time was measured to be 25 ps at 277 nm[10] and 69 ps at 307 nm[9]. At our two-photon energy, the 17 ps time is entirely consistent with the range of available energy for the barrier crossing. We determined the percentage of the radicals undergoing further dissociation to be 82%, again consistent with the available energy which exceeds both the I and I* thresholds.

Two more interesting observations can be made. First, we can compare the rates observed by molecular structural changes with time (i.e. certain internuclear separations) and those observed by probing spectroscopic states. An important consideration in this comparison is intramolecular vibrational-energy redistribution (IVR). The distribution of vibrational motions projected on the C-I reaction coordinate, monitored in these diffraction experiments, is different. This raises an important point regarding the role of IVR and the nature of reaction trajectories[41]. Such studies are under consideration, together with studies of the wavelength and intensity dependencies.

The second observation concerns the structure of the intermediate. The bridged radical model[42] has been postulated to explain the stereoselectivity observed in many reactions involving the haloethyl radicals. To explore this possibility, $\Delta I(t; +10\ ps; s)$ difference curves were also fitted with the bridged radical structure rather than the classical radical structures (anti and gauche). The fitting with the classical radical gives more satisfactory results than that with the bridged model. To further confirm this conclusion, another set of data was also collected with only four time points (-90, 0, 8, 188 ps) to increase the total integration time and signal-to-noise ratio at each delay time. As shown in Fig. 5.3.4, our experimental results for this set of data are also consistent with the classical structure. It is interesting to note that the time scale for C-C rotation relative to that of bond breakage may be the dominant effect for stereochemistry, in contrast with the real molecular structural rearrangement.

5.4 $C_2F_4I_2 \rightarrow C_2F_4I + I \rightarrow C_2F_4 + 2I$ @ 267 nm

5.4.1 Background

The elimination of iodine from 1,2-diiodotetrafluoroethane ($C_2F_4I_2$) is a prototypical reaction in ultrafast spectroscopic studies of non-concerted photoinitiated reactions.[9,10] Following the absorption of a UV photon, energy is deposited in one C-I bond coordinate, resulting in the rapid (~200 fs)[10] loss of the first iodine atom and the formation of the transient C_2F_4I radical intermediate. The remaining energy, left to equilibrate in the vibrational degrees of freedom of the C_2F_4I radical, is enough to cause the majority of the hot radicals to undergo a second fragmentation, resulting in the loss of the second iodine atom and the formation of the tetrafluoroethene product on the picosecond time scale.

The elimination of iodine from 1,2-diiodotetrafluoroethane ($C_2F_4I_2$) was also studied with the second-generation apparatus, providing early results which suggested that the molecular structure of the C_2F_4I radical intermediate is not bridged in nature, but instead is "classical", resembling the structure of the parent species.[47] Although the data permitted the course of reaction to be followed, and suggested the nature of the intermediate structure given two possible models, the signal–to–noise ratio and resolution was not yet sufficient to elucidate the molecular structures involved.

The need for greater sensitivity and resolution, as well as the desire to study more complex reactions, led to the development of our third-generation UED apparatus.[46] This new machine, with vast improvements in pulsed electron flux, repetition rate, detection sensitivity, and experimental stability, permits the direct

imaging of complex chemical reactions with unprecedented spatial and temporal resolution. In its first application,[46] the capabilities of the new apparatus were demonstrated in the study of two prototypical reactions: the non-concerted elimination of iodine from a haloethane ($C_2F_4I_2$), and the electrocyclic ring opening of 1,3-cyclohexadiene, a hydrocarbon with no heavy atoms. In the $C_2F_4I_2$ experiments, the spatial and temporal resolution of UED approached ~0.01 Å and ~1 ps, respectively, and we were sensitive to ~1% changes in the mole fractions of the various chemical species over the course of the reaction. Moreover, the molecular structure of the transient C_2F_4I radical was determined for the first time.

In general, the chemistry of halogen elimination reactions is of interest because the products are usually formed under stereochemical control with respect to the final positions of the functional groups about the newly formed double bond.[48-51] The origin of this well-known behavior has been hypothesized to lie in the geometry of the intermediate species of the reaction. For example, previous *ab initio* calculations[52] have shown that CH_2BrCH_2 and CH_2ICH_2 radicals should form stable, symmetrically "bridged" structures, consistent with the explanation for the origin of stereochemical control in such systems according to the Skell hypothesis.[42,53,54] In a symmetrically bridged structure, the primary halide (i.e., I or Br) is shared equally between the two -CR_2 moieties, whereas in a "classical" structure the primary halide (I or Br) would reside predominantly on one -CR_2 moiety.[42] Such a bridged structure would prevent rotation about the C-C bond, thereby maintaining the functional group positions in the final product. However, the substitution of hydrogens with highly electronegative

fluorines can cause dramatic changes in molecular structure (and reactivity); for example, it is well known that the CF_3 radical is highly non-planar while CH_3 is planar. While CF_2XCF_2 radicals can be readily detected in the photodissociation reactions of CF_2XCF_2X molecules, the molecular structure of these radicals has not been investigated spectroscopically. Thus, the elimination of iodine from $C_2F_4I_2$ is an ideal reaction to study with *ultrafast diffraction* for two reasons: 1) it is a complex, non-concerted reaction involving the loss of two highly-scattering heavy atoms (which provide a strong diffraction signal); and 2) it affords the opportunity to determine the molecular structure of a transient radical intermediate that belongs to an important family of chemical reactions. Here, we provide a full account of our recent UED studies on the elimination of iodine from $C_2F_4I_2$. Section II describes the experimental methods used to obtain the UED images. Section III provides a step-by-step explanation of the image processing procedures and data analysis utilized in our UED experiments. Section IV contains a comprehensive discussion of the results and analysis for the $C_2F_4I_2$ data. This discussion includes a comparison of ground-state $C_2F_4I_2$ diffraction data with a model derived from previous conventional GED experiments; the structural dynamics of the non-concerted iodine elimination reaction; and the molecular structure determination of the C_2F_4I radical intermediate. We determined the structure of the C_2F_4I radical to be non-bridged – a result that is relevant to the role of dynamics in stereochemical control of halogen elimination reactions. Section V concludes with a summary of the present work.

5.4.2 Experiment And Analysis

UED data was obtained with our third-generation apparatus. A schematic drawing is presented in Fig. 5.4.1. Briefly, the UED apparatus is comprised of an amplified femtosecond laser system (Spectra Physics), an electron gun, a high-vacuum scattering chamber, a molecular beam, a 2-D imaging system, and a time-of-flight mass spectrometer for the identification of molecular species. Amplified IR fs laser pulses provided by a Ti:Sapphire laser system (3 mJ, ~120 fs, 800 nm) are frequency-tripled with a third-harmonic generator to give high-power UV fs pulses (350 μJ, 267 nm). An optical beam splitter is used to direct part of this UV output into the scattering chamber to initiate the chemical reaction, while a smaller fraction of the laser power is first directed into a delay line with a computer-controlled translation stage, and then focussed onto a back-illuminated silver photocathode to generate electron pulses via the photoelectric effect. High intensity, picosecond electron bursts at 30 keV (de Broglie wavelength 0.067 Å) are produced by the home-built electron gun, which features magnetic focussing, electrostatic deflection, and built-in streaking capabilities for *in situ* measurement of the electron pulse width. The laser provides a 1 kHz repetition rate for the electron pulses, which were ~4 ps in duration in these experiments and contained ~25,000 electrons per pulse.

The sample was delivered into the scattering chamber as a molecular beam from an effusive-jet expansion source with a ~125 μm nozzle. The temperatures of the sample storage bulb, the gas inlet manifold, and the sample nozzle were monitored and controlled independently. The fs laser pulses, electron pulses, and molecular beam

intersect in a mutually perpendicular arrangement just below the sample nozzle. The interaction region, dictated by the overlap of the laser, electron, and molecular beam waists, was typically 400 ± 50 μm. Electron diffraction patterns were recorded with a low-noise 2-D CCD camera assembly capable of single-electron detection; the detector assembly is principally comprised of a phosphorous scintillator, an image intensifier (Hamamatsu), and finally the CCD camera (Photometrics, KAF-1000). Because the scattering intensity in electron diffraction decays rapidly with increasing scattering angle (usually varying over 6-8 orders of magnitude), a radially symmetric, variable neutral-density apodizing optical filter was coated onto the back side of the scintillator. This filter allows the simultaneous measurement of diffracted intensities varying over 7 orders of magnitude, thereby significantly extending the dynamic range of detected intensities and consequently, improving the precision of internuclear distance measurements in comparison with previous generations of UED.

The reaction zero-of-time was determined by the ion-induced lensing technique.[35] In this approach, a calibration gas (e.g., CF_3I) is delivered to the scattering chamber via the sample nozzle; the spatial profile of the undiffracted electron beam is then monitored while the arrival times of the electron pulses are varied with respect to those of the laser pulses. Fig. 5.4.2 shows a typical photoionization-induced lensing transient. When the electron and laser pulses coincide within the interaction region, the focused laser induces multi-photon ionization in the gas molecules, leading to charge separation and the formation of an electric field gradient. This field gradient effects a corresponding increase in the ellipticity of the

undiffracted electron beam. The time at which the ellipticity of the electron beam deviates from that of a symmetric profile is defined to be the reaction zero-of-time. The overall temporal resolution of the experiment, about 5 ps, includes contributions from the electron pulse width, the laser pulse width, and the group-velocity mismatch[34] (~3 ps) between light and electron pulses.

Samples of $C_2F_4I_2$ (Lancaster, 98%) were used without further purification, but were degassed with several freeze-pump-thaw cycles and stabilized with copper filings. High-purity xenon (Spectra Gases, 99.999%) was used as an atomic reference gas (see discussion below), and the CF_3I gas (99%) used for determining the zero-of-time in the lensing experiments was purchased from Aldrich. In order to maintain satisfactory sample pressure at the needle (estimated to be a few torr), the sample bulb, gas manifold, and nozzle temperatures were respectively maintained at 60 °C, 100 °C, and 120 °C for the $C_2F_4I_2$ experiments. The background pressure of the scattering chamber was typically ~2×10^{-4} torr during the experiment.

In order to obtain ground-state structures, we time the arrival of the electron pulse to occur prior to that of the initiation pulse (that is, at a negative time); diffraction patterns obtained at positive times, minus the negative one, give the images of transient structures involved in the reaction. The 2D ratio image at –95 ps is presented in Fig. 5.4.3.

In order to resolve structural changes during the course of the reaction, UED data was collected for $C_2F_4I_2$ over a range of time delays (t) from –95 ps to +405 ps. We directly monitored the net change in the diffraction pattern resulting from the

reaction by using the temporal difference method [4,47]. For example, $\Delta I^{2D}(t; t<0; pix) = I^{2D}(t) - I^{2D}(t<0)$ gives the difference image that reflects only changes in molecular structures involved in the formation and decay of transient species. Indeed, transient structural changes were observed in the 2D diffraction difference images [$\Delta I^{2D}(t; -95\ ps; pix)$], which are shown in Fig. 5.4.4. As expected, at $t = -45$ ps, no change was observed in the diffraction image because the electron pulses probe the molecules before the reaction. At $t = 0$ ps, we observed the instantaneous appearance (within our temporal resolution) of a periodic pattern – diffraction rings – that resulted from structural changes. The difference signal becomes more pronounced in the images with increasing time. The 2D ratio image, R^{2D}, was converted to a 1D total intensity curve, I^T, by calculating the average intensity as a function of pixel radius (*pix*) from the electron beam center. An experimental molecular scattering intensity curve, *sM(s)*, was generated [24] and subsequently fit to a theoretical *sM(s)* curve calculated from the structural parameters. A corresponding radial distribution curve, *f(r)*, which reflects the relative density of internuclear distances in a molecule, was obtained via a Fourier (sine) transform of *sM*(*s*):

$$f(r) = \int_0^{s_{max}} sM(s)\sin(sr)\exp(-ks^2)\,ds \qquad (5.4.2.1)$$

where s is the momentum transfer parameter given by $s = 4\pi/\lambda \cdot \sin(\theta/2)$, λ is the de Broglie wavelength of the electrons (0.067 Å at 30 keV), and θ is the scattering angle. The damping constant k accounts for the finite s range of the detector (≈1.5 to 18.5 Å^{-1}).

5.4.3 Analysis Of The Ground-State $C_2F_4I_2$ Data

The experimental results concerning the ground-state structures of $C_2F_4I_2$ are shown in Fig. 5.4.5. In order to observe the ground-state structures, we time the arrival of the electron pulse to occur prior to that of the initiation pulse (i.e., at a negative time). Figure 5.4.5(a) shows the raw 1-D diffraction data, $R^E(-95\ ps;\ s)$, obtained from the –95 ps data (following division by the Xe scattering intensity), and the corresponding $R_B^E(-95\ ps;\ s)$ baseline curve. Following subtraction of the $R_B^E(-95\ ps;\ s)$ baseline, the corresponding $sM^E(-95\ ps;\ s)$ curve was generated according to Eq. (4.5.1.14), and is shown as the solid line in Fig. 5.4.5(b). The experimental data was then compared with a theoretical model derived from structural parameters obtained by conventional electron diffraction.[36]

The $C_2F_4I_2$ molecule is known to have two conformational minima with respect to the energy surface parameterized by rotation about the C-C bond: an *anti* structure with a ∠ICCI torsion angle of 180° and C_{2h} symmetry, and a *gauche* structure with ∠ICCI ≈ 70° and C_2 symmetry. In the study by Hedberg and coworkers, the experimental structural parameters for $C_2F_4I_2$ were refined under the simplifying assumption that the *anti* and *gauche* conformers possess identical values for the structural parameters, except for the ∠ICCI dihedral angle. Correspondingly, identical *anti/gauche* parameter values were used in our analysis, although recent calculations have suggested that the C-C and C-F distances of the *anti* conformers may be slightly smaller, and the C-X distances slightly longer, than those of the *gauche* conformers.[44]

Both ground-state structures were observed in the electron diffraction data shown in Fig. 5.4.5; the ratio of these conformers was determined via least-squares refinement to be 76:24 ± 2 *anti*:*gauche*. This ratio, which is governed by the sample temperature and the energy difference between the conformers, was identical to the previous results obtained at 120 °C.[36] The theoretical $sM^T(-95\ ps;\ s)$ curve, obtained from the refinement of the conformer ratio, is shown as the shaded curve in Fig. 5.4.5(b). Excellent agreement can be seen between $sM^E(-95\ ps;\ s)$ and $sM^T(-95\ ps;\ s)$, and in the corresponding experimental and theoretical $f(-95\ ps;\ r)$ curves shown in Fig. 5.4.5(c). The various interatomic distances respectively contributed by the *anti* and *gauche* $C_2F_4I_2$ structures are indicated at the bottom of the figure, and can be summarized as follows: the peak at ~1.5 Å results from covalent C-F and C-C distances; the peak at ~2.2 Å results from covalent C-I and non-bonded F••F and C••F distances; the broad peak at ~3 Å is comprised of non-bonded F••I, C••I, and F••F distances; and the peaks at ~3.8 Å and ~5.1 Å respectively correspond to the non-bonded I••I distances for the *gauche* and *anti* conformers.

5.4.4 Structural Dynamics Of The Decomposition Of $C_2F_4I_2$

UED images were acquired for the decomposition of $C_2F_4I_2$ over a range of time delays (t) from –95 ps to +405 ps. The data at –95 ps served as a reference representing the signal contributed only by parent molecules; a set of diffraction-difference curves with t_{ref} = –95 ps was obtained from the images using the procedure described in Section III. Figure 5.4.6(a) shows the effects of the Fourier filter on a

raw diffraction-difference curve, $\Delta R^E(405\ ps;\ -95\ ps;\ s)$, while Fig. 5.4.7(a) shows the entire set of difference curves, $\Delta R^E(t;\ -95\ ps;\ s)$, and the corresponding residual background curves, $\Delta R_B^E(t;\ -95\ ps;\ s)$. Whereas no change is observed in the $t = -45$ ps data—the electron pulses probe the molecules prior to the initiation of the chemical reaction—at $t = 0$ ps, a periodic pattern instantaneously appears (within our time resolution), resulting from structural changes in the molecules. The difference signal becomes more pronounced with increasing time.

The corresponding $\Delta sM^E(t;\ -95\ ps;\ s)$ curves, created in part by subtraction of the baseline curves obtained for each time delay (shown as shaded lines in Fig. 5.4.7(a)), are shown in Fig. 5.4.7(b). The difference procedure removes most of the contribution from the background signal, resulting in a small, nearly linear background curve for the raw difference curves in Fig. 5.4.7(a). Finally, the corresponding time-dependent difference radial distribution curves, $\Delta f^E(t;\ -95\ ps;\ r)$, which directly indicate the structural changes occurring over the course of the reaction, are shown in Fig. 5.4.7(c). It is interesting to note that the peak intensity at ~5 Å in the $\Delta f(r)$ curves remains constant after 5 ps, whereas the peak intensities around 2~3 Å continue to increase over a longer time scale. As shown in the figure, the negative peak at ~5 Å results from the loss of the I··I internuclear separation of the *anti* conformer of the parent $C_2F_4I_2$ molecules, while those at 2~3 Å result primarily from the depletion of C-I, F··I, and C··I distances. These observations demonstrate the non-concerted nature of the structural changes in the reaction: The first step ($C_2F_4I_2 \rightarrow C_2F_4I + I$) is essentially complete within our 5 ps resolution—consistent with the ~200 fs time

constant measured previously in this laboratory,[10] whereas the second step ($C_2F_4I \rightarrow C_2F_4 + I$) is considerably slower, taking place over tens of picoseconds.

Theoretical $\Delta sM^T(t; -95\ ps; s)$ and $\Delta f^T(t; -95\ ps; s)$ curves (shaded lines in Figs. 7(b) and 7(c)) were obtained by refining the relative fractions of the species present against the corresponding experimental $\Delta sM^E(t; -95\ ps; s)$ curve at each time delay. These refinements were performed as follows. The depletion of the $C_2F_4I_2$ parent molecules was modeled using the structural parameters determined by Hedberg and co-workers, and with the *anti*:*gauche* conformer ratio held fixed at the 74:26 value determined above; the latter practice assumes that there is no disproportional selectivity in the depletion of *anti* vs. *gauche* $C_2F_4I_2$ conformers during the loss of the first iodine atom (i.e., that the C-I chromophores of the *anti* and *gauche* conformers have identical absorption cross sections and reactivity).

The C_2F_4I radical intermediate was modeled using the structural parameters provided by recent *ab initio* calculations.[44] While one goal of our studies was to experimentally determine the structure of this transient species (the subject of Section IV D), *ab initio* calculations suggested that the structure of this species is non-bridged in nature, with *anti* and *gauche* conformers qualitatively similar to the parent structures. Nevertheless, we initially included an *ab initio* bridged C_2F_4I structure in our early fraction refinements; doing so, however, had a detrimental effect on the overall fits—and typically resulted in negative values for the bridged fraction. Therefore, our final fraction refinements of the $\Delta sM(t; -95\ ps; s)$ data included only the non-bridged, "classical" *anti* and *gauche* C_2F_4I structures.

Thermal effects resulting from the high internal energy of the C_2F_4I radical following photoexcitation were included in our model. After each parent molecule absorbs a UV photon (107 kcal/mol) and fragments into C_2F_4I + I, 48 kcal/mol are available for the internal energy of the C_2F_4I radical and the translational motion of both particles (for the I channel, whereas only 26 kcal/mol is left over after the formation of I*, spin excited iodine); 59 kcal/mol of the incident energy is required to break the first C-I bond (in addition to the 22 kcal/mol needed to match the spin-orbit energy of I*). According to previous experiments from this group,[10] about 67% (for the I channel; 59% for I* channel) of the energy is partitioned into the translational degrees of freedom, whereas the remaining 33% [for the I channel (16 kcal/mol); 41% for the I* channel (11 kcal/mol)] goes into the internal energy of the C_2F_4I radical. Accounting for the branching ratio of 30:70 for the I and I* channels[10] yields 12.5 kcal/mol for the available internal energy acquired in the C_2F_4I radical by photoexcitation. However, because some thermal energy from the parent molecule at 393 K remains in C_2F_4I (~6.7 kcal/mol), the total available internal energy is about 19 kcal/mol. If a complete thermalization of the internal degrees of freedom is assumed, a vibrational temperature of ~800 K can be estimated for the C_2F_4I radical (based on the total remaining internal energy and *ab initio* estimates for the vibrational frequencies[44]).

Using *ab initio* values for the rotational barrier separating *anti* and *gauche* structures,[44] microcanonical RRKM rates may be calculated to predict that the time constant for the conversion from the *anti* conformer to the *gauche* conformer is ~13

ps, and that for the reverse isomerization is ~3 ps. These time constants yield a steady-state *anti*:*gauche* conformer ratio of 82:18. On the other hand, assuming complete thermalization of the internal degrees of freedom gives a similar conformer ratio of 81:19, estimated from the energy difference between the conformers (calculated to be ~3.3 kcal/mol [44]), and the internal temperature. In our refinements of the UED data, the *anti*:*gauche* conformer ratio of the C_2F_4I radicals was therefore held fixed at 81:19. Note that the *ab initio* calculations predicted that the conformational energy difference between *anti* and *gauche* radicals is *larger* than the corresponding value for the parent conformers (1.2 ~ 1.9 kcal/mol)[44], apparently resulting from a relative stabilization of the *anti* radicals that has been rationalized in terms of hyperconjugation between the radical center and the σ*(C-I) molecular orbital.[55]

Finally, the structural parameters reported in Ref. [56] were used to model the C_2F_4 product species. The following assumptions permitted the fraction refinements to be simplified to a two-parameter fit: 1) the total fraction of $C_2F_4I_2$ parent molecules depleted and 2) the total fraction of C_2F_4I radicals formed. The fraction of C_2F_4 product formed could then be determined from these values at each time point according to Eq. (4.5.3.3):

$$\begin{aligned}\Delta sM(t;-95ps;s) = &-|\Delta p_{C_2F_4I_2}|\cdot sM(s)_{C_2F_4I_2} + |\Delta p_{C_2F_4I}|\cdot sM(s)_{C_2F_4I} \\ &+|\Delta p_{C_2F_4}|\cdot sM(s)_{C_2F_4}\end{aligned} \quad ,(5.4.4.1)$$

with

$$\Delta p_{C_2F_4} + \Delta p_{C_2F_4I} = -\Delta p_{C_2F_4I_2} \,. \qquad (5.4.4.2)$$

The time evolution of the distribution of structures as determined from the

$\Delta sM(t; -95\ ps; s)$ data is shown in Fig. 5.4.8. Figure 5.4.8(a) shows the time dependence of the relative fraction of the $C_2F_4I_2$ parent molecules. An initial depletion of the parental signal is observed to follow the response function of the UED apparatus, a result that is consistent with the ~200 fs time constant measured previously by femtosecond mass spectrometry.[10] The amplitude of the diffraction-difference signals, when scaled to that of the ground state, shows that 8 ± 1% of the parent molecules participated in the reaction under the given experimental conditions. The temporal evolution of the relative fractions of the C_2F_4I radicals and C_2F_4 products are shown respectively in Figs. 5.4.8(b) and 5.4.8(c). The relative fraction of C_2F_4I rises briefly (within the response time of the apparatus) and then decays, while the fraction of C_2F_4 rises steadily. Fitting these time-dependent fractions results in an average time constant of 26 ± 7 ps for the depletion of C_2F_4I transient structures (20 ± 5 ps) and formation of C_2F_4 molecules (31 ± 4 ps); the overall temporal resolution of the apparatus was explicitly included in the determination of these time constants. Given the available internal energy of the C_2F_4I intermediate described above, this temporal behavior is entirely consistent with a barrier crossing process, as is the percentage of C_2F_4I radicals undergoing further dissociation to form C_2F_4 (55 ± 5%).

5.4.5 Isolation Of The $C_2F_4I \rightarrow C_2F_4 + I$ Process

As shown clearly in the previous section, any reaction involving the parent molecules is complete within the first 5 ps. Thus, in order to highlight the structural changes of the reaction intermediate and product only—with no contribution from any

other species present—we generated a set of additional diffraction-difference curves with t_{ref} = 5 ps through Eq. (16). Figure 5.4.9(a) shows raw difference curves [$\Delta R^E(t; 5\ ps; s)$] and the corresponding residual background curves [$\Delta R_B{}^E(t; 5\ ps; s)$, shaded lines]. The $\Delta sM^E(t; 5\ ps; s)$ curves, created in part by subtracting the baseline curves obtained for each time point, are shown in Fig. 5.4.9(b). As before, this difference procedure removes most of the background signal.

Fig. 5.4.9(c) shows the corresponding difference radial distribution curves, $\Delta f^E(t; 5\ ps; r)$. The $\Delta f(t; 5\ ps; r)$ signals arise only from the transient C_2F_4I and final product C_2F_4 species, with the depletion of the C_2F_4I radical being evident at C-I, C··I, and F··I separations; note that the populations of other internuclear separations (e.g. C-F, C-C, and F··F) are essentially unchanged, and make no contribution to the $\Delta sM^E(t; 5\ ps; s)$ or $\Delta f^E(t; -95\ ps; r)$ signals. The absence of an I··I component (~5 Å) in the $\Delta f^E(t; 5\ ps; r)$ curves clearly shows that we are observing solely the population change of the transient C_2F_4I structures forming C_2F_4, and that the contribution from the unreacted $C_2F_4I_2$ population is negligible. Theoretical $\Delta sM^T(t; 5\ ps; s)$ and $\Delta f^T(t; 5\ ps; s)$ curves (shaded lines in Figs. 5.4.9(b) and 5.4.9(c)) were obtained by a single-parameter fit (the fraction of C_2F_4 species) of the experimental $\Delta sM^E(t; 5\ ps; s)$ curves according to Eq. (4.5.3.3):

$$\Delta sM(t;5ps;s) = -|\Delta p_{C_2F_4I}| \cdot sM(s)_{C_2F_4I} + |\Delta p_{C_2F_4}| \cdot sM(s)_{C_2F_4},$$

(5.4.5.1)

with

$$\Delta p_{C_2F_4} = -\Delta p_{C_2F_4I} \,. \qquad (5.4.5.2)$$

The time-dependent fraction of C_2F_4 formed after 5 ps, shown in Fig. 5.4.10, yields a time constant of 25 ± 7 ps, in total agreement with the above analysis of the $\Delta f(t; -95\ ps; r)$ curves.

5.4.6 Molecular Structure Of The C_2F_4I Radical

The molecular structure of the C_2F_4I radical intermediate was determined from the diffraction-difference curves $\Delta sM(t; 5\ ps; s)$; both bridged and classical C_2F_4I structures were considered in the modeling of the diffraction data. The symmetrically bridged structure has C_{2v} symmetry, whereas the *anti* and *gauche* conformers of the classical structure have C_s and C_1 symmetry, respectively. The $\Delta R^E(t; 5\ ps; s)$ difference curves from t = +40 ps to +405 ps were averaged (prior to Fourier filtering) to improve the precision of the fits. No significant changes in the structure of the radical are expected (or were observed) over this temporal range, as the radical should already be thermally equilibrated, and collisional cooling should not become important until well into the nanosecond regime under the present experimental conditions. The averaged signal, denoted $\Delta R^E(\infty; 5\ ps; s)$, was then fit separately with either the *ab initio* bridged radical structure, or the 81:19 mixture of *ab initio* classical *anti* and *gauche* radical structures described in the previous section.[44] The $\Delta R^E(\infty; 5\ ps; s)$

curve, along with the background curve obtained by fitting through the theoretical zero-crossing points, is shown in Fig. 5.4.11 as an example of this procedure.

The results of this fitting procedure are contained in Fig. 5.4.12, where the experimental $\Delta sM^E(\infty; 5\ ps; s)$ and $\Delta f^E(\infty; 5\ ps; r)$ curves are shown as solid lines, and the corresponding theoretical curves produced with the two *ab initio* structural models are shown as shaded lines. As shown in Figs. 5.4.12(c) and (d), the theoretical curves for the mixture of *ab initio* classical structures reproduce the experimental data extremely well, whereas the fit provided by the *ab initio* bridged structure (Figs. 5.4.12(a) and (b)) is vastly inferior. Indeed, the $\Delta sM^E(\infty; 5\ ps; s)$ and $\Delta sM^T(\infty; 5\ ps; s)$ curves in Fig. 5.4.12(a) quickly go out of phase, yielding manifestly different positions for the two prominent negative peaks in the corresponding $\Delta f^E(\infty; 5\ ps; r)$ and $\Delta f^T(\infty; 5\ ps; r)$ curves (Fig. 5.4.12(b)). Thus, we concluded that the structure of the C_2F_4I radical intermediate is, in fact, classical in nature,[46] in general agreement with our qualitative interpretations of previous UED experiments.[47]

Significant improvements in sensitivity and resolution provided by our third-generation UED apparatus permitted the quantitative determination of the molecular structure of the C_2F_4I radical from our experimental data, thereby allowing a direct comparison with the *ab initio* calculations. A least-squares refinement of the $\Delta sM^E(\infty; 5\ ps; s)$ data was performed as follows. A theoretical model was implemented to simplify the fit and reduce the number of adjustable parameters in the final structural refinement. Assuming a dihedral angle of 180°, the *anti* conformer of the C_2F_4I radical has 9 independent parameters when the structure is constrained to be

geometrically consistent: four covalent bond distances and five bond angles. The *gauche* conformer was treated similarly: it was described by the same 9 independent parameters, but with small constant differences from the values of the 9 *anti* parameters as predicted by the *ab initio* calculations[44] (for example, the calculations suggested that the C-I distance of the *gauche* conformer [$r(\text{C-I})_{gauche}$] would be less than that of the *anti* conformer by 0.015 Å; thus, $r(\text{C-I})_{gauche}$ was obtained by subtracting 0.015 Å from the refined value of $r(\text{C-I})_{anti}$). Additionally, the primary dihedral angle of the *gauche* species was fixed at 56° (again, following the *ab initio* predictions)—the dihedral angle was poorly sensitive in the fitting, partially due to the low amount of *gauche* structures present. As before, the *anti*:*gauche* radical conformer ratio was held fixed at 81:19 (see Section IV B). Finally, values for the mean amplitudes of vibration (l) and centrifugal distortion corrections (dr) (summarized in Table 1), and the relationships between the refined geometrically consistent bond lengths (r_e) and the internuclear distances measured by electron diffraction (r_a), were calculated according to the procedures as follows. The ASYM40 program developed by Hedberg's group[43] was used to aid in the determination of the molecular structure of the C_2F_4I radical, specifically to account for the elevated temperature of this transient species. The program was used to calculate temperature-dependent values for the centrifugal distortion (dr) and the mean amplitude of vibration (l) relevant to each atom-atom pair (see Table 1). These values were then entered into the structural refinement of the (geometrically consistent) zero-Kelvin bond distances (r_e) and angles using the relation $r_a \approx r_e + (3/2)al^2 + dr - l^2/r$, where r_a

is the internuclear distance as measured by electron diffraction and *a* is the anharmonicity constant for the bond. The independent structural parameters obtained from the least-squares fit of the experimental data could then be compared to *ab initio* calculations. This simplifying theoretical model thus limited the structural refinement of the C_2F_4I radical to only 9 adjustable parameters.

The results of the least-squares structural refinement is shown in Fig. 5.4.13, and the values determined for the independent structural parameters are summarized in Table 2. The corresponding error matrix is given in Table 3; the diagonal elements of the matrix are the squares of the standard deviations of the least-squares refinement, and the off-diagonal elements are the average products of the standard deviations of each pairing of refined parameters. The *r*(C-I) and *r*(C-C) distances of the C_2F_4I radical are, respectively, longer and shorter than those of the parent molecule (for $C_2F_4I_2$, *r*(C-I) = 2.136 Å, *r*(C-C) = 1.534 Å)[36], while the C-F′ internuclear distance in the radical site (-CF'_2) is shorter than that of the -CF_2I site. Moreover, the ∠CCF′ and ∠F′CF′ angles become larger than the corresponding angles of the parent (by ~9° and ~12°, respectively [36]), suggesting that the radical center (-CF'_2) of the C_2F_4I intermediate relaxes following the loss of the I atom from the $C_2F_4I_2$ parent molecule (naturally, a similar comparison may be drawn between these ∠CCF′ and ∠F′CF′ angles and the ∠CCF and ∠FCF angles on the other side of the radical). These results are consistent with the increased C-C bond order expected from the formation of the transient C_2F_4I structure. These trends were also well-reproduced by the *ab initio*

calculations; indeed, the refined internuclear distances reported in Table 2 agree with the corresponding *ab initio* predictions to within 0.03 Å.[44]

It is interesting to compare the molecular structure of the C_2F_4I radical with the corresponding structure of the C_2H_4I radical, and consider the stereochemical implications for the respective geometries of these intermediate species. However, while the geometry of the C_2F_4I radical has now been studied with UED (see also Refs. [46,47]), to date only *ab initio* investigations of the C_2H_4I radical geometry have been performed (the high thermal instability of the $C_2H_4I_2$ parent molecule makes this substance notoriously difficult to work with in experimental studies).

The recent *ab initio* investigations by Ihee *et al.*[44] generalized this structural comparison to include a variety of CR_2XCR_2-type radicals, where R represents either H or F, and X refers to the heavy halides (Cl, Br, and I). These calculations predicted that when X = I (or Br) and if R = F, then the most energetically stable radical structure is classical; however, if R = H, then the structure is bridged. The *ab initio* structures of the C_2F_4I radical and the C_2H_4I radical are presented in Fig. 5.4.14. The dramatic difference between the C_2F_4I and C_2H_4I radical geometries in these calculations originated from the lower electron density of the π orbital of the C_2F_4 moiety compared to the C_2H_4 moiety (due to electron withdrawal by the electronegative F atoms), as the singly-occupied molecular orbital of the bridged structure involves significant interaction between the p orbital of the primary halogen atom (I) and the π orbital of the C-C bond.[44]

5.4.7 Discussion On The Stereochemical Selectivity

Much of the interest in the molecular structures of CR_2XCR_2-type radicals lies in the relevance of structure and dynamics to the stereochemistry of chemical reactions involving these transient species. For example, consider the generalized two-step elimination of 2X from $C_2R_4X_2$ giving C_2R_4, shown schematically in Fig. 5.4.15. A number of C_2R_4X intermediate structures could, in principle, be involved in the reaction, with different implications for the stereochemical control of the reaction with regard to the final positions of the –R groups about the C=C bond in the C_2R_4 product. The formation of a bridged C_2R_4X structure prevents rotation about the C-C bond, thereby ensuring stereochemical control in accordance with the Skell hypothesis[53,54] (a similar result would be obtained if the X atom were rapidly "shuttled" between the two $-CR_2$ moieties[42]). Alternatively, a classical structure could be formed, with either a "pyramidal" radical center (predicted for R=F)[44] or a nearly planar radical center (predicted for R=H [44]). Because rotation about the C-C bond is unhindered in classical structures, one might predict (contrapositively to the Skell hypothesis) that reactions involving C_2R_4X radical intermediates that lack bridged geometries would *not* maintain stereochemical control (for nearly planar radical centers (R=H), the final positions of $-R_3$ and $-R_4$ could be scrambled through simple rotation about the C-C bond, whereas in species with R=F the non-planar nature of the $-CF_2$ moiety might require some combination of rotation and inversion due to the high energy required to reach the "eclipsed" rotational transition state[44]). However, it should be considered that dynamical effects may also play a role in the retention of stereochemistry in such

reactions; if the time for the second C-X bond breakage is shorter than that of rotation around the C-C bond, stereochemistry will be retained even in reactions involving classical C_2R_4X structures. Future studies on other C_2R_4X species may shine new light on the respective roles of structure and dynamics in determining the stereochemical nature of the products formed by various reactions.

References

1. Kawasaki, M., Lee, S. J. & Bersohn, R. Photodissociation of molecular beams of methylene iodide and iodoform. *J. Chem. Phys.* **63**, 809-814 (1975).
2. Baughcum, S. L. & Leone, S. R. Photofragmentation infrared emission studies of vibrationally excited free radicals CH_3 and CH_2I. *J. Chem. Phys.* **72**, 6531-6545 (1980).
3. Williamson, J. C., Cao, J., Ihee, H., Frey, H. & Zewail, A. H. Clocking transient chemical changes by ultrafast electron diffraction. *Nature* **386**, 159-162 (1997).
4. Ihee, H., Cao, J. & Zewail, A. H. Ultrafast electron diffraction: structures in dissociation dynamics of $Fe(CO)_5$. *Chem. Phys. Lett.* **281**, 10-19 (1997).
5. Wannenmacher, E. A. J., Felder, P. & Huber, J. R. The simultaneous three-body dissociation of CF_2I_2. *J. Chem. Phys.* **95**, 986-997 (1991).
6. Baum, G., Felder, P. & Huber, J. R. Photofragmentation of CF_2I_2. Competition between radical and three-body dissociation. *J. Chem. Phys.* **98**, 1999-2010 (1993).
7. Boesl, U., Neusser, H. J. & Schlag, E. W. Secondary Excitation of Ions in a Multiphoton Mass Spectrometer. *Chem. Phys. Lett.* **87**, 1-6 (1982).
8. Bañares, L., Baumert, T., Bergt, M., Kiefer, B. & Gerber, G. The ultrafast photodissociation of $Fe(CO)_5$ in the gas phase. *J. Chem. Phys.* **108**, 5799-5811 (1998).

9. Khundkar, L. R. & Zewail, A. H. Picosecond photofragment spectroscopy. IV. Dynamics of consecutive bond breakage in the reaction $C_2F_4I_2$->C_2F_4+2I. *J. Chem. Phys.* **92**, 231-242 (1990).

10. Zhong, D., Ahmad, S. & Zewail, A. H. Femtosecond Elimination Reaction Dynamics. *J. Am. Chem. Soc.* **119**, 5978-5979 (1997).

11. Mathews, C. W. The Absorption Spectrum of CF_2. *Can. J. Phys.* **45**, 2355-2374 (1967).

12. Kirchhoff, W. H., Lide, D. R. J. & Powell, F. X. The Microwave Spectrum, Force Field and Dipole Moment of CF_2. *J. Mol. Spectrosc.* **47**, 491-498 (1973).

13. Cameron, M. R., Kable, S. H. & Bacskay, G. B. The electronic spectroscopy of jet-cooled difluorocarbene (CF_2): The missing A-state stretching frequencies. *J. Chem. Phys.* **103**, 4476-4483 (1995).

14. Cheong, B.-S. & Cho, H.-G. Ab Initio Studies of Haogenated Methyl and Methylene Radicals: Molecular Structure, Vibrational Frequencies, and Enthalpies of Formation. *J. Phys. Chem. A* **101**, 7901-7906 (1997).

15. Cai, Z.-L. Ab Initio Study of Several Electronic States of the CF_2 Radical. *J. Phys. Chem.* **97**, 8399-8402 (1993).

16. Russo, N., Sicilia, E. & Toscano, M. Geometries, singlet-triplet separations, dipole moments, ionization potentials, and vibrational frequencies in methylene (CH_2) and halocarbenes (CHF, CF_2, CCl_2, CBr_2, CI_2). *J. Chem. Phys.* **97**, 5031-5036 (1992).

17. Bauschlicher, C. W. J., Schefer, H. F. I. & Bagus, P. S. Structure and Energies of Simple Carbenes CH_2, CHF, CHCl, CHBr, CF_2, and CCl_2. *J. Am. Chem. Soc.* **99**, 7106-7110 (1977).

18. Sundström, V. *Femtochemistry and Femtobiology: Ultrafast Reaction Dynamics at Atomic-Scale Resolution* (World Scientific, Singapore, 1997).

19. Chergui, M. *Ultrafast Chemical and Physical Processes in Molecular Systems* (World Scientific, Singapore, 1996).

20. Manz, J. & Wöste, L. *Femtosecond Chemistry* (VCH, New York, 1995).

21. Zewail, A. H. *Femtochemistry: Ultrafast Dynamics of the Chemical Bond* (World Scientific, Singapore, 1994).

22. Castleman, A. W., Jr. 10 years of femtochemistry - A historical perspective. *J. Phys. Chem. A. - TEN YEARS OF FEMTOCHEMISTRY* **102**, June 4 issue (1998).

23. Williamson, J. C. & Zewail, A. H. Structural femtochemistry: Experimental methodology. *Proc. Natl. Acad. Sci.* **88**, 5021-5025 (1991).

24. Hargittai, I. & Hargittai, M. *Stereochemical Applications Of Gas-Phase Electron Diffraction* (VCH, New York, 1988).

25. Ischenko, A. A., Schäfer, L., Luo, J. Y. & Ewbank, J. D. Structural and Vibrational Kinetics by Stroboscopic Gas Electron Diffraction: The 193 nm Photodissociation of CS_2. *J. Phys. Chem.* **98**, 8673-8678 (1994).

26. Elsayed-Ali, H. E. Time-resolved reflection high-energy electron diffraction of metal surfaces. *Proc. SPIE* **2521**, 92-102 (1995).

27. Ráksi, F. *et al.* Ultrafast x-ray absorption probing of a chemical reaction. *J. Chem. Phys.* **104**, 6066-6069 (1996).

28. Schoenlein, R. W. *et al.* Femtosecond X-ray Pulses at 0.4 Å Generated by 90° Thomson Scattering: A Tool for Probing the Structural Dynamics of Materials. *Science* **274**, 236-238 (1996).

29. Perman, B. *et al.* Energy Transduction on the Nanosecond Time Scale: Early Structural Events in a Xanthopsin Photocyle. *Science* **279**, 1946-1950 (1998).

30. Tomov, I. V., Chen, P. & Rentzepis, P. M. Picosecond time-resolved x-ray diffraction during laser-pulse heating of an Au(111) crystal. *J. Appl. Cryst.* **28**, 358-362 (1995).

31. Larsson, J. *et al.* Ultrafast structural changes measured by time-resolved X-ray diffraction. *Appl. Phys. A* **66**, 587-591 (1998).

32. Rischel, C. *et al.* Femtosecond time-resolved X-ray diffraction from laser-heated organic films. *Nature* **390**, 490-492 (1997).

33. Cao, J., Ihee, H. & Zewail, A. H. Ultrafast electron diffraction: determination of radical structure with picosecond time resolution. *Chem. Phys. Lett.* **290**, 1-8 (1998).

34. Williamson, J. C. & Zewail, A. H. Ultrafast electron diffraction. Velocity mismatch and temporal resolution in crossed-beam experiments. *Chem. Phys. Lett.* **209**, 10-16 (1993).

35. Dantus, M., Kim, S. B., Williamson, J. C. & Zewail, A. H. Ultrafast Electron Diffraction. 5. Experimental Time Resolution and Applications. *J. Phys. Chem.*

98, 2782-2796 (1994).

36. Thomassen, H., Samdal, S. & Hedberg, K. Conformational Analysis. 15. 1,2-Dibromotetrafluoroethane and 1,2-Diiodotetrafluoroethane. Electron Diffraction Investigations of the Molecular Structures, Comparisons, and Anti-Gauche Energy and Entropy Differences. *J. Am. Chem. Soc.* **114**, 2810-2815 (1992).

37. Hedberg, K. & Iwasaki, M. Least-Squares Refinement of Molecular Structures from Gaseous Electron Diffraction Sector-Microphotometer Intensity Data. I. Method. *Acta Cryst.* **17**, 529-533 (1964).

38. Bartell, L. S. in *Physical Methods of Chemistry* (eds. Weissberger, A. & Rossiter, B. W.) (Wiley, New York, 1972).

39. Jaguar. (Schrödinger, Inc., Portland, OR, 1997).

40. Hay, P. J. & Wadt, W. R. *J. Chem. Phys.* **82**, 284-298 (1985).

41. Møller, K. B. & Zewail, A. H. Femtosecond dynamics of transition states: the classical saddle-point barrier reactions. *Chem. Phys. Lett.* **295**, 1-10 (1998).

42. Skell, P. S. & Traynham, J. G. Radical Brominations of Alkyl Bromides and the Nature of β-Bromoalkyl Radicals. *Acc. Chem. Res.* **17**, 160-166 (1984).

43. Hedberg, L. & Mills, I. M. ASYM20: A Program for Force Constant and Normal Coordinate Calculations, with a Critical Review of the Theory Involved. *J. Mol. Spectrosc.* **160**, 117-142 (1993).

44. Ihee, H., Kua, J., Goddard, W. A., III. & Zewail, A. H. CF2XCF2X and CF_2XCF_2 radicals (X = Cl, Br, I): Ab initio studies and Comparison with

Experiments. *J. Phys. Chem. A*, Accepted (2001).

45. Hassel, O. & Viervoll, H. Electron Diffraction Investigation of Molecular Structures

II. Results Obtained by the Rotating Sector Method. *Acta. Chem. Scand.* **1**, 149-168 (1947).

46. Ihee, H. *et al.* Direct Imaging of Transient Molecular Structures with Ultrafast Diffraction. *Science* **291**, 458-462 (2001).

47. Cao, J., Ihee, H. & Zewail, A. H. Ultrafast electron diffraction and direct observation of transient structures in a chemical reaction. *Proc. Natl. Acad. Sci. USA* **96**, 338-342 (1999).

48. Kochi, J. K. (ed.) *Free Radicals* (John Wiley & Sons, New York, 1973).

49. Beckwith, A. L. J. & Ingold, K. U. in *Rearrangements in Ground and Excited States* (ed. Mayo, P. d.) (Academic Press, New York, 1980).

50. Kerr, J. A. (ed.) *Handbook of Bimolecular and Termolecular Gas Reactions* (CRC Press, Boca Raton, FL, 1981).

51. Fossey, J., Lefort, D. & Sorba, J. (eds.) *Free Radicals in Organic Chemistry* (John Wiley & Sons, New York, 1995).

52. Ihee, H., Zewail, A. H. & Goddard, W. A., III. Conformations and Barriers of Haloethyl Radicals (CH_2XCH_2, X = F, Cl, Br, I): Ab Initio Studies. *J. Phys. Chem. A* **103**, 6638-6649 (1999).

53. Skell, P. S., Tuleen, D. L. & Readio, P. D. *J. Am. Chem. Soc.* **85**, 2849 (1963).

54. Skell, P. S. & Shea, K. J. in *Free Radicals* (ed. Kochi, J. K.) (John Wiley &

Sons, New York, London, Sydney, Toronto, 1973).

55. Bernardi, F., Bottoni, A., Fossey, J. & Sorba, J. Fragment Interaction Analysis In The Framework Of Ab Initio UHF MO Computations. *J. Mol. Struct.* **119**, 231-239 (1985).

56. Carlos, J. L., Karl, R. R. J. & Bauer, S. H. Gas Phase Electron Diffraction Study of Six Fluoroethylenes. *J. Chem. Soc. Farad. Trans. II* **70**, 177-187 (1973).

Table 5.2.1. The comparison of structural data of UED with conventional gas-phase electron diffraction*.

	UED		Gas phase diffraction	
	$r \pm 3\sigma$	$l \pm \sigma$	$r \pm 3\sigma$	$l \pm 3\sigma$
C-F	1.34 ± 0.08	0.04 ± 0.09	1.336 ± 0.005	0.036 ± 0.012
C-I	2.07 ± 0.07	0.04 ± 0.25	2.148 ± 0.004	0.060 ± 0.010
F··· F	2.18 ± 0.63	0.08 ± 0.22	2.182 ± 0.014	0.060
F··· I	2.84 ± 0.31	0.11 ± 0.02	2.870 ± 0.006	0.083 ± 0.004
I··· I	3.54 ± 0.03	0.11 ± 0.02	3.572 ± 0.008	0.090 ± 0.003

* For the detailed discussion of error analysis in UED, see text.

Table 5.2.2. Summary of results for the experimental diffraction- difference curves.

delay time	0 ps	12 ps	162 ps
$r(C\text{-}F) \pm 3\sigma$	1.27 ± 0.03	1.29 ± 0.02	1.30 ± 0.02
$r(F\cdots F) \pm 3\sigma$	2.07 ± 0.09	2.07 ± 0.06	2.06 ± 0.06
$l(C\text{-}F) \pm \sigma$	0.03 ± 0.06	0.04 ± 0.03	0.04 ± 0.05
$l(F\cdots F) \pm \sigma$	0.06 ± 0.08	0.06 ± 0.05	0.06 ± 0.06
CF_2 fraction (%) $\pm 3\sigma$*	18.0 ± 1.0	26.3 ± 1.0	26.6 ± 1.0
χ^2	274	205	301
R	0.102	0.061	0.073

* The scattering intensity fluctuations in I_{Tot} were also estimated and included.

Table 5.4.1. Mean amplitudes of vibration (*l*) and centrifugal distortions (*dr*) at 800 K for the *anti* conformer of the C_2F_4I radical as calculated using the ASYM40 program.[43] The atomic numbering follows the schematic below the table.

	l (Å)	*dr* (Å)
C_1-C_2	0.0657	0.0010
C_1-I_5	0.0889	0.0025
C_2-I_5	0.1268	0.0060
C_1-F_3	0.0572	0.0004
C_2-F_6	0.0590	0.0006
C_2-F_3	0.0983	0.0006
C_1-F_6	0.1148	0.0030
F_3-F_4	0.0886	0.0002
F_6-F_7	0.0844	0.0001
F_3-F_6	0.2047	0.0025
F_3-F_7	0.0999	0.0020
F_3-I_5	0.1193	0.0018
F_6-I_5	0.3307	0.0101

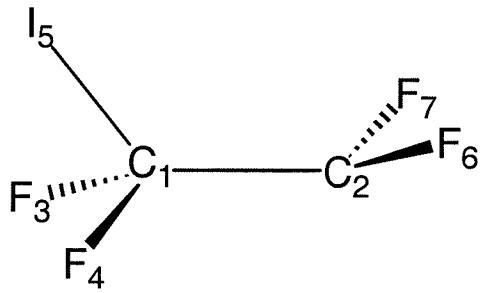

Table 5.4.2. Comparison of the experimental values of the independent structural parameters of the classical C_2F_4I radical intermediate with those obtained via *ab initio* calculations.[44] The bond distances are in Ångströms and the bond angles are in degrees.

	Experiment	***Ab initio* calculations**	
	Anti	*Anti*	*Gauche*
r(C=C)	1.478 ± 0.049	1.503	1.508
r(C-F)	1.340 ± 0.037	1.322	1.327, 1.323
r(C-I)	2.153 ± 0.013	2.164	2.149
r(C-F')	1.277 ± 0.027	1.304	1.309, 1.307
∠CCI	115.0 ± 3.1	112.7	111.8
∠CCF	108.6 ± 6.0	108.6	109.8, 108.1
∠FCF / 2	54.0 ± 5.6	54.4	54.0
∠CCF′	117.9 ± 3.1	114.0	112.3, 113.8
∠F′CF′ / 2	59.9 ± 3.9	55.9	55.6

Table 5.4.3. Error matrix for the least-squares refinement of the C_2F_4I radical intermediate structure.

	r(C-C)	r(C-F)	r(C-I)	r(C-F′)	∠CCI	∠CCF	∠FCF / 2	∠CCF′	∠F′CF′ / 2
r(C-C)	0.0024	-0.0018	-0.0005	0.0012	-0.1488	-0.2898	0.2669	0.1420	-0.1814
r(C-F)		0.0014	0.0003	-0.0010	0.1121	0.2160	-0.1990	-0.1058	0.1352
r(C-I)			0.0002	-0.0002	0.0284	0.0587	-0.0515	-0.0234	0.0309
r(C-F′)				0.0007	-0.0797	-0.1540	0.1413	0.0742	-0.0956
∠CCI					9.6844	18.4113	-17.1247	-9.3730	11.7735
∠CCF						35.8866	-33.1673	-17.8859	22.6619
∠FCF / 2							30.8816	16.8453	-21.3019
∠CCF′								9.8962	-12.0551
∠F′CF′ / 2									15.1277

Figure Captions

Figure 5.1.1: Top, Second-generation Ultrafast Electron Diffraction apparatus, consisting of an electron gun chamber, a diffraction chamber, and a detector chamber. Two fs laser pulses are used; the first initiates the chemical change and the second generates the electron pulse. Bottom, Detection Scheme. Incident electrons either directly bombard a small CCD or strike a phosphor-coated fused fiber optic window. Light emitted from the phosphor is amplified by an image intensifier and brought to a scientific-grade CCD. Both CCDs are thermoelectrically cooled.

Figure 5.1.2: (a) Surface contour plots of low and high-intensity streaked electron pulse pairs. Each pair comes from two incident light pulses, one of which is delayed by 66.7 ps. The horizontal coordinate is the streaking axis. The temporal durations of pulses with high electron numbers (top trace -- 7400 e^-, 6.6 ps; 3790 e^-, 4.3 ps) are broadened by space-charge effects. For low electron numbers (bottom trace -- 295 e^-, 0.5 ps; 150 e^-, 0.5 ps), measurement of the pulse width is limited by the resolution of the streak experiment. The electron pulse width was obtained by subtracting the width of the unstreaked electron beam (4 pix) from the width of the streaked pulses (Lorentzian profiles). (b) Measured electron pulse widths as a function of the number of electrons. The streak velocity was 2.1 pix/ps, or 1.6×10^8 m/s. The sweep voltage is ~1 kV/ns. (c) Experimental photoionization-induced lensing transient. The ordinate reflects the relative difference between the average profile of the electron beam spot in the presence of the excitation laser and a reference profile (no laser).

Figure 5.1.3: Experimental modified molecular scattering curves for two sets of data taken with 15 ps (left panel) and 30 ps (right panel) electron pulses. The delay times between the fs laser pulse and the ps electron pulse are shown. Theoretical calculations of *sM(s)* at -20 ps are presented (see text).

Figure 5.1.4: Radial distribution functions *f(r)* and $\Delta f(r)$ obtained from the *sM(s)* and $\Delta sM(s)$ curves of Fig. 5.1.3, also for two sets of data (15 ps and 30 ps electron pulse width). The corresponding theoretical *f(r)* curve is shown for the -20 ps data. The changes obtained are in the region of the C-I and I···I internuclear separations (see text). Note that in f(r) the peak corresponding to the I···I distance should have about twice the area of the first peak (C-I and H···I); the peak area scales ~ $n_{ij}Z_iZ_j/r_{ij}$ (Z is the atomic number and n_{ij} is the multiplicity for nuclear pairs). However, because of damping in equation (2), the peaks appear to be of equal areas, and this is evident in our simulations for different values of k. The theoretical simulations shown in the Figure are based on the structural data of ref. [45]. We have also used more recent data from K. Hedberg's group (private communication) and obtained very similar *f(r)* curves, within the reported resolution. We thank the referee for pointing out to us this recent reference.

Figure 5.2.1: The experimental *sM(s)* and *f(r)* curves at -150 ps and the difference $\Delta sM(s)$ and $\Delta f(r)$ curves at different delay times, relative to the data of CF_2I_2 at -150 ps (solid lines). Shaded lines represent the theoretical *sM(s)* and *f(r)*, derived with the structural parameters from conventional gas-phase electron diffraction[36], and the

fitting results for $\Delta sM(s)$ and $\Delta f(r)$. The delay time between the initiation laser pulse and the ps electron pulse are also shown.

Figure 5.2.2: Contribution of CF_2 radical to the diffraction intensity at each delay time. The radial distribution functions ($f(r)$) are shown in the left panel, and the modified molecular scattering intensity ($sM(s)$) curves are shown in the right panel. The experimental (solid line) and theoretical (shaded line) $sM(s)$ and $f(r)$ curves for parent CF_2I_2 at -150 ps are also shown. The heavy shaded line represents the difference between the experimental and theoretical radial distribution curves at -150 ps.

Figure 5.3.1: The experimental $sM(s)$ and $f(r)$ curves at t = -150 ps (solid lines). The shaded lines represent the theoretical calculations (see text). The different internuclear separations relevant to the chemical reaction under study are also shown in $f(r)$.

Figure 5.3.2: The experimental diffraction-difference $\Delta sM(t;\ -150\ ps;\ s)$ (left panel) and $\Delta f(t;\ -150\ ps;\ r)$ (right panel) curves at different reaction times referenced to the parent $C_2F_4I_2$ data at -150 ps (solid lines). The shaded lines are the theoretical difference curves. The reaction time t is indicated, and the relevant internuclear distances are also displayed.

Figure 5.3.3: (Upper panel) The temporal evolution of the reactant, the intermediate and the final product. The changes of the individual internuclear separations and the associated molecular structures are also shown. (Lower panel) Diffraction difference curves, labeled by the time of the reaction (t) and the reference time (t_{ref}).

Figure 5.3.4: (Upper panel) The experimental diffraction-difference $\Delta f(t;\ +10\ ps;\ r)$ curves at different reaction times referenced to t_{ref} = +10 ps (solid lines). Shaded lines are the theoretical difference curves. (Lower two panels) The comparison between theoretical and experimental $\Delta f(t;\ +8\ ps;\ r)$ for the two structures, the bridged (middle) and the classical, non-bridged (low) structure. The experimental data in the lower two panels are identical; the difference in appearance is due to values of zero points of ΔI determined by the theoretical analysis (see refs. 8, 17, 18). The reaction time t is indicated on each curve.

Figure 5.3.5: The fraction (%) change of transient C_2F_4I radicals (diamond), final product C_2F_4 (closed circle), and parent $C_2F_4I_2$ (open square), as a function of delay time. The error bars are one standard deviation. The solid curves are from the solution of the kinetic model, Eq. (5.3.5.1) , with $\tau_2 = 17 \pm 2$ ps for C_2F_4 data. For the decay of C_2F_4I, τ_2 was found to be 18 ps, but the error bars are somewhat bigger. In the fitting, the first C-I bond breakage was taken as a step function, since it occurs in ~200 fs; convolution with our time resolution was included (see text). The inset shows the clocking (zero-of-time) with better than 2 ps accuracy. Note that the fraction of reacted parent molecule detected at the time zero is half of the final fraction, and this is entirely consistent with the fact that the first bond breakage is much shorter than 10 ps. This confirms the accurate clocking (2 ps) of time zero in these experiments, as shown in the inset.

Figure 5.4.1: Schematic representation of the UED apparatus.

Figure 5.4.2: Experimental photoionization-induced lensing transient for a molecular beam of CF_3I. The ellipticity is defined as the ratio of vertical and horizontal e-beam widths (FWHM) on the screen. The insert shows an expanded view from –20 ps to 80 ps.

Figure 5.4.3: The ratio image at –95 ps, $R^{2D}(-95\ ps)$.

Figure 5.4.4: Diffraction difference ratio-images for $C_2F_4I_2$, $\Delta R^{2D}(t; -95\ ps)$. The top left one is the ratio image at –95 ps, $R^{2D}(-95\ ps)$.

Figure 5.4.5: The ground-state structure of $C_2F_4I_2$. (*a*) Raw electron diffraction data (solid line) obtained at –95 ps, following division by the atomic reference signal and radial summation of the 2-D data. The smooth background curve is shown as a shaded line. (*b*) Comparison of theoretical (shaded line) and experimental (solid line) *sM(s)* curves for the data in (a) following refinement of the relative fractions of the *anti* and *gauche* structures. (*c*) Comparison of corresponding theoretical (shaded line) and experimental (solid line) *f(r)* curves, obtained by sine transformation of the data in (b) according to Eq. 6. The major interatomic distances for the *anti* and *gauche* $C_2F_4I_2$ structures obtained by Hedberg and co-workers[36] are indicated for comparison.

Figure 5.4.6: The effect of Fourier filtering on 1-D raw diffraction-difference curves. The raw data is shown as a shaded line and the Fourier filtered data (obtained with a ≈8.7-Å low-pass filter) is shown as a solid line. The difference between the raw and filtered data shows the random noise removed by the filter. (a) $\Delta R^{E}(405\ ps; -95\ ps; s)$. (b) $\Delta R^{E}(\infty ps; 5\ ps; s)$.

Figure 5.4.7: Time-resolved structural changes from the elimination of iodine from $C_2F_4I_2$. (a) Raw diffraction-difference signals, *ΔR(t; -95 ps; s),* (solid lines), shown with the baseline curves (shaded lines). (b) Experimental (solid lines) and theoretical (shaded lines) *ΔsM(t; -95 ps; s)* curves obtained at varying time delays. (c) Experimental (solid lines) and theoretical (shaded lines) *Δf(t; -95 ps; r)* curves. Major internuclear distances showing temporal changes are indicated in (C).

Figure 5.4.8: Time dependence of the species fractions from the analysis of *ΔI(t; -95 ps; s)* data. (a) The depletion of the parent fraction (*anti* and *gauche* $C_2F_4I_2$). Depletion of the parent signal is essentially complete within the ~5 ps resolution of the experiment. (b) Time dependence of the transient C_2F_4I species. (c) Formation of the C_2F_4 product. The time constants measured for the depletion of the C_2F_4I radicals (20 ± 5 ps) and formation of C_2F_4 molecules (31 ± 4 ps) yields an average time constant of 26 ± 7 ps. In all three figures, the temporal pulse widths of the electron and laser pulses were accounted for in the determination of the reported time constants. Each error bar represents one standard deviation.

Figure 5.4.9: Time-resolved structural changes involving only the $C_2F_4I \rightarrow C_2F_4 + I$ contribution to the diffraction-difference signal. (a) Raw diffraction-difference signals, *ΔR(t; 5 ps; s)*, (solid lines), shown with the (nearly linear) baseline curves (shaded lines). (b) Experimental (solid lines) and theoretical (shaded lines) *ΔsM(t; 5 ps; s)* curves obtained at varying time delays. (c) Experimental (solid lines) and theoretical (shaded lines) *Δf(t; 5 ps; r)* curves. Note the absence of a peak at ~5 Å corresponding to the depletion of I···I internuclear distances.

Figure 5.4.10: Time dependence of the formation of C_2F_4 molecules from the decay of C_2F_4I transient molecules in the $\Delta I(t;\ 5\ ps;\ s)$ data. The curve is an exponential fit of the C_2F_4 fraction (with the temporal pulse widths of the electron and laser pulses taken into account); the apparent time constant for the formation of C_2F_4 was of 25 ± 7 ps. Each error bar represents one standard deviation.

Figure 5.4.11: Background fitting through the zero-crossing points of the experimental $\Delta R^E(\infty;\ 5\ ps;\ s)$ data. The experimental $\Delta R^E(\infty;\ 5\ ps;\ s)$ and the background $\Delta R^E{}_B(\infty;\ 5\ ps;\ s)$ obtained by fitting a low-order polynomial through the zero-crossing points.

Figure 5.4.12: Comparison of experimental data with *ab initio* calculations for the C_2F_4I radical structure.[46] (a,b) Comparison of experimental $\Delta sM(\infty\ ps;\ 5\ ps;\ s)$ and $\Delta f(\infty\ ps;\ 5\ ps;\ r)$ curves (solid lines) with corresponding theoretical curves (shaded lines) obtained via *ab initio* calculations of the bridged structure for C_2F_4I. (c,d) Comparison of experimental $\Delta sM(\infty\ ps;\ 5\ ps;\ s)$ and $\Delta f(\infty\ ps;\ 5\ ps;\ r)$ curves with theoretical curves obtained using the *ab initio* classical (*anti* and *gauche*) C_2F_4I structures.

Figure 5.4.13: Refinement of the C_2F_4I radical structure. (a,b) Comparison of experimental $\Delta sM(\infty;\ 5\ ps;\ s)$ (a) and $\Delta f(\infty;\ 5\ ps;\ r)$ (b) curves (solid lines) with corresponding theoretical curves (shaded lines) obtained from the least-squares refinement of the C_2F_4I structure (see text). The results are summarized in Table 1; the error correlation matrix is given in Table 2. Values for some of the major structural parameters (of the *anti* conformer) are indicated in the ball and stick model

of the radical.

Figure 5.4.14: Comparison of the *ab initio* molecular structures of the C_2F_4I and C_2H_4I radical intermediates.

Figure 5.4.15: Schematic of dihalide elimination reactions involving C_2R_4X radical intermediates. Once the parent molecule $C_2R_4X_2$ loses the first –X atom, the intermediate species C_2R_4X is formed. Two structural motifs for the C_2R_4X intermediate, namely the bridged and classical structures, have been discussed in the literature concerning stereochemical control in these reactions. In the case of the bridged structure (top brackets), the retention of stereochemical selectivity is clearly derived from the inhibition of rotation about the C-C bond (top product). However, in the case of the classical structure (bottom brackets), the situation is more complex. Rotation about the C-C bond is allowed, but the rate of rotation depends on the rotational barrier—the higher the barrier, the slower the rotation. If the time scale for the elimination of the second -X atom is much faster than the rotation, one can expect stereochemical selectivity (bottom product), whereas stereochemical control would be lost if the situation were reversed (middle product). With regard to the geometry of the radical site in the classical structure, simple rotation about the C-C bond (prior to the loss of the second –X atom) would suffice for the loss of stereochemical control for structures with planar radical centers (middle intermediate), whereas species with non-planar radical centers (bottom intermediate) may require a combination of rotation and inversion.

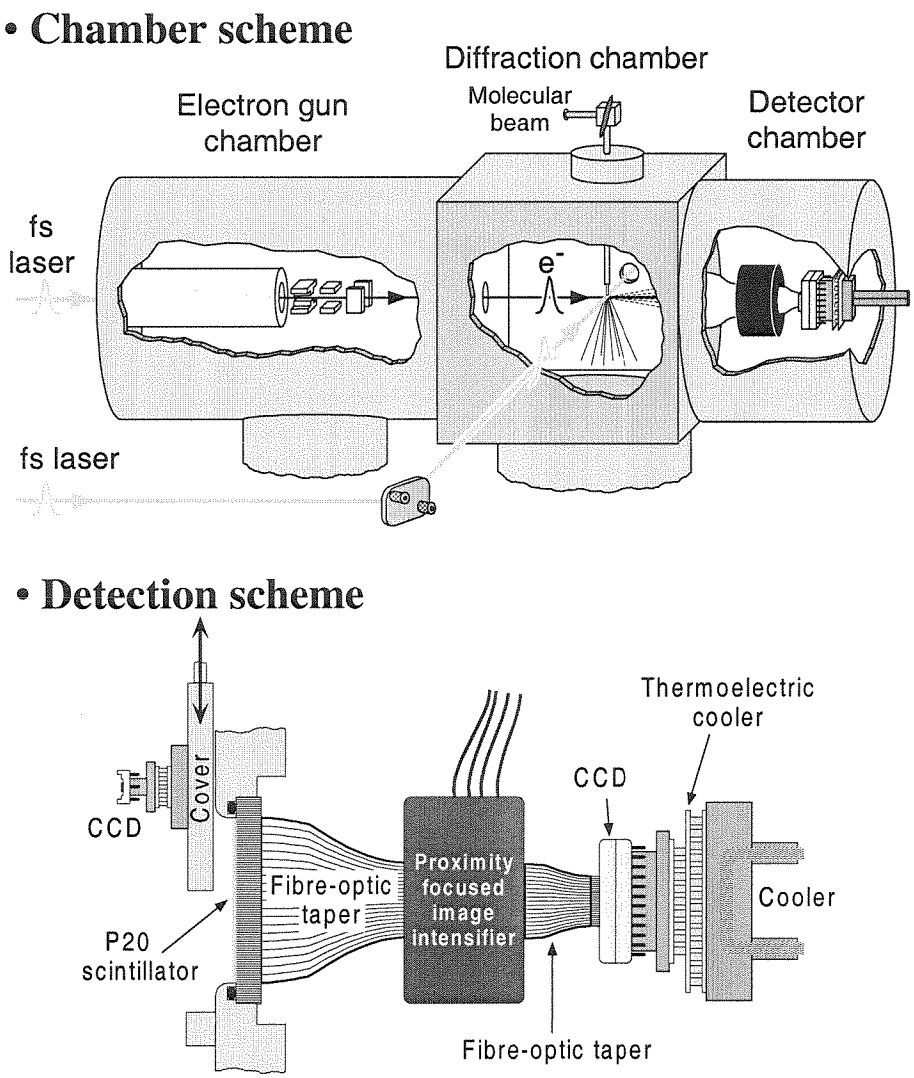
• Chamber scheme
Diffraction chamber
Electron gun chamber
Molecular beam
Detector chamber
fs laser
e⁻
fs laser
• Detection scheme
Thermoelectric cooler
CCD
Cover
CCD
Fibre-optic taper
Proximity focused image intensifier
Cooler
P20 scintillator
Fibre-optic taper

Figure 5.1.1

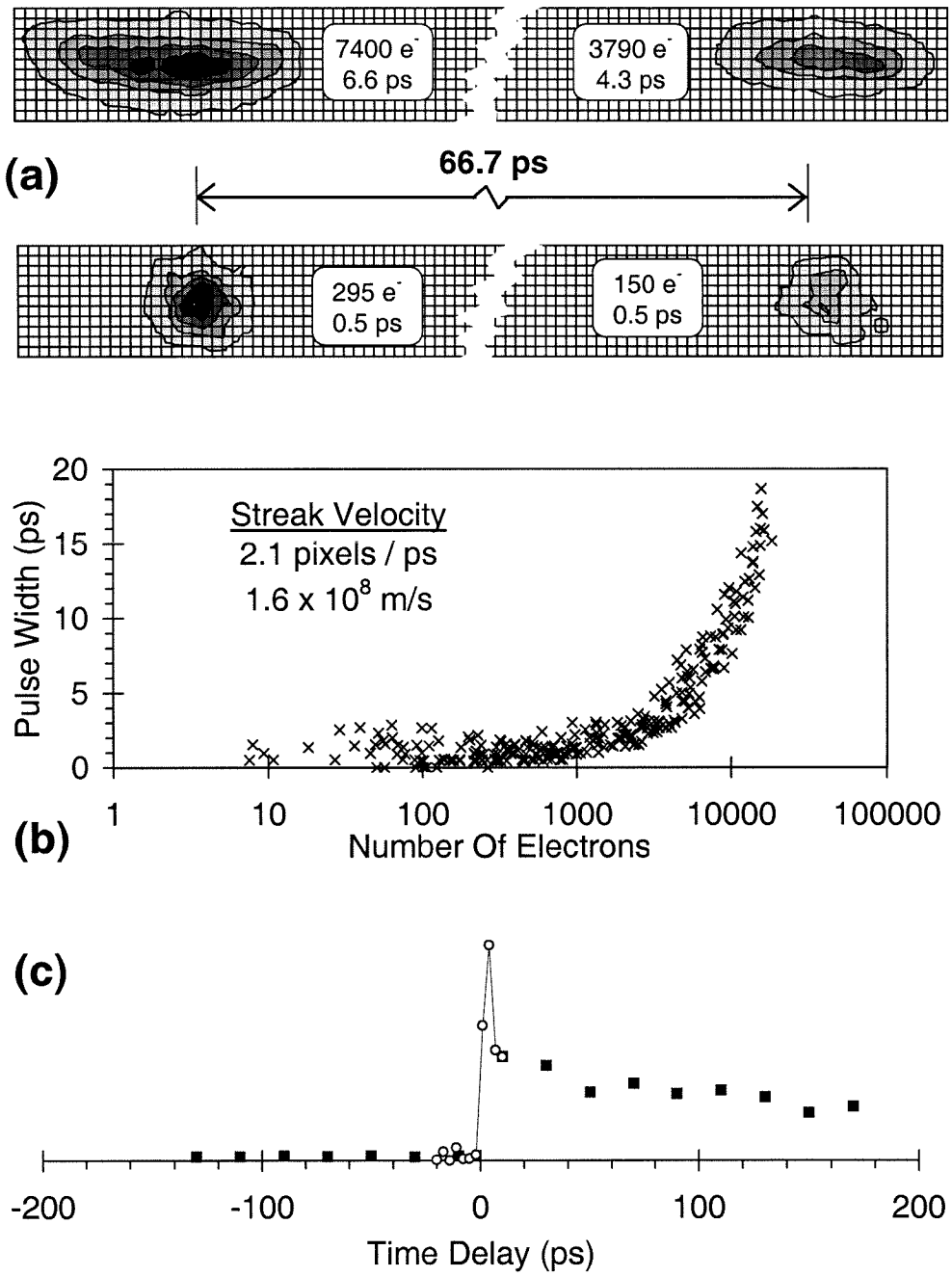
7400 e⁻
6.6 ps
3790 e⁻
4.3 ps
(a)
66.7 ps
295 e⁻
0.5 ps
150 e⁻
0.5 ps
Streak Velocity
2.1 pixels / ps
1.6 x 10⁸ m/s
Pulse Width (ps)
20
15
10
5
0
1
10
100
1000
10000
100000
Number Of Electrons
(b)
(c)
-200
-100
0
100
200
Time Delay (ps)

Figure 5.1.2

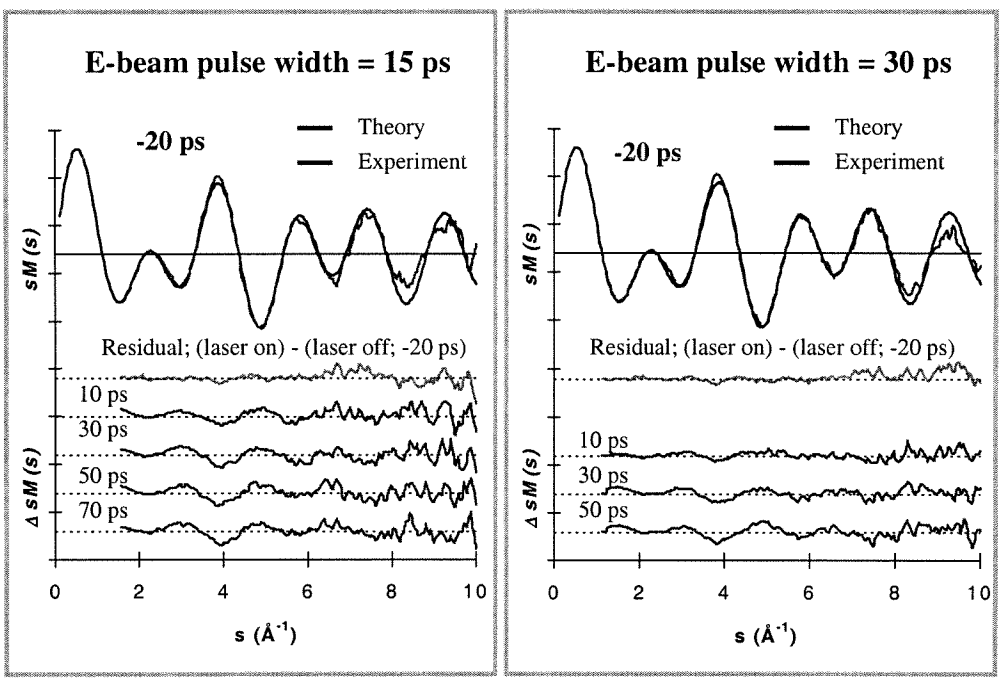
E-beam pulse width = 15 ps
-20 ps
Theory
Experiment
sM (s)
Residual; (laser on) - (laser off; -20 ps)
10 ps
30 ps
50 ps
70 ps
Δ sM (s)
0
2
4
6
8
10
s (Å-1)
E-beam pulse width = 30 ps
-20 ps
Theory
Experiment
sM (s)
Residual; (laser on) - (laser off; -20 ps)
10 ps
30 ps
50 ps
Δ sM (s)
0
2
4
6
8
10
s (Å-1)

Figure 5.1.3

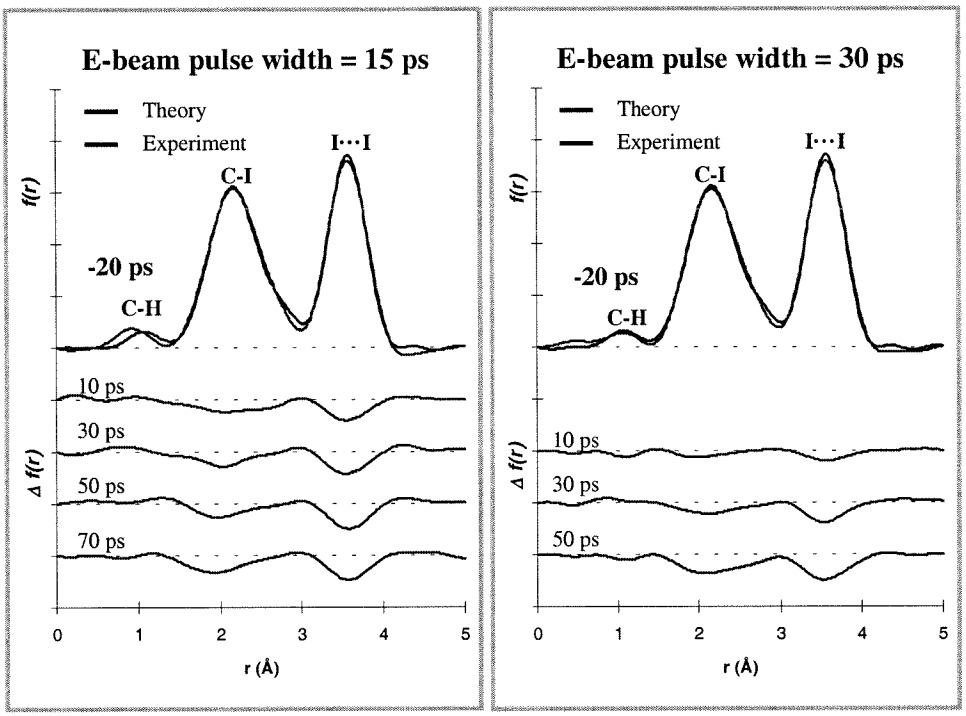
E-beam pulse width = 15 ps
Theory
Experiment
I···I
C-I
f(r)
-20 ps
C-H
10 ps
30 ps
50 ps
70 ps
Δ f(r)
0
1
2
3
4
5
r (Å)
E-beam pulse width = 30 ps
Theory
Experiment
I···I
C-I
f(r)
-20 ps
C-H
10 ps
30 ps
50 ps
Δ f(r)
0
1
2
3
4
5
r (Å)

Figure 5.1.4

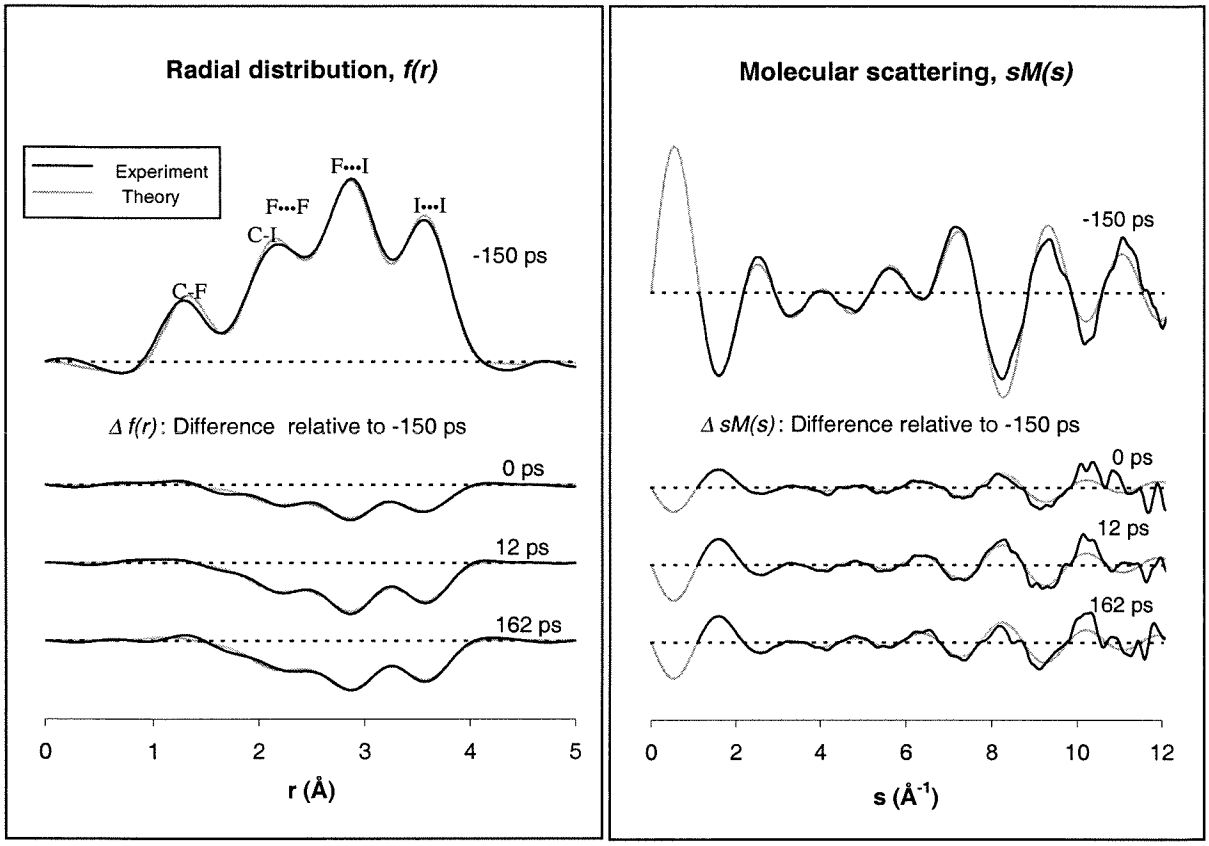
Radial distribution, f(r)
Experiment
Theory
C-F
C-I
F•••F
F•••I
I•••I
-150 ps
Δ f(r): Difference relative to -150 ps
0 ps
12 ps
162 ps
0
1
2
3
4
5
r (Å)
Molecular scattering, sM(s)
-150 ps
Δ sM(s): Difference relative to -150 ps
0 ps
12 ps
162 ps
0
2
4
6
8
10
12
s (Å-1)

Figure 5.2.1

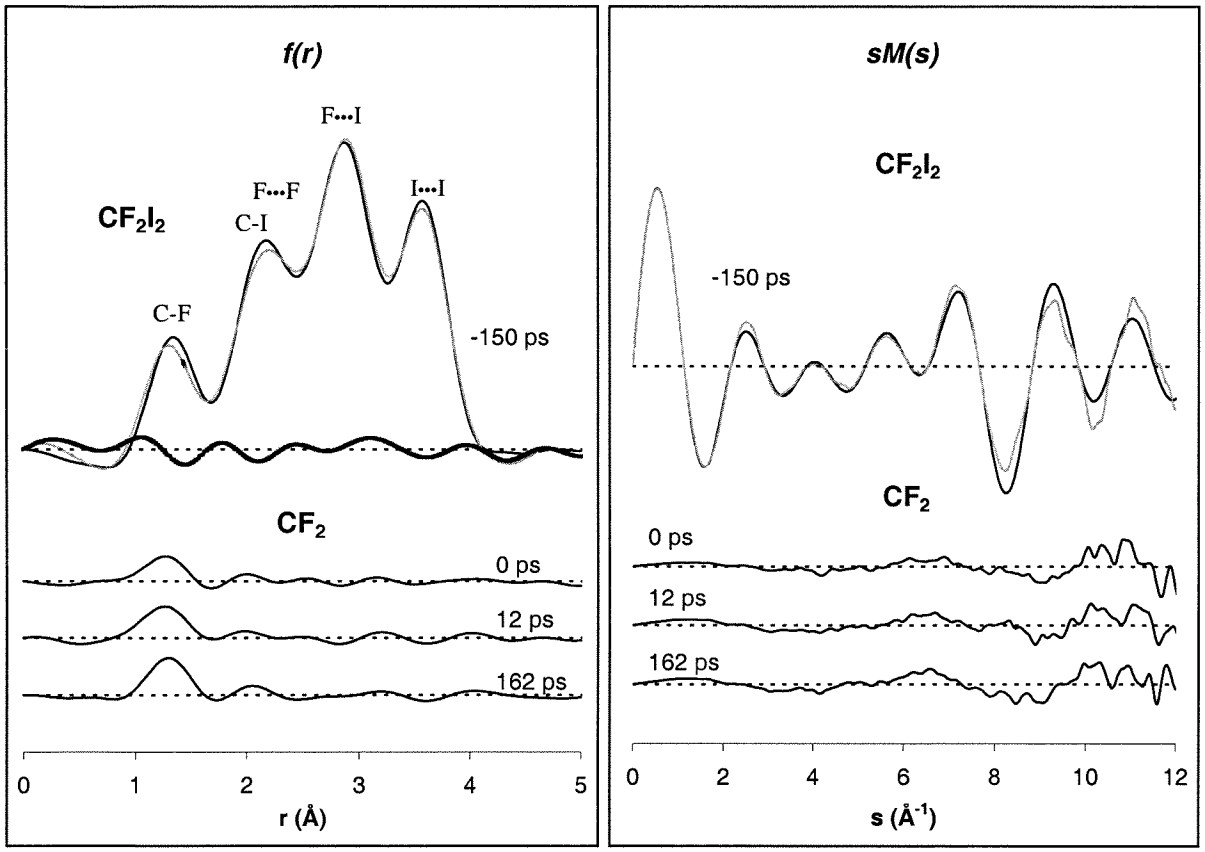
f(r)
F···I
F···F
I···I
C-I
C-F
CF2I2
-150 ps
CF2
0 ps
12 ps
162 ps
0
1
2
3
4
5
r (Å)
sM(s)
CF2I2
-150 ps
CF2
0 ps
12 ps
162 ps
0
2
4
6
8
10
12
s (Å-1)

Figure 5.2.2

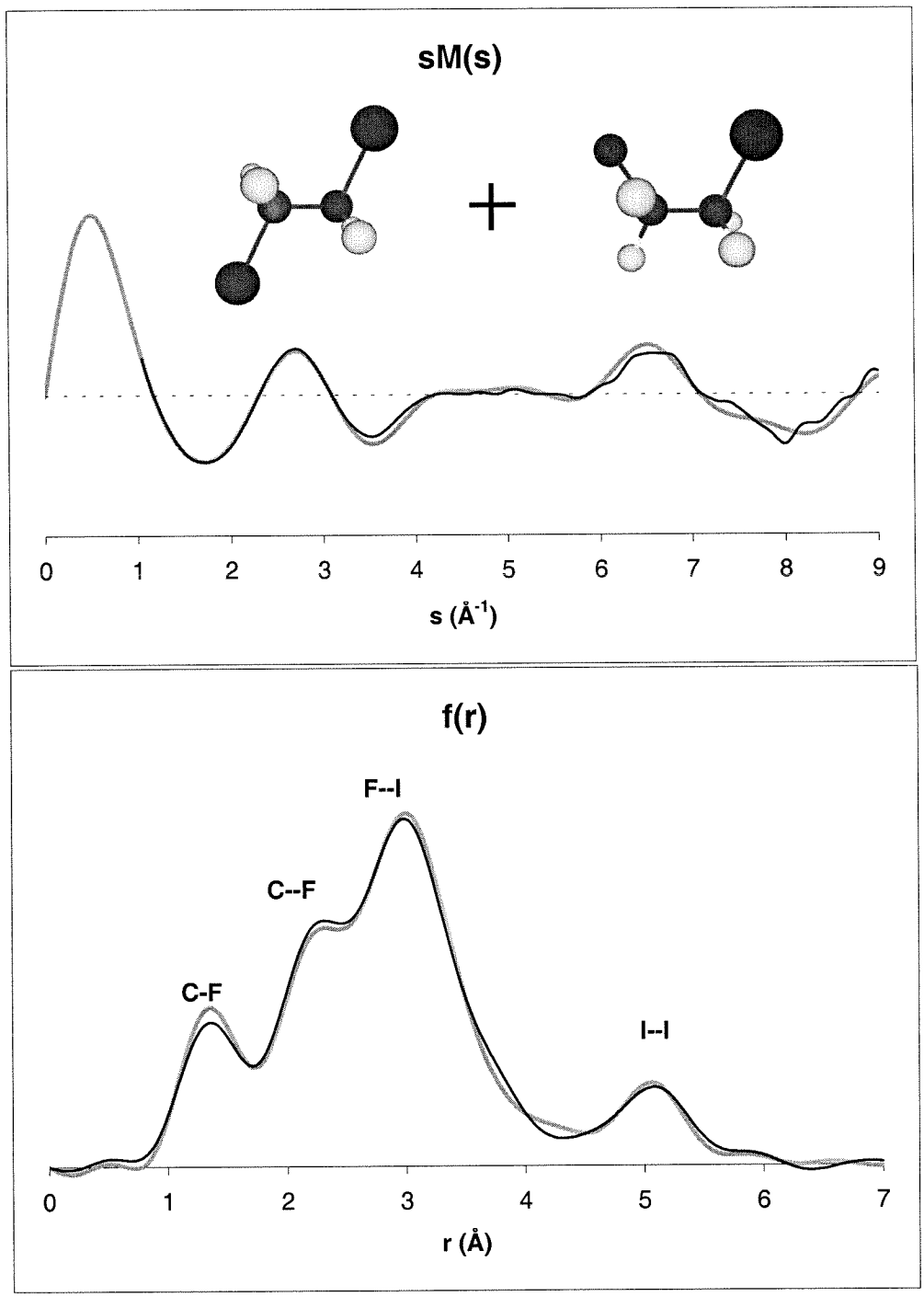

Figure 5.3.1

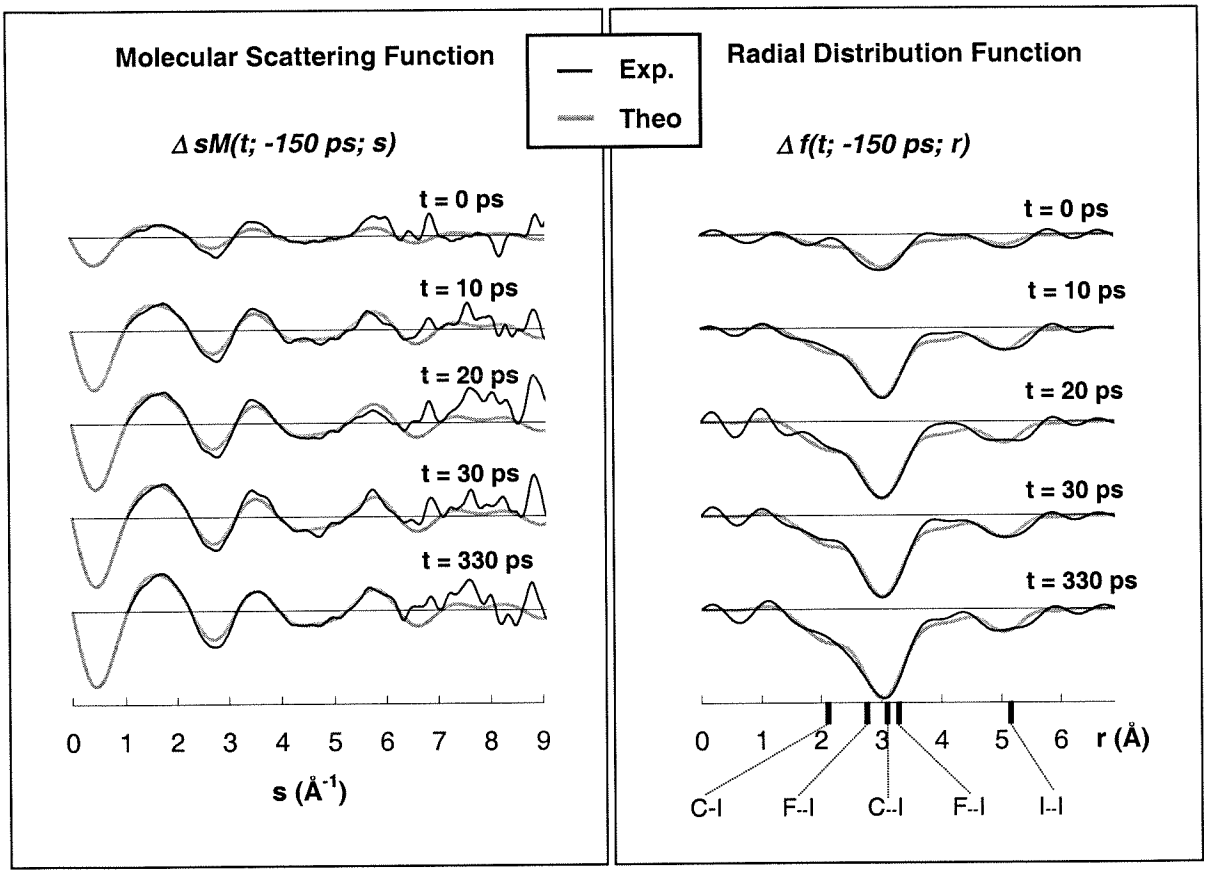
Molecular Scattering Function
Δ sM(t; -150 ps; s)
Exp.
Theo
Radial Distribution Function
Δ f(t; -150 ps; r)
t = 0 ps
t = 10 ps
t = 20 ps
t = 30 ps
t = 330 ps
0 1 2 3 4 5 6 7 8 9
s (Å-1)
0 1 2 3 4 5 6 r (Å)
C-I
F--I
C--I
F--I
I--I

Figure 5.3.2

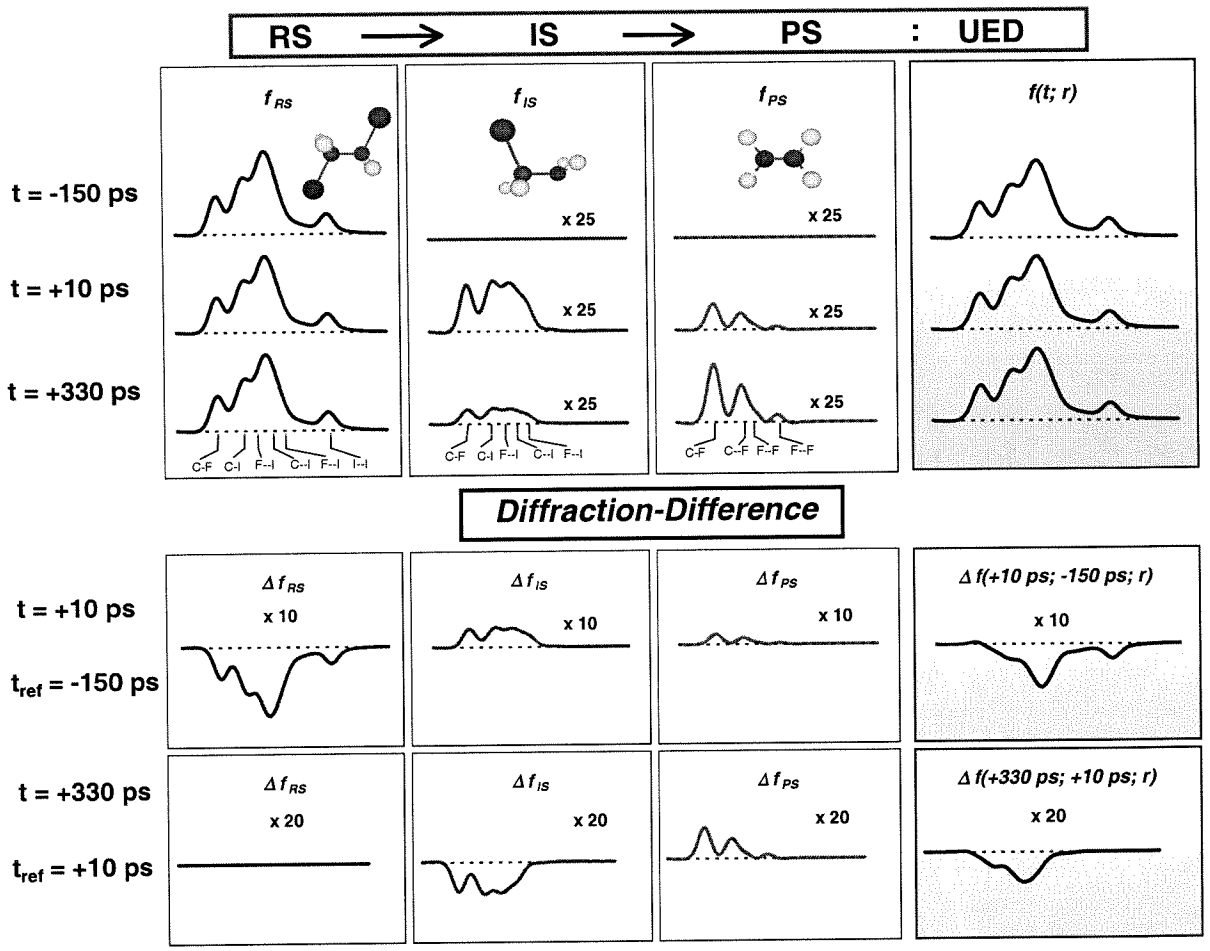
RS → IS → PS : UED
f_{RS}
f_{IS}
f_{PS}
f(t; r)
t = -150 ps
t = +10 ps
t = +330 ps
x 25
C-F C-I F--I C--I F--I I--I
C-F C-I F--I C--I F--I
C-F C--F F--F F--F
Diffraction-Difference
Δf_{RS}
Δf_{IS}
Δf_{PS}
Δf(+10 ps; -150 ps; r)
x 10
t = +10 ps
t_{ref} = -150 ps
Δf(+330 ps; +10 ps; r)
x 20
t = +330 ps
t_{ref} = +10 ps

Figure 5.3.3

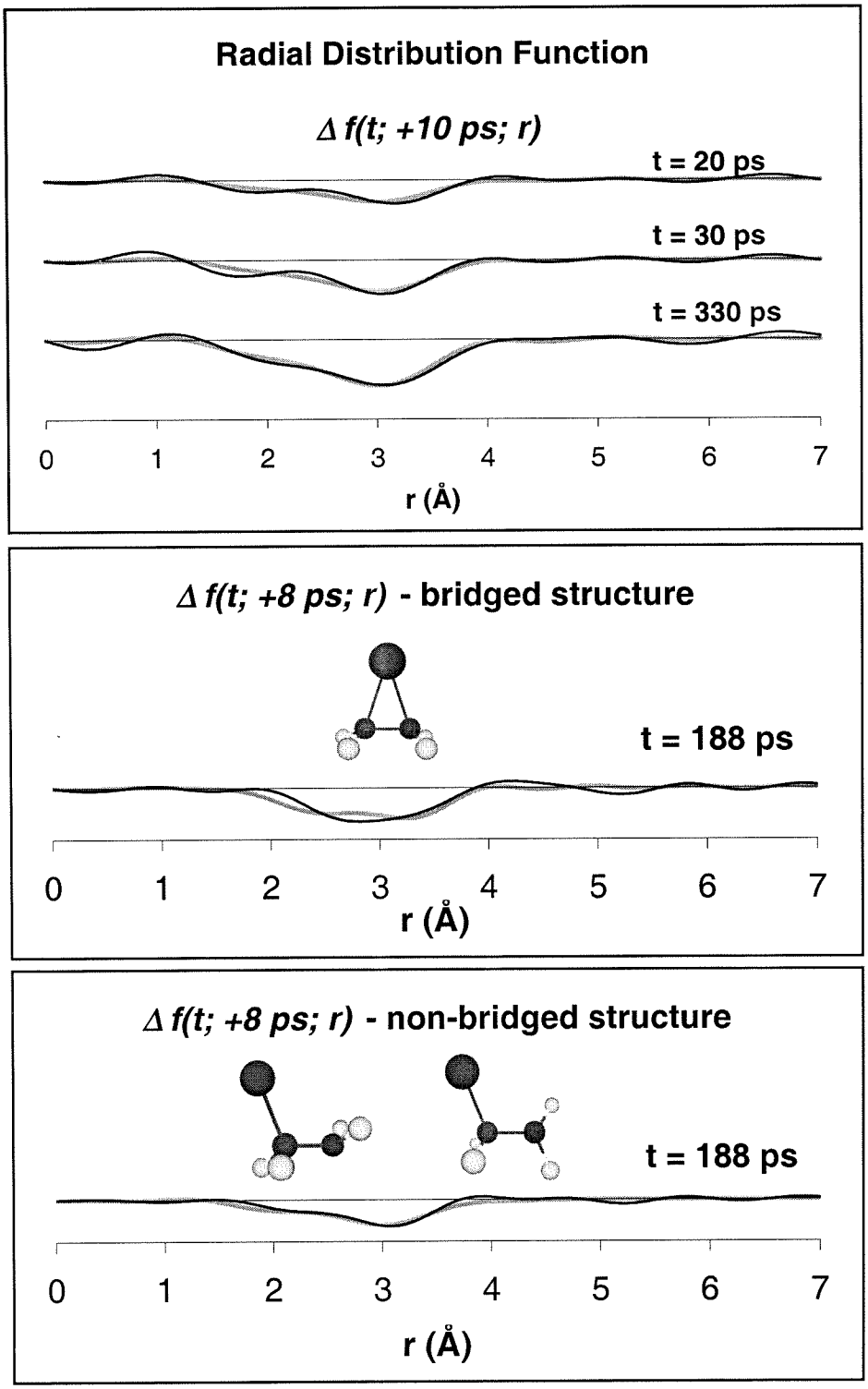
Radial Distribution Function
Δ f(t; +10 ps; r)
t = 20 ps
t = 30 ps
t = 330 ps
0 1 2 3 4 5 6 7
r (Å)
Δ f(t; +8 ps; r) - bridged structure
t = 188 ps
0 1 2 3 4 5 6 7
r (Å)
Δ f(t; +8 ps; r) - non-bridged structure
t = 188 ps
0 1 2 3 4 5 6 7
r (Å)

Figure 5.3.4

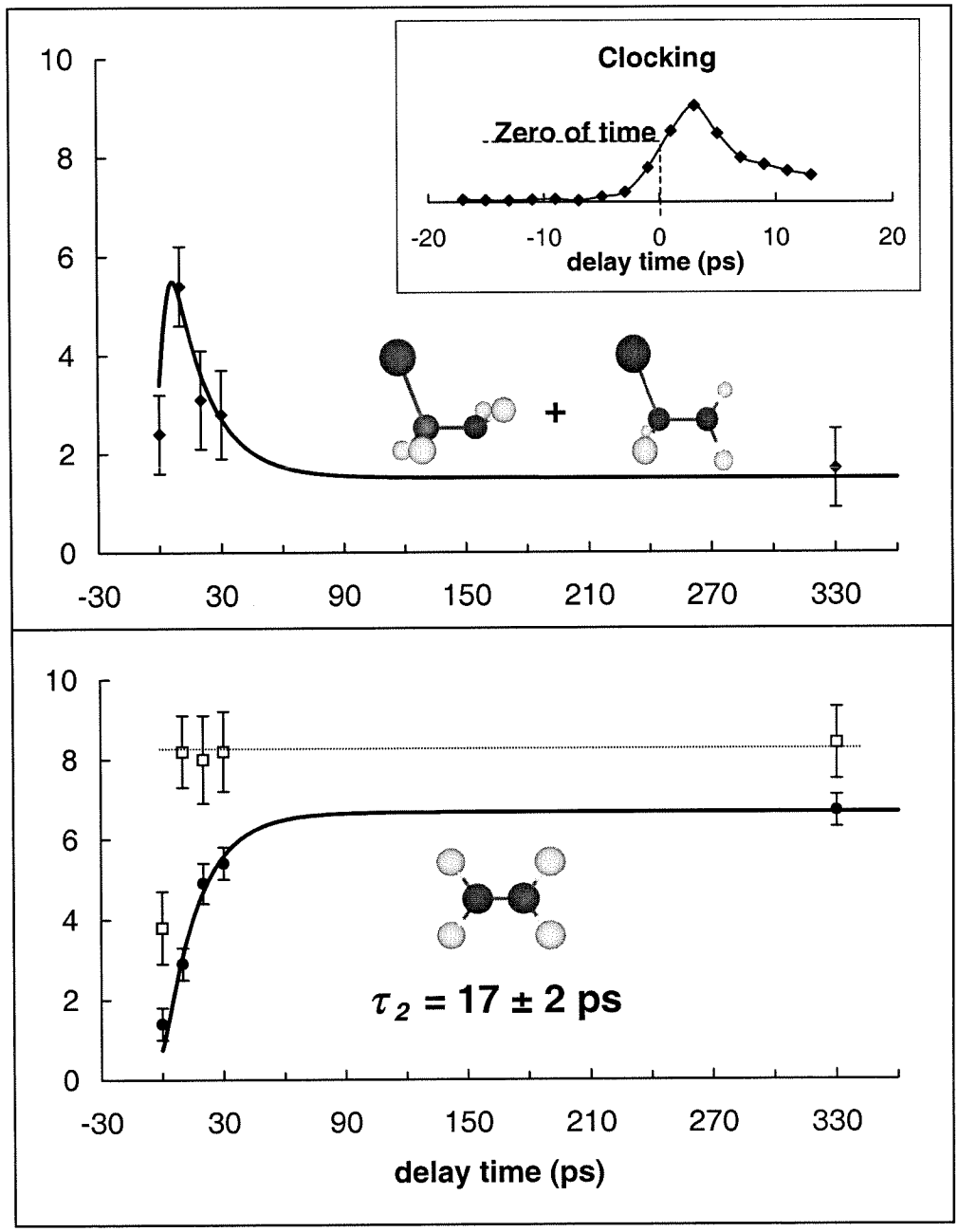
Clocking
Zero of time
-20
-10
0
10
20
delay time (ps)
10
8
6
4
2
0
-30
30
90
150
210
270
330
+
τ_2 = 17 ± 2 ps
delay time (ps)

Figure 5.3.5

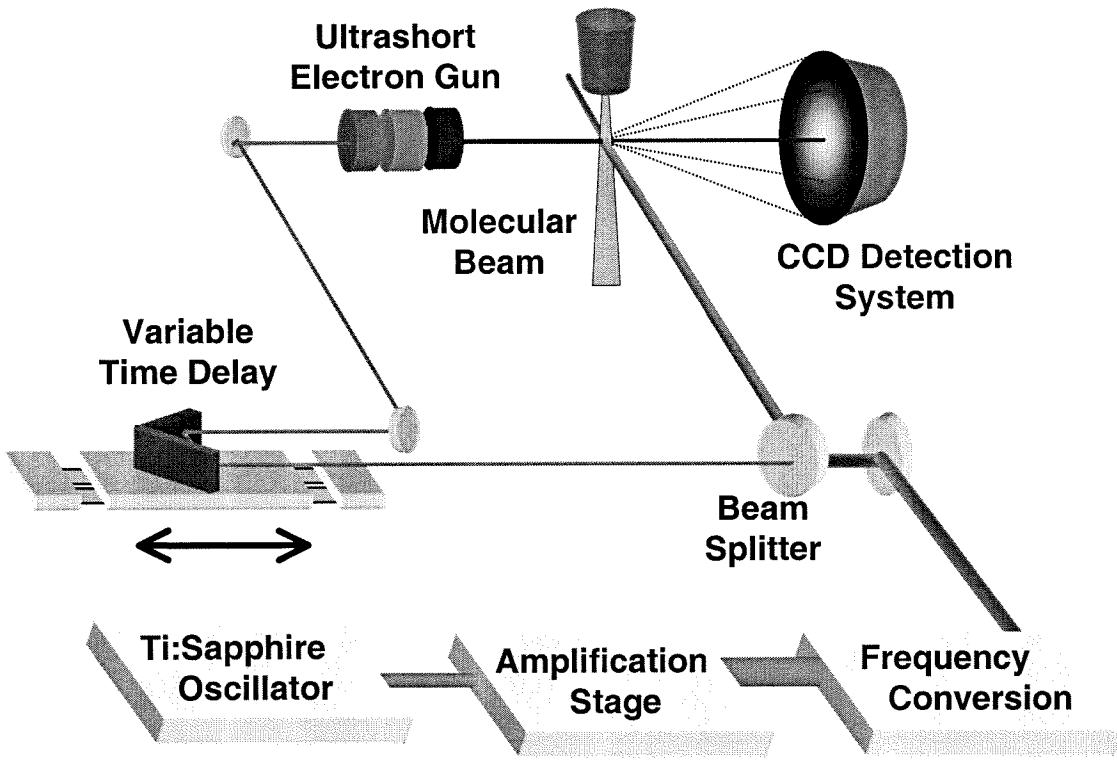
Ultrashort
Electron Gun
Molecular
Beam
CCD Detection
System
Variable
Time Delay
Beam
Splitter
Ti:Sapphire
Oscillator
Amplification
Stage
Frequency
Conversion

Figure 5.4.1

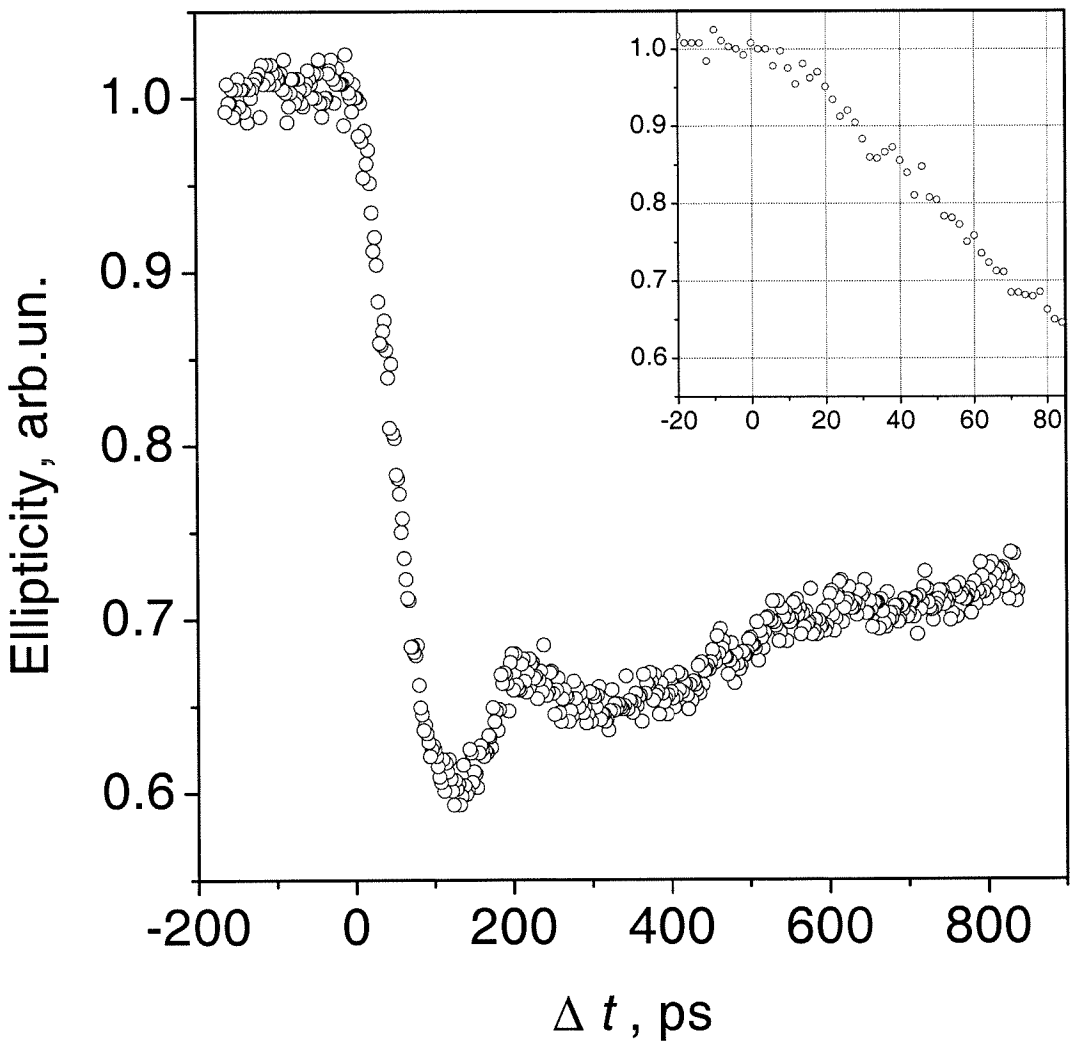
Ellipticity, arb.un.
1.0
0.9
0.8
0.7
0.6
-200
0
200
400
600
800
Δ t , ps
1.0
0.9
0.8
0.7
0.6
-20
0
20
40
60
80

Figure 5.4.2

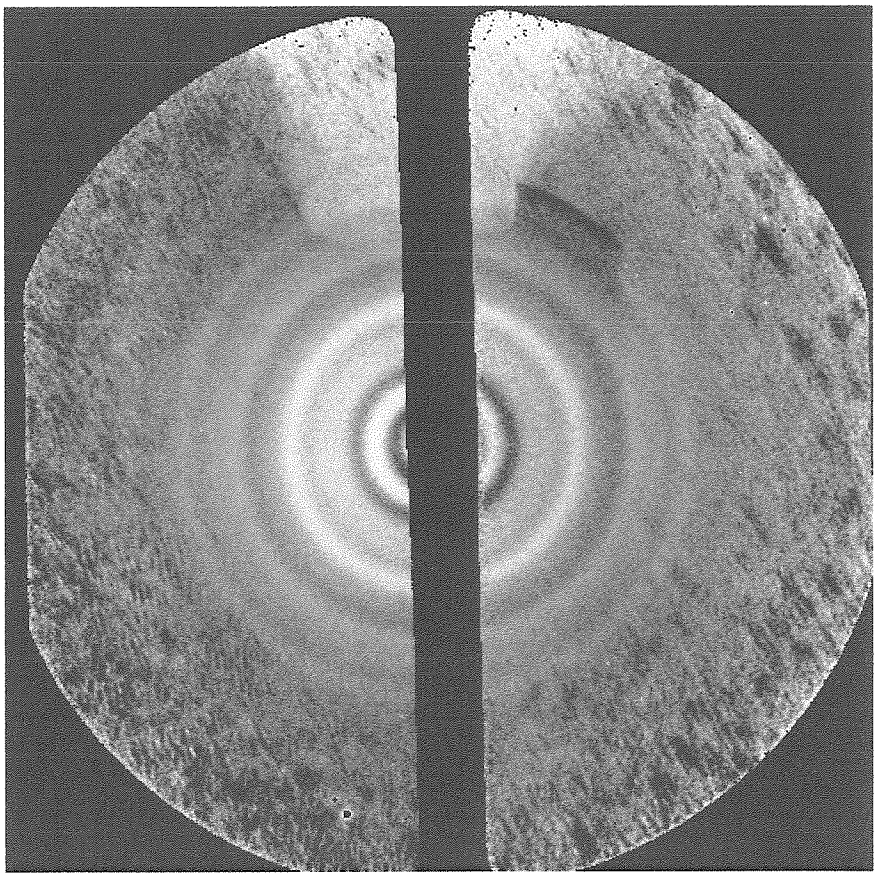

Figure 5.4.3

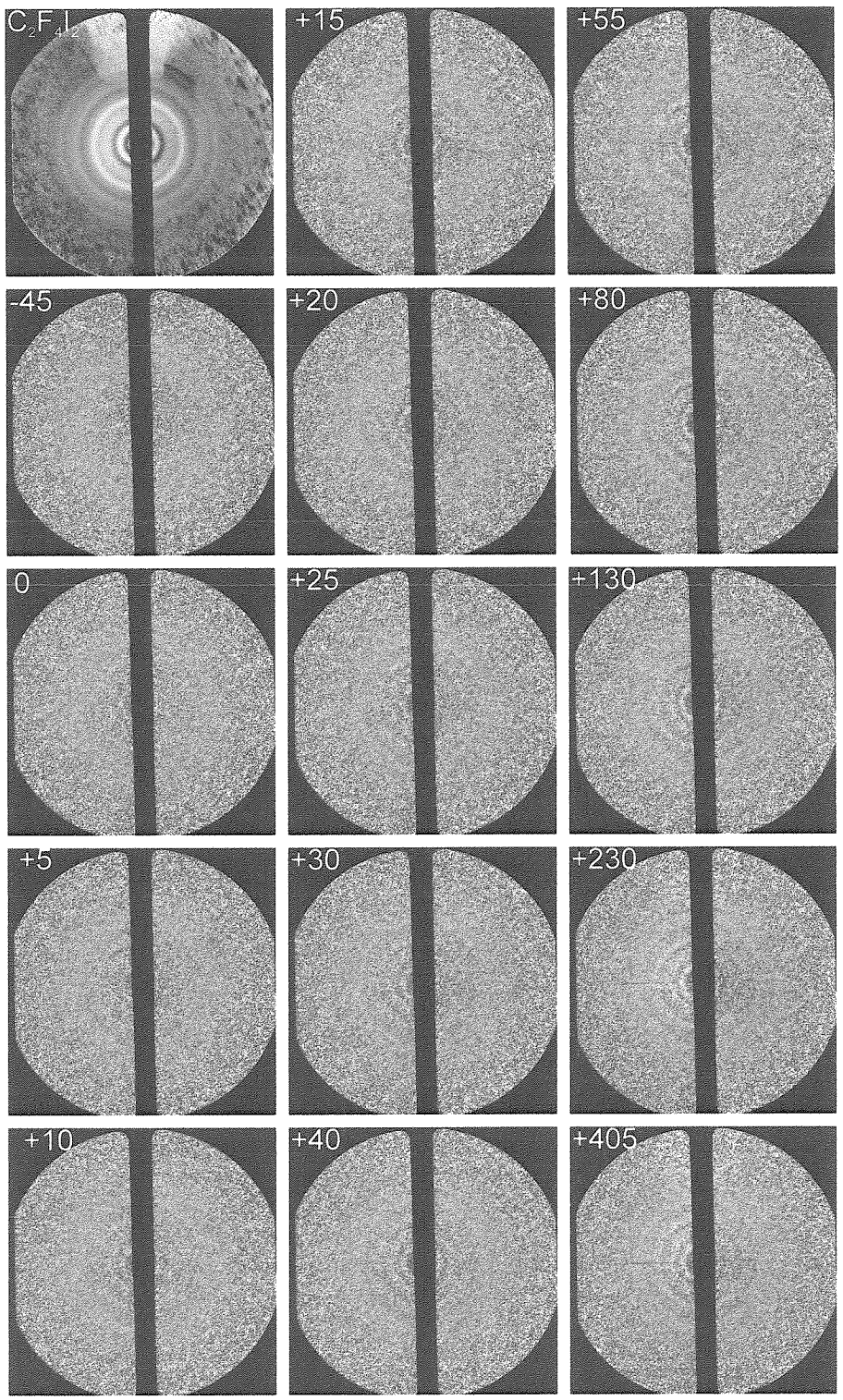

Figure 5.4.4

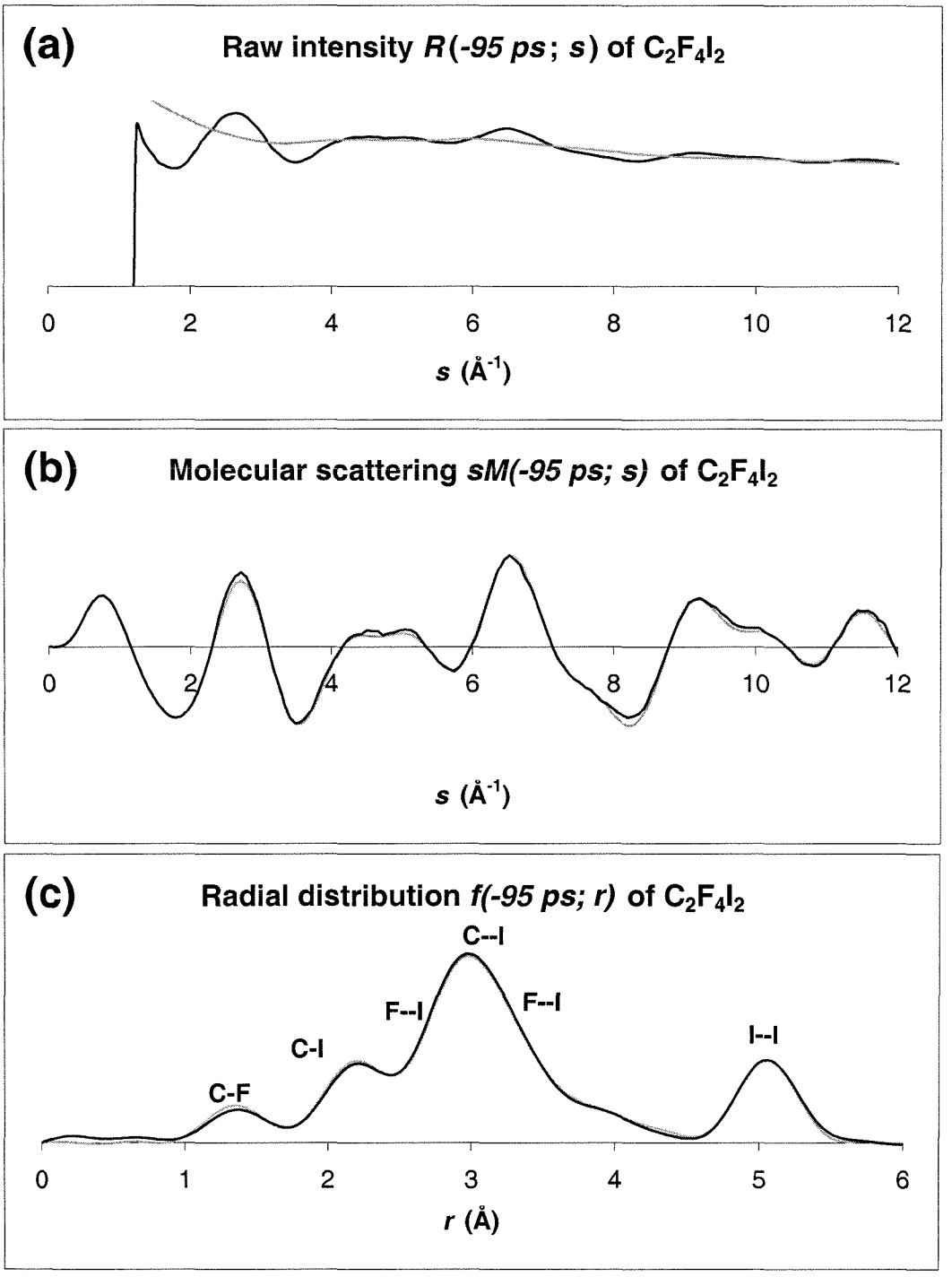
(a)
Raw intensity R(-95 ps; s) of C2F4I2
0
2
4
6
8
10
12
s (Å-1)
(b)
Molecular scattering sM(-95 ps; s) of C2F4I2
0
2
4
6
8
10
12
s (Å-1)
(c)
Radial distribution f(-95 ps; r) of C2F4I2
C--I
F--I
F--I
C-I
C-F
I--I
0
1
2
3
4
5
6
r (Å)

Figure 5.4.5

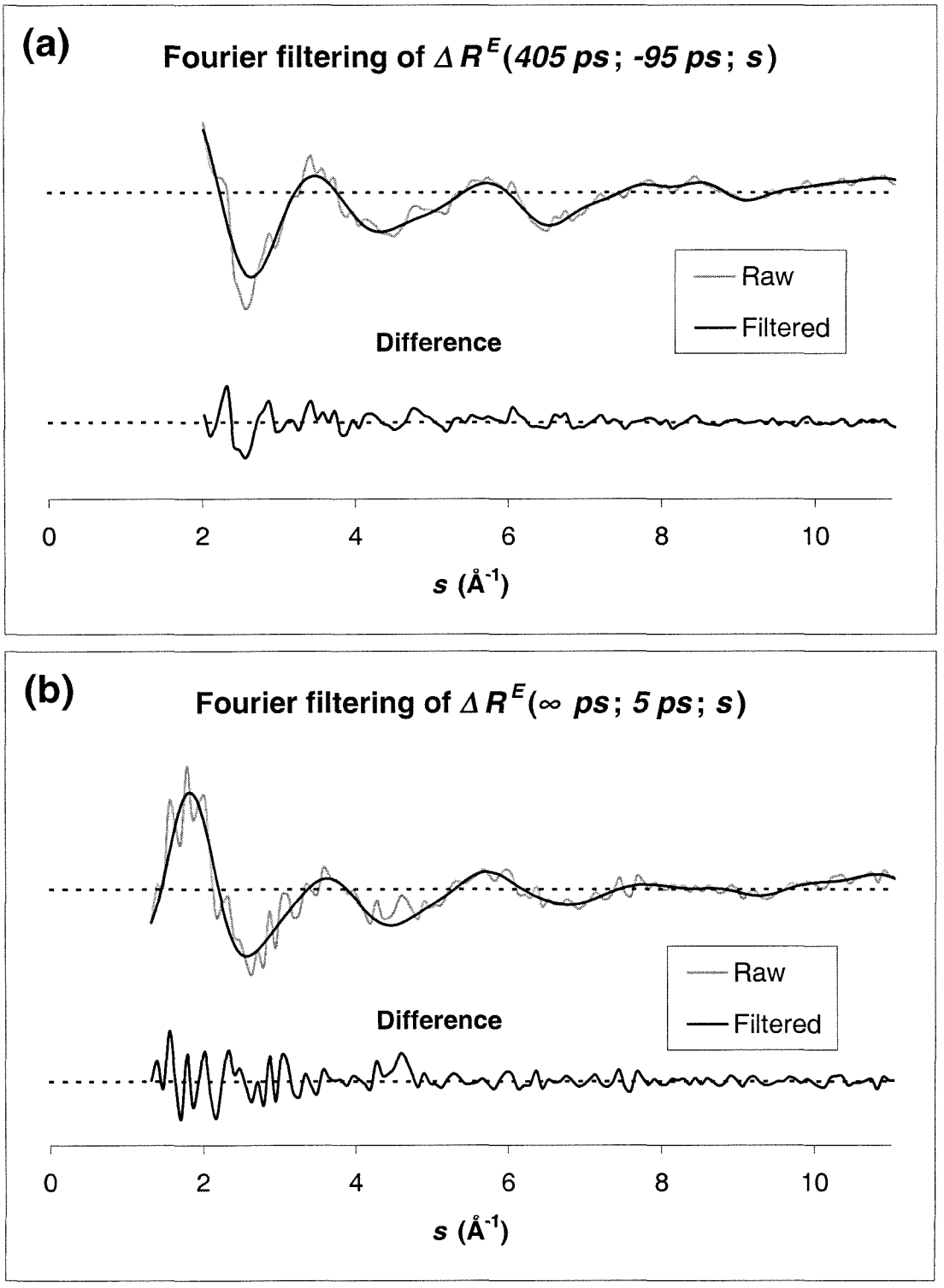
(a)
Fourier filtering of $\Delta R^E(405\ ps; -95\ ps; s)$
Raw
Filtered
Difference
0
2
4
6
8
10
s (Å^{-1})
(b)
Fourier filtering of $\Delta R^E(\infty\ ps; 5\ ps; s)$
Raw
Filtered
Difference
0
2
4
6
8
10
s (Å^{-1})

Figure 5.4.6

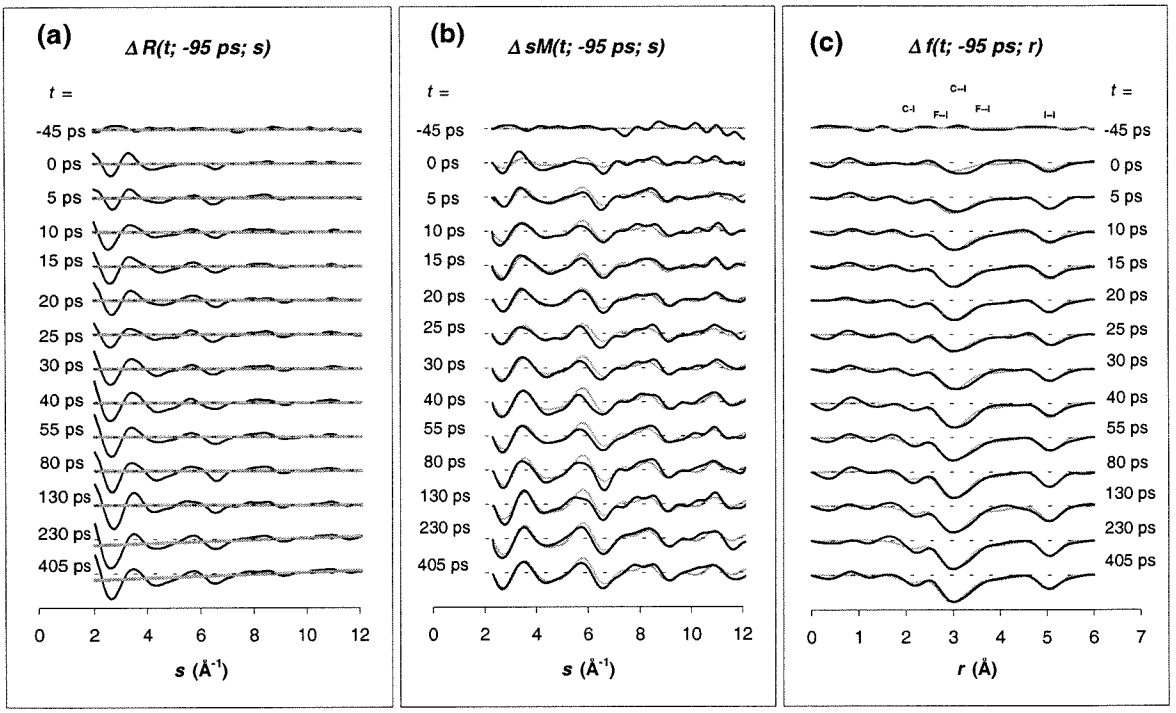
(a)
Δ R(t; -95 ps; s)
t =
-45 ps
0 ps
5 ps
10 ps
15 ps
20 ps
25 ps
30 ps
40 ps
55 ps
80 ps
130 ps
230 ps
405 ps
0 2 4 6 8 10 12
s (Å-1)
(b)
Δ sM(t; -95 ps; s)
t =
-45 ps
0 ps
5 ps
10 ps
15 ps
20 ps
25 ps
30 ps
40 ps
55 ps
80 ps
130 ps
230 ps
405 ps
0 2 4 6 8 10 12
s (Å-1)
(c)
Δ f(t; -95 ps; r)
C–I
C-I
F–I
F-I
I–I
t =
-45 ps
0 ps
5 ps
10 ps
15 ps
20 ps
25 ps
30 ps
40 ps
55 ps
80 ps
130 ps
230 ps
405 ps
0 1 2 3 4 5 6 7
r (Å)

Figure 5.4.7

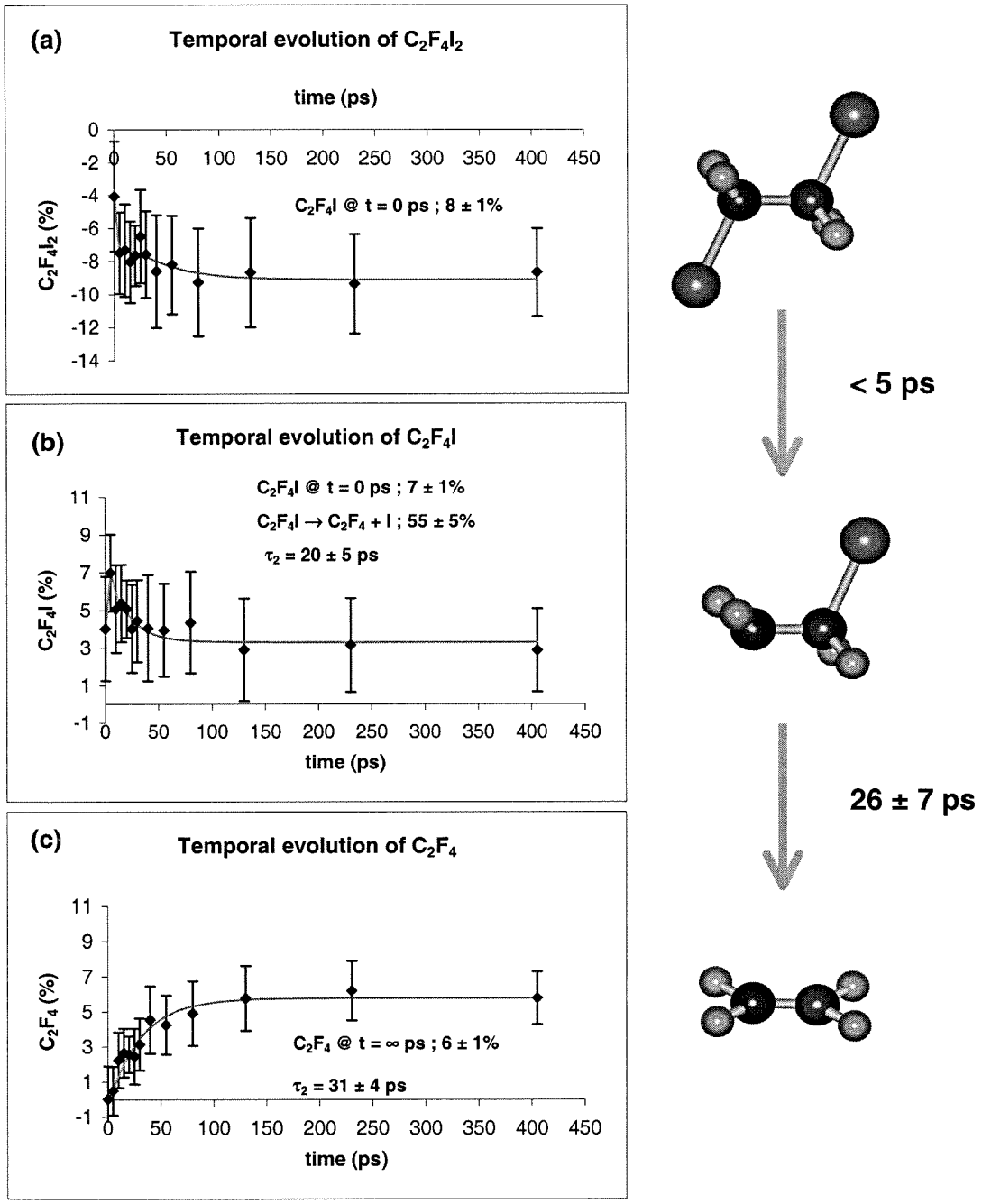
(a)
Temporal evolution of $C_2F_4I_2$
time (ps)
$C_2F_4I_2$ (%)
C_2F_4I @ t = 0 ps ; 8 ± 1%
(b)
Temporal evolution of C_2F_4I
C_2F_4I @ t = 0 ps ; 7 ± 1%
$C_2F_4I \rightarrow C_2F_4 + I$; 55 ± 5%
τ_2 = 20 ± 5 ps
C_2F_4I (%)
time (ps)
(c)
Temporal evolution of C_2F_4
C_2F_4 (%)
C_2F_4 @ t = ∞ ps ; 6 ± 1%
τ_2 = 31 ± 4 ps
time (ps)
< 5 ps
26 ± 7 ps

Figure 5.4.8

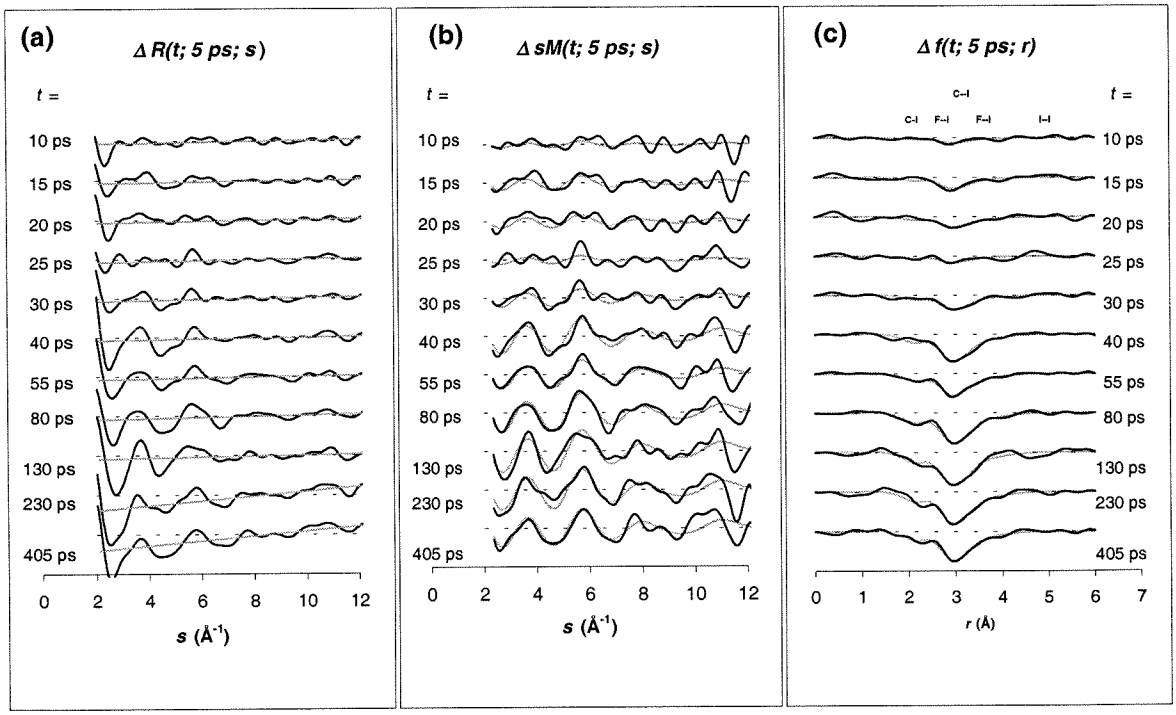
(a)
Δ R(t; 5 ps; s)
t =
10 ps
15 ps
20 ps
25 ps
30 ps
40 ps
55 ps
80 ps
130 ps
230 ps
405 ps
0 2 4 6 8 10 12
s (Å-1)
(b)
Δ sM(t; 5 ps; s)
t =
10 ps
15 ps
20 ps
25 ps
30 ps
40 ps
55 ps
80 ps
130 ps
230 ps
405 ps
0 2 4 6 8 10 12
s (Å-1)
(c)
Δ f(t; 5 ps; r)
C–I
C-I F–I F–I I–I
t =
10 ps
15 ps
20 ps
25 ps
30 ps
40 ps
55 ps
80 ps
130 ps
230 ps
405 ps
0 1 2 3 4 5 6 7
r (Å)

Figure 5.4.9

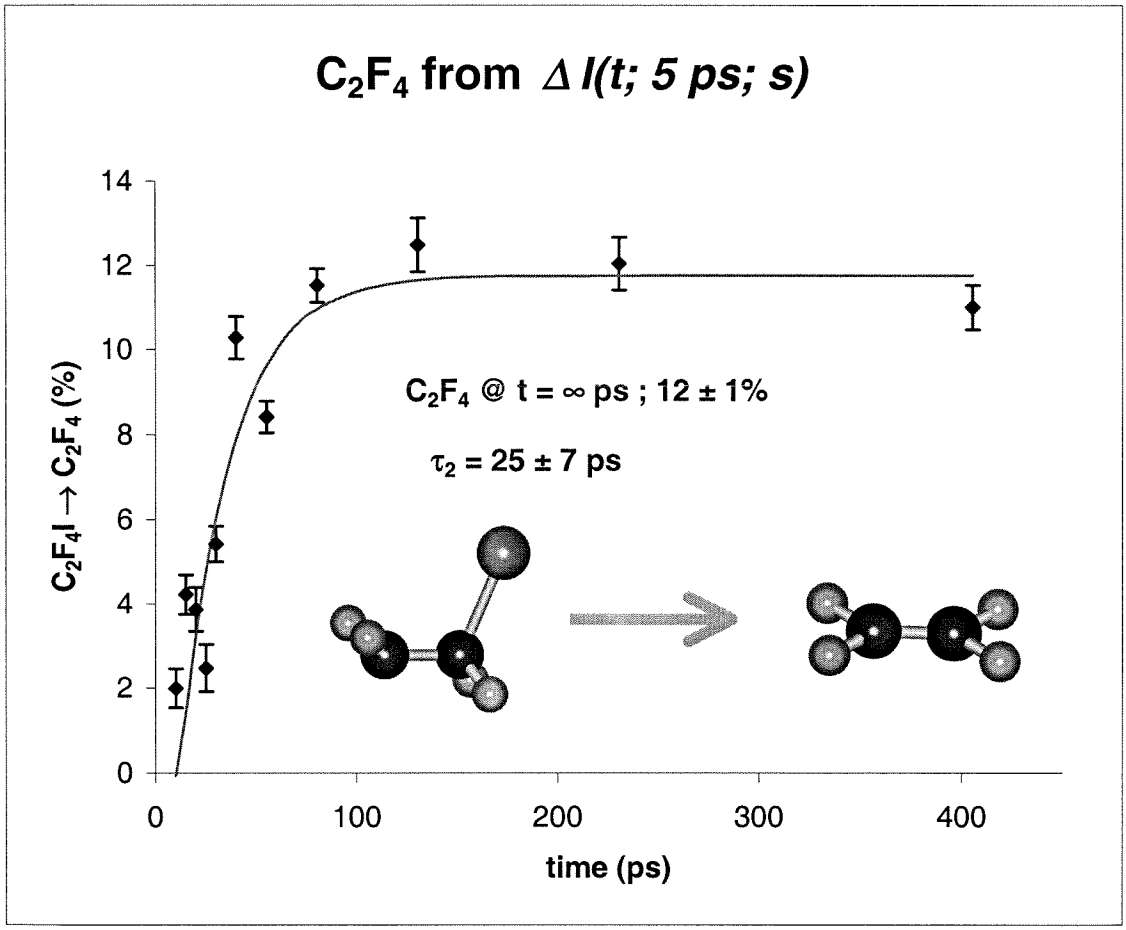
C2F4 from Δ I(t; 5 ps; s)
C2F4 @ t = ∞ ps ; 12 ± 1%
τ2 = 25 ± 7 ps
C2F4I → C2F4 (%)
time (ps)
0
2
4
6
8
10
12
14
0
100
200
300
400

Figure 5.4.10

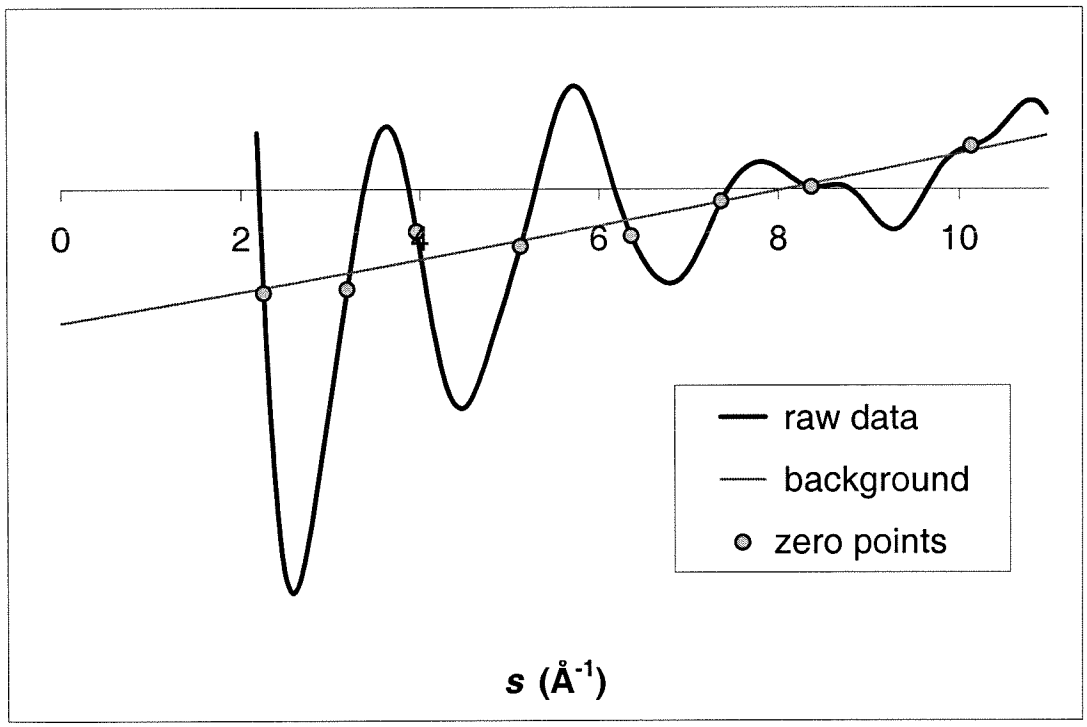

Figure 5.4.11

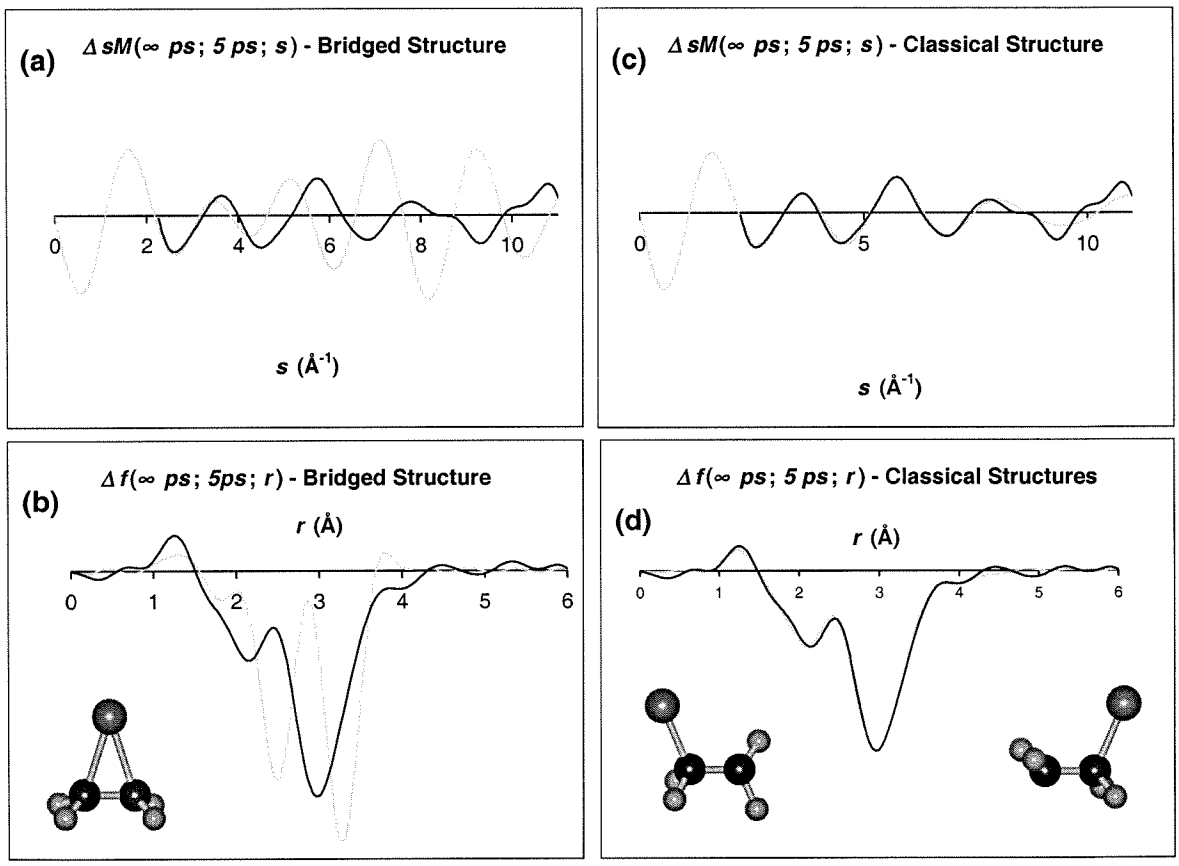
(a)
ΔsM(∞ ps; 5 ps; s) - Bridged Structure
0
2
4
6
8
10
s (Å-1)
(c)
ΔsM(∞ ps; 5 ps; s) - Classical Structure
0
5
10
s (Å-1)
(b)
Δf(∞ ps; 5ps; r) - Bridged Structure
r (Å)
0
1
2
3
4
5
6
(d)
Δf(∞ ps; 5 ps; r) - Classical Structures
r (Å)
0
1
2
3
4
5
6

Figure 5.4.12

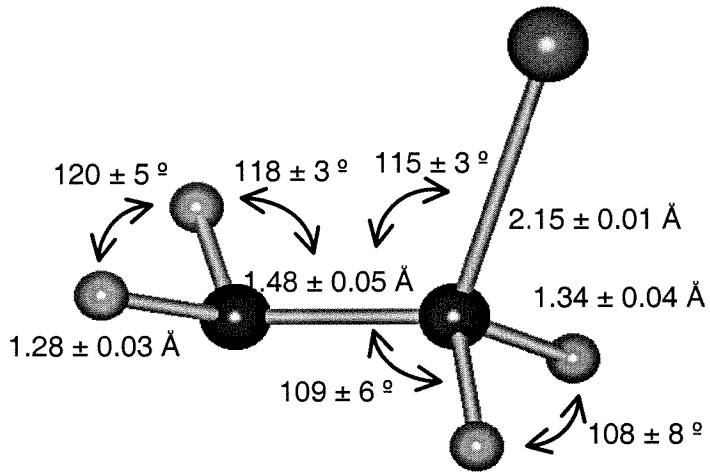
120 ± 5 º
118 ± 3 º
115 ± 3 º
2.15 ± 0.01 Å
1.48 ± 0.05 Å
1.34 ± 0.04 Å
1.28 ± 0.03 Å
109 ± 6 º
108 ± 8 º

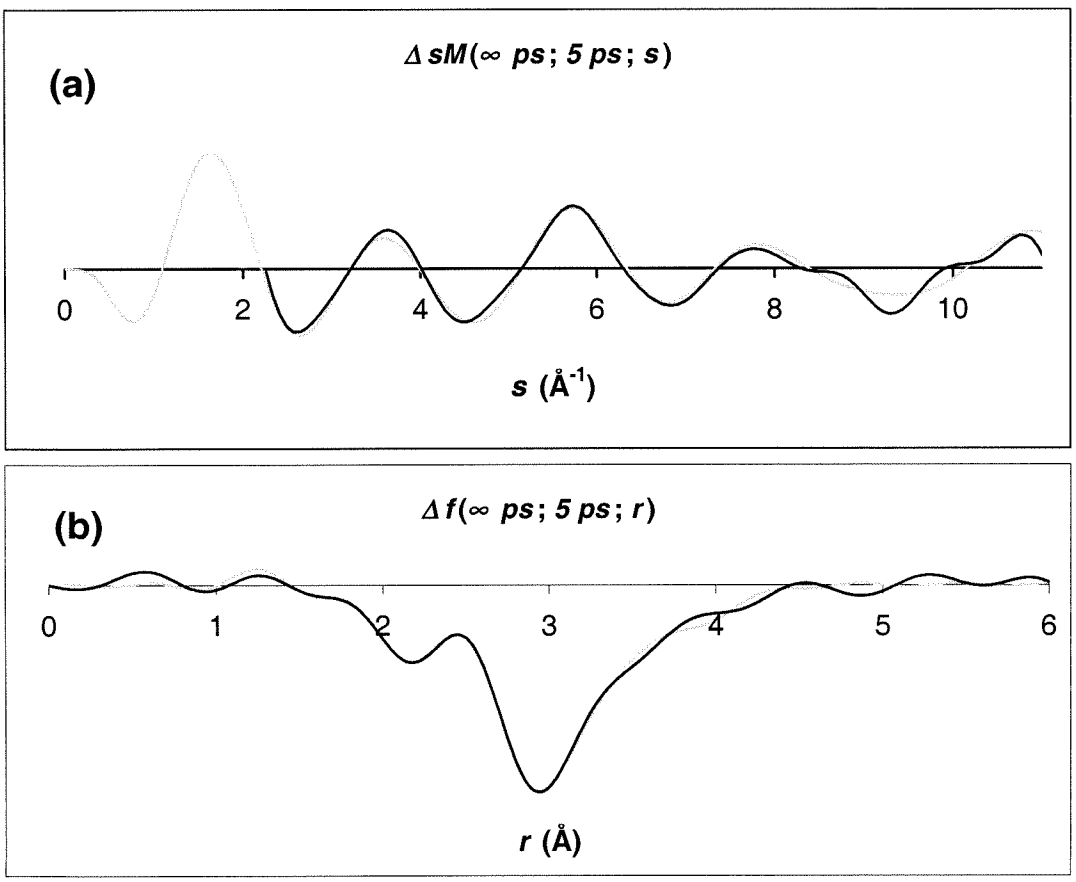
(a)
Δ sM(∞ ps; 5 ps; s)
0
2
4
6
8
10
s (Å-1)
(b)
Δ f(∞ ps; 5 ps; r)
0
1
2
3
4
5
6
r (Å)

Figure 5.4.13

CF_2ICF_2• radical

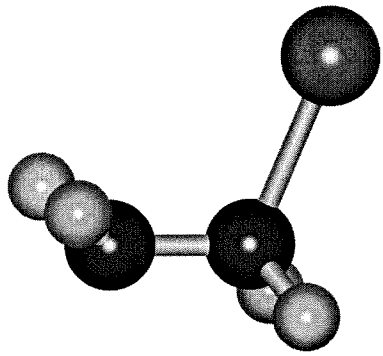

CH_2ICH_2• radical

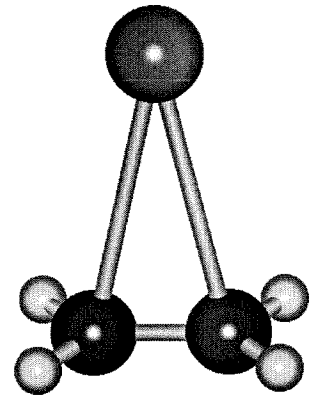

Figure 5.4.14

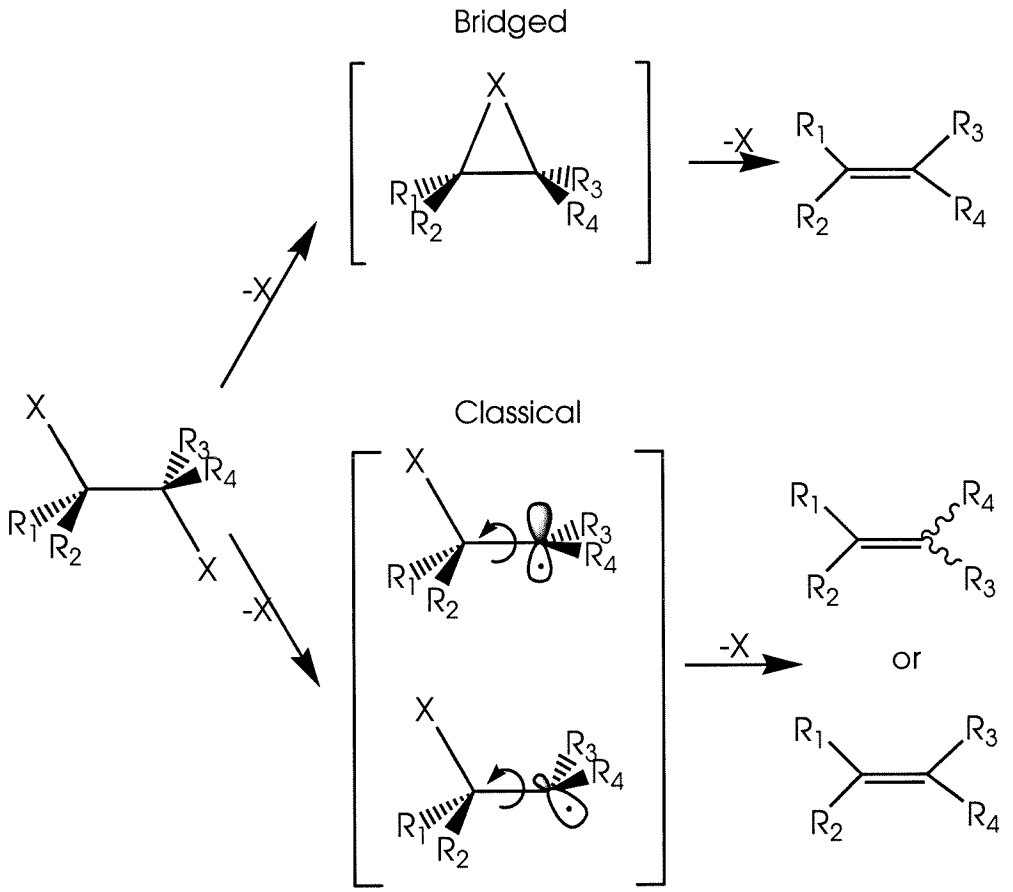

Figure 5.4.15

CHAPTER SIX

APPLICATIONS TO HYDROCARBONS

6.1 CHD → HT @ 267 nm

6.1.1 Background

A) General interest in the CHD reaction

Certainly, the 1,3-cyclohexadiene (CHD) → hexatriene (HT) reaction is interesting to the UED group for a variety of reasons. This system represents a complete departure from the types of reactions studied previously by UED, in that it involves neither heavy atoms nor fragmentation of the parent molecule but instead involves the subtle structural rearrangement of a hydrocarbon. The high absorption cross section (ε = ~1800 $l \cdot mol^{-1} \cdot cm^{-1}$)[1] of CHD is advantageous for study at our pump wavelength of 267 nm, helping us attain an exceptional signal-to-noise ratio in the difference UED data. Additionally, due to the complexity of CHD and its rich behavior upon photo-activation, the analysis has proved to be very demanding from a theoretical standpoint, forcing us to develop new approaches for treating UED data. Finally, the strong evidence for non-Boltzmann energy trapping behavior in the specific modes makes these results particularly exciting. Nevertheless, it should be noted that the photo-reaction of CHD is considered to be interesting and generally important to chemists for a variety of reasons.

From a purely chemical standpoint, the photo-reaction of CHD is a prototypical reaction for the large field of polyene photochemistry, involving various types of chemicals including dyes. This reaction belongs to the family of pericyclic rearrangements (reactions believed to proceed with a transition state possessing a closed loop of interacting orbitals); specifically, the photoreaction of CHD to form HT

is known as electrocyclic ring opening. In general, the outcomes of pericyclic rearrangements can be predicted by the Woodward-Hoffmann rules, which were constructed using relatively simple molecular orbital symmetry arguments.[2] For example, these rules predict that for a system with $4n$ π electrons (i.e., with two conjugated double bonds in the ring), photochemical ring opening will proceed with conrotatory specificity (that is, the ring opening will proceed such that the end groups at the ring opening position will rotate in the same direction), while systems with $4n+2$ π electrons will proceed via disrotatory motion of the end groups (for $n = 0,1,2\ldots$). The CHD reaction has also been used as a model system for studying the effects of substituents and solvent on the photo-reaction rate. For example, the effects of the presence of solvent on energy redistribution and transport—as well as the effects of friction of the solvent on bulk motion and morphological change of the solute over the course of a chemical reaction—have recently been studied. Additionally (and of direct importance to us), the ultrafast dynamics of this reaction have been studied experimentally and theoretically by a number of groups over the past 10 years, and there appears to be considerable disagreement regarding the interpretation of the various results regarding, for example, the rate of ring opening in the reaction.

The CHD/HT reaction has biological significance as well. Because this reaction is a model for polyene photochemistry in general, it is also relevant to a variety of polyene photo-isomerization reactions critical to many biological processes. Examples frequently cited in the literature include: the photo-isomerization of 11-*cis* retinal (a vitamin A derivative) to form all-*trans* retinal in rhodopsin (the fundamental

process in dim-light vision of vertebrates); the photo-isomerization of all-*trans* retinal to form 13-*cis* retinal in bacteriorhodopsin (a fundamental process of photosynthesis in certain types of bacteria); and the *cis-trans* isomerization of urocanic acid in the epidermis by UVB light (a process which has been implicated in the suppression of immune response that ultimately leads to skin cancer). Moreover, the light-induced ring opening of CHD is directly relevant to the synthesis of vitamin D *in vivo*. Specifically, CHD models the chromophoric subunit of 7-dehydrocholesterol, which forms *cZc*-previtamin D upon UV irradiation in the primary step of vitamin D synthesis.

B) General description of electronic transitions and ultrafast reaction dynamics in CHD

Although photochemical characteristics of CHD were studied long ago, various important investigations regarding its ultrafast dynamics have been carried out within the last decade. A schematic of the relevant potential energy surfaces, along with the static structures of CHD and the relevant HT conformers, is shown in Fig. 6.1.1. The initial UV excitation of CHD in its $1A_1$ ground state creates a population in the $1B_2$ state, which subsequently "decays" (using the word loosely) either by rapid motion out of the Frank-Condon region of the excited state potential energy surface, or by ultrafast internal conversion to an optically forbidden $2A_1$ state on a time scale of ~10 fs.[2,3] Many spectroscopic tools encompassing resonance Raman scattering,[3-5] UV absorption,[6-8] resonance enhanced multiphoton ionization (REMPI),[9] and dissociative

intense field ionization[10,11] have been incorporated to elucidate the photodynamics of the ring-opening reaction of CHD. The analysis of this reaction is, however, greatly complicated by the effects of vibrational excitation and the lack of information about the spectra of the possible conformers of HT, namely *cZc* and *cZt* (the spectrum for the lowest-energy conformer, *tZt*, is well-known).

One can easily see that at least four time scales are involved in this reaction; 1) the depopulation of the initially populated $1B_2$ state into another excited state (most probably $2A_1$); 2) the depopulation of the excited state into the vibrationally hot CHD ground state; 3) the depopulation of the excited state into the photoproduct of the ring-opening reaction (i.e., the step governed by the all-important ring opening rate); and 4) the isomerization of the initially formed photoproduct (most probably *cZc*) into other rotamers (*cZt* and *tZt*). In the condensed phase, the problem is complicated further due to possible vibrational relaxation (thermalization) caused by the solvent molecules. The apparent difficulties associated with these complicated processes are evident in the fact that the suggested time scales for the processes scatter over an order of magnitude, depending the detection methods and the various interpretations.

6.1.2 Experimental setup and method

UED data were obtained with our third-generation apparatus[12], which will be described in greater detail in a separate publication (V.A.L. et al., in preparation). Briefly, the amplified output from a Ti:Sapphire laser system (350 μJ, 120 fs, 267 nm, 1 kHz repetition rate) was split into two beams, with the stronger beam being directed

into the scattering chamber to initiate the reaction. The weaker beam was directed into a delay line, and then focused onto a back-illuminated photocathode to generate electron pulses via the photoelectric effect (30 kV, de Broglie wavelength: λ = 0.067 Å, ~25,000 electrons per pulse at ~4 ps). The molecular sample was introduced into the chamber via a jet expansion source. After interacting with the molecular beam, the diffracted electrons were detected with a low-noise CCD camera [active s range: ~1.5-18.5 Å; $s = (4\pi/\lambda)\cdot\sin(\theta/2)$, where θ is the scattering angle]. The reaction zero-of-time was determined by the ion-induced lensing technique[13] using CF_3I gas (Aldrich, 99%). Samples of CHD (Aldrich, 97%) were degassed with several freeze-pump-thaw cycles, and high-purity xenon (Spectra Gases, 99.999%) was used as an atomic reference gas[14]. The nozzle temperature for the diffraction experiments was maintained at 120 °C.

Ground-state diffraction images (Fig. 6.1.2 for the CHD ground state data) were obtained at "negative time" by timing the electron pulse to arrive before the laser pulse, whereas time-resolved diffraction snapshots were acquired by varying the delay between the light and electron pulses. 2D diffraction images were radially averaged to generate 1D total intensity curves, from which experimental $sM(s)$ curves were calculated[15]. Time-dependant difference curves were obtained by subtracting a reference diffraction signal (obtained at negative time) from the signals obtained at positive times. As they contain equal but opposite contributions from the parent and product structures, the difference curves permit the relative parent and product fractions to be determined at each point in time[16]. Product-isolated curves were

obtained by adding the appropriately scaled parent diffraction signal at negative time to the difference curves, thus canceling out the parent contribution in each curve.[17] Using *ab initio* or previously available experimental structural parameters, geometrically consistent molecular models were constructed, from which theoretical $sM(s)$ curves were derived. A Monte Carlo sampling procedure was then applied to seek out structures corresponding to minima in configuration space, followed by least-squares refinement of the structures. Vibrationally excited product structures were modeled by correcting for the increased l values (mean amplitude of vibration); l values for thermally equilibrated structures were either estimated with the ASYM40 program[18] or extrapolated to high temperatures[15] from the empirical equations given in Refs. [19-22]. Extrapolated l values were also used to relate r_e (the geometrically consistent zero-Kelvin equilibrium internuclear distance), to r_a (the internuclear distance measured by electron diffraction), using the equation: $r_a \approx r_e + (3/2)\cdot a\cdot l^2 + dr - l^2/r$, where a is the anharmonicity constant for the bond and dr is the small correction due to centrifugal distortion.[15]

6.1.3 Specifics Of Our CHD UED Data Analysis

A) Background subtraction

A significant, slowly-varying background curve underlies the (structurally relevant) molecular interference pattern at each time point. These seemingly time-delay-dependent background curves probably originate from two major potential sources: 1) the shift of the residual background seen in the ground-state diffraction

pattern, possibly caused by the defocused photo-electrons (as well as the stray photo-induced spurious electron emission from the surface of the vacuum chamber); and/or 2) an artifact of the ion-lensing effect. For quick examinations of the data, the slowly varying background curves are removed by fitting the difference data set with 4^{th}-order polynomials. Once the background curves are removed, the remaining high-frequency oscillation patterns for the 75-400 ps data set are almost identical (both in period and in amplitude). This procedure thus highlighted the robustness of the interference terms in the data, independent of the spurious background counts.

B) Generation of "Product-Isolated" curves from diffraction difference signals

The structure-rendering procedures used for the CHD data have been modified from our previously reported schemes in two aspects. First, the diffraction difference scheme is extended to include both difference curve and "product-isolated" curve procedures, performed in an iterative loop as shown schematically in Fig. 6.1.3. As described previously, the difference curve yields information regarding the proportions of the products obtained following photo-illumination. This procedure may also be used to determine the structure of a given photo-product in a theoretical model, which must include both the parent $sM(s)$ curve and that of the product. Both the experimental difference data [which is produced, for example, by subtracting positive time data (contributed mostly by the parents, with the remaining ~1-15% coming from the photo-products) from the negative time data (100% parent)] and the corresponding curve generated from a theoretical model are comprised of 50% parent

contributions and 50% product contributions. The diffraction-difference procedure has the advantages of removing systematic artifacts from the raw experimental data set, and concentrating on the results of photo-reactions by highlighting only those contributions to the molecular scattering signal originating from internuclear distances that change over the course of the reaction. However, the success of this procedure depends on the success of the ground state structure fitting; moreover, the sensitivity with respect to the product structure is reduced by the contribution from the parent signal.

In light of these difficulties, we implemented a second structural fitting loop which permits the contribution from the product only to be extracted from the total diffraction difference curve. In the first step of this new procedure, the values of the parent/product proportions are obtained at each time point from the usual diffraction difference analysis; these values are then used to fit the temporal behavior of the reaction dynamics. The resulting "exponential" temporal curve is then used to obtain "true" values for the proportions of parent and product species at each point in the reaction. Next (at each point in the reaction), the parent-only signal obtained at negative time points is scaled down according to the temporal curve, and subsequently added to the difference curve at a given time point—effectively canceling out the parent contribution, and leaving only the products to contribute to the diffraction signal. Finally, the product signal is fit (see below). These two fitting loops are connected interactively for successive refining; the refinement is repeated iteratively until the fits converge. The advantages of the new product-isolated procedure are

four-fold: 1) the experimental data is comprised of 100% products, giving greater sensitivity for studying the product structure(s) directly (particularly when the structural change is significant); 2) it provides a more intuitive framework for analysis and interpretation; 3) the data analysis is much less dependent on the parent structure fitting; and 4) it allows us to exploit the fact that the temporal behavior of the entire reaction is known with greater precision than that of the species distribution at any given time point. This approach was first suggested during the work on UED2, and was realized with the CF_2 study.[17]

C) Novel aspects of the product structure analysis used for "hot" HT product

The second major deviation in data analysis from our previous methods is the inclusion of non-single-gaussian probability functions for certain bond distances and those for the primary torsional angles. The former attempts to take into account the possibility of inverted (non-Boltzmann) vibrational populations in a given portion of the vibrational manifold relevant to our investigation; the latter accounts for the distribution of the HT conformers. Additionally, an alternative structure modeling/fitting scheme aimed at treating complicated molecular systems is proposed in this work; the methodology and its results should complement the current approach, and will be mentioned later in 6.1.6.B.

Before going further, it should be mentioned that these increasingly sophisticated (and increasingly deviant from conventional) procedures were implemented only after exhaustive attempts to fit the data with our previous, more

conventional methods were determined to be unsatisfactory. In our earlier approaches with the CHD data, equations governing geometrically consistent models were carefully constructed for CHD, *cZc*, *cZt*, and *tZt*; these models were then introduced into the UED fitting program in the usual way (these models were independently determined to be quite self-consistent, with the greatest error in mathematical self-consistency of predicted distances to be ~0.05 Å for one long-range non-bonded distance in *cZc*—nearly all other distances were within 0.005 Å for *cZc* and *cZt*, and all distances for CHD and *tZt* were within 0.001 Å. The relatively large error of ~0.05 Å was accepted because it was shown to be a result of the simplified geometrically-consistent model for *cZc*/*cZt*, and not a human error in algebraic formulation). An equilibrated vibrational temperature for the HT products was estimated to be ~2100 K, considering the left-over deposited energy and the vibrational frequencies of the 36 modes. Reasonable values for the mean amplitudes of vibration and the temperature corrections to the distances were obtained by meticulously constructing U-matrices for entry into ASYM40, along with appropriate Hessians from Gaussian for each species. Structural parameters for the various species were obtained from conventional ED, our own fit of the ground state, and from *ab initio* calculations. We could then perform our early fits, in which we could see qualitatively: 1) that the progress of the reaction was relatively slow (indeed, the time constant for the reaction was always in the ballpark of 30 ps, regardless of the model); 2) that the positive and negative contributions to $\Delta f(r)$ were consistent with ring-opening; and 3) that fitting the $\Delta f(r)$ curves to the different conformers gave relatively poor agreement (considering our

SNR) to the various possible static structures, but seemed to support *cZc* more than anything else.

1) The double-Gaussian probability distribution function for bond distances

In this approach, for each of the direct-bond distances in the CC skeleton, a double-Gaussian probability function is assigned; this may be compared with the single-Gaussian probability functions (characteristic normal Boltzmann thermal populations) normally used in static electron diffraction. The double Gaussians were allowed to vary in their mean positions and FWHMs, thereby giving the refinement freedom to qualitatively simulate an inverted vibrational population in which the density bifurcates towards the classical turning points of the local potential well. Naturally, if the mean positions of the two Gaussians merge together, then the normal single-Gaussian picture for a Boltzmann vibrational distribution is recovered.

2) The conformational evolution—the analysis of the torsional angle distribution

The first novel analysis of the structure and torsional angle distribution (which ultimately reflects the HT conformer distribution) was performed as follows. The geometrically-consistent model of the generalized HT (specifically, *cZt*) structure was put into the refinement routine. For each of the two torsional motions under consideration [i.e., those involving rotation about the two C-C single bonds, namely through the torsion angles τ_1(∠C1=C2-C3=C4) and τ_2(∠C3=C4-C5=C6)], a two-peak cyclic Gaussian probability function was assigned, with mean positions centered (and fixed) at 48° (*cis*-) and 180° (*trans*-). Additionally, the distributions of these angles

were fixed at 40° (FWHM); giving a distribution shown to give a better fit than that obtained by assuming delta functions for the dihedral angle distributions (but the value of 40° was not numerically optimized). The mean angle values, determined from *ab initio* calculations, and FWHM values were held fixed at this stage in the processing in order to reduce the number of adjustable parameters. The weighing prefactors before the *cis*- and *trans*- normalized Gaussian functions were allowed to vary (but naturally were required to have a sum of 1). The two torsional motions were regarded as independent. With 2×2=4 weighing prefactors (only two of which are independent parameters), the relative portions of the *cZc*, *cZt*, and *tZt* conformers could then (in principle) be determined.

With the increased complexity of the total fit, each major step within the complete iterative refinement is broken into smaller steps according to the sensitivity of the fit to each given type of parameter; i.e., in terms of the fit sensitivity, product fraction > bond distances > torsional angles / conformational prefactors (standard three-atom bond angles, which do not differ more than a few degrees among the different HT conformers, were held fixed at the ab initio values). The low-frequency (DC) background-removing procedures (and convergence tests for avoiding divergence) are embedded within the fitting iteration cycles for guidance towards the global minimum. For the sake of objectivity, the exact refinement sequences are directly coded into the software so that all time points are treated equivalently.

At this stage of structural refinement, there were 18 total independent fitting parameters. These included: 3 independent covalent C-C bond distributions (C1=C2,

C2-C3, and C3=C4), each described by 2 independent Gaussians [with their own mean values (2 params), FWHMs (2 params), and relative amplitudes (1 param)], giving 15 independent parameters for the covalent distances; torsional prefactors for the conformational distribution (described by 2 independent parameters); and finally the fraction of the product (only 1 parameter for difference curve fitting) (15+2+1=18). Other structure parameters were taken from ab initio calculations, with the mean amplitudes of vibration estimated using the ab inito force constants extrapolated to 2100 K with ASYM40. Although the total number of fitting parameters is large, it was found that only the fraction of the product, the C-C distances, and the torsional prefactors are very important for determining the global outcome of the fit (the other parameters (e.g., the FWHMs and deviations from 50/50 proportionality of the two-Gaussian distributions) can be regarded as mere "by-standers" to the overall fit; however, of course the values of these "secondary" parameters would not be trust-worthy if the global structure fitting did not yield good results). During the structure/conformation refinement of the CHD data, it was found that iterative background-removing procedures and convergence-checking procedures were crucial for the ultimate success of this step-wise process.

6.1.4 Summary Of Our Apparent Observations

A) Despite the lack of heavy atoms or molecular fragmentation in the CHD → HT reaction, we were able to obtain excellent signal-to-noise from this system,

demonstrating the general applicability of UED for studying ultrafast structural dynamics in diverse types of chemical reactions.

B) We see significant structural changes over the course of the UED experiment, directly resulting from chemical reactions.

1) The data best supports the depletion of CHD and formation of HT on the 30 ps time scale. This result seems extremely clear and robust, by our standards anyway. While this surprisingly long time constant can be rationalized to agree with the ~6 ps result from Mathies and co-workers in solution, it contradicts the interpretations of Fuss, Kompa, Sension, and others, who believe that the ring opening occurs in a few hundred fs only, basically regardless of the experimental conditions. They, no doubt, would not be pleased with our belief that excited CHD* exists for ~30 ps.
2) Fitting the data well requires a distribution of torsion angles for the HT product. Doing so results in a torsion angle distribution that doesn't change much over the course of the reaction; also, most of the HT is *cZc* in nature, with some *cZt*, and virtually no *tZt*. Thus, the molecules do not seem to reach any kind of thermally equilibrated structural partitioning on our 400 ps time scale (at 2100 K, a thermally equilibrated mixture should be roughly proportioned at ~14% *cZc* (=cCc), 45% *cZt* (=cCt), and 41% *tZt* (=*tZt*)).
3) About 9 or 10% of the CHD molecules undergo reaction.

C) We apparently see evidence of the effects of a non-thermal (non-Boltzmann) distribution of energy on the overall UED-detected structural aspects of the HT product. Our inability to fit the UED data well with a 0 K ab initio model of HT is believed to be a result of the extremely hot nature of the HT product. This seems to be manifested it two ways: First, by the distribution of torsion angles, and the apparent preference for *cZc*, the highest energy conformer (which can be rationalized classically in the following way: just in the same way that a high-energy harmonic oscillator spends most of its time at the periphery of the potential and very little time at the bottom of the well, our product HT spends most of its time in the high-energy *cZc*-like conformation, and virtually no time in the *tZt* conformation); second, by the presence of a highly-nonequilibrium internuclear separation of a C-C single bond (~1.75 Å). Using a conventional ED analysis—which employs temperature-dependent correction terms based on the available energy being thermally equilibrated throughout the molecule (in this case, at ~2100 K)—was not sufficient to give us a satisfactory fit of the data, and could not give anything close to a 1.75 Å C-C internuclear distance. We add that this long distance is apparently evident in our initial ("before-and-after") CHD run as well; therefore, the effect is reproducible.

D) A different data processing method was used to select the product molecular contribution only from the time-resolved diffraction signals. Not only does this process highlight the complete product signal, it removes any complications from the parent signal being present. This goal is achieved by adding a scaled amount of the

ground-state signal to the difference signal (thus, one doesn't even need to know the ground state structure well in order to perform this), thereby canceling out the parent contribution. One should note that any significant error in the scale of the reaction would re-introduce parent signal into the "pure" product, which would otherwise be unaccounted for.

E) We saw change in the –10 ps image, and seemed to have missed the zero-of-time by about 20 ps according to a fit of the data.

6.1.5 Review Of Previous Studies In Light of Our UED Results

A) The resonance Raman studies of Mathies and co-workers

Resonance Raman intensity analysis[3] has demonstrated that the initial excited-state evolution of CHD is along the conrotary reaction coordinate (as expected according to the Woodward-Hoffmann rules), and that depopulation of this state occurs in ~10 fs (determined from a linewidth analysis).

In 1993, Mathies and coworkers[5] reported time-resolved UV resonance Raman studies of CHD→HT in the condensed phase. In their results, the appearance time of the Stokes scattering from ground-state *cZc*-type HT is 6 ± 1 ps and the photoproduct anti-Stokes ethylenic intensity appears with a time constant of 8 ± 2 ps and decays in 9 ± 2 ps (this observation reflects the production and dissipation of "hot" HT-type product). Analysis of the photoproduct spectral evolution in the Stokes and anti-Stokes data as well as the observation of Raman lines characteristic of the *cZc* conformer in

the anti-Stokes data demonstrates that *cZc* first appears on the ground-state surface, and then subsequently undergoes conformational relaxation to produce *cZt* with a time constant of about 7 ps. The photoproduct anti-Stokes ethylenic and single-bond stretch intensities further demonstrate that the initial photoproduct temperature at 4 ps is 1500 ± 500 K [a very reasonable observation when compared to the value we calculated for the expected "fully thermalized" temperature (~2100 K; they estimated ~1950 K for the initial product temperature) neglecting any dissipation of heat to the solvent] and that the cooling time is ~15 ps. It was also shown that the time scale for any final conversion of *cZt* to *tZt* takes longer than 200 ps.

We believe that these time scales and their interpretation do *not* contradict our UED results and interpretations. While the appearance time (6 ps) for the HT species is significantly shorter than what we measured (~30 ps), we believe that their faster rate can be at least qualitatively rationalized by including the additional de-activation channel available in the condensed phase (i.e., the channeling of energy from CHD* into the bath via contact with the solvent, which efficiently quenches the reaction). If CHD* is quenched by the solvent with a time constant of about 7 ps, it would reduce the appearance time of HT from 30 ps to the 6 ps observed by Mathies et al. Alternatively, the solvent may alter the available phase-space in the excited state in some way, thus yielding a faster decay. However, since they were blind to the direct depletion of CHD*, it's hard to say anything more definitive that that. Moreover, we note that the "condensing" (relaxing) of HT product conformers takes considerable time, and requires the presence of the solvent; therefore, it is not surprising that we

still see a highly non-thermal conformer distribution (with *cZc* dominating).

If the Mathies results have a weakness, it is the (inevitable) reliance on ab initio-derived resonance-Raman spectra for the *cZc* and *cZt* conformers. For example, Mathies et al. claim: "The presence of scattering at 829 cm^{-1} (well into the ps regime) strongly argues for the presence of the all-*cis* conformer on the ground state surface." This particular argument is based on the fact that neither the ab initio *cZt* or *tZt* spectra have frequencies anywhere near this region, whereas *cZc* is predicted via ab initio methods to have one at 849 cm^{-1}. Still, one might question the relevance of ab initio predictions of resonant Raman spectra (specifically, the absence of certain lines) for species at zero temperature involved in the CHD→HT reaction, when we know there is an enormous amount of energy bouncing around in HT. Indeed, it is this potential weakness that is invoked (arguably, in a hypocritical manner) by Sension and co-workers to malign the Mathies' interpretation that supports long-time (many ps) ring-opening.

B) The initial work of Sension and co-workers

Sension and co-workers[6] used a complimentary technique of fs transient absorption spectroscopy to further investigate the rate of appearance of the *cZc* conformer from photoexcited CHD. One-color transient absorption signals of CHD in cyclohexane and methanol pumped at 262, 268, and 273 nm revealed a rising component of several ps. In their analysis, these authors made the following assumptions: 1) The *cZt* and *tZt* conformers, as well as the *cZc* conformer, are formed.

2) The quantum yield for the CHD→HT isomerization reaction was fixed at 0.4. 3) The oscillator strengths of the *cZc* and *cZt* conformers were restricted to be in the range of 0.25-0.5 and 0.5-1.0, respectively. 4) The oscillator strengths of the vibrationally hot *cZc* and *cZt* species were restricted to be smaller than those of the thermally equilibrated isomers. 5) The time constant of conformational relaxation from *cZc* to *cZt* was constrained to 7 ps as determined in the ps resonance Raman experiments of Mathies and coworkers described above.

Under the framework of their assumptions, the authors basically concluded that the ring-opening reaction is finished essentially completely within 1 ps of excitation and suggested that the 6 ps appearance of resonance Raman scattering (of Mathies and coworkers) from the initial *cZc* photoproduct is somehow limited by vibrational relaxation in the ground state manifold. While a "free" fit of the observed transient behavior would allow one to conclude just about what ever one wanted, Sension and coworkers concluded that the assignment of a 6 ps time constant for the appearance of the *cZc* photoproduct (i.e., ring opening) was physically unreasonable, as it would require that the absorption cross section for the initially formed, vibrationally hot *cZc* be two to three times higher than the absorption cross section of the thermally equilibrated *cZt* photoproduct at all three probe wavelengths (at least within the other constraints of their model).

Neglected is the possibility that only *cZc* is formed in their solution without significant conversion into *cZt* or *tZt*. We also note that these authors were selective in which results they liked and which results they didn't like from the same Mathies

paper—they disregard the 6 ps ring opening assignment, yet actually use the 7 ps time constant assigned to *cZc*→*cZt* conformational relaxation in their model. Moreover, they also suffer from the fact that the transient absorption spectra for *cZc* and *cZt* are unknown. They admit that while calculations proved quantitatively unreliable, the calculations did successfully reproduce the trend of CHD < *cZc* < *cZt* < *tZt*. Still, it is hard to pinpoint where, if anywhere, Sension and co-workers go "wrong", except to say that their conclusions are based on the application of somewhat complex models (with parameters that aren't well-known, especially over the various conditions of the experiment) to simple transient curves.

C) The work of Fuss, Kompa, and co-workers

More recently Fuss and co-workers used the same technique of fs transient absorption[7] to study the ring-opening dynamics of CHD and the subsequent processes such as isomerization and cooling in the condensed phase. The interpretations and time scales for the ring-opening and isomerization were drastically different from those of the Raman studies of Mathies and co-workers, and were mostly consistent with the FTS studies of Sension and co-workers (which is altogether not surprising, since the technique was the basically the same). The interpretation starts from the analysis of the transient absorption at 404 nm of CHD dissolved in ethanol after excitation at 267 nm. Since CHD, as well as HT, absorbs only at wavelengths shorter than 290 nm, this transient absorption at 404 nm was attributed to the excitation from the S_1 to higher electronic states S_n, requiring less energy than the excitation from the

ground state to the S_1 state. The transient absorption signal clearly showed that the species giving the transient signal disappears within 300 fs. From this observation, they concluded that the ring-opening completes within 300 fs (i.e., CHD*→HT).

Generally speaking, there are two ways that conclusions like this based on FTS experiments could be wrong. First, the observed behavior might not be representative [i.e., the conclusion is right (e.g., in this case, they are indeed seeing ring opening in 300 fs), but it is a picture only of what a small percentage of reacting molecules are doing, with rest of the molecules being dark for some reason). Correspondingly, the second possibility is that the behavior is indeed representative of the entire ensemble, but the conclusion is wrong (e.g., in this case, the time constant does not represent ring opening, but merely results from the wave packet passing through a narrow observation window that happens to have a high absorption cross section at 404 nm compared with other species. Thus, the species giving a high absorption at 404 nm may not represent the whole landscape of the excited states ($1B_2$ and $2A_1$) of CHD), and the ring hasn't opened yet, even after the wave packet passes through the 404 nm window).

The rest of the interpretation was merely based on this conclusion that CHD ring-opening occurs within 300 fs, and therefore would be easily falsified if the initial conclusion were wrong. In their model, the concentrations of the conformers reach thermal equilibrium in a few picoseconds; during the first 10-20 ps, the concentrations follow the cooling of the molecule by the solvent, staying near thermal equilibrium (i.e., rapidly tending toward *tZt* in great majority); and a small quantity of *cZt*-

hexatriene is trapped in its potential well on a time scale of 100 ps at the final temperature (300 K) (Note that this result is also very different from that of Mathies and co-workers). The reason that they were so confident about the short time scale for the ring-opening process seems to have originated from their previous studies[10] (also, see later work in [11]) in the gas phase where a short time scale was claimed. The earlier result of Sension and co-workers may have contributed to their biased assumption. Still, the authors spend a considerable amount of time deconstructing the results and interpretations of Mathies and co-workers, and make some strong arguments. While seemingly neglecting a few of Mathies' more qualitative yet convincing arguments (e.g., the presence/absence of particular resonances that could only be reasonably assigned to particular conformers), they directly challenge their quantitative interpretations, and come up with their own interpretations of what Mathies' group saw. For example, they believe that if differences in transition dipole moments of the HT conformers were included by Mathies' group in their analysis, they would have concluded that their 6 ps rise was actually due to conformer isomerization, not ring opening. Additionally, Fuss and co-workers believe that one resonance assigned to *cZt* should have been assigned to *tZt*, which is why Mathies thinks *tZt* was not appreciably formed over the course of their experiment, when in fact it was.

In the most recent study[11] in the gas phase, the same researchers used dissociative intense-laser field ionization in an attempt to substantiate the ultrafast nature of the dynamics of CHD ring opening. All the transient mass signals showed

very short time constants. On the basis of the rather different fragmentation pattern of CHD and HT when ionized by an intense-laser field, the H^+ mass transient was attributed to the formation of HT. However, neglected is the possibility that the extremely strong laser fields may perturb the potential energy surfaces of the whole process of ring-opening and isomerization, instantly accelerating the ring-opening process and creating the product, thereby giving an artificially fast appearance time for the product.

However, we note that the potential problem with the intense-field ionization may be absent with the resonance-enhanced multiphoton ionization (REMPI) experiments performed by this group. Actually, the same authors[9] utilized time-resolved REMPI and obtained a 600 fs rise time, which was attributed to product formation by ring opening. However, later on they reassigned the 600 fs to the conformer isomerization in the hot product.

In other work by Sension and coworkers[8], they expanded their transient absorption study in this system in solution. Their results and interpretations are almost identical to those of Fuss and coworkers.

One question is whether the authors from the gas-phase experiments thought that *tZt* was the complete final product or not? Even complete equilibration of thermal energy should give 13.6% *cZc*, 45.2% *cZt*, and 41.2% *tZt*. It should be noted that while a bias to *tZt* is probably assumed, no gas-phase study besides ours has been attempted to directly address the product conformer distribution.

D) A brief review of the work studying the ultrafast dynamics of 7-dehydrocholestrol (DHC)

As previously mentioned, the formation of previtamin D from UV photoactivation of DHC is directly relevant to our CHD experiment. Moreover, we believe that the experiments performed on this system provide an excellent example of how two different groups can perform nearly identical experiments on the same system, see mildly different results, and come to very different conclusions.

The photochemical reaction of DHC to form Previtamin D has been studied by two different research groups. Fuss and coworkers[23] were the first to apply femtosecond transient absorption spectroscopy to this system. DHC in ethanol was pumped with an tunable UV excitation pulse ranging from 267 to 292 nm, and was probed with a second UV pulse ranging from 267 to 316 nm. Two time components were observed in the transients. The "fast" component (with a time constant t_1 = 5.2 ps) was independent of temperature, pump wavelength, and probe wavelength. The "slow" component (t_2) varied between 60 ps at 315 K and 1300 ps at 247 K. Consequently, the authors assigned the fast time constant to the appearance of the first photoproduct (*cZc* Previtamin D), i.e. the ring opening and concomitant cross-over from the excited potential energy surface to the ground state surface, and suggested that the independence of t_1 on the excitation wavelength implies that it does not depend on the initial vibrational excess energy and deduced an activation entropy ΔS_a of about –3.4 k_B.

Sension and coworkers[24] also examined this system by using the exact same

technique—ultrafast transient absorption spectroscopy. In their experiment, the molecules were excited at 265 nm and probed at 20 different wavelengths from 261 to 650 nm. In addition to the two time scales observed by Fuss and coworkers, a shorter time scale of 0.95 ± 0.10 ps was observed in their experiment at all long probe wavelengths from 470 to 650 nm. This primary transient absorption was assigned to an $S_1 \rightarrow S_n$ transition that peaks near 470 nm. The second time scale, which was previously assigned to the lifetime of S_1 by Fuss and coworkers, showed wavelength dependence, going down to 1.3 ps at 340 nm. This observation led these authors to conclude that this time scale of 1-5 ps arises from vibrational cooling. On top of this conclusion, the authors also suggested that the observed cooling signal is in fact dominated by the DHC parent, rather than the product. Their results on the longest time components are relatively consistent with those of Fuss and coworkers. Based on the two different interpretations, one can see that it is not so obvious to unambiguously assign the time components in transient signals.

6.1.6 Results

A) Primary results obtained using the procedure described in 6.1.4

The results of the "product-isolated" fits are shown in Fig. 6.1.4. The refinement models/procedures were built based on different hypotheses, chosen in order to prove or disprove different arguments. For example, the hypothesis that there may be bifurcated probability functions associated with all covalent C-C distances (C-H contributions are small) was tested with the assignment of two-Gaussian models for

all C-C distances. The results show that while C-C single bonds show bifurcation distinctly and robustly, the bifurcated distributions for the C=C double bonds distances proved unnecessary. However, the most distinct result of the fit (which is easily seen even without high-level structure refinement) is the time-constant of the growth of the difference signal (Fig. 6.1.5). This growth is attributed to the time constant of the production of photo-products, based on the structural similarity with the "saturated" structure (400 ps data set) in the properly scaled experimental $sM(s)$ curves among different time frames. A second distinct feature is the introduction of frequency components corresponding to a C-C bond distance at ~1.7 Å in the product-isolated $sM(s)$ curves (it also shows up in the $\Delta sM(s)$ curves using the old data analysis); this very strange distance can be seen directly in the product-isolated $f(r)$ curves. Over the course of the refinement procedure, the third major result is the overall (non-thermal) favor of the *cZc* conformer (see Fig. 6.1.5(b)). The relative proportions of these species (small majority *cZc*, large minority *cZt*, and virtually no *tZt*), determined from the torsional prefactors, was relatively constant over the course of the reaction. This distribution is considered non-thermal because if the relative energies and degeneracies of the conformers are considered, a Boltzmann distribution of conformers at 2100 K would give about 14% *cZc*, 45% *cZt*, and 41% *tZt*.

The need for including other types of species into the fit was also tested. First, vibrationally hot (i.e., equilibrated at 2000 K) ground-state CHD was included as a part of the photo-products, but was determined unnecessary, being refuted at levels above 10% of the total photo-products generated. Additionally, the need for including

trans-HT (instead of the expected *cis*-HT) was also investigated. Fitting with *trans*-HT yielded relatively good results, but not as good as the results obtained with *cis*-HT. Instead, we tend to exclude the presence of *trans*-HT on the basis of energetics arguments. The presence of *trans*-HT would require isomerization about the center double bond after ring opening; however, this isomerization is unlikely because of the relatively high potential barrier involved (especially considering that the torsional motion for isomerization is not directly connected to the ring-opening reaction coordinates). Nevertheless, despite the unfavorable energetics, many other isomers, including MCPD, Tricyclo[3,1,0,0]hexane, Bicyclo[2,1,1]hex-2ene, Bicyclo[1,1,0] butane, and 3-Vinyl-cyclobutene were tested and their presence was subsequently reputed easily.

The final version of the product-isolated $sM(s)$ and radial distribution curves for data at all time frames are respectively depicted in Figs. 6.1.6(a) and 6.1.6(b), along with the corresponding curves produced theoretically for *cZc*, *cZt*, *tZt*, and hot CHD using ab initio structure parameters (assuming a thermal vibrational population at 2400 K for CHD). Note that in the product-isolated representation, the radial curves are constructed from the data set rather than the best fitted structural parameters, thus preserving all the information of bond distances carried by the data (even though the fit might not be perfect). Note that the radial distribution curve is the Fourier sine transform of the $sM(s)$ curve, but a theoretical model is required to amend the cut-off effects because only data in a finite s range are obtained.

The time-constant for the product formation is revealed in the growth of the product fraction, which in our case, connected monotonically from time zero to the 400 ps data set. A single-component model fits the product fraction relatively well, with a time constant of 32 ± 2 ps, and zero-of-time shift to -20 ps (Fig. 6.1.5(a)). The –20 ps offset is robust, and does not seem to depend on the nature of the model. The origin of the shift of time-zero is uncertain (see 6.1.8.C), but its presence suggests that (at least in the CHD experiment) the ion-lensing effect was not significant enough in this particular run for pin-pointing the exact onset time for the reaction. The lensing is a subtle effect on the isotropy of the electron beam shape, which also depends on the preparation of the electron beam (while the electron diffraction is not sensitive to the shape of the electron beam so long as it is small). The lagged time-zero is limited by the sensitivity of observing the anisotropy of the electron beam. However, we note that provided that the zero-of-time problem is not a symptom of a greater problem, it is irrelevant—it does not effect the results or conclusions. Thus in any case, we assign the 33 ps time constant to be the ensemble ring opening time for the CHD upon photo-absorption, and not for any conformational changes/equilibration. This conclusion is supported by the fact we see similar conformers at all time frames; more importantly, the diffraction patterns of the different HT product conformers are all much closer to each other in nature than any of them are to the parent CHD (indeed, the signals for HT and CHD are surprisingly different).

Upon a cursory examination of the product-isolated $f(r)$ curves, one can tell based on the relative heights of the covalently bonded (<2 Å) and indirectly bonded

(>2 Å) peaks that the product distribution favors a mixture composed predominantly of *cZc* and *cZt* (and not the thermally predicted mixture comprised predominantly of *cZt* and *tZt*). This observation agrees with the results reported by the refinement procedures in terms of the ratios among the different conformers, as shown in Fig. 6.1.5(b). Additionally, we note that the ~1.75 Å bond distance produced by the fit can be directly observed in the radial distribution curves for almost all time points. Naturally, this internuclear distance would be a highly unexpected result from considering any of the ab initio structures of possible products. While the origin of the exceptionally long distance is uncertain, the results of our refinement clearly point to this internuclear distance belonging exclusively to the C-C single bonds. In this procedure, the refinement clearly indicated that the C-C single bond probability distribution function generates this long-distance peak, as well as peak at a (more reasonable) shorter distance (at around 1.35-1.45 Å, just under the expected ab initio distance) with roughly the same probability. We believe that this strange result originates from a non-thermal population effect, and is (apparently) associated with the C-C single bonds exclusively; we saw no evidence of similar behavior for the C=C double bonds.

B) CHD results obtained with the generalized Monte Carlo method: A complimentary analysis

Although the significant features observed from the afore-mentioned modeling scheme should be robust, one could argue that certain specific structure features might

originate from the specific assumptions and constraints we have applied in the model (e.g., the values and distribution of the torsional angles and the bifurcation of the C-C bond distance probability function). Thus, it could be argued that there might be yet other (improved, or at least equally good) minima in the χ^2 hypersurface in the configuration space that are also well justified by the quality of our experimental data—and would be located if the structure were described differently—but are not reachable under the current constraints of the model.

In order to alleviate this doubt, global scanning was performed using a Monte Carlo approach over the configuration space (defined by a geometrically consistent Z-matrix representation of the structure) to probe for the existence of local minima for in each time delay. The Z-matrix representation of molecular structures is widely used in many ab initio and semiclassical methods in optimizing molecular geometry and dynamics. The flexibility of this construction allows us to treat the least-squares refinements of UED in the molecular hyper-configurational space, and to survey the landscape of the χ^2 hypersurface. By examining all the possible minima, the model-dependent "correlations" among structure parameters (e.g., pairs of similar covalent bond distances) can be noted for further analysis; moreover, the universal structure features, which should be model-independent, can also be established; the Monte Carlo survey helps us to locate the true, global minimum, and allows us to report global structure features with a high level of confidence.

This new modeling procedure has been applied to analyze our CHD data with two different initial conditions for the HT structure: 1) the ab initio structure of *tZt*;

and 2) the ab initio structure for *cZc* (both refinements gave similar results). Unlike conventionally applied least-squares fitting routines, no non-thermal probability distribution functions are presumed in the initial models. Additionally, this approach has the "built-in" predisposition of treating all dynamical effects as being effectively averaged, providing a single, static framework for the molecule (e.g., there are no distributions assigned to the dihedral angles—instead, average values are directly determined for τ_1 and τ_2 for each minimum on the χ^2 hypersurface).

Even without the assumption of non-thermal probability distribution functions, the averaged structure revealed in this complementary analysis shows clearly that one C-C single bond is extended to 1.7-1.8 Å, with the other C-C single bond being varying between 1.35-1.45 Å; additionally, the average skeletal structure of the HT product clearly takes on the shape of some intermediate structure between that of the "static" *cZc* and *cZt* conformers. These results are robust and apply for nearly all the time frames. Those averaged (static) general characteristics are very consistent with the results described in the previous Section obtained with the dynamically resolved non-thermal model.

6.1.7 Discussion

A) The possibility of Hot CHD

As described above, we have used two rather different modeling and refinement procedures to fit the molecular structure(s) of the photo-products of this reaction (both of which, we should add, deviate from previous GED methods of data

analysis to varying degrees). One assumption of these procedures is that the "back-reaction" pathway leading to internal conversion of the "hot" CHD would not create a structure drastically different from that of the parent, "cold" CHD. This assumption is based on the proposition that the vibrational manifold within the rigid frame work of the skeletal CC bond stretching will not favor any localized non-thermal behavior (at least not in the long-time limit).

In a thermal (Boltzmann-populated) model, the structure differences between hot and cold CHD would then arise only from the small bond elongation and the vibrational damping on the molecular interference pattern associated increased mean amplitudes of vibration which are roughly proportional to $T^{1/2}$. It has been reported that the quantum yields of internal conversion and ring opening of CHD upon illumination of ~260 nm light are ~60% and ~40% in solution. Thus, we analyzed the data in order to test if we also have a 3:2 hot-CHD:HT product ratio. We fit a thermal model of hot CHD (at 2373 K) for the 75-400 picosecond data set, but found the likelihood of a branching ratio of 3:2 for hot CHD and hot HT to be extremely low. As a matter of fact, the fitting of our UED data strongly suggests that the quantum yield of hot CHD in the gas phase is close to zero. On the other hand, a non-thermal "hot" CHD model clearly cannot fit all the features of the diffraction pattern of the photo-product. Indeed, our best fit requires that a non-thermal, hot HT must account for the structural feature of 1.75 Å.

B) Ramifications of the preliminary analysis of the CHT experiment

Nevertheless, the possible existence of non-thermally populated, hot CHD remains an interesting topic for consideration. To explore this possibility further—and to test other ideas about energy re-distribution in such systems—we performed UED on 1,3,5-cycloheptatriene (CHT), under the expectation that only an internal conversion process will take place (in addition to a hydrogen migration); thus, we expect that the only difference between "parent" and "product" in this reaction will be the vibrational temperature (see 6.2). The preliminary analysis of the CHT data suggests that a thermally-populated (energy-equipartioned among modes) hot CHT, formed through the internal conversion process, does in fact dominate the diffraction pattern. We see the formation of the hot CHT photo-product with a conversion time constant of 16 ± 3 ps. Thus, we believe that this result indicates that the thermalized model (energy-equipartioned among modes) of hot CHD presumed in modeling the CHD experiment is well-justified. Furthermore it supports that the ring-opening process is the dominant pathway in the CHD photo-reaction dynamics and that the back formation of hot CHD is not nearly as important in the gas phase as it is in the condensed phase.

C) On the long-time ring-opening of CHD; another point of view (see also 6.1.8.A)

Perhaps the most unambiguous feature of the CHD data that does *not* require rigorous structural fitting is the ~32 ps ring opening time. As stated previously, this result is in significant disagreement with the recent sub-ps results obtained by various femtosecond spectroscopic techniques. However, we believe that our long time

constant can be rationalized to agree with the earlier results of 6 ps obtained by Mathies and co-workers in solution, using resonant Raman spectroscopy. We believe that the presence of the solvent has a significant effect on the excited-state dynamics, because the CHD* molecules will have to "oscillate a few cycles" before a radiationless nonadiabatic decay can take place. We note that this conclusion is very different from the sub-ps interpretations, which generally suggest that the solvent plays no role in determining the rate and outcome of the CHD photo-reactions. In order to form HT, the molecule has to at least cross two excited vibronic manifolds. Doing so in the sub-ps picture would require that a coherent, collective mode of motion (driven by the shape of the potential) takes place, leading almost straight to the ring opening and internal conversions simultaneously. Additionally, because the solvent is expected to play no role in the reaction, the sub-ps picture would predict that in gas-phase reactions 60% of the products would be hot CHD, just as they would be in solution.

On the other hand, in our picosecond picture, CHD* has sufficient time to wander around in the two excited rovibronic surfaces before reaching the "appropriate" geometric configurations where the non-adiabatic decay can occur. Additionally, in this picture the presence of solvent molecules will undoubtedly affect the reactive space through rovibrational coupling with the excited-state surfaces and through the steric hindrance of solute molecular motion. Thus, we believe that the vibrational cooling by the solvent molecules of CHD* effectively quenches the skeletal vibrational motion generated upon photo-excitation, leading to a fast decay of

CHD*. Moreover, the steric hindrance of the solvent molecules likely plays a role in enhancing the reaction pathway leading to internal conversion ("back-reaction") to form vibrationally hot CHD instead of HT.

D) On slow IVR in ground state surfaces

General relevance

The photo-initiated, non-dissociative radiationless decay processes in CHD embody a prototypical IVR problem. Indeed, there are two universal characteristics associated with this process which make this photo-reaction a particularly interesting case: 1) A vast amount of the electronic energy is transferred to the vibrational energy of the molecule in a relative short period of time. 2) There is a direct coupling to the low-frequency skeletal torsion modes at higher vibrational levels. Because the reaction pathway connecting the ground and excited electronic levels is rather steep with regard to the energy potential surfaces, and often begins with a well-characterized geometry, the initial condition of IVR (e.g., the geometry of the molecule and the locality of non-thermalized population distributions) is probably similar for all the molecules in the ensemble, albeit there is probably not a universal onset time for the decay of the molecules (i.e., here we do not mean to imply that there is coherent ensemble wave packet evolution on this time scale).

For CHD in particular, the ring opening is directly coupled to large-amplitude torsional motions along a potential well where the conformational barrier is rather low compared to the initial available vibrational energy. Here two of questions come to

mind: 1) In a collisionless environment, how is the energy which is initially deposited in the torsional modes (with their relatively high densities of state) coupled to other, higher-frequency modes of bond stretches and more rigid (higher-energy) torsional motions? 2) What is the time scale of this coupling, and how does it vary depending on the molecular environment and the nature of the excited-state preparation? In the gas phase, a very similar process is the collision-induced level-crossing non-adiabatic decay in bi-molecular reactions involving electronically excited species. Even more common in condensed phases is solvent-mediated non-radiative decay, one of the primary energy channels in photolysis. Indeed, as indicated above, reaction dynamics may be greatly affected by the presence of solvent. Understanding the IVR process in the gas phase can also cast light on the effects of solvation in condensed phases. Additionally, while IVR is usually studied in the energy domain by following the frequency signatures associated with specific ro-vibrational motion of molecules, UED provides a different perspective in studying IVR by monitoring the structural evolution directly.

Attempts to understand our structural results, and the implications for IVR

First, our result of a highly unexpected 1.7-1.8 Å C-C peak in the radial distribution curves suggests a rather long IVR time for the molecular motions coupled with this internuclear separation. This observation begs the question: what are the reaction coordinates involved in the manifestation of this extremely long bond distance? Perhaps a clue to the answer of this question lies in the conclusion that the

averaged product structure is highly non-thermal, resembling an asymmetric *cZc*, or a more folded *cZt*, even up to 400 ps after the reaction began; thus, the non-thermal torsional motions around the C-C single bonds survive for at least 400 ps. As shown schematically at the top of Fig. 6.1.7, an inverted population in the torsional rotor mode has a higher probability to be seen in the geometries found near the classical turning points—i.e., the "folded" conformations found in both halves of *cZc* (and one half of *cZt*)—in qualitative agreement with our observations.

As described elsewhere in this document, two attempts were made to theoretically explain the presence of the 1.75 Å peak. We re-iterate that while the two fitting procedures used address the 1.75 Å peak in two rather different pictures, both models unmistakably assign the 1.75 Å peak to the C-C single bonds. In the first model, the origin of the averaged 1.75 Å peak is directly associated a non-Boltzmann population distribution of the local C-C stretching mode. A dual-Gaussian probability function was used to simulate a possible non-thermal bond-stretching. In such a scenario, the averaged 1.75 Å bond distance would originate from density at the *outer* classical turning point in the local Morse potential, whereas an averaged 1.4 Å distance would originate from density at the inner classical turning point. The energetics and eigenstate analysis showed that with 1.75 Å as the averaged outer turning position, the inner turning position should actually be around 1.2-1.3 Å, with a (demanding) mean vibrational energy of 25 kcal/mole per bond (see Figs 6.1.8(a) and 6.1.8(b)).

The second model, which employed a Monte Carlo search for the best-fitting Z-matrix representations of the averaged structure at each time point, instead indicated that one C-C bond was elongated to 1.75 Å while the other was somewhat shorter, at 1.35 Å (this is a subtle difference from the previous model, which considered *both* bonds to be in an *effective superposition* of long and short). If one performs a calculation that adiabatically follows the *ab initio cZc* structure (with $\tau_1=\tau_2\sim42°$), stretching one of the C-C bonds to 1.75 Å takes about 10 kcal/mole. Also it is interesting to note that as the C-C bond was stretched, and the rest of the molecule was allowed to re-organize adiabatically from its initial *cZc* conformation, the molecule adopted a more open, asymmetric structure that is *not that different* from that obtained from the Z-matrix representation refinement of the effective averaged structure (e.g., with "G" referring to Gaussian, and "Z" referring to the Z-matrix data-refinement procedure: $\tau_1(G) \sim 33°$, $\tau_1(Z) \sim 20°$; $\tau_2(G) \sim 59°$, $\tau_2(Z) \sim 63°$) (However, we don't want to make to big a deal of this fact, as other structural features don't compare as well—for example, Gaussian fails to make the second C-C bond shorter than the equilibrium value).

Thus, it could be argued that the second model—in which the long C-C distance really represents the time-averaged internuclear separation of one of the bonds, and which originates from coupling to the (manifestly non-thermal) torsional motion—provides a better, more self-consistent picture of the product structure and non-equilibrated behavior. Moreover, the preliminary analysis of the CHT data suggests that a thermalized model (energy-equipartioned among modes) of hot CHT

after internal conversion provides a good fit to the observed results without requiring the existence a 1.75 Å C-C bond; this suggests that the non-thermal behavior manifested by the HT product results from the presence of the "floppy" torsional modes. This evidence provides further support for the notion that the long CC single bond distance somehow originates from the non-thermal torsional mode vibrations.

An attempt at an intuitive classical picture for the interplay of the non-thermal torsional motion and the exceptional C-C bond distance

In a simple classical picture, one may visualize the two counter-propagating "rotors" of HT trying to pass by each other. At the classical turning points, the kinetic energy must be stored in the molecule, perhaps through stretching/compressing of the directly-coupled bond distances. In an asymmetric encounter (which we think we see), it is reasonable to stretch more on the faster moving arm as compared to the compression of the slow moving arm. This classical picture might be justified by the spatially localized initial preparation of a non-thermal ro-vibrational state resembling a wave-packet preparation on an excited vibrational manifold, and the close coupling of this motion to the reaction pathway following the ring-opening of CHD. (Note this classical "wavepacket" preparation refers to an intra-molecular vibrational mode of a single molecule which just landed in the ground state surface. However, because the molecules leave the excited electronic surface randomly (characterized by a 32 ps life time), the preparation of the ensemble of molecules in the ground state surface is not a coherent one.) Additionally, it has been proposed that it there is some long-lived

"combination mode" comprised of the torsional motion and an asymmetric CC skeletal stretch.

Some final thoughts on our ability to study IVR in these systems

Studies of vibrational motion with electron diffraction are complimentary to those performed with spectroscopic methods. The high-frequency local mode motions are associated with the mean amplitudes of vibration of the directly bonded distances. On the one hand, through the temperature effects seen via damping and frequency shifts in the molecular interference patterns caused by the increased mean amplitude motions, the local force fields can be extrapolated, complementing the spectroscopic information. On the other hand, the low-frequency large-amplitude motions can be studied through the changes of the indirect bond distances. The slow IVR processes associated with these motions, which usually are very hard to investigate directly by spectroscopic techniques, can now be studied by UED as suggested in this work. The latter behavior is particularly relevant to larger, biologically-relevant systems. We should add that the analytical difficulties expected from such macromolecules are also addressed in our newly developed data-analysis procedures, in which the Z-matrix becomes the central pivoting element linking the molecular dynamical modeling of the UED data with the vastly available biomolecular structure databanks (not to mention freeing us from having to manually develop geometrically consistent equations for such macromolecules—no doubt a Herculean task). The separation of rigid-frame molecular motions from the floppy, often classical-like, large-amplitude motions

provides an additional advantage for using UED for studying complex molecular systems.

6.1.8 Summary

We observed a long-lived, far-from-equilibrium molecular structure for 1,3,5-hexatriene (HT), formed by the ultrafast ring opening of CHD[2,7,11,25]. Figure 6.1.4a shows the evolution of radial distribution curves for the ring-opening reaction of CHD. The product-isolated HT diffraction signals were significantly damped at all time points (manifested as peak broadening in the $_{pi}f(t; r)$ curves), indicating the vibrationally hot nature of the product structure. Shown below the experimental data in Fig. 4b are theoretical $f(r)$ curves for three hot conformers of HT (labeled *cZc*, *cZt*, and *tZt* apropos the conformation of torsion angles about the C-C single bonds). Close inspection of the experimental $f(t; r)$ curves reveals greater similarity to the theoretical *cZc* curve than to that of the lower-energy *tZt* conformer. Furthermore, an anomalous peak at ~1.7 Å can be seen as a shoulder in all the experimental $f(t; r)$ curves; the presence of this peak—which is ~0.2 Å away from any expected equilibrium distance—was confirmed with a second diffraction experiment.

Least-squares refinement of the structural parameters, in conjunction with a Monte Carlo sampling procedure, yielded an average HT molecular structure at each time slice. These HT structures showed no *tZt* character, but consistently manifested a configuration intermediate between *cZc* and *cZt*—far removed from a thermally equilibrated conformer distribution of ~41% *tZt*, ~45% *cZt*, and ~14% *cZc* at 2100 K

(estimated from *ab initio* calculations of the conformer energies). Moreover, the ~1.7 Å peak observed in the $f(t; r)$ curves was assigned to one C-C single bond in HT—a highly non-equilibrium value for a C-C internuclear separation. The remarkable departure from the predicted equilibrium conformation, together with the unusual C-C bond length, demonstrates the far-from-equilibrium nature of the HT structure. The HT structures, formed with a time constant of 32 ± 2 ps (Fig. 6.1.5a), remained virtually unchanged over the course of the experiment (~400 ps). Time-averaged values for selected structural parameters are summarized in Table 1, along with corresponding ab initio values for the three HT conformers. The observation of far-from-equilibrium structures at all points in time indicates that unlike CHT (see section 6.2), energy partitioning within HT is slow with respect to both the rate of product formation and the time scale of the UED experiment.

This distinct non-equilibrium behavior exhibited by CHT (see section 6.2) and HT can be understood in terms of different energy flow pathways. Both systems exhibit damping of the $sM(t; s)$ curves, establishing the vibrationally hot nature of the product structures. However, while energy equipartitioning in CHT is complete within our time resolution of ~5 ps, incomplete energy partitioning in HT, even up to 400 ps, results in the far-from-equilibrium configuration. As shown schematically in Fig. 6.1.7, the *cZc*-like conformation of HT corresponds to an inverted population on the potential energy surface (projected along the coordinate of torsional motion), with significant density at the classical turning points. Moreover, the ~1.7 Å average distance attributed to one C-C bond would require depositing ~15 kcal/mol of the

available ~90 kcal/mol in that C-C bond (assuming a simple Morse oscillator model)—further evidence for an inequitable partitioning of energy. Coincidence of the inverted torsional configuration and the stretched C-C bond over time strongly suggests that these two structural features are coupled in some way, and may reflect a long-lived, low-frequency cooperative (hybrid) motion comprised of both torsion and asymmetric stretching of the carbon skeleton. Conceptually, one may picture that as the molecule oscillates between the turning points of the potential well (Fig. 6.1.7), the stretched C-C distance is shifted continuously from one C-C single bond to another and at the turning points, the torsional energy is partially stored in the C-C bond-stretching coordinates. The persistence of this far-from-equilibrium structure over 400 ps suggests a bottleneck in energy transfer from the inferred hybrid motion to other (higher frequency) modes after the initial energy deposition.

The dissimilar reaction pathways followed by CHT and CHD can be expected to affect the dynamical behavior of these molecules. Recent ab initio calculations[26] have suggested that at the point of descent from the excited state to the ground state, CHT adopts a near-planar geometry, as opposed to the minimum-energy boat-shaped geometry at equilibrium. Thus, all C-C skeletal modes are engaged in the initial structural motion on the ground state; because the ring remains intact, these modes remain strongly coupled—leading to rapid vibrational energy redistribution. For CHD, however, ring opening leads to a significant share of the energy being initially deposited in the torsional motion, much of which remains localized in the aforementioned hybrid motion for over 400 ps. The remaining internal energy is

rapidly randomized among the other HT modes in a manner akin to that in CHT. The non-equilibrium features of the HT structure may, in fact, reflect a memory of the asymmetric geometry at the instant of ring-opening, suggesting that ring opening of CHD follows a symmetry-breaking pathway (i.e., one that violates the C_2 symmetry of the parent structure)[27]. Thus, our results suggest that the initial ground-state product geometry profoundly influences the fate of energy disbursement in high-energy molecules.

It is interesting to note that while we found virtually no contribution from hot CHD in the HT product (despite our sensitivity to hot "parent" structures in CHT), condensed-phase experiments have shown a 60/40 branching ratio for the CHD reformation/ring-opening pathways[2]. This near-absence of hot parent structures, along with the long time observed for ring opening (~30 ps), signifies the crucial role played by the solvent in redirecting the fate of the reaction compared to the gas phase. For instance, the increased steric hindrance to ring opening in the solvent may favor the reformation of CHD over ring opening.

We have demonstrated the ability of UED to generate and observe isolated, high-energy molecular structures. While non-thermal effects have been previously reported in the literature[28-32], to our knowledge this is the first time that such a far-from-equilibrium structure—both in terms of torsional conformation and the stretched C-C bond in HT—has been directly observed in isolated polyatomic molecules. The long-lived, asymmetric HT structure shows that the relaxation dynamics of complex molecules at extreme energies can be highly non-intuitive. Future UED studies on

related and more complicated systems, including biomolecules, promise to shed more light on the intrinsic behavior of molecules at high energy. Electron diffraction has long been a powerful tool for studying conformations of static equilibrium molecular structures. With the added dimension of time, UED is now poised to explore the rich structural and energetic features underlying conformational changes in isolated molecular systems.

6.2 CHT → CHT @ 267 nm

6.2.1 Introduction

The photodynamics of 1,3,5-cyclohexatriene (CHT) are similar to those of CHD in that UV excitation involves two excited potential energy surfaces, and that vibrationally hot products are formed through two conical intersections (or avoided crossings). The major difference between the behavior of these two systems is that in the case of CHT, the product ("hot" CHT) formed via a [1,7]-H shift is indistinguishable from the product formed via the internal conversion (except possibly by the distribution of the high internal energy at short times—however, we do not expect to be able to resolve this). Like CHD, CHT has also received considerable attention in the literature,[33-42] and the ultrafast dynamics concerning its internal conversion and H-migration have been studied both experimentally[4,43-47] and theoretically[26,48].

Recent theoretical calculations showed that the initial UV excitation populates the 1A″ state.[26,48] The subsequent internal conversion proceeds via two conical intersections, and the hydrogen migration occurs on the 2A′ surface within the first electronically excited state. Early UV-Raman pump-probe spectroscopy with a time resolution of 1.7 ps obtained 26 ps as the appearance time for the photoproduct.[43] However, as with the case of CHD, this "long" time constant has been challenged by other recent theoretical and experimental work. For example, Steuhl et al., based on their theoretical study, suggested that 26 ps is much too long, and Borell et al. derived a decay time constant of the electronically excited CHT of about 55 fs from the total

ion yield in [1+1] multiphoton ionization experiments. However, the authors had to estimate the absorption cross-section for the ionization process by the second photon.

In a very recent work by Fuss and coworkers,[47] femtosecond dissociative intense-filed ionization was used to study the excited state dynamics, and three distinct time scales attributable to the excited states were observed. These authors assigned the first two time constants (10 fs and 60 fs) to the wave packet travelling through two regions of the 1A″ surface, and assigned the third constant (70 fs) to the departure from the 2A′ surface and subsequent repopulation of the ground state. On the basis of their observation, they suggested that the ultrafast nature of the rates prove the existence of a continuous pathway that leads the wave packet from the initially excited 1A″ state, through the dark state 2A′, finally to the ground-state surface via two easily accessible conical intersections.

Interestingly, the claimed ability of Fuss and coworkers to follow the stepwise excited-state dynamics using the intense-field ionization was challenged by a more recent study by Hertwig et al.[46] In this work, femtosecond transient absorption was used; CHT in the liquid phase was excited at 266 nm and the transient absorption at 400 nm was monitored. Based on the transient at 400 nm, they reported an excited-state lifetime of 110 fs, and concluded that the stepwise dynamics suggested by Fuss and coworkers can not be supported by their results.

In our UED study on CHT, a time constant of ~16 ps was obtained for the recovery of the thermally-equilibrated, hot CHT in our preliminary analysis. In principle, the time constant of 16 ps need not depend on our model for the

vibrationally hot CHT; in other words, 16 ps is merely the time constant of whatever changes are noticeable to electron diffraction. However, with the fact that our UED data agree with the thermally equilibrated photoproduct model surprisingly well, and with the assumption that the electronic energy in the excited states is released into the vibrational energy of the ground state (with either a thermal or non-thermal distribution), our time constant can be best assigned to the appearance of hot CHT molecules, and the relevant time constant for IVR is much faster than the time constant for the appearance.

6.2.2 Experimental Setup and Method

UED data were obtained with our third-generation apparatus[12]. Briefly, the output from an amplified Ti:Sapphire laser system (350 μJ, 120 fs, 267 nm, 1 kHz repetition rate) was split into two beams; the stronger beam was directed into the scattering chamber to initiate the excitations, while the weaker beam was directed into a delay line, and then focused onto a back-illuminated photocathode to generate electron pulses via the photoelectric effect (30 kV, de Broglie wavelength: λ =0.067 Å, ~25,000 electrons per pulse at ~4 ps). The molecular sample was introduced into the chamber via a jet expansion source. After interacting with the molecular beam, diffracted electrons were detected with a low-noise CCD camera (active *s* range: ~1.5-18.5 Å). The reaction zero-of-time was determined by the ion-induced lensing technique[13] using CF_3I gas (Aldrich, 99%). Samples of CHT (Fluka, 95%) were degassed with several freeze-pump-thaw cycles, and high-purity xenon (Spectra

Gases, 99.999%) was used as an atomic reference gas[14]. The nozzle temperature for the diffraction experiments was maintained at 130 °C.

2D diffraction images were radially averaged to generate 1D total intensity curves, and experimental $sM(s)$ curves were calculated[15] and fit to theoretical $sM(s)$ curves derived from structural parameters given by previous experimental or ab initio results; $s = (4\pi/\lambda)\cdot\sin(\theta/2)$, where θ is the scattering angle. Diffraction signals from ground-state structures are obtained by timing the arrival of the electron pulse to occur prior to that of the photo-initiating laser pulse, i.e., at a negative time (or with the laser blocked). Time-resolved diffraction images were obtained by varying the delay between the arrival of the light and electron pulses within the interaction region; we subtract a reference diffraction signal obtained at a negative time from the signals obtained at positive times, yielding a time-dependant difference signal comprised equally of 1) negative contributions from the parent structures, and 2) positive contributions from the product structures, thereby permitting the relative fractions of the parent and product structures to be determined at each point in time[16]. Diffraction signals from the product structures were isolated by adding the parent diffraction signal obtained at a negative time—scaled by the fraction of parent molecules depleted at each time point—to the diffraction difference curves, thereby canceling out the parent contribution.[16,17] Vibrationally excited product structures were modeled by correcting for the increased l values; l values for thermally equilibrated structures were estimated either with the ASYM40 program[18] or by extrapolating the empirical equations given in Refs. [19-22,49] to high temperatures[15]. Extrapolated l values were

also used to relate r_e (the geometrically consistent zero-Kelvin equilibrium internuclear distance), to r_a (the internuclear distance measured by electron diffraction), using the equation: $r_a \approx r_e + (3/2)\cdot a\cdot l^2 + dr - l^2/r$, where a is the anharmonicity constant for the bond and dr is the small correction due to centrifugal distortion.[15] The geometrically consistent molecular structures are built using internal coordinates of the molecules, defining the configuration space. The Monte Carlo sampling procedure is then applied to search the minima in the configuration space closest to the data, followed by least-squares refinement of the molecular structure.

6.2.3 Ground State Data

Figure 6.2.1 shows typical ground-state diffraction images for CHT and the corresponding structures. The vertical lines in $f(r)$ approximate the relative contributions from various internuclear pairs; the height of each line scales with $(Z_iZ_j)^2$ / r_{ij} multiplied by the degeneracy, where Z is the nuclear charge and r_{ij} is the internuclear distance. The first peak corresponds to the directly bonded C-C bonds and the second, third, and forth peaks are from indirectly bonded (non-bonded) C···C bonds. Note that CHT has three different kinds of non-bonded C···C internuclear distances, which are observed in the $f(r)$ curve.

6.2.4 Time-Resolved Data

The first system, CHT, undergoes an ultrafast hydrogen shift following UV

excitation[26,43,46,47], resulting in the subsequent reformation of CHT with high internal energy. Despite the likeness of the parent and product structures in this reaction, the sensitivity of our third-generation apparatus allowed us to directly monitor the subtle structural modifications induced by photo-excitation. Except for their relative intensities, all the product-isolated $sM(t; s)$ curves exhibited similar features. Figure 6.2.2 shows the experimental CHT curve averaged from 75 to 400 ps, along with the theoretical curves generated using the same internuclear distances (those of the parent structure[50]), but with varying l values. The experimental diffraction curve is clearly more damped than the theoretical one obtained from a vibrationally "cold" parent structure (403 K). However, improved agreement is obtained between experiment and theory with increasing l values. The l values giving the best agreement correspond to an effective vibrational "temperature" roughly three times that estimated for a Boltzmann energy distribution (~2200 K) among the vibrational modes of CHT[37]. That the product CHT structure has similar internuclear distances as the parent, but mean amplitudes of vibration dramatically higher than those resulting from a Boltzmann assumption, clearly indicates the vibrationally hot, near-equilibrium nature of the product. The near-equilibrium nature of the structure can be explained by equipartitioning of the available energy throughout the molecule, albeit with slightly inverted vibrational distributions. The prevalence of this near-equilibrium configuration at all time points suggests that energy partitioning is rapid with respect to the rate of formation (16 ± 3 ps; Fig. 6.2.2 inset) of the hot CHT product. Recent ab initio calculations[26] have suggested that at the point of descent from the excited state

to the ground state, CHT adopts a near-planar geometry, as opposed to the minimum-energy boat-shaped geometry at equilibrium. Thus, all C-C skeletal modes are engaged in the initial structural motion on the ground state; because the ring remains intact, these modes remain strongly coupled—leading to rapid vibrational energy redistribution.

References

1. McDiarmid, R. & Sabljic, A. Valence transitions in 1,3-cyclopentadiene, 1,3-cyclohexadiene, and 1,3-cycloheptadiene. *J. Chem. Phys.* **83**, 2147-2152 (1985).

2. Lawless, M. K., Wickham, S. D. & Mathies, R. A. Resonance Raman View of Pericyclic Photochemical Ring-Opening Reactions: Beyond the Woodward-Hoffmann Rules. *Acc. Chem. Res.* **28**, 493-502 (1995).

3. Trulson, M. O., Dollinger, G. D. & Mathies, R. A. Femtosecond Photochemical Ring Opening Dynamics of 1,3-Cyclohexadiene from Resonance Raman Intensities. *J. Am. Chem. Soc.* **109**, 586-587 (1987).

4. Reid, P. J., Wickham, S. D. & Mathies, R. A. Picosecond UV resonance Raman spectroscopy of the photochemical hydrogen migration in 1,3,5-cycloheptatriene. *J. Phys. Chem.* **96**, 5720-5724 (1992).

5. Reid, P. J., Doig, S. J., Wickham, S. D. & Mathies, R. A. Photochemical Ring-Opening Reactions Are Complete in Picoseconds: A Time-Resolved UV Resonance Raman Study of 1,3-Cyclohexadiene. *J. Am. Chem. Soc.* **115**, 4754-4763 (1993).

6. Pullen, S., II, L. A. W., Donovan, B. & Sension, R. J. Femtosecond transient absorption study of the ring-opening reaction of 1,3-cyclohexadiene. *Chem. Phys. Lett.* **242**, 415-420 (1985).

7. Lochbrunner, S., Fuss, W., Schmid, W. E. & Kompa, K. L. Electronic

relaxation and ground-state dynamics of 1,3-cyclohexadiene and *cis*-hexatriene in ethanol. *J. Phys. Chem. A* **102**, 9334-9344 (1998).

8. Pullen, S. H., Anderson, N. A., II, L. A. W. & Sension, R. J. The ultrafast photochemical ring-opening reaction of 1,3-cyclohexadiene in cyclohexane. *J. Chem. Phys.* **108**, 556-563 (1998).

9. Fuß, W., Schikarski, T., Schmid, W. E., Trushin, S. & Kompa, K. L. Ultrafast dynamics of the photochemical ring opening of 1,3-cyclohexadiene studied by multiphoton ionization. *Chem. Phys. Lett.* **262**, 675-682 (1996).

10. Trushin, S. A., Fub, W., Schikarski, T., Schmid, W. E. & Kompa, K. L. Femtosecond photochemical ring opening of 1,3-cyclohexadiene studied by time-resolved intense-field ionization. *J. Chem. Phys.* **106**, 9386-9389 (1997).

11. Fuß, W., Schmid, W. E. & Trushin, S. A. Time-resolved dissociative intense-laser field ionization for probing dynamics: Femtosecond photochemical ring opening of 1,3-cyclohexadiene. *J. Chem. Phys.* **112**, 8347-8362 (2000).

12. Ihee, H. *et al.* Direct Imaging of Transient Molecular Structures with Ultrafast Diffraction. *Science* **291**, 458-462 (2001).

13. Dantus, M., Kim, S. B., Williamson, J. C. & Zewail, A. H. Ultrafast Electron Diffraction. 5. Experimental Time Resolution and Applications. *J. Phys. Chem.* **98**, 2782-2796 (1994).

14. Lobastov, V. A., Ewbank, J. D., Schäfer, L. & Ischenko, A. A. Instrumentation for time-resolved electron diffraction spanning the time domain from microseconds to picoseconds. *Rev. Sci. Instrum.* **69**, 2633-2643 (1998).

15. Hargittai, I. & Hargittai, M. *Stereochemical Applications Of Gas-Phase Electron Diffraction* (VCH, New York, 1988).

16. Ihee, H., Cao, J. & Zewail, A. H. Ultrafast electron diffraction: structures in dissociation dynamics of $Fe(CO)_5$. *Chem. Phys. Lett.* **281**, 10-19 (1997).

17. Cao, J., Ihee, H. & Zewail, A. H. Ultrafast electron diffraction: determination of radical structure with picosecond time resolution. *Chem. Phys. Lett.* **290**, 1-8 (1998).

18. Hedberg, L. & Mills, I. M. ASYM20: A Program for Force Constant and Normal Coordinate Calculations, with a Critical Review of the Theory Involved. *J. Mol. Spectrosc.* **160**, 117-142 (1993).

19. Mastryukov, V. S. & Cyvin, S. J. Relations between mean amplitudes of vibration and corresponding internuclear distances I. Bonded and nonbonded carbon-carbon distances. *J. Mol. Struct.* **29**, 15-25 (1975).

20. Cyvin, S. J. & Mastryukov, V. S. Relations between mean amplitudes of vibration and corresponding internuclear distances II. Bonded carbon-carbon distances. *J. Mol. Struct.* **30**, 333-337 (1976).

21. Mastryukov, V. S. & Osina, E. L. The relationship between vibrational amplitudes and internuclear distances IV. Amplitudes for element-hydrogen distances. *Zhu. Struk. Khim.* **17**, 172-174 (1976).

22. Mastryukov, V. S., Osina, E. L., Vilkov, L. V. & Cyvin, S. The relationship between vibrational amplitudes and internuclear distances V. Bonded and nonbonded CH distances. *Zhu. Struk. Khim.* **17**, 80-85 (1976).

23. Fuss, W. *et al.* Ring Opening in the Dehydrocholesterol--Previtamin D System Studied by Ultrafast Spectroscopy. *J. Phys. Chem.* **100**, 921-927 (1996).

24. Anderson, N. A., Shiang, J. J. & Sension, R. J. Subpicosecond Ring Opening of 7-Dehydrocholesterol Studied by Ultrafast Spectroscopy. *J. Phys. Chem. A* **103**, 10730-10736 (1999).

25. Andersen, N. A., Pullen, S. H., II, L. A. W., Shiang, J. J. & Sension, R. J. Ultrafast polyene dynamics in solution: The conformational relaxation and thermalization of highly excited cis-hexatriene as a function of initial conformation and solvent. *J. Phys. Chem. A* **102**, 10588-10598 (1998).

26. Steuhl, H.-M., Bornemann, C. & Klessinger, M. The Mechanism of the Photochemical Hydrogen Migration in 1,3,5-Cycloheptatriene: A Theoretical Study. *Chem. Eur. J* **5**, 2404-2412 (1999).

27. Garavelli, M. *et al.* Potential-energy surfaces for ultrafast photochemistry. *Faraday Discuss.* **110**, 51-70 (1998).

28. Zewail, A. H. *Femtochemistry: atomic-scale dynamics of the chemical bond using ultrafast lasers in Les Prix Nobel* (Almqvist & Wiksell, Stockholm, 1999).

29. Mizutani, Y., Uesugi, Y. & Kitagawa, T. Intramolecular vibrational energy redistribution and intermolecular energy transfer in the (d,d) excited state of nickel octaethylporphyrin. *J. Chem. Phys.* **111**, 8950-8962 (1999).

30. Helliwell, J. R. & Renzepis, P. M. (eds.) *Time-Resolved Diffraction* (Oxford University Press, New York, 1997).

31. Rousse, A. *et al.* Non-thermal melting in semiconductors measured at femtosecond resolution. *Nature* **410**, 65-68 (2001).

32. Techert, S., Schotte, F. & Wulff, M. Picosecond x-ray diffraction probed transient structureal changes in organic solids. *Phys. Rev. Lett.* **86**, 2030-2033 (2001).

33. Jensen, F. R. & Smith, L. A. The Structure and Interconversion of Cycloheptatriene. *J. Am. Chem. Soc.* **86**, 956-957 (1964).

34. Maier, G. The Norcaradiene Problem. *Angew. Chem. Int. Ed.* **6**, 402-413 (1967).

35. Jarzecki, A. A., Gajewski, J. & Davidson, E. R. Thermal Rearrangements of Norcaradiene. *J. Am. Chem. Soc.* **121**, 6928-6935 (1999).

36. Rubin, M. B. Photolysis of Two Trichclic Nonenediones. Direct Observation of Norcaradiene. *J. Am. Chem. Soc.* **103**, 7791-7792 (1981).

37. Paulick, W., Jung, C., Kempka, U., Suhnel, J. & Gustav, K. Interpretation of the vibraional spectra and calculation of the geometries of cycloheptatriene, 7-d-cycloheptatriene and phenyl substituted cycloheptatrienes. *J. Mol. Struct.* **85**, 235-240 (1981).

38. Manner, W. L., Hostetler, M. J., Girolami, G. S. & Nuzzo, R. G. Structures and Reativities of Cycloheptane, Cycloheptene, 1,3-Cycloheptadiene, and Cycloheptatriene on Pt(111). *J. Phys. Chem. B* **103**, 6752-6763 (1999).

39. Toyota, A., Koseki, S. & Shiota, M. Ab Initio MCSCF Study on the Pseudo-Jahn-Teller Distortion from Planarity in Cycloheptatriene, Heptalene, and

Heptafulvalene. *J. Phys. Chem. A* **104**, 5343-5350 (2000).

40. Eis, M. J. v., Linde, B. S. E. v. d., Kanter, F. J. J. d., Wolf, W. H. d. & Bickelhaupt, F. Dichlorocarbene Addition to [5]Metacyclophane; Experimental and Calculational Evidence for a [1,5] Sigmatropic Chlorine Shift in a Bridged Cycloheptatriene. *J. Org. Chem.* **65**, 4348-4354 (2000).

41. Anet, F. A. L. Ring Inversion in Cycloheptatriene. *J. Am. Chem. Soc.* **86**, 458-460 (1964).

42. Aonuma, S., Komatsu, K. & Takeuchi, K. Energy Barriers for the Ring Inversion of 1,2:3,4:5,6-Tris(bicyclo[2.2.2]octeno)- and 1,2,3,4,5,6-Hexamethylcycloheptatrienes. *Chem. Lett.*, 2107-2110 (1989).

43. Reid, P. J., Shreve, A. P. & Mathies, R. A. Resonance Raman Intensity Analysis of the Photochemical Hydrogen Migration in 1,3,5-Cycloheptatriene. *J. Phys. Chem.* **97**, 12691-12699 (1993).

44. Fuß, W. *et al.* Ultrafast Photochemical Pericyclic Reactions and Isomerizations of Small Polyenes. *Ber. Bunsenges. Phys. Chem.* **101**, 500-509 (1997).

45. Samuni, U., Kahana, S. & Haas, Y. Matrix Photochemistry of Cycloheptatriene: Site Effects. *J. Phys. Chem. A* **102**, 4758-4768 (1998).

46. Hertwig, A., Hippler, H., Schmid, H. & Unterreiner, A.-N. Direct time-resolved UV-absorption study on the ultrafast internal conversion of cycloheptatriene in solution. *Phys. Chem. Chem. Phys.* **1**, 5129-5132 (1999).

47. Trushin, S. A., Diemer, S., Fub, W., Kompa, K. L. & Schmid, W. E. Femtosecond dynamics of hydrogen migration and internal conversion in

cycloheptatriene and derivatives studied by intense-filed dissociative ionization. *Phys. Chem. Chem. Phys.* **1**, 1431-1440 (1999).

48. Bornemann, C. & Klessinger, M. Excited-State Energy and Geometry Changes during the [1,7]H-Shift Reaction of Cycloheptatriene. *Org. Lett.* **1**, 1889-1891 (1999).

49. E.L. Osina, V. S. M., L.V. Vilkov, S. Cyvin. Relationship between the vibration amplitudes and the internuclear distances. III. Amplitudes for the CCH, CH distances and Badger's rule. *J. Struct. Chem.* **17** (1976).

50. Traetteberg, M. The molecular structure of 1,3,5-cycloheptatriene in the vapor phase as determined by the sector electron diffraction method. *Act. Chem. Scand.* **86**, 4265-4270 (1964).

51. Lauro, C. D. & Neto, N. Vibrational spectrum and normal mode analysis of 1,3-cyclohexadiene. *J. Mol. Struct.* **3**, 219-226 (1969).

52. Panchenko, Y. N., Krasnoshchiokov, S. V., George, P. & Bock, C. W. An Ab Initio Structural and Vibrational Analysis of gauche, Trans, trans-and gauche, Cis, trans-Hexa-1,35-trienes. *Struct. Chem.* **3**, 15-26 (1992).

Table 6.1.1 Selected refined structural parameters for the far-from-equilibrium HT structure

Structural Parameter	**Mean value**[†]	σ_{mean}[‡]	σ_{fit}[§]	*cZc*[¶]	*cZt*[¶]	*tZt*[¶]
r(C1=C2)	**1.29 Å**	0.06 Å	0.04 Å	1.338 Å	1.342 Å	1.342 Å
r(C2-C3)	**1.40 Å**	0.10 Å	0.02 Å	1.471 Å	1.453 Å	1.452 Å
r(C3=C4)	**1.41 Å**	0.08 Å	0.04 Å	1.350 Å	1.353 Å	1.355 Å
r(C4-C5)	**1.71 Å**	0.05 Å	0.02 Å	1.471 Å	1.465 Å	1.452 Å
r(C5=C6)	**1.32 Å**	0.04 Å	0.03 Å	1.338 Å	1.341 Å	1.342 Å
ϕ_1(C1C2-C3C4)	**84°**	41°	11°	35.5°	-174.7°	180°
ϕ_2(C3C4-C5C6)	**15°**	22°	11°	35.5°	37.7°	180°

[†]Structural parameters obtained from averaging over all time points.

[‡]Standard deviation (spread) of the mean value.

[§]Standard deviation (error) of the least-squares fit.

[¶]Structural parameters for the HT conformers, calculated using ab initio methods (B3LYP/6-31G** basis set), shown for comparison.

Figure Captions

Figure 6.1.1: Schematic of the relevant potential energy surfaces for the CHD photoreaction. Ball-and-stick models for CHD and the relevant static structures of HT are also shown within the figure.

Figure 6.1.2: Ground-state diffraction images and the corresponding *f(r)* curve for CHD. The vertical lines in *f(r)* approximate the relative contributions from various internuclear pairs; the height of each line scales with $(Z_iZ_j)^2$ / r_{ij} multiplied by the degeneracy, where Z is the nuclear charge and r_{ij} is the internuclear distance.

Figure 6.1.3: Schematic of data processing procedures used for the CHD data, including the generation of the "diffraction-difference" signal and the "product-isolated" signal.

Figure 6.1.4: Product-isolated UED data for the CHD experiment obtained at various delays, along with the corresponding experimental curves for the CHD parent (top curve), and *ab initio* curves for the three canonical HT conformers extrapolated to 2100 K, and CHD extrapolated to 2400 K. **(a)** The UED data shows Experimental ${}_{pi}sM(t; s)$ curves, along with theoretical curves (solid lines), superimposed on corresponding theoretical curves generated using the first analytical approach (i.e., with Gaussian distribution functions for covalent CC distances, and a distribution of dihedral angles for a geometrically consistent model of HT). **(b)** Corresponding experimental and theoretical ${}_{pi}f(t; r)$ curves. Note the small peak at ~1.7 Å (more prevalent in the experimental curves).

Figure 6.1.5: (Top) Time dependence of HT fraction obtained upon final refinement of the CHD data, showing the time scale of ring opening. After consideration of the electron and laser pulse widths, the time constant for the observed exponential rise is 33 ± 3 ps. **(Bottom)** Relative fractions of the canonical HT conformers obtained from the refinements shown in Fig. 6.1.4. The data generally supports a non-thermal distribution of torsion angles, showing a majority of *cZc*, with significant *cZt* and virtually no *tZt*.

Figure 6.1.6: Product-isolated UED data for the CHD experiment obtained at various delays, along with the corresponding experimental curves for the CHD parent (top curve), and *ab initio* curves for the three canonical HT conformers extrapolated to 2100 K, and CHD extrapolated to 2400 K. **(a)** The UED data shows Experimental ${}_{pi}sM(t;\ s)$ curves, along with theoretical curves (solid lines), superimposed on corresponding theoretical curves generated using the second analytical approach (i.e., with the Monte Carlo χ^2 minimization and Z-matrix representation of an effectively averaged static structure). **(b)** Corresponding experimental and theoretical ${}_{pi}f(t;\ r)$ curves. Note the improved results compared to Fig. 6.1.4.

Figure 6.1.7: Schematic potential energy landscape relevant to the formation of HT. A probability density curve (blue) on the HT ground-state surface depicts the high-energy nature of the product structure. The higher density near the classical turning points reflects significant population in *cZc*-type conformations; the refined molecular structures shown at these points represent the average far-from-equilibrium structure over 400 ps. The "faded" configurations portray the possible intermediate stages of

the molecule as it oscillates between the turning points. The inset shows the corresponding ab initio 2D potential energy surface governing HT torsion angles (ϕ_1 and ϕ_2) about the C-C single bonds. The white curves illustrate possible trajectories leading to a time-averaged structure with considerable *cZc* and *cZt* character, but virtually no contribution from *tZt*.

Figure 6.1.8: (a) Results for a best-fit of a Gaussian distribution (in energy, P(r)) of a population of Morse oscillators to a two-Gaussian fit (centers at 1.42 and 1.75 Å, effective *l* values (σ) are 0.07 Å for both, normalized amplitudes are 0.475 and 0.525) of the C-C probability density obtained from UED. **(b)** The Gaussian energy distribution optimized to get the results in (a); E_0 = 8830 cm^{-1}, ΔE = 1945 cm^{-1}. The points mark the Morse eigenenergies; the distribution peaks at $v = 7$.

Figure 6.1.9: Time-resolved formation of far-from-equilibrium HT structures following the ring opening of CHD. **a**, Fourier-filtered $f(t; r)$ curves showing product evolution; note the small shoulder at ~1.7 Å. The inset depicts the time dependence of the HT fraction, elucidating the apparent time scale of ring opening ($\tau = 32 \pm 2$ ps). **b**, Top: *ab initio* $f(r)$ curve (red) for the CHD parent structure at 403 K. Middle: comparison of selected experimental product-isolated $f(t; r)$ curves (blue) with corresponding structural fits (green). Bottom: *ab initio* $f(r)$ curves (red) for the three HT conformers (extrapolated to 2100 K) and for hot CHD (extrapolated to 2400 K) shown for comparison. These equilibrated temperatures were estimated from frequencies reported in Refs. [51] and [52] respectively.

Figure 6.2.1: Ground-state diffraction images and corresponding *f(r)* curve for CHT. The vertical lines in *f(r)* approximate the relative contributions from various internuclear pairs; the height of each line scales with $(Z_iZ_j)^2$ / r_{ij} multiplied by the degeneracy, where Z is the nuclear charge and r_{ij} is the internuclear distance.

Figure 6.2.2: Product-isolated *sM(s)* curves for CHT. The (green) experimental curve averaged from 75 to 400 ps is shown, along with corresponding theoretical curves (calculated using an equipartitioned model of the CHT structure) for increasing values of mean *l*. The inset shows the time dependence of the hot CHT fraction. After deconvolution of the instrument function, the time constant for the observed exponential rise is 16 ± 3 ps.

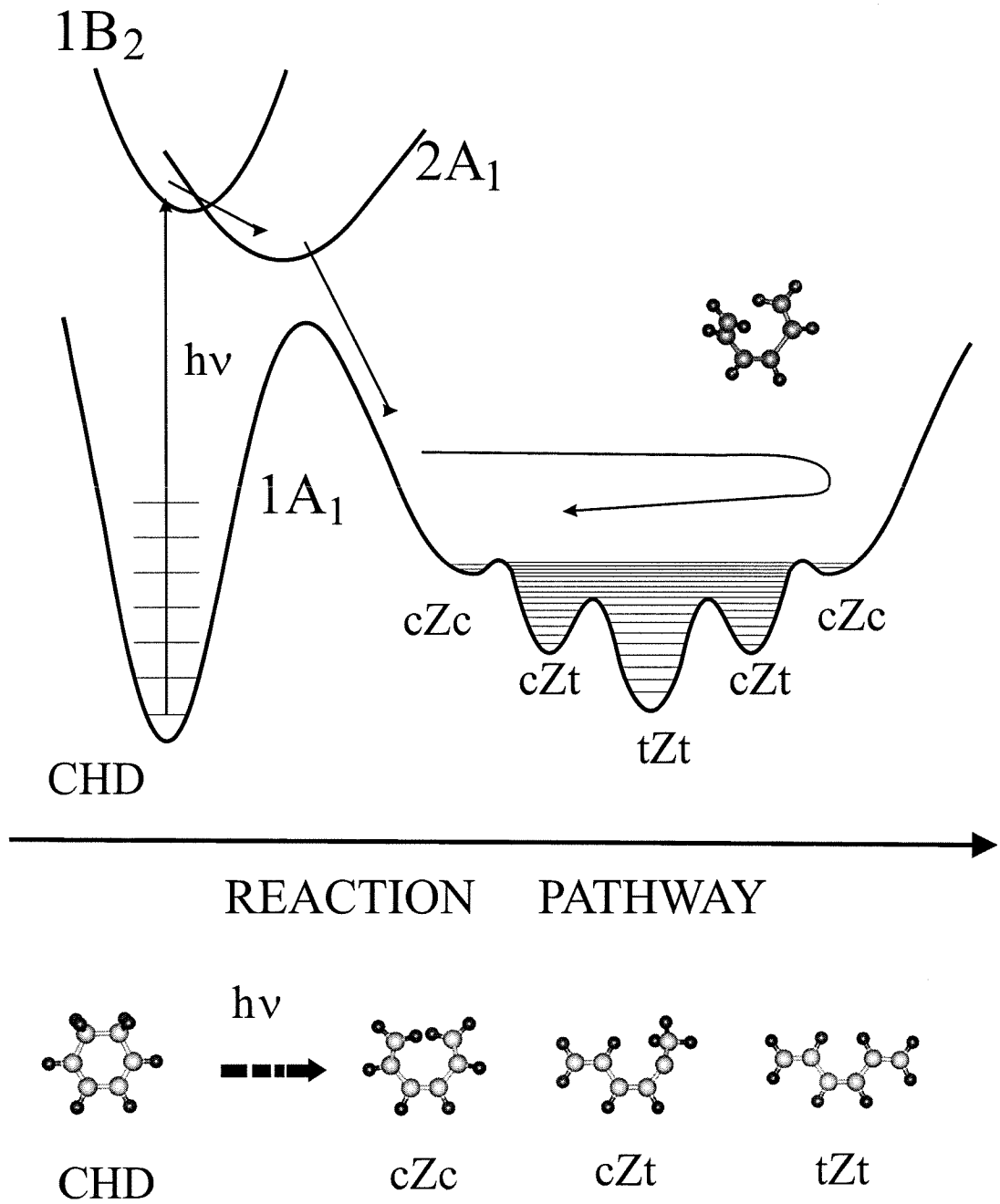
1B2
2A1
hν
1A1
cZc
cZt
cZt
cZc
tZt
CHD
REACTION PATHWAY
hν
CHD
cZc
cZt
tZt

Figure 6.1.1

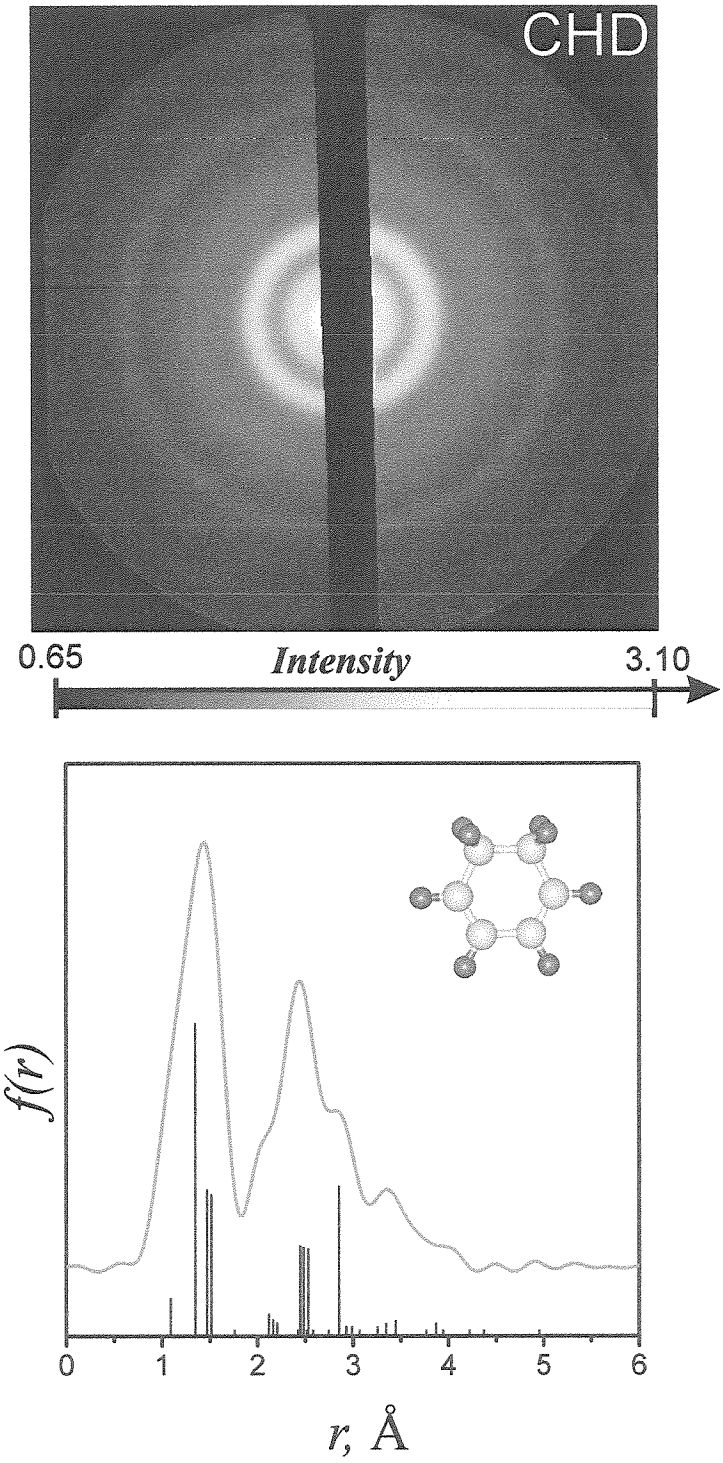

Figure 6.1.2

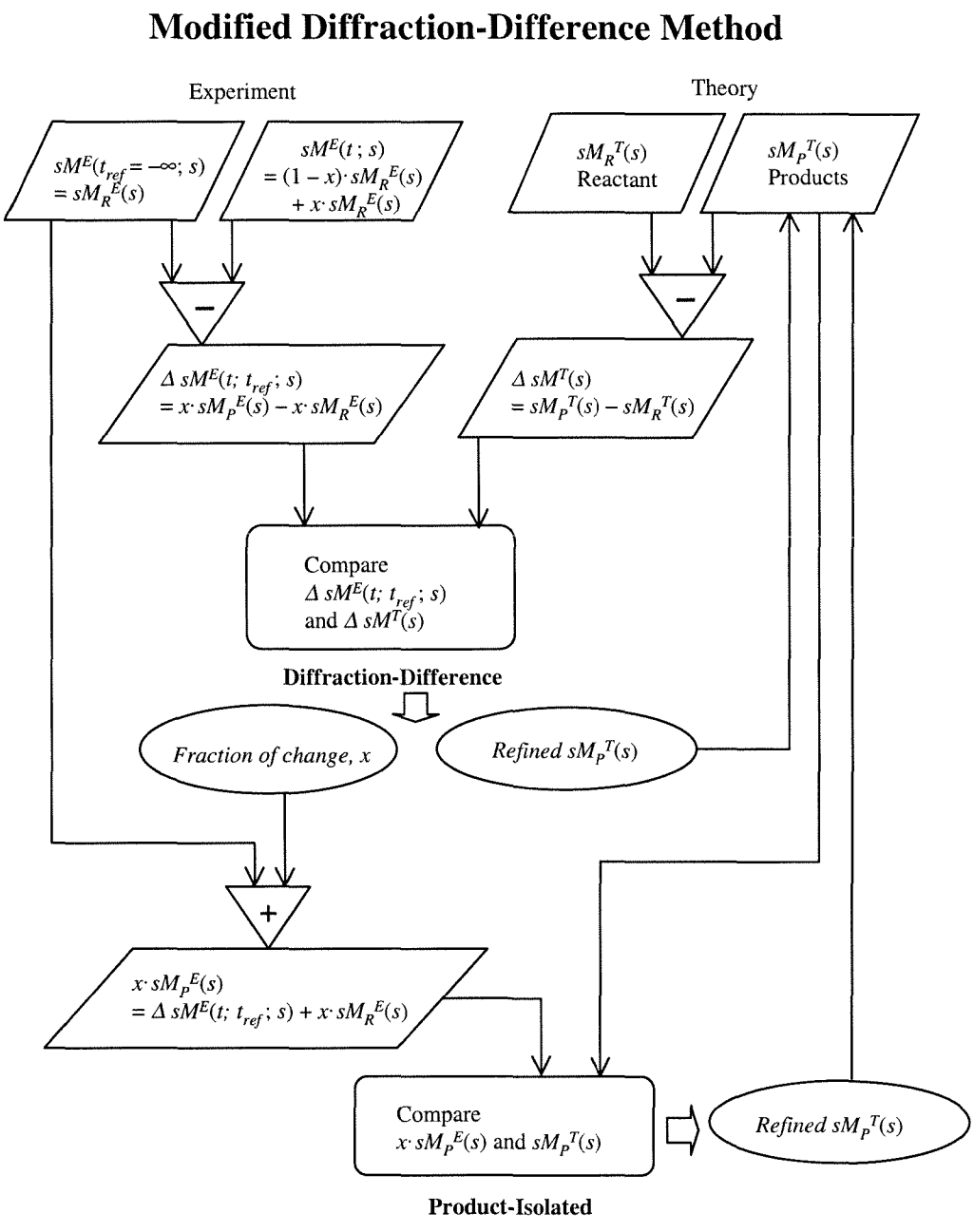
Modified Diffraction-Difference Method
Experiment
Theory
$sM^E(t_{ref} = -\infty; s) = sM_R^E(s)$
$sM^E(t; s) = (1 - x)\cdot sM_R^E(s) + x\cdot sM_R^E(s)$
$sM_R^T(s)$ Reactant
$sM_P^T(s)$ Products
$\Delta\, sM^E(t; t_{ref}; s) = x\cdot sM_P^E(s) - x\cdot sM_R^E(s)$
$\Delta\, sM^T(s) = sM_P^T(s) - sM_R^T(s)$
Compare $\Delta\, sM^E(t; t_{ref}; s)$ and $\Delta\, sM^T(s)$
Diffraction-Difference
Fraction of change, x
Refined $sM_P^T(s)$
$x\cdot sM_P^E(s) = \Delta\, sM^E(t; t_{ref}; s) + x\cdot sM_R^E(s)$
Compare $x\cdot sM_P^E(s)$ and $sM_P^T(s)$
Refined $sM_P^T(s)$
Product-Isolated

Figure 6.1.3

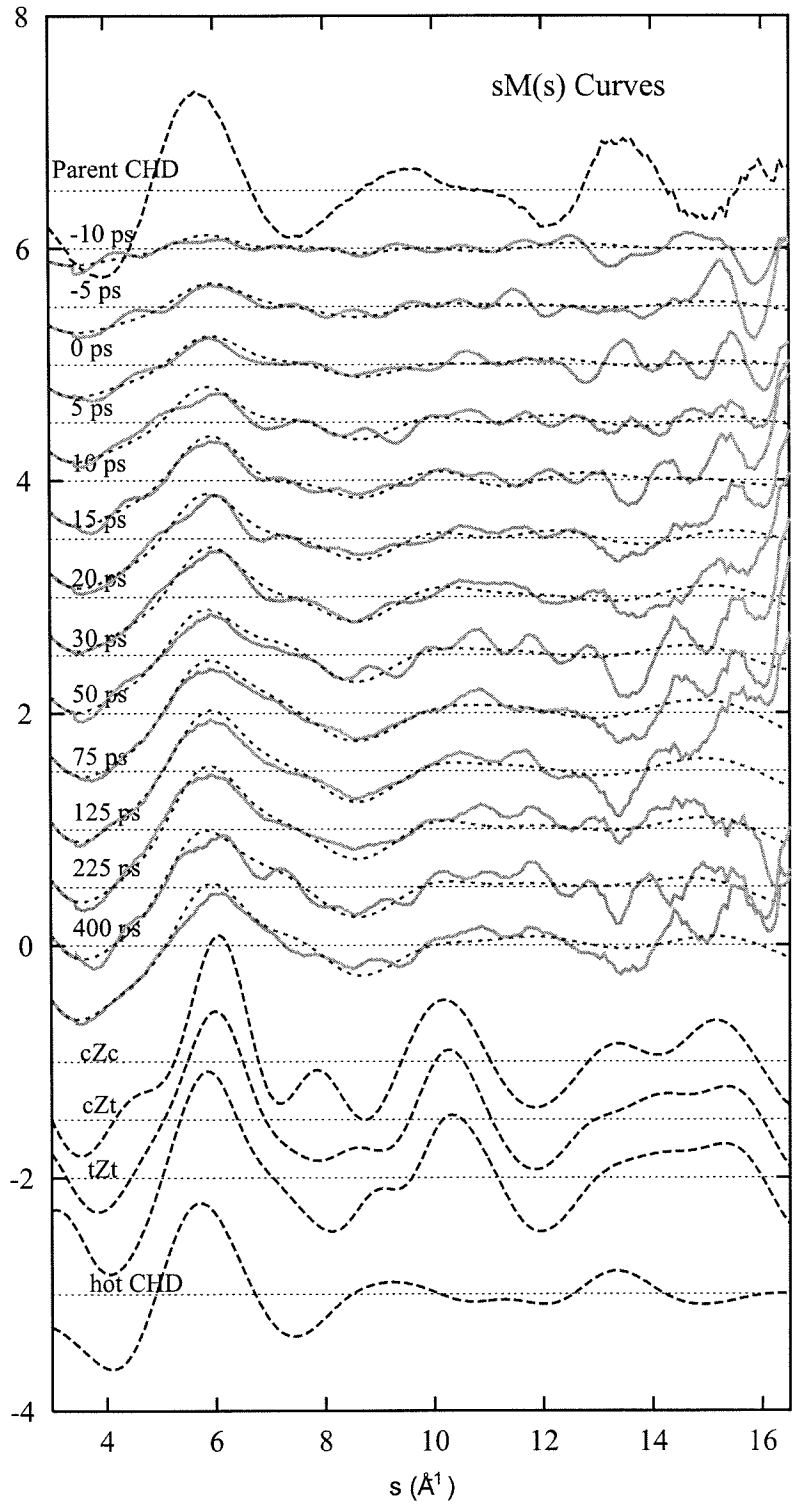
sM(s) Curves
Parent CHD
-10 ps
-5 ps
0 ps
5 ps
10 ps
15 ps
20 ps
30 ps
50 ps
75 ps
125 ps
225 ps
400 ps
cZc
cZt
tZt
hot CHD
8
6
4
2
0
-2
-4
4
6
8
10
12
14
16
s (Å-1)

Figure 6.1.4a

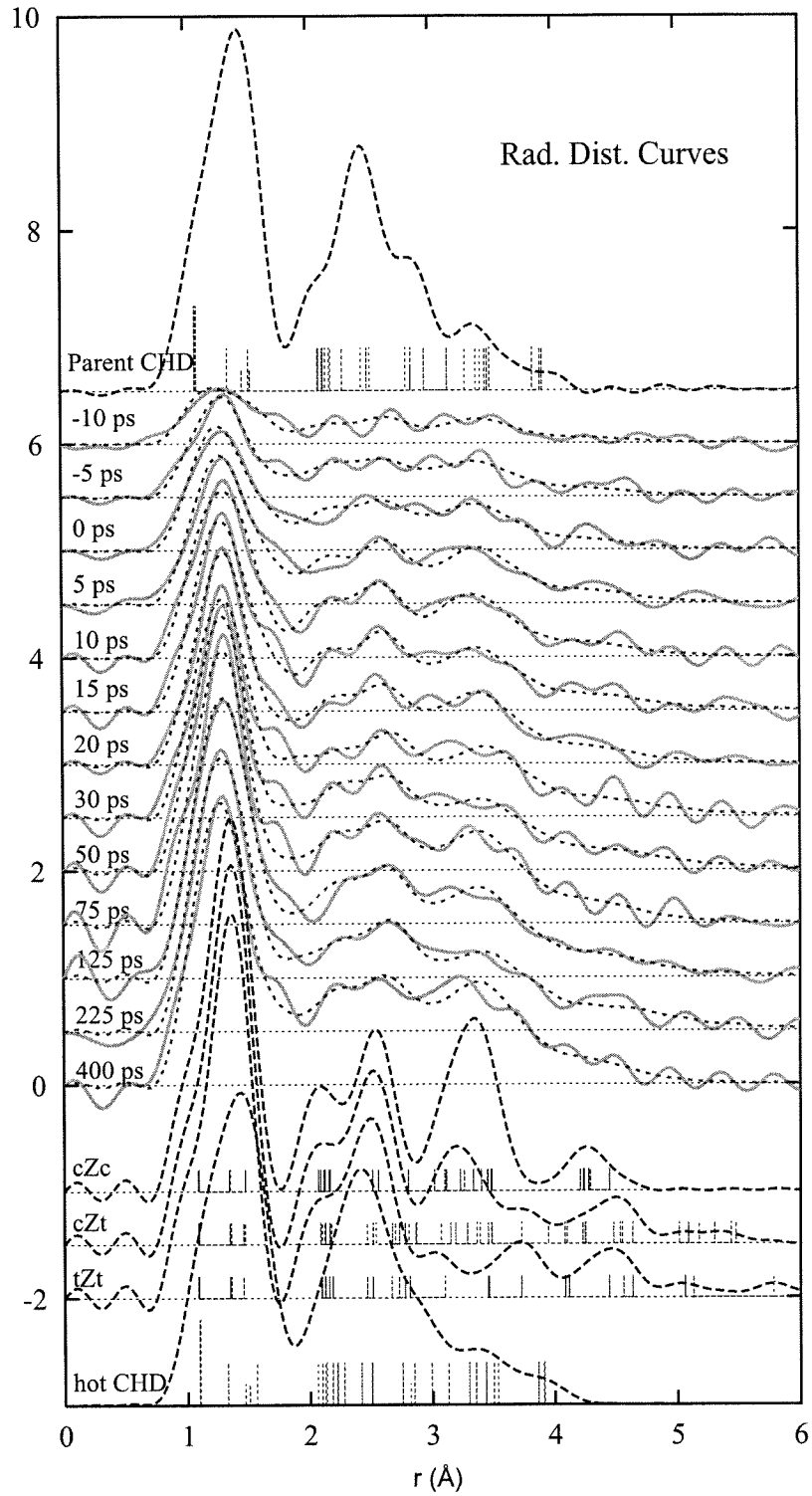
Rad. Dist. Curves
Parent CHD
-10 ps
-5 ps
0 ps
5 ps
10 ps
15 ps
20 ps
30 ps
50 ps
75 ps
125 ps
225 ps
400 ps
cZc
cZt
tZt
hot CHD
10
8
6
4
2
0
-2
0
1
2
3
4
5
6
r (Å)

Figure 6.1.4b

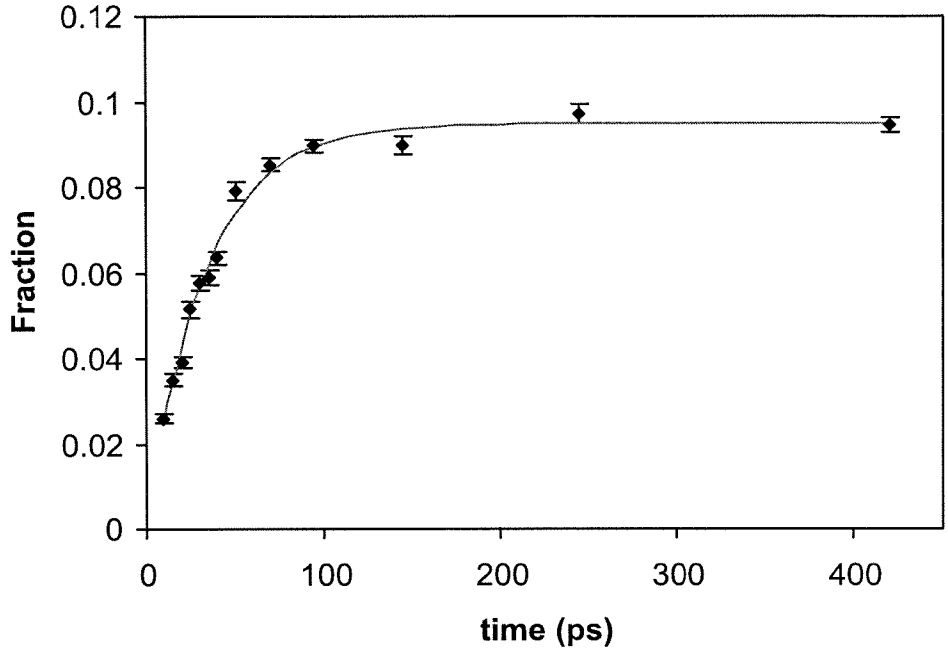
0.12
0.1
0.08
0.06
0.04
0.02
0
Fraction
0
100
200
300
400
time (ps)

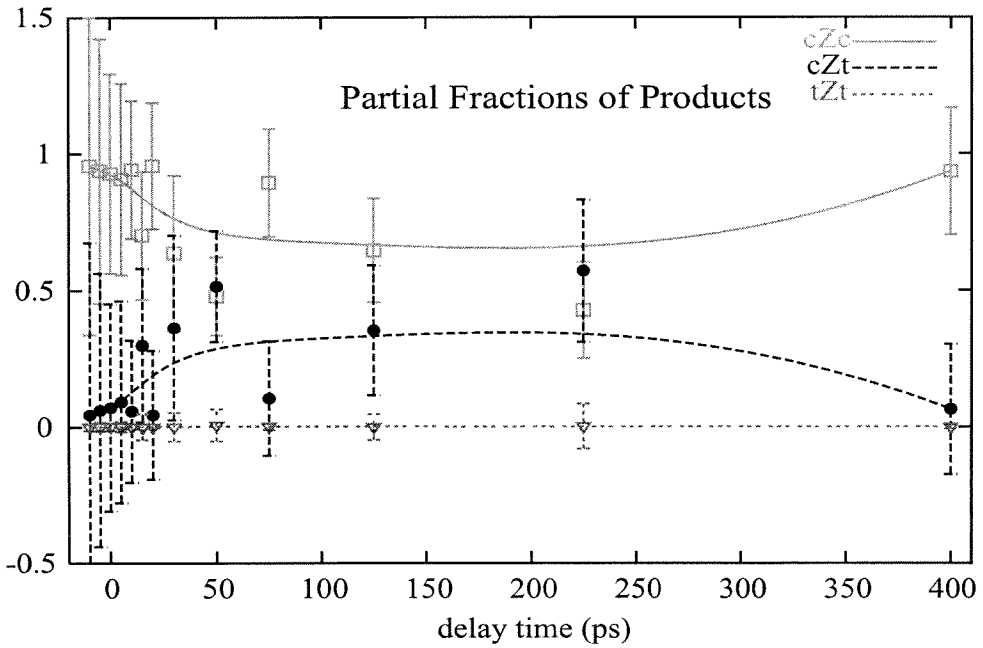
Partial Fractions of Products
cZc
cZt
tZt
1.5
1
0.5
0
-0.5
0
50
100
150
200
250
300
350
400
delay time (ps)

Figure 6.1.5

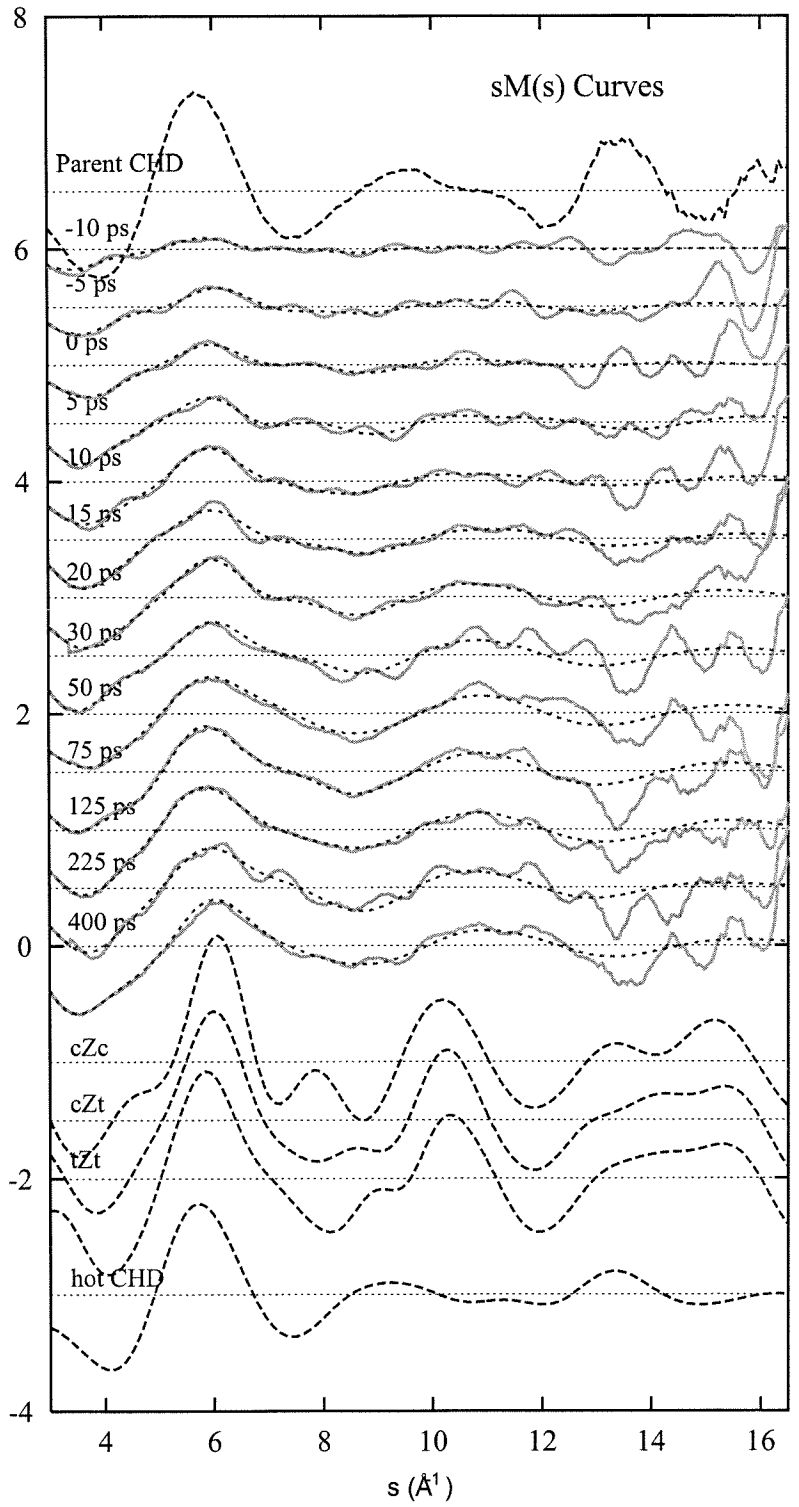
sM(s) Curves
Parent CHD
-10 ps
-5 ps
0 ps
5 ps
10 ps
15 ps
20 ps
30 ps
50 ps
75 ps
125 ps
225 ps
400 ps
cZc
cZt
tZt
hot CHD
8
6
4
2
0
-2
-4
4
6
8
10
12
14
16
s (Å-1)

Figure 6.1.6a

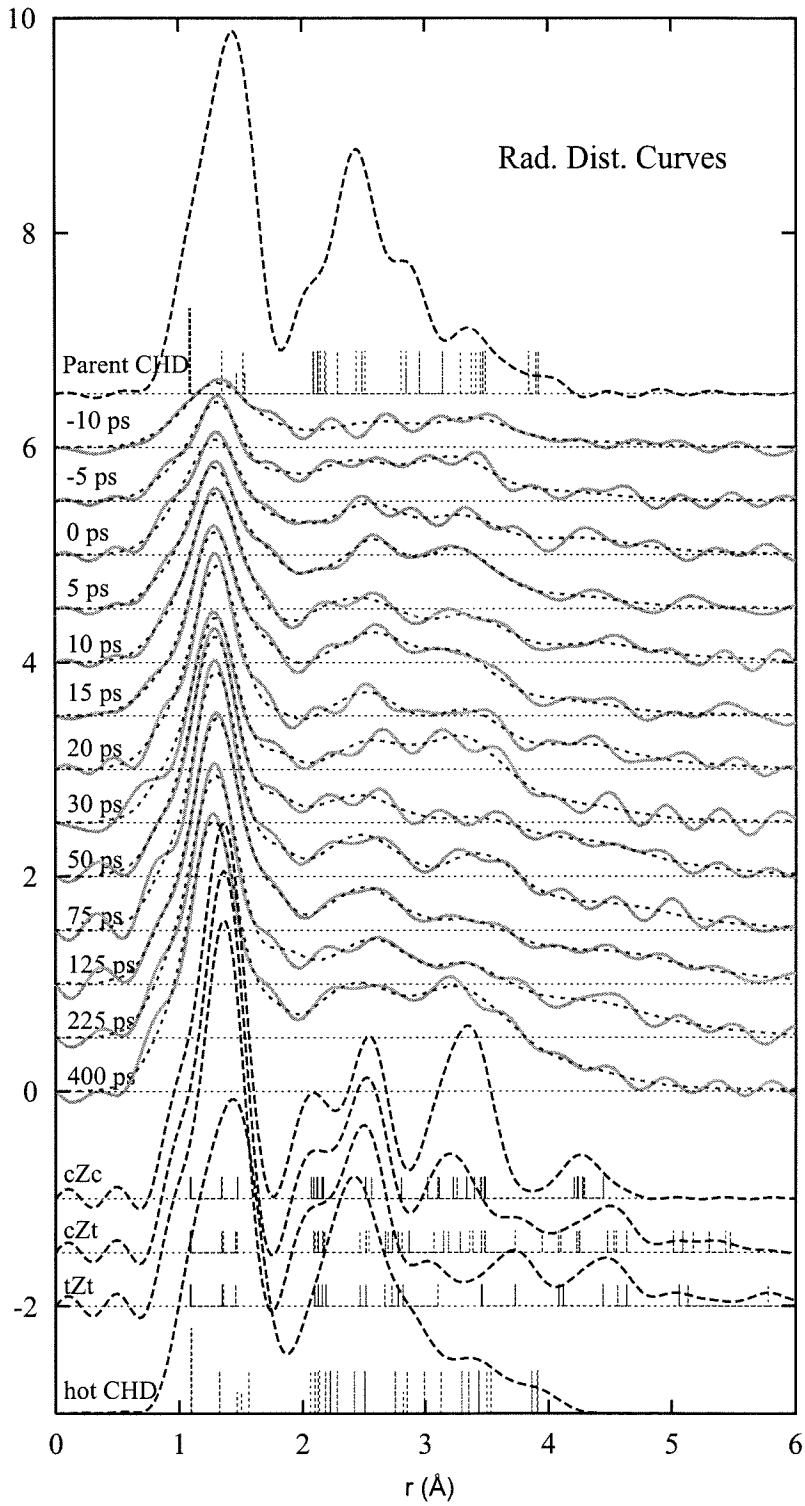
Rad. Dist. Curves
Parent CHD
-10 ps
-5 ps
0 ps
5 ps
10 ps
15 ps
20 ps
30 ps
50 ps
75 ps
125 ps
225 ps
400 ps
cZc
cZt
tZt
hot CHD
10
8
6
4
2
0
-2
0
1
2
3
4
5
6
r (Å)

Figure 6.1.6b

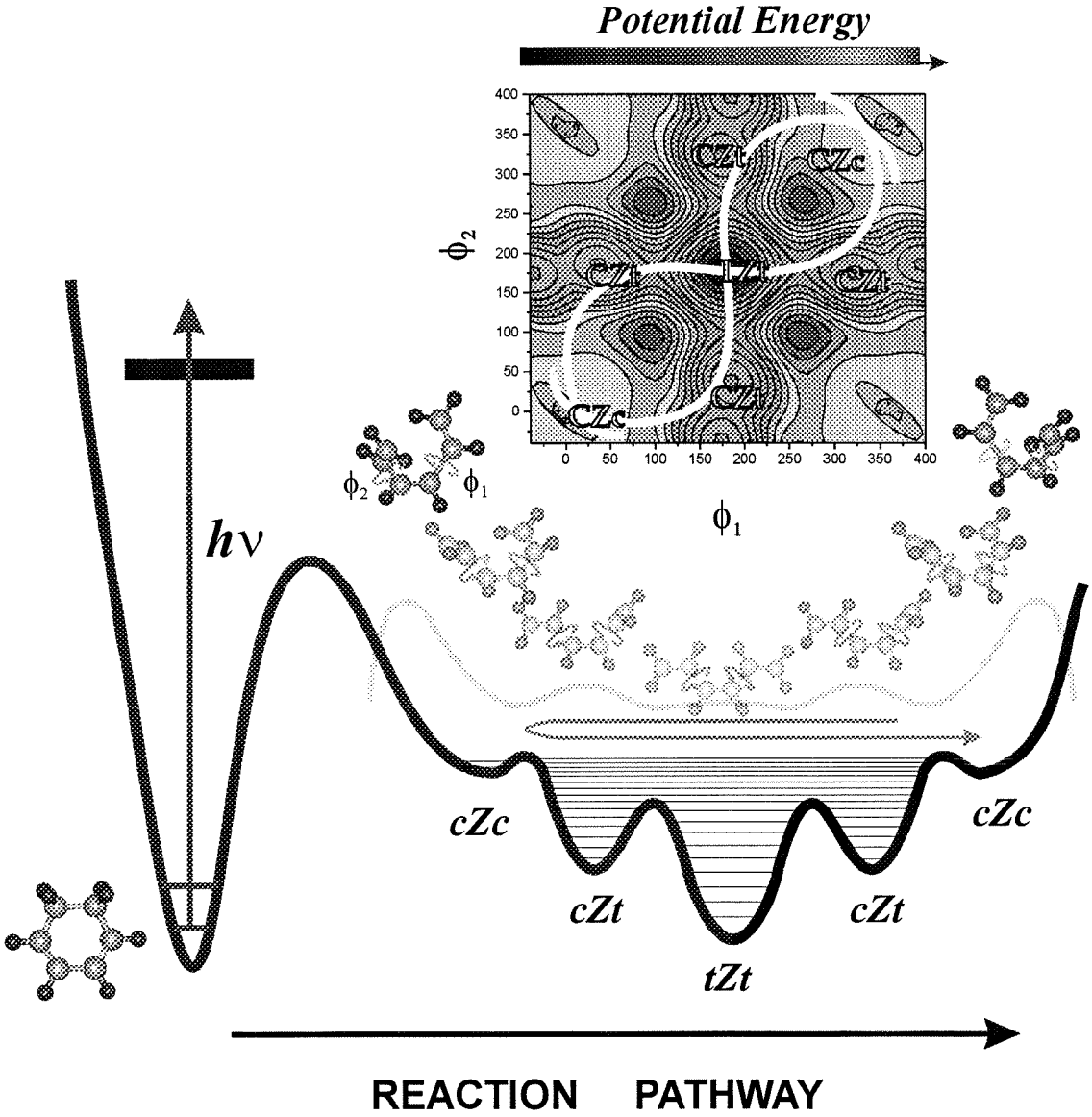
Potential Energy
400
350
300
250
200
150
100
50
0
0 50 100 150 200 250 300 350 400
ϕ_2
ϕ_1
CZt
CZc
CZt
CZt
CZc
CZt
$h\nu$
cZc
cZt
tZt
cZt
cZc
REACTION PATHWAY

Figure 6.1.7

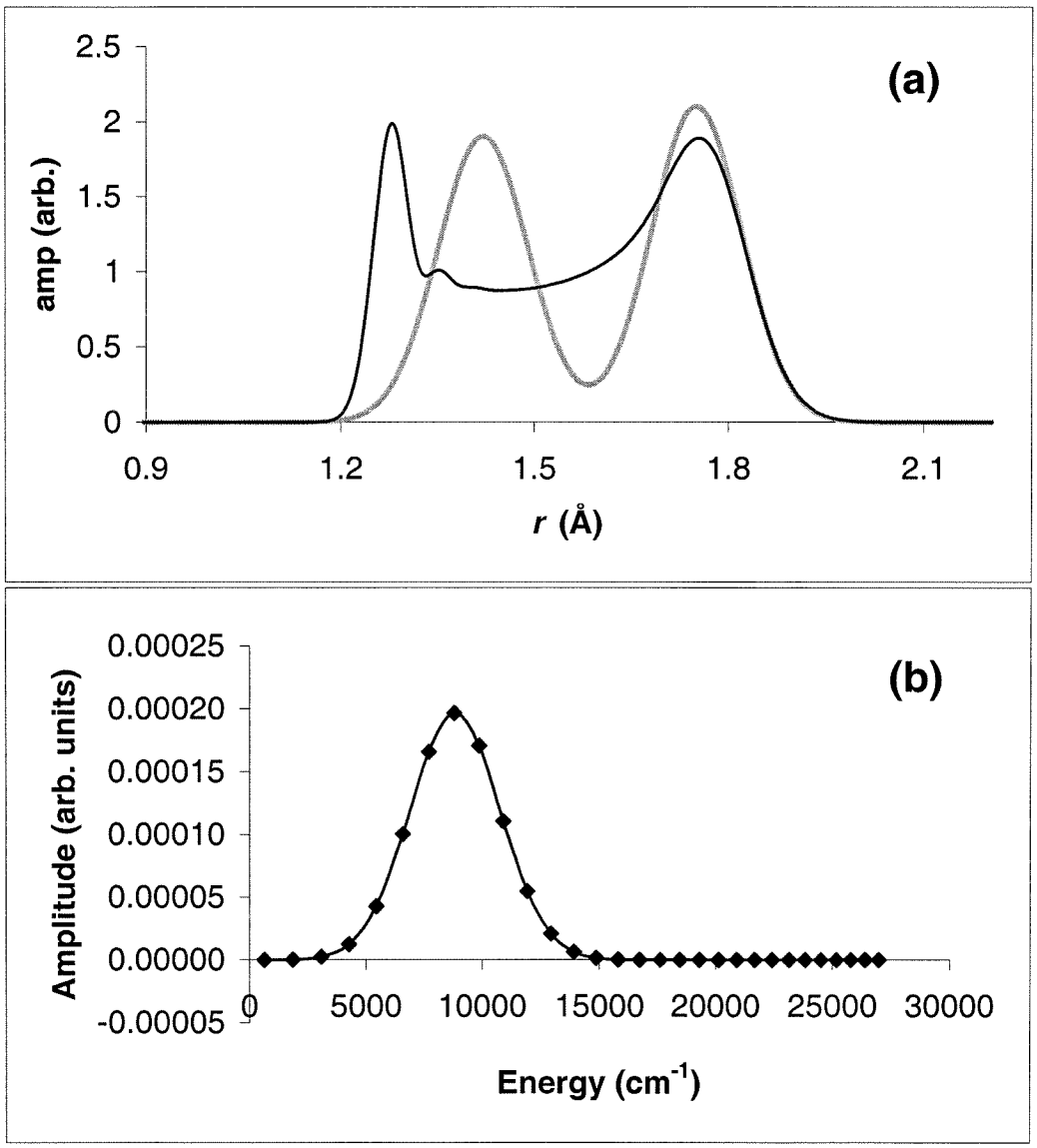
(a)
amp (arb.)
2.5
2
1.5
1
0.5
0
0.9
1.2
1.5
1.8
2.1
r (Å)
(b)
Amplitude (arb. units)
0.00025
0.00020
0.00015
0.00010
0.00005
0.00000
-0.00005
0
5000
10000
15000
20000
25000
30000
Energy (cm-1)

Figure 6.1.8

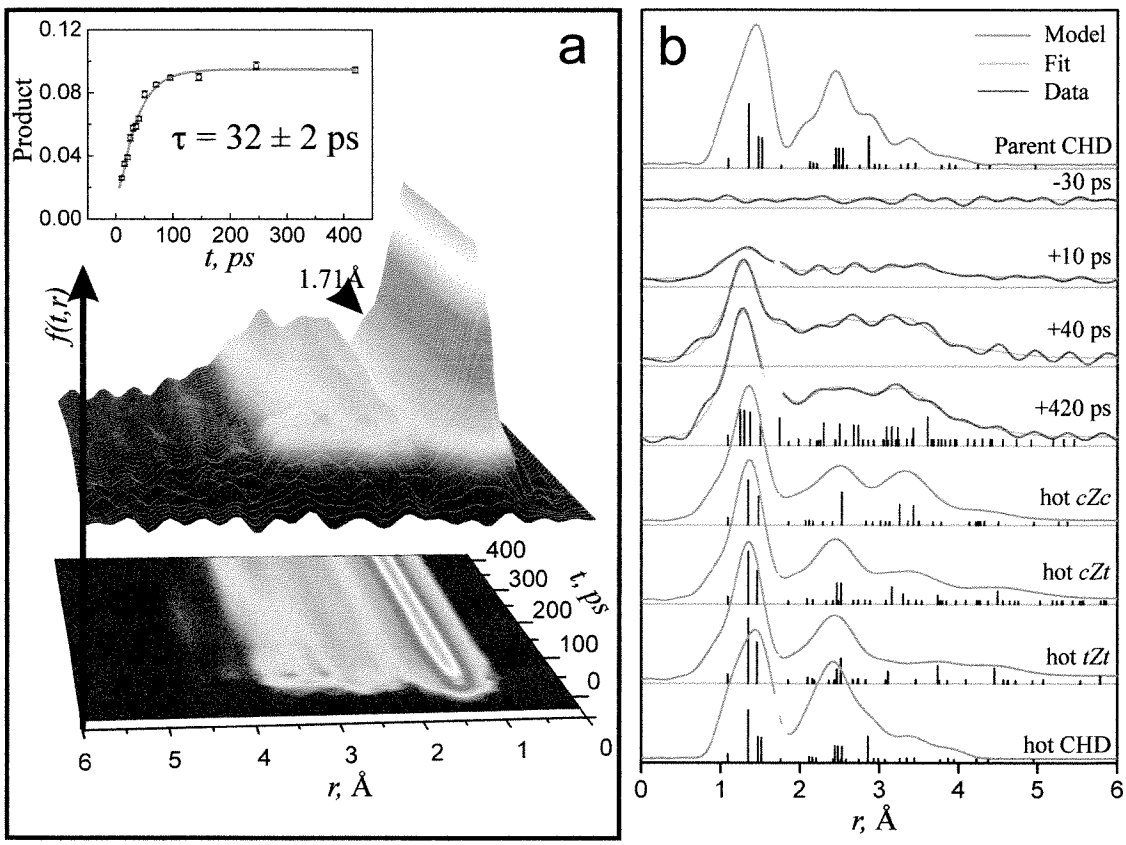
a
Product
0.12
0.08
0.04
0.00
0
100
200
300
400
t, ps
τ = 32 ± 2 ps
1.71Å
f(t,r)
400
300
200
100
0
t, ps
6
5
4
3
2
1
0
r, Å
b
Model
Fit
Data
Parent CHD
-30 ps
+10 ps
+40 ps
+420 ps
hot cZc
hot cZt
hot tZt
hot CHD
0
1
2
3
4
5
6
r, Å

Figure 6.1.9

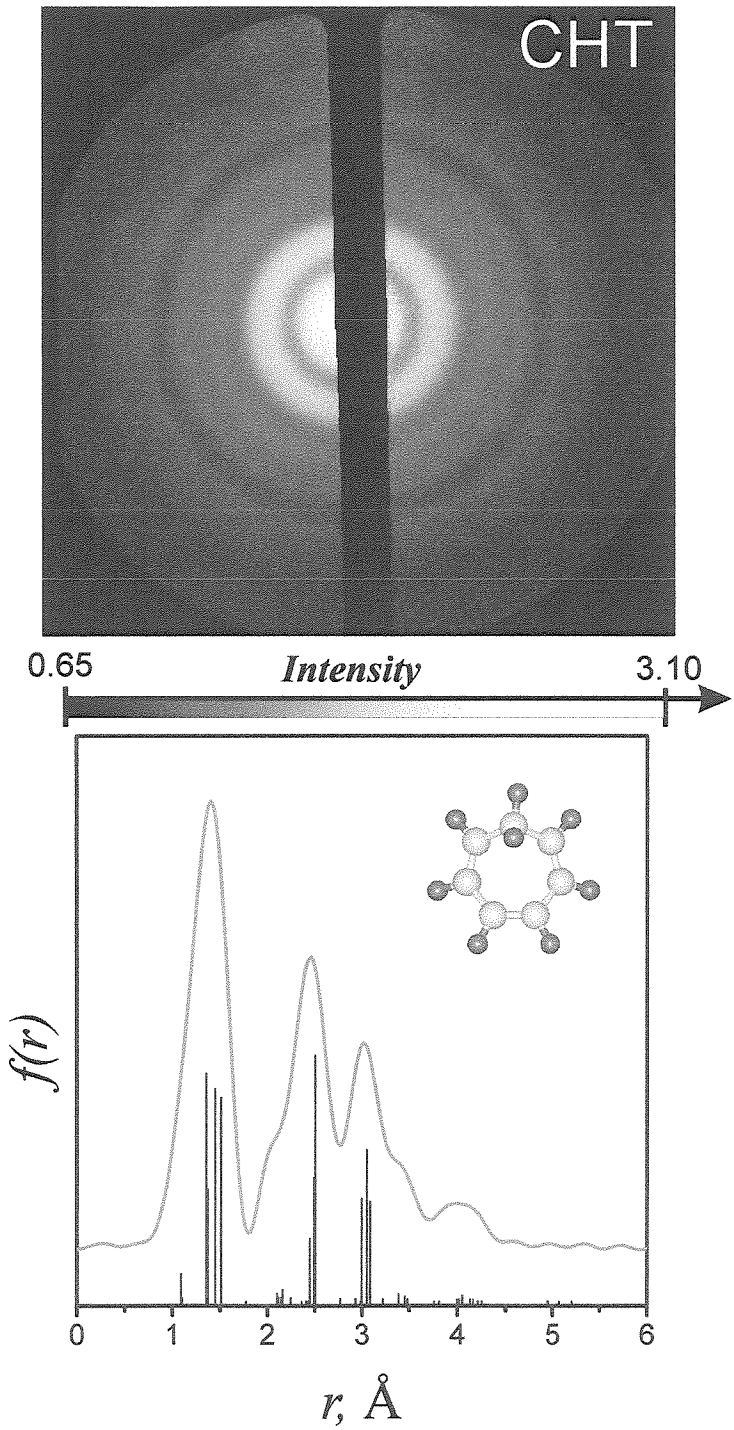

Figure 6.2.1

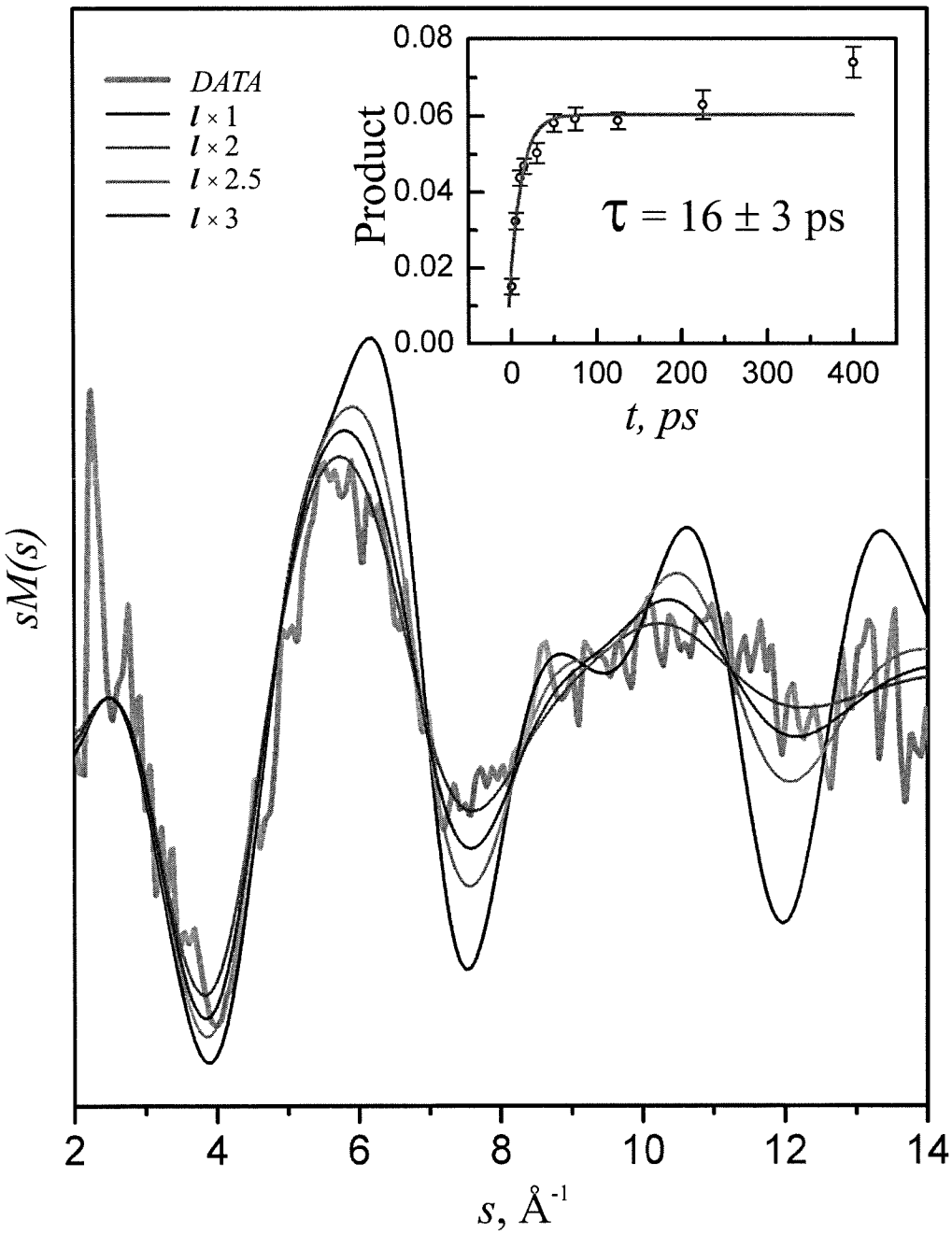
DATA
l × 1
l × 2
l × 2.5
l × 3
Product
0.08
0.06
0.04
0.02
0.00
0
100
200
300
400
t, ps
τ = 16 ± 3 ps
sM(s)
2
4
6
8
10
12
14
s, Å-1

Figure 6.2.2

CHAPTER SEVEN

APPLICATIONS TO ORGANOMETALLICS

7.1 $Fe(CO)_5 \rightarrow Fe(CO)_n + (5 - n)\ CO$, n = 2, 1, 0 @ 310 nm

7.1.1 Background

Transition metal carbonyls display rich photochemistry[1,2]. After absorbing ultraviolet photons, they dissociate into reactive unsaturated carbonyls, which are known to catalyze a variety of interesting reactions[3,4]. Over the decades, the photochemistry of coordinately unsaturated species has been the subject of studies of increasing depth and detail. Of particular interest are the reaction pathways, the binding energies of successive CO ligands, and the structures of the unsaturated species.

The majority of gas-phase photochemistry work on metal carbonyls has been devoted to $Fe(CO)_5$ and its unsaturated radicals, and much experimental and theoretical information about their molecular and electronic structures is available. $Fe(CO)_5$ is known to absorb strongly in the ultraviolet starting at ~ 350 nm (3.5 eV)[5,6]. The spectrum is rather featureless and thought to be dominated by ligand field d-d transitions at low energies and metal-to-ligand charge transfer transitions at high energies. The complete fragmentation of $Fe(CO)_5$ requires about 6.1 eV[7] and the successive CO binding energies were determined to be ~2.0, ~0.5, ~1.5, ~1 and ~1 eV respectively[8-11]. Fig. 7.1.1 presents the structures of $Fe(CO)_5$ and its unsaturated photofragments. The ground state of $Fe(CO)_5$ has a D_{3h} structural symmetry[9,12-14]. After losing one CO ligand, $Fe(CO)_4$ develops a structure of Jahn-Teller distorted tetrahedron with C_{2v} symmetry[15]. The further dissociation of a CO produces $Fe(CO)_3$ of C_{3v} symmetry with an out of plane bend angle θ of 21 degree[15,16]. Both $Fe(CO)_2$

and FeCO have linear structures due to the Fe-C σ-bond and C-O π-bond[14,17]. However, except the structure of $Fe(CO)_5$ parent molecule which was determined by gas phase electron diffraction (GED), all the internuclear distances of its unsaturated photofragments have not been precisely determined.

Several research groups have investigated the fundamental photochemistry such as how the reaction depends on the excitation wavelength, and whether the dissociation occurs in a concerted or sequential manner when multiple CO fragments depart. By chemical trapping method, Yardley *et al.* were the first to measure the distribution of $Fe(CO)_n$ (n= 2, 3, 4) resulting from one-photon absorption at 193, 248 and 352 nm[5,18]. They showed that more CO ligands are lost as the pump laser photon energy increases and proposed a photodissociation process in which the CO ligands are lost sequentially. Later studies by Grant[19], Waller and Hepburn[20,21], Vernon[22], and by Weitz[23,24], with different techniques, support the mechanism that the photofragmentation of $Fe(CO)_5$ proceeds in a sequential liberation of CO ligands. Although there are some quantitative disagreement of final product distribution in their results, all of them observed the general trend that $Fe(CO)_5$ loses more carbonyl groups with higher excitation photon energy.

The first femtosecond photodissociation study of gas phase metal carbonyl was carried out in our group on $M_2(CO)_{10}$ [25]. In their experiment, the temporal dynamics for both metal-metal and metal-ligand bond cleavage, occurring on a time scale of hundreds of femtoseconds, was clearly identified. Very recently, a femtosecond transition spectroscopy (FTS) study were performed on $Fe(CO)_5$ by Bañares *et al.*[26,27].

In their experiment, $Fe(CO)_5$ absorbed two photons of 400 nm light from a pump laser and the transient mass spectra of each intermediate species was recorded following a 800 nm probe laser pulse. Again, the time scale of photodissociation was observed as a few hundred femtoseconds. In contrast to the previous one-photon studies, which support a step-wise elimination of ligands, the authors suggested that Fe(CO) formed in a concerted manner from $Fe(CO)_5$ and further dissociated into Fe.

Time zero was determined within 2 ps by a lensing experiment. $Fe(CO)_5$ was pumped by a femtosecond (fs) laser pulse, and snapshots of the diffraction images were recorded at different delay times before and after time zero. No further changes were observed after 10 ps (up to 270 ps) time delay, which indicates that the photodissociation of $Fe(CO)_5$ is faster than our temporal resolution of ~10 ps. In addition, the final major products were found to be $Fe(CO)_2$, FeCO and Fe with the branching ratio 2: 5: 5. The Fe-C and C-O bond distances of $Fe(CO)_2$ and Fe(CO) were also obtained.

7.1.2 Experimental Setup and Method

The ps time-resolved gas phase electron diffraction experiments of $Fe(CO)_5$ were performed on the second generation UED apparatus developed in our laboratory. Briefly, it is composed of a femtosecond laser, a picosecond electron gun, a free-jet expansion sample source, and a two-dimensional single electron detection system. Femtosecond laser pulses from a colliding-pulse mode-locked ring dye laser were amplified in a four-stage pulsed dye amplifier pumped by a Nd:YAG laser at 30 Hz.

The amplified pulses (620 nm, 2-3 mJ/pulse, 30 Hz, ~300 fs pulse width) were then split with a beam splitter into pump and probe laser. 95% of the laser pulse (pump) was first frequency-doubled with a KDP crystal (250 μJ at 310 nm), then directed and focused to the scattering gas sample beneath the needle of the free-jet expansion source in the scattering chamber. The remaining 5% (probe), also doubled, was focused onto a back-illuminated photocathode in the electron gun to generate the ps electron pulse. The ultrashort electron pulse was then accelerated to 18.1 KeV (de Broglie wavelength is 0.0904 Å) and focused to the scattering volume. The two-dimensional diffraction images at certain delay times were recorded using a charge-coupled device (CCD) chip at the end of a phosphor scintillator/fiber optic/image intensifier chain in the detection chamber. Time delays between the fs pump laser pulse and the ps electron pulse were controlled by a computer-driven translational stage.

$Fe(CO)_5$ was purchased from Aldrich (98%). The sample was purified through the vacuum distillation and then transferred into a sample cell *in situ*. After being connected to the diffraction chamber, the sample was further purified *in situ* by three cycles of freeze-and-thaw to remove the residual impurities. The final sample purity was estimated to be better than 99 %. In order to give enough molecular density in the scattering volume, the sample cell, gas line and nozzle were heated to 38, 65 and 68 $^{\circ}C$, respectively. The gas pressure in the scattering chamber during the experiment was about 4×10^{-4} torr, and the pressure at the scattering volume was estimated to be about a few torr.

The electron pulse, laser pulse and molecular beam were arranged in a cross-beam geometry, and the alignment of the three beams were controlled within 10 μm. The camera length was measured to be 102.7 mm. For our current setup, the time resolution is determined by the electron pulse width. With an electron flux of ~10^4 electrons per pulse, the corresponding temporal width is 10 ps[28]. The total temporal resolution, including the contributions from pump laser pulse width and group velocity mismatch effect[29], was then calculated to be less than 12 ps. After establishing the time zero by a lensing experiment within ± 2 ps accuracy[28], the time-resolved data were taken at -20, +10, +40, +70 and +270 ps delay time relative to the pump laser pulse.

The diffraction data was subjected to a standard procedure of data analysis developed in our laboratory[28]. First, each raw image underwent a visual examination to identify blatant problems such as electron gun arcing, sudden shift in the electron beam position, or CCD readout failures. Then, the center of each image and the background offset (CCD dark noise) was identified with home-developed software. With this information, the software computed the average intensity as a function of pixel distance from the center of each diffraction pattern. The abnormally high or low values of pixels (out of the range of four standard deviations of the mean), mainly caused by spontaneous emission from the image intensifier, were filtered out. Finally, the results from all images at a given delay time were combined into a single, one-dimensional data file: the experimental total scattering intensity curve I_{Tol} *(pix)*. After normalization of the total scattering intensity fluctuation of I_{Tol} *(pix)*(less than 1%) at

each time point and conversion of pixel number to momentum transfer s, the experimental modified molecular scattering intensity, $sM(s)$, was obtained at each time point

$$sM(s) = s\frac{I_{Tot}(s) - I_{Back}(s)}{|f_a||f_b|}, \qquad (7.1.2.1)$$

where I_{Tot} is the total scattering intensity, I_{Back} is the background (including atomic) scattering intensity, and f_a and f_b are atomic scattering amplitudes. The corresponding radial distribution curves were then calculated from the $sM(s)$ curves according to the standard GED equation[30]:

$$f(r) = \int_0^{s_{max}} sM(s)\sin(sr)\exp(-ks^2)ds \qquad (7.1.2.2)$$

where the constant k is a damping coefficient included for the limited s range (k = 0.02 Å^2 in our data analysis)

7.1.3 Results and Discussion

Fig. 7.1.2 shows the experimental $sM(s)$ and $f(r)$ curves at -20 ps and the difference $\Delta sM(s)$ and $\Delta f(r)$ curves at different delay times relative to the data at -20 ps of $Fe(CO)_5$. The theoretical $sM(s)$ and $f(r)$ with the structural parameters from a static gas phase electron diffraction study[13] were also imposed on -20 ps data for comparison. The fit between theory and experiment is not as perfect as the conventional gas phase electron diffraction experiment, but very good if the low electron flux of our ps electron pulse is considered. Since time zero was unambiguously clocked within 2 ps and the experimental temporal resolution was less

than 12 ps, the data at -20 ps established the reference curve which was not perturbed by the excitation laser[31-33]. To visualize the changes induced by the fs excitation laser, difference curves ΔI_{Tot} at each of the positive time points were first obtained by subtracting the I_{Tot} at -20 ps. By correcting the background drift in ΔI_{Tot}, as will be explained in more detail later on, the difference experimental modified molecular scattering intensity $\Delta sM(s)$ and difference radial distribution curves $\Delta f(r)$ were obtained with Eqs. (7.1.2.1) and (7.1.2.2).

As shown in Fig. 7.1.2, the difference curves of each positive time point are identical within our experimental error. The absence of temporal evolution after 10 ps sets the upper bound of the time constant for the whole photofragmentation process to be less than 10 ps. This is consistent with the recent FTS study on $Fe(CO)_5$ using 400 nm pump and 800 nm probe laser[26,27], where they found that the final photofragments were formed within 500 fs. The step-function behavior of our time resolved diffraction patterns is, therefore, natural with our present temporal resolution of 10 ps. The two main dips centered at 1.82 Å and 2.98 Å in the difference curves indicate the depletion of the Fe-C and Fe···O internuclear contribution after some of $Fe(CO)_5$ parent molecules have dissociated into $Fe(CO)_x$ (x = 4, 3, 2, 1, 0), and the shoulder after 3.5 Å is due to other internuclear contributions such as C···O and O···O.

Having five carbonyl moieties, a $Fe(CO)_5$ molecule excited by a ultraviolet photon can dissociate into five different products depending on the excitation wavelength. Several research groups have studied the product distribution following photolysis with different approaches in observing the unsaturated iron carbonyl

species. Yardley *et al.* were the first to study the photolysis of $Fe(CO)_5$ in the gas phase[5,18]. In their chemical trapping experiment, low concentrations of $Fe(CO)_5$ in a flow cell containing PF_3 gas was irradiated by a photolysis laser with a wavelength of 193, 248 or 352 nm. PF_3 substituted photofragments were detected and analyzed with a gas chromatography and mass spectrometry apparatus under the assumption of uniform sensitivity of the thermolysis detector to each species. Since the detected species depended on the collision of unsaturated fragments with PF_3 and other types of ligand exchange could occur as well, the true product distribution could not be obtained. To remove the collision effects, Waller and Hepburn conducted the $Fe(CO)_5$ photofragmentation experiment in a molecular beam at 193, 248, 266, and 351 nm[21]. They probed the rotational, vibrational, and translational energy distributions of nascent CO fragments by VUV induced LIF. The product distributions were derived from a theoretical fit to their data with the assumption of step-wise photodissociation and statistical energy randomization between each photofragmentation step. Vernon and coworkers also studied the photolysis of $Fe(CO)_5$ in a molecular beam using a pump laser at 193 and 248 nm[22]. The products were ionized and detected after traveling 20 cm to the entrance of a mass spectrometer. Like Waller and Hepburn's approach, product distributions were obtained by fitting a theoretical model of the mechanism to the experimental angle and velocity distributions of mass peaks corresponding to $Fe(CO)_2^+$, $Fe(CO)^+$ and Fe^+. The methods of Waller and Hepburn or Vernon and coworkers were indirect in detecting the neutral photoproducts. The only direct detection of $Fe(CO)_x$ fragments was performed by Weitz and coworkers[23,24].

$Fe(CO)_5$ buffered by Ar gas in a flow cell was irradiated by the pump laser at 193, 248 or 351 nm, and IR absorption spectra were recorded on the ns-μs time scale. The absorption peaks were assigned to photoproducts based on the temporal evolution and the IR spectra of $Fe(CO)_4$ and $Fe(CO)_3$ isolated in matrices. Not surprisingly, the results on the product distribution were not convergent between each group. Therefore, it is a very interesting issue whether our UED technique can reveal the product distribution or not. Like the time-resolved IR study, UED techniques detect the photoproducts in a direct manner; it has a high possibility of providing the true product distribution.

For a starting point, we assumed that just one product could be generated following the whole photoprocess. This assumption cannot be justified in reality, but it at least can give us some clues on the identities of the major products, because any molecules with significant concentration would produce an acceptable fit between theory and experiment. For each assumed product, the initial structural parameters in the fitting were assigned based on the IR study in matrix and the ab initio calculation. The IR absorption study on $Fe(CO)_4$ in Ar and SF_6 matrices at 20 K showed that $Fe(CO)_4$ has a C_{2v} symmetry with bond angles of 145° (α) and 120° (β)[15]. The same IR study of $Fe(CO)_3$ isolated in a methane matrix at 20 K supported a C_{3v} symmetry and yielded an out-of-plane bend angle θ of 21°.[16] Theoretical calculations also qualitatively agree with the experimental results[14]. Both theoretical calculations and matrix-isolated IR studies of low temperature suggest linear structures for $Fe(CO)_2$ and Fe(CO).[17] In the fitting, the structural symmetries of all photofragments were kept

fixed (see Fig. 7.1.1). The Fe-C distance and the C-O distance were assumed to be 1.82 Å and 1.16 Å respectively for all the products ($Fe(CO)_x$, x = 4, 3, 2, 1) initially and then would be refined later. The difference total intensity data, ΔI_{Tol}, were used for the analysis instead of the usual I_{Tol}, because of several advantages. First, atomic scattering is a common contribution regardless of time and photofragmentation, therefore it can be removed automatically by subtracting the -20 ps data from each positive time point. Second, any intrinsic systematic error of the detection system will be eliminated or greatly reduced after subtraction. Third, the difference curve contains the -1:1 ratio mixture of parent and products while the original raw data contains a very small fraction of product compared to a majority of parent. Therefore, the significance of product contribution is dramatically enhanced in ΔI_{Tol}.

Theoretically, the difference total intensity ΔI_{Tot} should be same as the difference molecular scattering intensity (ΔI_{mol}) and free from any background, because the atomic scattering should not be changed before and after time zero. However, a small residual background was detected in our experimental ΔI_{Tot}. The origin of this residual background is not fully understood, but tentatively assigned to the unique scattering effect of positive ions generated by a strong excitation laser through multiphoton ionization. The investigation to account for this effect is in progress. This residual background was fitted with the zero points of theoretical $\Delta sM(s)$ and was subtracted from ΔI_{Tot} to get the background-free ΔI_{Tot}. Then experimental $\Delta sM(s)$ and $\Delta f(r)$ were obtained with the corrected ΔI_{Tot} through Eq. (7.1.2.1) and (2), where Fe and O were chosen as scaling atoms. For each assumed

product, the fraction and the structural parameters were fitted iteratively in least-square manner to give the best fit between theoretical and experimental $\Delta sM(s)$ curve[34,35].

Fig. 7.1.3 shows the best fits with each assumed product. The fits with $Fe(CO)_4$ and $Fe(CO)_3$ are unacceptable while those with $Fe(CO)_2$, Fe(CO) and Fe are very good. This implies that the concentrations of $Fe(CO)_4$ and $Fe(CO)_3$ are negligible in our molecular beam after photofragmentation, whereas those of $Fe(CO)_2$, Fe(CO) and Fe are significant. The first, second, and third bond dissociation energies of $Fe(CO)_5$ were known to be ~2.0, ~0.4 and ~1.2 eV respectively[11] and Waller and Hepburn showed that each CO fragment possesses ~0.5 eV internal energy[21,24]. With excitation photon energy of about 4.0 eV (310 nm) and no multiphoton effects, $Fe(CO)_4$ and $Fe(CO)_3$ are the only energetically possible products. Our result suggests that the photoexcitation process in our experiment is two-photon rather than one-photon. Since the peak power of our pump laser is several orders of magnitude higher than those used for one-photon process, the two-photon process highly favorable in our experimental setup.

Having ruled out the $Fe(CO)_4$ and $Fe(CO)_3$ as significant products, we further tried the data fitting with the mixture of $Fe(CO)_2$, Fe(CO), and Fe, rather than just one component. In the fitting, the mean amplitudes of vibration of the intermediates were kept fixed at the same value as those of parent. Fig. 7.1.4 shows the result of this trial. The fitting result showed that the fractions for the product were 2% (± 1%), 5% (± 2%) and 5% (± 1%) for $Fe(CO)_2$, Fe(CO), and Fe, respectively. This indicates that

12% of the total parent $Fe(CO)_5$ molecules in the molecular beam dissociated into 2% $Fe(CO)_2$, 5% Fe(CO) and 5% Fe. In comparison, the FTS result of Bañares *et al.* showed that Fe(CO) forms in a concerted manner from $Fe(CO)_5$ and that some of the Fe(CO) loses the last carbonyl group to form Fe.[14,36] Their result suggests that the final products were Fe(CO) and Fe. Our result is highly consistent with their result although their excitation wavelength (400 nm) is different from ours (310 nm).

Another interesting aspect to our results is the fitted structural parameters of $Fe(CO)_2$ and Fe(CO). Since the signal-to-noise ratio of UED data is relatively low due to the low electron flux, the statistical standard deviations of fitted parameters were more than ten times bigger than the usual standard deviations of conventional electron diffraction studies[30]. However, the fitting result might give us a relative trend in the structural parameters compared with the parent. The fitted Fe-C and C-O distances of $Fe(CO)_2$ were 1.67 (± 0.25) Å and 1.34 (± 0.10) Å, and those of Fe(CO) were 1.78 (± 0.32) Å and 1.20 (± 0.16) Å, respectively. The errors are one standard deviation of the fitting and do not account for any systematic errors. Compared with the GED results of $Fe(CO)_5$, where the equatorial and axial Fe-C distances are 1.827 Å and 1.807 Å, and the C-O distance is 1.152 Å, it is noteworthy that the Fe-C distances of the products become shorter while the C-O distance becomes longer than those of parent molecule. Interestingly, in IR studies on the matrix-isolated iron carbonyls formed upon cocondensation of iron atoms with noble gas / CO gas mixture at 12 K,[17] Peden *et al.* observed that infrared C-O stretching frequencies of $Fe(CO)_2$ and Fe(CO) were smaller than those of $Fe(CO)_5$, $Fe(CO)_4$, and $Fe(CO)_3$. This indicates that the C-O

bonds of $Fe(CO)_2$ and Fe(CO) are relatively weaker than the others. The frequency (~1860 cm^{-1}) of $Fe(CO)_2$ was dramatically smaller than those (~2000 cm^{-1}) of $Fe(CO)_5$. In the conventional model describing the bonding between a transition-metal atom and a carbon monoxide with σ-bonding and π-back bonding[1], CO donates its filled weakly antibonding 5σ orbital to the metal orbital, strengthening the C-O bond. The metal may back-donate a filled d orbital into the empty 2π* orbital of CO , thereby weakening the C-O bond. The authors noticed Ozin's proposal[37] that each individual CO may experience increased σ- and π- effects for a less saturated metal carbonyl, and suggested that their results indicated increased that π-back bonding is more important than increased σ- bonding in $Fe(CO)_2$ and Fe(CO). The smaller C-O stretching frequencies of $Fe(CO)_2$ and Fe(CO) infer that the C-O bond lengths of these molecules are larger than those of less unsaturated iron carbonyls. Therefore, our results from structural analysis are consistent with their conclusion from IR study. A more meaningful analysis of structural changes demands better signal-to-noise ratio, which is the focus of an ongoing project in our laboratory.

7.2 $Fe(CO)_5 \rightarrow Fe(CO)_4 + CO$ @ 620 nm

7.2.1 Background

Transition metal carbonyls[2,37] respond to ultraviolet light by losing one or more CO ligands and subsequently forming coordinatively unsaturated carbonyls, which are known to catalyze a variety of reactions.[3,4,38] The photochemistry governing the formation of these coordinatively unsaturated species has been an active area of research both experimentally[18,19,21,23,24,27,39,40] and theoretically[8,14,41-44], often focusing on the reaction pathways and molecular structures of these transient species. Among the transition metal carbonyls, $Fe(CO)_5$ is one of the most extensively studied molecular systems. $Fe(CO)_5$ absorbs strongly in the ultraviolet starting at ~350 nm (3.5 eV)[5,6,45]. The spectrum is rather featureless, and is dominated by ligand-field d-d transitions[6] at low energies and metal-to-ligand charge transfer transitions[6] at high energies. Having five carbonyl ligands, an $Fe(CO)_5$ molecule can dissociate into five different products ($Fe(CO)_x$, $x = 4, 3, 2, 1, 0$) depending on the excitation wavelength.

In these reactions, $Fe(CO)_4$ is the primary intermediate and serves as a "doorway" molecule for various subsequent reactions,[1,46] such as decomposition, recombination with the carbonyl ligand, and coordination with solvent molecules. Elucidating the nature of $Fe(CO)_4$, including its electronic states and the corresponding molecular geometry, is important for understanding the role of intermediates in the photolysis of transition metal carbonyls.

Herein we report direct determination of the molecular structure (Fig. 7.2.1) of the transient $Fe(CO)_4$ using diffraction with ultrashort pulses of electrons. In this way,

we are able to identify the primary reaction pathway and provide details of bond lengths and angles of the intermediate structure. Because of the picosecond time resolution used in these ultrafast electron diffraction (UED) experiments, it is possible to "freeze" the intermediate and determine its structure and its resulting reaction pathway. For $Fe(CO)_4$, we provide direct evidence that the molecular structure involved is that of the singlet, not triplet, pathway contrary to many suggestions in past studies.

The potential energy levels of the $Fe(CO)_x$ species relevant to the photolysis of $Fe(CO)_5$ are shown in Figure 7.2.2. The ground state of $Fe(CO)_5$ is a singlet ($^1A'_1$; D_{3h}) and can be pumped into excited singlet states by absorbing ultraviolet photons. Two possible reaction pathways, the singlet and the triplet, following UV excitation have been postulated.[23,41,47]. In the singlet pathway[23,47], the $^1E'$ state molecules of $Fe(CO)_5$ dissociate into the singlet excited state ($^1A_1$) of $Fe(CO)_4$, while for the triplet pathway,[21,23,42] spin-orbit coupling to the $^3E'$ state of $Fe(CO)_5$ is required prior to dissociation to the triplet ground state ($^3B_2$) of $Fe(CO)_4$. From photolysis in solid matrices at low temperature, $Fe(CO)_4$ product was characterized[15] to have a structure with C_{2v} symmetry and to be in the triplet electronic ground state. This observation is consistent with other experimental results in which secondary fragments [$Fe(CO)_3$, $Fe(CO)_2$, and Fe(CO)] in their triplet electronic ground states were observed as major products, indicating that the ground state ($^3B_2$) of $Fe(CO)_4$ played a determining role.[21,39,48]

However, it was still unclear whether $Fe(CO)_4$ is formed directly into the triplet state or through relaxation via singlet states (Fig. 2), and how the reaction proceeded to generate the subsequent secondary fragments. Early studies on the nanosecond time scale have suggested that the fragmentation follows the triplet pathway.[21,39] A more recent study has suggested that the $^1A_1$ state is initially formed, favoring the singlet pathway.[40] The discrepancy may originate from the difficulty associated with directly monitoring the identity of the transient intermediate structure during the course of the reaction. In this respect, UED[28,49-52] is a powerful method for studying the molecular structure of transient $Fe(CO)_4$. As with conventional ultrafast spectroscopies,[31,53] UED utilizes a femtosecond (fs) laser pulse to initiate a desired chemical reaction; however, in UED, the subsequent laser pulses normally used to probe the progress of the reaction are replaced with ultrashort pulses of electrons. Diffraction patterns are then recorded to provide the internuclear distances of the molecular species involved.

The UED experiments on $Fe(CO)_5$ were performed using the second generation apparatus[28] developed in this laboratory. The time zero, when the excitation laser pulse and the probing electron pulse temporally overlap in the molecular beam, was determined by an ion-induced lensing experiment[28] with $\pm$ 2 ps accuracy. To initiate the reaction, a fs laser pulse was focused into the gas sample beneath the needle of the free-jet expansion. The snapshots of diffraction images at a certain delay time t (−180 and +200 ps) were recorded and converted to the diffraction

intensity data $I_{Tot}(t; s)$, where $s = (4\pi/\lambda)\sin(\theta/2)$, λ is the de Broglie wavelength of the electrons and θ is the scattering angle.

7.2.2 Experimental Setup And Method

The second-generation UED apparatus[28] is composed of a femtosecond laser, a picosecond electron gun, a free-jet expansion sample source, and a two-dimensional single electron detection system. Femtosecond laser pulses from a colliding-pulse mode-locked ring dye laser were amplified in a four-stage pulsed dye amplifier pumped by a Nd:YAG laser. The amplified pulses (620 nm, 3 mJ/pulse, 30 Hz, ~300 fs pulse width) were then split into pump and probe laser pulses; 95% of each laser pulse (pump) was directed and focused into the gas sample beneath the needle of the free-jet expansion source in the scattering chamber. The remaining 5% (probe) was first frequency-doubled with a KDP crystal, and then focused onto a back-illuminated photocathode in the electron gun to generate the ps electron pulses.

The ultrashort electron pulses were accelerated to 18.8 KeV (de Broglie wavelength is 0.088 Å) and focused into the scattering volume. The two-dimensional diffraction images were then recorded at chosen delay times by a charge-coupled device camera at the end of a phosphor scintillator/fiber optic/image intensifier chain in the detection chamber. The electron pulse, laser pulse, and molecular beam were arranged in a cross-beam geometry, and the alignment of the three beams was controlled to within 10 μm. Time delays between the fs pump laser pulse and the ps electron pulse were controlled by a computer-driven translational stage. The

diffraction images were taken with ultrashort electron pulses (~2×10^4 electrons per pulse, with temporal width of 15 ps), and the total temporal resolution is less than 20 ps. The beam waist of both the electron beam and the laser beam was adjusted to be ~300 μm, and the camera length was measured to be 102.9 mm. This second generation apparatus has now been replaced with a third generation machine which provides orders of magnitude improvement in time resolution and sensitivity.[52]

$Fe(CO)_5$ was purchased from Aldrich (98% purity). The sample was first purified through vacuum distillation and then transferred into a sample cell *in situ*. Following connection to the diffraction chamber, the sample was degassed by three cycles of freeze-pump-thaw. In order to provide enough molecular gas density in the scattering volume, the sample cell, gas line, and nozzle were heated to 47, 64, and 72 °C, respectively. The gas pressure in the scattering chamber during the experiment was about 4.6×10^{-4} torr, and the pressure at the scattering volume was estimated to be about a few torr.

7.2.3 Results And Discussion

In our experiments, the time zero was determined with 2 ps accuracy and the overall temporal resolution was less than 20 ps. Thus the diffraction data obtained when the probe electron pulses arrived 180 ps ahead of the first excitation laser pulses (I_{Tot} (*−180 ps*; *s*)) provided a reference signal originated only from the parent molecules $Fe(CO)_5$, as these parent molecules were not excited by the initiating laser. In contrast, the data at +200 ps, I_{Tot} (*+200 ps*; *s*), is comprised of the

contributions from both the remaining parent molecules, $Fe(CO)_5$, and newly formed photoproducts, $Fe(CO)_x$. Thus, the difference between them,[49-52]

$$\Delta I_{Tot}(+200\ ps;\ -180\ ps;\ s) = I_{Tot}\ (+200\ ps;\ s) - I_{Tot}\ (-180\ ps;\ s), \qquad (7.2.3.1)$$

selects the reaction change induced by the fs laser pulse. In the diffraction difference signal, ΔI_{Tot}, the contributions from unreacted molecules and the background signal, which do not change in the course of the chemical reaction, are eliminated, thus highlighting the signal from the change in molecular structure under consideration. A smooth residual background with extremely small amplitude, a likely result of the interaction of probe electrons with positive ions in the gas sample generated by the intense laser pulses, was observed in our experimental ΔI_{Tot}. The background was removed by fitting a smooth curve through the zero-crossing points of the theoretical ΔI_{Tot}. The experimental ΔI_{Tot} curve was smoothed via Fourier filtering (9 Å low-pass) and pixel regions showing systematic abnormalities were removed.. For data analysis, the difference modified molecular scattering intensity, $\Delta sM(t;\ t_{ref};\ s)$, was obtained following the conventional definition:[30]

$$\Delta sM(t;\ t_{ref};\ s) = s \cdot \Delta I(t;\ t_{ref};\ s)/(I_{Atom}), \qquad (7.2.3.2)$$

where I_{Atom} is the atomic scattering intensity (t = +200 ps and t_{ref} = −180 ps in the present case). The corresponding difference radial distribution curves, $\Delta f(r)$, which directly give the change in internuclear distances (r) of the reaction, were then calculated from the $\Delta sM(s)$ curves according to the standard gas-phase electron diffraction equation[30]:

$$\Delta f(r) = \int_0^{s_{max}} \Delta s M(s) \sin(sr) \exp(-ks^2) ds \qquad (7.2.3.3)$$

where the constant k = 0.02 Å^2, is a damping coefficient included to account for the limited s range.

With two-photon excitation at the wavelength of 620 nm, only $Fe(CO)_4$ (both $^1A_1$ and $^3B_2$ states) and $Fe(CO)_3$ (the $^3A_2$ state only) are energetically possible. energy, The singlet $Fe(CO)_3$ may be in principle generated through subsequent loss of a CO ligand from the singlet $Fe(CO)_4$. However, consideration of the energetics eliminates this possibility. The total energy available following the dissociation of $Fe(CO)_5$ into $Fe(CO)_4$ and CO upon two-photon excitation at 620 nm (92 kcal/mol) is 33 kcal/mol, and at most ~65% (21 kcal/mol) of this remaining energy is retained as the internal excitation of $Fe(CO)_4$.[18,21,24] Since the energy gap between the singlet $Fe(CO)_4$ and the singlet $Fe(CO)_3$ is at least 22 kcal/mol, the available energy for the reaction coordinate (mostly r(Fe-C)) is not enough to liberate another CO ligand, even if all the remaining internal energy was transferred to the reaction coordinate. The possibility of generating the singlet $Fe(CO)_3$ by concerted loss of two CO ligands from $Fe(CO)_5$ can not be excluded based on our UED experiment because a fit including the singlet $Fe(CO)_3$ was not performed mainly due to the lack of ab initio structure. However, the elimination process is known to be sequential rather than concerted.[18,21,39,40,42]. A fit with these three possible products was performed by floating the fraction (relative to 100% parent fraction before the photolysis) of each species, and by using the

structural parameters obtained from *ab initio* calculations[44]. The fraction of the singlet $Fe(CO)_4$ was 14 ± 1% while the total fraction of the triplet $Fe(CO)_4$ and triplet $Fe(CO)_3$ was less than 1%, indicating that the singlet $Fe(CO)_4$ is the primary product and the formation of other species is negligible. To trace other possible secondary photofragments, a fit including triplet $Fe(CO)_2$, triplet Fe(CO) and Fe was also performed by floating the fraction of each species while keeping their structural parameters fixed at the values obtained from *ab initio* calculations[44]. The resulting total fraction of $Fe(CO)_2$, Fe(CO) and Fe was less than 1%, confirming that these secondary products are negligible.

Figure 7.2.3 shows the comparison between the UED data fits with $Fe(CO)_4$ for the two different reaction pathways. The $Fe(CO)_4$ structure in the $^1A_1$ state is very similar to that of $Fe(CO)_5$ with one equatorial carbonyl removed, while the structure of $Fe(CO)_4$ in the $^3B_2$ state is significantly distorted.[44] The C-Fe-C angles of the $^3B_2$ state are smaller and the Fe-C distances are longer than those of $Fe(CO)_5$. As shown in Figure 7.2.3, the fit for the $^3B_2$ state is clearly inferior to that of the $^1A_1$ state, which gives a very good agreement between the experiment and theory. Therefore, $Fe(CO)_4$ is formed following the singlet pathway of the reaction in its singlet excited state, $^1A_1$, rather than the ground state, $^3B_2$, at the excitation used. In our previous attempt[49] to isolate the $Fe(CO)_4$ species, 310 nm fs laser pulses were used to photolyze $Fe(CO)_5$. Although one photon of 310 nm just falls short of the threshold for generating $Fe(CO)_2$, Fe(CO) and Fe, it was found that in fact the two-photon absorption dominated. Consequently, the major products obtained were actually $Fe(CO)_2$, Fe(CO)

and Fe rather than $Fe(CO)_4$ or $Fe(CO)_3$. In the present experiment, 620 nm photon excitation was used instead of 310 nm and the main absorption is two-photon. This excitation provides enough energy to break at most two Fe-C bonds, leaving $Fe(CO)_4$ and $Fe(CO)_3$ as the major products. The $^1A_1$ state $Fe(CO)_4$ may eventually convert into the $^3B_2$ state through intersystem crossing (thereby providing a more efficient route for the formation of the $^3A_2$ state $Fe(CO)_3$), but intersystem crossing needs more than 200 ns,[6,23,41,47] which is beyond our investigated time range of up to 200 ps.

A closer examination of the $\Delta f(+200\ ps; -180\ ps; r)$ curve (Fig. 7.2.3) reveals rich details of the structural changes due to the depletion of $Fe(CO)_5$ and formation of $Fe(CO)_4$. The two main peaks centered at ~2 Å and ~3 Å, respectively, indicate the depletion of the Fe-C and Fe···O internuclear contributions due to the liberation of CO. The shoulders beyond 3.5 Å are due to the reduction of other internuclear contributions, C···O and O···O, in the liberation process. The small peak for the C-O bond at ~1.12 Å is negative because the liberated CO ligand has a shorter bond distance than that of the bound ligand (~1.15 Å), but the negative amplitude of the peak is small because the change (from 1.15Å to 1.12 Å) is minute, causing the positive and negative contributions to nearly cancel out.

The structure of $Fe(CO)_4$ obtained from our UED experiment was further refined by limiting the fit to a single product and floating all the independent structural parameters. The results are shown in Figure 7.2.4 and give the following structural parameters: $r(Fe\text{-}C_1) = 1.81 \pm 0.03$ Å, $r(C_1\text{-}O_1) = 1.14 \pm 0.05$ Å, $r(Fe\text{-}C_2) = 1.77 \pm 0.03$ Å; $r(C_2\text{-}O_2) = 1.15 \pm 0.06$ Å, $\angle C_1\text{-}Fe\text{-}C_1 = 169 \pm 2°$, $\angle C_2\text{-}Fe\text{-}C_2 = 125 \pm 3°$. The

error bars represent one standard deviation and do not account for systematic errors. The structure determined here is in good agreements with the ab initio calculation[44] for the $^1A_1$ state. Much earlier, Poliakoff and Turner in their studies of $Fe(CO)_4$ found a species other than the triplet ground state and tentatively assigned the species to be in the singlet state stabilized by a CH_4 matrix at low temperatures. Their careful analysis of IR intensities led them to obtain 173.5 ± 1° and 125 ± 2.5° for C-Fe-C angles,[15] which are remarkably close to our experimental UED values obtained for the isolated species.

In summary, the UED technique was used in this contribution to study the reaction of $Fe(CO)_5$ to liberate CO ligands. The molecular structure of the transient was identified using the temporal diffraction-difference approach of UED. Our results clearly showed that the major product, up to 200 ps, is the transient $Fe(CO)_4$ formed in the $^1A_1$ state, rather than the $^3B_2$ ground state. The structure obtained from the diffraction data was further refined to give the bond lengths and angles of the transient $Fe(CO)_4$ with a resolution of ~0.05 Å. These combined temporal and structural resolutions should be of significant value in identifying transition configurations and pathways of other reactions.

References

1. Wrighton, M. The Photochemistry of Metal Carbonyls. *Chem. Rev.* **74**, 401-430 (1974).
2. Geoffroy, G. L. & Wrighton, M. S. *Organometallic Photochemistry* (Academic Press, New York, 1979).
3. Wender, I. & Pino, P. *Organic Synthesis via Metal Carbonyls* (Wiley, New York, 1977).
4. Wrighton, M. S., Ginley, D. S., Schroeder, M. A. & Morse, D. L. Generation of Catalysts by Photolysis of Transition Metal Complexes. *Pure & Appl. Chem.* **41**, 671-697 (1975).
5. Nathanson, G., Gitlin, B., Rosan, A. M. & Yardley, J. T. Ultraviolet laser photolysis: Primary photochemistry of $Fe(CO)_5$ in PF_3. *J. Chem. Phys.* **74**, 361-369 (1981).
6. Kotzian, M., Rosch, N., Schroder, H. & Zerner, M. C. Optical Spectra of Transition-Metal Carbonyls: $Cr(CO)_6$, $Fe(CO)_5$ and $Ni(CO)_4$. *J. Am. Chem. Soc.* **111**, 7687-7696 (1989).
7. Housecroft, C. E., Wade, K. & Smith, B. C. Reorganization Energies and Site Preferences of Carbonyl Ligands: Bond Energies of the Bridging and Terminal Carbonyl Groups of the Iron Carbonyls $Fe_2(CO)_9$ and $Fe(CO)_5$. *J. Organomet. Chem.* **170**, C1-C5 (1979).
8. Guenzburger, D., Saitovitch, E. M. B., De Paoli, M. A. & Manela, H. On the

photofragmentation of $Fe(CO)_5$. II. Molecular orbital studies of $Fe(CO)_n$, 1 >= n >=5. *J. Chem. Phys.* **80**, 735-744 (1984).

9. Li, J., Schreckenbach, G. & Ziegler, T. A reassessment of the first metal-carbonyl dissociation energy in $M(CO)_4$ (M = Ni, Pd, Pt), $M(CO)_5$ (M = Fe, Ru, Os), and $M(CO)_6$ (M = Cr, Mo, W) by a Quasirelativistic Density Functional Method. *J. Am. Chem. Soc.* **117**, 486-494 (1995).

10. Engelking, P. C. & Lineberger, W. C. Laser Photoelectron Spectrometry of the Negative Ions of Iron and Iron Carbonyls. Electron Affinity Determination for the Series $Fe(CO)_n$, n = 0, 1, 2, 3, 4. *J. Am. Chem. Soc.* **101**, 5569-5573 (1979).

11. Lewis, K. E., Golden, D. M. & Smith, G. P. Organometallic Bond Dissociation Energies: Laser Pyrolysis of $Fe(CO)_5$, $Cr(CO)_6$, $Mo(CO)_6$, and $W(CO)_6$. *J. Am. Chem. Soc.* **106**, 3905-3912 (1984).

12. Beagley, B., Cruickshank, D. W. J., Pinder, P. M., Robiette, A. G. & Sheldrick, G. M. The Molecular Structure of $Fe(CO)_5$ in the Gas Phase. *Acta Cryst.* **B25**, 737-744 (1969).

13. Beagley, B. & Schmidling, D. G. A Re-Evaluation Of The Molecular Structure Of Iron Pentacarbonyl. *J. Mol. Struct.* **22**, 466-468 (1974).

14. Barnes, L. A., Rosi, M. & Bauschlicher, C. W. J. An ab initio study of $Fe(CO)_n$, n = 1, 5, and $Cr(CO)_6$. *J. Chem. Phys.* **94**, 2031-2039 (1991).

15. Poliakoff, M. & Turner, J. J. Structure and Reactions of Matrix-isolated

Tetracarbonyliron(0). *J. Chem. Soc. Dalton Trans.*, 2276-2285 (1974).

16. Poliakoff, M. Infrared Spectrum of Matrix Isolated Tricarbonyliron. *J. Chem. Soc. Dalton. Trans.*, 210-212 (1974).

17. Peden, C. H. F., Parker, S. F., Barrett, P. H. & Pearson, R. G. Mossbauer and Infrared Studies of Matrix-Isolated Iron-Carbonyl Complexes. *J. Phys. Chem.* **87**, 2329-2336 (1983).

18. Yardley, J. T., Gitlin, B., Nathanson, G. & Rosan, A. M. Fragmentation and molecular dynamics in the laser photodissociation of iron pentacarbonyl. *J. Chem. Phys.* **74**, 370-378 (1981).

19. Whetten, R. L., Fu, K.-J. & Grant, E. R. Photodissociation dynamics of $Fe(CO)_5$: Excited state lifetimes and energy disposal. *J. Chem. Phys.* **79**, 4899-4911 (1983).

20. Waller, I. M., Davis, H. F. & Hepburn, J. W. Photofragment Spectroscopy of Metal Carbonyls: A Molecular Beam Study of $Fe(CO)_5$ Photolysis at 193 nm. *J. Phys. Chem.* **91**, 506-508 (1987).

21. Waller, I. M. & Hepburn, J. W. State-resolved photofragmentation dynamics of $Fe(CO)_5$ at 193, 248, 266, and 351 nm. *J. Chem. Phys.* **88**, 6658-6669 (1988).

22. Ray, U. *et al.* A crossed laser-molecular beam study of the photodissociation dynamics of $Fe(CO)_5$ at 193 nm. *J. Chem. Phys.* **89**, 4092-4101 (1988).

23. Seder, T. A., Ouderkirk, A. J. & Weitz, E. The wavelength dependence of excimer laser photolysis of $Fe(CO)_5$ in the game phase. Transient infrared

spectroscopy and kinetics of the $Fe(CO)_x$ (x = 4, 3, 2) photofragments. *J. Chem. Phys.* **85**, 1977-1986 (1986).

24. Ryther, R. J. & Weitz, E. Reaction Kinetics of Coordinatively Unsaturated Iron Carbonyls Formed on Gas-Phase Excimer Laser Photolysis of $Fe(CO)_5$. *J. Phys. Chem.* **95**, 9841-9852 (1991).

25. Kim, S. K., Pedersen, S. & Zewail, A. H. Femtochemistry of organometallics: dynamics of metal-metal and metal-ligand bond cleavage in $Mn_2(CO)_{10}$. *Chem. Phys. Lett.* **233**, 500-508 (1995).

26. Bañares, L., Baumert, T., Bergt, M., Kiefer, B. & Gerber, G. Femtosecond photodissociation dynamics of $Fe(CO)_5$ in the gas phase. *Chem. Phys. Lett.* **267**, 141-148 (1997).

27. Bañares, L., Baumert, T., Bergt, M., Kiefer, B. & Gerber, G. The ultrafast photodissociation of $Fe(CO)_5$ in the gas phase. *J. Chem. Phys.* **108**, 5799-5811 (1998).

28. Williamson, J. C., Cao, J., Ihee, H., Frey, H. & Zewail, A. H. Clocking transient chemical changes by ultrafast electron diffraction. *Nature* **386**, 159-162 (1997).

29. Williamson, J. C. & Zewail, A. H. Ultrafast Electron Diffraction. 4. Molecular Structures and Coherent Dynamics. *J. Phys. Chem.* **98**, 2766-2781 (1994).

30. Hargittai, I. & Hargittai, M. *Stereochemical Applications Of Gas-Phase Electron Diffraction* (VCH, New York, 1988).

31. Zewail, A. H. *Femtochemistry: Ultrafast Dynamics of the Chemical Bond*

(World Scientific, Singapore, 1994).

32. Zewail, A. H. *Femtochemistry: atomic-scale dynamics of the chemical bond using ultrafast lasers in Les Prix Nobel* (Almqvist & Wiksell, Stockholm, 1999).

33. Zewail, A. H. Femtochemistry: Atomic-Scale Dynamics of the Chemical Bond. *J. Phys. Chem. A* **104**, 5660-5694 (2000).

34. Hedberg, K. & Iwasaki, M. Least-Squares Refinement of Molecular Structures from Gaseous Electron Diffraction Sector-Microphotometer Intensity Data. I. Method. *Acta Cryst.* **17**, 529-533 (1964).

35. Bartell, L. S. in *Physical Methods of Chemistry* (eds. Weissberger, A. & Rossiter, B. W.) (Wiley, New York, 1972).

36. Barnes, I., Becker, K. H. & Starcke, J. The gas-phase infrared spectra of formyl iodide and carbonyl iodide. *Chem. Phys. Lett.* **246**, 594-600 (1995).

37. Ozin, G. A. & Hanlan, A. J. L. Rhodium and Iridium Atom Chemistry: Binary Carbonyls of Rhodium and Iridium. *Inorg. Chem.* **18**, 2091-2101 (1979).

38. Schroeder, M. A. & Wrighton, M. S. Pentacarbonyliron(0) photocatalyzed hydrogenation and isomerization of olefins. *J. Am. Chem. Soc.* **98**, 551-558 (1976).

39. Venkataraman, B. K., Bandukwalla, G., Zhang, Z. & Vernon, M. One- and two- photon photodissociation of $Fe(CO)_5$ at 248 nm. Application of an accurate method for calculating angle resolved velocity distributions for multiple sequential bond rupture processes. *J. Chem. Phys.* **90**, 5510-5526

(1989).

40. Trushin, S. A., Fuss, W., Kompa, K. L. & Schmid, W. E. Femtosecond dynamics of $Fe(CO)_5$ photodissociation at 267 nm studies by transient ionization. *J. Phys. Chem. A* **104**, 1997-2006 (2000).

41. Daniel, C., Benard, M., Dedieu, A., Wiest, R. & Veillard, A. Theoretical Aspects of the Photochemistry of Organometallics. 3. Potential Energy Curves for the Photodissociation of Fe(CO)5. *J. Phys. Chem.* **88**, 4805-4811 (1984).

42. Veillard, A., Strich, A., Daniel, C. & Siegbahn, P. E. M. A CAS SCF CCI Study of The Lowest Excited States of $HMn(CO)_5$ and $Fe(CO)_5$. *Chem. Phys. Lett.* **141**, 329-333 (1987).

43. Rubner, O., Engel, V., Hachey, M. R. & Daniel, C. A CASSCF/MR-CCI study of the excited states of Fe(CO)5. *Chem. Phys. Lett.* **302**, 489-494 (1999).

44. González-Blanco, O. & Branchadell, V. Density functional study of the Fe-CO bond dissociation energies of Fe(CO)5. *J. Chem. Phys.* **110**, 778-783 (1999).

45. Dartiguenave, M., Dartiguenave, Y. & Gray, H. B. Spectre electronique du fer pentacarbonyle. Etude theorique et experimentale. *Bul. Soc. Chem. Fran.* **12**, 4223-4225 (1969).

46. Poliakoff, M. & Weitz, E. Shedding Light on Organometallic Reactions: The Characterization of Fe(CO)4, a Prototypical Reaction Intermediate. *Acc. Chem. Res.* **20**, 408-414 (1987).

47. Ryther, R. J. & Weitz, E. Diode Laser Probes of the Product Distribution of Coordinatively Unsaturated Iron Carbonyls Produced following Excimer Laser

Photolysis of Fe(CO)5 in the gas phase. *J. Phys. Chem.* **96**, 2561-2567 (1992).

48. Ouderkirk, A. J., Wermer, P., Schultz, N. L. & Weitz, E. Observation of Coordinatively Unsaturated Intermediates following the Pulsed UV Photolysis of Fe(CO)5. *J. Am. Chem. Soc.* **105**, 3354-3355 (1983).

49. Ihee, H., Cao, J. & Zewail, A. H. Ultrafast electron diffraction: structures in dissociation dynamics of $Fe(CO)_5$. *Chem. Phys. Lett.* **281**, 10-19 (1997).

50. Cao, J., Ihee, H. & Zewail, A. H. Ultrafast electron diffraction: determination of radical structure with picosecond time resolution. *Chem. Phys. Lett.* **290**, 1-8 (1998).

51. Cao, J., Ihee, H. & Zewail, A. H. Ultrafast electron diffraction and direct observation of transient structures in a chemical reaction. *Proc. Natl. Acad. Sci. USA* **96**, 338-342 (1999).

52. Ihee, H. *et al.* Direct Imaging of Transient Molecular Structures with Ultrafast Diffraction. *Science* **291**, 458-462 (2001).

53. Manz, J. & Wöste, L. *Femtosecond Chemistry* (VCH, New York, 1995).

Figure Captions

Figure 7.1.1: Structures of $Fe(CO)_5$ and its unsaturated photofragments, where α= 145°, β = 120° [14], and θ = 21° [14, 30].

Figure 7.1.2: Experimental modified molecular scattering curves (left) and radial distribution curves (right) taken with 10-ps electron pulses. The delay time between the fs laser pulse and the ps electron pulse are shown. Shaded lines represent theoretical calculation with structural parameters from other electron diffraction study.

Figure 7.1.3: Difference modified molecular scattering curves (left) and difference radial distribution curves (right) obtained by fitting one component product. Solid lines are experimental curves and shaded lines are the best fits.

Figure 7.1.4: Best fits obtained by fitting $Fe(CO)_2$, Fe(CO) and Fe as products. The fractions of $Fe(CO)_2$, Fe(CO) and Fe are 2% (± 1%), 5% (± 2%) and 5% (± 1%), respectively. The fitted Fe-C and C-O distance of $Fe(CO)_2$ are 1.67 (± 0.25) Å and 1.34 (± 0.10) Å, and the fitted Fe-C and C-O distance of Fe(CO) were 1.78 (± 0.32) Å and 1.20 (± 0.16) Å, respectively.

Figure 7.2.1: Structural changes in the reaction of $Fe(CO)_5$ to liberate CO ligands.

Figure 7.2.2: Scheme of the potential energy levels and pathways of the UV dissociation of $Fe(CO)_5$. The following energies (in kcal/mol) relative to the ground state ($1A'_1$) of $Fe(CO)_5$ are from the literature.[8,14,39,41,43] $Fe(CO)_5$: $^3E'$, 78.1; a^1E',

77.2; $^1A''_2$, 105.8; b$^1E'$, 114.4; $Fe(CO)_4$: $^3B_2$, 41.5; $^1A_1$, 59.0; $Fe(CO)_3$: $^3A_2$, 53.0; $^1E'$, 80.7. The two pathways, singlet and triplet, are indicated in the two panels.

Figure 7.2.3: Ultrafast electron diffraction of the intermediate $Fe(CO)_4$ species. Top panel: The structures of two possible electronic states ($^1A_1$ and $^3B_2$) for $Fe(CO)_4$. The values for the angles are from *ab initio* calculations[44]. Bottom panel: Comparison of experimental $-\Delta f(+200\ ps;\ -180\ ps;\ r)$ curves (red) with corresponding theoretical calculations (blue) obtained via *ab initio* structures of the $^1A_1$ state (Left panel) and the $^3B_2$ state (Right panel).

Figure 7.2.4: The refined molecular structure of $Fe(CO)_4$ in the $^1A_1$ state, determined by ultrafast electron diffraction. (see text).

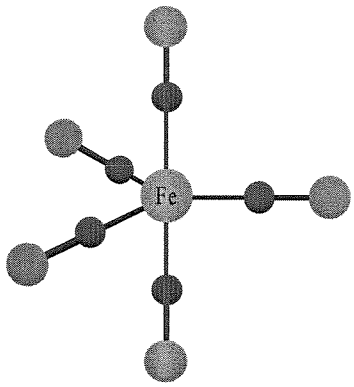

$Fe(CO)_5$, D_{3h}

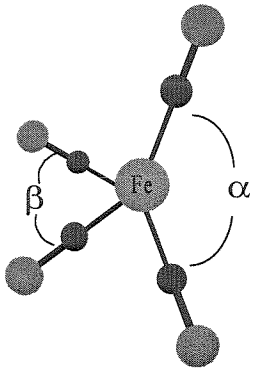

$Fe(CO)_4$, C_{2v}

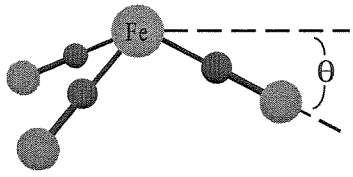

$Fe(CO)_3$, C_{3v}

$Fe(CO)_2$, $D_{\infty h}$

$Fe(CO)$, $C_{\infty v}$

Figure 7.1.1

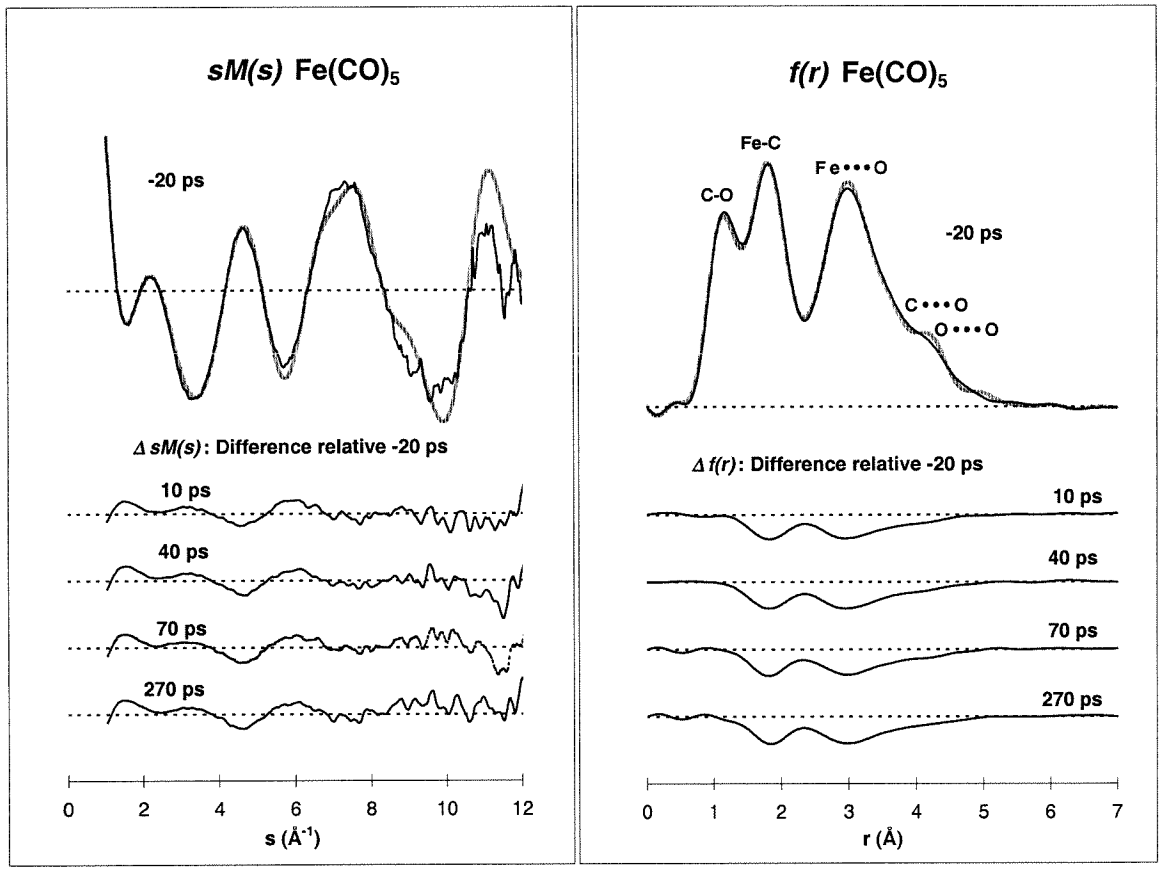
sM(s) Fe(CO)5
-20 ps
Δ sM(s): Difference relative -20 ps
10 ps
40 ps
70 ps
270 ps
0 2 4 6 8 10 12
s (Å-1)
f(r) Fe(CO)5
Fe-C
Fe•••O
C-O
-20 ps
C•••O
O•••O
Δ f(r): Difference relative -20 ps
10 ps
40 ps
70 ps
270 ps
0 1 2 3 4 5 6 7
r (Å)

Figure 7.1.2

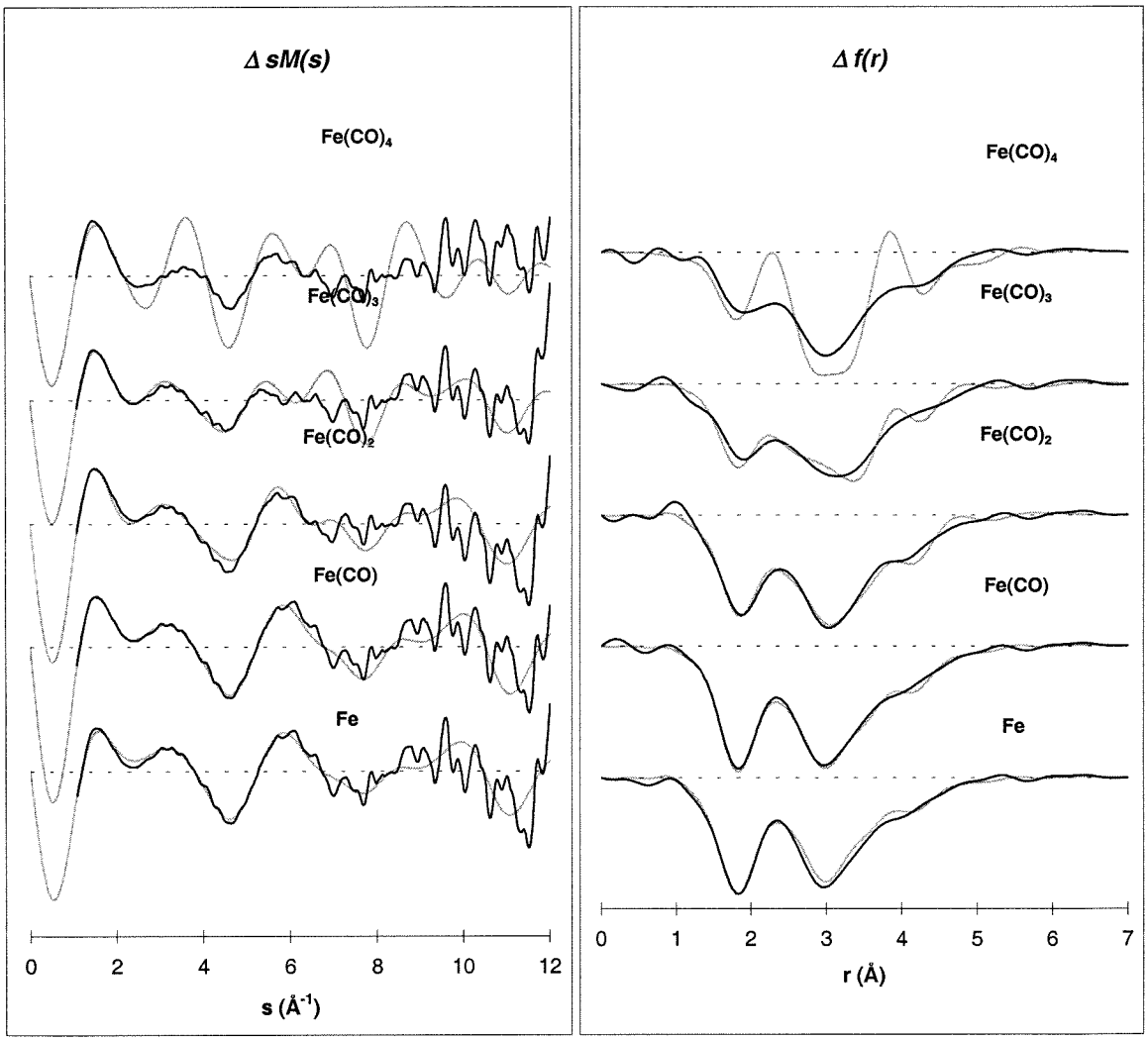
Δ sM(s)
Fe(CO)4
Fe(CO)3
Fe(CO)2
Fe(CO)
Fe
0
2
4
6
8
10
12
s (Å-1)
Δ f(r)
Fe(CO)4
Fe(CO)3
Fe(CO)2
Fe(CO)
Fe
0
1
2
3
4
5
6
7
r (Å)

Figure 7.1.3

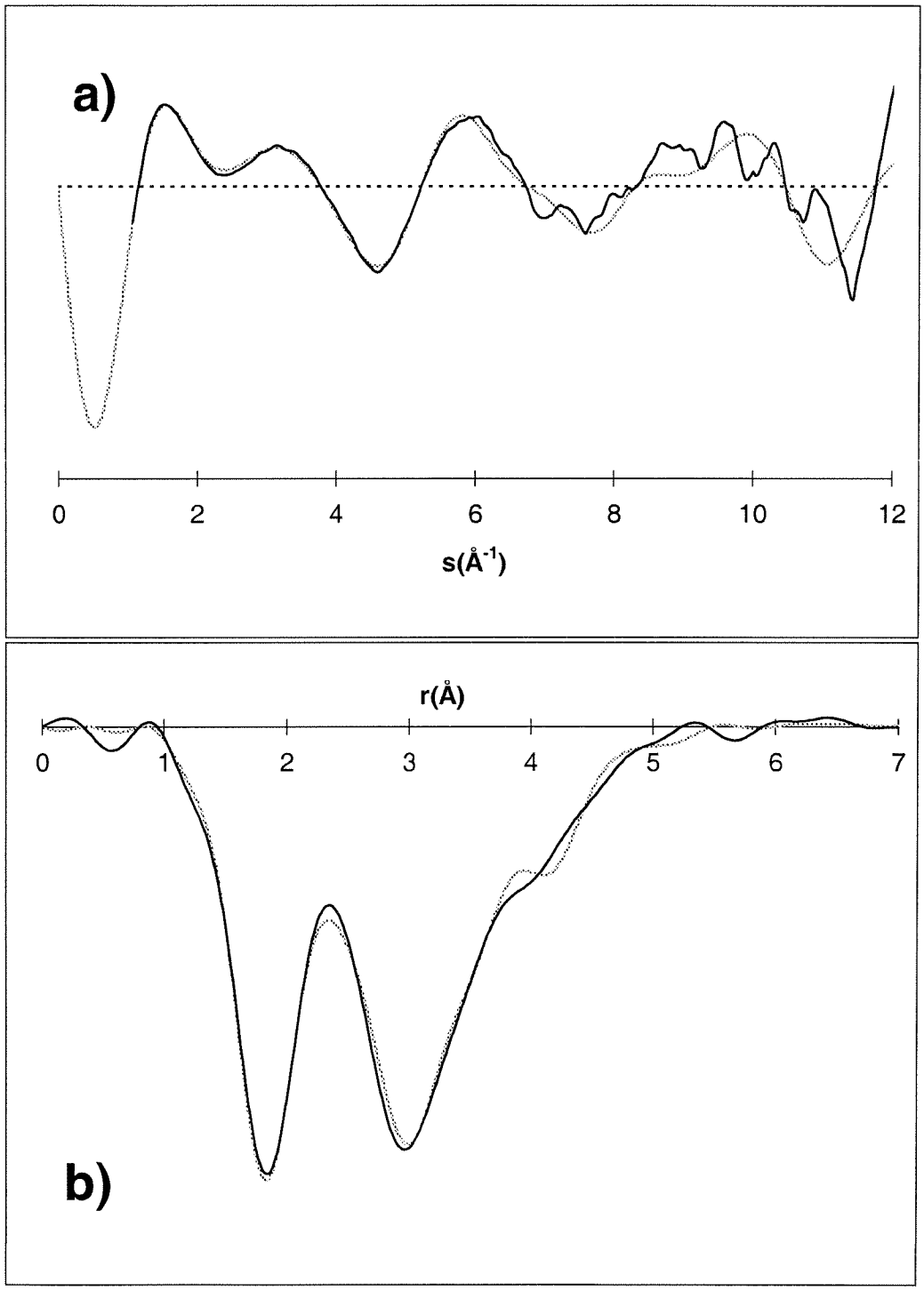

Figure 7.1.4

Structural Changes: Ligand Elimination Reaction

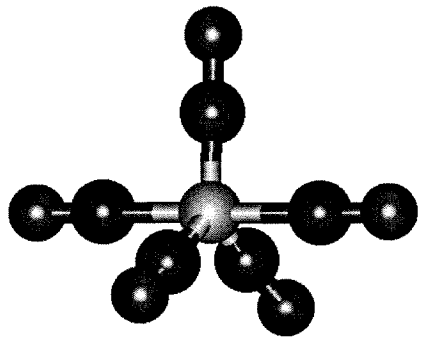

$Fe(CO)_5$

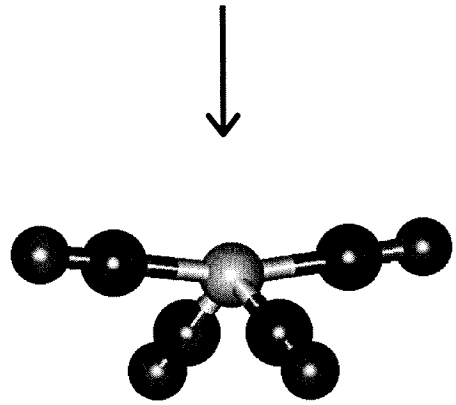

$Fe(CO)_4$

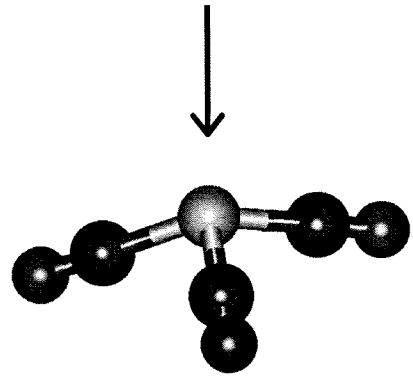

$Fe(CO)_3$

Figure 7.2.1

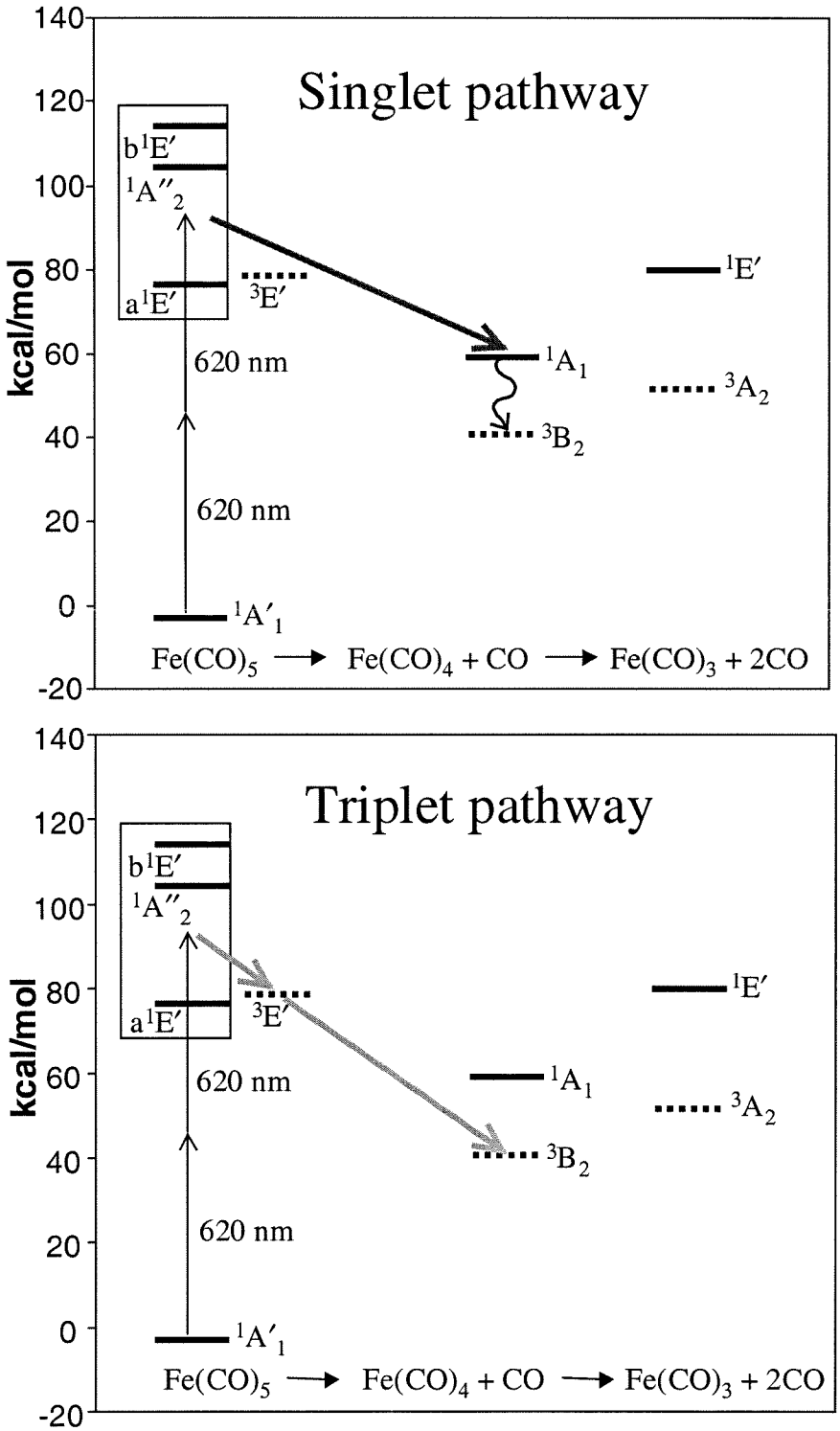
Singlet pathway
kcal/mol
140
120
100
80
60
40
20
0
-20
b1E′
1A″2
a1E′
3E′
620 nm
620 nm
1A′1
1A1
3B2
1E′
3A2
Fe(CO)5 → Fe(CO)4 + CO → Fe(CO)3 + 2CO
Triplet pathway
kcal/mol
140
120
100
80
60
40
20
0
-20
b1E′
1A″2
a1E′
3E′
620 nm
620 nm
1A′1
1A1
3B2
1E′
3A2
Fe(CO)5 → Fe(CO)4 + CO → Fe(CO)3 + 2CO

Figure 7.2.2

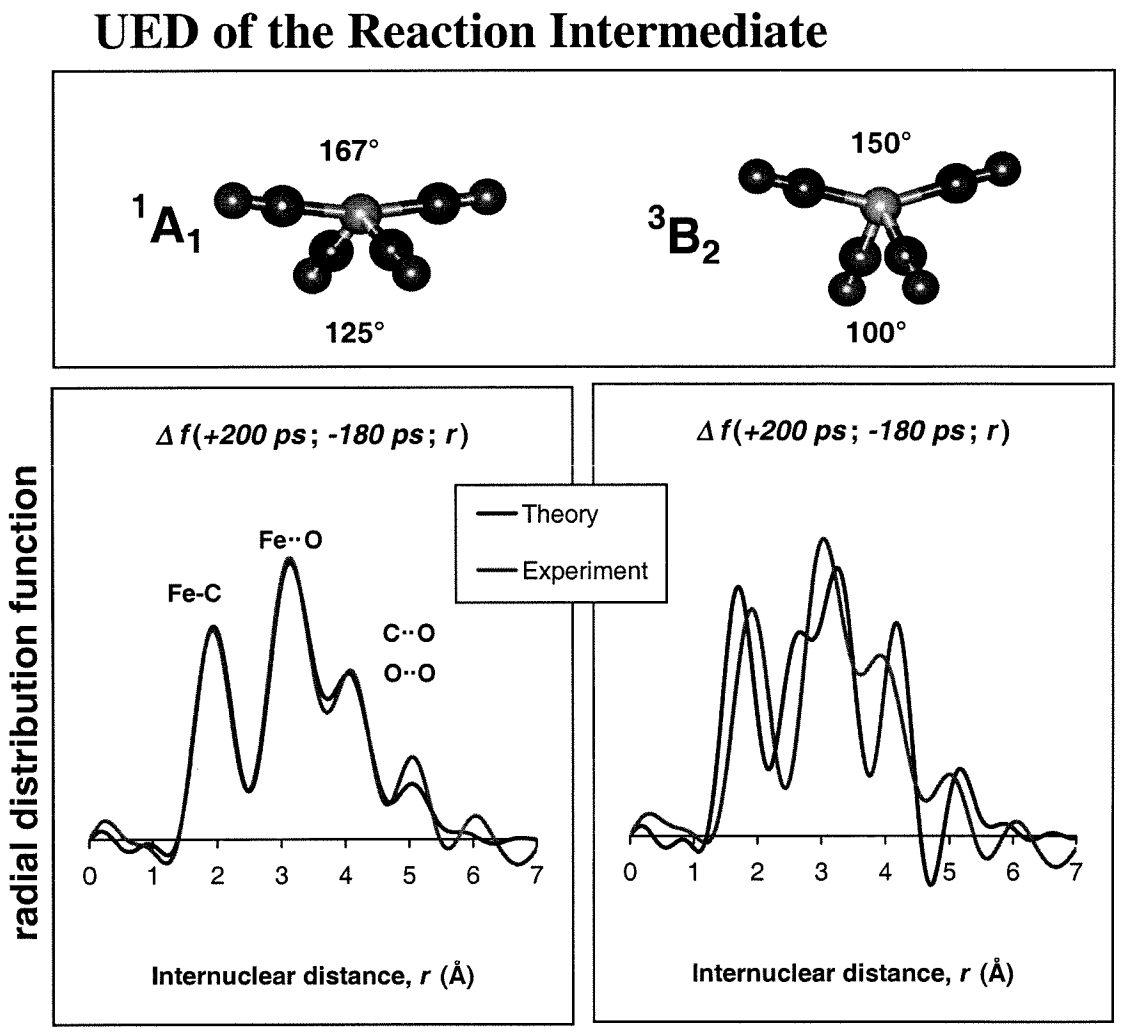
UED of the Reaction Intermediate
167°
$^1A_1$
125°
150°
$^3B_2$
100°
radial distribution function
Δf(+200 ps; -180 ps; r)
Theory
Experiment
Fe··O
Fe-C
C··O
O··O
0 1 2 3 4 5 6 7
Internuclear distance, r (Å)
Δf(+200 ps; -180 ps; r)
0 1 2 3 4 5 6 7
Internuclear distance, r (Å)

Figure 7.2.3

Molecular Structure of Intermediate $[Fe(CO)_4]$

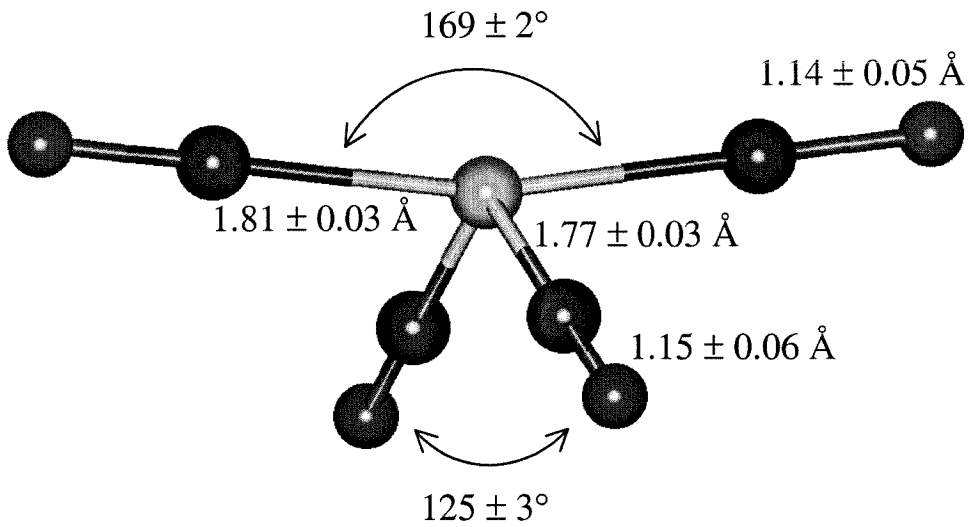

Figure 7.2.4

APPENDIX

A.1 Ab Initio Calculation Of C_2H_4X and $C_2H_4X_2$ (X = F, Cl, Br, I)

A.1.1 Introduction

The class of halo radicals such as CH_2XCH_2• is important in a number of chemical processes[1-4] and determines the stereoselectivity of the reaction products from the halogenation[1,2,5-9] of alkenes and alkanes. Their role in stereoselective control is determined by whether the radical is classical (Figure A.1.1c) or bridged and if bridged whether the structure is symmetric (Figure A.1.1a) or asymmetric (Figure A.1.1b). The possible minima and transition structures for rotation around the C-C bond are schematically represented in Figure A.1.2. Anti (I) and gauche (III) rotamers are candidates for local energy minima on the rotational energy surface because Pauli repulsion between bonding pairs would be minimized at these two conformations. The other two structures (II and IV) possessing eclipsed bonds are also possible transition states on the rotational energy surface.

If the structure of the radical is bridged, we expect retention of the stereochemistry. However, if the radical prefers a classical asymmetric conformation, additional conditions must be fulfilled to exert stereochemical control. Namely, a strong preference for high population of the anti conformer and non-planarity of the radical center are required. Experimental[10-20] and theoretical[21-43] studies have led to a good understanding of the structure and energetics for the cases of X = H, F, and Cl; however, little is known about X = Br and I. The motivation for our studies was to elucidate the X = Br and I systems. But we also studied the X = H, F, Cl cases as a comparison to previous experiments and theories.

In this paper we use four techniques of first principles quantum mechanics (QM) methods to examine the potential surface for CH_2XCH_2• with X = H, F, Cl, Br, and I. These

QM methods are HF, local MP2 (LMP2) and two kinds of DFT (B3LYP and B3PW91). We find that X = Br and I are significantly different from the cases of X = H, F, and Cl.

Section 2 reviews the current level of understanding for these systems. Section 3 explains the QM methods being used, and Section 4 presents the results.

A.1.2 Previous Studies

A.1.2.1 Experiments

It is well established that the carbonium ion $C_2H_4X^+$ (where X = H, F, Cl, Br, I) has a bridged structure with one X^+ shared equally between the two carbons.[44-46] However, there is no general agreement on whether the radical $C_2H_4X\bullet$ is bridged or not.[47] Based on the stereochemical control observed in the free radical addition of HBr to 1-bromocyclohexene and 1-methylcyclohexene, Goering et al.[5] introduced the concept of a bridged radical to explain the results. Also, Thaler[6] reported the unexpected preponderance of *trans*-1, 2-dibromide in the product mixture from the radical bromination of several alkyl bromides and suggested that the intermediate bromoalkyl radical may exist as a three-membered ring species. To understand this stereoselectivity, many researchers have studied the β-substituted alkyl radicals both experimentally[10-20] and theoretically.[21-43]

Three possible structures (Figure A.1.1) could play a role in the stereochemical retention observed in many reactions containing β-haloalkyl radicals[47]:

a. symmetrically bridged radical

b. asymmetrically bridged radical

c. classical radical (asymmetric and non-bridged).

The early proposal by Goering et al. did not distinguish between symmetrically or asymmetrically bridged species. Later, Skell and co-workers[7,48] advocated a *symmetrically* bridged structure for β-substituted alkyl radicals containing third- and higher-row elements to explain the stereochemical control observed in many reactions. However, based on the hyperfine coupling constants from the ESR spectrum, Bowles et al.[13] suggested that the β-chloroethyl radical prefers the anti conformation in which the Cl atom is in the same plane as the singly occupied carbon 2p orbital. Also, Kochi and coworkers[49] disputed Skell's hypothesis based on the inequivalence of α- and β-splittings of ESR spectrum in $R_nMCH_2CH_2\bullet$ radicals containing third- and higher-row elements. Instead, they suggested asymmetrically bridged structures. Semiempirical INDO calculations[43] on ethyl and β-chloroethyl radicals supported this asymmetric bridging hypothesis. However, β-bromo and β-iodo radicals have not been identified by ESR[10], hence, the argument of Kochi and coworkers cannot be applied generally. In response, Skell and co-workers[47] suggested that stereochemical control could be explained also with a *dynamic* asymmetric bridging (shuttle motion) where the substituent oscillates rapidly between the two carbon atoms. Alternatively, Lloyd and Wood[50] pointed out that the stereoselectivity can be explained in terms of a high rotational barrier around the C-C bond in conjunction with a non-planar radical center for β-chloro, β-bromo, and β-iodo alkyl radicals (based on the ESR study of β-halo-*tert*-butyl radicals and INDO calculations). Most investigations using ESR techniques have been limited to β-substituted radicals containing H, F, Cl, S, Si, and Sn as a

substituent. For the CH_2FCH_2• radical, Chen et al.[12] observed unusual selective line broadening in the ESR spectra and strong temperature dependence of the β-proton and β-fluorine coupling constants. They suggested that a rapid interconversion takes place between two or more different equilibrium conformations which differ in energy by <0.3 kcal/mol and which are separated by a barrier <1.5 kcal/mol. Edge and Kochi[10] could not observe the β-bromoalkyl (both the β-bromoethyl and the β-bromopropionyl) radical in solution even at –120° by ESR. As they pointed out, their inability to observe the ESR spectra of the β-bromoalkyl radical *in solution* does not mean that such is not possible. For example, the ESR spectra of β-bromo and β-iodoalkyl radicals were obtained in frozen solution at 77 K by ^{60}Co γ-radiolysis.[51]

A.1.2.2 Theoretical Studies

Since the experimental results hardly distinguish the possibilities, many theoretical calculations have been performed to determine the most stable structures. Most theoretical studies have been devoted to β-fluoroethyl radical (CH_2FCH_2•)[21-36] and to β-chloroethyl radical (CH_2ClCH_2•)[31-43] with very little attention to β-bromoethyl radical (CH_2BrCH_2•)[35] and β-iodoethyl radical (CH_2ICH_2•).

CH_2FCH_2•

Early *ab initio* calculations[27-29,36] generally considered only two structures; the eclipsed structure (IV in Figure A.1.2) where the carbon 2p orbital is perpendicular to the

FCC plane and the anti structure (I in Figure A.1.2) where the 2p orbital is coplanar with FCC plane. Pople and coworkers[29] studied the rotational barriers in substituted ethyl radicals using *ab initio* unrestricted HF (UHF) calculations with a minimal basis set (STO-3G). They pointed out that the barriers of the radicals are smaller than those of corresponding cations. For the $CH_2FCH_2\bullet$ radical, their calculation showed no energy difference between the eclipsed form and the anti conformation. They rationalized the general decrease of rotational barrier in the radicals by suggesting that the hyperconjugative interaction between the $2p(CH_2\bullet)$ orbital and the $\pi_x(CH_2F)$ or $\pi_y(CH_2F)$ orbital at the β-carbon is reduced in the radicals because the 2p orbital is no longer vacant. Pross and Radom[28] reported UHF calculations (UHF/4-31G or UHF/5-31G) of β-substituted ethyl radicals where the substituents are second-row elements. They observed that the eclipsed form shows only slight conformational preferences (0.6 kcal/mol) to the anti conformation of $CH_2FCH_2\bullet$ and rationalized such behavior in terms of opposing changes in positive and negative hyperconjugation between the CH_2F group and the $CH_2\bullet$ center. In contrast, Kato and Morokuma[27] reported that the eclipsed form is the saddle point for the internal rotation around the CC bond while the anti structure is the minimum (at the UHF/4-31G level of calculation).

Fossey and Nedelec[26] used the UHF method with the STO-3G basis set to study 1,2 migrations observed in many free radical reactions. They considered only the anti conformation and the symmetrically bridged form. They reported that they could not find an energy minimum for the bridged structure of the $CH_2FCH_2\bullet$ radical. Schlegel[25] studied the $F + C_2H_4$ reaction by fully optimizing the equilibrium geometries and transition structures

using UHF/3-21G, HF/6-31G* and MP2/3-21G methods. In contrast with previous *ab initio* calculations, they reported that the CH_2FCH_2 radical adopts a gauche conformation (III in Figure A.1.2). They also reported that the anti structure is at the saddle point with one imaginary vibrational frequency at UHF/3-21G level. Based on UHF and MP2 calculations, Clark and coworkers reported that protonation[34] and addition of a metal cation[52] enhance the stability of the symmetrically bridged structures. Bernardi and coworkers[24,32] used perturbational MO approaches to rationalize the conformational preference in β-substituted ethyl radical in the framework of the UHF calculations. They suggested that the hyperconjugation between the singly occupied carbon 2p orbital and the σ*(C-X) MO plays the major role in determining the preferred conformation. Engels and Peyerimhoff[22] reported that the bridged form of CH_2FCH_2• is stable with respect to the dissociation but too high to allow any shuttle motion in their large scale multi referenced configuration interaction (MRD-CI) calculation. They found only one minimum (gauche form) along the rotation around CC bond. In contrast, Tschuikow-Roux and coworkers[53] reported there are two minima and two saddle points along the rotational surface at UHF and MP2//UHF levels of theory.

CH_2ClCH_2•

Based on INDO calculations, Biddles and Hudson[43] claimed that β-chloroethyl radical has a ClCC bond angle of 92°, supporting the asymmetric bridged structure proposed by Kochi and coworkers[49]. Except for this early INDO calculation, there seems to have

been no *ab initio* calculations supporting an asymmetrically bridged structure for the CH_2ClCH_2• radical. Hopkinson et al.[42] performed UHF/4-31G* calculations on CH_2ClCH_2 with minimal and split-valence shell basis sets. They reported a rotational barrier of 2 kcal/mol and concluded that there is no evidence of bridging of the Cl atom. Molino et al.[36] studied the conformational preferences and structural trends for a series of fluorine- and chlorine-substituted methyl and ethyl radicals using MNDO type calculations with UHF and half-electron formalisms. Their calculations suggested that the CH_2FCH_2 radical prefers the eclipsed conformation and the CH_2ClCH_2 radical prefers the anti conformation. Fossey and Nedelec[26] reported that the bridged CH_2ClCH_2 radical is 53 kcal/mol higher than the anti structure. Schlegel et al.[41] studied the Cl + C_2H_4 reaction using UHF/3-21G*, HF/6-31G* and MP2/3-21G methods and reported that the CH_2ClCH_2 radical adopts a anti conformation with rotational energy barrier of 4 kcal/mol. Hoz et al.[40] studied the 1,2-rearrangement in β-substituted ethyl radicals using active space multiconfiguration self-consistent field calculations. They reported that the symmetric bridged structure is above the Cl + C_2H_4 dissociation energy limit, suggesting that symmetric bridging in CH_2ClCH_2 is not likely. In contrast, Engels et al.[38] performed large scale MRD-CI calculations and reported that the symmetrically bridged form is stable to the dissociation and only 6.2 kcal/mol higher than the anti conformation. Recently, Tschuikow-Roux and coworkers studied the rotation/inversion barriers of CH_2ClCH_2.[37] They reported that the rotational barrier for CH_2ClCH_2 is only 1.5 kcal/mol at MP2/6-311G*//HF/6-31G* level with the anti conformation preferred. They did not study the bridged structure for the radicals.

CH_2BrCH_2•

Based on *ab initio* large scale MRD-CI studies of the β-haloethyl radicals for X = F, Cl, and Br, Engels and Peyerimhoff[35] reported that the absolute minimum in the potential energy surface is an asymmetric radical for all three cases. The structures of the asymmetric radicals in their calculations did not show evidence for asymmetric bridging. Based on the energy difference between the absolute minimum and the symmetric conformation, they suggested that the shuttle motion is highly probable in CH_2BrCH_2 but less favorable for CH_2FCH_2 and CH_2ClCH_2. It should be noted that the shuttle motion in the Engels and Peyerimhoff discussion is different from the Skell's dynamic asymmetric bridging in that the latter refers to the rapid oscillation between two asymmetrically bridged radicals while the former involves a symmetrically bridged structure between two asymmetric non-bridged radicals (classical radicals).

In the most recent study on the β-substituted ethyl radicals, Guerra[31] concluded that the observed stereochemical control could be accounted for by:

(i) a high population of the anti conformer in radicals bearing third-row substituents in conjunction with the nonplanarity of the radical site and/or

(ii) steric hindrance of the β-substituent due to bridging.

To distinguish between these two possibilities for explaining the stereoselective control, it is important to study simultaneously the rotational barrier and the stability of the bridged structure. The CH_2BrCH_2 and CH_2ICH_2 radicals have rarely been studied by *ab initio* methods. We know of just one *ab initio* study[35] on the CH_2BrCH_2 radical and could not

find any theoretical study on the CH_2ICH_2 radical. Moreover, simultaneous studies on both the bridged structure and the rotational barrier have been sparse and no systematic study encompassing all the β-substituted haloethyl radicals has been reported. This contribution is meant to remedy this situation.

A.1.3 Calculations

All calculations were performed using the Jaguar 3.0 program,[54] which utilizes pseudospectral algorithms. The H, C, and F atoms were described using the 6-31G** basis set. The I, Br, and Cl atoms were described using the LAV3P relativistic effective core potential (RECP)[55] and basis set. The LAV3P basis set consists of 3s3p valence primitive Gaussian functions contracted to 3s2p. The RECP was based on atomic calculations including relativistic effects.

For each system, the geometry was optimized at three levels of theory restricted to be proper spin states:

- Hartree-Fock (HF)
- second-order local Møller-Plesset[56] perturbation theory (LMP2) to account for electron correlation, and
- density functional theory (DFT).

In addition, we carried out LMP2 calculations[57,58] at the optimized HF geometry, denoted LMP2//HF. We did not include spin orbital coupling. This has negligible effect for the molecular radicals since the states are orbitally nondegenerate. For the dissociated halo

radials, the calculated bond energies should be decreased by ~(1/3)E($^2P_{1/2}$ – $^2P_{3/2}$). This is significant only for Iodine where the adiabatic bond energy would be ~8 kcal/mol lower.

Two flavors of DFT method were used, B3PW91 and B3LYP. Both include gradient corrections, exact HF exchange, making them much more accurate than the simple local density approximation (LDA). B3LYP employs a combination of exchange terms: exact HF, the Becke 1988 non-local gradient correction,[59] and the original Slater local exchange functional.[60] In addition, it uses the Vosko-Wilk-Nusair (VWN) local functional[61] and the Lee-Yang-Parr local and non-local electron correlation functional.[62] B3PW91 uses the same exchange functional as B3LYP but uses the Perdew-Wang 1991 local correlation functional and the GGA-II non-local correlation functional.[63]

For the minima and transition states, we calculated harmonic vibrational frequencies at the HF, B3PW91, and B3LYP levels of theory. This was used to obtain the zero point energy. All minima were found to have all real frequencies and all transition states were found to have just one imaginary frequency except for the case of CH_2FCH_2• radical. The relative energies and dissociation energies were corrected for the zero point energy using a scaling factor of 0.92 for HF and 0.98 for DFT methods. For the LMP2//HF and LMP2 calculations, we used the HF zero point corrections. All (unscaled) zero point energies and total energies are provided in Table A.1.1.

A.1.4 Results for β-substituted haloethyl radicals; CH_2XCH_2 (X = F, Cl, Br, I)

A.1.4.1 Asymmetric Structures and the Rotational Barriers

To find the global minima and correlate the structural changes with the relative energies between each conformation, we optimized the geometries at a HF level as a function of the torsion angle ω at 5° steps. Single point calculations with LMP2, B3PW91, and B3LYP methods were then performed at the geometries optimized at the HF level of theory. Figure A.1.3 displays the resulting rotational energy curves. Then, the geometries of the minima and the transition structures were fully optimized also at LMP2, B3PW91 and B3LYP levels of theory. The calculated total energies at minima and transition states are given in Table A.1.1 and the relative energies are provided in Table A.1.2. The optimized structures at various levels of theory are presented in Table A.1.3.

At all levels of calculations, the CH_2ClCH_2, CH_2BrCH_2 and CH_2ICH_2 radicals have only one minimum [the anti conformation (I)] and only one transition state (IV). In contrast, the CH_2FCH_2 radical shows different behavior for the various methods. The HF calculation finds two minima (I and III) and two transition states (II and IV) while the LMP2 and DFT calculations show only one minima (II) and two saddle points (I and IV).

All methods give somewhat similar overall descriptions of the various CH_2XCH_2 cases. Thus, in all cases:

- X = H slightly favors anti (with ω = 0°); the rotational barrier through the IV* rotamer is less than 0.2 kcal/mol except for HF.
- X = F rather strongly favors gauche (III) with ω = 64 to 70°. Here the barrier through the IV* rotamer (ω = 90°) ranges from 0.16 to 0.4 kcal except for HF. While HF finds a

minimum at the anti conformation (ω = 0°), the MP2 and DFT calculations do *not* lead to a minima; they find a saddle point instead.

- X = Cl, Br, I strongly favors the anti (ω = 0°) conformation and the rotational barrier through the IV rotamer increases in the order of Cl, Br, and I.

For the C_2H_5 and CH_2FCH_2 radicals, the internal rotation is almost free. Our HF results on the CH_2FCH_2 radical generally agree with the estimates based on ESR data[12] and are close to the results from recent *ab initio* calculations at the UHF and MP2//HF levels of theory by Tschuikow-Roux and coworkers.[21] In contrast, the LMP2 and DFT methods give only one stable conformation (gauche) rather than two minima (anti and gauche) for CH_2FCH_2. Instead, the anti structure is located at the saddle point at the LMP2 and DFT methods. There is no general agreement on the nature of the anti rotamer. Some[25,32] previous *ab initio* calculations suggest a saddle point for the anti structure (ω = 0°) while others[21,31] find a minimum there. For the C_2H_5 and CH_2FCH_2 radicals only, the energy difference between rotamers is comparable to the difference of the zero point energies. Indeed, some of the rotational barriers become negative after the correction for the zero point energies. This reversal of the Born-Oppenheimer potential energy surface was also observed in previous *ab initio* calculations[21] on the CH_2FCH_2 radical.

Early UHF calculations[42] with the 4-31G* basis set suggested that CH_2ClCH_2 has two minima and two transition states, just as for CH_2FCH_2. However, later UHF results[37] with the 6-31G* basis set showed that the CH_2ClCH_2 radical has only one minimum and one

transition state for internal rotation about the C-C bond. Our results also support this conclusion.

For CH_2BrCH_2 and CH_2ICH_2, the potential energy curves for the internal rotation have not been previously reported. The general form for the rotational energy curves for the CH_2BrCH_2 and CH_2ICH_2 radicals are very similar to that of the CH_2ClCH_2 radical. They also have only one minimum at the anti conformation and only one saddle point at the IV rotamer. The LMP2//HF and HF calculations show comparable barriers while both DFT//HF methods (B3PW91//HF and B3LYP//HF) lead to barriers twice as high.

Compared with the C_2H_5 and CH_2FCH_2 radicals, the haloethyl radicals containing third row or higher substituents have relatively high rotational barriers. The rotational barriers increase in the order of Cl, Br and I. The results calculated at LMP2 level were very close to those of LMP2//HF. Kochi and coworkers[15] estimated ~4 kcal/mol for the rotational barrier about the C-C bond of the CH_2ClCH_2 radical from their ESR investigation. DFT calculations, led to results in good agreement with experiment (3.9 kcal/mol for B3PW91 and 3.5 kcal/mol for B3LYP) with larger errors for HF (2.6 kcal/mol), LMP2//HF (1.7 kcal/mol), and LMP2 (1.8 kcal/mol).

The structures optimized using LMP2 method are very similar to those with HF while DFT geometries show considerable deviation from the LMP2 geometries. The DFT methods (B3PW91 and B3LYP) yield similar geometries.

The XCC bond angles in the haloethyl radicals at the asymmetric bridging minima in the rotational energy curve are only slightly less than the tetrahedral bond angle. At the anti

conformations, the radical centers are slightly distorted from the perfectly planar form so that the singly occupied carbon 2p orbital is anti to the halogen.

Early INDO calculations[43] showed that CH_2ClCH_2 has the asymmetric bridged structure. However, later *ab initio* studies[31-42] showed no evidence of asymmetric bridging.

Figure A.1.4 displays the changes in the structural parameters as a function of the torsion angle. The behavior observed for C_2H_5 and CH_2FCH_2 radicals is quite different from that in the other haloethyl radicals. For C_2H_5 and CH_2FCH_2 radicals, the C-C bond length and C-X bond length are independent of the torsion angle while the XCC bond angle decreases from the I to IV rotamers. However, for the CH_2ClCH_2, CH_2BrCH_2, and CH_2ICH_2 radicals the C-C bond length increases and C-X bond length decreases from the I to the IV rotamer. The shape of the XCC bond angle as a function of the torsion angle has minima at the I and III conformations and maxima at II and IV conformations. The trends of the C-C bond length and the XCC bond angle might be explained solely by Pauli repulsion between the singly occupied carbon 2p orbital and the halogen doubly occupied orbitals. However, the trend in the C-X bond length is not rationalized by the same argument because it would increase with the torsion angle to minimize the repulsion rather than decrease with it as observed in Figure A.1.4.

Based on UMP2 calculations,[31] Guerra explained the unexpected trend of the C-X bond length in terms of the highly stabilizing interaction between the singly occupied carbon 2p orbital and σ^*(C-X) MO. This interaction (referred to as hyperconjugation) was studied extensively by Bernardi and coworkers.[24,32,39] They performed fragment interaction analysis of the UHF calculations and concluded that the contribution of hyperconjugation

between the singly occupied carbon 2p orbital and σ*(C-X) MO is dominant in determining conformational preference in the β-chloroethyl radical. The trends of the relative energies and other structural parameters are also consistent with this hyperconjugation. Figure A.1.5 shows a schematic of the singly occupied highest molecular orbital (SOMO) we find for rotamers I and IV. The hyperconjugation is maximum in the anti conformation (rotamer I) and decreases with increasing torsion angle. The SOMO of rotamer I results from hyperconjugation between the carbon 2p orbital and the σ*(C-X) MO. In contrast, the SOMO of IV has hyperconjugation between the 2p orbital and σ*(C-H) MO, which is much weaker. Thus, the IV rotamer has the maximum energy due to the absence of this stabilizing hyperconjugation between the carbon 2p orbital and the σ*(C-X) MO. Since hyperconjugation enhances the C-C double bond character and weakens the C-X bond, the anti conformer has the minimum C-C bond length and the maximum C-X bond length.

By means of the electron transmission spectroscopy on *tert*-butyl halides $(CH_3)_3CX$, Modelli et al.[64] observed that the σ*(C-X) MOs lie low in energy only for X = Br, I, and higher rows. They reproduced these experimental results using MXSα calculations (an approximation to the LDA approximation of DFT). We also examined the SOMO and LUMO energies for CH_2XCH_2 radicals. Table A.1.4 lists the SOMO and LUMO energies and also the differences for the rotamer IV calculated at various levels of theory as discussed above. The rotamer IV is expected to have the least hyperconjugation. It is clear that the LUMO energies are very low for X = Cl, Br, and I compared to X = H and F. The LUMO energies calculated at DFT methods seem to especially emphasize these trends. This might explain the higher rotational barriers (energy difference between I and IV) calculated with

DFT methods compared to the LMP2 results. The more electronegative halogen (F) disfavors hyperconjugation by raising the energy of the σ*(C-X) MO. This is also consistent with the magnitudes of the changes in the structural parameters, which increase in the order X = Cl < Br < I. From Table A.1.3, we see that the C-C bond lengths of rotamer I dramatically decrease from X=F to X=I while rotamer IV shows little change. This observation is also consistent with the hyperconjugation explanation.

A.1.4.2 Bridged Structures

At all levels of theory in this study, the radicals with X = Cl, Br, and I lead to symmetrically bridged minima with no imaginary frequency. For the CH_2ClCH_2 radical, all methods predict that the bridged structure is less stable than the anti conformer. In contrast, the bridged structures are the global minima for CH_2BrCH_2 and CH_2ICH_2 radicals at all levels of calculation. At the LMP2 level, the bridged form is more stable than the anti form by more than 7 kcal/mol for CH_2BrCH_2 and 12 kcal/mol for CH_2ICH_2. The B3PW91 and B3LYP methods indicate that the anti conformation of CH_2ICH_2 radical is not a local energy minimum. Also, the anti CH_2BrCH_2 radical optimized with B3LYP converged to the bridged structure. The calculated total energies and the relative energies for the symmetrically bridged structures at various levels of theory are presented in Table A.1.1 and Table A.1.2, respectively. The optimized structural parameters calculated at various levels of theory are also given in Table A.1.5, and Table A.1.6 lists the vibrational frequencies and assignments.

The symmetrically bridged conformation of CH_2ClCH_2 was studied previously. Fossey and Nedelec[26] used UHF with the STO-3G basis set to study the 1,2 migrations observed in many free radical reactions. They reported that the bridged CH_2ClCH_2 radical is 53 kcal/mol higher than the anti structure, but still stable with respect to dissociation. However, Hoz et al.[40] studied 1,2-rearrangement of CH_2ClCH_2 using active space multiconfiguration SCF method and reported that the bridged structure is above the C_2H_4 + Cl dissociation limit. Like Fossey and Nedelec, Engels et al.[38] reported MRD-CI calculations indicating that the symmetric bridged structure is stable with respect to the dissociation reaction. Their bridged conformation corresponds to the transition state for the shuttle motion. From unrestricted MP2 calculations, Guerra[31] also reported that $^2A_1$ state of the symmetrically bridged CH_2ClCH_2 radical is below the dissociation limit while the $^2B_2$ state is dissociative without a minimum and lies above $^2A_1$ state. The vibrational frequencies calculated for the symmetrically bridged CH_2ClCH_2 radical are all real in our calculation indicating that it is located at a local minimum rather than a saddle point. Engels et al. also studied CH_2BrCH_2 radical[35] where they reported that the bridged form has a local minimum. But they did not fully optimize the geometries (due to high computational cost for obtaining the whole potential energy hypersurface). While their results indicate that the symmetrically bridged structure is less stable than the anti conformer, the symmetrically bridged form is a global minimum in our calculation.

The C_2H_4 moiety of the bridged structure has almost same structure as the free C_2H_4 molecule except that the C-C bond length is elongated, reflecting the interaction between the halogen atom and the π orbital of the C_2H_4 moiety. However, the C-C bond length of the

bridged structure is much closer to that of the double bond than that of the single bond. In Table A.1.6, the vibrational frequency showing the most apparent change from C_2H_4 to the bridged CH_2XCH_2 is the C-C stretch mode. Due to the weakened C-C bond in the bridged CH_2XCH_2, the vibrational frequency for the C-C stretch is reduced, but still closer to that of C_2H_4 than the anti form of CH_2XCH_2. The SOMO of the symmetrically bridged form is represented schematically in Figure A.1.5. This SOMO is the result of the interaction between the halogen p orbital and the π orbital of the C_2H_4 moiety. The C-X bond length in the bridged structure is about 30% longer than that of anti conformation due to the relatively weak interaction between halogen and carbon atoms. Engels et al.[38] reported a C-Cl bond length of 2.98 Å for the symmetrically bridged conformation of CH_2ClCH_2 radical. Our HF and LMP2 calculations give higher values and the DFT methods give slightly lower values. Actually, our DFT values are very close to those reported by Guerra (2.58 Å)[31] and Fossey and Nedelec (2.68 Å).[26] The C-Br internuclear distances calculated with DFT for the CH_2BrCH_2 radical are also very close to the 2.98 Å distance taken from Engels et. al.[35] The geometries optimized with the LMP2 method are slightly asymmetric. However, the amount of deviation from the perfectly symmetric form is too small to be attributed to the asymmetrically bridged radical. The DFT methods describe the symmetrically bridged structures better than the HF and LMP2 methods.

A.1.4.3 Shuttle motion and Dissociation

To study the shuttle motion and the dissociation mechanism, the geometries were optimized as a function of the position of the halogen atom with the B3PW91 method. The

resulting potential energy surfaces for CH_2ClCH_2, CH_2BrCH_2, and CH_2ICH_2 are depicted in Figures A.1.6, A.1.7, and A.1.8, respectively. In the calculation, the halogen atom was confined in the XCC plane bisecting the HCH angle.

The contour maps clearly show the relative stability of the anti conformer and the symmetrically bridged structure. For the CH_2ClCH_2 radical, the global minimum corresponds to the anti conformer while the symmetric conformation is a local minimum. The region around the symmetric conformation is very flat along the C-C axis leading to the lowest vibrational frequency of only 33 cm^{-1}. The barrier from the symmetrically bridged form to the anti conformation is almost zero. The relative stability is reversed in the CH_2BrCH_2 radical and the anti conformation is no longer stable for the CH_2ICH_2 radical. The potential energy surfaces for the region of the symmetrically bridged conformations are bounded and also very flat. Therefore, we can expect high amplitude shuttle motion around the symmetric conformation especially for the CH_2BrCH_2 and CH_2ICH_2 radicals. The shuttle motion should be considered as a rocking motion of the ethylene moiety around the heavy halogen atom rather than the direct movement of the halogen atom. These shuttle motions can be visualized by examining the vibrational modes of the bridged radicals. The lowest vibrational frequency corresponds to the rocking motion of C_2H_4 moiety along C-C axis and the second lowest one corresponds to the X-(C_2H_4) stretch motion perpendicular to the C-C axis. The rocking motion out of the XCC plane bisecting the HCH angle is the third lowest frequency. The rocking motion of C_2H_4 moiety along C-C axis is conceptually similar to the dynamic shuttle motion proposed by Skell and coworkers[47] except that the symmetrically bridged conformation actually corresponds to a minimum rather than a saddle

point. In other word, it is more compatible with the shuttle motion of Engels and Peyerimhoff[35].

It is evident from the results that the bridged structures should play an important role in the dissociation process of CH_2XCH_2 for the cases of X = Cl, Br and I. In particular, the bridged structures should be the dominant conformers for the CH_2BrCH_2 and CH_2ICH_2 radicals. This suggests that Skell's hypothesis of symmetric bridging[7,48] *can* explain the stereochemical control of the CH_2BrCH_2 and CH_2ICH_2 radicals. Engels and Peyerimhoff also proposed that symmetrically bridged radicals play an important role in the dissociation process of the CH_2ClCH_2 radical.[38] They suggested that a symmetrically bridged structure can be an intermediate species in the dissociation process.

The DFT methods lead to energetics considerably different than those obtained through HF and LMP2 methods. Table A.1.7 lists the dissociation energies for the C-X bond cleavage. The global minimum of the radical was used for obtaining the dissociation energy. Correcting for zero point energy, we see that for X = H, DFT is too high by 3 to 4 kcal/mol, LMP2 is too low by 3 to 4 kcal/mol and HF is within 1 kcal/mol. For X = F, DFT is within the range of experimental uncertainty while LMP2 is too low by at least 3 kcal/mol and HF is too low by 22 kcal/mol (50%). For X = Cl, DFT is too low by 3 to 6 kcal/mol while LMP is too low by ~19 kcal/mol (over 100%) and HF is too low by 14 kcal/mol. For X = Br, DFT is within the experimental range while LMP2 is too low by 9 kcal/mol (over 100%) and HF is too low by 7 kcal/mol. Including a correction for spin-orbit interaction in the I atom, we see that for X = I, DFT is high by 7 kcal/mol while LMP2 is within experimental range. It should be noted that the experimental values for X = Cl, Br, and I are

similar species, namely CF_2ICF_2 radical, was observed recently by means of ultrafast electron diffraction techniques.[66] The structure of the short-lived (~17 ps life time) CF_2ICF_2 radical was consistent with a mixture of anti and gauche conformers rather than the symmetrically bridged structure. The experimental observation is consistent with our *ab initio* calculations.[66,67] In addition, the Zewail lab is currently using ultrafast electron diffraction techniques to investigate the molecular structures of the CH_2BrCH_2 and CH_2ICH_2 radicals.[73]

References

1)Kochi, J. K. *Free Radicals*; John Wiley & Sons: New York, 1973; Vol. II.

2)Beckwith, A. L. J.; Ingold, K. U. *Free-Radical Rearrangements*; Mayo, P. d., Ed.; Academic Press: New York, 1980.

3)Kerr, J. A. *Handbook of Bimolecular and Termolecular Gas Reactions*; CRC Press: Boca Raton, FL, 1981; Vol. I.

4)Fossey, J.; Lefort, D.; Sorba, J. *Free Radicals in Organic Chemistry*; John Wiley & Sons: New York, 1995.

5)Goering, H. L.; Abell, P. I.; Aycock, B. F. *J. Am. Chem. Soc.* **1952**, *74*, 3588.

6)Thaler, W. *J. Am. Chem. Soc.* **1963**, *85*, 2607.

7)Skell, P. S.; Tuleen, D. L.; Readio, P. D. *J. Am. Chem. Soc.* **1963**, *85*, 2849.

8)Tanner, D. D.; Darwish, D.; Mosher, M. W.; Bunce, N. J. *J. Am. Chem. Soc.* **1969**, *91*, 7398.

9)Traynham, J. G.; Lee, Y.-S. *J. Am. Chem. Soc.* **1974**, *96*, 3590.

10)Edge, D. J.; Kochi, J. K. *J. Am. Chem. Soc.* **1972**, *94*, 6485.

11)Kawamura, T.; Edge, D. J.; Kochi, J. K. *J. Am. Chem. Soc.* **1972**, *94*, 1752.

12)Chen, K. S.; Krusic, P. J.; Meakin, P.; Kochi, J. K. *J. Phys. Chem.* **1974**, *78*, 2014.

13)Bowles, A. J.; Hudson, A.; Jackson, R. A. *Chem. Phys. Lett.* **1970**, *5*, 552.

14)Elson, I. H.; Chen, K. S.; Kochi, J. K. *Chem. Phys. Lett.* **1973**, *21*, 72.

15)Chen, K. S.; Elson, I. H.; Kochi, J. K. *J. Am. Chem. Soc.* **1973**, *95*, 5341.

16)Cooper, J.; Hudson, A.; Jackson, R. A. *Tetrahedron Lett.* **1973**, 831.

17)Krusic, P. J.; Bingham, R. C. *J. Am. Chem. Soc.* **1976**, *98*, 230.

18)Parson, J. M.; Lee, Y. T. *J. Chem. Phys.* **1972**, *56*, 4658.

19)Farrar, J. M.; Lee, Y. T. *J. Chem. Phys.* **1976**, *65*, 1414.

20)Jacox, M. E. *Chem. Phys.* **1981**, *58*, 289.

21)Chen, Y.; Rauk, A.; Tschuikow-Roux, E. *J. Chem. Phys.* **1990**, *93*, 6620.

22)Engels, B.; Peyerimhoff, S. D. *J. Phys. Chem.* **1989**, *93*, 4462.

23)Pasto, D. J.; Krasnansky, R.; Zercher, C. *J. Org. Chem.* **1987**, *52*, 3062.

24)Bernardi, F.; Bottoni, A.; Fossey, J.; Sorba, J. *J. Mol. Struct.* **1985**, *119*, 231.

25)Schlegel, H. B. *J. Phys. Chem.* **1982**, *86*, 4678.

26)Fossey, J.; Nedelec, J.-Y. *Tetrahedron* **1981**, *37*, 2967.

27)Kato, S.; Morokuma, K. *J. Chem. Phys.* **1980**, *72*, 206.

28)Pross, A.; Radom, L. *Tetrahedron* **1980**, *36*, 1999.

29)Radom, L.; Paviot, J.; Pople, J. A. *J. Chem. Soc. Chem. Commun.* **1974**, 58.

30)Hoffmann, R.; Radom, L.; Pople, J. A.; Schleyer, P. v. R.; Hehre, W. J.; Salem, L. *J. Am. Chem. Soc.* **1972**, *94*, 6221.

31)Guerra, M. *J. Am. Chem. Soc.* **1992**, *114*, 2077.

32)Bernardi, F.; Fossey, J. *J. Mol. Struct.* **1988**, *180*, 79.

33)Guerra, M. *Chem. Phys. Lett.* **1987**, *139*, 463.

34)Clark, T.; Symons, M. C. R. *J. Chem. Soc. Chem. Commun.* **1986**, 96.

35)Engels, B.; Peyerimhoff, S. D. *J. Mol. Struct.* **1986**, *138*, 59.

36)Molino, L. M.; Poblet, J. M.; Canadell, E. *J. Chem. Soc. Perkin Trans. II* **1982**, 1217.

37)Chen, Y.; Tschuikow-Roux, E. *J. Phys. Chem.* **1992**, *96*, 7266.

38)Engels, B.; Peyerimhoff, S. D.; Skell, P. S. *J. Phys. Chem.* **1990**, *94*, 1267.

39)Bernardi, F.; Bottoni, A.; Fossey, J.; Sorba, J. *Tetrahedron* **1986**, *42*, 5567.

40)Hoz, T.; Sprecher, M.; Basch, H. *J. Phys. Chem.* **1985**, *89*, 1664.

41)Schlegel, H. B.; Sosa, C. *J. Phys. Chem.* **1984**, *88*, 1141.

42)Hopkinson, A. C.; Lien, M. H.; Csizmadia, I. G. *Chem. Phys. Lett.* **1980**, *71*, 557.

43)Biddles, I.; Hudson, A. *Chem. Phys. Lett.* **1973**, *18*, 45.

44)Creary, X. *Advances in Carbocation Chemistry*; JAI Press: London, 1989; Vol. I.

45)Raghavachari, T.; Haddon, R. C.; Jr, W. H. S. *J. Am. Chem. Soc.* **1982**, *104*, 5054.

46)Reynolds, C. H. *J. Am. Chem. Soc.* **1992**, *114*, 8676.

47)Skell, P. S.; Traynham, J. G. *Acc. Chem. Res.* **1984**, *17*, 160.

48)Skell, P. S.; Shea, K. J. *Bridged Free Radicals*; Kochi, J. K., Ed.; John Wiley & Sons: New York, London, Sydney, Toronto, 1973.

49)Krusic, P. J.; Kochi, J. K. *J. Am. Chem. Soc.* **1971**, *93*, 846.

50)Lloyd, R. V.; Wood, D. E. *J. Am. Chem. Soc.* **1975**, *97*, 5986.

51)Lysons, A. R.; Symons, M. C. R. *J. Am. Chem. Soc.* **1971**, *93*, 7330.

52)von Onciul, A.; Clark, T. *J. Chem. Soc. Chem. Commun.* **1989**, 1082.

53)Chen, Y.; Rauk, A.; Tschuikow-Roux, E. *J. Chem. Phys.* **1990**, *93*, 1187.

54)Jaguar 3.0; Schrödinger, Inc.: Portland, OR, 1997. Greeley, B. H.; Russo, T. V.; Mainz, D. T.; Friesner, R. A.; Langlois, J-M.; Goddard III, W. A.; Donnelly, R. E.; Ringnalda, M. N. *J. Chem. Phys.* **1994**, *101*, 4028. Tannor, D. J.; Marten, B.;

Murphy, R.; Friesner, R. A.; Sitkoff, D.; Nicholls, A.; Ringnalda, M.; Goddard III, W. A.; Honig, B. *J. Am. Chem. Soc.* **1994**, *116*, 11875.

55)Hay, P. J.; Wadt, W. R. *J. Chem. Phys.* **1985**, *82*, 284.

56)Møller, C.; Plesset, M. S. *Phys. Rev.* **1934**, *46*, 618.

57)Sæbø, S.; Pulay, P. *Ann. Rev. Phys. Chem.* **1993**, *44*, 213.

58)Murphy, R. B.; Beachy, M. D.; Friesner, R. A.; Ringnalda, M. N. *J. Chem. Phys.* **1995**, *103*, 1481.

59)Becke, A. D. *Phys. Rev. A* **1988**, *38*, 3098.

60)Slater, J. C. *Quantum Theory of Molecules and Solids*; McGrow-Hill: New York, 1974.

61)Vosko, S. H.; Wilk, L.; Nusair, M. *Can. J. Phys.* **1980**, *58*, 1200.

62)Lee, C.; Yang, W.; Parr, R. G. *Phys. Rev. B* **1988**, *37*, 785.

63)Perdew, J. P.; Chevary, J. A.; Vosko, S. H.; Jackson, K. A.; Pederson, M. R.; Singh, D. J.; Fiolhais, C. *Phys. Rev. B* **1992**, *46*, 6671.

64)Modelli, A.; Scagnolari, F.; Distefano, G.; Guerra, M.; Jones, D. *Chem. Phys.* **1990**, *145*, 89.

65)Nathanson, G. M.; Minton, T. K.; Shane, S. F.; Lee, Y. T. *J. Chem. Phys.* **1989**, *90*, 6157.

66)Cao, J.; Ihee, H.; Zewail, A. H. *Proc. Natl. Acad. Sci.* **1999**, *96*, 338.

67)Ihee, H.; Kua, J.; Zewail, A. H.; Goddard III, W. A. , In preparation.

68)Castelhano, A. L.; Marriott, P. R.; Griller, D. *J. Am. Chem. Soc.* **1981**, *103*, 4262.

69)*JANAF Thermochemical Tables, Natl. Stand. Ref. Data. Ser. U. S. Natl. Bur. Stand. 37*; 2nd ed.; U. S. GPO: Washington D. C., 1971.

70)Schlegel, H. B.; Bhalla, K. C.; Hase, W. L. *J. Phys. Chem.* **1982**, *86*, 4883.

71)Holmes, J. L.; Lossing, F. P. *J. Am. Chem. Soc.* **1988**, *110*, 7343.

72)Franklin, J. A.; Huybrechts, G. H. *Int. J. Chem. Kinet.* **1969**, *1*, 3.

73)Ihee, H; Zewail, A. H., work in progress.

Figure Captions

Figure A.1.1: Hypothesized structures for β-substituted alkyl radical. (a) Symmetrically bridged, (b) asymmetrically bridged, and (c) classical non-bridged.

Figure A.1.2: A schematic view of the possible rotational minima and the transition structures of the CH_2XCH_2 (X = F, Cl, Br, and I).

Figure A.1.3: The energy of CH_2XCH_2 as a function of the torsion angle (ω). In these calculations the torsion angle was fixed and all structural parameters optimized. **(a)** HF. **(b)** LMP2//HF. **(c)** B3PW91//HF. **(d)** B3LYP//HF.

Figure A.1.4: The geometric parameters optimized as a function of the torsion angle (ω) with the HF method. **(a)** C-C bond length (Å). **(b)** XCC angle in degree. **(c)** C-X bond length (Å).

Figure A.1.5: A schematic representations of the singly occupied highest molecular orbital (SOMO) of CH_2XCH_2 radical (X = Cl, Br, and I). **(a)** rotamer I, **(b)** rotamer IV, and **(c)** symmetrically bridged structure.

Figure A.1.6: The contour map constructed for CH_2ClCH_2 with the B3PW91 method. The position of the halogen atom is referenced to the middle point of two carbon atoms. The zero of energy corresponds to the global minimum (anti rotamer (I)).

Figure A.1.7: The contour map constructed for CH_2BrCH_2 with the B3PW91 method. The position of the halogen atom is referenced to the middle point of two carbon atoms. The zero of energy corresponds to the global minimum (symmetrically bridged form).

Figure A.1.8: The contour map constructed for CH_2ICH_2 with the B3PW91 method. The position of the halogen atom is referenced to the middle point of two carbon atoms. The zero of energy corresponds to the global minimum (symmetrically bridged form).

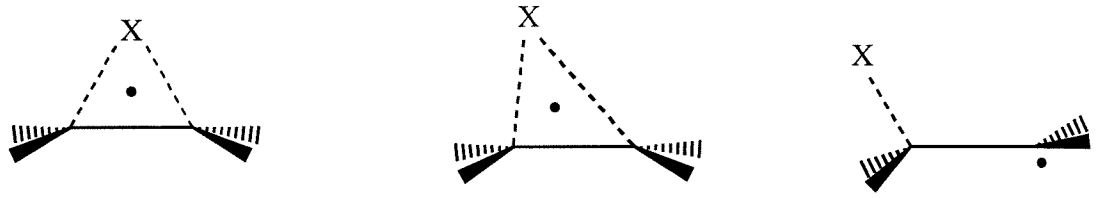

a) symmetrically bridged b) asymmetrically bridged c) classical non-bridged

Figure A.1.1

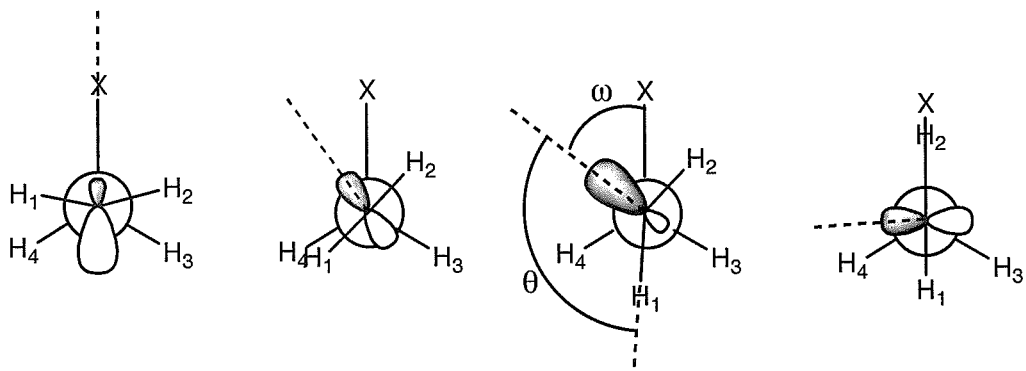

I II III IV

Figure A.1.2.

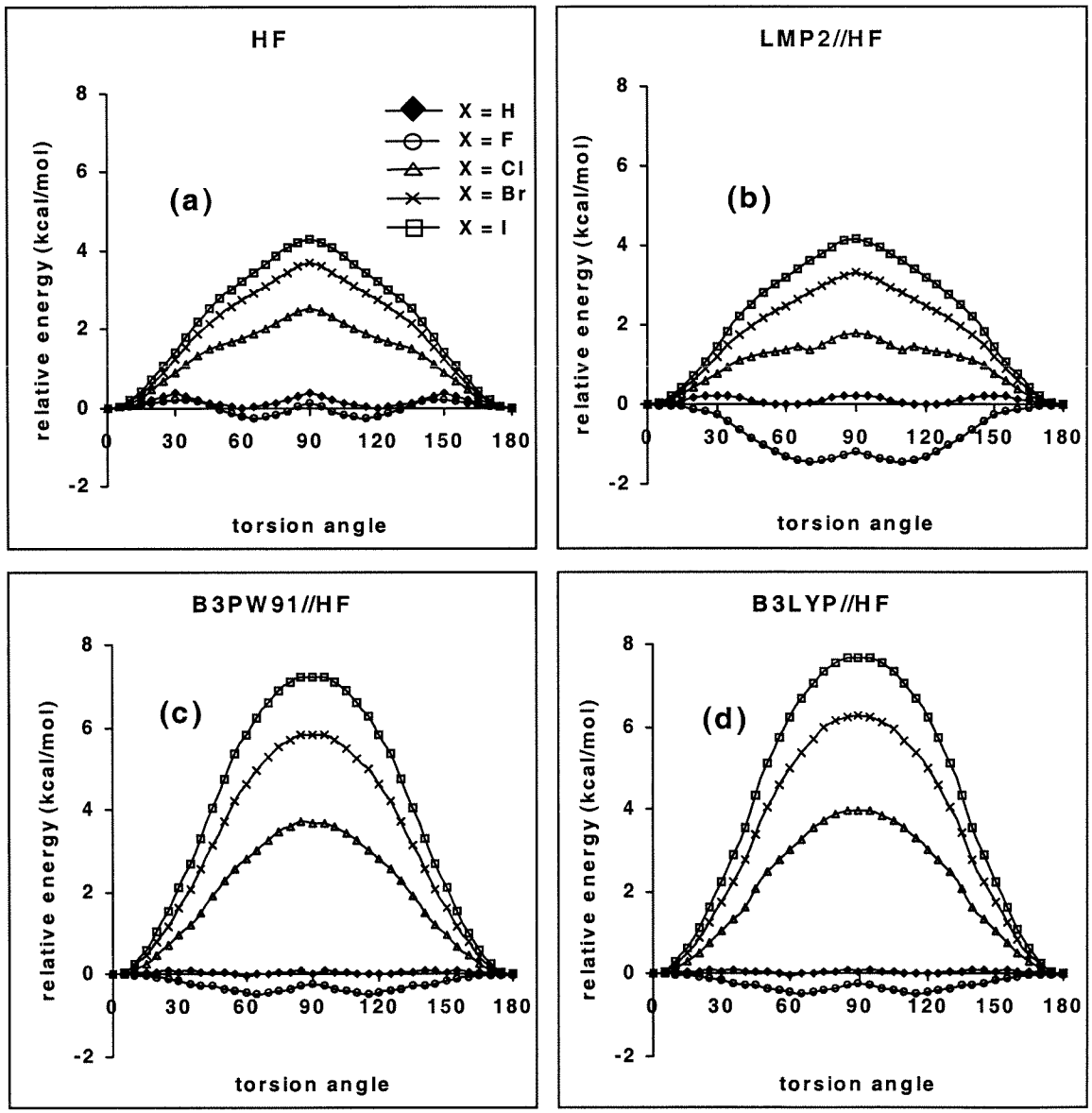
HF
(a)
X = H
X = F
X = Cl
X = Br
X = I
relative energy (kcal/mol)
torsion angle
LMP2//HF
(b)
B3PW91//HF
(c)
B3LYP//HF
(d)
8
6
4
2
0
-2
0
30
60
90
120
150
180

Figure A.1.3.

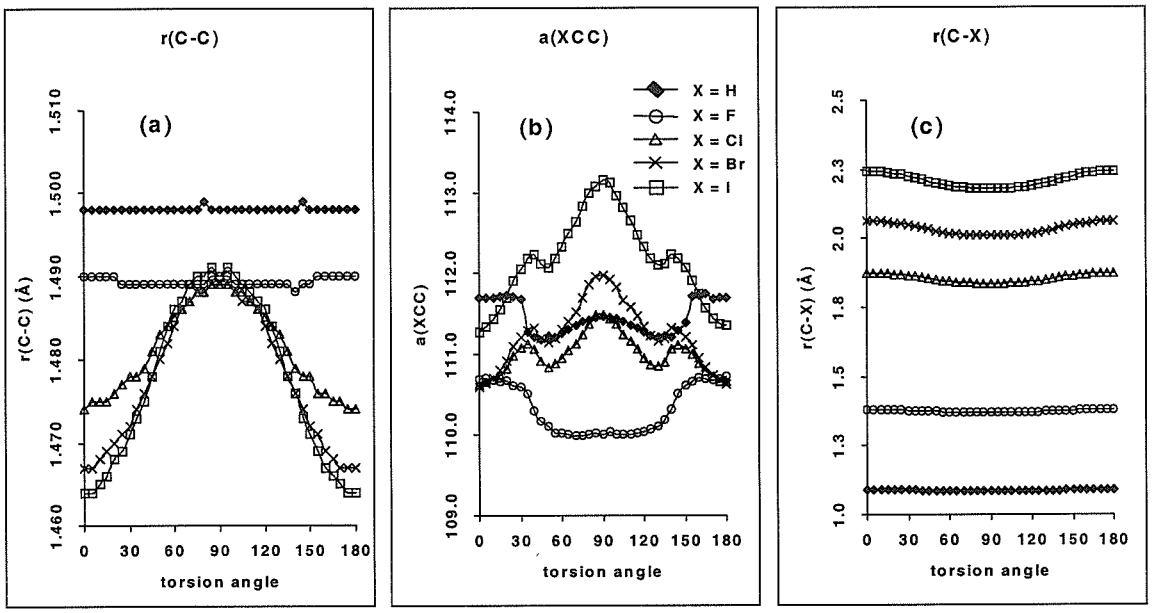
r(C-C)
(a)
r(C-C) (Å)
1.460
1.470
1.480
1.490
1.500
1.510
0 30 60 90 120 150 180
torsion angle
a(XCC)
(b)
X = H
X = F
X = Cl
X = Br
X = I
a(XCC)
109.0
110.0
111.0
112.0
113.0
114.0
0 30 60 90 120 150 180
torsion angle
r(C-X)
(c)
r(C-X) (Å)
1.0
1.3
1.5
1.8
2.0
2.3
2.5
0 30 60 90 120 150 180
torsion angle

Figure A.1.4.

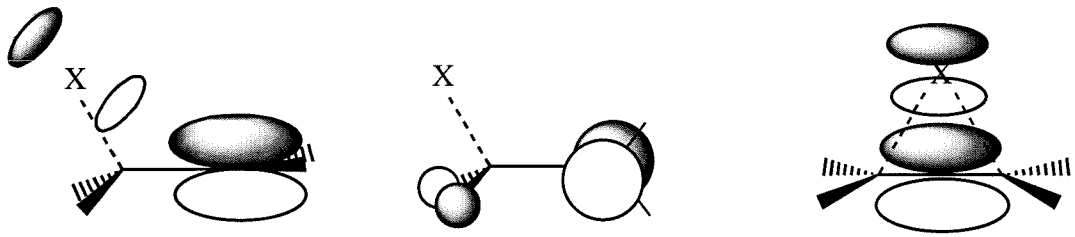

a) SOMO of rotamer I b) SOMO of rotamer IV c) SOMO of a bridged structure

Figure A.1.5.

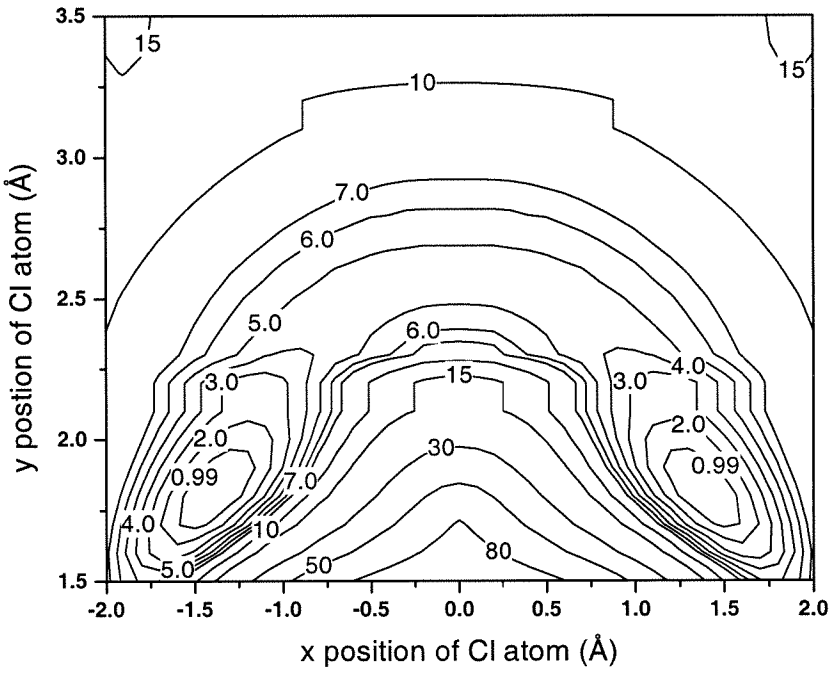
y postion of Cl atom (Å)
x position of Cl atom (Å)
3.5
3.0
2.5
2.0
1.5
-2.0
-1.5
-1.0
-0.5
0.0
0.5
1.0
1.5
2.0
15
15
10
7.0
6.0
5.0
6.0
3.0
15
3.0
4.0
2.0
2.0
0.99
30
0.99
7.0
4.0
10
5.0
50
80

Figure A.1.6.

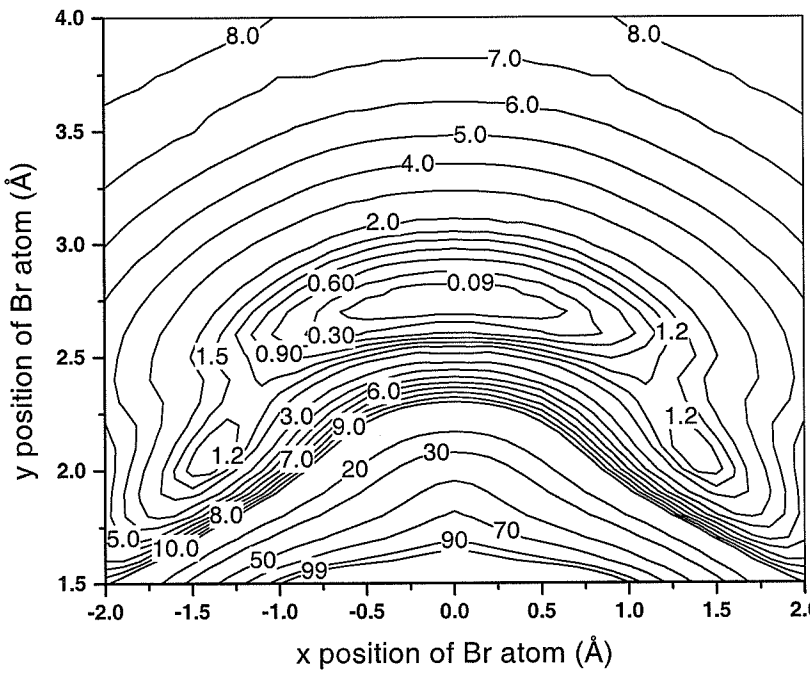
y position of Br atom (Å)
x position of Br atom (Å)
4.0
3.5
3.0
2.5
2.0
1.5
-2.0
-1.5
-1.0
-0.5
0.0
0.5
1.0
1.5
2.0
8.0
8.0
7.0
6.0
5.0
4.0
2.0
0.60
0.09
0.30
1.5
0.90
1.2
6.0
3.0
9.0
1.2
7.0
20
30
8.0
5.0
10.0
90
70
50
99

Figure A.1.7.

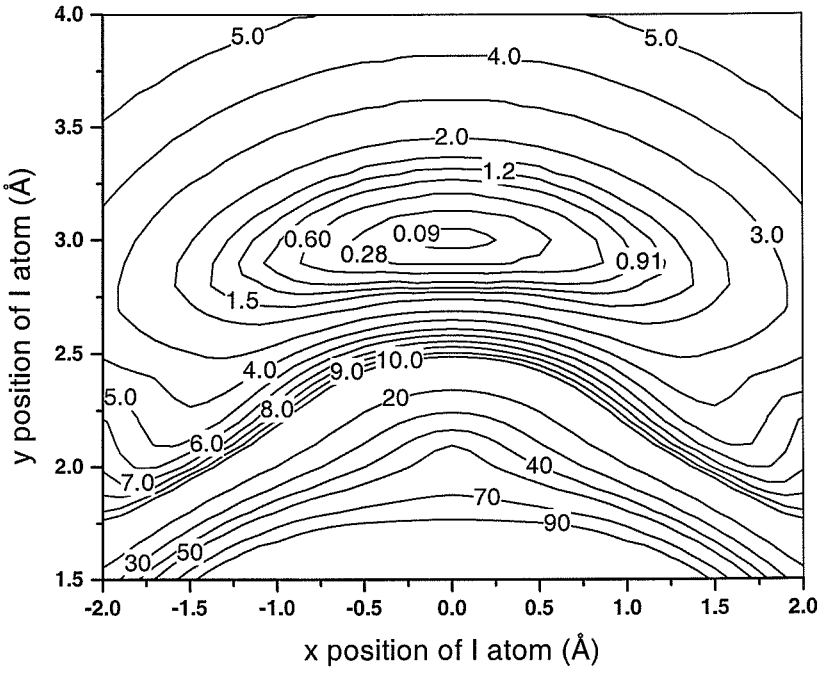
y position of I atom (Å)
x position of I atom (Å)
4.0
3.5
3.0
2.5
2.0
1.5
-2.0
-1.5
-1.0
-0.5
0.0
0.5
1.0
1.5
2.0
5.0
4.0
2.0
1.2
0.60
0.09
0.28
0.91
3.0
1.5
4.0
9.0
10.0
20
8.0
6.0
7.0
40
70
90
30
50

Figure A.1.8.

Table A.1.1. Total energy (Hartree) of CH_2XCH_2 radicals calculated at various levels of theory. The unscaled zero point energies (kcal/mol) are also presented in parentheses. The anti conformer has a prefix of a- and the eclipsed form has a prefix of te-. The symmetrically bridged structure has a prefix of b-.

Method	**C_2H_4**	**I**	**Br**	**Cl**	**F**	**H**
HF	-78.03887 (34.19)	-11.15723	-12.91863	-14.68120	-99.36175	-0.49823
LMP2//HF	-78.31376	-11.17128	-12.93869	-14.70823	-99.48943	-0.49823
LMP2	-78.31430 (32.89)	-11.17128	-12.93869	-14.70823	-99.48943	-0.49823
B3PW91	-78.56139 (32.10)	-11.38531	-13.15084	-14.91530	-99.67926	-0.50217
B3LYP	-78.59380 (32.07)	-11.36306	-13.13069	-14.89608	-99.71429	-0.50027

Method	**a-CH_3CH_2 (I)**	**te-CH_3CH_2 (IV)**
HF	-78.60129 (39.75)	-78.60072 (39.07)
LMP2//HF	-78.87128	-78.87102
LMP2	-78.87139	-78.87108
B3PW91	-79.13431 (37.43)	-79.13416 (37.17)
B3LYP	-79.16369 (37.35)	-79.16354 (37.08)

Method	**a-CH_2FCH_2 (I)**	**g-CH_2FCH_2 (III)**	**tex-CH_2FCH_2 (IV)**	**teh-CH_2FCH_2 (II)**
HF	-177.44560 (35.76)	-177.44600 (35.65)	-177.44535 (35.24)	-177.44526 (34.87)
LMP2//HF	-177.87046	-177.87244	-177.87218	-177.87082
LMP2	-177.87101	-177.87324	-177.87293	Converge to I
B3PW91	-178.31942 (33.58)	-178.32024 (33.29)	-178.31993 (32.81)	Converge to I
B3LYP	-178.38507 (33.49)	-178.38582 (33.19)	-178.38549 (32.70)	Converge to I

Method	**a-CH_2ClCH_2 (I)**	**b-CH_2ClCH_2**	**te-CH_2ClCH_2 (IV)**
HF	-92.72628 (34.89)	-92.72150 (34.55)	-92.72221 (33.68)
LMP2//HF	-93.02238	-93.02078	-93.01971
LMP2	-93.02272	-93.02137	-93.01986
B3PW91	-93.50166 (32.89)	-93.49428 (32.86)	-93.49547 (31.94)
B3LYP	-93.50936 (32.77)	-93.50664 (32.86)	-93.50220 (31.82)

Method	**a-CH_2BrCH_2 (I)**	**b-CH_2BrCH_2**	**te-CH_2BrCH_2 (IV)**
HF	-90.94928 (34.55)	-90.95898 (34.57)	-90.94336 (33.25)
LMP2//HF	-91.23914	-91.25103	-91.23406
LMP2	-91.23956	-91.25164	-91.23488
B3PW91	-91.72445 (32.62)	-91.72603 (32.93)	-91.71438 (31.57)
B3LYP	Converge to bridge	-91.73727 (32.82)	-91.71997 (31.46)

Method	**a-CH_2ICH_2 (I)**	**b-CH_2ICH_2**	**te-CH_2ICH_2 (IV)**
HF	-89.17801 (34.30)	-89.19758 (34.57)	-89.17114 (32.99)
LMP2//HF	-89.46416	-89.48363	-89.45770
LMP2	-89.46458	-89.48425	-89.45832
B3PW91	Converge to bridge	-89.95607 (32.88)	-89.93640 (31.49)
B3LYP	Converge to bridge	-89.96520 (32.70)	-89.93985 (31.24)

Table A.1.2. Relative energies (kcal/mol) of CH_2XCH_2 radicals calculated at various levels of theory. The values in parentheses are corrected for the zero point energies. The anti conformer has a prefix of a- and the eclipsed form has a prefix of te-. The symmetrically bridged structure has a prefix of b-.

CH_3CH_2				
Method	**a-CH_3CH_2 (I)**		**te-CH_3CH_2 (IV)**	
HF	0		0.360 (-0.259)	
LMP2//HF	0		0.167 (-0.452)	
LMP2	0		0.193 (-0.426)	
B3PW91	0		0.095 (-0.160)	
B3LYP	0		0.098 (-0.167)	
CH_2FCH_2				
Method	**a-CH_2FCH_2 (I)**	**g-CH_2FCH_2 (III)**	**tex-CH_2FCH_2 (IV)**	**teh-CH_2FCH_2 (II)**
HF	0.253 (0.353)	0	0.413 (0.040)	0.465 (-0.255)
LMP2//HF	1.246 (1.346)	0	0.164 (-0.209)	1.015 (0.295)
LMP2	1.401 (1.501)	0	0.194 (-0.179)	Converge to I
B3PW91	0.513 (0.797)	0	0.193 (-0.277)	Converge to I
B3LYP	0.469 (0.753)	0	0.205 (-0.275)	Converge to I
CH_2ClCH_2				
Method	**a-CH_2ClCH_2 (I)**	**b-CH_2ClCH_2**	**te-CH_2ClCH_2 (IV)**	
HF	-2.998 (-2.689)	0	-0.444 (-1.236)	
LMP2//HF	-1.000 (-0.691)	0	0.673 (-0.122)	
LMP2	-0.852 (-0.543)	0	0.942 (0.150)	
B3PW91	-4.629 (-4.600)	0	-0.745 (-1.647)	
B3LYP	-1.705 (-1.793)	0	2.786 (1.767)	
CH_2BrCH_2				
Method	**a-CH_2BrCH_2 (I)**	**b-CH_2BrCH_2**	**te-CH_2BrCH_2 (IV)**	
HF	6.089 (6.071)	0	9.800 (8.599)	
LMP2//HF	7.457 (7.439)	0	10.648 (9.447)	
LMP2	7.583 (7.565)	0	10.519 (9.318)	
B3PW91	0.991 (0.687)	0	7.310 (5.997)	
B3LYP	Converge to bridge	0	10.855 (9.522)	
CH_2ICH_2				
Method	**a-CH_2ICH_2 (I)**	**b-CH_2ICH_2**	**te-CH_2ICH_2 (IV)**	
HF	12.281 (12.035)	0	16.591 (15.153)	
LMP2//HF	12.219 (11.973)	0	16.272 (14.834)	
LMP2	12.345 (12.099)	0	16.268 (14.830)	
B3PW91	Converge to bridge	0	12.343 (10.981)	
B3LYP	Converge to bridge	0	15.912 (14.481)	

Table A.1.3. Optimized structural parameters of β-substituted ethyl radicals ($C_\beta H_2X\text{-}C_\alpha H_2$). The bond lengths are in Å and the angles are in degrees. The blanks indicate that the corresponding structure can not be located either in a minimum or in a saddle point.

(a) HF level

	X = H		X = F				X = Cl		X = Br		X = I	
	I	IV*	I	II*	III	IV*	I	IV*	I	IV*	I	IV*
$r(C_\alpha\text{-}C_\beta)$	1.498	1.497	1.490	1.489	1.489	1.489	1.474	1.488	1.467	1.488	1.464	1.490
$r(C_\beta\text{-}X)$	1.090	1.085	1.379	1.376	1.371	1.370	1.875	1.836	2.062	2.009	2.246	2.181
$\angle XC_\beta C_\alpha$	111.7	111.4	110.7	110.5	110.0	110.0	110.6	111.5	110.6	112.0	111.3	113.1
$r(C_\beta\text{-}H_{3\beta})$	1.086	1.088	1.083	1.086	1.088	1.087	1.077	1.081	1.076	1.080	1.077	1.081
$r(C_\beta\text{-}H_{4\beta})$	1.086	1.089	1.083	1.083	1.085	1.087	1.077	1.081	1.076	1.080	1.077	1.081
$\angle H_{3\beta}CC$	111.3	111.5	111.2	111.5	111.8	111.6	113.4	112.8	114.1	113.0	114.1	112.7
$\angle H_{4\beta}CC$	111.3	111.6	111.3	111.4	111.3	111.6	113.4	112.7	114.1	113.0	114.1	112.7
$\angle H_{3\beta}CH_{4\beta}$	108.0	106.8	108.8	108.5	108.1	107.8	110.7	109.0	111.3	109.2	111.2	108.7
$r(C_\alpha\text{-}H_{1\alpha})$	1.075	1.074	1.074	1.072	1.074	1.073	1.073	1.074	1.073	1.074	1.073	1.075
$r(C_\alpha\text{-}H_{2\alpha})$	1.075	1.072	1.074	1.073	1.074	1.071	1.073	1.070	1.073	1.070	1.073	1.070
$\angle H_{1\alpha}CC$	119.7	120.5	119.6	121.5	119.5	120.0	119.4	118.4	119.6	118.1	119.8	118.0
$\angle H_{2\alpha}CC$	119.7	121.6	119.6	119.4	118.6	119.9	119.4	121.6	119.6	122.2	119.8	122.7
θ	78.5	90.1	79.5	87.2	101.9	89.9	80.0	90.0	80.7	90.0	81.2	90.0
ω	0.0	90.0	0.0	34.6	65.6	90.0	0.0	90.0	0.0	90.0	0.0	90.0

(b) LMP2 level

	X = H		X = F				X = Cl		X = Br		X = I	
	I	IV*	I*	II	III	IV*	I	IV*	I	IV*	I	IV*
$r(C_\alpha\text{-}C_\beta)$	1.497	1.496	1.496		1.489	1.489	1.481	1.484	1.472	1.485	1.468	1.491
$r(C_\beta\text{-}X)$	1.096	1.089	1.405		1.399	1.398	1.855	1.822	2.035	1.986	2.212	2.153
$\angle XC_\beta C_\alpha$	111.6	111.4	111.3		110.0	109.8	111.6	111.4	111.3	112.5	111.8	112.5
$r(C_\beta\text{-}H_{3\beta})$	1.090	1.094	1.091		1.097	1.096	1.086	1.091	1.086	1.090	1.086	1.091
$r(C_\beta\text{-}H_{4\beta})$	1.090	1.094	1.090		1.093	1.095	1.086	1.091	1.086	1.091	1.086	1.090
$\angle H_{3\beta}CC$	111.3	111.4	110.6		111.5	111.7	111.2	112.2	112.8	111.8	112.8	111.7
$\angle H_{4\beta}CC$	111.4	111.5	110.9		111.3	111.8	112.3	111.4	112.9	112.0	112.9	111.8
$\angle H_{3\beta}CH_{4\beta}$	108.1	106.7	107.9		107.9	107.6	109.7	108.0	110.1	108.1	109.9	107.6
$r(C_\alpha\text{-}H_{1\alpha})$	1.080	1.079	1.079		1.080	1.078	1.079	1.081	1.080	1.087	1.080	1.082
$r(C_\alpha\text{-}H_{2\alpha})$	1.080	1.078	1.079		1.079	1.077	1.079	1.077	1.080	1.078	1.080	1.077
$\angle H_{1\alpha}CC$	120.2	120.5	120.5		119.2	120.1	119.6	118.7	119.8	116.4	119.9	118.4
$\angle H_{2\alpha}CC$	120.1	121.6	119.8		118.8	119.7	119.8	121.7	119.9	120.9	120.0	122.5
θ	80.7	91.2	82.5		100.4	90.0	80.7	90.8	81.0	101.4	80.9	91.0
ω	0.0	90.0	0.0		69.5	90.0	0.0	90.0	0.0	78.0	0.0	90.0

(c) B3PW91 level of DFT

	X = H		X = F				X = Cl		X = Br		X = I	
	I	IV*	I*	II	III	IV*	I	IV*	I	IV*	I	IV*
$r(C_\alpha\text{-}C_\beta)$	1.485	1.485	1.482		1.478	1.478	1.451	1.476	1.427	1.476		1.477
$r(C_\beta\text{-}X)$	1.103	1.094	1.404		1.387	1.384	1.931	1.843	2.170	2.014		2.191
$\angle XC_\beta C_\alpha$	112.1	111.9	110.8		111.0	111.0	109.7	112.1	108.2	112.5		113.4
$r(C_\beta\text{-}H_{3\beta})$	1.096	1.100	1.096		1.105	1.104	1.089	1.096	1.087	1.096		1.094
$r(C_\beta\text{-}H_{4\beta})$	1.096	1.100	1.096		1.100	1.104	1.089	1.096	1.087	1.096		1.096
$\angle H_{3\beta}CC$	111.8	111.9	111.3		111.6	111.5	114.5	112.9	116.4	113.2		112.9
$\angle H_{4\beta}CC$	111.8	111.9	111.3		111.2	111.5	114.5	112.8	116.4	113.2		113.1
$\angle H_{3\beta}CH_{4\beta}$	108.0	105.8	108.5		106.9	106.5	114.4	107.7	113.1	108.0		107.8
$r(C_\alpha\text{-}H_{1\alpha})$	1.085	1.085	1.085		1.084	1.084	1.084	1.085	1.084	1.086		1.087
$r(C_\alpha\text{-}H_{2\alpha})$	1.085	1.084	1.085		1.084	1.082	1.084	1.082	1.084	1.081		1.083
$\angle H_{1\alpha}CC$	120.8	120.6	120.5		120.2	120.2	120.4	118.6	120.6	118.3		117.6
$\angle H_{2\alpha}CC$	120.8	121.7	120.5		119.5	120.1	120.4	121.8	120.6	122.4		122.2
θ	84.3	90.0	83.3		96.5	89.6	83.9	90.0	85.0	90.0		98.5
ω	0.0	90.0	0.0		64.4	90.0	0.0	90.0	0.0	90.0		81.5

(d) B3LYP level of DFT

	X = H		X = F				X = Cl		X = Br		X = I	
	I	IV*	I*	II	III	IV*	I	IV*	I	IV*	I	IV*
$r(C_\alpha\text{-}C_\beta)$	1.489	1.489	1.484		1.480	1.481	1.447	1.479		1.479		1.480
$r(C_\beta\text{-}X)$	1.104	1.094	1.411		1.393	1.390	1.970	1.858		2.030		2.204
$\angle XC_\beta C_\alpha$	112.1	111.9	110.6		110.8	110.8	109.2	112.1		112.5		113.5
$r(C_\beta\text{-}H_{3\beta})$	1.096	1.101	1.096		1.105	1.104	1.087	1.096		1.095		1.095
$r(C_\beta\text{-}H_{4\beta})$	1.096	1.101	1.096		1.100	1.104	1.087	1.096		1.095		1.095
$\angle H_{3\beta}CC$	111.8	112.0	111.4		111.8	111.5	115.2	113.0		112.4		113.1
$\angle H_{4\beta}CC$	111.8	112.0	111.4		111.3	111.6	115.2	113.0		113.4		113.1
$\angle H_{3\beta}CH_{4\beta}$	108.1	105.7	108.7		106.9	106.6	112.0	107.8		108.1		107.7
$r(C_\alpha\text{-}H_{1\alpha})$	1.085	1.083	1.084		1.084	1.083	1.084	1.085		1.086		1.081
$r(C_\alpha\text{-}H_{2\alpha})$	1.085	1.084	1.084		1.084	1.082	1.084	1.081		1.081		1.086
$\angle H_{1\alpha}CC$	120.8	121.7	120.5		120.2	120.2	120.5	118.5		118.2		123.0
$\angle H_{2\alpha}CC$	120.8	120.6	120.5		119.5	120.0	120.5	121.8		122.5		118.1
θ	84.3	90.0	83.3		91.0	89.5	84.1	90.1		90.0		90.1
ω	0.0	90.0	0.0		69.5	90.0	0.0	90.0		90.0		90.0

Table A.1.4. SOMO and LUMO energy (Hartrees) of the IV rotamer of CH_2XCH_2.

HF	SOMO	LUMO	LUMO - SOMO
C_2H_5	-0.1746	0.25865	0.43325
CH_2FCH_2	-0.18469	0.25851	0.44320
CH_2ClCH_2	-0.19116	0.18879	0.37995
CH_2BrCH_2	-0.19098	0.14300	0.33398
CH_2ICH_2	-0.18978	0.10579	0.29557
LMP2			
C_2H_5	-0.17462	0.25781	0.43243
CH_2FCH_2	-0.18536	0.25583	0.44119
CH_2ClCH_2	-0.19032	0.19282	0.38314
CH_2BrCH_2	-0.19497	0.14994	0.34491
CH_2ICH_2	-0.18872	0.11009	0.29881
B3PW91			
C_2H_5	-0.10000	0.12519	0.22519
CH_2FCH_2	-0.10881	0.10513	0.21394
CH_2ClCH_2	-0.11457	0.01644	0.13101
CH_2BrCH_2	-0.11455	-0.01626	0.09829
CH_2ICH_2	-0.11541	-0.03897	0.07644
B3LYP			
C_2H_5	-0.09759	0.11733	0.21492
CH_2FCH_2	-0.10658	0.10192	0.20850
CH_2ClCH_2	-0.11213	0.01378	0.12591
CH_2BrCH_2	-0.11208	-0.01880	0.09328
CH_2ICH_2	-0.11132	-0.04026	0.07106

Table A.1.5. Optimized structure of the bridged radicals at various levels of theory. The bond lengths are in Å and the angles are in degrees.

	C_2H_4			
	HF	**LMP2**	**B3PW91**	**B3LYP**
r(C-X)				
∠CXC				
r(C-C)	1.317	1.336	1.329	1.330
r(C-H)	1.077	1.082	1.087	1.087
∠HCC	121.7	121.5	121.8	121.8
	CH_2ClCH_2			
	HF	**LMP2**	**B3PW91**	**B3LYP**
r(C-X)	3.515	3.500 3.562	2.660	2.705
∠CXC	21.6	21.9	29.5	29.0
r(C-C)	1.319	1.340	1.355	1.354
r(C-H)	1.076	1.082	1.085	1.085
∠HCC	121.7	121.4	121.4	121.5
	CH_2BrCH_2			
	HF	**LMP2**	**B3PW91**	**B3LYP**
r(C-X)	3.620	3.704 3.752	2.829	2.889
∠CXC	21.0	20.7	27.7	27.7
r(C-C)	1.319	1.340	1.352	1.352
r(C-H)	1.076	1.082	1.086	1.085
∠HCC	121.7	121.4	121.5	121.5
	CH_2ICH_2			
	HF	**LMP2**	**B3PW91**	**B3LYP**
r(C-X)	3.894	4.028 4.042	3.079	3.159
∠CXC	19.5	19.1	25.3	25.1
r(C-C)	1.319	1.339	1.348	1.347
r(C-H)	1.076	1.082	1.086	1.086
∠HCC	121.7	121.5	121.5	121.6

Table A.1.6. Vibrational frequencies of CH_2XCH_2 radicals and C_2H_4 calculated with DFT methods (B3PW91 and B3LYP). The anti conformer has a prefix of a- and the symmetrically bridged structure has a prefix of b-. Symmetry species in each row are symmetrically correlated.

	C_{2v}	b-CH_2ClCH_2	b-CH_2BrCH_2	b-CH_2ICH_2	D_{2h}	C_2H_4		C_s	a-CH_2ClCH_2	a-CH_2BrCH_2
cis CH stretch	B_1	3300[a] (3286[b])	3294 (3280)	3288 (3273)	B_{2u}	3258 (3244)	asym. CH stretch of $\bullet CH_2$	A"	3301 (3287)	3300
trans CH stretch	A_2	3278 (3263)	3272 (3257)	3265 (3250)	B_{3g}	3234 (3219)	asym. CH stretch of XCH_2	A"	3222 (3220)	3249
symm. CH stretch	A_1	3192 (3182)	3188 (3178)	3184 (3174)	A_g	3170 (3159)	symm. CH stretch of $\bullet CH_2$	A'	3188 (3177)	3187
anti. CH stretch	B_2	3185 (3176)	3180 (3171)	3176 (3166)	B_{1u}	3154 (3145)	symm. CH stretch of XCH_2	A'	3142 (3141)	3162
CC stretch	A_1	1639 (1641)	1644 (1647)	1654 (1657)	A_g	1720 (1717)	CC stretch	A'	1132 (1127)	1103
anti. HCH bend	B_2	1470 (1479)	1471 (1481)	1471 (1481)	B_{1u}	1471 (1480)	anti. HCH bend	A'	1465 (1473)	1463
symm. HCH bend	A_1	1358 (1360)	1361 (1362)	1365 (1367)	A_g	1385 (1387)	symm. HCH bend	A'	1512 (1520)	1521
anti. HCH wag	A_2	1234 (1239)	1234 (1240)	1234 (1240)	B_{3g}	1233 (1239)	anti. HCH wag	A"	1252 (1250)	1241
H_2C-CH_2 twist	A_2	961 (965)	988 (988)	1009 (1005)	A_u	1070 (1071)	XCH_2 scissor + $\bullet CH_2$ wag	A"	1052 (1039)	998
symm. out of plane	A_1	993 (993)	997 (996)	998 (994)	B_{3u}	976 (978)	CH_2 rock of $\bullet CH_2$	A'	688 (705)	750
anti. out of	B_2	971 (973)	975 (974)	977 (974)	B_{2g}	964	CH_2 rock of	A'	1229	1178

plane						(963)	XCH_2		(1210)	
symm. HCH wag	B_1	829 (832)	828 (832)	827 (831)	B_{2u}	825 (828)	symm. HCH wag	A"	781 (784)	780
shuttle perp. to CC	B_1	323 (300)	327 (293)	300 (246)			torsion	A"	277 (299)	356
X-(C_2H_4) stretch	A_1	218 (212)	178 (166)	141 (126)			$\bullet CH_2$ rock + XCH_2 rock	A'	466 (403)	232
shuttle along CC	B_2	33 (86)	97 (96)	111 (90)			XCC bend	A'	300 (291)	298

[a] unscaled values and represented in cm^{-1}

[b] B3LYP values are presented in parentheses

Table A.1.7. Dissociation energy (kcal/mol) for $CH_2XCH_2\bullet \rightarrow CH_2{=}CH_2 + X$ reaction. The values in the parenthesis are corrected for the zero point energies.

Method	X = H	X = F	X = Cl	X = Br	X = I
HF	40.28	24.48	3.90	0.93	0.93
	(35.22)	(23.15)	(2.47)	(0.58)	(-0.58)[e]
LMP2//HF	37.21	43.45	0.24	-0.89	-0.88
	(32.15)	(42.12)	(-1.19)	(-1.24)	(-1.23)[e]
LMP2	36.94	43.62	0.12	-0.85	-0.83
	(31.88)	(42.29)	(-1.31)	(-1.20)	(-1.18)[e]
B3PW91	44.40	49.94	15.67	8.66	5.88
	(39.18)	(48.77)	(14.90)	(7.75)	(5.12)[e]
B3LYP	43.69	48.78	12.23	8.02	5.23
	(38.52)	(47.68)	(11.54)	(7.29)	(4.61)[e]
Experiment	35.5 ± 1.0 [a]	45 ~ 50 [b]	18.2 ± 2.2 [c]	8.4 ± 2.2 [c]	-10.1 ± 1.6 [d]

[a]Estimated using $\Delta H_{f,300K}(C_2H_5)$ = 28.0 ± 1.0 kcal/mol,[68] and $\Delta H_{f,0K}(C_2H_4)$ and $\Delta H_{f,0K}(H)$ from JANAF.[69] The thermal enthalpy is corrected for 0 K.

[b]Estimated by Schlegel et al.[70]

[c]Estimated using $\Delta H_f(CH_2ClCH_2\bullet)$ and $\Delta H_f(CH_2ClCH_2\bullet)$ from Ref. 71 and $\Delta H_f(C_2H_4)$ and $\Delta H_f(X)$ from the JANAF table[69]. The thermal enthalpy is corrected for 0 K. The estimated value for CH_2ClCH_2 is close to the 21.3 kcal/mol estimated in different way.[72]

[d]Estimated assuming that $D_0(CH_2XCH_2\text{-}H) = D_0(CH_3CH_2\text{-}H)$. The $\Delta H_f(C_2H_4)$, $\Delta H_f(CH_2XCH_3)$, $\Delta H_f(H)$, and $\Delta H_f(X)$ are taken from the JANAF table.[69]

[e]The calculated bond energy should be decreased by ~8 kcal/mol to reflect the spin-orbit coupling in the case of X = I.

A.2. Ab initio calculations of CF_2XCF_2X and CF_2XCF_2• (X = Cl, Br, I)

A.2.1 Introduction

In our previous paper,[1] we reported *ab initio* calculations of the haloethyl radicals (CH_2XCH_2•, X = I, Br, and Cl) aimed at elucidating the origin of the stereochemical control[2-8] observed in chemical reactions involving such radicals. We found that CH_2XCH_2• has one minimum and one saddle point in the rotational energy surface along the C-C bond. In addition, we suggested that the symmetrically bridged structures[7,9,10] are highly probable and should be responsible for stereochemical control in CH_2BrCH_2• and CH_2ICH_2• radicals.

To our knowledge, there has not yet been an experimental determination of the molecular structures of CH_2XCH_2• radicals. However, the molecular structure of the fluorine substituted analog, namely the CF_2ICF_2• radical, has recently been observed[11] and determined by[12] means of ultrafast electron diffraction techniques[13-16] developed in the Zewail laboratory. In this experiment, a CF_2ICF_2I molecule was irradiated by femtosecond laser pulses and molecular structures of transients and products were probed by picosecond electron pulses during the course of the dissociation process ($CF_2ICF_2I \rightarrow CF_2ICF_2$• + $I \rightarrow$ $CF_2{=}CF_2$ + 2I). The experimental diffraction patterns as a function of time were analyzed by incorporating geometries from the *ab initio* calculations reported here. We showed that the structure of the short-lived (picosecond time scale)[11,12] CF_2ICF_2• radical is consistent with the mixture of classical anti and gauche conformers found in the theory rather than the bridged structure expected for CH_2ICH_2•. Herein we provide a full account of the *ab initio*

calculations relevant to our experimental work and a comparison with our preliminary analysis of some recent experimental results[12].

Substitution of hydrogens with highly electronegative fluorines often causes dramatic changes in properties such as molecular structure and reactivity. For example, it is well-known that CF_3 is highly non-planar while CH_3 is planar.[17-19] The origin of this difference was explained by Goddard and Harding[20]. Another example is that 1,2-difluoroethane[21,22] (CH_2FCH_2F) strongly prefers the gauche conformer over the anti form, whereas, for CH_2ClCH_2Cl, CH_2BrCH_2Br, and CH_2ICH_2I, the anti conformer predominates over the gauche conformer (as expected from steric effects). Numerous experimental and theoretical studies have been performed to explain this effect of fluorine substitution. The comparison between CH_2XCH_2• radicals and CF_2XCF_2• radicals should provide a good platform for understanding the fluorine-substitution effect in ethyl radicals.

Along with CF_2XCF_2• radicals, 1,2-dihalotetrafluoroethanes (CF_2XCF_2X, X = I, Br and Cl) were also studied. As pointed out by Hedberg,[23] the CF_2XCF_2X system is unique because (1) it has more fluorine atoms than other heavier halogen atoms and (2) both steric and gauche effects are expected to play a role in determining the relative stability of the anti and gauche conformers. Despite the considerable number of experiments,[23-30] *ab initio* calculations of these molecules are quite sparse, especially for the molecules containing iodine atoms. In this work, we report studies of the structures, conformations, and dissociation energies for 1,2-dihalotetrafluoroethanes and their radicals.

A.2.2 Calculations

A.2.2.1 Methods

All calculations were performed using the Jaguar 3.5 program,[31,32] which utilizes pseudospectral algorithms. The C and F atoms were described using the 6-31G* basis set. The I, Br, and Cl atoms were described using the LAV3P relativistic effective core potential (RECP)[33] and basis set for the geometry scans of the rotational energy surface around the C-C bond. The LAV3P basis set consists of 3s3p valence primitive Gaussian functions contracted to 3s2p. The RECP was based on atomic calculations including relativistic effects. In addition, the stationary points were optimized with an additional basis set at the DFT-B3PW91 level.

- LAV3P(d): similar to LAV3P with an additional d-polarization function added for I, Br, and Cl atoms.[34]
- MSV: an all electron basis set equivalent to 4-31G[35]
- MSV(d): an all electron basis set equivalent to 4-31G*[35]

The DFT method (B3PW91) employs a combination of exchange terms: exact HF, the Becke 1988 non-local gradient correction,[36] and the original Slater local exchange functional.[37] In addition, it uses the Perdew-Wang 1991 local correlation functional and the GGA-II non-local correlation functional.[38]

We did not include spin-orbit coupling. This has negligible effect on the molecular radicals since the states are orbitally nondegenerate. For the dissociated halo radicals, the calculated bond energies should be decreased by ~(1/3)E($^2P_{1/2}$ – $^2P_{3/2}$). This is significant only for iodine where the adiabatic bond energy would be ~8 kcal/mol lower.

A.2.2.2 Procedure

For each system, the geometry was optimized with both Hartree-Fock (HF) and density functional theory (DFT). For the optimized HF geometries, we carried out local MP2 calculations[39,40] to account for electron correlation effects, denoted LMP2//HF. All calculations were restricted to proper spin states (singlet for CF_2XCF_2X and doublet for CF_2XCF_2•).

The total energies of each molecule and radical (CF_2XCF_2X, CF_2XCF_2•, CH_2XCH_2X, CH_2XCH_2• for X = Cl, Br and I) calculated at various levels of theory and basis sets are given in the supplementary tables. The complete lists of optimized structural parameters are also provided in the supplement. Selected structural parameters of the stable CF_2XCF_2X molecules are collected in Table A.2.1 and compared with the available experimental data. In addition, selected structural parameters of the anti CF_2XCF_2• radicals are listed in Table A.2.2 with recent experimental values[12] from ultrafast electron diffraction. For the minima and transition states, we calculated the vibrational frequencies at the HF and B3PW91 levels of theory. These frequencies were then used to obtain the zero point energy. All minima were found to have all real frequencies and all transition states were found to have only one imaginary frequency. The vibrational frequencies and mode assignments are included in supplementary tables. The relative energies and dissociation energies were corrected for the zero point energy using a scaling factor of 0.94 for HF and 0.97 for DFT methods.[41,42] Where the zero point energies were not calculated, values obtained with the same level of theory were used. For example, for energies with

LMP2//HF (LAV3P), we used the zero point corrections from HF (LAV3P) calculations. Table A.2.3 lists the conformational energy differences and rotational barriers.

A.2.3 Results and Discussion

A.2.3.1 CF_2XCF_2X (X = I, Br, Cl)

The CF_2XCF_2X molecule has two conformational minima, A (anti) and G (gauche), on the rotational energy surface. The two rotational transition structures connecting A and G are denoted as T1 (G $\leftrightarrow$ G) and T2 (G $\leftrightarrow$ A). The structures are schematically represented in Figure A.2.1, with the rotational energy surfaces calculated at the LMP2//HF level. The anti conformer exhibits C_{2h} symmetry while the gauche conformer has C_2 symmetry. The structures of these molecules have been well studied by gas phase electron diffraction.[23,24,30] The experimental values from the literature[23,24,30] are also listed in Table A.2.1 for comparison.

Geometries

The experimental structural parameters were obtained assuming that the anti and gauche conformers have identical geometry except for the ICCI dihedral angle.[23,24] At the HF level of theory with the LAV3P(d) basis set, we find for CF_2ICF_2I:

CC bond distances of 1.532 Å for A and 1.540 Å for G (1.534 ± 0.013 experiment);

CF bond distances of 1.320 Å for A and 1.323 Å for G (1.328 ± 0.003 experiment);

CI bond distances of 2.159 Å for A and 2.147 Å for G (2.136 ± 0.007 experiment);

CCF bond angles of 109.0° for A and 107.6° for G (109.4° ± 1.0° experiment);

CCI bond angles of 111.9° for A and 114.8° for G (111.6° ± 1.0° experiment);

FCF bond angles of 108.7° for A and 107.9° for G (107.8° ± 1.0° experiment).

Generally the geometries optimized at the HF and B3PW91 levels are very close to the experimental structures. Compared with the HF structures, the DFT (B3PW91) structures differ by less than 0.02 Å for the CC and CF bond distances, less than 0.04 Å for the CX bond distances, less than 1° for the CCF and FCF bond angles, and less than 2° for the CCX bond angles (see Table A.2.1). A closer examination reveals that the B3PW91 method gives longer CC, CF, and CX bond distances than those of the HF method, and within the B3PW91 method, the LAV3P(d) basis set provides the closer values to the available experimental values than the LAV3P basis set. Compared with the available experimental values, the B3PW91(LAV3P(d)) optimized values have longer CC, CF, and CX bond distances. For the CX bond distance, the HF (LAV3P(d)) gives better agreement with the experiment than the B3PW91 method. For the CC and CF distances, the B3PW91 method gives better agreement with the experiment than the HF method. As mentioned previously, the experimental values were obtained with a simplifying assumption that the anti and gauche conformers have the exact same structural parameters except for the XCCX dihedral angle. Our calculations suggest that the C-C and C-F distances of the anti conformers are smaller and C-X distances are longer than those of the gauche conformers.

Based on electron diffraction studies, Hedberg and coworkers reported that the internuclear distances between halogen atoms, which are gauche to each other, are smaller than the corresponding van der Waals distances by 0.2 to 0.6 Å. They suggested that the small root-mean square amplitudes of the torsional motion could be explained by the

minimization of van der Waals repulsion.[23] The C-C distances in the rotational transition structures are even longer than those of anti and gauche structures by 0.03 Å. The elongation of C-C bonds in gauche conformers and the transition structures (provided in the supplement) can be readily explained by the same argument.

Energies

The conformational energy differences and rotational barriers are listed in Table A.2.3. The correction for the thermal energies (0 K to 300 K) are less than 0.1 kcal/mol and are not included. The energy differences between the anti and gauche conformers of CF_2XCF_2X were investigated by infrared spectroscopy[25-29] and gas phase electron diffraction.[23,24] For all three molecules, anti conformers were found to be more stable than gauche conformers, in agreement with our calculations.

Serboli and Minasso[29] measured the infrared spectrum of CF_2ICF_2I at various temperatures and phases, and deduced $\Delta E_{A\rightarrow G}$ = 1.835 ± 0.100 kcal/mol. Using the same approach, Kagarise and Daasch[27,28] reported $\Delta E_{A\rightarrow G}$ = 0.925 ± 0.050 kcal/mol for CF_2BrCF_2Br and 0.5 ± 0.2 kcal/mol for CF_2ClCF_2Cl. Hedberg and coworkers[23,30] obtained a slightly lower value of 1.22 ± 0.36 kcal/mol for CF_2ICF_2I, 0.86 ± 0.26 kcal/mol for CF_2BrCF_2Br, and 0.45± 0.11 kcal/mol for CF_2ClCF_2Cl by measuring mole fractions of gauche conformers at various temperatures. Iwasaki[24] also used the gas phase electron diffraction technique and obtained 0.44 ± 0.11 kcal/mol for CF_2ClCF_2Cl.

The conformational energy differences obtained using the single-point energies calculated at LMP2//HF (LAV3P(d)) level of theory are in good agreement with the

experimentally obtained values for all three molecules. Thus, at the LMP2//HF level, we find:

$\Delta E_{A\rightarrow G}$ = 1.90 for X=I (experiment 1.835 ± 0.1 and 1.22 ± 0.36);

$\Delta E_{A\rightarrow G}$ = 1.05 for X=Br (experiment 0.925 ± 0.05 and 0.81 ± 0.26);

$\Delta E_{A\rightarrow G}$ = 0.44 for X=Cl (experiment 0.5 ± 0.2 and 0.44 ± 0.11).

In general, the inclusion of a d function reduces the energy differences between the conformers giving closer values to the experiment. Both experiment and *ab initio* calculations show that the conformational energy difference increases in the order of Cl, Br, and I. This trend is consistent with the idea that the main source for the different stabilities of anti and gauche conformers is steric. Indeed, the X...X distance for G at the HF level of theory is 3.396 Å for Cl, 3.668 Å for Br, and 4.002 Å for I, all less than the standard van der Waals parameters: 3.92 Å for Cl, 4.19 Å for Br , and 4.50 Å for I (values from the DREIDING force field[43]). The X...X distance calculated with the B3PW91 method is also smaller than the van der Waals parameters. The supplementary materials provide graphs showing such correlations in the conformational energy differences.[44] The barriers for the internal rotation also follow the same trend; the bigger the halogen atom, the higher the barrier.

Since the discovery of rotational barriers and conformational energies, there have been numerous discussions[21,44-61] regarding their origin. Although this is not the focus of this paper, a few comments are relevant. In the force fields used for molecular dynamics, the energy is composed of additive interactions.[45] Here, the steric interactions between the nonbonded substituents are described in terms of van der Waals and electrostatic

interactions. This is supplemented with a torsional term to obtain a more precise fit. The van der Waals term accounts for Pauli orthogonalization of nonbonded orbitals (repulsive) and long-range attraction (dispersion). These pair repulsions dominate the steric interaction responsible for the conformational energy difference between the anti and gauche forms of the CF_2XCF_2X molecules.[48] There have been many attempts to analyze the QM conformational energies and rotational barriers in terms of orbital interactions[21,56,62] or energy decompositions.[46,49,50] One energy decomposition[46] partitions the total HF energy into the attractive energy (total one-electron energy terms) and the repulsive energy (nuclear repulsion energy plus total two-electron energy terms). This is shown for CF_2ICF_2I in Figure A.2.2. Figure A.2.2 shows that the rotational barriers are attractive-dominant while the conformational energy is repulsive-dominant. For example, transforming the gauche conformer into the transition states, the change of the attractive energy is bigger than that of the repulsive energy and therefore is more responsible for the origin of the barriers (attractive-dominant). In contrast, the opposite is true for converting the gauche to the anti form (repulsive-dominant). The repulsive-dominant interaction is due to the steric effect in the force field. The energy decompositions for CF_2ICF_2•, CH_2ICH_2I and CH_2ICH_2• are included in the supplement. Comparing the rotational barriers and conformational energy differences (presented in the supplements) between CF_2XCF_2X and CH_2XCH_2X shows that the barriers of CF_2XCF_2X are generally higher and the conformational energy difference is lower than those of CH_2XCH_2X.

A.2.3.2 CF_2XCF_2• radicals (X = I, Br, and Cl)

Classical asymmetric structure

The CF_2XCF_2 radicals can be readily observed in the photodissociation reactions of CF_2XCF_2X molecules.[11,63-67] As with the parent molecules, each radical has two minima, A (anti) and G (gauche), and two rotational transition states, T1 and T2, on the rotational energy surface. The structures are schematically illustrated in Fig. A.2.3 with the rotational energy surfaces calculated at the LMP2//HF level. The anti conformers have C_s symmetry and the gauche conformers have C_1 symmetry. The geometries of these radicals have not yet been studied experimentally except for the ultrafast electron diffraction study[11,12] on the CF_2ICF_2• radical.

Table A.2.2 presents selected structural parameters of the anti CF_2XCF_2 radicals. The general trend of the structural parameters in the radicals is the same as for the parent molecules. The gauche conformers have longer C-C bonds and shorter C-X bonds than the anti conformers. The structures in the rotational transition state structures also have highly elongated C-C bonds.

The B3PW91 method generally gives longer CF, CF′, and CX bond distances than those of the HF method, and the HF (LAV3P(d)) method actually provides the closest C-I distance to the experimental value from the analysis of recent data[12] using ultrafast electron diffraction. This result is consistent with the trend observed in the parent molecules, which also show that the HF (LAV3P(d)) values are the closest values to the experiment. For the CC and CF distances, the B3PW91 methods gives better values than the HF method. This trend is also valid for the parent molecule (CF_2ICF_2I). The experimentally determined

structural parameters of the CF_2ICF_2I and CF_2ICF_2 show the same trend as predicted by calculations. The C-I bond distance becomes longer (~0.02 Å) and the C-C bond distance becomes shorter (~0.05 Å) for the CF_2ICF_2 radical compared with the CF_2ICF_2I molecule. In addition the CCF′ and F′CF′ angles become larger by 9° and 11°, suggesting that the radical center (-CF'_2) of the CF_2ICF_2 radical is relaxed after removing the I atom from the CF_2ICF_2I molecule.

Table 3 presents the relative energies for different conformations of the CF_2XCF_2 radicals. No experimental values for the radicals have been reported yet. We find that these anti conformers are more stable than the gauche conformers by 1.8 kcal/mol (at LMP2//HF (LAV3P(d))) for Cl, 2.8 kcal/mol for Br, and 3.3 kcal/mol for I; thus, the radicals follow the same trend as seen in the parent molecules, but with much greater magnitude. The barriers also increase in the order of Cl, Br, and I, as for the parent, but with much lower magnitude. Both T1 and T2 rotational barriers are significantly lowered compared to those of the parent molecules. The lowered rotational barriers in the radicals can be readily explained by the absence of the steric repulsion between two heavy halogen atoms (I, Br, and Cl). However, the larger conformational energy differences in the radicals cannot be explained solely by the steric effect since steric repulsion in the gauche conformer should be less severe for the radicals than for the parent molecules.

The larger conformational energy differences in the radicals suggest that the anti form of the radical gains extra stability. Indeed, the anti conformer has a hyperconjugative interaction[1] between the radical center and the σ*(C-X) MO while the gauche form has hyperconjugation between the radical center and the σ*(C-F) MO. The more

electronegative atom will disfavor the hyperconjugation by raising the energy of the σ*(C-X) MO. To further confirm our conclusion, we compared the (B3PW91) relative energies of the CI_2FCI_2F molecule with the CI_2FCI_2 radical. For CI_2FCI_2F, the anti conformer is more stable than the gauche form by 1.41 kcal/mol mainly due to steric effects. For the radical, the relative stability is *reversed* with the gauche form more stable than the anti form by 7.43 kcal/mol. This is highly consistent with the hyperconjugation explanation since the anti form of the CI_2FCI_2 radical has hyperconjugation between the radical center and the σ*(C-F) MO while the gauche form has hyperconjugation between the radical center and the σ*(C-I) MO.

In Table A.2.3, the comparison of B3PW91 (LAV3P) and B3PW91 (LAV3P(d)) shows that the inclusion of a d function to the halogen atom does not change the general energetics of the conformers. The CH_2XCH_2 radicals have only one minima and one saddle point (see Fig. A.2.4) while the CF_2XCF_2 radicals have two minima and two saddle points on the rotational energy surface. This rather dramatic change is due to the difference in the radical center; in CH_2XCH_2 radicals, the radical center is almost planar; however, the radical center of CF_2XCF_2 is highly non-planar due to the electronegative F atoms. The effect of fluorine substitution was systematically studied by Bernardi, *et al.*[19] for the fluorine substituted methyl radicals ($CH_{3-n}F_n$, n = 0 – 3). They showed that the pyramidality of the radical center increases with fluorination due to conjugative and inductive effects. The non-planarity of the CF_2XCF_2 radicals can be explained by the same argument.

We explored the rotational potential energy surfaces of CF_2ClCF_2•, CF_2ClCH_2•, CH_2ClCF_2•, CH_2ClCH_2• radicals as shown in Figure A.2.4. Indeed, we found that every

species having a $-CH_2\bullet$ radical center has only one stable conformation (which is anti with one rotational transition structure) while radicals with a $-CF_2\bullet$ center have two minima and two transition states on the rotational energy surface along the C-C bond.

Bridged structure

Our previous study[1] of CH_2BrCH_2 and CH_2ICH_2 radicals showed that the symmetrically bridged form is stable in the potential energy surfaces, confirming the Skell hypothesis[7,9,10] that symmetrical bridging is predominantly responsible for stereochemical control. In our previous study on the CH_2XCH_2 radicals (X = I, Br, and Cl), the LAV3P basis set was used without a d function. To test the effect of a d function, the geometries of the CH_2XCH_2 radicals were optimized with the LAV3P(d) basis set at the B3PW91 level of theory and compared with the previous values[1] in Table A.2.4. Inclusion of a d function shortens the C-X bond distances, but not dramatically. Moreover, the anti structures get added stabilization compared with the bridged structures, and for the CH_2BrCH_2 radical, the bridged structure is less stable than the anti structure. Therefore, our previous conclusion that the bridged form of the CH_2BrCH_2 radical is more stable than the anti form should be modified; the anti form is more stable than the bridged form in the B3PW91 (LAV3P(d)) calculation. This new conclusion is consistent with a MRD-CI calculation[68] of Engels and Peyerimhoff. However, the bridged structure is still the global minimum for the CH_2ICH_2 radical.

The bridged structures were also explored in an attempt to elucidate the relative stability of the bridged CF_2XCF_2 radicals. Table A.2.3 shows the relative energy of the

bridged structure compared to the gauche structure for each radical. In contrast to the CH_2BrCH_2 and CH_2ICH_2 radicals, the symmetrically bridged conformations of the CF_2XCF_2 radicals are *not* favorable. We could not find any minimum structure with all real frequencies for the symmetrically bridged conformation in any but the CF_2ClCF_2 radical calculated at HF level.

Our conclusion that the symmetrically bridged form is not favorable for the CF_2XCF_2 radicals is consistent with recent experimental observations.[11,12] Indeed, the current calculations were motivated by the experiment and the structures and energetics reported herein were used as the initial guess in refining the structure.[11,12] The potential energy surfaces, relevant to the stability of the bridged conformation of CF_2ICF_2 radical, are shown in Figure A.2.5. Using B3PW91, the geometries were optimized as a function of the position of the primary halogen atom. In this calculation, this halogen atom was confined in the XCC plane bisecting the FCF angle. For comparison, the corresponding contour map[1] for the CH_2ICH_2 radical is also presented. The dramatic difference between the CH_2ICH_2 radical and the fluorinated analog (CF_2ICF_2) is clear. The singly-occupied molecular orbital of the bridged structure[1] involves an interaction between the p orbital of halogen atom and the π orbital of the CC bond. The relative instability of the bridged structure in CF_2XCF_2 radicals compared with CH_2XCH_2 radicals is not surprising since the electron density of the π orbital of the C_2F_4 moiety is relatively smaller than that of the C_2H_4 moiety due to presence of highly electronegative F atoms. This was confirmed by calculating the electron density surfaces of C_2H_4 and C_2F_4.

Dissociation energy

Using the energies for CF_2XCF_2X and CF_2XCF_2, we calculated the dissociation energy for the reaction of CF_2XCF_2X into CF_2XCF_2 and X. To calculate the dissociation energy for the further dissociation of CF_2XCF_2 into $CF_2{=}CF_2$ and X, the energy of $CF_2{=}CF_2$ was also calculated at the HF, LMP2//HF, B3PW91 and LMP2 levels using the 6-31G* basis set. Table A.2.5 lists the calculated dissociation energy for each reaction.

There has been no direct measurement of these dissociation energies. Nathanson, *et al.*[64] measured the upper limit of 59.1 ± 1 kcal/mol for the reaction enthalpy of CF_2ICF_2I to CF_2CF_2 + I + I using photofragment translational spectroscopy. They also estimated the upper limits to the dissociation energies, CF_2CF_2-I(Br) → $CF_2{=}CF_2$ + I(Br), to be 7.1 ± 2.5 kcal/mol for $D_0(CF_2CF_2\text{-I})$ and 22.3 ± 2.5 kcal/mol for $D_0(CF_2CF_2\text{-Br})$. We note that these values were obtained by assuming that the C-I bond energies in the CF_2BrCF_2I and CF_2ICF_2I molecules are the same, and equal to $D_0(CF_3CF_2\text{-I})$ = 52 ± 1.3 kcal/mol. The dissociation energies for CF_2CF_2-I and CF_2CF_2-Br were also estimated by Krajnovich, *et al.*[67] using the available thermodynamic data for the related molecules and halogen atoms. They found $D_0(CF_2CF_2\text{-I})$ to be 0 kcal/mol and $D_0(CF_2CF_2\text{-Br})$ to be 16 kcal/mol by assuming that the C-F bond dissociation energies in CF_2ICF_2 and CF_2BrCF_2 radical are the same as in C_2F_6. They also assigned 19.3 kcal/mol as the upper limit of $D_0(CF_2CF_2\text{-Br})$ based on their experimental results.

The values from the B3PW91 (LAV3P(d)) and B3PW91 (MSV(d)) seem to converge to each other and give the best value compared with experiments. The calculated dissociation energies do not contradict these experimental estimates. Based on the spread in

dissociation energies in Table A.2.5, a conservative estimate for the error bar of the calculations relative to experiment would be 4 kcal/mol. The values calculated at each level of theory follow the same trend; the dissociation energies decrease in the order of Cl, Br, and I. The second dissociation energies (D_2) are much smaller than the first dissociation energies (D_1) mainly due to π-bond formation in CF_2=CF_2. The C-X bond in the CF_2XCF_2 radical might be weaker than that of CF_2XCF_2X since the hyperconjugative interaction in the radical weakens the C-X bond. As noted before, the C-C bond length of the CF_2XCF_2 radical is considerably shorter and the C-X bond is longer than in the parent molecule. Indeed, $D_1 - D_2 = \pi$, the thermochemical CC π-bond for C_2F_4. Thus, we expect D_1-D_2 to be nearly the same independent of X, which is observed (Table A.2.5).

A.2.4 Conclusion

The rotational energy barriers of the CF_2XCF_2 radicals (Figs. 1, 3) are smaller than those of the parent molecules (CF_2XCF_2X) owing to the absence of steric repulsion between the two heavy halogen atoms. However, the conformational energy differences (Figs. 1, 3) in the radicals were found to be larger than those in the parent molecules. It is suggested that the hyperconjugation between the radical center and the σ*(C-X) MO stabilizes the anti conformer of the radical.

Compared with haloethyl radicals (CH_2XCH_2), the CF_2XCF_2 radicals show dramatically different behavior. The CF_2XCF_2 radical has two minima and two saddle points while the CH_2XCH_2 radical has only one minima and one saddle point on the rotational energy surface along the C-C bond. We found that every radical with a $-CH_2$•

center has only one stable conformation (anti with one rotational transition structure) while radicals with a $-CF_2\bullet$ center have two minima and two transition states on the rotational energy surface along the C-C bond. We show that the CF_2XCF_2 radicals cannot form stable bridged structures while such bridged structures *are* favorable in the corresponding CH_2XCH_2 radicals. For the case of X = I, the current calculations were used as the initial guess in refining the structure for a recent ultrafast electron diffraction experiment[11,12].

Supporting Information Available: Figure A.2.S1 shows correlation between the van der Waals radii / group electronegativity and the relative energy difference, and Figures S2-S4 shows the energy decomposition for CH_2ICH_2I, $CF_2ICF_2\bullet$ and $CH_2ICH_2\bullet$, respectively. Table A.2.S1 presenting the complete structural parameters of the CF_2XCF_2X and $CF_2XCF_2\bullet$ radicals (X = I, Br and Cl) optimized at various levels of theory (HF and B3PW91) and basis set (LAV3P, LAV3P(d), MSV, MSV(d)). Table A.2.S2 presents the total energies calculated at various levels of theory and basis set for CF_2XCF_2X and CF_2XCF_2 radicals. Tables S3 and S4 presenting the total energies and relative energies of CH_2XCH_2X calculated at various levels of theory and basis set. Tables S5-S8 presents the vibrational frequencies and mode analysis for CF_2XCF_2X and CF_2XCF_2 at various levels of theory and basis set. Table A.2.S9 lists the exponents and coefficients of MSV(d) basis set.

References

1)Ihee, H.; Zewail, A. H.; Goddard, W. A., III. *J. Phys. Chem. A* **1999**, *103*, 6638.

2)Kochi, J. K. *Free Radicals*; John Wiley & Sons: New York, 1973; Vol. II.

3)Beckwith, A. L. J.; Ingold, K. U. *Free-Radical Rearrangements*; Mayo, P. d., Ed.; Academic Press: New York, 1980.

4)Fossey, J.; Lefort, D.; Sorba, J. *Free Radicals in Organic Chemistry*; John Wiley & Sons: New York, 1995.

5)Goering, H. L.; Abell, P. I.; Aycock, B. F. *J. Am. Chem. Soc.* **1952**, *74*, 3588.

6)Thaler, W. *J. Am. Chem. Soc.* **1963**, *85*, 2607-2613.

7)Skell, P. S.; Tuleen, D. L.; Readio, P. D. *J. Am. Chem. Soc.* **1963**, *85*, 2849.

8)Tanner, D. D.; Darwish, D.; Mosher, M. W.; Bunce, N. J. *J. Am. Chem. Soc.* **1969**, *91*, 7398.

9)Skell, P. S.; Shea, K. J. *Bridged Free Radicals*; Kochi, J. K., Ed.; John Wiley & Sons: New York, London, Sydney, Toronto, 1973.

10)Skell, P. S.; Pavlis, R. P.; Lewis, D. C.; Shea, K. J. *J. Am. Chem. Soc.* **1973**, *95*, 6735.

11)Cao, J.; Ihee, H.; Zewail, A. H. *Proc. Natl. Acad. Sci. USA* **1999**, *96*, 338.

12)Ihee, H.; Lobastov, V. A.; Gomez, U.; Goodson, B. M.; Srinivasan, R.; Ruan, C.-Y.; Zewail, A. H. *Science* **2001**, *291*, 458.

13)Ihee, H.; Cao, J.; Zewail, A. H. *Chem. Phys. Lett.* **1997**, *281*, 10.

14)Cao, J.; Ihee, H.; Zewail, A. H. *Chem. Phys. Lett.* **1998**, *290*, 1.

15)Williamson, J. C.; Cao, J.; Ihee, H.; Frey, H.; Zewail, A. H. *Nature* **1997**, *386*, 159.

16)Ihee, H.; Cao, J.; Zewail, A. H. *Angew. Chem. Int. Ed.* **2001**, in press.

17)Koenig, T.; Ball, T.; Snell, W. *J. Am. Chem. Soc.* **1975**, *97*, 662.

18)Fessenden, R. W.; Schuler, R. H. *J. Chem. Phys.* **1965**, *43*, 2704.

19)Bernardi, F.; Cherry, W.; Shaik, S.; Epiotis, N. D. *J. Am. Chem. Soc.* **1978**, *100*, 1352.

20)Goddard III, W. A.; harding, L. B. *Ann. Rev. Phys. Chem.* **1978**, *29*, 363.

21)Wiberg, K. B.; Murcko, M. A.; Laidig, K. E.; MacDougall, P. J. *J. Phys. Chem.* **1990**, *94*, 6956.

22)Engkvist, O.; Karlström, G.; Widmark, P.-O. *Chem. Phys. Lett.* **1997**, *265*, 19.

23)Thomassen, H.; Samdal, S.; Hedberg, K. *J. Am. Chem. Soc.* **1992**, *114*, 2810.

24)Iwasaki, M. *Bull. Chem. Soc. Jap.* **1958**, *31*, 1071.

25)Glockler, G.; Sage, C. *J. Chem. Phys.* **1941**, *9*, 387.

26)Simpson, D.; Plyler, E. K. *J. Res. Natl. Bur. Stand.* **1953**, *50*, 223.

27)Kagarise, R. E. *J. Chem. Phys.* **1957**, *26*, 380.

28)Kagarise, R. E.; Daasch, L. W. *J. Chem. Phys.* **1955**, *23*, 130.

29)Serboli, G.; Minasso, B. *Spect. Acta* **1968**, *24A*, 1813.

30)Thomassen, H.; Hedberg, K. *J. Phys. Chem.* **1992**, *96*, 7983.

31)Jaguar *Jaguar*; 3.0 ed.; Schrödinger, Inc.: Portland, OR, 1997.

32)Greeley, B. H.; Russo, T. V.; Mainz, D. T.; Friesner, R. A.; Langlois, J.-M.; Goddard, I., W. A.; Donnelly, R. E.; Ringnalda, M. N. *J. Chem. Phys.* **1994**, *101*, 4028.

33)Hay, P. J.; Wadt, W. R. *J. Chem. Phys.* **1985**, *82*, 284.

34)Exponent , Exponents for d-polarization functions for I, Br, Cl are 0.226, 0.380 and 0.750 respectively.

35)Rappe, A. K.; Goddard III, W. A., unpublished results: Exponents and coefficients for C, F, Cl, Br, and I are presented in the supporting information.

36)Becke, A. D. *Phys. Rev. A* **1988**, *38*, 3098.

37)Slater, J. C. *Quantum Theory of Molecules and Solids*; McGraw-Hill: New York, 1974.

38)Perdew, J. P.; Chevary, J. A.; Vosko, S. H.; Jackson, K. A.; Pederson, M. R.; Singh, D. J.; Fiolhais, C. *Phys. Rev. B* **1992**, *46*, 6671.

39)Sæbø, S.; Pulay, P. *Ann. Rev. Phys. Chem.* **1993**, *44*, 213.

40)Murphy, R. B.; Beachy, M. D.; Friesner, R. A.; Ringnalda, M. N. *J. Chem. Phys.* **1995**, *103*, 1481.

41)Scott, A. P.; Radom, L. *J. Phys. Chem.* **1996**, *100*, 16502.

42)Wong, M. W. *Chem. Phys. Lett.* **1996**, *256*, 391.

43)Mayo, S. L.; Olafson, B. D.; Goddard III, W. A. *J. Phys. Chem.* **1990**, *94*, 8897.

44)Phillips, L.; Wray, V. *J. Chem. Soc. Chem. Comm.* **1973**, 90.

45)Hill, T. L. *J. Chem. Phys.* **1948**, *16*, 399.

46)Allen, L. C. *Chem. Phys. Lett.* **1968**, *2*, 597.

47)Lowe, J. P. *Barriers to Internal Rotation about Single Bonds*; Streitwieser, J. A. and Taft, R. W., Ed., 1968; Vol. 6, pp 1-80.

48)Abraham, R. J.; Parry, K. *J. Chem. Soc. B* **1970**, 539.

49)Wolfe, S.; Rauk, A.; Tel, L. M.; Csizmadia, I. G. *J. Chem. Soc. B* **1971**, 136.

50)Wolfe, S. *Acc. Chem. Res.* **1972**, *5*, 102-111.

51)Radom, L.; Hehre, W. J.; Pople, J. A. *J. Am. Chem. Soc.* **1972**, *94*, 2371.

52)Kaloustian, M. K. *J. Chem. Edu.* **1974**, *51*, 777.

53)Eliel, E. L. *J. Chem. Edu.* **1975**, *52*, 762.

54)Eliel, E. L.; Juaristi, E. *J. Am. Chem. Soc.* **1978**, *100*, 6114.

55)Smart, B. E. *J. Org. Chem.* **1973**, *38*, 2039.

56)Brunck, T. K.; Weinhold, F. *J. Am. Chem. Soc.* **1979**, *101*, 1700.

57)Kveseth, K. *Acta Chem. Scand. A* **1978**, *32*, 51.

58)Juaristi, E. *J. Chem. Edu.* **1979**, *56*, 438.

59)Wiberg, K. B.; Murcko, M. A. *J. Phys. Chem.* **1987**, *91*, 3616.

60)Dixon, D. A.; Matsuzawa, N.; Walker, S. C. *J. Phys. Chem.* **1992**, *96*, 10740.

61)Chang, Y.-P.; Su, T.-M.; Li, T.-W.; Chao, I. *J. Phys. Chem.* **1997**, *101*, 6107.

62)Bernardi, F.; Bottoni, A.; Fossey, J. *Theo. Chim. Acta* **1982**, *61*, 251.

63)Knee, J. L.; Khundkar, L. R.; Zewail, A. H. *J. Chem. Phys.* **1985**, *83*, 1996.

64)Nathanson, G. M.; Minton, T. K.; Shane, S. F.; Lee, Y. T. *J. Chem. Phys.* **1989**, *90*, 6157.

65)Khundkar, L. R.; Zewail, A. H. *J. Chem. Phys.* **1990**, *92*, 231.

66)Zhong, D.; Ahmad, S.; Zewail, A. H. *J. Am. Chem. Soc.* **1997**, *119*, 5978.

67)Krajnovich, D.; Butler, L. J.; Lee, Y. T. *J. Chem. Phys.* **1984**, *81*, 3031.

68)Engels, B.; Peyerimhoff, S. D. *J. Mol. Struct.* **1986**, *138*, 59.

Figure Captions

Figure A.2.1: The rotational potential energy curves for the CF_2XCF_2X (X = I, Br, and Cl) molecules calculated at LMP2//HF (LAV3P). The torsion angle is the XCCX dihedral angle.

Figure A.2.2: Energy decomposition for CF_2ICF_2I calculated at HF (LAV3P) level. Total HF energy is sum of the attractive energy (Total one-electron term) and repulsive energy (Nuclear repulsion + Total two-electron terms). See 3.1.2 for a discussion.

Figure A.2.3: The rotational potential energy curves for the CF_2XCF_2 (X = I, Br, and Cl) radicals calculated at LMP2//HF (LAV3P). The torsion angle is the dihedral angle of XCC-radical center.

Figure A.2.4: The rotational potential energy curves for various radicals calculated at LMP2//HF (LAV3P). The torsion angle is the dihedral angle of XCC-radical center. Note that the lower two cases correspond to equivalent isomers for ϕ = 0 to 180° because the radical center is CH_2 which prefers to be planar.

Figure A.2.5: The energy contours for CH_2ICH_2 and CF_2ICF_2 using the B3PW91 (LAV3P) method. The position of halogen atom is referenced to the middle point of two carbon atoms. The zero of energy corresponds to the global minimum. Thus CH_2ICH_2 is bridged while CF_2ICF_2 has the classical structure.

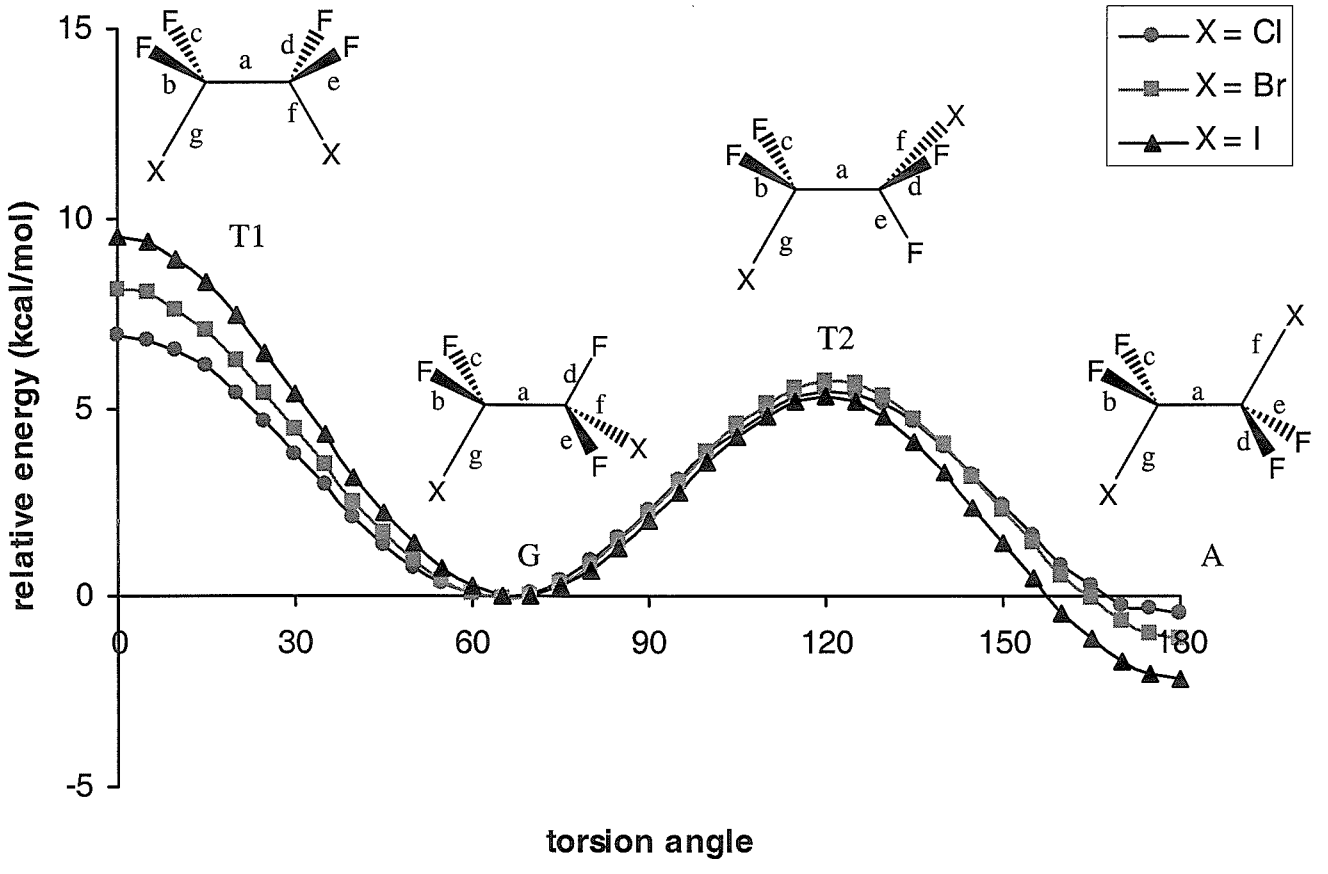
X = Cl
X = Br
X = I
relative energy (kcal/mol)
torsion angle
T1
T2
G
A
15
10
5
0
-5
0
30
60
90
120
150
180

Figure A.2.1

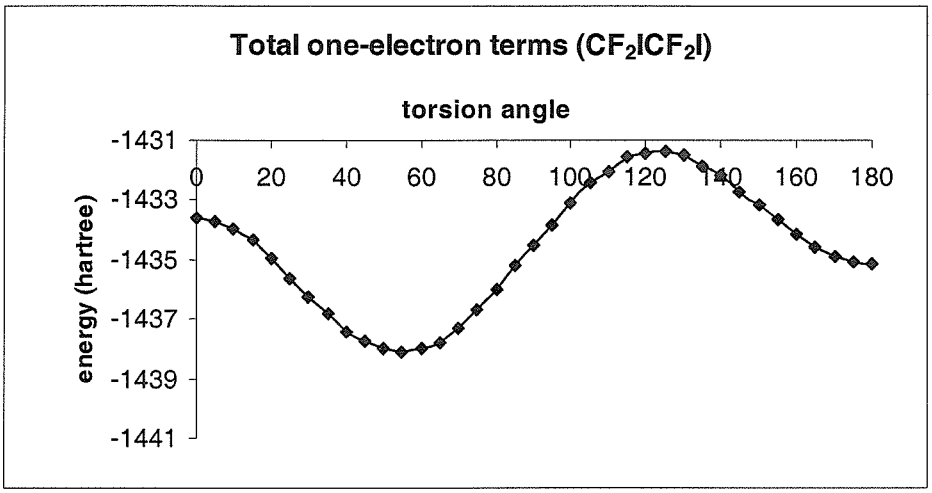
Total one-electron terms (CF_2ICF_2I)
torsion angle
energy (hartree)
-1431
-1433
-1435
-1437
-1439
-1441
0
20
40
60
80
100
120
140
160
180

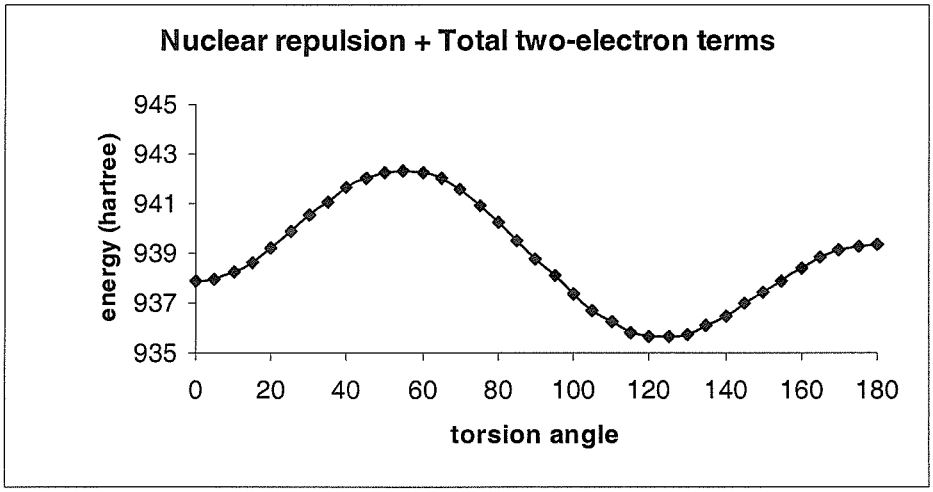
Nuclear repulsion + Total two-electron terms
energy (hartree)
945
943
941
939
937
935
0
20
40
60
80
100
120
140
160
180
torsion angle

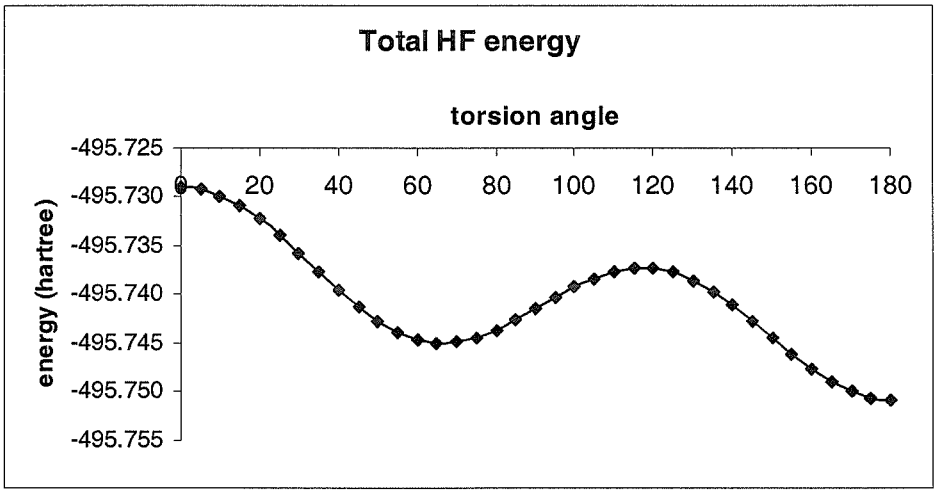
Total HF energy
torsion angle
energy (hartree)
-495.725
-495.730
-495.735
-495.740
-495.745
-495.750
-495.755
0
20
40
60
80
100
120
140
160
180

Figure A.2.2

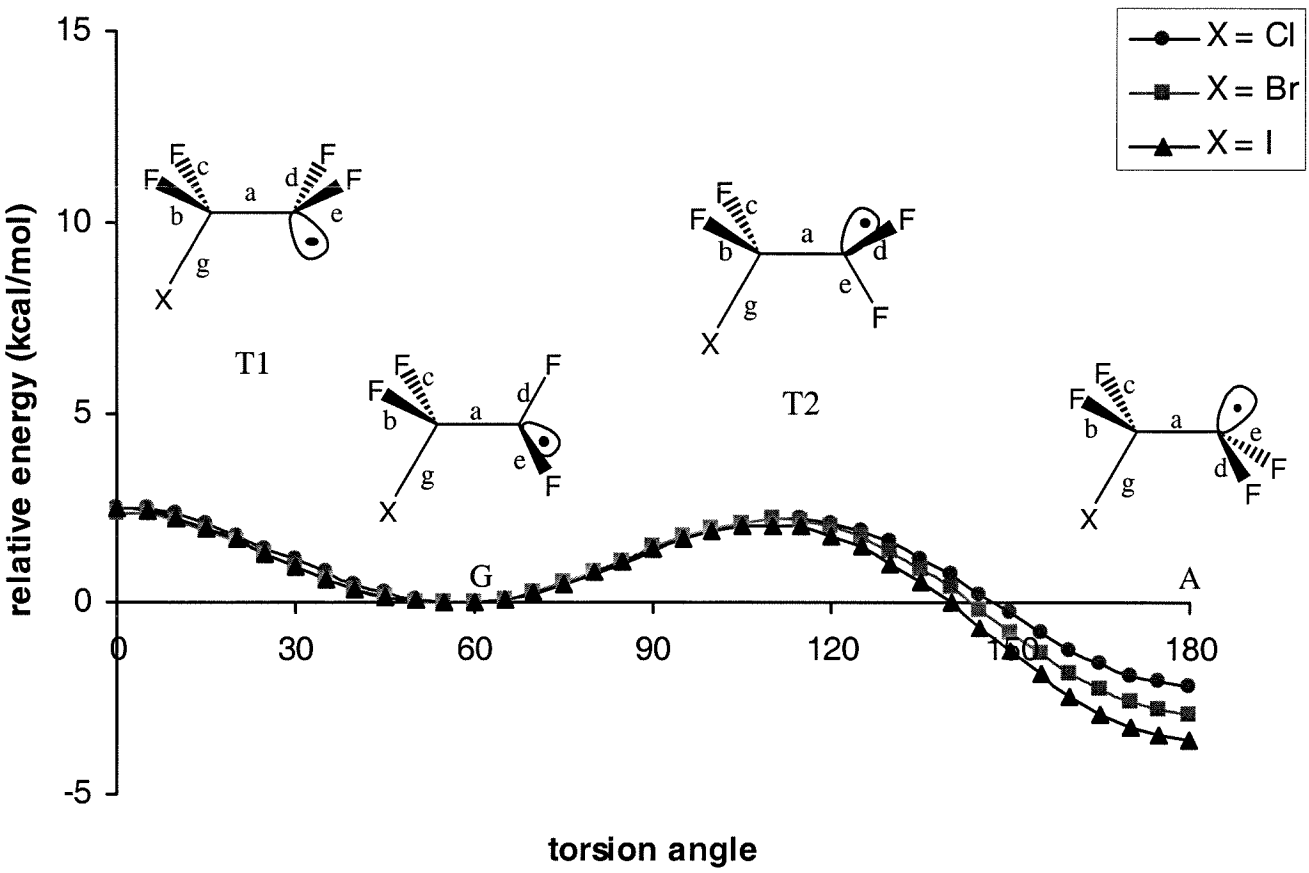
X = Cl
X = Br
X = I
relative energy (kcal/mol)
torsion angle
T1
T2
G
A
15
10
5
0
-5
0
30
60
90
120
150
180

Figure A.2.3.

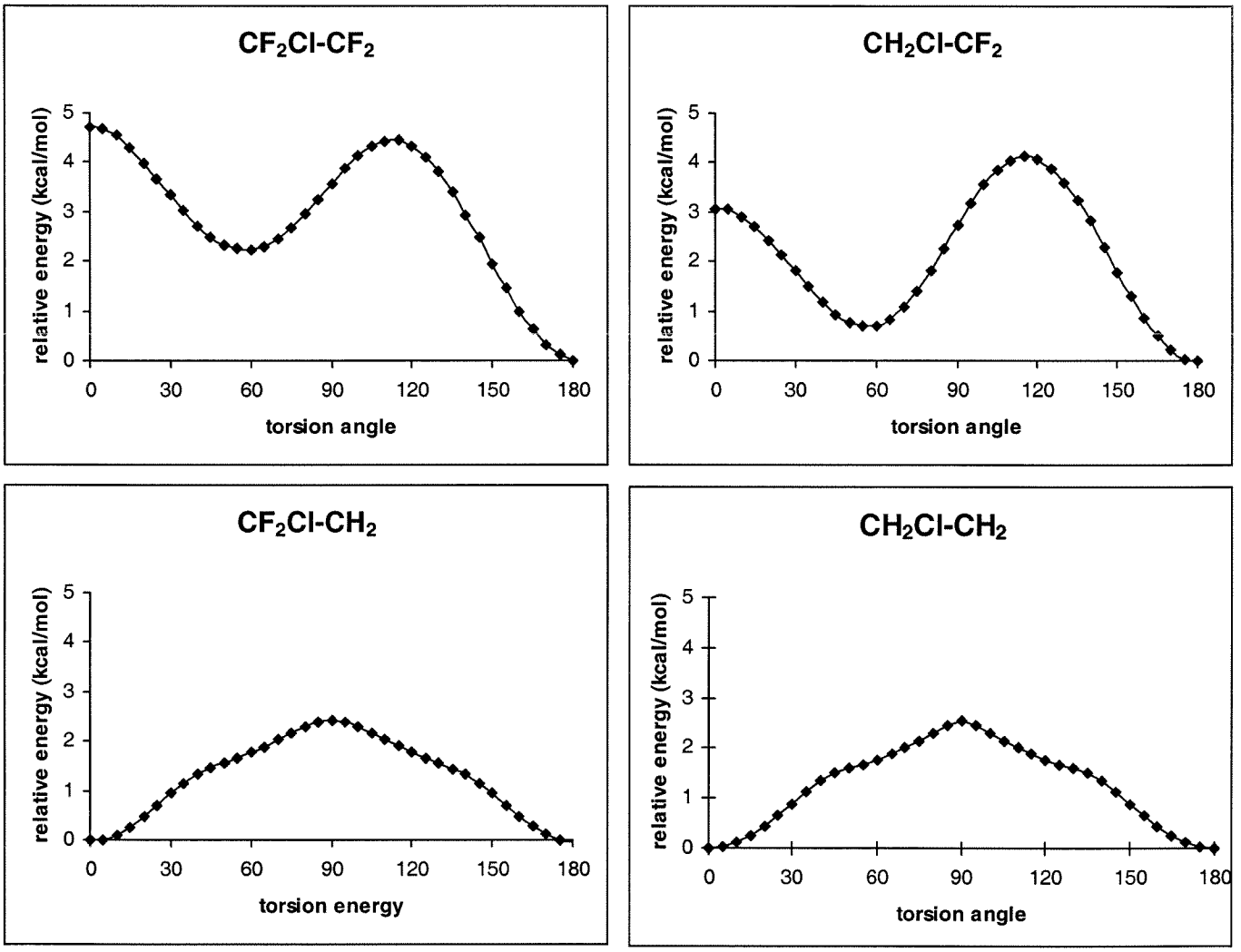
CF2Cl-CF2
relative energy (kcal/mol)
0
1
2
3
4
5
0
30
60
90
120
150
180
torsion angle
CH2Cl-CF2
relative energy (kcal/mol)
0
1
2
3
4
5
0
30
60
90
120
150
180
torsion angle
CF2Cl-CH2
relative energy (kcal/mol)
0
1
2
3
4
5
0
30
60
90
120
150
180
torsion energy
CH2Cl-CH2
relative energy (kcal/mol)
0
1
2
3
4
5
0
30
60
90
120
150
180
torsion angle

Figure A.2.4.

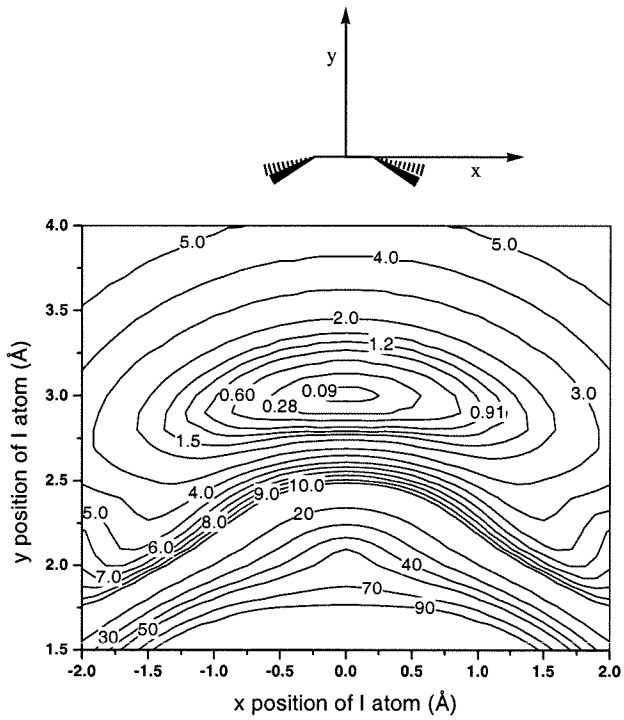

CH_2ICH_2 radical

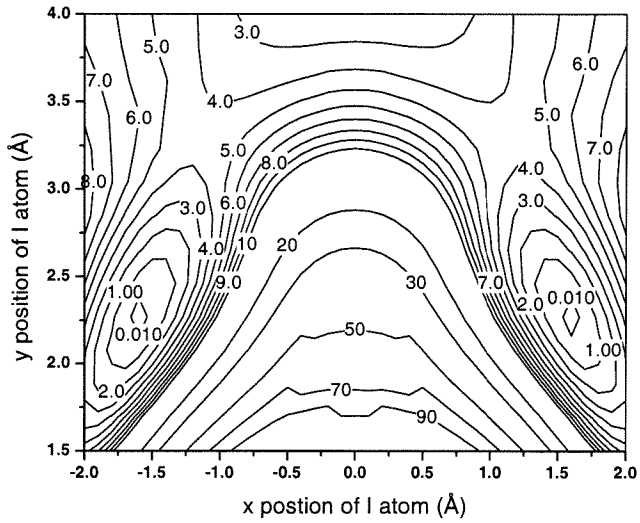

CF_2ICF_2 radical

Figure A.2.5.

Table A.2.1. Selected structural parameters of CF_2XCF_2X (X = I, Br, Cl). The experimental data and the calculated values at various levels of theory (HF and B3PW91) and basis set (LAV3P, LAV3P(d), MSV, and MSV(d)) are presented for comparison. The prefix A- and G-mean anti- and gauche-, respectively. For F...F, X...X, and F...X, only the shortest pairs are listed. We recommend the HF (LAV3P(d)) values for structures.

X=I

	A						
	expt[a]	HF (LAV3P)	**HF (LAV3P(d))**	B3PW91 (LAV3P)	B3PW91 (LAV3P(d))	B3PW91 (MSV)	B3PW91 (MSV(d))
C-C	1.534 (13)	1.531	**1.532**	1.545	1.547	1.529	1.542
C-F	1.328 (3)	1.319	**1.320**	1.333	1.335	1.394	1.336
C-X	2.136 (7)	2.169	**2.159**	2.207	2.187	2.167	2.198
CCF	109.4 (10)	109.0	**109.0**	109.7	109.6	108.4	109.5
CCX	111.6 (10)	112.0	**111.9**	110.4	110.5	113.9	110.6
FCF	107.8 (10)	107.8	**108.7**	109.4	109.3	107.5	109.3
XCCX	180 (fixed)	180.0	**180.0**	180.0	180.0	180.0	180.0
F...F	2.734 (13)	2.708	**2.712**	2.746	2.749	2.784	2.743
X...X	5.054 (7)	5.112	**5.092**	5.161	5.129	5.146	5.146
F...X	3.256 (9)	3.274	**3.267**	3.304	3.293	3.319	3.295
	G						
C-C	1.534 (13)	1.537	**1.540**	1.555	1.556	1.538	1.552
C-F	1.328 (3)	1.321	**1.323**	1.337	1.339	1.395	1.340
C-X	2.136 (7)	2.159	**2.147**	2.193	2.173	2.167	2.186
CCF	109.4 (10)	107.4	**107.6**	108.0	108.2	107.7	107.9
CCX	111.6 (10)	115.0	**114.8**	113.3	113.0	115.6	113.7
FCF	107.8 (10)	108.0	**107.9**	108.5	108.4	107.0	108.5
XCCX	70 (3)	67.3	**67.8**	67.8	68.2	63.8	60.5
F...F	2.62 (3)	2.535	**2.540**	2.744	2.594	2.640	2.645
X...X	3.87 (5)	4.002	**3.987**	3.985	3.952	3.988	3.873
F...X	3.17 (3)	3.307	**3.293**	3.311	3.284	3.377	3.385

a) r_e values estimated from electron diffraction data[23]

X=Br

	A						
	expt[a]	HF (LAV3P)	HF (LAV3P(d))	B3PW91 (LAV3P)	B3PW91 (LAV3P(d))	B3PW91 (MSV)	B3PW91 (MSV(d))
C-C	1.548 (13)	1.531	**1.536**	1.547	1.552	1.529	1.544
C-F	1.332 (3)	1.312	**1.316**	1.329	1.333	1.387	1.335
C-X	1.922 (5)	1.976	**1.944**	2.011	1.972	1.963	1.948
CCF	109.9 (4)	109.5	**109.2**	110.0	109.6	109.0	109.5
CCX	110.5 (5)	110.7	**111.1**	109.6	109.0	112.5	110.0
FCF	108.4 (8)	109.3	**108.9**	109.8	109.4	108.0	109.3
XCCX	180 (fixed)	180.0	**180.0**	180.0	180.0	180.0	180.0
F...F	2.774 (12)	2.707	**2.712**	2.746	2.750	2.784	2.744
X...X	4.631 (8)	4.714	**4.666**	4.749	4.708	4.727	4.655
F...X	3.123 (7)	3.123	**3.108**	3.159	3.139	3.164	3.111
	G						
C-C	1.548 (13)	1.536	**1.540**	1.553	1.556	1.534	1.549
C-F	1.332 (3)	1.315	**1.319**	1.333	1.336	1.388	1.338
C-X	1.922 (5)	1.966	**1.935**	1.997	1.960	1.958	1.936
CCF	109.9 (4)	108.0	**107.9**	108.6	108.3	108.4	108.4
CCX	110.5 (5)	113.4	**113.6**	112.1	112.3	113.7	111.8
FCF	108.4 (8)	108.6	**108.2**	108.9	108.6	107.7	108.6
XCCX	67 (3)	66.0	**65.9**	66.6	66.1	65.4	63.6
F...F	2.71 (3)	2.568	**2.569**	2.620	2.622	2.660	2.644
X...X	3.52 (5)	3.668	**3.639**	3.668	3.628	3.662	3.539
F...X	3.06 (4)	3.147	**3.134**	3.158	3.142	3.173	3.134

a) r_e values estimated from electron diffraction data[23]

X=Cl

	A						
	expt[a]	HF (LAV3P)	HF (LAV3P(d))	B3PW91 (LAV3P)	B3PW91 (LAV3P(d))	B3PW91 (MSV)	B3PW91 (MSV(d))
C-C	1.557 (7)	1.533	**1.538**	1.549	1.555	1.533	1.551
C-F	1.330 (2)	1.310	**1.316**	1.329	1.335	1.379	1.336
C-X	1.747 (3)	1.783	**1.743**	1.817	1.768	1.846	1.770
CCF	108.9 (3)	109.4	**108.9**	109.8	109.2	109.7	109.2
CCX	110.7 (4)	110.3	**111.0**	109.5	110.4	110.7	110.3
FCF	108.7 (3)	109.5	**108.9**	109.8	109.2	108.7	109.1
XCCX	180 (fixed)	180.0	**180.0**	180.0	180.0	180.0	180.0
F...F	2.745 (7)	2.703	**2.708**	2.743	2.747	2.792	2.745
X...X	4.305 (9)	4.342	**4.286**	4.400	4.330	4.470	4.330
F...X	2.994 (6)	2.991	**2.973**	3.029	3.006	3.072	3.003
	G						
C-C	1.557 (7)	1.536	**1.540**	1.552	1.557	1.537	1.553
C-F	1.330 (2)	1.313	**1.318**	1.332	1.337	1.382	1.340
C-X	1.747 (3)	1.776	**1.739**	1.807	1.762	1.838	1.763
CCF	108.9 (3)	108.2	**107.9**	108.7	108.3	109.2	108.4
CCX	110.7 (4)	112.8	**113.1**	111.6	112.1	111.7	111.8
FCF	108.7 (3)	108.9	**108.4**	109.1	108.6	108.2	108.6
XCCX	62.5 (13)	64.6	**64.0**	65.7	64.7	65.4	63.7
F...F	2.695 (13)	2.588	**2.587**	2.640	2.634	2.699	2.645
X...X	3.273 (20)	3.396	**3.361**	3.411	3.370	3.432	3.343
F...X	2.986 (17)	3.017	**3.007**	3.028	3.018	3.057	3.019

b) r_e values estimated from electron diffraction data[30]

Table A.2.2. Selected structural parameters of the anti $CF_2XCF'_2$• (X = I, Br, Cl) radicals. The calculated values at various levels of theory (HF and B3PW91) and basis set (LAV3P, LAV3P(d), MSV, and MSV(d)) are presented. Values from preliminary analysis of recent ultrafast electron diffraction experiment are also given for comparison. We recommend the HF (LAV3P(d)) values for structures.

X = I

	Experiment[a]	HF (LAV3P)	**HF (LAV3P(d))**	B3PW91 (LAV3P)	B3PW91 (LAV3P(d))	B3PW91 (MSV)	B3PW91 (MSV(d))
r(C=C)	1.478 ± 0.049	1.502	**1.503**	1.489	1.492	1.486	1.490
r(C-F)	1.340 ± 0.037	1.320	**1.322**	1.334	1.336	1.394	1.337
r(C-X)	2.153 ± 0.013	2.180	**2.164**	2.266	2.233	2.193	2.229
r(C-F')	1.277 ± 0.027	1.304	**1.304**	1.315	1.316	1.363	1.318
∠CCX	115.0 ± 3.1	113.0	**112.7**	111.3	111.5	115.2	109.8
∠CCF	108.6 ± 6.0	108.5	**108.6**	110.1	109.9	108.4	110.2
∠FCF/2	54.0 ± 5.6	54.4	**54.4**	55.0	54.9	54.2	54.9
∠CCF'	117.9 ± 3.1	114.0	**114.0**	116.1	115.9	116.1	115.3
∠F'CF'/2	59.9 ± 3.9	55.9	**55.9**	56.4	56.4	56.0	56.4

a) r_e values from recent ultrafast electron diffraction data[11,12]

X = Br

	Experiment	HF (LAV3P)	**HF (LAV3P(d))**	B3PW91 (LAV3P)	B3PW91 (LAV3P(d))	B3PW91 (MSV)	B3PW91 (MSV(d))
r(C=C)	Not available	1.502	**1.505**	1.493	1.500	1.486	1.497
r(C-F)		1.315	**1.319**	1.331	1.336	1.388	1.337
r(C-X)		1.989	**1.952**	2.063	2.006	2.001	1.982
r(C-F')		1.303	**1.304**	1.316	1.317	1.361	1.319
∠CCX		111.9	**112.1**	111.0	111.6	113.9	111.3
∠CCF		109.1	**108.8**	110.3	109.7	109.0	109.6
∠FCF/2		54.7	**54.4**	55.1	54.9	54.4	54.8
∠CCF'		113.9	**113.9**	115.8	115.5	116.1	115.2
∠F'CF'/2		54.4	**56.0**	56.4	56.4	56.1	56.4

X = Cl

	Experiment	HF (LAV3P)	**HF (LAV3P(d))**	B3PW91 (LAV3P)	B3PW91 (LAV3P(d))	B3PW91 (MSV)	B3PW91 (MSV(d))
r(C=C)	Not available	1.504	**1.507**	1.501	1.508	1.486	1.504
r(C-F)		1.313	**1.319**	1.331	1.338	1.382	1.339
r(C-X)		1.797	**1.752**	1.856	1.793	1.885	1.795
r(C-F')		1.303	**1.304**	1.318	1.319	1.360	1.320
∠CCX		111.6	**112.2**	111.2	112.3	111.9	112.2
∠CCF		109.3	**108.6**	110.0	109.1	110.0	109.1
∠FCF/2		54.7	**54.4**	53.9	54.7	54.6	54.7
∠CCF'		113.6	**113.6**	115.1	114.9	116.0	114.9
∠F'CF'/2		56.0	**55.9**	56.4	56.2	56.3	56.3

Table A.2.3. The relative energies calculated at various levels of theory (HF and B3PW91) and basis sets (LAV3P, LAV3P(d), MSV, and MSV(d)) for CF_2XCF_2X and CF_2XCF_2• radicals (X = I, Br, Cl). The energies are given in kcal/mol. The prefix A-, G-, T- and B- mean anti-, gauche-, transition state, and bridged structure, respectively. For energies, we recommend the LMP2//HF (LAV3P(d)) values.

CF_2XCF_2X

Method	A-CF_2ICF_2I	G-CF_2ICF_2I	T1-CF_2ICF_2I	T2-CF_2ICF_2I
HF (LAV3P)	-3.59	0	10.09	4.90
HF (LAV3P(d))	-2.97	0	10.01	5.16
LMP2//HF (LAV3P)	-2.17	0	9.42	5.28
LMP2//HF (LAV3P(d))	**-1.90**	**0**	**8.96**	**4.83**
B3PW91 (LAV3P)	-3.16	0	7.41	3.36
B3PW91 (LAV3P(d))	-3.13	0	6.74	2.88
B3PW91 (MSV)	-3.70	0	7.90	3.19
B3PW91 (MSV(d))	-2.98	0	7.24	3.23
Expt[a]	-1.835 ± 0.10	0		
Expt[b]	-1.22 ± 0.36	0		
Method	A-CF_2BrCF_2Br	G-CF_2BrCF_2Br	T1-CF_2BrCF_2Br	T2-CF_2BrCF_2Br
HF (LAV3P)	-2.27	0	9.17	5.37
HF (LAV3P(d))	-1.52	0	8.99	5.82
LMP2//HF (LAV3P)	-1.06	0	8.13	5.49
LMP2//HF (LAV3P(d))	**-1.05**	**0**	**7.82**	**5.12**
B3PW91 (LAV3P)	-1.62	0	7.01	4.26
B3PW91 (LAV3P(d))	-1.12	0	6.60	4.21
B3PW91 (MSV)	-1.79	0	7.28	4.15
B3PW91 (MSV(d))	-1.17	0	6.83	4.50
Expt[c]	-0.925 ± 0.05	0		
Expt[b]	-0.86 ± 0.26	0		
Method	A-CF_2ClCF_2Cl	G-CF_2ClCF_2Cl	T1-CF_2ClCF_2Cl	T2-CF_2ClCF_2Cl
HF (LAV3P)	-1.24	0	8.10	5.96
HF (LAV3P(d))	-0.83	0	8.20	6.35
LMP2//HF (LAV3P)	-0.49	0	6.90	5.40
LMP2//HF (LAV3P(d))	**-0.44**	**0**	**7.28**	**5.75**
B3PW91 (LAV3P)	-0.82	0	6.22	4.39
B3PW91 (LAV3P(d))	-0.37	0	6.10	4.64
B3PW91 (MSV)	-0.91	0	6.69	4.63
B3PW91 (MSV(d))	-0.27	0	6.04	4.76
Expt[d]	-0.5 ± 0.2	0		
Expt[e]	-0.44 ± 0.11	0		
Expt[f]	-0.45 ± 0.11	0		

CF_2XCF_2• radicals

Method	A-CF_2ICF_2	G-CF_2ICF_2	T1-CF_2ICF_2	T2-CF_2ICF_2	B-CF_2ICF_2
HF (LAV3P)	-2.83	0	2.61	2.41	58.85
HF (LAV3P(d))	-2.61	0	2.58	2.52	56.65
LMP2//HF (LAV3P)	-3.55	0	2.44	1.95	34.48
LMP2//HF (LAV3P(d))	**-3.33**	**0**	**2.26**	**1.61**	**31.78**
B3PW91 (LAV3P)	-5.02	0	1.51	1.09	30.10
B3PW91 (LAV3P(d))	-4.62	0	1.50	1.08	27.77
B3PW91 (MSV)	-2.96	0	1.76	0.88	29.61
B3PW91 (MSV(d))	-4.76	0	1.56	1.033	27.06
Method	A-CF_2BrCF_2	G-CF_2BrCF_2	T1-CF_2BrCF_2	T2-CF_2BrCF_2	B-CF_2BrCF_2
HF (LAV3P)	-2.83	0	2.47	2.56	71.30
HF (LAV3P(d))	-2.07	0	2.53	2.76	70.16
LMP2//HF (LAV3P)	-2.90	0	2.33	2.22	44.60
LMP2//HF (LAV3P(d))	**-2.75**	**0**	**2.12**	**1.93**	**41.77**
B3PW91 (LAV3P)	-3.94	0	1.57	1.42	39.37
B3PW91 (LAV3P(d))	-3.22	0	1.69	1.45	38.62
B3PW91 (MSV)	-2.44	0	2.04	1.35	40.89
B3PW91 (MSV(d))	-3.09	0	1.88	1.47	40.02
Method	A-CF_2ClCF_2	G-CF_2ClCF_2	T1-CF_2ClCF_2	T2-CF_2ClCF_2	B-CF_2ClCF_2
HF (LAV3P)	-1.80	0	2.61	2.62	84.14
HF (LAV3P(d))	-1.53	0	2.81	2.75	25.16
LMP2//HF (LAV3P)	-2.07	0	2.55	2.29	59.29
LMP2//HF (LAV3P(d))	**-1.79**	**0**	**2.45**	**2.05**	**31.26**
B3PW91 (LAV3P)	-2.70	0	1.90	1.55	10.64
B3PW91 (LAV3P(d))	-2.05	0	2.23	1.63	18.16
B3PW91 (MSV)	-2.27	0	1.89	1.54	10.83
B3PW91 (MSV(d))	-1.98	0	2.19	1.64	17.34

a) IR spectroscopy[29]
b) Electron diffraction[23]
c) IR spectroscopy[28]
d) IR spectroscopy[27]
e) Electron diffraction[24]
f) Electron diffraction[30]
g) MSV corrected with difference between MSV and MSV(d) for Br

Table A.2.4. The relative energies (in kcal/mol) calculated at various levels of theory (HF and B3PW91) and basis sets (LAV3P and LAV3P(d)) for CH_2XCH_2• radicals (X = I, Br, Cl). The energies are given in kcal/mol. The prefix A- and B- mean anti and bridged structure. The values in the parentheses are the C-X bond distances.

CH_2XCH_2

Method	A-CH_2ICH_2	B-CH_2ICH_2
HF (LAV3P)	12.28 (2.246 Å)	0 (3.894 Å)
B3PW91 (LAV3P)	Converged to bridge	0 (3.079 Å)
B3PW91 (LAV3P(d))	Converged to bridge	0 (3.046 Å)
Method	A-CH_2BrCH_2	B-CH_2BrCH_2
HF (LAV3P)	6.09 (2.062 Å)	0 (3.620 Å)
B3PW91 (LAV3P)	0.99 (2.170 Å)	0 (2.829 Å)
B3PW91 (LAV3P(d))	-1.98 (2.074 Å)	0 (2.774 Å)
Method	A-CH_2ClCH_2	B-CH_2ClCH_2
HF (LAV3P)	-3.00 (1.875 Å)	0 (3.515 Å)
B3PW91 (LAV3P)	-4.63 (1.931 Å)	0 (2.660 Å)
B3PW91 (LAV3P(d))	-10.01 (1.847 Å)	0 (2.633 Å)

Table A.2.5. Dissociation energies from the optimized energies calculated at various levels of theory (HF and B3PW91) and basis sets (LAV3P and LAV3P(d)) for CF_2XCF_2X and CF_2XCF_2• radicals (X = I, Br, Cl). Energies are given in kcal/mol. We recommend B3PW91 with a d function (either LAV3P(d) or MSV(d)).

	Total dissociation energy		
	$CF_2XCF_2X \rightarrow CF_2CF_2 + X + X$		
Method	X = I[a]	X = Br	X = Cl
HF (LAV3P)	11.8	27.5	53.9
HF (LAV3P(d))	21.0	45.2	77.0
LMP2//HF (LAV3P)	46.8	60.0	84.0
LMP2//HF (LAV3P(d))	54.1	76.8	110.7
B3PW91 (LAV3P)	48.0	66.2	91.9
B3PW91 (LAV3P(d))	**55.8**	**80.4**	**110.8**
B3PW91 (MSV)	58.5	74.0	80.6
B3PW91 (MSV(d))	**58.7**	**90.8**	**109.8**
Experiment	$\leq 59.1 \pm 1$[b]		
	First dissociation energy (D_1)		
	$CF_2XCF_2X \rightarrow CF_2XCF_2 + X$		
Method	X = I[c]	X = Br	X = Cl
HF (LAV3P)	19.8	27.4	40.7
HF (LAV3P(d))	24.3	36.2	52.6
LMP2//HF (LAV3P)	51.4	58.1	70.4
LMP2//HF (LAV3P(d))	46.2	57.4	75.2
B3PW91 (LAV3P)	45.8	55.4	69.3
B3PW91 (LAV3P(d))	**50.4**	**63.4**	**79.8**
B3PW91 (MSV)	51.9	59.7	62.6
B3PW91 (MSV(d))	**50.1**	**67.4**	**77.7**
Experiment	52 ± 1.6[d]	67.6 ± 1.6[e]	
	Second dissociation energy (D_2)		
	$CF_2XCF_2 \rightarrow CF_2CF_2 + X$		
Method	X = I[c]	X = Br	X = Cl
HF (LAV3P)	-8.0	0.1	13.1
HF (LAV3P(d))	-3.1	7.9	24.4
LMP2//HF (LAV3P)	-4.6	-1.1	13.5
LMP2//HF (LAV3P(d))	7.9	19.4	35.5
B3PW91 (LAV3P)	2.2	10.8	22.7
B3PW91 (LAV3P(d))	**5.5**	**17.0**	**31.1**
B3PW91 (MSV)	6.6	14.3	17.9
B3PW91 (MSV(d))	**8.6**	**23.5**	**32.2**
Experiment	0[f]	16[f]	
	$\leq 7.1 \pm 2.5$[b]	$\leq 22.3 \pm 2.5$[b]	
	$D_1 - D_2$		
Method	X = I[c]	X = Br	X = Cl
HF (LAV3P)	27.8	27.3	27.1
HF (LAV3P(d))	27.4	28.3	28.2
LMP2//HF (LAV3P)	56.0	56.2	56.9
LMP2//HF (LAV3P(d))	38.3	38.0	39.7
B3PW91 (LAV3P)	43.6	44.6	46.6
B3PW91 (LAV3P(d))	**44.9**	**46.4**	**48.7**

B3PW91 (MSV)	45.3	45.4	44.7
B3PW91 (MSV(d))	**41.5**	**43.9**	**45.5**
Experiment	~45	~45	~45

[a]The calculated bond energy should be decreased by ~16 kcal/mol to reflect the spin-orbit coupling in the case of X = I.

[b]An upper limit obtained by photofragment translational spectroscopy[64].

[c]The calculated bond energy should be decreased by ~8 kcal/mol to reflect the spin-orbit coupling in the case of X = I.

[d]$D_0(CF_3CF_2\text{-}I)$. Direct measured data for $D_0(CF_2ICF_2\text{-}I)$ is not available[64].

[e]$D_0(CF_3CF_2\text{-}Br)$. Direct measured data for $D_0(CF_2BrCF_2\text{-}Br)$ is not available[64].

[f]Estimated values by using the available thermodynamic data[67].

Supporting Information

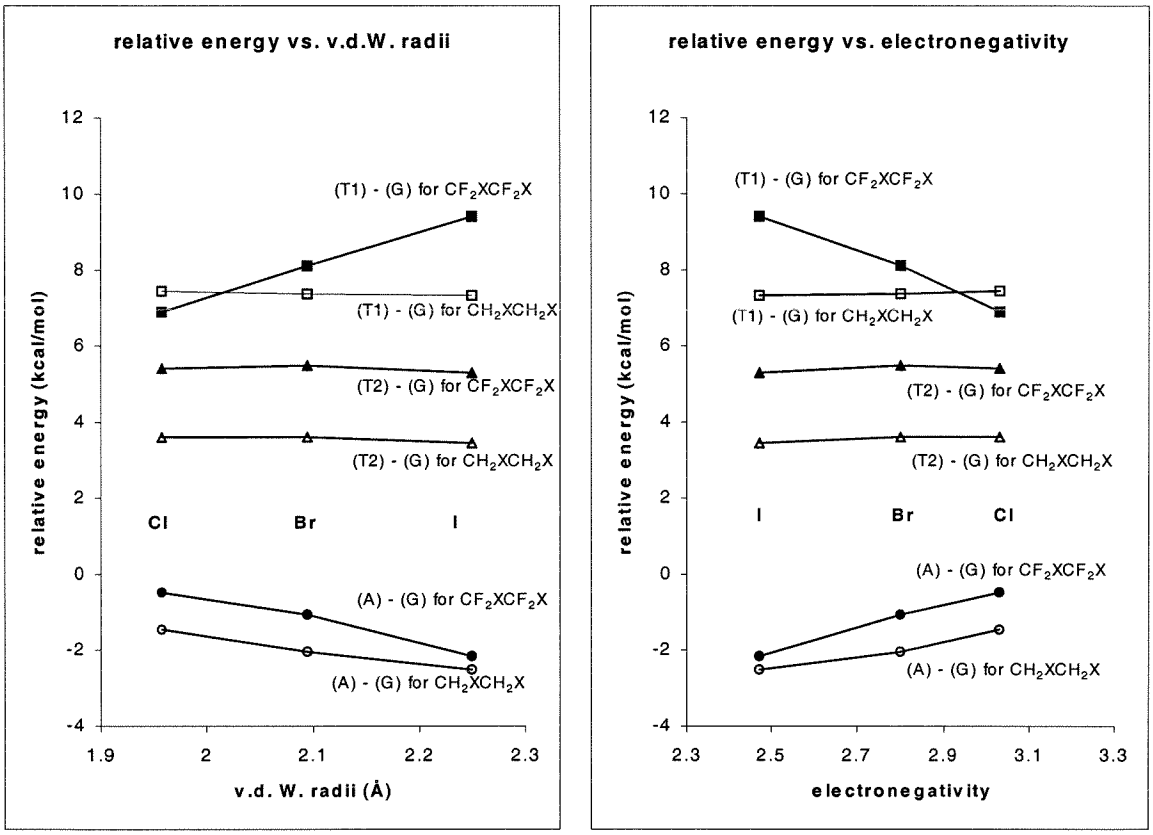

Figure A.2.S1. Correlation between the van der Waalls radii or group electronegativity and the relative energy differences.

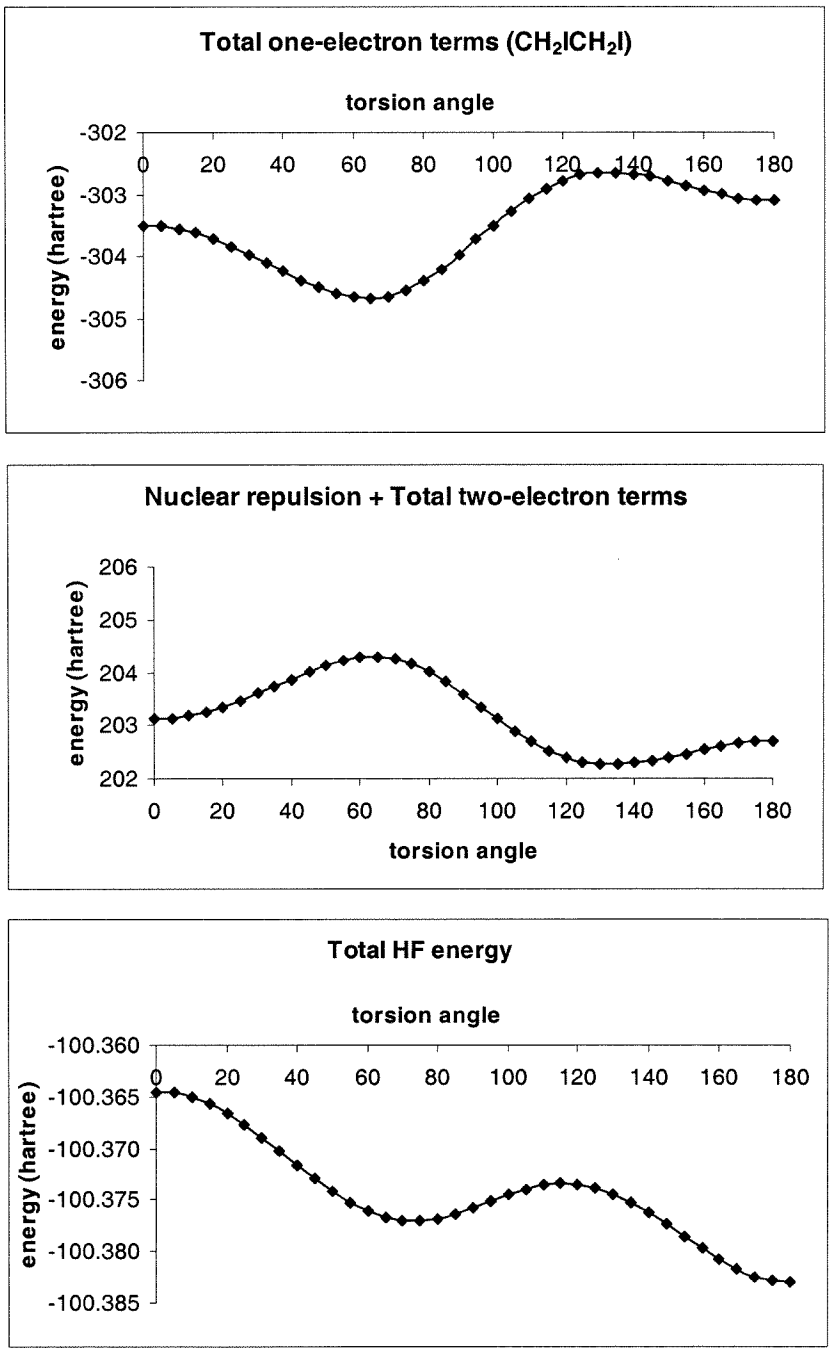

Figure A.2.S2. Energy decomposition for CH_2ICH_2I calculated at HF (LAV3P) level. Total HF energy is sum of the attractive energy (Total one-electron term) and repulsive energy

(Nuclear repulsion + Total two-electron terms). The energy is in hartrees and the angles are in degrees.

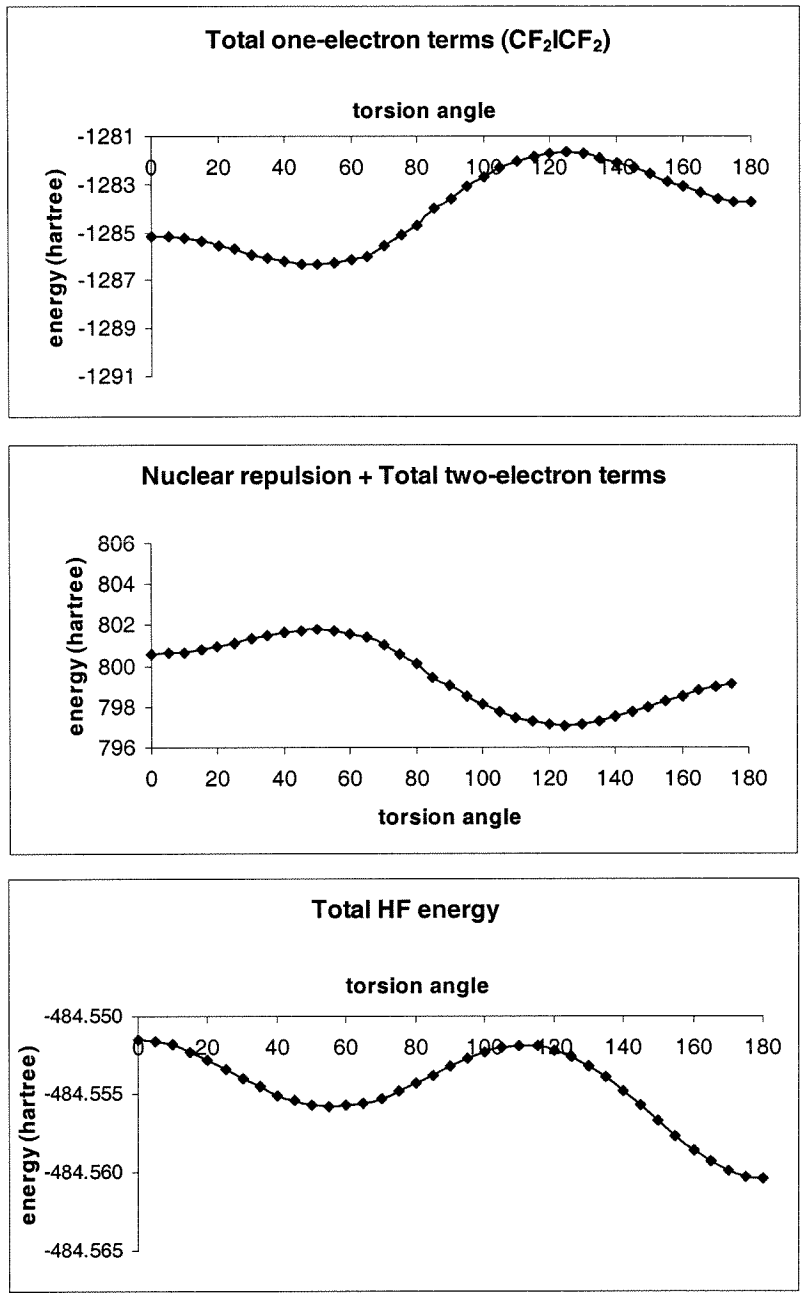

Figure A.2.S3. Energy decomposition for CF_2ICF_2 calculated at HF (LAV3P) level. Total HF energy is sum of the attractive energy (Total one-electron term) and repulsive energy (Nuclear repulsion + Total two-electron terms). The energy is in hartrees and the angles are in degrees.

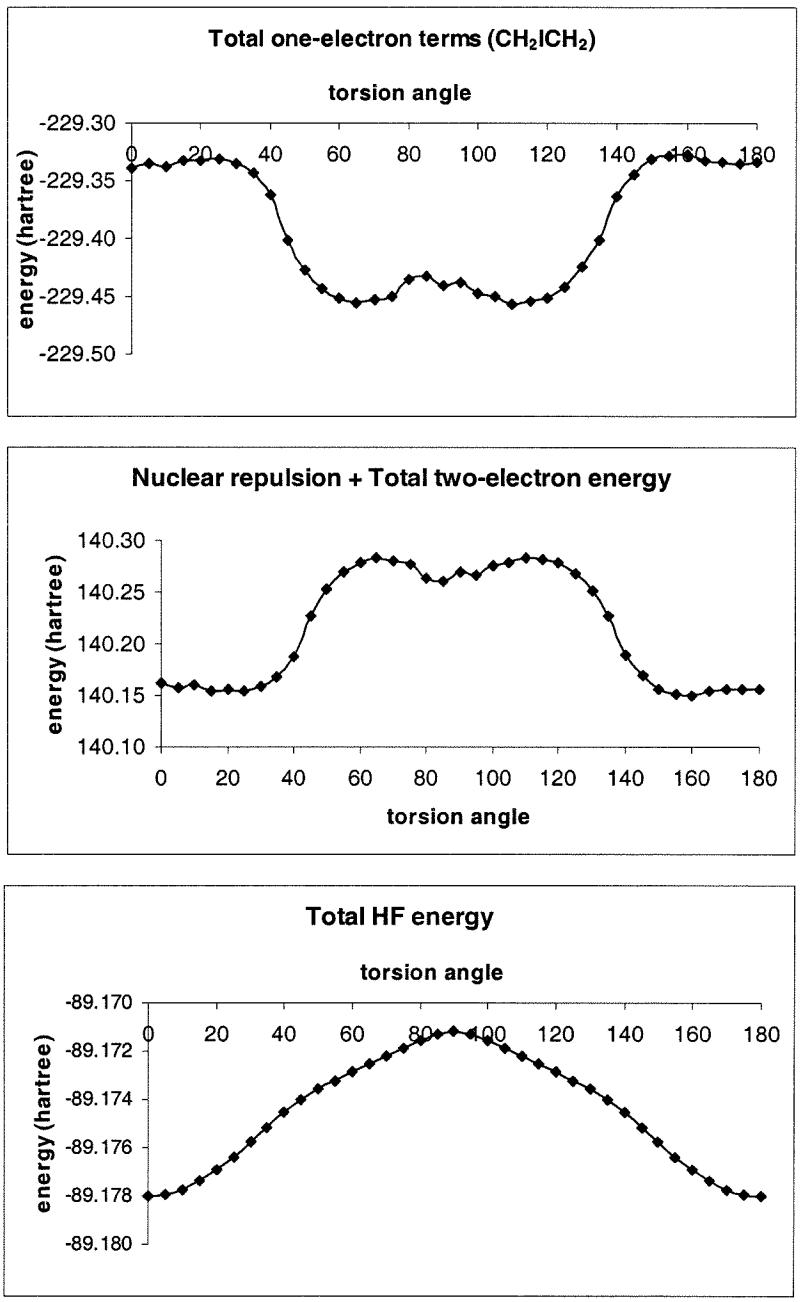

Figure A.2.S4. Energy decomposition for CH_2ICH_2 calculated at HF (LAV3P) level. Total HF energy is sum of the attractive energy (Total one-electron term) and repulsive energy (Nuclear repulsion + Total two-electron terms). The energy is in hartrees and the angles are in degrees.

Table A.2.S1a. The structural parameters of the CF_2XCF_2X and CF_2XCF_2• radicals (X = I, Br and Cl) optimized at HF (LAV3P) level of theory. The bond length is given in angstrom and the angle is in degree. The prefix A-, G-, and T- mean anti-, gauche-, and transition state, respectively. *a* corresponds to the C-C bond, *b, c, d* and *e* correspond to C-F bonds, and *f* and *g* corresponds to C-X bonds.

X = I (HF (LAV3P))

	CF_2ICF_2I						CF_2ICF_2•			
	A		G		T1	T2	A	G	T1	T2
	HF	Expt[a]	HF	Expt[a]	HF	HF	HF	HF	HF	HF
a	1.531	1.540 (13)	1.537	1.540 (13)	1.583	1.570	1.502	1.508	1.522	1.524
b	1.319	1.328 (3)	1.323	1.328 (3)	1.321	1.319	1.320	1.326	1.320	1.322
c	1.319		1.319		1.320	1.319	1.320	1.321	1.320	1.326
d	1.319		1.323		1.321	1.319	1.304	1.309	1.306	1.306
e	1.319		1.319		1.320	1.319	1.304	1.307	1.306	1.305
f	2.169	2.139 (7)	2.159	2.139 (7)	2.167	2.170				
g	2.169		2.159		2.167	2.170	2.180	2.162	2.173	2.168
ab	109.0	109.4 (10)	106.2	109.4 (10)	107.3	108.1	108.5	109.6	109.9	109.2
ac	109.0		108.6		107.3	110.8	108.5	108.0	109.9	107.9
ad	109.0		106.2		107.3	108.1	114.0	112.2	113.7	113.2
ae	109.0		108.6		107.3	110.8	114.0	113.8	113.7	116.9
af	112.0	111.6 (10)	115.0	111.6 (10)	119.9	114.2				
ag	112.0		115.0		119.9	114.2	113.0	112.1	110.9	114.6
bc	108.7	107.8 (10)	108.0	107.8 (10)	107.6	107.2	108.8	108.0	108.5	107.4
bg	109.1		108.7		107.1	108.7	108.8	109.5	108.8	109.0
cg	109.1		109.9		107.1	107.8	108.8	109.5	108.8	108.4
de	108.7		108.0		107.6	107.2	111.8	111.3	111.7	110.9
df	109.1		108.7		107.1	108.7				
ef	109.1		109.9		107.1	107.8				
bad	61.5		-52.1		-114.9	0.1	55.9	-65.6	-124.5	-11.3
bae	180.0		63.9		0.5	117.2	-174.0	61.9	4.9	119.4
baf	-59.3		-172.4		122.8	-120.9				
cad	180.0		63.9		0.5	117.2	174.0	51.8	-5.1	105.2
cae	-61.5		179.9		115.9	-125.7	-55.9	179.4	124.3	-124.1
caf	59.3		-56.4		-121.8	-3.8				
gad	-59.3		-172.4		122.8	-120.9	-65.0	172.6	115.2	-133.9
gae	59.3		-56.4		-121.8	-3.8	65.0	-59.9	-115.4	-3.3
gaf	180.0	180 (fixed)	67.3	70 (3)	0.5	118.1				

a) Electron diffraction data[23]

X = Br (HF (LAV3P))

	CF_2BrCF_2Br						CF_2BrCF_2•			
	A		G		T1	T2	A	G	T1	T2
	HF	Expt[a]	HF	Expt[a]	HF	HF	HF	HF	HF	HF
a	1.531	1.557 (13)	1.536	1.557 (13)	1.578	1.570	1.502	1.508	1.521	1.524
b	1.312	1.334 (3)	1.317	1.334 (3)	1.315	1.314	1.315	1.320	1.314	1.316
c	1.312		1.313		1.315	1.312	1.315	1.316	1.314	1.321
d	1.312		1.317		1.315	1.314	1.303	1.308	1.305	1.305
e	1.312		1.313		1.315	1.312	1.303	1.305	1.305	1.302
f	1.976	1.925 (5)	1.966	1.925 (5)	1.970	1.975				
g	1.976		1.966		1.970	1.975	1.989	1.973	1.985	1.976
ab	109.5	109.9 (4)	106.8	109.9 (4)	107.8	108.2	109.1	110.4	110.5	109.8
ac	109.5		109.3		107.8	111.4	109.1	108,7	110.5	108.5
ad	109.5		106.8		107.8	108.2	113.9	112.0	113.5	112.9
ae	109.5		109.3		107.8	111.4	113.9	113.8	113.6	116.9
af	110.7	110.5 (5)	113.4	110.5 (5)	117.8	112.9				
ag	110.7		113.4		117.8	112.9	111.9	110.8	109.8	113.4
bc	109.3	108.4 (8)	108.6	108.4 (8)	108.2	107.8	109.3	108.5	109.0	107.9
bg	109.0		108.8		107.5	108.5	108.7	109.1	108.5	108.8
cg	109.0		109.8		107.5	108.0	108.7	109.3	108.5	108.3
de	109.3		108.6		108.2	108.0	108.7	111.5	111.8	111.1
df	109.0		108.8		107.5	108.0				
ef	109.0		109.8		107.5	108.5				
bad	60.2		-54.3		-116.5	-1.2	55.3	-66.9	-125.0	-11.3
bae	180.0		63.0		0.0	117.2	-174.6	60.7	4.2	119.3
baf	-59.9		-174.1		121.8	-121.2				
cad	180.0		63.0		0.0	117.2	174.6	52.1	-4.3	106.4
cae	-60.2		179.7		116.5	-124.5	-55.3	179.6	124.9	-122.9
caf	59.9		-56.8		-121.7	-2.8				
gad	-59.9		-174.1		121.8	-121.2	-65.1	172.2	115.4	-133.3
gae	59.9		-56.8		-121.7	-2.8	65.1	-60.3	-115.4	-2.6
gaf	180.0	180 (fixed)	66.0	67 (3)	0.0	118.8				

a) Electron diffraction data[23]

X = Cl (HF (LAV3P))

	CF_2ClCF_2Cl						CF_2ClCF_2•			
	A		G		T1	T2	A	G	T1	T2
	HF	Expt[b]	HF	Expt[b]	HF	HF	HF	HF	HF	HF
a	1.533	1.563 (7)	1.536	1.563 (7)	1.576	1.572	1.504	1.508	1.523	1.525
b	1.310	1.331 (2)	1.314	1.331 (2)	1.313	1.312	1.313	1.318	1.313	1.314
c	1.310		1.311		1.313	1.310	1.313	1.314	1.313	1.319
d	1.310		1.314		1.313	1.312	1.303	1.307	1.305	1.305
e	1.310		1.311		1.313	1.310	1.303	1.304	1.305	1.302
f	1.783	1.748 (3)	1.776	1.748 (3)	1.777	1.782				
g	1.783		1.776		1.777	1.782	1.797	1.783	1.793	1.786
ab	109.4	108.9 (3)	107.1	108.9 (3)	108.1	108.3	109.3	110.6	110.6	110.0
ac	109.4		109.3		108.1	111.2	109.3	108.8	110.5	108.7
ad	109.4		107.1		108.1	108.3	113.6	111.9	113.5	112.9
ae	109.4		109.3		108.1	111.2	113.6	113.7	113.5	116.5
af	110.3	110.7 (4)	112.8	110.7 (4)	116.2	112.3				
ag	110.3		112.8		116.2	112.4	111.6	110.8	110.0	113.0
bc	109.5	108.7 (3)	108.9	108.7 (3)	108.4	108.2	109.3	108.6	109.0	108.1
bg	109.1		109.0		108.0	108.4	108.6	108.9	108.3	108.8
cg	109.1		109.7		108.0	108.2	108.6	109.2	108.3	108.2
de	109.5		108.9		108.4	108.2	112.0	111.6	111.8	111.3
df	109.1		109.0		108.0	108.4				
ef	109.1		109.7		108.0	108.2				
bad	60.0		-55.7		-117.2	-0.8	55.4	-65.9	-125.1	-9.6
bae	180.0		62.1		-0.1	118.0	-175.0	61.7	4.0	121.1
baf	-60.0		-175.5		121.4	-120.6				
cad	180.0		62.1		-0.1	118.0	175.0	53.3	-4.3	108.5
cae	-60.0		180.0		117.0	-123.2	-55.4	-179.1	124.8	-120.8
caf	60.0		-57.7		-121.5	-1.8				
gad	-60.0		-175.5		121.4	-120.6	-64.8	173.3	115.3	-131.3
gae	60.0		-57.7		-121.5	-1.8	64.8	-59.1	-115.6	-0.7
gaf	180.0	180 (fixed)	64.6	62.5 (13)	-0.1	119.7				

b) Electron diffraction data[30]

Table A.2.S1b. The structural parameters of the CF_2XCF_2X and CF_2XCF_2• radicals (X = I, Br and Cl) optimized at HF (LAV3P) level of theory. The bond length is given in angstrom and the angle is in degree. The prefix A-, G-, and T- mean anti-, gauche-, and transition state, respectively. *a* corresponds to the C-C bond, *b, c, d* and *e* correspond to C-F bonds, and *f* and *g* corresponds to C-X bonds.

X = I (HF (LAV3P(d)))

	CF_2ICF_2I				CF_2ICF_2•			
	A	G	T1	T2	A	G	T1	T2
a	1.532	1.540	1.584	1.573	1.503	1.508	1.523	1.525
b	1.320	1.324	1.322	1.320	1.322	1.327	1.321	1.323
c	1.320	1.321	1.322	1.321	1.322	1.323	1.321	1.328
d	1.320	1.324	1.322	1.320	1.304	1.309	1.307	1.306
e	1.320	1.321	1.322	1.321	1.304	1.307	1.307	1.305
f	2.159	2.147	2.153	2.157				
g	2.159	2.147	2.153	2.157	2.164	2.149	2.159	2.154
ab	109.0	106.4	107.3	108.0	108.6	109.8	110.0	109.3
ac	109.0	108.7	107.3	110.7	108.6	108.1	110.0	107.9
ad	109.0	106.4	107.3	108.0	114.0	112.3	113.7	113.1
ae	109.0	108.7	107.3	110.7	114.0	113.8	113.7	117.0
af	111.9	114.8	119.7	114.2				
ag	111.9	114.8	119.7	114.2	112.7	111.8	110.6	114.5
bc	108.7	107.9	107.5	107.1	108.7	108.0	108.4	107.3
bg	109.1	110.1	107.3	108.6	109.1	109.6	109.0	109.1
cg	109.1	108.7	107.2	107.9	109.1	109.6	109.0	108.5
de	108.7	107.9	107.5	107.1	111.8	111.2	111.7	110.8
df	109.1	108.7	107.3	108.6				
ef	109.1	110.1	107.2	107.2				
bad	61.5	-51.6	-115.3	-0.4	56.0	-66.1	-124.2	-11.1
bae	180.0	64.3	0.0	116.5	-174.0	61.4	5.0	119.5
baf	-59.3	-171.9	122.3	-121.4				
cad	180.0	64.3	0.0	116.5	174.0	51.4	-5.0	105.3
cae	-61.5	-179.7	115.4	-126.6	-56.0	178.9	124.3	-124.1
caf	59.3	-56.0	-122.3	-4.5				
gad	-59.3	-171.9	122.4	-121.4	-65.0	172.1	115.4	-133.7
gae	59.3	-56.0	-122.3	-4.5	65.0	-60.4	-115.3	-3.1
gaf	180.0	67.8	0.0	117.6				

X = Br (HF (LAV3P(d)))

	CF_2BrCF_2Br				CF_2BrCF_2•			
	A	G	T1	T2	A	G	T1	T2
a	1.536	1.540	1.583	1.576	1.505	1.509	1.524	1.527
b	1.316	1.321	1.318	1.317	1.319	1.323	1.318	1.320
c	1.316	1.316	1.318	1.316	1.319	1.319	1.318	1.324
d	1.316	1.321	1.318	1.317	1.304	1.309	1.306	1.306
e	1.316	1.316	1.318	1.316	1.304	1.306	1.306	1.303
f	1.944	1.935	1.939	1.943				
g	1.944	1.935	1.939	1.943	1.952	1.940	1.949	1.943
ab	109.2	106.7	107.6	108.0	108.8	110.2	110.2	109.5
ac	109.2	109.0	107.6	111.1	108.8	108.5	110.2	108.2
ad	109.2	106.7	107.6	108.0	113.9	112.1	113.6	113.0
ae	109.2	109.0	107.6	111.1	113.9	113.8	113.6	116.9
af	111.1	113.6	117.6	113.1				
ag	111.1	113.6	117.6	113.1	112.1	111.0	110.1	113.6
bc	108.9	108.2	107.8	107.4	108.8	108.1	108.5	107.5
bg	109.2	109.0	107.9	108.8	109.1	109.4	108.9	109.2
cg	109.2	110.1	107.9	108.2	109.1	109.6	108.9	108.6
de	108.9	108.2	107.8	107.4	112.0	111.4	111.7	111.0
df	109.2	109.0	107.9	108.8				
ef	109.2	110.1	107.9	108.2				
bad	61.1	-53.8	-115.9	0.4	55.8	-66.5	-124.4	-9.6
bae	180.0	62.9	0.0	118.0	-174.2	61.0	4.6	121.2
baf	-59.5	-173.9	122.0	-120.0				
cad	180.0	62.9	0.0	118.0	174.2	51.7	-4.8	107.4
cae	-61.1	179.6	116.0	-124.4	-55.8	179.2	124.3	-121.9
caf	59.5	-57.2	-122.0	-2.4				
gad	-59.5	-173.9	122.0	-120.0	-65.0	172.1	115.5	-131.9
gae	59.5	-57.2	-122.0	-2.4	65.0	-60.4	-115.5	-1.2
gaf	180.0	65.9	0.0	119.5				

X = Cl (HF (LAV3P(d)))

	CF_2ClCF_2Cl				CF_2ClCF_2•			
	A	G	T1	T2	A	G	T1	T2
a	1.538	1.540	1.581	1.577	1.507	1.510	1.526	1.528
b	1.316	1.319	1.317	1.317	1.319	1.324	1.319	1.320
c	1.316	1.316	1.318	1.316	1.319	1.319	1.319	1.324
d	1.316	1.319	1.317	1.317	1.304	1.307	1.306	1.306
e	1.316	1.316	1.318	1.316	1.304	1.306	1.306	1.304
f	1.743	1.739	1.741	1.743				
g	1.743	1.739	1.741	1.743	1.752	1.744	1.751	1.745
ab	108.9	106.9	107.8	108.1	108.6	110.0	110.0	109.5
ac	108.9	108.8	107.8	110.7	108.6	108.3	110.0	108.2
ad	108.9	106.9	107.8	108.1	113.6	112.1	113.6	113.2
ae	108.9	108.8	107.8	110.7	113.6	113.7	113.6	116.4
af	111.0	113.1	116.2	112.7				
ag	111.0	113.1	116.2	112.7	112.2	111.2	110.6	113.3
bc	108.9	108.4	107.9	107.6	108.7	108.0	108.4	107.5
bg	109.5	109.4	108.4	109.0	109.3	109.4	108.9	109.3
cg	109.5	110.1	108.5	108.6	109.3	109.7	108.9	108.8
de	108.9	108.4	107.8	107.6	111.8	111.5	111.6	111.1
df	109.5	109.4	108.5	109.0				
ef	109.5	110.1	108.5	108.6				
bad	61.4	-55.1	-116.3	1.3	56.3	-64.7	-124.4	-7.8
bae	180.0	61.8	-0.1	118.8	-174.4	62.9	4.6	122.8
baf	-59.3	-175.6	121.8	-119.3				
cad	180.0	61.8	-0.1	118.9	174.4	53.2	-5.1	109.1
cae	-61.4	178.6	116.1	-123.6	-56.3	179.2	123.9	-120.3
caf	59.3	-58.7	-121.9	-1.7				
gad	-59.3	-175.6	121.8	-119.3	-64.6	173.9	115.3	-130.1
gae	59.3	-58.7	-122.0	-1.7	64.6	-58.6	-115.7	0.4
gaf	180.0	64.0	0.0	120.2				

Table A.2.S1c. The structural parameters of the CF_2XCF_2X and CF_2XCF_2• radicals (X = I, Br and Cl) optimized at B3PW91 (LAV3P) level of theory. The bond length is given in angstrom and the angle is in degree. The prefix A-, G-, and T- mean anti-, gauche-, and transition state, respectively. *a* corresponds to the C-C bond, *b, c, d* and *e* correspond to C-F bonds, and *f* and *g* corresponds to C-X bonds.

X = I (B3PW91 (LAV3P))

	CF_2ICF_2I						CF_2ICF_2•			
	A		G		T1	T2	A	G	T1	T2
	HF	Expt[a]	HF	Expt[a]	HF	HF	HF	HF	HF	HF
a	1.545	1.540 (13)	1.555	1.540 (13)	1.604	1.589	1.489	1.510	1.512	1.523
b	1.333	1.328 (3)	1.340	1.328 (3)	1.336	1.335	1.334	1.347	1.337	1.342
c	1.333		1.334		1.336	1.333	1.334	1.337	1.337	1.343
d	1.333		1.340		1.336	1.333	1.315	1.322	1.323	1.323
e	1.333		1.334		1.336	1.333	1.315	1.326	1.323	1.318
f	2.207	2.139 (7)	2.193	2.139 (7)	2.197	2.204				
g	2.207		2.193		2.197	2.204	2.266	2.201	2.226	2.208
ab	109.7	109.4 (10)	106.7	109.4 (10)	107.2	108.0	110.1	111.5	110.8	19.9
ac	109.7		109.4		107.2	111.5	110.1	108.5	110.8	108.9
ad	109.7		106.7		107.2	108.0	116.1	113.3	114.8	113.3
ae	109.7		109.4		107.2	111.5	116.1	115.2	114.8	118.5
af	110.4	111.6 (10)	113.3	111.6 (10)	118.8	112.9				
ag	110.4		113.3		118.8	112.9	111.3	110.2	109.8	113.1
bc	109.4	107.8 (10)	108.5	107.8 (10)	108.3	107.9	110.0	108.2	109.5	107.5
bg	108.8		108.9		107.5	108.7	107.6	108.9	108.0	109.3
cg	108.8		109.9		107.5	107.7	107.6	109.4	108.0	108.0
de	109.4		108.5		108.3	107.9	112.8	111.8	112.7	111.5
df	108.8		108.9		107.5	108.7				
ef	108.8		109.9		107.5	107.7				
bad	59.8		-52.5		-116.1	-0.4	51.2	-68.7	-127.8	-21.6
bae	180.0		64.6		0.0	118.0	-172.7	61.7	5.3	111.9
baf	-60.1		-172.3		122.0	-120.5				
cad	180.0		64.6		0.0	118.0	172.7	50.3	-6.0	95.9
cae	-59.8		-178.2		116.1	-123.6	-51.2	-179.2	127.1	-130.7
caf	60.1		-55.2		-121.9	-2.2				
gad	-60.1		-172.3		122.0	-120.5	-68.0	170.1	113.1	-144.0
gae	60.1		-55.2		-121.9	-2.2	68.0	-59.4	-113.8	-10.5
gaf	180.0	180 (fixed)	67.8	70 (3)	0.0	119.3				

a) Electron diffraction data[23]

X = Br (B3PW91 (LAV3P))

	CF_2BrCF_2Br						CF_2BrCF_2•			
	A		G		T1	T2	A	G	T1	T2
	HF	Expt[a]	HF	Expt[a]	HF	HF	HF	HF	HF	HF
a	1.547	1.557 (13)	1.553	1.557 (13)	1.598	1.589	1.493	1.510	1.513	1.523
b	1.329	1.334 (3)	1.335	1.334 (3)	1.332	1.331	1.331	1.342	1.333	1.337
c	1.329		1.330		1.332	1.327	1.331	1.333	1.333	1.339
d	1.329		1.335		1.332	1.331	1.316	1.326	1.322	1.323
e	1.329		1.330		1.332	1.327	1.316	1.321	1.322	1.317
f	2.011	1.925 (5)	1.997	1.925 (5)	1.999	2.007				
g	2.011		1.997		1.999	2.007	2.063	2.009	2.031	2.013
ab	110.0	109.9 (4)	107.3	109.9 (4)	107.7	108.2	110.3	112.1	111.1	110.3
ac	110.0		109.9		107.7	111.9	110.3	109.0	111.1	109.4
ad	110.0		107.3		107.7	108.2	115.8	113.2	114.7	113.1
ae	110.0		109.9		107.7	111.9	115.8	115.2	114.8	118.4
af	109.6	110.5 (5)	112.1	110.5 (5)	116.9	111.8				
ag	109.6		112.1		116.9	111.8	111.0	109.5	109.2	112.2
bc	109.8	108.4 (8)	108.9	108.4 (8)	108.7	108.4	110.2	108.5	109.8	107.8
bg	108.7		108.9		107.8	108.5	107.5	108.5	107.8	109.1
cg	108.7		109.8		107.8	107.9	107.5	109.3	107.8	107.9
de	109.8		108.9		108.7	108.4	112.8	112.0	112.8	111.7
df	108.7		108.9		107.8	108.5				
ef	108.7		109.8		107.8	107.9				
bad	58.9		-54.5		-117.0	-1.0	51.3	-69.5	-128.4	-19.7
bae	180.0		63.8		0.1	118.4	-173.2	61.2	4.5	113.8
baf	-60.5		-173.9		121.6	-120.4				
cad	180.0		63.8		0.1	118.4	173.2	50.5	-5.9	98.8
cae	-58.9		-178.0		117.2	-122.3	-51.3	-178.4	127.1	-127.7
caf	60.5		-55.7		-121.3	-1.0				
gad	-60.5		-173.9		121.6	-120.4	-67.7	170.0	112.8	-141.5
gae	60.5		-55.7		-121.3	-1.0	67.7	-59.3	-114.2	-8.0
gaf	180.0	180 (fixed)	66.6	67 (3)	0.1	120.2				

a) Electron diffraction data[23]

X = Cl (B3PW91 (LAV3P))

	CF_2ClCF_2Cl						CF_2ClCF_2•			
	A		G		T1	T2	A	G	T1	T2
	HF	Expt[b]	HF	Expt[b]	HF	HF	HF	HF	HF	HF
a	1.549	1.563 (7)	1.552	1.563 (7)	1.594	1.590	1.501	1.512	1.519	1.525
b	1.329	1.331 (2)	1.334	1.331 (2)	1.331	1.331	1.331	1.342	1.333	1.336
c	1.329		1.329		1.331	1.327	1.331	1.333	1.333	1.338
d	1.329		1.334		1.331	1.331	1.318	1.324	1.322	1.322
e	1.329		1.329		1.331	1.327	1.318	1.320	1.322	1.317
f	1.817	1.748 (3)	1.807	1.748 (3)	1.807	1.814				
g	1.817		1.807		1.807	1.814	1.856	1.818	1.834	1.822
ab	109.8	108.9 (3)	107.6	108.9 (3)	108.1	108.3	110.0	112.0	110.9	110.4
ac	109.8		109.8		108.1	111.6	110.0	109.0	111.0	109.6
ad	109.8		107.6		108.1	108.3	115.1	113.2	114.5	113.4
ae	109.8		109.8		108.1	111.6	115.1	115.1	114.5	117.8
af	109.5	110.7 (4)	111.6	110.7 (4)	115.5	111.4				
ag	109.5		111.6		115.5	111.4	111.2	109.7	109.6	111.9
bc	109.8	108.7 (3)	109.1	108.7 (3)	108.8	108.7	110.0	108.4	109.6	108.0
bg	108.9		108.9		108.1	108.5	107.8	108.4	107.9	109.0
cg	108.9		109.6		108.1	108.3	107.8	109.3	107.9	107.9
de	109.8		109.1		108.8	108.7	112.7	112.1	112.6	111.9
df	108.9		108.9		108.1	108.5				
ef	108.9		109.6		108.1	108.3				
bad	59.1		-55.4		-117.5	-1.0	52.5	-66.7	-127.7	-16.0
bae	180.0		63.3		0.0	118.6	-173.8	64.0	4.5	117.5
baf	-60.4		-174.8		121.3	-120.2				
cad	180.0		63.3		0.0	118.6	173.8	53.2	-5.6	102.8
cae	-59.1		-178.0		117.6	-121.8	-52.5	-176.0	126.5	-123.7
caf	60.4		-56.2		-121.2	-0.6				
gad	-60.4		-174.8		121.3	-120.2	-66.8	172.9	113.3	-137.6
gae	60.4		-56.2		-121.2	-0.6	66.8	-56.4	-114.5	-4.0
gaf	180.0	180 (fixed)	65.7	62.5 (13)	0.0	120.5				

b) Electron diffraction data[30]

Table A.2.S1d. The structural parameters of the CF_2XCF_2X and CF_2XCF_2• radicals (X = I, Br and Cl) optimized at B3PW91 (LAV3P(d)) level of theory. The bond length is given in angstrom and the angle is in degree. The prefix A-, G-, and T- mean anti-, gauche-, and transition state, respectively. *a* corresponds to the C-C bond, *b, c, d* and *e* correspond to C-F bonds, and *f* and *g* corresponds to C-X bonds.

X = I (B3PW91 (LAV3P(d))

	CF_2ICF_2I				CF_2ICF_2•			
	A	G	T1	T2	A	G	T1	T2
a	1.547	1.555	1.604	1.589	1.492	1.510	1.514	1.523
b	1.335	1.341	1.338	1.337	1.336	1.348	1.339	1.343
c	1.335	1.336	1.338	1.335	1.336	1.338	1.339	1.345
d	1.335	1.341	1.338	1.335	1.316	1.326	1.323	1.324
e	1.335	1.336	1.338	1.337	1.316	1.322	1.323	1.319
f	2.187	2.173	2.176	2.183				
g	2.187	2.173	2.176	2.183	2.233	2.180	2.198	2.185
ab	109.6	107.0	107.4	108.1	109.9	111.6	110.8	109.9
ac	109.6	109.4	107.4	111.3	109.8	108.5	110.8	109.0
ad	109.6	107.0	107.4	111.3	115.9	113.4	114.8	113.3
ae	109.6	109.4	107.4	108.1	115.9	115.2	114.8	118.3
af	110.6	113.0	118.3	112.8				
ag	110.6	113.0	118.3	112.8	111.5	110.1	109.5	112.9
bc	109.3	108.4	108.2	107.8	109.8	108.1	109.4	107.4
bg	108.8	110.0	107.6	108.8	107.8	109.0	108.2	109.3
cg	108.8	109.0	107.6	108.0	107.8	109.4	108.2	108.1
de	109.3	108.4	108.2	107.8	112.8	111.8	112.6	111.5
df	108.8	109.0	107.6	108.0				
ef	108.8	110.0	107.6	108.8				
bad	60.0	-52.0	-116.0	-1.5	51.8	-69.1	-127.5	-21.0
bae	180.0	65.2	0.2	116.7	-172.7	61.5	5.3	112.2
baf	-60.0	-171.9	112.1	-121.8				
cad	180.0	65.2	0.2	116.7	172.7	50.0	-6.0	96.4
cae	-60.0	-177.6	116.3	-125.1	-51.8	179.4	126.9	-130.3
caf	60.0	-54.7	-121.8	-3.6				
gad	-60.0	-171.9	122.1	-121.8	-67.8	169.7	113.3	-143.4
gae	60.0	-54.7	-121.8	-3.6	67.8	-59.7	-113.9	-10.1
gaf	180.0	68.2	0.2	118.0				

X = Br (B3PW91 (LAV3P(d))

	CF_2ICF_2I				CF_2ICF_2•			
	A	G	T1	T2	A	G	T1	T2
a	1.552	1.556	1.602	1.593	1.500	1.512	1.519	1.526
b	1.333	1.339	1.336	1.335	1.336	1.347	1.337	1.341
c	1.333	1.333	1.336	1.332	1.336	1.337	1.337	1.343
d	1.333	1.339	1.336	1.335	1.317	1.326	1.323	1.323
e	1.333	1.333	1.336	1.332	1.317	1.321	1.323	1.318
f	1.972	1.960	1.960	1.968				
g	1.972	1.960	1.960	1.968	2.006	1.967	1.983	1.971
ab	109.6	107.2	107.6	108.1	109.7	111.8	110.8	110.1
ac	109.6	109.5	107.7	111.4	109.7	108.7	110.8	109.2
ad	109.6	107.2	107.7	108.1	115.5	113.3	114.6	113.3
ae	109.6	109.5	107.7	111.4	115.5	115.1	114.6	118.2
af	110.1	112.3	116.7	112.0				
ag	110.1	112.3	116.7	112.0	111.6	109.9	109.4	112.4
bc	109.4	108.6	108.4	108.1	109.7	108.1	109.3	107.5
bg	109.0	109.1	108.1	108.8	108.1	108.8	108.3	109.3
cg	109.0	110.0	108.1	108.3	108.1	109.5	108.3	108.3
de	109.4	108.6	108.4	108.1	112.7	111.9	112.6	111.7
df	109.0	109.1	108.1	108.8				
ef	109.0	110.0	108.1	108.3				
bad	59.9	-54.2	-116.3	-0.4	52.6	-68.6	-127.4	-17.4
bae	180.0	63.5	0.3	118.2	-173.1	62.0	4.9	116.0
baf	-60.1	-174.1	112.0	-120.2				
cad	180.0	63.5	0.3	118.2	173.1	50.7	-5.9	100.4
cae	-59.9	178.9	116.9	-123.2	-52.6	-178.8	126.4	-126.2
caf	60.1	-56.4	-121.4	-1.6				
gad	-60.1	-174.1	122.0	-120.2	-67.2	170.5	113.3	-139.5
gae	60.1	-56.4	-121.4	-1.6	67.2	-58.9	-114.4	-6.1
gaf	180.0	66.1	0.3	119.9				

X = Cl (B3PW91 (LAV3P(d))

	CF_2ICF_2I				CF_2ICF_2•			
	A	G	T1	T2	A	G	T1	T2
a	1.555	1.557	1.601	1.597	1.508	1.515	1.526	1.529
b	1.335	1.339	1.337	1.336	1.338	1.349	1.339	1.341
c	1.335	1.335	1.336	1.333	1.338	1.339	1.339	1.345
d	1.335	1.339	1.336	1.336	1.319	1.324	1.323	1.322
e	1.335	1.335	1.337	1.334	1.319	1.322	1.323	1.319
f	1.768	1.762	1.762	1.766				
g	1.768	1.762	1.763	1.767	1.793	1.768	1.780	1.772
ab	109.2	107.4	107.8	108.0	109.1	111.3	110.2	109.7
ac	109.2	109.2	107.8	110.9	109.1	108.4	110.3	109.0
ad	109.2	107.4	107.8	108.0	114.9	113.2	114.3	113.8
ae	109.2	109.2	107.8	110.9	114.9	115.1	114.4	117.5
af	110.4	112.1	108.3	111.8				
ag	110.4	112.1	108.7	111.9	112.3	110.5	110.2	112.5
bc	109.2	108.6	108.2	108.1	109.4	107.8	108.9	107.5
bg	109.5	109.5	108.7	109.1	108.5	109.0	108.6	109.5
cg	109.5	110.1	108.7	108.8	108.5	109.8	108.5	108.5
de	109.2	108.6	108.3	108.1	112.4	112.0	112.3	111.8
df	109.5	109.5	108.7	109.1				
ef	109.5	110.1	108.7	108.8				
bad	60.7	-54.8	-116.7	1.2	54.0	-64.3	-126.4	-12.3
bae	180.0	62.7	0.0	119.5	-173.4	66.3	5.1	121.1
baf	-59.6	-175.1	121.7	-118.9				
cad	180.0	62.7	0.0	119.4	173.4	54.1	-6.0	105.1
cae	-60.7	-179.7	116.7	-122.3	-54.0	-175.3	125.4	-121.5
caf	59.6	-57.5	-121.7	-0.7				
gad	-59.6	-175.1	121.6	-118.9	-66.3	174.5	113.8	-134.5
gae	59.6	-57.5	-121.7	-0.7	66.3	-54.9	-114.7	-1.1
gaf	180.0	64.7	0.0	121.0				

Table A.2.S1e. The structural parameters of the CF_2XCF_2X and CF_2XCF_2• radicals (X = I, Br and Cl) optimized at B3PW91 (MSV) level of theory. The bond length is given in angstrom and the angle is in degree. The prefix A-, G-, and T- mean anti-, gauche-, and transition state, respectively. *a* corresponds to the C-C bond, *b, c, d* and *e* correspond to C-F bonds, and *f* and *g* corresponds to C-X bonds.

X = I (B3PW91 (MSV)

	CF_2ICF_2I				CF_2ICF_2•			
	A	G	T1	T2	A	G	T1	T2
a	1.529	1.538	1.582	1.566	1.486	1.491	1.497	1.500
b	1.394	1.396	1.394	1.393	1.394	1.410	1.397	1.402
c	1.394	1.394	1.394	1.395	1.394	1.395	1.397	1.405
d	1.394	1.396	1.394	1.393	1.363	1.367	1.366	1.365
e	1.394	1.394	1.394	1.395	1.363	1.367	1.366	1.365
f	2.167	2.167	2.174	2.173				
g	2.167	2.167	2.174	2.173	2.193	2.165	2.174	2.161
ab	108.4	107.1	107.5	108.2	108.4	111.1	110.3	109.5
ac	108.4	108.2	107.5	109.8	108.4	107.8	110.3	108.1
ad	108.4	107.1	107.5	108.2	116.1	115.9	116.4	115.7
ae	108.4	108.2	107.5	109.8	116.1	116.0	116.5	118.7
af	113.9	115.6	120.0	115.8				
ag	113.9	115.6	120.0	115.8	115.2	112.1	111.5	115.1
bc	107.5	107.0	106.7	106.0	108.4	106.5	108.0	105.9
bg	109.2	109.6	107.3	108.3	108.1	109.3	108.4	109.3
cg	109.2	109.0	107.3	108.3	108.1	109.8	108.3	108.5
de	107.5	107.0	106.7	106.0	111.9	111.6	112.5	111.2
df	109.2	109.0	107.3	108.3				
ef	109.2	109.6	107.3	108.3				
bad	63.6	-52.8	-114.4	-3.2	53.9	-67.9	-127.9	-18.9
bae	180.0	62.3	0.1	112.1	-171.4	65.9	8.6	117.3
baf	-58.2	-174.5	122.9	-125.0				
cad	180.0	62.3	0.1	112.1	171.4	48.5	-8.7	96.1
cae	-63.6	177.3	114.7	-132.6	-53.9	177.7	127.8	-127.8
caf	58.2	-59.4	-122.6	-9.7				
gad	-58.2	-174.5	122.9	-125.0	-67.3	169.4	111.7	-142.5
gae	58.2	-59.4	-122.6	-9.7	67.3	-56.8	-111.8	-6.3
gaf	180.0	63.8	0.2	113.3				

X = Br (B3PW91 (MSV)

	CF_2ICF_2I				CF_2ICF_2•			
	A	G	T1	T2	A	G	T1	T2
a	1.529	1.534	1.574	1.565	1.486	1.492	1.498	1.502
b	1.387	1.390	1.388	1.387	1.388	1.402	1.390	1.394
c	1.387	1.386	1.388	1.387	1.388	1.389	1.390	1.398
d	1.387	1.390	1.388	1.387	1.361	1.367	1.365	1.365
e	1.387	1.386	1.388	1.387	1.361	1.365	1.365	1.362
f	1.963	1.958	1.963	1.964				
g	1.963	1.958	1.963	1.964	2.001	1.964	1.985	1.967
ab	109.0	107.8	108.2	108.6	109.0	111.7	110.7	110.0
ac	109.0	109.0	108.2	110.6	109.0	108.4	110.7	108.7
ad	109.0	107.8	108.2	108.6	116.1	115.3	116.3	115.6
ae	109.0	109.0	108.2	110.6	116.1	116.2	116.3	118.8
af	112.5	113.7	117.5	114.1				
ag	112.5	113.7	117.5	114.1	113.9	111.3	110.9	114.0
bc	108.0	107.7	107.3	106.7	108.8	107.0	108.4	106.5
bg	109.1	109.0	107.7	108.4	108.0	108.8	108.0	109.3
cg	109.1	109.6	107.7	108.1	108.0	109.6	108.1	108.2
de	108.0	107.7	107.3	106.7	112.2	111.8	112.4	111.5
df	109.1	108.9	107.7	108.4				
ef	109.1	109.6	107.7	108.1				
bad	62.3	-53.0	-115.8	-0.2	53.2	-66.2	-128.0	-15.7
bae	180.0	63.6	0.1	116.6	-171.8	67.5	7.9	120.9
baf	-58.9	-173.8	122.2	-121.2				
cad	180.0	63.6	0.1	116.6	171.8	51.4	-7.8	100.5
cae	-62.3	-179.7	116.0	-126.6	-53.2	174.9	128.1	-122.9
caf	58.9	-57.2	-121.9	-4.4				
gad	-58.9	-173.8	122.2	-121.2	-67.5	172.1	112.1	-138.8
gae	58.9	-57.2	-121.9	-4.4	67.5	-54.2	-112.0	-2.2
gaf	180.0	65.4	0.1	117.8				

X = Cl (B3PW91 (MSV)

	CF_2ICF_2I				CF_2ICF_2•			
	A	G	T1	T2	A	G	T1	T2
a	1.533	1.537	1.573	1.568	1.486	1.494	1.498	1.503
b	1.379	1.384	1.382	1.381	1.382	1.396	1.384	1.389
c	1.379	1.379	1.382	1.378	1.382	1.383	1.385	1.391
d	1.379	1.384	1.382	1.381	1.360	1.367	1.364	1.364
e	1.379	1.379	1.382	1.378	1.360	1.363	1.363	1.360
f	1.846	1.838	1.840	1.845				
g	1.846	1.838	1.840	1.845	1.885	1.848	1.868	1.851
ab	109.7	108.5	108.7	108.9	110.0	112.5	111.4	110.8
ac	109.7	109.8	108.7	111.4	110.0	109.1	111.4	109.5
ad	109.7	108.5	108.7	108.9	116.0	115.0	116.2	115.2
ae	109.7	109.8	108.7	111.4	116.0	116.1	116.2	118.7
af	110.7	111.7	115.3	112.1				
ag	110.7	111.7	115.3	112.1	111.9	109.8	109.5	112.3
bc	108.7	108.2	107.9	107.5	109.2	107.5	108.8	106.9
bg	109.0	108.9	108.0	108.6	107.9	108.4	107.8	109.1
cg	109.0	109.7	108.0	108.2	107.9	109.4	107.8	108.0
de	108.7	108.2	107.9	107.5	112.5	112.0	112.7	111.8
df	109.0	108.9	108.0	108.6				
ef	109.0	109.7	108.0	108.2				
bad	60.6	-54.4	-117.3	-0.1	52.3	-68.2	-129.1	-16.3
bae	180.0	63.7	-0.1	118.4	-172.5	65.3	7.1	120.3
baf	-59.7	-174.5	121.3	-120.2				
cad	180.0	63.7	-0.1	118.4	172.5	51.0	-7.4	101.4
cae	-60.6	-178.3	117.1	-123.2	-52.23	175.5	128.8	-122.1
caf	59.7	-56.4	-121.5	-1.8				
gad	-59.7	-174.5	121.3	-120.2	-67.6	170.9	111.7	-138.6
gae	59.7	-56.4	-121.5	-1.8	67.6	-55.5	-112.1	-2.1
gaf	180.0	65.4	-0.1	119.6				

Table A.2.S1f. The structural parameters of the CF_2XCF_2X and CF_2XCF_2• radicals (X = I, Br and Cl) optimized at B3PW91 (MSV(d)) level of theory. The bond length is given in angstrom and the angle is in degree. The prefix A-, G-, and T- mean anti-, gauche-, and transition state, respectively. *a* corresponds to the C-C bond, *b, c, d* and *e* correspond to C-F bonds, and *f* and *g* corresponds to C-X bonds.

X = I (B3PW91 (MSV(d))

	CF_2ICF_2I				CF_2ICF_2•			
	A	G	T1	T2	A	G	T1	T2
a	1.542	1.552	1.601	1.586	1.490	1.506	1.511	1.520
b	1.336	1.343	1.339	1.338	1.337	1.350	1.340	1.345
c	1.336	1.337	1.339	1.337	1.337	1.339	1.340	1.346
d	1.336	1.343	1.339	1.338	1.318	1.327	1.324	1.325
e	1.336	1.337	1.339	1.337	1.318	1.324	1.324	1.321
f	2.198	2.186	2.189	2.193				
g	2.198	2.186	2.189	2.193	2.229	2.194	2.203	2.194
ab	109.5	106.7	107.4	108.0	110.2	111.5	111.0	110.1
ac	109.5	109.0	107.4	111.1	110.2	108.8	111.0	108.9
ad	109.5	106.7	107.4	108.0	115.3	113.9	114.9	113.4
ae	109.5	109.0	107.4	111.1	115.3	114.5	114.8	118.1
af	110.6	113.7	118.4	113.1				
ag	110.6	113.7	118.4	113.1	109.8	109.5	108.5	112.4
bc	109.3	108.5	108.2	107.8	109.8	108.3	109.3	107.3
bg	108.9	109.7	107.6	108.5	108.4	109.4	108.5	109.4
cg	108.9	109.1	107.6	108.1	108.4	109.3	108.5	108.5
de	109.3	108.5	108.2	107.8	112.7	112.0	112.8	111.6
df	108.9	109.1	107.6	108.5				
ef	108.9	109.7	107.6	108.1				
bad	60.1	-58.9	-116.6	-2.9	52.3	-75.2	-127.4	-23.6
bae	180.0	58.1	-0.5	115.2	-173.6	55.5	5.8	109.6
baf	-59.9	-179.2	121.4	-123.1				
cad	180.0	58.1	-0.5	115.2	173.6	44.2	-5.6	93.8
cae	-60.1	175.1	115.6	-126.7	-52.3	174.9	127.6	-132.9
caf	59.9	-62.2	-122.5	-5.0				
gad	-59.9	-179.2	121.4	-123.1	-67.0	163.5	113.5	-145.9
gae	59.9	-62.2	-122.5	-5.0	67.0	-65.7	-113.3	-12.6
gaf	180.0	60.5	-0.5	116.8				

X = Br (B3PW91 (MSV(d))

	CF_2ICF_2I				CF_2ICF_2•			
	A	G	T1	T2	A	G	T1	T2
a	1.544	1.549	1.594	1.587	1.497	1.508	1.516	1.521
b	1.335	1.341	1.337	1.336	1.337	1.349	1.339	1.343
c	1.335	1.335	1.337	1.334	1.337	1.339	1.339	1.345
d	1.335	1.341	1.337	1.336	1.319	1.323	1.324	1.324
e	1.335	1.335	1.337	1.334	1.319	1.323	1.324	1.319
f	1.948	1.936	1.938	1.944				
g	1.948	1.936	1.938	1.944	1.982	1.944	1.958	1.948
ab	109.5	107.4	107.8	108.2	109.6	111.6	110.7	110.1
ac	109.5	109.4	107.8	111.3	109.6	108.7	110.7	109.1
ad	109.5	107.4	107.8	108.2	115.2	113.4	114.6	113.5
ae	109.5	109.4	107.8	111.3	115.2	114.9	114.6	118.1
af	110.0	111.8	116.2	112.0				
ag	110.0	111.8	116.2	112.0	111.3	109.8	109.3	112.3
bc	109.3	108.6	108.3	107.9	109.6	108.2	109.2	107.5
bg	109.2	109.3	108.2	108.9	108.3	109.0	108.4	109.3
cg	109.2	110.1	108.2	108.4	108.3	109.6	108.4	108.4
de	109.3	108.6	108.3	107.9	112.7	112.0	112.5	111.8
df	109.2	109.3	108.2	108.9				
ef	109.2	110.1	108.2	108.4				
bad	60.1	-56.5	-116.8	-0.1	52.8	-69.6	-126.7	-17.9
bae	180.0	61.3	-0.1	118.4	-173.2	61.1	5.5	115.8
baf	-60.0	-176.4	121.6	-120.1				
cad	180.0	61.3	-0.1	118.4	173.2	49.6	-5.4	99.8
cae	-60.0	179.1	116.6	-123.2	-52.8	179.8	126.8	-126.5
caf	60.0	-58.6	-121.7	-1.6				
gad	-60.0	-176.4	121.6	-120.1	-67.0	169.5	113.9	-139.9
gae	60.0	-58.6	-121.7	-1.6	67.0	-59.9	-113.9	-6.3
gaf	180.0	63.6	-0.1	119.9				

X = Cl (B3PW91 (MSV(d))

	CF_2ICF_2I				CF_2ICF_2•			
	A	G	T1	T2	A	G	T1	T2
a	1.551	1.553	1.597	1.592	1.504	1.511	1.523	1.525
b	1.336	1.340	1.338	1.337	1.339	1.350	1.340	1.343
c	1.336	1.336	1.337	1.334	1.339	1.340	1.340	1.346
d	1.336	1.340	1.338	1.337	1.320	1.326	1.324	1.324
e	1.336	1.336	1.337	1.335	1.320	1.322	1.324	1.319
f	1.770	1.763	1.763	1.768				
g	1.770	1.763	1.764	1.768	1.795	1.770	1.781	1.773
ab	109.2	107.5	107.9	108.1	109.1	111.2	110.3	109.9
ac	109.2	109.2	107.9	110.9	109.1	108.5	110.3	108.9
ad	109.2	107.5	107.9	108.1	114.9	113.2	114.4	113.8
ae	109.2	109.2	107.9	110.9	114.9	115.0	114.4	117.5
af	110.3	111.8	115.1	111.7				
ag	110.3	111.8	115.1	111.7	112.2	110.4	110.1	112.3
bc	109.1	108.6	108.2	108.0	109.4	107.9	108.9	107.4
bg	109.5	109.5	108.8	109.2	108.5	109.0	108.6	109.6
cg	109.5	110.2	108.8	108.8	108.5	109.9	108.6	108.6
de	109.1	108.6	108.2	108.1	112.5	112.1	112.4	111.9
df	109.5	109.5	108.8	109.2				
ef	109.5	110.2	108.8	108.8				
bad	60.8	-55.8	-116.7	1.3	53.8	-65.2	-126.3	-13.1
bae	180.0	61.8	0.1	119.6	-173.3	65.4	5.5	120.5
baf	-59.6	-176.0	121.7	-118.8				
cad	180.0	61.8	0.0	119.5	173.3	53.3	-5.9	104.4
cae	-60.8	179.4	116.8	-122.2	-53.8	176.1	125.9	-122.1
caf	59.6	-58.4	-121.6	-0.6				
gad	-59.6	-176.0	121.7	-118.9	-66.4	173.7	113.9	-135.3
gae	59.6	-58.4	-121.6	-0.6	66.4	-55.7	-114.4	-1.8
gaf	180.0	63.7	0.0	121.0				

Table A.2.S2. The total energies calculated at various levels of theory for CF_2XCF_2X and CF_2XCF_2• radicals (X = I, Br, Cl). Zero point energies are given in the parenthesis. The energies are in hartrees and the difference energies, zero point energies and experimental values are in kcal/mol.

CF_2XCF_2X

Method	A-CF_2ICF_2I	G-CF_2ICF_2I	T1-CF_2ICF_2I	T2-CF_2ICF_2I
HF (LAV3P)	-495.75091 (15.31)	-495.74518 (15.30)	-495.72891 (15.18)	-495.73732 (15.27)
HF (LAV3P(d))	-495.76559	-495.76084	-495.74470	-495.75257
LMP2//HF (LAV3P)	-496.73633	-496.73285	-496.71765	-496.72439
LMP2//HF (LAV3P(d))	-496.89951	-496.89646	-496.88199	-496.88871
B3PW91 (LAV3P)	-498.17647 (14.39)	-498.17208 (14.80)	-498.15940 (14.27)	-498.16599 (14.33)
B3PW91 (LAV3P(d))	-498.18764	-498.18330	-498.17171	-498.17796
B3PW91 (MSV)	-14304.37211	-14304.36686	-14304.35343	-14304.36102
B3PW91 (MSV(d))	-14304.64320	-14304.63910	-14304.62672	-14304.63321
Method	A-CF_2BrCF_2Br	G-CF_2BrCF_2Br	T1-CF_2BrCF_2Br	T2-CF_2BrCF_2Br
HF (LAV3P)	-499.29963 (15.85)	-499.29599 (15.83)	-499.28135 (15.82)	-499.28713 (15.65)
HF (LAV3P(d))	-499.32776	-499.32531	-499.31096	-499.31575
LMP2//HF (LAV3P)	-500.29297	-500.29125	-500.27828	-500.28222
LMP2//HF (LAV3P(d))	-500.48345	-500.48175	-500.46927	-500.47330
B3PW91 (LAV3P)	-501.73728 (14.85)	-501.73464 (14.81)	-501.72339 (14.76)	-501.72787 (14.82)
B3PW91 (LAV3P(d))	-501.75803	-501.75618	-501.74559	-501.74948
B3PW91 (MSV)	-5617.83150	-5617.82859	-5617.81691	-5617.82200
B3PW91 (MSV(d))	-5618.15262	-5618.15069	-5618.13973	-5618.14354
Method	A-CF_2ClCF_2Cl	G-CF_2ClCF_2Cl	T1-CF_2ClCF_2Cl	T2-CF_2ClCF_2Cl
HF (LAV3P)	-502.86834 (16.80)	-502.86640 (16.83)	-502.85346 (16.80)	-502.85688 (16.81)
HF (LAV3P(d))	-502.90520	-502.90392	-502.89080	-502.89377
LMP2//HF (LAV3P)	-503.87189	-503.87115	-503.86011	-503.86252
LMP2//HF (LAV3P(d))	-504.09539	-504.09473	-504.08308	-504.08554
B3PW91 (LAV3P)	-505.30851 (15.71)	-505.30714 (15.67)	-505.29724 (15.68)	-505.72787 (15.69)
B3PW91 (LAV3P(d))	-505.33587	-505.33521	-505.32551	-505.32785
B3PW91 (MSV)	-1393.97389	-1393.97238	-1393.96173	-1393.96503
B3PW91 (MSV(d))	-1394.13947	-1394.13897	-1394.12936	-1394.13142

CF_2XCF_2• radicals

Method	A-CF_2ICF_2	G-CF_2ICF_2	T1-CF_2ICF_2	T2-CF_2ICF_2	B-CF_2ICF_2
HF (LAV3P)	-484.56037 (14.20)	-484.55579 (14.16)	-484.55149 (14.07)	-484.55183 (14.09)	-484.46074 (13.37)
HF (LAV3P(d))	-484.56793	-484.56370	-484.55945	-484.55957	-484.47216
LMP2//HF (LAV3P)	-485.48135	-485.47563	-485.47160	-485.47241	-485.41942
LMP2//HF (LAV3P(d))	-485.57701	-485.57164	-485.56789	-485.56896	-485.51973
B3PW91 (LAV3P)	-486.71635 (13.27)	-486.70835 (13.27)	-486.70551 (13.00)	-486.70640 (13.13)	-486.65886 (12.31)
B3PW91 (LAV3P(d))	-486.72154	-486.71418	-486.71133	-486.71224	-486.66830
B3PW91 (MSV)	-7389.50604	-7389.50133	-7389.49810	-7389.49970	-7389.45262
B3PW91 (MSV(d))	-7389.70407	-7389.69648	-7389.69357	-7389.69461	-7389.65182
Method	A-CF_2BrCF_2	G-CF_2BrCF_2	T1-CF_2BrCF_2	T2-CF_2BrCF_2	B-CF_2BrCF_2
HF (LAV3P)	-486.33507 (14.45)	-486.33114 (14.42)	-486.32705 (14.33)	-486.32697 (14.37)	-486.21793 (13.68)
HF (LAV3P(d))	-486.34914	-486.34579	-486.34161	-486.34131	-486.23280
LMP2//HF (LAV3P)	-487.25946	-487.25479	-487.25093	-487.25117	-487.18413
LMP2//HF (LAV3P(d))	-487.36917	-487.36474	-487.36122	-487.36159	-487.29700
B3PW91 (LAV3P)	-488.49597 (13.50)	-488.48955 (13.41)	-488.48681 (13.26)	-488.48723 (13.37)	-488.42624(13.06)
B3PW91 (LAV3P(d))	-488.50548	-488.50020	-488.49726	-488.49783	-488.43807
B3PW91 (MSV)	-3046.23564	-3046.23161	-3046.22812	-3046.22940	-3046.16589
B3PW91 (MSV(d))	-3046.45685	-3046.45178	-3046.44854	-3046.44938	-3046.38745
Method	A-CF_2ClCF_2	G-CF_2ClCF_2	T1-CF_2ClCF_2	T2-CF_2ClCF_2	B-CF_2ClCF_2
HF (LAV3P)	-488.11909 (14.93)	-488.11616 (14.90)	-488.11187 (14.81)	-488.11188 (14.83)	-487.97955 (13.42)
HF (LAV3P(d))	-488.13714	-488.13466	-488.13004	-488.13016	-488.09235
LMP2//HF (LAV3P)	-489.04824	-489.04489	-489.04068	-489.04114	-488.94788
LMP2//HF (LAV3P(d))	-489.17387	-489.17097	-489.16693	-489.16759	-489.11880
B3PW91 (LAV3P)	-490.27995 (13.90)	-490.27556 (13.84)	-490.27235 (13.73)	-490.27301 (13.79)	-490.25819 (13.58)
B3PW91 (LAV3P(d))	-490.29261	-490.28925	-490.28559	-490.28658	-490.25986
B3PW91 (MSV)	-934.30735	-934.30364	-934.30045	-934.30110	-934.28597
B3PW91 (MSV(d))	-934.44897	-934.44572	-934.44205	-934.44303	-934.41767

Halogen atoms and CF_2=CF_2

Method	I	Br	Cl	CF_2=CF_2
HF (LAV3P)	-11.15723	-12.91863	-14.68120	-473.41578 (14.13)
HF (LAV3P(d))	-11.15723	-12.91863	-14.68120	-473.41578
LMP2//HF (LAV3P)	-11.17128	-12.93869	-14.70823	-474.31729
LMP2//HF (LAV3P(d))	-11.24707	-13.02050	-14.79872	-474.31729
B3PW91 (LAV3P)	-11.38531	-13.15084	-14.91530	-475.32740 (13.20)
B3PW91 (LAV3P(d))	-11.38531	-13.15084	-14.91530	-475.32740
B3PW91 (MSV)	-6914.78155	-2571.49856	-459.56382	-474.71385
B3PW91 (MSV(d))	-6914.85751	-2571.58622	-459.56382	-474.83278

Table A.2.S3. Total energy (hartree) of CH_2XCH_2X calculated at various levels of theory. The zero point energies (kcal/mol) are also presented in the parenthesis.

Method	A-CH_2ClCH_2Cl	G-CH_2ClCH_2Cl	T1-CH_2ClCH_2Cl	T2-CH_2ClCH_2Cl
HF (LAV3P)	-107.48309	-107.47967	-107.46583	-107.47488
	(36.71)	(36.71)	(36.68)	(36.61)
LMP2//HF (LAV3P)	-107.84102	-107.83872	-107.82677	-107.83283
LMP2 (LAV3P)	-107.84155	-107.83917	-107.82709	-107.83332
	(36.70)	(36.63)	(36.55)	(36.43)
B3PW91 (LAV3P)	-108.53653	-108.53386	-108.52146	-108.52900
	(35.60)	(35.53)	(35.49)	(35.38)
B3LYP (LAV3P)	-108.52082	-108.51794	-108.50562	-108.51333
	(35.48)	(35.41)	(35.36)	(35.25)

Method	A-CH_2BrCH_2Br	G-CH_2BrCH_2Br	T1-CH_2BrCH_2Br	T2-CH_2BrCH_2Br
HF (LAV3P)	-103.92640	-103.92161	-103.90824	-103.91738
	(35.89)	(35.85)	(35.79)	(35.80)
LMP2//HF (LAV3P)	-104.27160	-104.26830	-104.25643	-104.26246
LMP2 (LAV3P)	-104.27218	-104.26877	-104.25679	-104.26303
	(35.89)	(35.81)	(35.68)	(35.64)
B3PW91 (LAV3P)	-104.97538	-104.97124	-104.95956	-104.96683
	(34.80)	(34.75)	(34.67)	(34.62)
B3LYP (LAV3P)	-104.95736	-104.95290	-104.94133	-104.94891
	(34.68)	(34.61)	(34.54)	(34.50)

Method	A-CH_2ICH2I	G-CH_2ICH_2I	T1-CH_2ICH_2I	T2-CH_2ICH_2I
HF (LAV3P)	-100.38301	-100.37718	-100.36450	-100.37339
	(35.38)	(35.32)	(35.24)	(35.32)
LMP2//HF (LAV3P)	-100.71969	-100.71558	-100.70376	-100.71011
LMP2 (LAV3P)	-100.72028	-100.71602	-100.70416	-100.71070
	(35.42)	(35.34)	(35.17)	(35.19)
B3PW91 (LAV3P)	-101.42044	-101.41519	-101.40448	-101.41086
	(34.33)	(34.26)	(34.17)	(34.18)
B3LYP (LAV3P)	-101.39825	-101.39259	-101.38195	-101.38883
	(34.22)	(34.20)	(34.05)	(34.07)

Table A.2.S4. Relative energies (kcal/mol) of CH_2XCH_2X calculated at various levels of theory.

Method	A-CH_2ClCH_2Cl	G-CH_2ClCH_2Cl	T1-CH_2ClCH_2Cl	T2-CH_2ClCH_2Cl
HF	-2.15	0	8.65	2.90
LMP2//HF	-1.44	0	7.47	3.60
LMP2	-1.42	0	7.50	3.47
B3PW91	-1.61	0	7.74	2.90
B3LYP	-1.74	0	7.68	2.73
experiment	-1.0 ~ -1.5	0		

Method	A-CH_2BrCH_2Br	G-CH_2BrCH_2Br	T1-CH_2BrCH_2Br	T2-CH_2BrCH_2Br
HF	-2.97	0	8.33	2.61
LMP2//HF	-2.03	0	7.39	3.62
LMP2	-2.06	0	7.39	3.43
B3PW91	-2.55	0	7.25	2.64
B3LYP	-2.71	0	7.19	2.39
experiment	-1.4 ~ -2.2	0		

Method	A-CH_2ICH_2I	G-CH_2ICH_2I	T1-CH_2ICH_2I	T2-CH_2ICH_2I
HF	-3.60	0	7.88	2.38
LMP2//HF	-2.52	0	7.34	3.44
LMP2	-2.60	0	7.27	3.19
B3PW91	-3.22	0	6.63	2.64
B3LYP	-3.54	0	6.52	2.23
experiment	-1.38 ~ -2.6	0		

Table A.2.S5. Vibrational frequencies and mode analysis for CF_2XCF_2X parent molecules (B3PW91 (LAV3P))

a. Anti conformer

Freq(cm-1)		CF_2ClCF_2Cl	Freq(cm^{-1})		CF_2BrCF_2Br	Freq(cm^{-1})		CF_2ICF_2I
1330	A_g	C-C str	1308	A_g	C-C str	1280	A_g	C-C str
1292	A_u	C-F str asym	1286	A_u	C-F str asym	1263	A_u	C-F str asym
1277	B_g	C-F str asym	1274	B_g	C-F str asym	1255	B_g	C-F str asym
1189	B_u	C-F str sym, F-C-F scissor	1185	B_u	F-C-F scissor	1174	B_u	C-F str sym, F-C-F scissor
1039	A_g	C-Cl str	998	A_g	C-Br str sym	985	A_g	C-I str
802	B_u	C-Cl str	727	B_u	C-Br str	693	B_u	C-I str
707	A_g	C-F str sym Cl-C-C bend	694	A_g	Br-C-C bend sym	684	A_g	C-F str sym F-C-F scissor, I-C-C bend
604	B_u	F-C-F scissor	589	B_u	C-F str sym	578	B_u	F-C-F scissor
536	B_g	twist	521	B_g	twist	517	B_g	twist
415	B_u	C-Cl str	361	A_g	C-F str sym	360	A_g	F-C-C bend
408	A_g	wag, C-Cl str	317	B_u	C-Br str	287	A_u	twist
370	A_u	twist	308	A_u	twist	276	B_u	C-I str
358	A_g	F-C-C bend	296	A_g	wag, C-Br str	262	B_g	rock
318	B_g	rock	280	B_g	Rock	261	A_g	wag
249	A_g	Cl-C-C bend	207	A_u	F-C-C bend	205	A_u	F-C-C bend
213	A_u	F-C-C bend	170	A_g	C-Br str Br-C-C bend	130	A_g	C-I str
165	B_u	Cl-C-C bend	126	B_u	Br-C-C bend	109	B_u	I-C-C bend
68	A_u	torsion	62	A_u	torsion	57	A_u	torsion

b. gauche conformer

Freq(cm^{-1})		CF_2ClCF_2Cl	Freq(cm^{-1})		CF_2BrCF_2Br	Freq(cm^{-1})		CF_2ICF_2I
1323	A	C-C str	1295	A	C-C str	1260	A	C-C str
1273	B	C-F str asym	1263	B	C-F str asym	1242	B	C-F str asym
1264	A	C-F str asym	1254	A	C-F str asym	1234	A	C-F str asym
1164	B	C-F str sym F-C-F scissor	1151	B	C-F str sym F-C-F scissor	1135	B	C-F str sym F-C-F scissor
1036	A	C-Cl str F-C-F scissor	1008	A	C-Br str F-C-F scissor	994	A	C-I str F-C-F scissor
883	B	C-Cl str	842	B	C-Br str	821	B	C-I str
670	A	C-F str sym	650	A	C-F str sym	640	A	C-F str sym
618	B	F-C-F scissor	601	B	F-C-F scissor	587	B	F-C-F scissor
482	A	twist F-C-C bend	456	A	twist, F-C-C bend	447	A	twist, F-C-C bend
422	B	rock, C-Cl str	354	B	twist, Br-C-C bend F-C-C bend	333	B	twist, I-C-C bend F-C-C bend
418	A	rock, C-Cl str	320	A	F-C-C bend	305	A	F-C-C bend
393	B	twist, Cl-C-C bend F-C-C bend	309	B	rock	276	B	rock
323	A	F-C-C bend	302	A	rock	276	A	rock
305	A	F-C-C bend	271	A	Br-C-F bend	245	A	I-C-F bend
303	B	rock	259	B	F-C-C bend	231	B	F-C-C bend
195	B	F-C-C bend	173	B	rock, F-C-C bend	156	B	rock, I-C-C bend
165	A	Cl-C-C bend	113	A	Br-C-C bend	93	A	I-C-C bend
62	A	torsion	58	A	torsion	55	A	torsion

c. Rotational transition state T1

Freq(cm^{-1})		CF_2ClCF_2Cl	Freq(cm^{-1})		CF_2BrCF_2Br	Freq(cm^{-1})		CF_2ICF_2I
1271	A	C-C str C-F str asym	1261	B	C-F str asym	1241	B	C-F str asym
1270	B	C-F str asym	1250	A	C-F str asym	1231	A	C-F str asym
1262	A	C-F str sym	1243	A	C-C str, C-F str sym	1213	A	C-C str, C-F str sym
1164	B	C-F str sym	1149	B	C-F str sym	1134	B	C-F str sym
991	A	C-C str C-Cl str	947	A	C-C str C-Br str	919	A	C-C str C-I str
900	B	C-Cl str	861	B	C-Br str	841	B	C-I str
634	A	C-Cl str, F-C-F scissor	603	B	F-C-F scissor	589	B	F-C-F scissor
624	B	F-C-F scissor Cl-C-C bend	600	A	F-C-F scissor	586	A	F-C-F scissor
525	A	twist	504	A	twist	491	A	twist
424	A	C-Cl str	370	A	wag	369	A	wag
416	B	C-Cl str, rock	338	B	F-C-C bend	333	B	F-C-C bend
378	B	rock	311	B	rock, C-Br str	275	B	rock
363	A	wag	310	A	C-Br str	266	B	rock
310	A	rock	282	B	rock	264	A	C-I str
298	B	F-C-C bend	273	A	rock	256	A	rock
274	B	Cl-C-C bend	213	B	Br-C-C bend	181	B	I-C-C bend
200	A	Cl-C-C bend	128	A	Br-C-C bend	103	A	I-C-C bend
66*i*	A	torsion	53*i*	A	torsion	53*i*	A	torsion

d. Rotational transition state T2

Freq(cm^{-1})		CF_2ClCF_2Cl	Freq(cm^{-1})		CF_2BrCF_2Br	Freq(cm^{-1})		CF_2ICF_2I
1281	A	C-C str C-F str asym	1270	A	C-F str asym	1248	A	C-F str asym
1276	A	C-C str, C-F str asym	1266	B	C-F str asym	1243	B	C-F str asym
1274	B	C-F str sym	1256	A	C-C str, C-Br str	1228	A	C-C str, C-I str
1176	B	C-F str sym	1170	B	C-F str sym, C-Br str	1158	B	C-F str sym, C-I str
1021	A	C-C str C-Cl str	988	A	C-C str C-F str sym	971	A	C-C str C-F str sym
824	B	C-Cl str, wag	768	B	C-Br str, F-C-C bend	742	B	C-I str, F-C-C bend
694	A	F-C-F scissor	678	A	F-C-F scissor	669	A	F-C-F scissor
623	B	F-C-F scissor	608	B	F-C-F scissor	598	B	F-C-F scissor
475	B	rock	437	B	rock	422	B	rock
418	A	rock	396	A	wag	394	A	wag
414	B	rock	331	A	F-C-C bend	325	A	F-C-C bend
407	A	twist	318	B	rock	283	A	rock
356	A	wag	310	A	rock	282	B	rock
317	B	F-C-C bend	287	A	twist	250	A	twist
312	B	F-C-C bend	273	B	F-C-C bend	245	B	F-C-C bend
227	A	Cl-C-C bend	175	B	Br-C-C bend	150	B	I-C-C bend
223	B	Cl-C-C bend	157	A	Br-C-C bend	124	A	I-C-C bend
61*i*	A	torsion	51*i*	A	torsion	44*i*	A	torsion

Table A.2.S6. Vibrational frequencies and mode analysis for CF_2XCF_2 radicals (B3PW91 (LAV3P))

a. Anti conformer

Freq(cm^{-1})		CF_2ClCF_2	Freq(cm^{-1})		CF_2BrCF_2	Freq(cm^{-1})		CF_2ICF_2
1243	A'	C-C str	1230	A'	C-C str	1246	A'	C-C str
1355	A"	C-F str asym (rad)	1365	A"	C-F str asym (rad)	1366	A"	C-F str (rad)
1277	A"	C-F str asym (Cl)	1276	A"	C-F str asym (Br)	1261	A"	C-F str (I)
1188	A'	C-F str sym	1186	A'	C-F str sym	1178	A'	C-F str sym
889	A'	C-F str sym	845	A'	C-F str sym	822	A'	C-F str sym, C-C str
676	A'	wag, C-Cl str	660	A'	wag, C-Br str	647	A'	wag, C-I str
623	A'	wag, C-Cl str	588	A'	F-C-F scissor	575	A'	F-C-F scissor
567	A'	F-C-F scissor	552	A'	wag, C-Br str	541	A'	wag, C-I str
519	A"	twist	512	A"	twist	511	A"	twist
377	A'	C-Cl str	366	A'	F-C-C bend	365	A'	F-C-C bend
364	A'	F-C-C bend	287	A"	rock	265	A"	rock
331	A"	rock	269	A'	C-Br str	225	A'	C-I str
200	A"	F-C-C bend	199	A"	F-C-C bend	198	A"	F-C-C bend
162	A'	Cl-C-C bend	130	A'	Br-C-C bend	115	A'	I-C-C bend
70	A"	torsion	70	A"	torsion	72	A"	torsion

b. Gauche conformer

Freq(cm^{-1})	CF_2ClCF_2	Freq(cm^{-1})	CF_2BrCF_2	Freq(cm^{-1})	CF_2ICF_2
1394	C-C str	1383	C-C str	1368	C-C str
1331	C-F str asym (rad)	1326	C-F str asym (rad)	1319	C-F str asym (rad)
1238	C-F str asym (Cl)	1234	C-F str asym (Br)	1216	C-F str asym (I)
1138	C-F str sym	1131	C-F str sym	1117	C-F str sym
955	C-Cl str, C-F str sym	922	C-Br str, C-F str sym	911	C-F str sym, C-I str
772	wag, C-Cl str	764	wag, C-Br str	761	wag, C-I str
627	wag, C-Cl str	613	wag, C-Br str	608	wag, C-I str
578	F-C-F scissor	571	F-C-F scissor	564	F-C-F scissor
448	twist	438	twist	434	twist
410	C-Cl str	307	F-C-C bend	294	F-C-C bend
340	rock	295	rock	267	rock
317	F-C-C bend	288	C-Br str, rock	249	C-I str
210	F-C-C bend	208	F-C-C bend	206	F-C-C bend
176	Cl-C-C bend, F-C-C bend	148	Br-C-C bend	133	I-C-C bend
46	torsion	44	torsion	42	torsion

c. Rotational transition state T1

Freq(cm^{-1})	CF_2ClCF_2	Freq(cm^{-1})	CF_2BrCF_2	Freq(cm^{-1})	CF_2ICF_2
1391	C-C str	1387	C-C str	1374	C-C str
1339	C-F str asym (rad)	1340	C-F str asym (rad)	1336	C-F str asym (rad)
1264	C-F str asym (Cl)	1262	C-F str asym (Br)	1245	C-F str asym (I)
1153	C-F str sym	1145	C-F str sym	1132	C-F str sym
904	C-Cl str, C-F str sym	868	C-Br str, C-F str sym	851	C-I str, C-F str sym
753	wag, C-Cl str	734	wag, C-Br str	725	wag, C-I str
576	F-C-F scissor	565	F-C-F scissor	558	F-C-F scissor
508	wag, C-Cl str	495	twist	490	twist
504	twist	474	wag, C-Br str	461	wag, C-I str
403	C-Cl str	310	F-C-C bend sym	302	F-C-C bend sym
330	rock	292	C-Br str	265	rock
325	F-C-C bend sym	288	rock	248	C-I str
246	F-C-C bend asym	243	F-C-C bend asym	242	F-C-C bend asym
201	Cl-C-C bend	161	Br-C-C bend	139	I-C-C bend
60*i*	torsion	53*i*	torsion	58*i*	torsion

d. Rotational transition state T2

Freq(cm^{-1})	CF_2ClCF_2	Freq(cm^{-1})	CF_2BrCF_2	Freq(cm^{-1})	CF_2ICF_2
1388	C-C str	1380	C-C str	1367	C-C str
1339	C-F str asym (rad)	1334	C-F str asym (rad)	1328	C-F str asym (rad)
1225	C-F str asym (Cl)	1216	C-F str asym (Br)	1196	C-F str asym (I)
1159	C-F str sym	1152	C-F str sym	1140	C-F str sym
945	C-Cl str, C-F str sym	920	C-Br str, C-F str sym	910	C-I str, C-F str sym
700	wag, C-Cl str	687	wag, C-Br str	681	wag, C-I str
632	F-C-F scissor sym	625	F-C-F scissor sym	622	F-C-F scissor sym
583	F-C-F scissor asym	579	F-C-F scissor asym	576	F-C-F scissor asym
414	C-Cl str	390	twist	391	twist
390	F-C-C bend	357	F-C-C bend	342	rock
389	twist	303	C-Br str	273	F-C-C bend
320	rock	274	rock	255	wag, F-C-C bend
259	wag, F-C-C bend	257	wag, F-C-C bend	239	C-I str
207	Cl-C-C bend	169	Br-C-C bend	149	I-C-C bend
64*i*	torsion	61*i*	torsion	61*i*	torsion

Table A.2.S7. Vibrational frequencies and mode analysis for CF_2XCF_2X parent molecules (HF (LAV3P))

a. Anti conformer

Freq(cm-1)		CF_2ClCF_2Cl	Freq(cm^{-1})		CF_2BrCF_2Br	Freq(cm^{-1})		CF_2ICF_2I
1492	A_g	C-C str	1460	A_g	C-C str	1420	A_g	C-C str
1422	A_u	C-F str asym	1410	A_u	C-F str asym	1377	A_u	C-F str asym
1414	B_g	C-F str asym	1402	B_g	C-F str asym	1372	B_g	C-F str asym
1298	B_u	C-F str sym, F-C-F scissor	1287	B_u	F-C-F scissor	1272	B_u	C-F str sym, F-C-F scissor
1163	A_g	C-Cl str	1127	A_g	C-Br str sym	1119	A_g	C-I str
895	B_u	C-Cl str	811	B_u	C-Br str	776	B_u	C-I str
763	A_g	C-F str sym Cl-C-C bend	748	A_g	Br-C-C bend sym	735	A_g	C-F str sym F-C-F scissor, I-C-C bend
652	B_u	F-C-F scissor	634	B_u	C-F str sym	621	B_u	F-C-F scissor
588	B_g	twist	571	B_g	twist	567	B_g	twist
459	B_u	C-Cl str	392	A_g	C-F str sym	392	A_g	F-C-C bend
459	A_g	wag, C-Cl str	353	B_u	C-Br str	316	A_u	twist
405	A_u	twist	340	A_u	twist	307	B_u	C-I str
391	A_g	F-C-C bend	330	A_g	wag, C-Br str	291	A_g	wag
351	B_g	rock	311	B_g	rock	288	B_g	rock
270	A_g	Cl-C-C bend	229	A_u	F-C-C bend	226	A_u	F-C-C bend
230	A_u	F-C-C bend	190	A_g	C-Br str Br-C-C bend	146	A_g	C-I str
179	B_u	Cl-C-C bend	134	B_u	Br-C-C bend	112	B_u	I-C-C bend
68	A_u	torsion	69	A_u	torsion	55	A_u	torsion

b. Gauche conformer

Freq(cm^{-1})		CF_2ClCF_2Cl	Freq(cm^{-1})		CF_2BrCF_2Br	Freq(cm^{-1})		CF_2ICF_2I
1486	A	C-C str	1448	A	C-C str	1405	A	C-C str
1407	B	C-F str asym	1389	B	C-F str asym	1360	B	C-F str asym
1402	A	C-F str asym	1385	A	C-F str asym	1356	A	C-F str asym
1279	B	C-F str sym F-C-F scissor	1257	B	C-F str sym F-C-F scissor	1239	B	C-F str sym F-C-F scissor
1164	A	C-Cl str F-C-F scissor	1128	A	C-Br str F-C-F scissor	1119	A	C-I str F-C-F scissor
981	B	C-Cl str	930	B	C-Br str	911	B	C-I str
728	A	C-F str sym	704	A	C-F str sym	691	A	C-F str sym
671	B	F-C-F scissor	650	B	F-C-F scissor	633	B	F-C-F scissor
534	A	twist F-C-C bend	501	A	twist, F-C-C bend	490	A	twist, F-C-C bend
470	B	rock, C-Cl str	387	B	twist, Br-C-C bend F-C-C bend	364	B	twist, I-C-C bend F-C-C bend
463	A	rock, C-Cl str	356	A	F-C-C bend, C-Br str	338	A	F-C-C bend
432	B	twist, Cl-C-C bend F-C-C bend	342	B	rock	306	B	rock
356	A	F-C-C bend	329	A	F-C-C bend	301	A	rock
341	B	F-C-C bend	306	A	Br-C-F bend	274	A	I-C-F bend
340	A	Cl-C-F bend	292	B	F-C-C bend	261	B	F-C-C bend
215	B	F-C-C bend	189	B	F-C-C bend, Br-C-C bend	170	B	rock, I-C-C bend
182	A	Cl-C-C bend	125	A	Br-C-C bend	102	A	I-C-C bend
76	A	torsion	64	A	torsion	62	A	torsion

c. Rotational transition state T1

Freq(cm^{-1})		CF_2ClCF_2Cl	Freq(cm^{-1})		CF_2BrCF_2Br	Freq(cm^{-1})		CF_2ICF_2I
1427	A	C-C str C-F str asym	1389	A	C-C str	1355	A	C-C str
1400	B	C-F str asym	1384	B	C-F str asym	1355	B	C-F str asym
1399	A	C-F str sym	1383	A	C-F str sym	1347	A	C-F str sym
1278	B	C-F str sym	1252	B	C-F str sym	1232	B	C-F str sym
1114	A	C-C str C-Cl str	1064	A	C-Br str, C-C str	1040	A	C-I str, C-C str
995	B	C-Cl str	949	B	C-Br str	929	B	C-I str
688	A	C-Cl str, F-C-F scissor	651	B	F-C-F scissor	634	B	F-C-F scissor
675	B	F-C-F scissor Cl-C-C bend	649	A	F-C-F scissor	634	A	F-C-F scissor
580	A	twist	556	A	twist	543	A	twist
468	A	C-Cl str	402	A	wag	399	A	wag
464	B	C-Cl str, rock	372	B	F-C-C bend	366	B	F-C-C bend
420	B	rock	344	B	rock, C-Br str	301	B	rock
397	A	wag	343	A	C-Br str	292	A	C-I str
347	A	rock	302	B	rock	283	B	rock
323	B	F-C-C bend	302	A	rock	277	A	rock
307	B	Cl-C-C bend	237	B	Br-C-C bend	203	B	I-C-C bend
218	A	Cl-C-C bend	138	A	Br-C-C bend	102	A	I-C-C bend
76*i*	A	torsion	72*i*	A	torsion	77*i*	A	torsion

d. Rotational transition state T2

Freq(cm^{-1})		CF_2ClCF_2Cl	Freq(cm^{-1})		CF_2BrCF_2Br	Freq(cm^{-1})		CF_2ICF_2I
1433	A	C-C str	1402	A	C-C str	1370	A	C-C str
1407	A	C-F str asym,	1390	A	C-F str asym	1359	A	C-F str asym
1407	B	C-F str asym	1390	B	C-F str asym	1353	B	C-C str,
1269	B	C-F str sym	1275	B	C-F str sym, C-Br str	1260	B	C-F str sym, C-I str
1154	A	C-C str C-Cl str	1118	A	C-C str C-F str sym	1107	A	C-C str C-F str sym
919	B	C-Cl str, wag	855	B	C-Br str, F-C-C bend	829	B	C-I str, F-C-C bend
751	A	F-C-F scissor	732	A	F-C-F scissor	721	A	F-C-F scissor
673	B	F-C-F scissor	657	B	F-C-F scissor	644	B	F-C-F scissor
524	B	rock	478	B	rock	461	B	rock
468	A	rock	433	A	wag	431	A	wag
458	B	rock	364	A	F-C-C bend	355	A	F-C-C bend
448	A	twist	352	B	rock	311	B	rock
391	A	wag	339	A	twist	308	A	twist
351	B	F-C-C bend	318	A	rock	276	A	rock
348	B	F-C-C bend	303	B	F-C-C bend	273	B	F-C-C bend
249	A	Cl-C-C bend	193	B	Br-C-C bend	165	B	I-C-C bend
245	B	Cl-C-C bend	172	A	Br-C-C bend	137	A	I-C-C bend
-68*i*	A	torsion	57*i*	A	torsion	48*i*	A	torsion

Table A.2.S8. Vibrational frequencies and mode analysis for CF_2XCF_2 radicals (HF (LAV3P))

a. Anti conformer

Freq(cm^{-1})		CF_2ClCF_2	Freq(cm^{-1})		CF_2BrCF_2	Freq(cm^{-1})		CF_2ICF_2
1545	A'	C-C str	1532	A'	C-C str	1515	A'	C-C str
1457	A"	C-F str asym (rad)	1457	A"	C-F str asym (rad)	1451	A"	C-F str (rad)
1408	A"	C-F str asym (Cl)	1395	A"	C-F str asym (Br)	1370	A"	C-F str (I)
1294	A'	C-F str sym	1286	A'	C-F str sym	1274	A'	C-F str sym
1080	A'	wag, C-Cl str	1050	A'	wag, C-Br str	1043	A'	wag, C-I str
739	A'	C-F str sym	730	A'	C-F str sym	722	A'	C-F str sym
715	A'	wag, C-Cl str	664	A'	wag, C-Br str	642	A'	wag, C-Br str
618	A'	F-C-F scissor	610	A'	F-C-F scissor	605	A'	F-C-F scissor
565	A"	twist	555	A"	twist	552	A"	twist
443	A'	C-Cl str	393	A'	F-C-C bend	390	A'	F-C-C bend
391	A'	F-C-C bend	327	A"	rock	295	A"	rock
368	A"	rock	319	A'	C-Br str	282	A'	C-I str
220	A"	F-C-C bend	217	A"	F-C-C bend	218	A"	F-C-C bend
192	A'	Cl-C-C bend	149	A'	Br-C-C bend	138	A'	I-C-C bend
75	A"	torsion	70	A"	torsion	74	A"	torsion

b. Gauche conformer

Freq(cm^{-1})	CF_2ClCF_2	Freq(cm^{-1})	CF_2BrCF_2	Freq(cm^{-1})	CF_2ICF_2
1536	C-C str	1520	C-C str	1502	C-C str
1441	C-F str asym (rad)	1436	C-F str asym (rad)	1429	C-F str asym (rad)
1381	C-F str asym (Cl)	1370	C-F str asym (Br)	1345	C-F str asym (I)
1274	C-F str sym	1262	C-F str sym	1248	C-F str sym
1078	C-Cl str	1044	C-Br str,	1037	C-F str sym
	C-F str sym		C-F str sym		C-I str
887	wag,	876	wag,	872	wag,
	C-Cl str		C-Br str		C-I str
691	F-C-F scissor	676	F-C-F scissor	670	F-C-F scissor
627	F-C-F scissor	619	F-C-F scissor	612	F-C-F scissor
494	twist	477	twist	473	twist
456	C-Cl str	340	F-C-C bend	322	F-C-C bend
377	rock	325	rock	295	rock
346	F-C-C bend	319	C-Br str, rock	279	C-I str
241	F-C-C bend	240	F-C-C bend	239	F-C-C bend
194	Cl-C-C bend, F-C-C bend	163	Br-C-C bend	147	I-C-C bend
64	torsion	62	torsion	62	torsion

c. Rotational transition state T1

Freq(cm^{-1})	CF_2ClCF_2	Freq(cm^{-1})	CF_2BrCF_2	Freq(cm^{-1})	CF_2ICF_2
1525	C-C str	1514	C-C str	1497	C-C str
1446	C-F str asym (rad)	1444	C-F str asym (rad)	1440	C-F str asym (rad)
1403	C-F str asym (Cl)	1392	C-F str asym (Br)	1367	C-F str asym (I)
1276	C-F str sym	1254	C-F str sym	1250	C-F str sym
1024	C-Cl str, C-F str sym	984	C-Br str, C-F str sym	972	C-I str, C-F str sym
876	wag, C-Cl str	869	wag, C-Br str	865	wag, C-I str
628	F-C-F scissor	618	F-C-F scissor	610	F-C-F scissor
616	F-C-F scissor	593	F-C-F scissor	586	F-C-F scissor
555	twist	542	twist	537	twist
453	C-Cl str	347	wag	342	wag
366	rock	332	C-Br str	295	rock
356	F-C-C bend sym	318	rock	286	C-I str
266	F-C-C bend asym	263	F-C-C bend asym	260	F-C-C bend asym
227	Cl-C-C bend	183	Br-C-C bend	161	I-C-C bend
67*i*	torsion	65*i*	torsion	65*i*	torsion

d. Rotational transition state T2

Freq(cm^{-1})	CF_2ClCF_2	Freq(cm^{-1})	CF_2BrCF_2	Freq(cm^{-1})	CF_2ICF_2
1516	C-C str	1503	C-C str	1485	C-C str
1448	C-F str asym (rad)	1445	C-F str asym (rad)	1436	C-F str asym (rad)
1374	C-F str asym (Cl)	1360	C-F str asym (Br)	1334	C-F str asym (I)
1281	C-F str sym	1271	C-F str sym	1257	C-F str sym
1083	C-Cl str, C-F str sym	1053	C-Br str, C-F str sym	1044	C-I str, C-F str sym
780	wag, C-Cl str	759	wag, C-Br str	751	wag, C-I str
720	F-C-F scissor sym	711	F-C-F scissor sym	705	F-C-F scissor sym
635	F-C-F scissor asym	629	F-C-F scissor asym	624	F-C-F scissor asym
470	C-Cl str	421	twist	420	twist
436	F-C-C bend	410	F-C-C bend	396	rock
420	twist	339	C-Br str	309	F-C-C bend
357	rock	311	rock	287	wag, F-C-C bend
288	wag, F-C-C bend	293	wag, F-C-C bend	271	C-I str
231	Cl-C-C bend	188	Br-C-C bend	166	I-C-C bend
69*i*	torsion	67*i*	torsion	67*i*	torsion

Table A.2.S9. MSV(d) basis set for C, F, Cl, Br, and I.

Atom	Function	Exponent	Coefficient
C	S	426.100000000000	2.097797009752951E-02
		64.2200000000000	0.142886782983173
		14.3200000000000	0.479230978943563
		3.78400000000000	0.500827619941020
	S	5.02000000000000	-0.195941725088570
		0.528500000000000	1.07271908501021
	S	0.163200000000000	1.00000000000000
	P	9.55800000000000	5.637939631776828E-02
		2.02100000000000	0.311876407098290
		0.550000000000000	0.761900208240117
	P	0.152400000000000	1.00000000000000
	D	0.800000000000000	1.00000000000000
F	S	992.800000000000	2.049937459807006E-02
		149.500000000000	0.141169621986709
		33.4800000000000	0.479134790954891
		8.96300000000000	0.500751942952856
	S	12.6700000000000	-0.194997008079080
		1.37600000000000	1.07425918492655
	S	0.406300000000000	1.00000000000000
	P	22.6700000000000	6.486085724363115E-02
		4.98400000000000	0.340386062228974
		1.34900000000000	0.734731037494245
	P	0.347700000000000	1.00000000000000
	D	0.800000000000000	1.00000000000000

Cl	S	3644.00000000000	2.020008079827341E-02
		549.300000000000	0.139814876988049
		123.700000000000	0.480948279958891
		33.5100000000000	0.498428707957397
	S	47.9800000000000	-0.110538798010178
		6.68100000000000	0.475462701043779
		2.43600000000000	0.610153027056181
	S	4.40300000000000	-0.312627131952709
		0.561300000000000	1.12043444624658
	S	0.196100000000000	1.00000000000000
	P	133.900000000000	3.395905409223948E-02
		30.7700000000000	0.203104193953585
		9.12300000000000	0.518451969881520
		2.89400000000000	0.436301064900294
	P	1.76700000000000	8.502592820462777E-02
		0.701500000000000	0.932834217050772
	P	0.196000000000000	1.00000000000000
	D	0.750000000000000	1.00000000000000

Br	S	15690.0000000000	2.005409390159184E-02
		2366.00000000000	0.139148767011045
		534.600000000000	0.483172871038353
		145.800000000000	0.495763820039352
	S	209.000000000000	-0.129402412033746
		36.4100000000000	0.437059346113978
		14.2700000000000	0.655277576170886
	S	21.9700000000000	-0.261951703832504
		4.72000000000000	0.476204836695508
		1.87200000000000	0.677155797567016
	S	2.61000000000000	-0.558403306892908
		0.415300000000000	1.20759135544325
	S	0.153100000000000	1.00000000000000
	P	733.400000000000	2.932212709920819E-02
		171.900000000000	0.189532181994882
		53.2100000000000	0.521445373985919
		18.3000000000000	0.429631047988398
	P	12.3000000000000	6.465841919522045E-02
		6.19900000000000	0.510100782962293
		2.15900000000000	0.519376689961608
	P	4.95800000000000	-7.274844476209696E-02
		0.517000000000000	1.01656167505982
	P	0.153800000000000	1.00000000000000
	D	65.3100000000000	7.369196417280957E-02
		18.2500000000000	0.364265144865596
		5.97700000000000	0.714869328736232
	D	1.91500000000000	1.00000000000000
	D	0.338000000000000	1.00000000000000

I	S	36220.0000000000	1.996342370082851E-02
		5461.00000000000	0.138714698005757
		1235.00000000000	0.483557477020068
		337.400000000000	0.495477801020563
	S	482.000000000000	-0.135193513988191
		92.1400000000000	0.407543355964401
		36.3300000000000	0.688051319939898
	S	52.0200000000000	-0.336253055192589
		16.6000000000000	0.342699923196281
		6.84500000000000	0.859161714492084
	S	8.81800000000000	-0.471446175039328
		3.12300000000000	0.484940710040453
		1.24400000000000	0.808677575067459
	S	1.52600000000000	-0.756445126797422
		0.318800000000000	1.31909915313437
	S	0.123800000000000	1.00000000000000
	P	1808.00000000000	2.819335490447407E-02
		425.600000000000	0.186557030029605
		133.300000000000	0.523205440083029
		46.7800000000000	0.426506076067683
	P	28.9900000000000	6.684416238993790E-02
		19.0000000000000	0.490127391926221
		7.67100000000000	0.511428958923014
	P	14.3300000000000	-3.500068521310603E-02
		3.20100000000000	0.575302814215423
		1.25800000000000	0.502370060188113
	P	1.77900000000000	-2.152339671826118E-02
		0.348300000000000	1.00996065616450
	P	0.112800000000000	1.00000000000000
	D	231.200000000000	4.065184528411743E-02
		67.3300000000000	0.230875547909798
		23.8200000000000	0.532546493791935
		8.83100000000000	0.404395711842004
	D	8.14000000000000	0.217929100943697
		3.23900000000000	0.835574883784124
	D	1.14300000000000	1.00000000000000
	D	0.26600000000000	1.00000000000000

A.3 Data Analysis Of The Ground State Data

This section surveys the literature regarding the data processing and analysis, especially background correction. The purpose of this section is to provide the scope and variations of the data processing and data analysis that can be found in the literature for the ground state molecules. The data processing procedures and formalisms of theoretical intensity and the weighting factors used to remove the *s*-dependence of the total intensity are very confusing mainly due to (a) the two different ways to manipulate the original data ((i) dividing by the sector function and multiplying s^n (usually $n = 4$)→ background subtraction → (I_m) multiplying by s (ii) dividing by the sector function and dividing by theoretical atomic scattering function → background subtraction → ($M(s)$) multiplying by s.) (b) advancement of theory accuracy (from using Z/s^2 to $(Z - f)/s^2$ (first Born approximation) to the scattering factors ($f_i(s)$) from the partial wave calculation). (c) the numerous forms of the functions, and each depending on the preferences of the investigator (d) the least-square refinements which have been performed both on the molecular scattering function and the radial distribution function to a degree defined by each investigator. The following are approaches in data analysis developed by several groups.

A.3.1 Hargittai group[1]

The experimental background is usually determined empirically, whether by hand-drawing a smooth line through the oscillations of the total experimental intensity or fitting a high-order polynomial, which satisfies the criteria. The empirical

background usually can be improved during the structure analysis. The need for background improvement may be reflected in the nonstructural inner part of the smooth base line of the radial part of the $f^E(r)$, where nothing is expected. Ideally, background corrections should not influence structure parameters, only their uncertainties. Structural findings that appreciably change upon background modifications are suspect.

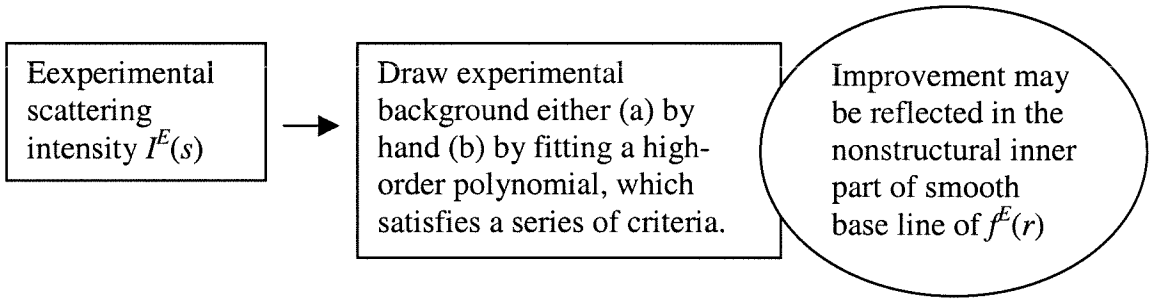

A.3.2 Bartell 1[2]

He divides the general approaches into two major schools; the Eastern U.S.-Eastern European-Japanese school and the Western U.S.-Western European school. The former works with the ratio I_M/I_A, reasoning that certain theoretical errors will cancel, and compensates radial distribution analyses for effects of planetary electrons by additive corrections. The latter[3-12] works with I_M itself, reasoning that extraneous scattering errors will drop out, and compensates for planetary electrons in radial distribution analyses by multiplicative corrections. The author deals with the former, where $M(s) = I/I_A - 1 = I_M/I_A$. The advantages for the former method are (a) the s-

dependence is almost removed in $M(s)$ compared to I_M. (b) any theoretical imperfections are presumably canceled out. (c) more sensitive $I_B(s)$ can be obtained with $M(s)$ rather than $I(s)$. First, I_0, "the leveled intensity", is obtained by dividing the experimental total intensity by the theoretical atomic scattering intensity ($I_0 = I^E/I_A{}^T$). The initial trial background function may be drawn by a visual estimate to cleave the molecular oscillations more or less evenly, or it may be derived by a polynomial fit with a computer as discussed elsewhere.[13] It is desirable to refine the initial trial background function as the analysis progresses, according to the criteria proposed by Karles[14-16], namely, the background must be kept smooth and the derived $f_c(r)$ radial distribution function be everywhere nonnegative. Once a trial background function has been selected, it is possible to compute a trial reduced intensity function $M^E(s) = \{[I_0^E(s)/I_B(s)] - 1\}$. The index of resolution R is then introduced for a better fit; $M^E(s) = R \cdot M^T(s)$. Usually, R is first kept as unity for every s, and then after obtaining the l_m's, $R(s)$ is allowed to vary.

A.3.3 Bartell 2[13]

Bartell et al. claim that the procedures in this paper differ from all previously published by directly using the observed quantities in place of the customary "reduced intensities" derived subjectively from manually smoothed data. Due to the cancellation of certain theoretical and experimental errors and the removal of the s-dependence, the reduced intensity function $M(s)(= I_M/I_A = (I/I_A) -1)$ is usually utilized. The principal difficulty in obtaining $M(s)$ is that I_A is itself not directly observable. Nevertheless,

$M(s)$ may be established within limits by applying a certain criteria[15]. Heretofore, one of the less desirable features of automatic analyses of reduced intensity functions has been that background functions, obtained subjectively, have been frozen until $f(r)$ is analyzed. Bartell et al. developed a new semi-automatic method to draw the background, which, in principle, requires no manual plotting of the data and no manual drawing of the background. Instead, the raw intensity data, unsmoothed by arbitrary procedures, could be utilized at the nonintegral values of s corresponding to the original intensity measurements. It has proven entirely feasible to allow the computer to select the background and refine it. The procedure is as follows: (a) $I_0^E(s) = I^E/I^T_A$ (b) minimize $\Sigma_i w_i[I_0^T(s) - I_0^E(s)]^2$, where $I_0^T(s) = I_B(s)[1 + R{\cdot}M^T(s)]$. $I_B(s) = A{\cdot}\exp(-\alpha s) + \Sigma_n a_n s^n$.

$I_0^E(s) = I^E/I^T_A$ →

minimize $\Sigma_i w_i[I_0^T(s) - I_0^E(s)]^2$,
where $I_0^T(s) = I_B^T(s)[1 + R{\cdot}M^T(s)]$.
$M(s) = \Sigma_i\Sigma_j C_{ij}\cos\Delta\eta_{ij}\exp(-l_m^2 s^2/2)\sin s[r_g(1)+\phi(s)]_{ij}/(sr_e)_{ij}$,
Where $C_{ij} = [Z - F(s)]_i[Z - F(s)]_j/\Sigma_i\{[Z - F(s)]_i^2 + S_i(s)\}$

$I_B^E(s) = I_0^E(s) / [1 + R{\cdot}M^E(s)]$.
Fit $I_B^E(s)$ with $I_B^T(s) = A{\cdot}\exp(-\alpha s) + \Sigma_n a_n s^n$.

For experimental data which do not include the region below s ≈ 7 Å^{-1}, it is sufficient to neglect the exponential term. Background smoothness is guaranteed by limiting the degree of the polynomial. At scattering angles corresponding s smaller than 6 or 7 Å^{-1}, the division of experimental by calculated atomic intensities does not level the data as

satisfactorily as it does at larger angles. Inside this limit, the derived background functions usually fall off rapidly as the scattering angle decreases. The imperfect leveling might be from a deficiency in the theory. The coefficient A is allowed to vary freely and α is kept constant at a value in the range of 0.5 to 2. Bartell et al. note that the atomic background intensity function, I_A, itself, has gentle bumps in it arising from the shell-like structure of atoms. Unless the total intensity function is leveled by a suitably bumpy calculated $I_A{}^T$ as described above, the smoothness criterion breaks down and the accuracy of the analysis is diminished. An initial trial background need not involve the manual plotting and visual selection typical of the previous scheme. The simplest procedure is to feed the initial background in as a constant representing the approximate mean leveled intensity. A procedure which may be somewhat more accurate is to obtain, by least squares, the parameters of a low-order polynomial which best follows the trends of $I_0(s)$. Another procedure is to calculate $I_B{}^T$ from $I_0{}^T(s) = I_B{}^T(s)[1 + R{\cdot}M^T(s)]$ assuming trial values for the molecular parameters and using the experimental $I_0(s)$. The calculated $I_B{}^T$ can then be fitted using $I_B{}^T(s) = A{\cdot}\exp(-\alpha s) + \Sigma_n a_n s^n$ with a least-squares method. All of these procedures have been used successfully. The last alternative is the most accurate, of course, if good guesses are available for bond lengths and amplitudes. It is obviously the procedure most likely to introduce an operator bias into the analysis, however.

A.3.4 Hedberg[3-5,17-19]

Not much is mentioned regarding background correction procedure. They compare their experimental data ($I^E(s)$) with the theoretical curve $kI_t(s) = k\Sigma_n A_n r_n^{-1}\exp(-\frac{1}{2}l_n^2 s^2)\sin(sr_n)$, where the amplitude A_n may be constant or vary with s. In this equation, they have obviously omitted η factors. A_n is the scattering amplitude from nth type of symmetry equivalent atomic pairs. $A_n = A_0$ or $A_n = A_{ij}$. A_0 is the constant scattering amplitude and A_{ij} is the variable amplitude. $A_{ij} = n'Z_iZ_jF_iF_j\cos\Delta\eta_{ij}$. F_k is the atomic coefficient of atom k normalized to an arbitrary reference atom M. $F_k = (Z_k - f_k)(Z_M - f_M)^{-1}Z_MZ_k^{-1}$. In conclusion, their $I_t(s)$ (and accordingly $I^{obs}(s)$) corresponds to $s\cdot s^4I_{mol}(s)$ and $s^4I_{mol}(s)$ actually corresponds to $M(s)$ of the Eastern U.S.-Eastern European-Japanese school.

A.3.5 Bastiansen[20]

The gas-scattered electron intensity striking the photographic plate is related to the total scattered intensity per unit solid angle according to the equation $I_p = I_t\cdot\alpha(s)\cdot P(\varphi)$, where $\alpha(s)$ is the sector function (carefully calibrated by direct measurement) and $P(\varphi) = \cos^3\varphi$ (φ is the scattering angle) takes into account the fact that the photographic plate is perpendicular to the undiffracted beam instead of being everywhere equidistant from the scattering point. The molecular scattering is then $I_m = \Sigma_{i,j}[(Z - f)_i(Z - f)_j/sr_{ij}]\cdot V_{ij}(s)\sin(sr_{ij}) = k(s\cdot I_p/(\Phi(s)P(\varphi)) - B_T)$, where the V terms are vibration factors, $\Phi(s) = \alpha(s)/s^3$ is a function differing only slightly from constancy, B_T

$= k\Sigma_i[(Z-f)_i^2 + Z_iS_i]$ is a background function and Z, f and S are the atomic numbers, the atomic form factors, and the Heisenberg incoherent scattering factors for x-rays, respectively. In summary, their $I_m = k(s \cdot I_p/(\Phi(s)P(\varphi)) - B_T) = k(s^4 I_t - B_T)$.

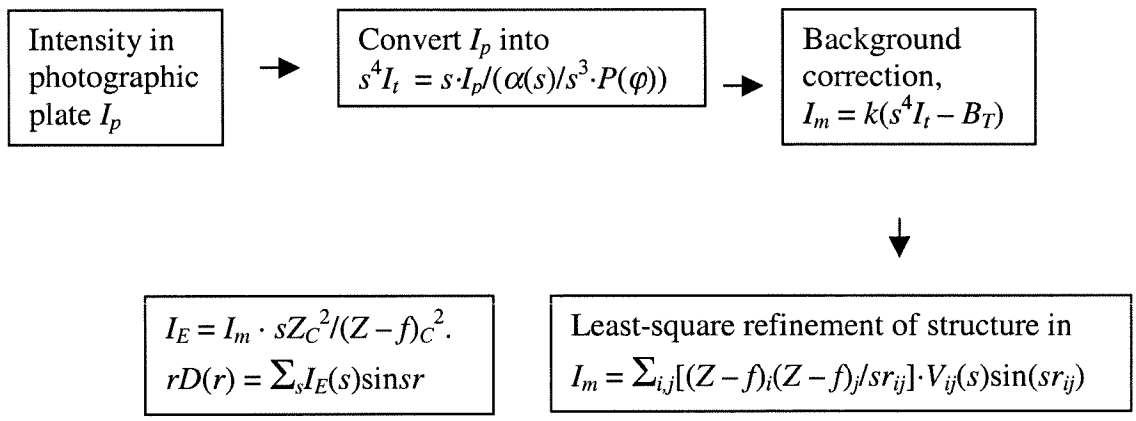

Largely owing to miscellaneous apparatus scattering, the experimental background usually differs considerably from the theoretical, so that it is customary to simply draw in a smooth background function. They essentially followed this procedure after multiplying the intensity curves by $s/(\Phi(s)P(\varphi)) = s^4/(\alpha(s)P(\varphi))$.

Actually, they attempted to use the theoretical background curves and found that the calculated function could be made to fit the middle parts of the curves fairly well. Unfortunately, it began to deviate in the direction of greater density over the inner parts of the curves and lesser density over the outer parts of the curves. The overlapping regions were joined by averaging points. Finally, I_m is multiplied by $sZ_C^2/(Z-f)_C^2$ to yield the more convenient (This function yields a Fourier transform, the peaks of which are essentially Gaussian.[21]) experimental intensity function (I_E).

The radial distribution curves $rD(r) = \Sigma_s I_E(s)\sin sr$. Inspection of the low r region reflects the adequacy of the empirical background. Failing to get rid of the negative area at $r < 0.75$ Å (reflecting errors in the background at small scattering angles), they used intensity data in the range $0 < s < 2.5$ from a theoretical curve. The analysis of the radial distribution curve was carried out by comparing it with theoretical curves composed of a sum of Gaussians, each Gaussian with center corresponding to an equilibrium interatomic distance, half-width equal to $(4a\ln 2)^{1/2}$, and area proportional to nZ_iZ_j/r_{ij}. The comparison with the theoretical radial distribution curves allowed them to distinguish between a good model and bad models. However, the actual refinement of the structure was performed by incorporating a least-square fitting.

A.3.6 Viervoll[22]

This paper provides a good source to look at the early stages of electron diffraction theory. The terms $I_t(s)$, $I_m(s)$ and $I_a(s)$, defined here, correspond to the intensities of the scattered beam before it strikes the rotating sector. $I_t'(s)$, $I_m'(s)$ and $I_a'(s)$ represent the same intensities after passing the sector and $P_t(s)$ is the ordinate of the photometric record. $P_a(s)$ can be defined by the equation $I_t(s)/I_a(s) = I_t'(s)/I_a'(s) = P_t(s)/P_a(s)$. Since $I_t(s) = I_a(s) + I_m(s)$, the following relationship can be drawn; $I_m(s)/I_a(s) = P_t(s)/P_a(s) - 1$. This function consists of a sum of modified $(\sin x) / x$ functions. For a sufficiently great interval of s the mean value of this function is near to zero.

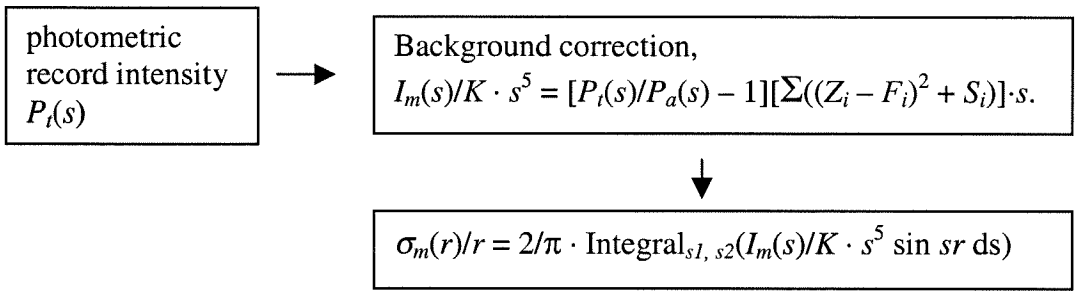

Their experience indicates that it is possible to make a reliable determination of the curve $P_a(s)$ by applying these relations: $I_m(s)/K \cdot s^5 = [P_t(s)/P_a(s) - 1][\Sigma((Z_i - F_i)^2 + S_i)] \cdot s$ and $\sigma_m(r)/r = 2/\pi \cdot \text{Integral}_{s1,\, s2}(I_m(s)/K \cdot s^5 \sin sr\, ds)$. This experimental $\sigma_m(r)/r$ has many wiggles (spurious undulations of period $2\pi/s_2$) due to the limited range of the integration. They called this "diffraction effects". To remedy this effect, a new function, $\sigma(r)$, was defined by inserting the damping factor $\exp(-ks^2)$. They also introduced so called normal curves. They pointed out that $\sigma_m(r)/r$ or $\sigma(r)/r$ may be written as a sum of functions each belonging to a single interatomic distance.

A.3.7 Karle 1[14]

The main difference between Karle's procedure and the Norwegian school (Viervoll) procedure concerns the method of analyzing the scattering data. Karl's $I_m(s) = \Sigma_i \Sigma_j c_{ij} A_{ij}$ $(i \neq j)$, where the coefficients c_{ij} are characteristic of the ith and jth atoms and in the subsequent analysis they are assumed to be constant. In practice, this is a good approximation, except for very small scattering angles, if the molecular scattering is obtained by dividing the total scattering by the background scattering.

This definition of I_m causes a confusion because this I_m is definitely not the same as the I_m in $I_t = I_m + I_a$. Introduction of $f(r)$ and its relationship with $D(r)$ is discussed. The procedure of data processing is as follows: The microphotometer reading is converted to intensity readings which are plotted against the variable s and a smooth background is drawn through the oscillations. Usually, it is easier to draw the background line beyond s values of 5 or 6 if the experimental intensity curve is multiplied by s or s^2 to accentuate the oscillations about the background. Uncertainties in the position of the background line mainly affect the shapes but not the positions of the maxima in the radial distribution curve. Hence, fairly reliable equilibrium distances for a molecule can be obtained from the radial distribution curve and then an intensity curve based on these distances may be computed. The background line may then be corrected if necessary to correspond to the position of the zero axis (this remark hints the use of zero points although they did not utilize this concept) in the intensity curve provided that no sudden changes occur in curvature of this line. This procedure may be repeated until it is evident that no additional improvement is possible. The improvement in the position of the background line should ordinarily be accompanied by a decrease in the magnitude of the negative portions of the radial distribution curve. Ideally, the radial distribution curve is positive. The molecular scattering is obtained by dividing the experimental intensity by the background curve. The main analyses were performed with the $f(r)$ curve.

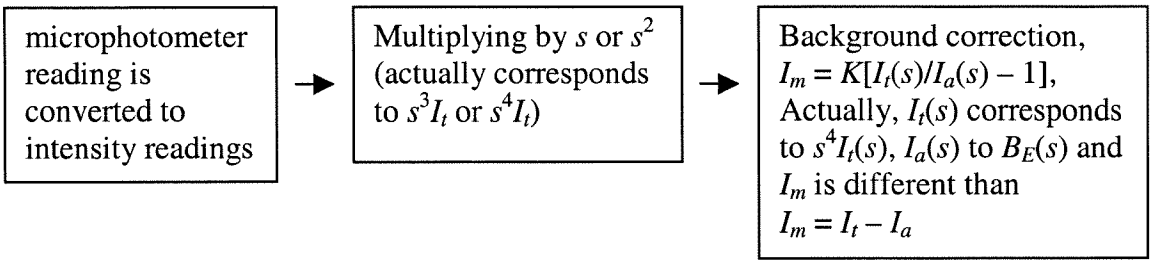

In the experimental intensity curve there is no useful data when s < 2 $Å^{-1}$ and the region when s < 3 or 4 $Å^{-1}$ does not represent a molecular scattering curve with constant coefficients. Hence, the region between s values of zero to three or four is replaced by an intensity curve computed with constant coefficients from an assumed model. Computed molecular intensity curves are used mainly to establish the range of uncertainty. They emphasize that there is a sufficient enough difference between the procedure developed by the Norwegian school and the one presented here to merit some comment. In the Norwegian school, the molecular scattering curve is obtained using the expression $I_m(s) = K \cdot [P_t(s)/P_a(s) - 1][\Sigma((Z_i - F_i)^2 + S_i) / s^4]$. Karle's procedure differs in that the molecular scattering function with constant coefficients is obtained from the expression $I_m = K[I_t(s)/I_a(s) - 1]$, where the photographic density readings have been converted to intensity readings. In addition, they do not reintroduce the variable scattering factors once they have been eliminated by dividing by the background.

A.3.8 Karle 2[16,23]

One of the steps in the procedure for extracting the molecular scattering from the total scattering involves drawing a background line through the oscillations of the curve representing the total intensity. The total intensity is then divided by this background line and yields the molecular scattering curve. Dividing the total intensity curve by the background line not only eliminates the atomic scattering but replaces the variable coefficients in the molecular scattering expression by constants to a good approximation, except at low s values,. It is not possible to use theoretical values for the background shape since these values are not sufficiently accurate. The best possible background line which may be drawn is one which produces a molecular scattering curve whose Fourier sine transform is essentially positive everywhere. The purpose in computing intensity curves is to determine the range of uncertainty in the structural parameters as obtained from the radial distribution curve.

The method for performing the decomposition of a composite peak is illustrated in the determination of the structures of CH_2CF_2 and CF_2CF_2. The photographic signal is converted into a scattering intensity. The total intensity of scattering is composed of a steeply falling background due to atomic scattering upon which is superimposed an oscillating curve due to molecular scattering. Since an s sector was used, the photographs register the total intensity, I, multiplied by s. It was convenient to multiply $I \cdot s$ by s^2 for s values greater than 5 or 6 to accentuate the oscillations. A smooth background line was drawn through the oscillations and the molecular scattering curve was obtained by dividing the total intensity curve by the

background line. They discuss the effects of the width of the electron beam, finite sample size, and multiple scattering. They are all negligible. Data analysis is based on the correlation method using the parameter chart and the estimation of errors does not seem to be rigorous.

A.3.9 Bauer[24]

Bauer and coworkers present a detailed account for the experimental apparatus including the rotating sector, sample holder, vacuum system, etc. They also compare the old visual method with the new sector-microphotometer method. Their sector function has a quite complicated form in an effort to thoroughly compensate for the atomic scattering. Their background should correspond to almost unity. Two objective procedures have been used in drawing the background. (A) Average values are computed for the ratios of intensities of adjacent maxima to minima from several theoretical curves. Points are then selected on the microphotometer record for which, if the background were drawn through them, the corresponding ratios for adjacent maxima to minima would result. The best smooth curve through these points is taken as the background. (B) Average values are computed for the s positions at which the theoretical curves cross from positive to negative values, and vice versa. These are plotted on the microphotometer record and the best smooth curve drawn through them is taken as the background. Experience has shown that the background curves are not sensitive to the selection of models used in the averaging processes when these nearly represent the correct structure. Also, the backgrounds deduced by means of procedures

(A) and (B) differ very little from each other. Models which depart appreciably from the correct structure will lead to points which scatter badly from a smooth curve. Then, as a first approximation, the intensity of the molecular term relative to the atomic terms (taken as unity) is the ratio of the density indicated by the microphotometer trace to that of the background at each value of s. The comparison of experimental $f(r)$ and theoretical $f(r)$ from several trial models (correlation method) allowed them to draw some conclusion. Then, they compared the experimental modified intensity with several theoretical modified intensities and reached the final structural parameters with an estimation of errors.

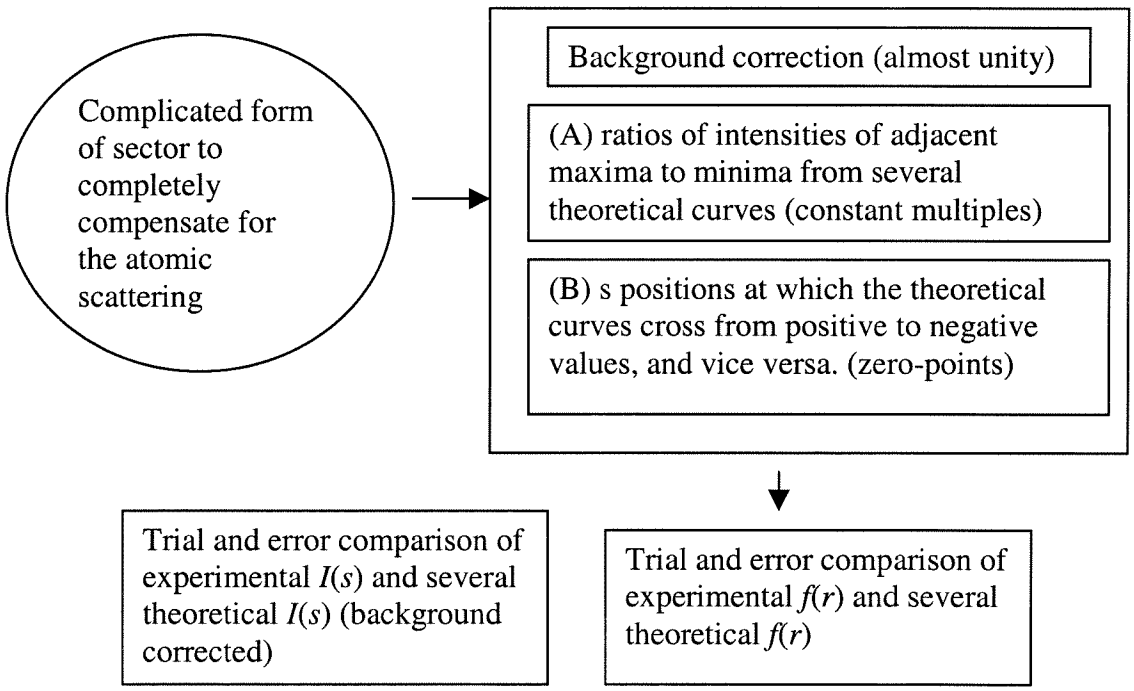

A.3.10 Bauer 2[25]

Visual estimates of the intensity and position of the maxima and minima were made from both sector and non-sector pictures. Microphotometer traces of the sector pictures were also obtained and treated as described below. The usual comparison of the observed intensity curves with computed curves for various models were made, both with the visual data and the reduced microphotometer trace. These intensity curves were computed according to the equation $I(s) = 1 + (\sum_{ij} f_i f_j \exp(-\alpha_{ij}^2 s^2) \sin sr_{ij}/sr_{ij}) / (\sum_{ij}(f_i^2 + g_i)$ to be comparable with the sector data (the f_i and f_j are atomic form factor, not scattering factor and $I(s)$ should be $I(s)/I_{bg}$). The comparison, the "specific contrast", defined as $[I(s)/I_{bg}]_{obs}/[I(s)/I_{bg}]_{calc}$ and computed at the observed maxima and minima, provides another criterion by which postulated models may be judged. The microphotometer traces of the sector photographs must be corrected to take out extraneous contributions to the scattering, and for variation of the atomic scattering function with angle, before they can be used in calculations as a measure of the molecular scattering. This process, drawing in a background on the microphotometer trace, yields structural information. The background can be positioned using the theoretical intensity curves as follows: (1) the microphotometer densities at those s values for which the molecular contribution to the scattering is zero (the "cross-over points" where the atomic and molecular curves intersect) would lie on a straight line if the theoretical model provides a set of such points which can be marked on the photometer record. Even if no set lies on a straight line, those sets of

points given by fairly satisfactory models scatter about a line whose curvature changes slowly compared to the molecular oscillations. This curve may be considered to be a "reasonable background." In addition, the better the model, the closer the cross-over points lie to the background. Thus variations in parameters can be followed quantitatively. (2) A similar procedure is possible using the maxima and minima of the photometer trace. The heights of the maxima and minima of the computed intensity curves can be reduced so that they all have the same value at one peak. Then for each model, at the positions of the computed maxima, multiples of these reduced heights can be marked on the graph of the photometer data, measuring downward from the microphotometer trace. Correspondingly, at the positions of the computed minima, multiples of the reduced depth can be marked on the graph, measuring upward from the trace. For accurate data and the correct structures, the points corresponding to some multiple should lie on a straight line. Experimentally they do not. However, the requirements that the background should only slowly curve and that the multiples which fall on it should change slowly with s, allow a " reasonable background" to be drawn. And the better the model, the more nearly will this background lie on points of a constant multiple.

A.3.11 Bauer 3[26]

Electron diffraction data taken with a sector apparatus are presented. Procedures for the reduction of such data are discussed. Theoretical backgrounds (the sum of atomic coherent plus incoherent scattering) based on Pauling-Sherman and on

Hartree atom form factors are compared with the curves observed. Structural information was derived from the resolution of radial distribution curves, and the final molecular models were checked by comparing theoretical molecular scattering curves with the reduced microphotometer traces. The photographic densities were converted to intensities with the aid of the characteristic emulsion curves. The data was then corrected for the fact that sectors cut specifically for phenylsilane were used for all three compounds. Because data for which the background is a straight line have not yet been obtained (because of the use of improper atomic form factors, and unavoidable extraneous scattering), estimation of the background position is not a simple matter. However, for the purposes of obtaining molecular structures, it is most important only that the experimentally determined background have no rapidly fluctuating errors. Small-amplitude low-frequency errors produce serious errors in the radial distribution curve only near the origin where no intramolecular distances are represented. If initially the molecular structure is known approximately, theoretical intensity curves may be used to help position the background. The experimental molecular intensity contribution should be zero at approximately the same values of s as is the theoretical curve for a good model. Thus, a reasonable experimental background is that smooth curve which comes closest to passing through all of these "cross-over points" Furthermore, the height of any experimental peak should bear the same relation to the heights of its neighboring peaks as is the case for the corresponding peaks in the theoretical curve. This is the basis of the method of "constant multiples" which is also useful in determining experimental backgrounds. In

the case that a theoretical intensity curve that corresponded fairly closely to the observed intensity pattern was available, these aids were of greatest advantage. In the case of somewhat larger discrepancy, a tentative structure first must be obtained using an uncertain background. The intensity curve for this trial structure can then be used to determine a much more accurate background.; i.e., a procedure of successive approximations is followed. With the background estimated, the intensity amplitudes obtained with the two sectors over separate overlapping regions of q were carefully matched and the ratio J_m/J_a, defined by the equation J_m/J_a = [(phot. dens.) × (all corrections) – (assumed back)] / (assumed back) was computed for integral q. Before J_m/J_a can be used to compute the desired nuclear radial distribution function, however, compensation must be made for the fact that each of the damped sinusoidal contributions to this function is also multiplied by some factors (two methods).

A.3.12 Kuchitsu[27,28]

Optical densities were converted in to relative intensities by Karle's procedure. The scattering intensity curve obtained with a short camera length was corrected to eliminate a small amount of extraneous scattering. A smooth background line was drawn through the intensity curve multiplied by q or $q^{1/2}$ and the molecular intensity curve M(q) was obtained by dividing the total intensity I_T by the background intensity I_B: $M(q) = (I_T - I_B) / I_B$. The data analysis was done by a correlation method using parameter charts.

The usual technique of drawing the background line cannot be applied in this region. Karle's criterion of the non-negative Gaussian RD peaks is not applicable because the influence of *f*-factors upon the molecular intensity curve is not negligible in this region; nor can the background line be drawn through the zero-points of a reasonable theoretical curve, because there is no zero-point from q = 5 to 15. Consequently, they have to use some alternative standard for obtaining a reasonable background line. To each theoretical $M_c(q)$ curve the corresponding "background function" $I_b(q)$ was computed by the following formula: $I_b(q) = q^{1/2}I_0(q)/\{1 + 0.84M_c(q)\}$ where $I_0(q)$ is the observed total scattering intensity, which was multiplied by $q^{1/2}$ to accentuate the oscillations in the region q = 8~15. The absolute molecular intensity M_c was multiplied by 0.84 to make it fit the experimental curve in the region q = 16.7 to 20.0. If the diffraction experiment were ideally performed and the assumed model were strictly correct, the I_b should have no sudden fluctuations of the frequency on the order of the molecular intensity; in general, the corresponding I_b will approach to a smooth curve as the assumed model becomes better. A factor σ defined by the following equation may be used as a numerical measure of the overall inconsistency between the qM_c and qM_0 curves: $\sigma = \Sigma_q\{qM_0(q) - cqM_c(q)\}^2$.

A.3.13 Morino[29]

The procedure used in the analysis of the small-angle region (q = 5~15) is described in detail. A microphotometer was used to measure the optical density as a function of the radius. The plates were rotated rapidly about their centers during

scanning. A smooth background line $I_B(q)$ was drawn through the relative intensity curve $I_0(q)$ multiplied by a uniform function $f(q)$ and the molecular intensity curve $qM(q)$ was obtained by the following formula: $qM(q) = q[f(q)I_0(q)/I_B(q) - 1]$. For small-angle regions, a number of theoretical molecular intensity curves $qM_c(q)$ were computed based on various assumed models, and to each curve the corresponding background function $I_b(q)$ was computed by the following equation: $I_b(q) = f(q)I_0(q)/[1 + cM_c(q)]$, where $I_0(q)$ is the observed scattering intensity, and c is a resolution constant[30,31]. The constant c corresponds to the index of resolution discussed by the above two papers. In general, it is slightly less than unity, and it is a function of q dependent on the condition of the diffraction experiment (double scattering, extraneous scattering, etc). Although its actual functional form was not known, it was found by examining the experimental intensity curves taken at different conditions that c is a function which varies so slowly in this region, that it can be regarded as constant. This is in agreement with the discussion of Harvey *et al.* $I_0(q)$ is multiplied by an algebraic function $f(q)$ in order to accentuate its oscillations and to make the background line nearly flat. A simple multiplication function, q or q^2, usually used for this purpose, was not adequate in the small-angle region. The following function was chosen by roughly fitting the function to the inverse of the experimental background line. The form of $f(q)$ depends on the shape of the sector used in the experiment. No further attempt was made to obtain a completely flat background line. The function $f(q) = q + 0.005(q - 8.5)^2$, for $q > 8.5$ and $f(q) = 1 + 0.005(q - 8.5)^2 - 0.003(q - 8.5)^3$ for $q < 8.5$ was used. The meaning of the background function I_b is that it is the

residual part of the intensity (background) after the fluctuation due to the molecular scattering is subtracted from the total scattering intensity curve. If the diffraction experiment were ideally conducted, and if the assumed model were strictly correct, the I_b function should correspond exactly to the atomic scattering intensity plus the inelastic scattering intensity, and therefore should have no sudden fluctuations (i.e., no fluctuations with frequencies on the order of the molecular intensity). In general, the better the model, the closer the corresponding I_b function will approach a smooth curve. Thus the extent of its fluctuation from a smooth curve can be used as a criterion for selecting a reasonable model, provided that the corrections for a nonideal experiment are properly taken into account. The data analysis was a correlation method using parameter charts.

A.3.14 Morino [32]

Morino and coworkers applied two methods of analysis of the observed data: one is to use the radial distribution function and the other is to use the trial and error or correlation method. The modified radial distribution function usually used is obtained by Fourier transformation of the observed molecular intensity multiplied by an artificial factor $\exp(-bs^2)$. If the intensity curves beyond smax and inside smin are spliced by a curve calculated with some plausible model, then by integration from zero to infinity the intensity curve can be transformed without any artificial factor. This type of radial distribution function will be called the unmodified radial distribution function (UMRD) as opposed to the usual, modified radial distribution function. The

observed intensity contains large errors in a large s region, and the multiplication of the observed intensity by s without the factor $\exp(-bs^2)$, is apt to exaggerate these errors in the UMRD curve. Error estimation of $sM(s) = s(I_T - I_B)/I_B$ are given. The formula for the corrected $sM(s)^I$ is: $sM(s)^I = sM(s)_{calc} + W(s)[sM(s)_{obs} - sM(s)_{calc}]$, where $W(s) = (s\Delta M_{max} - s\Delta M) / s\Delta M_{max}$. A more understandable form of this formula is: $sM(s)^I = sM(s)_{obs} + [sM(s)_{calc} - sM(s)_{obs}][\ s\Delta M / s\Delta M_{max}]$. Finally, UMRD in the first approximation is given by $rD(r) = \text{Integral}_{0,\infty} sM(s)_{calc} \sin srds + \text{Integral}_{smax,smin} s[M(s)_{obs} - M(s)_{calc}]W(s)\sin srds$. Next, by using the parameters corrected, the whole procedure is repeated until a self-consistent model is obtained. They also introduced a reliability factor of the UMRD curve as a criteria. A rather detailed description of the calculation of mean square amplitudes of vibration is given the paper.

A.3.15 Bonham 1[33]

The procedure described by Bonham et al. resembles that of Bartell, Brockway, and Schwndeman[31] except that digital computation replaced manual handling of data wherever possible and structural parameters were obtained more objectively by a least squares method. $M = [(I_{tot}/I_{background}) - 1]$. After good values for the important skeletal parameters are deduced from a least squares analysis of the radial distribution curve, it is informative to examine the background. The correlation background function $I_b(q) = I_0(q)/(1 - RM(q)_{theor})$ is calculated and compared with the experimental background, where $I_0(q)$ is the leveled experimental intensity curve, and

$M(q)_{theor}$ is the reduced theoretical intensity curve calculated for an assumed model, and R is the index of resolution. At its best, this method is more powerful than the conventional intensity correlation procedure. It is reassuring to note that the model giving the smoothest background function agrees very well with the model deduced by the radial distribution method.

A.3.16 Bonham 2[34]

Provided is possibly the best account of the least-square method of the radial distribution function. Notation: z = radius of diffraction pattern, $D(z)$ = optical density readings of diffraction patterns, ϕ = scattering angle, $q = (40/\lambda)\sin(\phi/2)$, Z_k = atomic number, $F_k(q)$ = coherent x-ray atom form factor, $S_k(q)$ = incoherent x-ray atom form factor, $I(q)$ = intensity of diffraction pattern at plate, $I_e(q)$ = extraneous intensity, $\Phi(q)$ = intensity without rotating sector/intensity with rotating sector, $I_B(q)$ = experimental background function, $M(q)$ = reduced intensity function = $[I_0(q)/I_B(q)] - 1$, $M_c(q)$ = reduced nuclear intensity function, R = index of resolution = $M(q)_{expt}/M(q)_{theor}$, $I_b(q)$ = correlation background function = $I_0(q)/[1 + RM(q)_{theor}]$, $f(r)$ = experimental radial distribution function $\approx (\pi^2/100)\text{Integral}_{0,\infty}\{qM_c(q)\exp(-\pi^2bq^2/100)\sin(\pi qr/10)\}dq$, $f_c(r)$ = calculated synthetic radial distribution function, $w(r)$ = weighting function for analysis of $f(r)$, $r_g(0)_{ij}$ = center of gravity of probability distribution linking atoms i and j, l_{ij} = root-mean-square amplitude of vibration of atom pair i and j. The present procedure requires, apart from simple control instructions, only the reading and punching of three quantities: the microphotometer readings, $D(z)$, of the patterns, the

leveled intensities $I_0(q)$, and the experimental background, $I_B(q)$. At the end of program *I*, it is necessary to stop the sequence and plot the processed data and select a smooth background function, $I_B(q)$ (maybe by hand, I guess). The least-square fitting is performed in $f(r)$ and an error estimation method is provided. It is helpful to include at an early state the structural parameters associated with one or more trial models because rigorous analysis requires corrections to be made which depend mildly on molecular structure. It is possible, if desired, to defer any introduction of structural parameters until a preliminary Fourier analysis is made of intensity data.

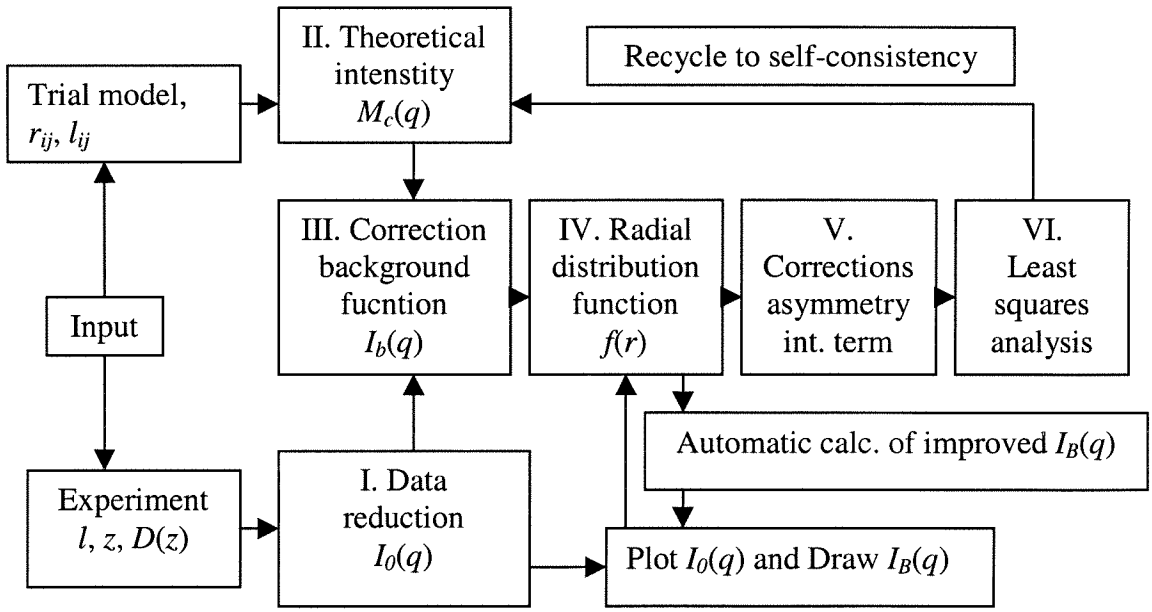

A.3.17 DeNeui[35]

The densities were converted to intensities using the equation, $E = D(1 + cD)$ with $c = 0.05$. Imperfections in the sector shape were measured using diffraction

photographs of argon. The indices of resolution $R = M_{expt}(s)/M_{calc}(s)$, as measured directly from the patterns or as inferred from the radial distribution curves were approximately 100% for the middle distance patterns and 90% for the long distance patterns. Good discussion regarding comparison between the electron diffraction and spectroscopic distances can be found in this reference.

A.3.18 Shibata 1[36]

Structural parameters were deduced by three methods and compared by: (a) a conventional radial distribution analysis (b) a least-squares "smooth background" method (c) a least squares fit of the total intensity.

A.3.19 Murata 1[37]

This is a cornerstone paper regarding the weighting matrix for both $qM(q)$ and $f(r)$.

A.3.20 Seip 1[38]

Norwegian method of data analysis can be found in this reference. The molecular intensity may be expressed as $I(s) = \text{const}\Sigma(A_i(s)/r_i)\exp(-\frac{1}{2}u_i^2s^2)\sin r_i s$ and $A_i(s)$ may be expressed as follows: $A_i(s) = n_{kl}Z_kZ_l[1 - (F/Z)]_k[1 - (F/Z)]_l/([1 - (F/Z)]_m[1 - (F/Z)]_n)$. Actually, this $I(s)$ is almost the same as our $sM(s) = sI_m(s)/|f_i||f_j|$.

A.3.21 Shibata 2[39]

Analyses were based on (a) the radial distribution method and (b) on a new automatic "smooth-background" method. The resulting discrepancy led to a greater uncertainty in the structural parameters than the random experimental intensity errors. This almost universally neglected source of error is briefly discussed. Experimental intensities were corrected for imperfections in the sector shape and for background of extraneous scattering in the apparatus. This scattering was not serious but was significant at the relatively low pressures used for the rather weakly scattering molecules. Corrections ranged from 0.4% at small scattering angles to about 3% at q = 120. In subsequent analyses, corrections were also made for anharmonicity, the failure of the Born approximation, and the effect of scattering by planetary electrons. The data was processed in essentially the same manner as described elsewhere to yield a corrected total intensity curve I_{tot} leveled by dividing the observed intensity by the theoretical atomic intensity. The leveled curves have background functions which are distinctly nonconstant. The marked deviation at small scattering angles undoubtedly corresponds to a failure of simple scattering theory. The smooth-background method is related to earlier qualitative methods but differs significantly in that it defines a quantitative criterion for background smoothness which can be utilized in automatic least-squares refinements of trial structures. In the new method, the total leveled intensity is equated to a calculated intensity, and molecular parameters are adjusted automatically to give the smoothest implied atomic background line. The criterion used was the minimization of the sum over experimental points of the following

functions: $S_1 = \Sigma_i w_i[I_B(q_{i+1}) - I_B(q_i)]^2$ or $S_2 = \Sigma_i w_i[I_B(q_{i+2}) - 2I_B(q_{i+1}) + I_B(q_i)]^2$, where w_i is a suitable weighting function, $I_B = I_{tot}/(1 + RM_{the})$, R is the index of resolution, and M_{the} is the calculated reduced intensity function. The sums S_1 and S_2 are related to the mean-square slope and the mean-square curvature of I_B, respectively. The second criterion seems superior to the first. Since there is no unique objective scheme for specifying the criterion for smoothness at present, there is no way of deducing unique structural parameters by electron diffraction even if the random intensity errors are zero.

A.3.22 Murata 2[40]

In an ordinary least-squares analysis of gas electron diffraction, the standard deviation for the most probable value of a parameter for a molecule depends on the interval of measurements Δs on a microphotometer recording, that is, on the number of observed points on an intensity curve. It is shown that a reasonable estimate of the standard deviation of a parameter can be obtained by taking into account the effect of 'correlation' among the points of observations.

A.3.23 Beagley[41]

This paper presents a good example of the least square application of the Norwegian school.

A.3.24 Bartell 3[42]

A more rigorous way of error analysis in the least squares method is proposed in this paper.

A.3.25 Seip 2[43]

They show that the standard deviations obtained for the structure parameters were typically from 1.2 to 2.5 times larger than those obtained with a diagonal weight matrix.

A.3.26 Bohn[44]

They show that the standard deviations are 2.2 to 4.0 times greater than those obtained using diagonal weight matrices.

A.3.27 Bartell 4[45]

This paper provides a good historical summary of the least square methods. A more detailed account of the smooth-background method is given. In general, the atomic background I_b associated with the leveled total intensity I_t is not a horizontal line and deviates from constancy because of imperfections in the theory and experiment.

In tests of the new method, several alternative schemes to deal with these imperfections were tried.

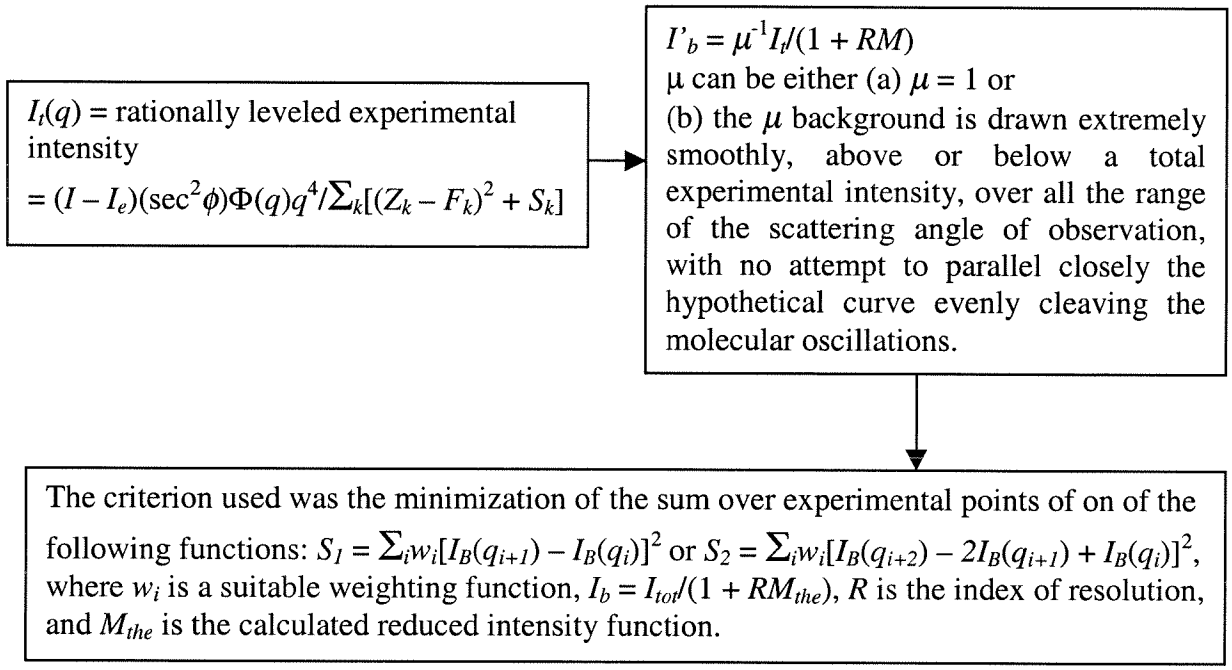

The smooth background criterion was applied either to the original leveled total intensity points ($\mu = 1$) or to a releveled set of intensities. In the latter scheme a hand-drawn background, referred to as the μ background, was introduced, leading to a revised atomic background $I'_b = \mu^{-1}I_t/(1 + RM)$. While this method is subjective, it seemed to introduce less bias than the usual backgrounds if the following conditions were scrupulously adhered to: the μ background is drawn extremely smoothly, above or below a total experimental intensity, over all the range of scattering angle of observation, with no attempt to parallel closely the hypothetical curve evenly cleaving the molecular oscillations. It could be shown in the analysis that the final values of molecular parameters obtained did not significantly depend on how the μ background

was drawn. The criterion used was the minimization of the sum over the experimental points of the following functions: $S_1 = \Sigma_i w_i[I_B(q_{i+1}) - I_B(q_i)]^2$ or $S_2 = \Sigma_i w_i[I_B(q_{i+2}) - 2I_B(q_{i+1}) + I_B(q_i)]^2$, where w_i is a suitable weighting function, $I_b = I_{tot}/(1 + RM_{the})$, R is the index of resolution, and M_{the} is the calculated reduced intensity function.

A.3.28 D'Antonio[46]

The average total intensities were processed with an automated background correction routine based on the positivity and area criteria. The function used in the calculation of a background line was $b_p(s) = \exp(\alpha_p + \beta_p s^{\gamma_p})$. The actual background line $B_n(s)$ is generated from a weighted average of segments $b_p(s)$, each having independent values for the background constants, α_p, β_p, and γ_p, $B_p(s) = [u_p(s)B_{p-1}(s) + v_p(s)b_p(s)]$, $p = 1, \ldots, n$, where p represents the number of the segment in a set of n segments and $u_p(s)$ and $v_p(s)$ are weighting coefficients in the overlap range of the two segments. $B_0(s) = 0$, and $B_1(s) = b_1(s)$, the first segment.

The values for the background constants α_p, β_p, and γ_p were determined in two ways: (1) The experimental total intensity function at the null points of a theoretical model is divided into three-point segments (1, 2, 3; 2, 3, 4; etc., or 1, 3, 5; 2, 4, 6; etc., where the digits label the successive null points). The background constants are then determined for each segment by a three-point fit.

Method (1)
α_p, β_p, γ_p

Background function
$b_p(s) = \exp(\alpha_p + \beta_p s^{\gamma_p})$
$B_p(s) = [u_p(s)B_{p-1}(s) + v_p(s)b_p(s)]$, $p = 1, \ldots, n$,

Method (2)
α_p, β_p, γ_p

The experimental total intensity function at the null points of a theoretical model is divided into three-point segments. The background constants are then determined for each segment by a three-point fit.

The initial molecular intensity functions were obtained from $I_m(s) = [I_t(s) / B_n(s)] - 1$, using the background function, $B_n(s) \sim I_b(s)$, developed in step (1) by means of the three-point fits.

The resulting $I_m(s)$ were averaged and a theoretical $I_m(s)$ was attached in the inner region. This molecular intensity curve was corrected for nonconstant scattering factors prior to being transformed into the corresponding radial distribution curve, $f(r)$.

$$sI_m(s) = K\sum_{i\neq j}^{N}\sum \sigma_{ij}(s)\cos\Delta\eta_{ij}(s)\cdot\exp(-\tfrac{1}{2}<l_{ij}^{\,2}>s^2)\cdot\sin(sr_{ij})/r_{ij}$$

$$sI_c(s) = K\sum_{i\neq j}^{N}\sum g_{ij}(s)\cos\Delta\eta_{ij}(s)\cdot\exp(-\tfrac{1}{2}<l_{ij}^{\,2}>s^2)\cdot\sin(sr_{ij})/r_{ij}$$

$$\Delta sI_m(s) = sI_m(s) - sI_c(s),$$

$$f(r) = \sqrt{2/\pi}\int_0^{s_{\max}}[sI_m(s) - \Delta sI_m(s)]\cdot\exp(-as^2)\cdot\sin(sr)ds$$

The resulting $f(r)$ was adjusted by positiveness criteria and an improved $I_m(s)$ was obtained from the Fourier sine transform of the positivized $f(r)$ and was adjusted by adding the correction term $\Delta sI_m(s)$.

$I_b(s)$ is segmented into intervals, Δs, ranging from 8 to 1 s unit. Each segment may be displaced from the preceding one by an arbitrary amount. The background constants are determined from a least squares fit to each segment using the first equation for $b_p(s)$.

$I_b(s) = I_t(s) / [I_m(s) + 1]$
$I_m(s)$ may be (a) a trial theoretical molecular intensity function or (b) the corrected Fourier sine transform of a positivized radial distribution curve, $f(r)$.

A preliminary least squares fit was made to both the combined $I_m(s)$ and the constant coefficient $f(r)$. From these procedures a further improved $I_m(s)$ was obtained. The positivity adjustment of the radial distribution function and the least squares procedures were repeated while decreasing the fitting range, Δs, until a positive radial distribution curve was obtained from smooth background lines, $B_n(s)$, for each of the photographic plates used in the analysis.

(2) The background function, $I_b(s)$, is generated from the experimental total intensity function, $I_m(s)$, using the following relation: $I_b(s) = I_t(s) / [I_m(s) + 1]$. $I_m(s)$ may be obtained from either of two types of calculation which will be described in detail below. It can be either (a) a trial theoretical molecular intensity function or (b) the corrected Fourier sine transform of a positivized radial distribution curve, $f(r)$. $I_b(s)$ is segmented into intervals, Δs, ranging from 8 to 1 s unit. Each segment may be displaced from the preceding one by an arbitrary amount. The background constants are determined from a least squares fit to each segment using the first equation for $b_p(s)$. The initial molecular intensity functions were obtained from $I_m(s) = [I_t(s) / B_n(s)] - 1$, using the background function, $B_n(s) \sim I_b(s)$, developed in step (1) by means of the three-point fits. The correction term $\Delta I_m(s)$ was calculated from the following equations. The theoretical expression for the molecular intensity $sI_m(s)$ is given by

$$sI_m(s) = K\sum_{i\neq j}^{N}\sum \sigma_{ij}(s)\cos\Delta\eta_{ij}(s)\cdot\exp(-\tfrac{1}{2}<l_{ij}^{\,2}>s^2)\cdot\sin(sr_{ij})/r_{ij},$$

where $\sigma_{ij}(s) = f_i(s)f_j(s)/\sum_{k}^{N}[f_k^{\,2}(s) + S_k(s)/s^4]$. K is a scale factor, N is the total number of atoms, $<l_{ij}^2>$ is the mean-squared amplitude of vibration, $f_i(s)$ and $\eta_i(s)$ are the magnitude and phase of the partial wave elastic scattering factor for the ith atom. The functional counterpart of $sI_m(s)$ with constant coefficients, $sI_c(s)$, is given by

$$sI_c(s) = K\sum_{i\neq j}^{N}\sum g_{ij}(s)\cos\Delta\eta_{ij}(s)\cdot\exp(-\tfrac{1}{2}<l_{ij}^{\,2}>s^2)\cdot\sin(sr_{ij})/r_{ij},$$

where $g_{ij} = <\sigma_{ij}(s)>_{S_r}$, and s_r represents s values restricted to the experimental range. The nonconstant coefficient correction is $\Delta sI_m(s) = sI_m(s) - sI_c(s)$, and the constant coefficient radial distribution curve is computed from $f(r) = \sqrt{2/\pi}\int_0^{s_{max}} [sI_m(s) - \Delta sI_m(s)] \cdot \exp(-as^2) \cdot \sin(sr) ds$. In this experiment the damping factor a was set so that $as_{max}^2 = 3.$. A new set of background curves, $I_b(s)$, were generated with the improved molecular intensity function using $I_b(s) = I_t(s) / [I_m(s) + 1]$. These background lines were fit as described in step (2) and a corresponding new set of molecular intensity curves was obtained from $I_m(s) = [I_t(s) / B_n(s)] - 1$. The intensity curves were averaged, an inner region from the improved molecular intensity function was added, and the combined curve was transformed. A preliminary least squares fit was made to both the combined molecular intensity curve and the constant coefficient radial distribution curve. From these procedures a further improved molecular intensity function was obtained. The positivity adjustment of the radial distribution function and the least squares procedures were repeated while decreasing the fitting range, Δs, until a positive radial distribution curve was obtained from smooth background lines, $B_n(s)$, for each of the photographic plates used in the analysis. After each cycle $I_m(s)$, $I_b(s)$, $I_t(s)$, and $B_n(s)$ were displayed for inspection. The last three curves were leveled by multiplying each by the first equation in which the values for α, β, and γ were determined from a fit to three widely spaced points on the $B_n(s)$ curve. As the data reduction procedure progressed, the generated background

lines, $I_b(s)$, more closely resembled their smooth counterparts, $B_n(s)$. In the final cycle the generated background lines were featureless curves.

A.3.29 Shibata 3[47]

The characteristic of the present method is that it does not need any bias depending upon human judgement throughout an analysis. The criterion for smoothness of a background is expressed as follows: $P_n = \Sigma_i w_i[I_b(q_i) - \Sigma_n a_n q_i^n]^2 =$ minimum. In the case of having non-zero off-diagonal weighting matrix, the expression is more complicated. A consideration of the correlation between data points increased the errors by a factor of about 1.4.

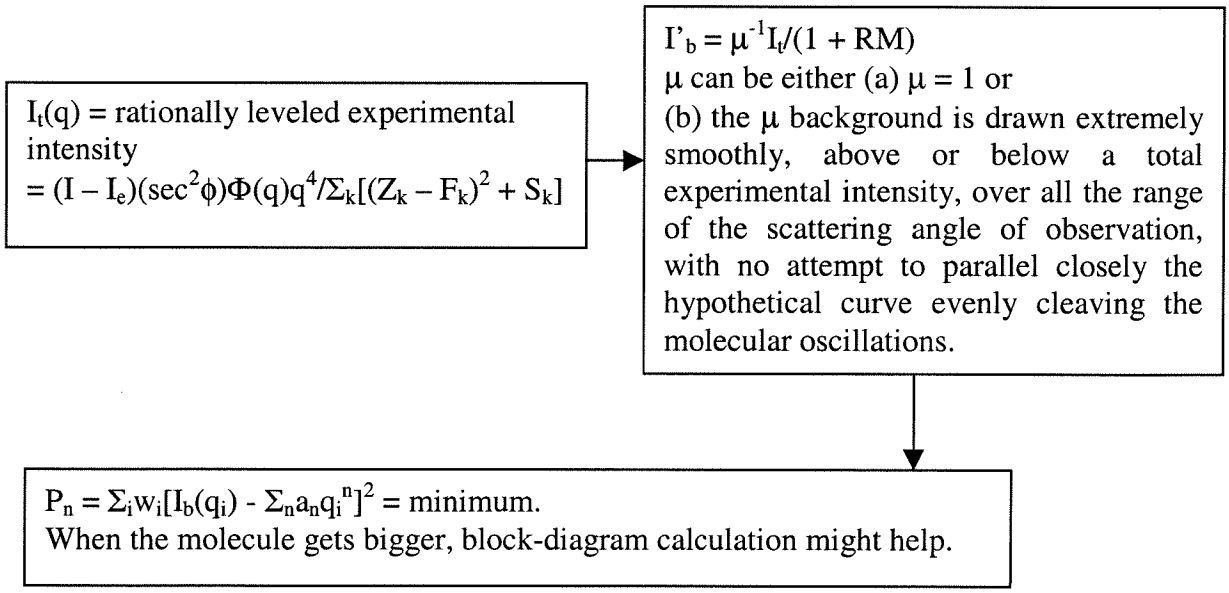

When the molecule gets bigger, a block-diagram calculation might help. In general, a background for a short camera range of $q > 20$ is leveled fairly well; and it can be approximated satisfactory with the polynomials of low degree, e.g., $n = 5$. A background for a long camera range of $q > 10$ has often a hump in the range of small scattering angles. In such a case, polynomials of higher degree, e.g., $n = 7$, can fit the background.

A.3.30 Mijlhoff[48]

Spline function is suggested as a form of background either by making it pass through a few points or by letting it smooth the background with an appropriately large tolerance.

A.3.31 Spiridonov[49]

The authors provide a very good historical summary of the efforts to prevent hand-drawing the background. New procedures are developed for computer background generation. They are based on spline smoothing and on filtering the total intensities. Background generation is an old and tedious problem in electron-diffraction data processing. For a long time this was done graphically by plotting the total intensity on a large scale and drawing a line through the fluctuations representing the so-called molecular scattering. The smoothness of the background and the non-negativeness of the resulting radial distribution function is the usual criteria. However,

the background routines depended crucially upon human judgement. Moreover, such routines involve operator bias, they are not suited for computer adaptation.

A.3.32 Novikov[50]

The author provides a very good historical summary of the efforts to prevent hand-drawing the background. Frequently, the most common problem is to find a smooth function $g(s)$ which approximates some function $y(s_i)$ originating from experimental data at the points s_i (i = 1, ..., n; n is the number of observations). The cubic spline $g(s)$ is composed of cubic parabolae $g(s) = a_i + b_i(s - s_i) + c_i(s - s_i)^2 + d_i(s - s_i)^3$, $s_i < s < s_i + 1$, which join each other at their common endpoints si (i = 1, ..., n-1) so that g, g', g'' are continuous. All the coefficients are shown to be strictly determined by a constant of smoothing C according to the conditions $\sum_{i=1}^{n}[g(s_i) - y(s_i)]^2 \leq nC^2$ and $\int_{s_1}^{s_n}[g''(s)]^2 ds = \min$. The first condition ensures that the spline approximates closely to the desired function, while the latter is responsible for the smoothness of this spline.

References

1)Hargittai, I.; Hargittai, M. *Stereochemical Applications Of Gas-Phase Electron Diffraction*; VCH: New York, 1988.

2)Bartell, L. S. *Electron Diffraction By Gases*; Weissberger, A. and Rossiter, B. W., Ed.; Wiley: New York, 1972.

3)Hedberg, K.; Iwasaki, M. *Acta Cryst.* **1964**, *17*, 529-533.

4)Iwasaki, M.; Fritsch, F. N.; Hedberg, K. *Acta Cryst.* **1964**, *17*, 533-537.

5)Bastiansen, O.; Fritsch, F. N.; Hedberg, K. *Acta Cryst.* **1964**, *17*, 538-543.

6)Seip, H. M. *Acta Chem. Scand.* **1965**, *19*, 1955-1968.

7)Seip, H. M.; Stølevik, R. *Acta Chem. Scand.* **1966**, *20*, 385-394.

8)Seip, H. M.; Seip, R. *Acta Chem. Scand.* **1966**, *20*, 2698-2710.

9)Seip, H. M.; Stølevik, R. *Acta Chem. Scand.* **1966**, *20*, 1535-1545.

10)Arnesen, S.; Seip, H. M. *Acta Chem. Scand.* **1966**, *20*, 2711-2727.

11)Andersen, B.; Andersen, P. *Acta Chem. Scand.* **1966**, *20*, 2728-2736.

12)Andersen, B.; Seip, H. M.; Strand, T. G.; Stølevik, R. *Acta Chem. Scand.* **1969**, *23*, 3224-3234.

13)Bartell, L. S.; Kohl, d. A.; Carroll, B. L.; Gavin, J. R. M. *J. Chem. Phys.* **1965**, *42*, 3079-3084.

14)Karle, I. L.; Karle, J. *J. Chem. Phys.* **1949**, *17*, 1052-1058.

15)Karle, I. L.; Karle, J. *J. Chem. Phys.* **1950**, *18*, 565.

16)Karle, I. L.; Karle, J. *J. Chem. Phys.* **1950**, *18*, 957-962.

17)Gundersen, G.; Hedberg, K. *J. Chem. Phys.* **1969**, *51*, 2500-2507.

18)Hagen, K.; Hedberg, K. *J. Am. Chem. Soc.* **1973**, *95*, 1003-1009.

19)Hedberg, L. *Determination Of Molecular Structures By Analysis Of Electron Diffraction Data. Method For Automatic Removal Of Background*: Austin, TX, 1974, pp 37-43.

20)Bastiansen, O.; Hedberg, L.; Hedberg, K. *J. Chem. Phys.* **1957**, *27*, 1311-1317.

21)Waser, J.; Schomaker, V. *Rev. Mod. Phys.* **1953**, *25*, 671-690.

22)Viervoll, H. *Acta Chem. Scand.* **1947**, *1*, 120-132.

23)Karle, I. L.; Karle, J. *J. Chem. Phys.* **1950**, *18*, 963-971.

24)Hastings, J. M.; Bauer, S. H. *J. Chem. Phys.* **1950**, *18*, 13-26.

25)Bregman, J.; Bauer, S. H. *J. Am. Chem. Soc.* **1955**, *77*, 1955-1965.

26)Keidel, F. A.; Bauer, S. H. *J. Chem. Phys.* **1956**, *25*, 1218-1227.

27)Kuchitsu, K. *Bul. Chem. Soc. Japan.* **1957**, *30*, 391-399.

28)Kuchitsu, K. *Bul. Jap. Chem. Soc.* **1957**, *30*, 399-402.

29)Morino, Y.; Kuchitsu, K. *J. Chem. Phys.* **1958**, *28*, 175-184.

30)Harvey, R. B.; Keidel, F. A.; Bauer, S. H. *J. Appl. Phys.* **1950**, *21*, 860-874.

31)Bartell, L. S.; Brockway, L. O.; Schwendeman, R. H. *J. Chem. Phys.* **1955**, *23*, 1854-1859.

32)Morino, Y.; Kuchitsu, K. *J. Chem. Phys.* **1958**, *28*, 185-197.

33)Bonham, R. A.; Bartell, L. S. *J. Am. Chem. Soc.* **1959**, *81*, 3491-3498.

34)Bonham, R. A.; Bartell, L. S. *J. Chem. Phys.* **1959**, *31*, 702-708.

35)Bartell, L. S.; Kuchitsu, K.; DeNeui, R. J. *J. Chem. Phys.* **1961**, *35*, 1211-1218.

36)Shibata, S.; Bartell, L. S.; Gavin, J. R. M. *J. Chem. Phys.* **1964**, *41*, 717-722.

37)Morino, Y.; Kuchitsu, K.; Murata, Y. *Acta Cryst.* **1965**, *18*, 549-557.

38)Almeningen, A.; Bastiansen, O.; Seip, R.; Seip, H. M. *Acta Chem. Scand.* **1964**, *18*, 2115-2124.

39)Shibata, S.; Bartell, L. S. *J. Chem. Phys.* **1965**, *42*, 1147-1151.

40)Murata, Y.; Morino, Y. *Acta Cryst.* **1966**, *20*, 605-609.

41)Beagley, B.; cruickshank, W. J.; Hewitt, T. G. *Trans. Frad. Soc.* **1967**, *63*, 836-845.

42)Bartell, L. S. *Acta Cryst.* **1969**, *A25*, S76.

43)Seip, H. M.; Strand, T. G.; Stolevik, R. *Chem. Phys. Lett.* **1969**, *3*, 617-623.

44)MacGregor, M. A.; Bohn, R. K. *Chem. Phys. Lett.* **1971**, *11*, 29-34.

45)Shibata, S.; Bartell, L. S. *J. Mol. Struct.* **1971**, *9*, 1-9.

46)D'Antonio, P.; George, C.; Lowrey, A. H.; Karle, J. *J. Chem. Phys.* **1971**, *55*, 1071-1075.

47)Shibata, S. *Bul. Chem. Soc. Jap.* **1972**, *45*, 1631-1634.

48)Mijlhoff, F. C. *J. Mol. Struct.* **1975**, *27*, 447.

49)Spiridonov, V. P.; Prikhod'ko, A. Y.; Butayev, B. S. *Chem. Phys. Lett.* **1979**, *65*, 605-609.

50)Novikov, V. P. *J. Mol. Struct.* **1979**, *55*, 215-221.